UNIVERSITY OF CALIFORNIA
SANTA CRUZ

BULK PROPERTIES AND FLOW STRUCTURES IN TURBULENT FLOWS

A dissertation submitted in partial satisfaction of the
requirements for the degree of

DOCTOR OF PHILOSOPHY

in

APPLIED MATHEMATICS

by

Anuj Kumar

June 2023

The Dissertation of Anuj Kumar
is approved:

Professor Pascale Garaud, Chair

Professor Daniele Venturi

Professor David Goluskin

Professor Maria Colombo

Peter Biehl
Vice Provost and Dean of Graduate Studies

Table of Contents

List of Figures vii

List of Tables xvii

Abstract xviii

Dedication xxii

Acknowledgments xxiii

1 Introduction 1
- 1.1 Turbulent flows . . . 1
  - 1.1.1 The onset of turbulence . . . 1
  - 1.1.2 Turbulent flows in nature and engineering . . . 2
  - 1.1.3 Questions of primary importance . . . 3
- 1.2 Flow modeling and various approaches in turbulent flow . . . 4
- 1.3 Content of the thesis . . . 7
- 1.4 Organization and summary of different chapters . . . 9

2 The background method 15
- 2.1 Introduction . . . 15
- 2.2 Understanding the background method through a simple example 17
- 2.3 Applications of the background method . . . 25
  - 2.3.1 Surface-velocity driven flows . . . 25
  - 2.3.2 Pressure driven flow in a conduit . . . 27
  - 2.3.3 External flows . . . 28
  - 2.3.4 Rayleigh–Bénard convection . . . 28
  - 2.3.5 Internally heated convection . . . 34

3 Bound on the drag coefficient for a flat plate in a uniform flow 37
- 3.1 Introduction . . . 37
- 3.2 Flow configuration . . . 41

3.2.1 Drag coefficient . . . 42
3.2.2 The relationship between drag coefficient and non-dimensional dissipation . . . 43
3.3 Background method formulation . . . 46
3.4 Upper bound on drag coefficient . . . 48
3.4.1 Background flow construction . . . 49
3.4.2 Bounds in subdomain R_1 . . . 52
3.4.3 Bounds in subdomain R_2 . . . 54
3.4.4 Bound on drag coefficient . . . 55
3.4.5 Comparison with observations . . . 58
3.5 Discussion and Concluding Remarks . . . 61
Appendix 3.A Proof of Lemma 3.4.1 and 3.4.2 . . . 66
Appendix 3.B Sketch of the construction of the background flow (3.35) 70
Appendix 3.C Optimal condition for the bound (3.55) . . . 73

4 Pressure-driven flows in helical pipes: bounds on flow rate and friction factor 76
4.1 Introduction . . . 76
4.2 Problem Setup . . . 80
4.2.1 Flow configuration . . . 80
4.2.2 Coordinate system . . . 81
4.2.3 Choice of forcing . . . 84
4.2.4 Quantities of interest . . . 86
4.3 The background method formulation . . . 87
4.4 Bounds on flow rate and friction factor . . . 91
4.4.1 Choice of background flow . . . 91
4.4.2 The spectral constraint . . . 94
4.4.3 Bound on mean quantities . . . 100
4.5 Discussion and Concluding Remarks . . . 104
Appendix 4.A The (s, r, ϕ) coordinate system . . . 111
Appendix 4.B A few useful inequalities . . . 113
Appendix 4.C Some useful calculations . . . 115
4.C.1 Calculation of $\boldsymbol{\nabla U}$ . . . 115
4.C.2 Reason behind choice 4.55 . . . 117

5 Geometrical dependence of optimal bounds in Taylor–Couette flow 119
5.1 Introduction . . . 119
5.2 Problem setup . . . 124
5.3 Energy stability analysis . . . 129
5.4 An analytical bound . . . 136
5.5 Optimal bounds . . . 141

5.5.1 Numerical Algorithm . . . 142
5.5.2 Optimal bound results . . . 145
5.5.3 Wavenumber spectrum of perturbation . . . 151
5.6 A note on the applicability of the background method . . . 157
5.7 Discussion and conclusion . . . 163
5.7.1 Summary and implications . . . 163
5.7.2 Comparison with the DNS . . . 168
5.7.3 Further generalizations . . . 169
Appendix 5.A The background method . . . 172
Appendix 5.B A useful lemma . . . 178
Appendix 5.C Analytical solution of the Euler–Lagrange equations in case 1 at high Reynolds number . . . 181

6 Analytical bounds on the heat transport in internally heated convection 185
6.1 Introduction . . . 185
6.2 Problem setup . . . 190
6.3 The auxiliary functional method . . . 192
6.4 Bound on heat flux in IH1 configuration . . . 200
6.5 Bound on heat flux in IH3 . . . 207
6.6 Discussion and concluding remarks . . . 212
Appendix 6.A Proof of Hardy and Rellich inequalities . . . 216
6.A.1 Proof of the Hardy inequality in Lemma 6.3.1 . . . 216
6.A.2 Proof of the Rellich inequality in Lemma 6.3.2 . . . 217

7 Three dimensional branching pipe flows for optimal scalar transport between walls 219
7.1 Introduction . . . 219
7.1.1 Motivation . . . 219
7.1.2 Problem setup . . . 221
7.1.3 Previous work and the present results . . . 226
7.1.4 Overview and philosophy of the proof . . . 229
7.1.5 Organization of the paper . . . 239
7.2 Notation and preliminaries . . . 240
7.3 Step III of the construction: Proof of Theorem 7.1.4 . . . 242
7.4 Construction of three-dimensional branching pipe flow: Step I and Step II . . . 247
7.4.1 An overivew of the construction . . . 247
7.4.2 Step I: Construction of the parent copies . . . 250
7.4.3 Main copies $\overline{\boldsymbol{u}}_N$ and $\overline{\xi}_N$: Proof of Proposition 7.3.1 . . . 268
7.5 Discussion . . . 277
7.5.1 Anomalous dissipation in a passive scalar . . . 277

7.5.2 Rayleigh–Bénard convection . . . 279
Appendix 7.A A useful estimate for the solution of the Poisson's equation: Proof of Proposition 7.3.2 . . . 281
7.A.1 Proof of Proposition 7.A.2 . . . 287
Appendix 7.B Derivation of the variational principle for heat transfer (7.11) . . . 296
Appendix 7.C Bounds on a few integrals . . . 299
Appendix 7.D A few basic lemmas . . . 301

8 Nonuniqueness of trajectories on a set of full measure for Sobolev vector fields 304
8.1 Introduction . . . 304
8.1.1 Notation . . . 307
8.1.2 Organization of the paper . . . 308
8.2 Cantor set construction . . . 308
8.3 Overview of the approach . . . 317
8.4 Proof of Theorem 8.1.1 and the design of vector field $\boldsymbol{v}$ . . . 321
8.4.1 Modifications required to prove Theorem 8.1.2 . . . 327
8.5 Blob flow . . . 328
8.5.1 A stationary blob flow . . . 328
8.5.2 A moving blob . . . 330
8.5.3 Assembly of moving blobs: A proof of Proposition 8.4.2 . . . 334
8.6 Conclusion and Future work . . . 337

9 Conclusion 339
9.1 Rigorous bounds on bulk quantities . . . 340
9.1.1 Summary of the thesis results . . . 340
9.1.2 Open problems and future prospects . . . 342
9.2 The design of incompressible flows in fluid problems . . . 347
9.2.1 Open problems and future prospects . . . 348

List of Figures

2.1 A schematic of Couette flow. 18
2.2 shows the one-dimensional background flow profile as defined in (2.20) 22
2.3 depicts convection between two differentially heated walls driven by buoyancy. 29

3.1 The solid line in the middle represents the plate. Γ is the domain enclosed between the plate and the thick dashed rectangular envelope (the spanwise direction is not visible in this figure). Also shown is the division of Γ into the eight subdomains R_1 through R_8. 50
3.2 a) Streamwise velocity profile at different positions x_1. b) Streamlines of the background flow field given by (3.35). In both panels, the dashed line marks the boundary of Γ. 52

3.3 The solid black line is the leading order term in the bound (3.58) on the drag coefficient. For the range of Reynolds number considered in this figure, a bound obtained by solving (3.55) and (3.56) would differ only by 0.3% from this leading term at most. The blue line shows the analytical expression for the drag coefficient in the laminar regime given by (3.59). The red line shows the empirical formula for the drag coefficient in the turbulent regime for a smooth plate given by (3.60). In both of these cases a solid line denotes the region of validity of the formulae. For $5 \cdot 10^5 \lesssim Re \lesssim 10^7$ the experimental data seems to fall in between these two lines (see Schlichting and Gersten, 2016, p. 10). The green dashed lines show the drag coefficient variation for two rough plates with different roughnesses (see Schlichting and Gersten, 2016, p. 584). 59

3.4 An elementary choice of the background flow ($\boldsymbol{U}$): (a) case of flow past a cylinder and (b) case of flow past a flat plate with nonzero angle of attack. In both cases the streamlines have to squezee around the body because of the incompressiblity of the background flow. As a result, $|\boldsymbol{\nabla U}| = O(\delta^{-2})$ as opposed to the present case where $|\boldsymbol{\nabla U}| = O(\delta^{-1})$ inside the boundary layer. 62

3.5 This figure shows a few flow configurations where the present analysis can be generalized. The arrow shows the direction of the uniform flow, and in all the above configurations, the objects are kept at zero incidence and are of zero thickness. These configurations are: (a) a yawed flat plate (top view), (b) a flat plate with irregular leading edge (top view), and (c) a group of flat plates (side view). 64

3.6 The thick line in the middle is the plate. Γ is the domain enclosed between the plate and the dashed rectangle (the spanwise direction is not visible in this figure). The shaded triangular region is R_T as defined in (3.70). Here, p_1, p_2, and p_3 are the points (x_1, x_2, x_3), $(0, x_2, x_3)$, and $(x_2, 0, x_3)$. The point p_1 belongs to R_1. 69

3.7 (a) Illustration of the piecewise linear choice of background flow on top of the plate. Here, U_p, the maximum value of the streamwise component of $\boldsymbol{U}$ and δ_p denotes the height from the plate where this value is achieved. (b) Illustration of the region R_1, where the streamfunction Ψ of the background flow $\boldsymbol{U}$ remains to be determined once the Ψ is constructed on top of the plate. 72

4.1 (a) Schematic diagram of a helical pipe with radius R_p, radius of the centerline helix R_h, and pitch of the centerline helix $2\pi l$. The dashed line is the axis of rotation of the helical pipe. (b) Illustration of the coordinate system (s, r, ϕ) used in this paper. 82

4.2 Variation of the streamwise component U_s of the background flow (4.36) across a cross-section of the pipe. In this example, the pipe's curvature is $\kappa = 0.5$ and torsion is $\tau = 0.25$. The solid black curve shows the edge of the boundary layer with variable thickness $\delta g(s, \phi)$. The point O denotes the outer edge of the pipe, i.e., the point on the cross-section, which is farthest from the axis of rotation of the helical pipe. The background flow in this figure corresponds to $\Lambda = 1$, and the boundary layer shape $g(s, \phi)$ is given by (4.56), which is the shape obtained in the process of optimizing the bound. 92

4.3 Ratio of the bound on the friction factor for a helical pipe as compared to a straight pipe $(\lambda_b/\lambda_{b,st})$, as a function of curvature κ and torsion τ. Here, λ_b is given by (4.74) and $\lambda_{b,st} = 27/8$. 103

4.4 Ratio of the bound on the friction factor for a helical pipe as compared to a straight pipe $(\lambda_b/\lambda_{b,st})$, as a function of the non-dimensional geometric parameters a and b as defined earlier. . . . 105

4.5 (a) Data from Cioncolini and Santini (2006), showing the friction factor (λ_{exp}) as a function of Reynolds number for four different helical pipes: (i) $\kappa = 0.028,\ \tau = 0.49\times10^{-3}$ (∇), (ii) $\kappa = 0.042,\ \tau = 1.87\times10^{-3}$($\square$), (iii) $\kappa = 0.059,\ \tau = 2.97\times10^{-3}$ ($*$), and (iv) $\kappa = 0.143,\ \tau = 11.4\times10^{-3}$ ($\times$). (b) Scaled friction factor ($\lambda_{exp}/I(\kappa,\tau)$) as a function of Reynolds number for the same four helical pipes. 107

4.6 Pressure driven flow (a) through a helical pipe with a square cross-section, (b) through a toroidal pipe with a square cross-section, (c) through an axially twisted pipe with an elliptical cross-section, (d) between grooved walls where the grooves are aligned in the direction of the pressure gradient, (e) through a helical pipe with varying pitch, and (f) between rough walls (two-dimensional view). Arrows indicate the direction of the mean flow. 109

5.1 Panel (a) shows the critical Taylor number Ta_c^{nc} (green line), Ta_c^{3D} (blue line) and Ta_c^{2D} (red line) as a function of the radius ratio η and (b) shows a close-up view of the same plot for small η. The dashed blue line corresponds to the marginally stable axisymmetric Taylor vortices, while Ta_c^{3D} is continued to be shown with the solid blue line. Panels (c) and (d) shows the critical Taylor number Ta_c^{3D} and Ta_c^{2D} normalized by Ta_c^{nc} as a function of η. 131

5.2 Variation of the critical axial wavenumber $2\pi/L_c$ and critical azimuthal wavenumber m_c with radius ratio η for (a) case 2 and (b) case 3. In panel (a), the critical azimuthal wavenumber changes from $m_c = 0$ above $\eta = \eta_s = 0.0556$ to $m_c = 1$ below η_s, as discussed in the main text. 133

5.3 Panel (a) shows selected streamlines of the marginally stable 3D flow and panel (b) shows selected streamlines of the marginally stable axisymmetric Taylor vortices, in both cases at a radius ratio ($\eta_s = 0.0556$). The corresponding critical Taylor numbers in both cases are equal. The streamlines are colored according to the magnitude of the velocity. In both the cases the velocity field has been scaled such that the maximum magnitude is 1. A typical vortex is shown using relatively thicker lines in both cases. Note that only half the vortex is shown in the axial direction. 135

5.4 The optimal background flow $U_\theta(r)$ at parameter values $Ta = 10^6$ and $\eta = 0.6$. The orange color is used for case 1, brown color for case 2 and blue color for case 3. Also, shown as a black thick line is the background flow (5.33) used to construct the analytical bound in §5.4, with the values of Λ, δ_i and δ_o given by (5.43) in definition (5.33). 146

5.5 The left column shows the optimal bound Nu_b compensated with $Ta^{\frac{1}{2}}$ in case 1, case 2 and case 3 (top to bottom) as a function of the Taylor number for a wide range of radius ratios. The right column shows the same plots but further scaled with the analytical geometrical scaling $\chi(\eta)$ given by (5.47). The collapse of the curves at high Taylor numbers suggests that the bound on Nusselt number Nu_b asymptotes to $c\chi(\eta)Ta^{\frac{1}{2}}$ in all three cases where the unknown constant c is given in (5.53a-c) 147

5.6 The left column shows the wavenumbers of the critical modes in the optimal perturbation as a function of Ta at $\eta = 0.2, 0.4, 0.6$ and 0.8 (top to bottom). The color indicates if the critical mode is active near the inner cylinder (blue), outer cylinder (red), both cylinders (green) and in the bulk (black), according to the classification given in the main text. The blue and red solid lines are the theoretical predictions for the critical mode with the largest wavenumber active near the inner and the outer cylinder, (see equation (5.57)), respectively. The right column shows the corresponding azimuthal component $\tilde{v}_{\theta,n_c}(r)$ of critical modes at the same radius ratios, at $Ta = 10^8$. 152

5.7 The plots in the left column shows the wavenumber m_c of the critical modes that constitutes the two dimensional optimal perturbation as a function of the Taylor number for radius ratios $\eta = 0.2, 0.4, 0.6$ and 0.8 (top to bottom). We use the same color scheme as in figure 5.6 to distinguish different critical modes. The solid green line is the relation (5.58) which predicts the largest critical wavenumber. The right column shows the plots of $\tilde{v}^c_{\theta,m_c}$, the coefficient of $\cos m_c\theta$ in the azimuthal component of the velocity, at $Ta = 10^8$ and the same radius ratios as the left-hand side plots. 155

5.8 A cartoon of the streamlines of the flow field given by (5.72). . . . 160

5.9 (a) The Nusselt number (Nu) from DNS as a function of the Taylor number (Ta). (b) The Nusselt number (Nu) scaled with the geometrical scaling $X(\eta)$ given by (5.47) as a function of Taylor number (Ta). In these figures the DNS results are taken from (Ostilla-Mónico et al., 2014) for $\eta = 0.5, 0.714$ and 0.909 and from (Froitzheim et al., 2019) for $\eta = 0.357$. 167

6.1 The two configurations considered in this paper. (a) IH1: Isothermal boundaries, (b) IH3: Isothermal top boundary and insulating bottom boundary. In both configurations the heating is uniform, so the non-dimensional thermal source term is $H = 1$. Dashed lines show the temperature profiles in the pure conduction state, while solid lines sketch the temporally- and horizontally-averaged temperature profiles in a typical turbulent state (also shown using the color plot). 187

6.2 Sketch of the functions $\psi(z)$ and $q(z)$ from (6.32), used to obtain a bound on the heat flux $\langle wT \rangle$ in the IH1 configuration. 201

6.3 Sketch of the functions $\psi(z)$ and $q(z)$ from (6.55), used to obtain bound on the heat flux $\langle wT \rangle$ in the IH3 configuration. 208

6.4 Bottom boundary layer structure of the numerically optimal functions $\psi(z)$ and $q(z)$ computed by Arslan et al. (2021b) for the IH1 configuration. The results shown are for $R = 2.67 \times 10^5$ but are typical of the behaviour observed at all sufficiently large R values. The boundary layer in $\psi(z)$ has an approximately linear inner sublayer ($0 \leq z \lessapprox 0.001$) followed by an outer sublayer where $\psi(z) \sim z^{-1}$ ($0.001 \leq z \lessapprox 0.002$). The transition between the two is nonsmooth. The optimal q approximately satisfies $q(z) = \psi'(z)$ in the boundary layer. This boundary layer structure is modelled similar to the analytical ψ and q sketched in Figure 6.2. 214

7.1 Panel (a) illustrates good and bad strategies to maximize term I defined in (7.12a-c). In the good scenario, ξ is positive (indicated by red color) where the flow is moving upward (positive z-direction) and is negative (blue color) where the flow is moving downward. Therefore, u_z and ξ are positively correlated. This is not the case in the bad scenario. Panel (b) illustrates good and bad strategies to minimize term II. In the good scenario, $\nabla\xi$ is perpendicular to $\boldsymbol{u}$, hence $\boldsymbol{u}\cdot\nabla\xi\equiv 0$, i.e., ξ is constant along the streamlines and therefore the term II zero. In the bad scenario, $\nabla\xi$ is parallel to $\boldsymbol{u}$, so the term II is nonzero. 230

7.2 Panel (a) shows the streamlines of a set of typical convective rolls. Panel (b) shows the streamlines of a steady two dimensional branching flow. In both figures, the streamlines have been overlayed with a ξ field according to the good scenario described in figure 7.1a (i.e. ξ is positive whenever u_z is positive, and ξ is negative whenever u_z is negative). The red color indicates a positive value of ξ, whereas the blue color indicates a negative value. The dashed circles in both figures show regions where $\boldsymbol{u}\cdot\nabla\xi$ is nonzero. 233

7.3 Illustration of the branching pipe flow. Panel (a): the parent construct $\overline{\boldsymbol{u}}$. It consists of red and blue pipes which are the part of pipelines $\boldsymbol{P}_{up}$ and $\boldsymbol{P}_{down}$, respectively. In panel (a), arrows are used in some pipes to show the direction of the flow. The reducer region of a pipe, in which the radius of the pipe decreases by a factor of half to ensure that the velocity remains, is also shown using a dashed circle. Panel (b): the branching skeleton. To build the main copy $\overline{\boldsymbol{u}}_N$ away from the boundary layer, we place the appropriately dilated version of the parent construct $\overline{\boldsymbol{u}}$ along the skeleton up to N levels. Panel (c): the parent construct $\overline{\boldsymbol{u}}_b$, used in the boundary layer. In the construct $\overline{\boldsymbol{u}}_b$, the flow from red pipes turn back to blue pipes (shown in the pink color). A 2D cartoon of the resultant pipe flow is shown in figure 7.4. 236

7.4 shows a 2D cartoon of the main copy $\overline{\boldsymbol{u}}_N$. The pipeline $\boldsymbol{P}_{up}$ is shown in red color and the pipeline $\boldsymbol{P}_{down}$ is shown in blue color. In the blow-up figure of a section of the pipeline, the graph of $\overline{\xi}_N$ is also shown. Notice is that $\overline{\xi}_N$ is constant in the support of $\overline{\boldsymbol{u}}_N$. 239

8.1 An illustration of the construction process of the Cantor set $\mathcal{C}_\Phi$ in two dimensions. The sequence Φ is given by (8.20), and we have chosen $\nu = \frac{3}{4}$. The figure shows the collection of first four generations of cubes, C_Φ^1, C_Φ^2, C_Φ^3 and C_Φ^4, in increasingly less pale red color. In the figure, $\boldsymbol{x}_0 = (1/2, 1/2)$, $\boldsymbol{x}_1 = P_\Phi^1(\mathfrak{s}_1)$, $\boldsymbol{x}_2 = P_\Phi^2(\mathfrak{s}_2)$ and $\boldsymbol{x}_3 = P_\Phi^3(\mathfrak{s}_3)$. Here, $\mathfrak{s}_1$, $\mathfrak{s}_2$ and $\mathfrak{s}_3$ are the elements of S_1, S_2 and S_3, respectively, given by $\mathfrak{s}_1 = \{(-1,-1)\}$, $\mathfrak{s}_2 = \{(-1,-1),(-1,-1)\}$ and $\mathfrak{s}_3 = \{(-1,-1),(-1,-1),(-1,-1)\}$. 312

8.2 The motion of the first four generations of cubes in the Cantor set construction process under the flow of vector field $\boldsymbol{v} = \sum_{i=0}^{\infty} \boldsymbol{v}_i$. At the ith stage, the vector field $\boldsymbol{v}_i$ translates the cubes of the ith generation so that their centers align with the dyadic cubes of the ith generation. In the first step, by definition of the centers (8.12), we have this alignment at $t = \tau_0$ itself. Therefore, in the first step, we simply choose $\boldsymbol{v}_0 \equiv 0$. The arrows in the figure indicate the direction of the motion of cubes. In panels (b), (c) and (d), the tails of the arrow lie at the shifted center (see (8.13)), $\widetilde{P}_\Phi^1(\mathfrak{s}_1)$, $\widetilde{P}_\Phi^2(\mathfrak{s}_2)$ and $\widetilde{P}_\Phi^3(\mathfrak{s}_3)$, respectively, for $\mathfrak{s}_1 \in S_1$, $\mathfrak{s}_2 \in S_2$ and $\mathfrak{s}_3 \in S_3$. Finally, in our construction, the vector field $\boldsymbol{v}_{i-1}$ is supported near the ith generation cubes in the Cantor set construction process as they move around in space. The size of these ith generation cubes becomes increasingly smaller compared to ith generation dyadic cubes, as can be seen in panel (e), for example. This shrinking of the support of the vector field $\boldsymbol{v}_i$ with large i is one of the main reasons that allow us to bound the Sobolev norm of the vector field uniformly in time. 318

8.3 An illustration of the blob flow $\widetilde{\boldsymbol{v}}$ in two dimensions. The vector field $\widetilde{\boldsymbol{v}}$ translates a cube of length λ centered at $\boldsymbol{x}_s$ at time $t = t_s$ to a cube centered at $\boldsymbol{x}_e$ at $t = t_e$. The cube is shown in red color. As the cube moves, the vector field $\widetilde{\boldsymbol{v}}$ inside the red cube is always uniform, and the support of the vector field lies in a slightly bigger cube of length $\lambda(1+\delta)$ (shown in dashed). 331

9.1 (a) A background decomposition of the flow as described in the main text. (b) One flow unit as described in the main text. The main property of this flow unit is that at level $z = 1$, the flow field is made up of four self-similar copies at level $z = 0$. 352

List of Tables

4.1 The first column shows the pipe type, the second column shows the lower bound on the flow rate Q (4.73) and the third column shows the upper bound on the friction factor λ (4.74) in different limits of curvature κ and torsion τ. In the table $\mathscr{C} = (32\pi^2/27)^{\frac{1}{2}}$ and $\mathscr{D} = 27/8$. 102

5.1 Variation of the ratio $A(\eta)/\chi(\eta)$, where $A(\eta)$ is from the relation (5.52) and $\chi(\eta)$ is given in (5.47), in case 1, case 2 and case 3 where we have respectively added 'nc', '$3D$' and '$2D$' in the superscript to signify the case. Notice that $A(\eta)$ when scaled with $\chi(\eta)$ becomes almost invariant in η. 148

7.1 A few useful definitions: line segments or rays (column one), vectors in $\mathbb{R}^3$ (column two) and vector-valued measures (column three). . 253

Abstract

Bulk properties and flow structures in turbulent flows

by

Anuj Kumar

Turbulence is ever-present: from flows in engineering, such as a wake behind a submarine, the boundary layer over an aircraft wing, and the swirl in an internal combustion engine, to flows in nature, such as convection in lakes, riffles on rivers and ocean currents. Turbulence can be found in flows at relatively small scales, such as blood flow in arteries and while mixing cream in a morning coffee, to flows at astrophysical scales, for instance, in accretion disks around stars or black holes. Because of their ubiquitous nature, progress in science and technology often hinges on progress in research on turbulent flows. In many situations described above, two lines of inquiry are of most interest. In the first direction, we are interested in quantities that are the "net" outcome of a fluid system, i.e., bulk quantities or global mean quantities such as drag force, rate of energy dissipation, mass, momentum and heat transport and mixing rate, which are usually long-time and volume averages and therefore depend only on the system's input parameters such as viscosity and diffusivity of the fluid, characteristics velocity scale, domain shape. The second direction, which is complementary to the first one, is the study of different structures in turbulent flows, for example, quantifying the range of scales and the energy distribution through this range in turbulent flows. In this thesis, we study a few problems that are related to and inspired by these two directions of questioning. While working on a problem, we always try to incorporate different perspectives: engineering, physics and mathematics. It is our intention to work at the interface of physical and mathematical fluid dynamics, as there appears to

be great potential for an exchange of ideas that can eventually benefit both fields. On the one hand, having knowledge of various phenomenological theories from the physics literature gives one the advantage in tackling the various pressing problems considered in the mathematical community. On the other hand, putting various theoretical predictions on a rigorous mathematical footing can allow us to gain a deeper understanding of the physical mechanism/phenomenon. In accordance with this theme, below we describe the problems considered in this thesis, which is divided into two parts.

In the first part of the thesis, we are interested in quantifying bulk properties of turbulent flows, such as energy dissipation, drag force, heat and mass transfer. We obtain rigorous bounds on these quantities using a well-known technique known as the background method. We consider four problems in the first part: (1) uniform flow past a flat plate, (2) pressure-driven flow in a helical pipe, (3) Taylor–Couette flow (flow between two independently rotating concentric cylinders), and (4) internally heated convection. In the flat plate study, we show that the energy dissipation rate for uniform flow past a flat plate remains bounded. This is the first and only example so far of an external flow problem (flow past a body) where such a bound has been established. In the second and third problems, we derive bound on mean quantities such as friction factor, volume flow rate, energy dissipation, torque on the cylinder and angular momentum transport not just as a function of the principal flow parameter, the Reynolds number, but more importantly, as a function of the geometry of the domain (i.e., curvature and torsion in the case of helical pipe flow and the ratio of the radii of two cylinders in Taylor–Couette flow). These studies are motivated by several engineering applications where the geometry of the domain plays an important role. In the fourth study, we consider the problem of convection between two solid boundaries driven by a source of

internal heating and derive a bound on the mean vertical heat flux, an inquiry that is motivated, for example, by convection in the earth's mantle and the sun's radiative zone.

In the second part of the thesis, we are concerned with designing incompressible flows that possess some specific desired properties. The first problem in this direction is related to the optimal heat transport from a hot to a cold wall using a flow whose enstrophy is bounded by a given constant. The bound on the enstrophy can also be thought of as a bound on the power supply needed to generate this flow (using a body-force in the momentum equation) Navier–Stokes system. An upper bound on the heat transfer that scales as 1/3-power of the power supply had formally been derived previously, but whether a flow exists that transports heat at that rate remained an outstanding question. For this problem, we design three-dimensional branching flows to prove that the corresponding heat transfer saturates this known upper bound, which then establishes the exact asymptotic behavior of the optimal heat transport between two plates. Beyond the mathematical proof, our method also reveals why three-dimensional branching flows are so efficient in transferring heat. Finally, in the second part, we study a problem related to the nonuniqueness of flow maps in an ODE system for the class of velocity fields that are divergence-free and belong to Sobolev space $W^{1,p}$. We reprove and improve the known result that had been previously established using the method of convex integration. Our goal for this problem is simple: provide explicit constructions and use them to gain insights into the exact mechanism of the nonuniqueness of solutions of the ODE and the PDEs, transport and continuity equation with the same vector field. Beyond proving the nonuniqueness results, we anticipate that such explicit constructions will be helpful for designing velocity fields in the convection-diffusion equation or the body-forced Navier–Stokes

equation to demonstrate the phenomenon of anomalous dissipation, an intrinsic characteristic of turbulent flows.

To my brother Ajay Kumar

Acknowledgments

I am grateful to my advisor Prof. Pascale Garaud for the continuous help, support and encouragement over the last five years in academics and beyond. I thank Pascale for introducing me to the wonderful summer program, GFD, at Woods Hole, which I attended in 2019 and had a great time. My Ph.D. research started during that program and gradually morphed into what I do today. I thank Pascale for the freedom, support and guidance to pursue topics of my interest. I learned the importance of organization and hard work from Pascale. I would also like to thank her for giving me valuable feedback on my writing, which enabled me to improve and develop my writing style. Pascale is someone who works hard for their students even in matters that are outside her duties. This is something I am inspired to do for my students in the future if I become an academic.

I thank the administrative staff and advisors in the last five years: Lisa, Theo, Jennifer and Tracie, for their work behind the scenes, which made my life easier as a student.

I thank my dissertation and advancement committee members, Prof. Daniele Venturi, Prof. David Goluskin, Prof. Maria Colombo and Prof. Charlie Doering, for taking the time to read the thesis and providing helpful comments and guidance at different junctures.

I would also like to thank Professors Dongwook Lee, Abhishek Halder, Rich Kerswell, Theodore Drivas, Colm Caulfield and Peter Constantin for their support at various stages.

Several people for the talk invitations and academics visits in the past few years: Ian Tobasco, Giovanni Fantuzzi, Pedram Hassanzadeh, Keaton Burns, Dan Ginsberg, Laurel Ohm, Dallas Albritton, Franziska Weber, Jon Wilkening,

Michele Dolce and Elia Brué.

Ali Arslan, Giovanni Fantuzzi, John Craske and Andrew Wynn for fun collaborating on the internally heated convection project.

To all my friends from the last five years, Arstan, Bhishek, Evan, Ian, Peter, Shruta, Zach and many others, for all the fun and laughs.

I thank two of my close teachers for their encouragement, who made an impact on me in growing as a researcher.

Finally, I am indebted to my parents and my brother for their unconditional love and support. I thank them for their sacrifices that ensured my success throughout the years. Without their presence, I would not be half the researcher that I am today.

Chapter 1

Introduction

1.1 Turbulent flows

1.1.1 The onset of turbulence

Turbulence is usually described as the chaotic motion of a fluid characterized by the presence of a wide range of flow scales, increased mixing of a scalar field, high rate of momentum transport and large energy dissipation rates. The properties described above can only be obtained when the flow is sufficiently energetic. Indeed, at low flow speeds, the fluid does not possess enough inertia to overcome the damping effect of viscosity. As a result, the flow stays "organized," which we call laminar flow. The momentum transport in laminar flows is primarily through viscous diffusion and is slower than in turbulent flows. As the flow speed becomes sufficiently large, the damping effect of viscosity is no longer adequate to keep the fluid's inertia in check, leading to the disorganized motion of the fluid, which we call turbulent flow. The transition from laminar to turbulent flows at intermediate speeds is often complex and can happen in several ways depending on the forces

applied to generate the flow and geometry of the domain. In some cases, the flow slowly becomes more intricate with increasing flow speed, undergoing a series of bifurcations that are each associated with a particular instability, and eventually becoming turbulent. Examples include the flow between two concentric cylinders (Taylor–Couette flow) with the inner cylinder rotating (Coles, 1965; DiPrima and Swinney, 1981). In other cases, such as pipe flow, the transition from laminar flow to turbulence is more sudden and happens at a certain flow speed threshold (Barkley, 2016).

1.1.2 Turbulent flows in nature and engineering

Turbulence is ever-present: from flows in engineering, such as a wake behind a submarine, the boundary layer over an aircraft wing, and the swirl in an internal combustion engine, to flows in nature, such as convection in lakes, riffles on rivers and ocean currents. Turbulence can be found in flows at relatively small scales, such as blood flow in arteries and while mixing cream in a morning coffee, to flows at astrophysical scales as, for instance, in accretion disks around stars or black holes. Because of their ubiquitous nature, progress in science and technology often hinges on progress in research on turbulent flows.

For example, the answer to one of the leading questions in astrophysics, which is about the formation of a star, rests on determining the transport of angular momentum rate in turbulent accretion disks (Shakura and Sunyaev, 1973; Ji et al., 2006; Avila, 2012; Balbus, 2017) and is currently an active area of research. Understanding energy and mass transfer by thermal convection is critical to understanding stellar evolution (Spruit et al., 1990). In the oceans, turbulent mixing is required to maintain the meridional overturning circulation, which in turn, is

responsible for the state of the climate (Munk and Wunsch, 1998; Wunsch and Ferrari, 2004). Turbulence also plays a crucial role in increased mixing and brings nutrients from the bottom to the surface in the oceans, an essential component for plankton growth (Caldwell and Mourn, 1995). From the engineering side, the design of airfoils, ship hulls, and rockets requires the calculation of the turbulent aerodynamic drag (Milgram, 1998; Pena and Huang, 2021). The design of heat exchangers and steam generators often involves the analysis of friction factors and heat transfer coefficients for turbulent flow in a helical coil (Naphon and Wongwises, 2006; Vashisth et al., 2008).

1.1.3 Questions of primary importance

In many situations concerning turbulent flows, such as the ones described above, we are often interested in quantities that are the "net" outcome of a fluid system, i.e., bulk quantities or global mean quantities such as drag force, rate of energy dissipation, mass, momentum and heat transport and mixing rate, which are usually long-time and volume averages and therefore depend only on the system's input parameters such as viscosity and diffusivity of the fluid, characteristic velocity scale and domain shape. The fundamental question in turbulence research is to quantify how these bulk quantities depend on these system parameters. The practical importance of answering this question can hardly be overstated, and there is rarely a study on turbulent flow that does not try to answer this question in one way or another. Complementary to this question, another significant research direction is the qualitative and quantitative study of turbulent flow structures. For example, given a fluid system, one is often interested in characterizing the range of scales of different flow structures and how the energy is distributed

across the scales. The study of bulk properties and flow structure in turbulent flows are, in fact, closely related to one another. Having the knowledge of flow structures, one can predict the bulk properties associated with the flow (Pope, 2000). Similarly, knowing the bulk properties, one can try to infer the flow structure by simply asking the question: what essential features must the flow possess to match the required values of bulk properties (Lumley, 1992; Vassilicos, 2015)? To cast some of these important questions on a more quantitative level, we now turn to the mathematical description of turbulent flows.

1.2 Flow modeling and various approaches in turbulent flow

The model of fluid motion that is extensively used in many scenarios inspired by previously described natural and engineering situations are the incompressible Navier–Stokes equations:

$$\nabla \cdot \boldsymbol{u} = 0, \tag{1.1a}$$

$$\frac{\partial \boldsymbol{u}}{\partial t} + \boldsymbol{u} \cdot \boldsymbol{\nabla} \boldsymbol{u} = -\frac{1}{\rho} \nabla p + \nu \Delta \boldsymbol{u}. \tag{1.1b}$$

In these equations, $\boldsymbol{u}$ is the velocity field, and p is the potential (commonly referred to as pressure but is different from thermodynamic pressure) responsible for maintaining the velocity field divergence-free. The quantities ρ (density) and ν (viscosity) are the fluid properties. Equation 1.1a is the mass conservation, and 1.1b is Newton's second law of motion written down for a small fluid volume. After appropriately scaling the variables, only one (nondimensional) parameter

that governs the flow dynamics emerges,

$$Re = \frac{[U][L]}{\nu},$$

known as the Reynolds number. Here $[L]$ is a typical length scale, and $[U]$ is a characteristic velocity scale of the flow. The Reynolds number is the ratio of the diffusive time scale to the convective time scale and can be seen as a competition between the fluid's inertia to the damping effect of the viscosity. At small Reynolds numbers, the flow is laminar, and it becomes turbulent at sufficiently large Reynolds numbers.

Given an initial condition of the velocity field, the Navier–Stokes equations supposedly describe the evolution of the flow. However, knowing the exact form of these equations does not necessarily allow us to answer the questions raised in section 1.1.3 about bulk properties and flow structure exactly. Indeed, the main difficulty is that the solutions of the Navier–Stokes equation are usually chaotic at high Reynolds numbers (consistent with the appearance of turbulence) and therefore lack analytical solutions in that regime. In such situations, one can make progress using one or a combination of the following approaches: field observations, performing experiments or direct numerical simulations (DNS), developing phenomenological theories and, finally, proving precise mathematical statements.

In some instances, experimental or numerical observations are sufficient to predict the behavior of bulk properties as a function of system parameters. For example, in large-scale body-forced flows or flows past a blunt object, there is plenty of evidence that the rate of energy dissipation becomes independent of viscosity at large Reynolds number (Roshko, 1961; Sreenivasan, 1984; Sreenivasan and Antonia, 1997; Kaneda et al., 2003), a phenomenon known as anomalous dissipation

(sometimes also dubbed as "zeroth law of turbulence" because of its fundamental nature). Using this observation as an assumption, along with the assumptions of homogeneity, isotropy and self-similarity, Kolmogorov further predicted the structure of the flow in his 1941 theory of isotropic turbulence (Kolmogorov, 1941a,b, 1991).

However, there are many instances where experiments or numerical simulations are insufficient to predict bulk properties or the flow structure. For example, in the design of many engineering applications, one crucial question is how bulk properties vary as a function of the shape of the domain in a fully turbulent regime (Duvigneau et al., 2003; Kim and Choi, 2005; Mohammadi and Pironneau, 2009; Mooneghi and Kargarmoakhar, 2016). Answering this question, especially for complex geometries, is very challenging and costly for both experiments and numerical computations as it requires building a new apparatus or starting a new simulation every time for a different geometry. Likewise, modeling the conditions relevant to astrophysical and geophysical flows in a laboratory setting or direct numerical simulations is generally very difficult or impossible. The first reason is that canonical problems associated with astrophysical and geophysical flows typically involve many different physical processes that are characterized by several input parameters. In nondimensional form, it could be the Reynolds number, the Péclet number, one or several diffusivity ratios, the Rossby number, the magnetic Reynolds number, etc. In addition, the values of these parameters relevant to astrophysical or geophysical flows are usually extreme, making it difficult for experiments or numerical simulations to achieve them in practice.

With sparse experimental and numerical data, phenomenological theories and empirical relations are often proposed as a less-than-ideal but necessary way forward. For example, the mixing length theory in stellar convection (Vitense, 1953;

Böhm-Vitense, 1958; Gough, 1977), α-viscosity model in accretion disks (Shakura and Sunyaev, 1973; Pringle, 1981), ocean diffusivity models and $k-\varepsilon$ model for turbulence in engineering (Mohammadi and Pironneau, 1993). These theories and relations are frequently based on unwarranted assumptions that may not always be verifiable through observations.

The content of this thesis is inspired and guided by an overarching aim of revisiting and grounding these theories and empirical relations into a mathematically rigorous framework to a feasible extent. While pursuing this course, we are interested in better understanding and articulating the physical mechanism of a process or phenomenon with the goal of using this new knowledge in real-world applications.

1.3 Content of the thesis

In this thesis, we attempt to bring together ideas from a broad range of disciplines, engineering, physics, analysis and numerical computations to make progress on the matter. Our work can be roughly divided into two broad categories. The first aspect of the work looks at obtaining rigorous bounds on turbulent bulk quantities, such as energy dissipation, drag force, heat and mass transfer, as a function of system parameters such as viscosity, thermal diffusivity and domain shape. As mentioned before, in a turbulent regime, obtaining a mathematical expression of the solution to the Navier–Stokes equation is not possible. However, in the absence of a solution, it is still possible to formally bound a resultant bulk quantity, either from above (upper bound) or from below (lower bound). These bounds are obtained as a function of the parameter(s) involved in the problem directly from the governing equations without making any assumption. The main

advantage of obtaining such bounds is that they are valid in extreme parameter regimes often of interest to engineering and naturally occurring flows.

On this important topic of bounding theory, we present four studies. One of these studies is on uniform flow past a flat plate at a large Reynolds number, where we obtain an upper bound on the energy dissipation rate (equivalently a bound on the drag coefficient), which is constant in the Reynolds number. This study was partially motivated by engineering considerations such as flow past an airfoil. The two subsequent studies are on pressure-driven helical pipe flow and Taylor–Couette flow (flow between two concentric cylinders), where we bound energy dissipation, volume flow rate, friction factor or angular momentum transport as a function of the geometrical parameters at high Reynolds numbers. These studies were motivated by several fluid-related engineering applications, where domain shapes play an essential role in the design. The final study from the first aspect of our work concerns bounds on heat transport in internally heated convection, a study inspired by convection in the Earth's mantle, radiative planet atmospheres and exothermic chemical reactions in various engineering flows. We use the well-known background method to obtain bounds in all four studies and present it in detail in Chapter 2.

The second aspect of our work looks at flow design problems, that is, the construction of incompressible fluid flows that satisfy a constraint (which can be thought of as a cost to generate these flows) and have given desired properties. We have been interested in two different yet related problems along those lines. The first one is related to optimal scalar transport, a problem in the community sometimes also known as wall-to-wall optimal transport (Hassanzadeh et al., 2014). In this work, we design an incompressible flow field, with a constraint on the mean enstrophy, that maximizes the advective transport of heat between differentially

heated parallel plates. This problem can equivalently be seen as the design of forcing in the Navier–Stokes equation, such that the resultant flow maximizes the transport of a passive temperature between two differentially heated walls for a given power supply budget. We demonstrate that the optimal flows take the form of self-similar "branching flows", and explain the physical reason why this should be the case.

In the second part, we use some of the ideas of flow design inspired by optimal heat transport flows to prove a theorem on the nonuniqueness of flow maps in a system of ODEs for "rough" vector fields. The problem is related to the modern theory of ordinary differential equations (DiPerna and Lions (1989) theory).

1.4 Organization and summary of different chapters

Even though there is a variety in the choice of flow problems considered in this thesis, there is one common theme that runs through every chapter and unites the whole thesis. It is creation: the construction of incompressible flows, whether it is the background flow to obtain bounds or flow design for optimal heat transport or to prove the nonuniqueness of flow map in an ODE system. The novel results we have obtained that have been published, submitted, or are about to be submitted for publication, are contained in the following chapters:

Chapter 3: Bound on the drag coefficient for a flat plate in a uniform flow

Based on: A. Kumar and P. Garaud [2020]

In Chapter 3, we look at the classical problem of uniform flow past a flat plate of finite length at zero angle of incidence and use the background method to obtain

a bound on the drag coefficient. The background method has been a successful tool in obtaining strict bounds on global mean quantities for several prototypical fluid problems. However, all applications of this method until now have focused on flows confined between solid boundaries. An important class of problems that, by contrast, has received no attention is the class of external flows, i.e., flow past a body. In this context, obtaining the dependence of the drag coefficient on the Reynolds number is of crucial relevance for many engineering applications. Assuming a statistically steady state and appropriate far-field decay rates for the flow variables, in this chapter, we show that at large Reynolds numbers, the drag coefficient is bounded by a constant. The bound obtained thus is within a logarithmic factor of what phenomenological theories, based on experimental data, predict.

Chapter 4: Pressure-driven flows in helical pipes: bounds on flow rate and friction factor

Based on: A. Kumar [2020]

Chapter 4 investigates pressure-driven flow in a helical pipe from a bounding perspective. We use the background method to obtain a rigorous lower bound on the volume flow rate through a helical pipe in the limit of a large Reynolds number. As a consequence, we also obtain an equivalent upper bound on the friction factor. These bounds are also valid for toroidal and straight pipes as limiting cases. Using a two-dimensional background flow with varying boundary layer thickness along the circumference of the pipe, we obtain these bounds as a function of the curvature and torsion of the pipe and therefore capture the geometrical aspects of the problem. In this chapter, we also present a sufficient criterion for determining the class of pressure-driven flow and surface-velocity-

driven flow problems that can be tackled using the background method.

Chapter 5: Geometrical dependence of optimal bounds in Taylor–Couette flow

Based on: A. Kumar [2022]

This chapter is concerned with the optimal upper bound on mean quantities (torque, dissipation and the Nusselt number) obtained in the framework of the background method for the Taylor–Couette flow with a stationary outer cylinder. In this chapter, we also study the energy stability analysis of the laminar flow. We demonstrate that below radius ratio 0.0556, the marginally stable perturbations are not the axisymmetric Taylor vortices but rather a fully three-dimensional flow. The main result of the chapter is an analytical expression of the optimal bound as a function of the radius ratio. To obtain this bound, we begin by deriving a suboptimal analytical bound using analysis techniques. We use a definition of the background flow with two boundary layers, whose relative thicknesses are optimized to obtain the bound. In the limit of high Reynolds number, the dependence of this suboptimal bound on the radius ratio (the geometrical scaling) turns out to be the same as that of numerically computed optimal bounds in three different cases: (1) the perturbed flow only satisfies the homogeneous boundary conditions but need not be incompressible; (2) the perturbed flow is three-dimensional and incompressible; (3) the perturbed flow is two-dimensional and incompressible. We compare the geometrical scaling with the observations from the turbulent Taylor–Couette flow, and find that the analytical result indeed agrees well with the available direct numerical simulations data. In this chapter, we also dismiss the applicability of the background method to certain flow problems and therefore establish the limitation of this method.

Chapter 6: Analytical bounds on the heat transport in internally heated convection

Based on: A. Kumar, A. Arslan, G. Fantuzzi, J. Craske and A. Wynn [2022]

In this chapter, we obtain an analytical bound on the mean vertical convective heat flux $\langle wT \rangle$ between two parallel boundaries driven by uniform internal heating. We consider two configurations, one with both boundaries held at the same constant temperature, and the other one with a top boundary held at constant temperature and a perfectly insulating bottom boundary. For the first configuration, Arslan *et al.* (*J. Fluid Mech.* 919:A15, 2021) recently provided numerical evidence that Rayleigh-number-dependent corrections to the only known rigorous bound $\langle wT \rangle \leq 1/2$ may be provable if the classical background method is augmented with a minimum principle stating that the fluid's temperature is no smaller than that of the top boundary. Here, we confirm this fact rigorously for both configurations by proving bounds on $\langle wT \rangle$ that approach $1/2$ exponentially from below as the Rayleigh number is increased. The key to obtaining these bounds are inner boundary layers in the background fields with a particular inverse-power scaling, which can be controlled in the spectral constraint using Hardy and Rellich inequalities. These allow for qualitative improvements in the analysis not available to standard constructions.

Chapter 7: Three dimensional branching pipe flows for optimal scalar transport between walls

Based on: A. Kumar [2022] arxiv: 2205.03367 , in preparation)

In this chapter, we look at the problem of "wall-to-wall optimal transport" in which we attempt to maximize the transport of a passive temperature field between hot

and cold plates using divergence-free velocity fields in the advection-diffusion equation subject to an enstrophy constraint. We are interested in the design of forcing in the Navier–Stokes equation such that the resultant flow maximizes the heat transfer between two differentially heated walls for a given power supply budget. Previous work established that heat transport cannot scale faster than 1/3-power of the power supply. Recently, Tobasco & Doering (*Phys. Rev. Lett.* vol.118, 2017, p.264502) and Doering & Tobasco (*Comm. Pure Appl. Math.* vol.72, 2019, p.2385–2448) constructed self-similar two-dimensional steady branching flows saturating this bound up to a logarithmic correction. This logarithmic correction appears to arise due to a topological obstruction inherent to two-dimensional steady branching flows. We present a construction of three-dimensional "branching pipe flows" that eliminates the possibility of this logarithmic correction and therefore identifies the optimal scaling as a clean 1/3-power law. Our flows resemble previous numerical studies of the three-dimensional wall-to-wall problem by Motoki, Kawahara & Shimizu (*J. Fluid Mech.* vol.851, 2018, p.R4). We also discuss the implications of our result to the heat transfer problem in Rayleigh–Bénard convection and the problem of anomalous dissipation in a passive scalar.

Chapter 8: Nonuniqueness of trajectories on a set of full measure for Sobolev vector fields

Based on: A. Kumar [2023] (arxiv: 2301.05185, in preparation)

In the theory of DiPerna–Lions for Sobolev vector fields $W^{1,p}$, an important question was whether the uniqueness of regular Lagrangian flow could be implied by proving almost everywhere uniqueness of trajectories. In this work, we construct an explicit example of divergence-free vector fields in $W^{1,p}$ with $p < d$ such that the set of initial conditions for which trajectories are not unique is a set of full

measure. To prove this, we build a vector field $\boldsymbol{u}$ and a corresponding flow map $X^{\boldsymbol{u}}$ such that after finite time $T > 0$, the flow map takes the whole domain $\mathbb{T}^d$ to a Cantor set $\mathcal{C}_\Phi$, i.e., $X^{\boldsymbol{u}}(T, \mathbb{T}^d) = \mathcal{C}_\Phi$ and the Hausdorff dimension of this Cantor set is strictly less than d. The flow map $X^{\boldsymbol{u}}$ constructed as such is not a regular Lagrangian flow. The nonuniqueness of trajectories on a full measure set is then deduced from the existence of the regular Lagrangian flow in the DiPerna–Lions theory.

Chapter 2

The background method

2.1 Introduction

The background method is an important tool in fluid dynamics that enables us to obtain bounds on the global mean quantities such as drag force, energy dissipation, heat and mass transfer in turbulent flows. Doering and Constantin first developed it in a series of four papers (Doering and Constantin, 1992, 1994; Constantin and Doering, 1995; Doering and Constantin, 1996). Their first two papers considered the Couette flow system (flow between two parallel boundaries subject to surface-velocity differential), where they showed that the rate of energy dissipation stays bounded in the limit of vanishing viscosity, or in other words, the upper bound is independent of viscosity. While this statement is relatively intuitive given the vast range of experiments confirming it in various flow setups (Dryden, 1943; Cadot et al., 1997; Sreenivasan, 1984, 1998; Pearson et al., 2002; Kaneda et al., 2003), proving was non-trivial, and in fact, such proofs are generally quite rare even today. For example, there is presently no equivalent proof that the energy dissipation rate stays bounded (by a quantity that is independent

of viscosity) for uniform flow past a sphere or cylinder. In their second paper, Constantin and Doering looked at pressure-driven flow in a channel and obtained a lower bound on the volume flow rate that is proportional to the square root of the pressure differential and independent of viscosity. Their final paper investigated Rayleigh–Bénard convection (the motion of fluid between two differentially heated walls driven by buoyancy), where they derived an upper bound on the Nusselt number (the non-dimensional heat transfer), which is proportional to the square root of Rayleigh number (a parameter governing the intensity of convection).

Doering and Constantin were not the first to obtain bounds on global mean quantities in fluid mechanics: this concept goes back to Howard (Howard, 1963, 1972). In his 1963 paper, Howard obtained an upper bound on the Nusselt number for the Rayleigh–Bénard problem under a statistical stationarity assumption. His bound is similar to that of Doering and Constantin but with a different prefactor. (Busse, 1969, 1970) further extended Howard's approach to Couette flow and pressure-driven flows. (Kerswell, 1997, 1998) showed that the best bounds obtained using the Howard–Busse technique and the Doering–Constantin technique are one and the same for turbulent shear flows. However, the Doering–Constantin approach is much more flexible than the Howard–Busse approach and does not require any assumption about the statistical stationarity of the flow. As a result, the Doering–Constantin background method has become more popular and has been used in several canonical flow configurations, some of which we discuss below.

2.2 Understanding the background method through a simple example

To understand the background method, we consider the example of the plane Couette flow, which is the flow of fluid between two parallel plates, where the top plate moves with the velocity U_0 and the bottom plate is stationary. Figure 2.1, shows the configuration. We study the problem using the incompressible Navier–Stokes equations

$$\nabla \cdot \boldsymbol{u} = 0, \tag{2.1a}$$

$$\frac{\partial \boldsymbol{u}}{\partial t} + \boldsymbol{u} \cdot \boldsymbol{\nabla} \boldsymbol{u} = -\frac{1}{\rho} \nabla p + \nu \Delta \boldsymbol{u}, \tag{2.1b}$$

where $\boldsymbol{u} = (u_x, u_y, u_z)$ is the velocity field, p denotes the pressure, ν is the viscosity of the fluid and ρ is the density. We assume that the flow satisfies periodic boundary conditions in the horizontal directions. The solid boundaries are situated at $z = -H/2$ and $z = H/2$. Therefore the domain of interest is $\Omega \coloneqq \mathbb{T}_{L_x} \times \mathbb{T}_{L_y} \times (-H/2, H/2)$. The flow field satisfies the following boundary condition:

$$\boldsymbol{u} = (0,0,0) \quad \text{at} \quad z = -H/2, \qquad \boldsymbol{u} = (U_0,0,0) \quad \text{at} \quad z = H/2. \tag{2.2}$$

The quantity that we are interested in is the rate of energy dissipation given by

$$\varepsilon_\nu \coloneqq \nu \langle |\nabla \boldsymbol{u}|^2 \rangle, \tag{2.3}$$

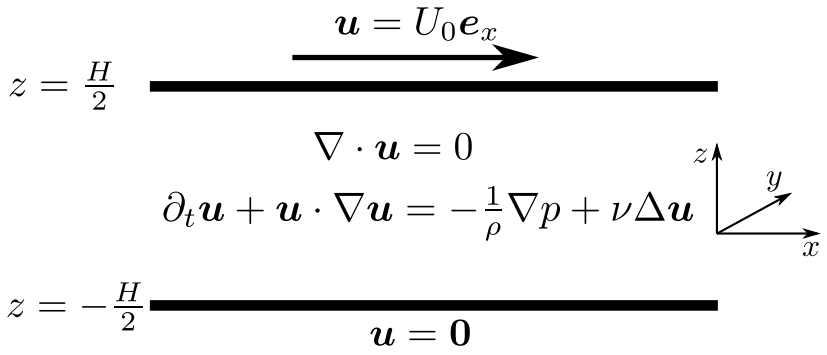

Figure 2.1: A schematic of Couette flow.

where the angle brackets denote the long-time volume average:

$$\langle [\,\cdot\,] \rangle \coloneqq \fint_\Omega \overline{[\,\cdot\,]}\,\mathrm{d}\boldsymbol{x} \coloneqq \frac{1}{|\Omega|}\int_\Omega \overline{[\,\cdot\,]}\,\mathrm{d}\boldsymbol{x}, \qquad \text{where} \qquad \overline{[\,\cdot\,]} \coloneqq \limsup_{T\to\infty} \frac{1}{T}\int_{t=0}^{t=T} [\,\cdot\,]\,\mathrm{d}t. \tag{2.4}$$

For the Couette flow system, it is easy to show by considering the long-time average kinetic energy equation that the rate of energy dissipation is linked to the rate of momentum transport as follows:

$$\varepsilon_\nu = \underbrace{\frac{U_0}{HL_xL_y}\int_0^{L_x}\int_0^{L_y}\left[\overline{u_x u_z} - \nu\overline{\frac{\partial u_x}{\partial z}}\right]_{z=z_0} dxdy}_{\text{Momentum Transport}}, \tag{2.5}$$

and therefore can also be related to the average force applied at the top wall to maintain a constant speed U_0:

$$\varepsilon_\nu = \frac{U_0}{HL_xL_y}F, \tag{2.6}$$

where

$$F = -\nu\int_0^{L_x}\int_0^{L_y}\left.\overline{\frac{\partial u_x}{\partial z}}\right|_{z=H/2} dxdy. \tag{2.7}$$

We now give a presentation of the background method to obtain an upper bound on the rate of energy dissipation. Using the relations (2.5) and (2.6), we will then also be able to obtain equivalent upper bounds on the momentum transport from one wall to the other, and on the force required to maintain the top plate at constant speed U_0. Our presentation here is an adaptation of the one given in ((Doering and Constantin, 1994)).

We start by writing the total flow $\boldsymbol{u}$ as a sum of two divergence-free flow fields: (1) $\boldsymbol{v}$, which we call the perturbed flow and (2) $\boldsymbol{U}$, which we call the background flow. The background flow $\boldsymbol{U}$ satisfies the same boundary conditions as the total flow $\boldsymbol{u}$:

$$\boldsymbol{U} = (0,0,0) \quad \text{at} \quad z = -H/2, \qquad\qquad \boldsymbol{U} = (U_0,0,0) \quad \text{at} \quad z = H/2. \tag{2.8}$$

As a result, the perturbed flow satisfies the homogeneous version of the boundary conditions:

$$\boldsymbol{v} = (0,0,0) \quad \text{at} \quad z = -H/2, H/2. \tag{2.9}$$

We choose the background flow $\boldsymbol{U}$ to be independent of time. Using the decomposition $\boldsymbol{u} = \boldsymbol{U} + \boldsymbol{v}$ in the governing equations (2.1) leads to

$$\nabla \cdot \boldsymbol{v} = 0, \tag{2.10a}$$

$$\frac{\partial \boldsymbol{v}}{\partial t} + \boldsymbol{U}\cdot\boldsymbol{\nabla}\boldsymbol{U} + \boldsymbol{U}\cdot\boldsymbol{\nabla}\boldsymbol{v} + \boldsymbol{v}\cdot\boldsymbol{\nabla}\boldsymbol{U} + \boldsymbol{v}\cdot\boldsymbol{\nabla}\boldsymbol{v} = -\frac{1}{\rho}\nabla p + \nu\Delta\boldsymbol{v} + \nu\Delta\boldsymbol{U}. \tag{2.10b}$$

Next, we obtain the equation for the evolution of the kinetic energy of the perturbed flow. We first take the dot product of equation (2.10b) with $\boldsymbol{v}$ and using

the divergence-free condition (2.10a), we obtain:

$$\frac{1}{2}\frac{\partial|\boldsymbol{v}|^2}{\partial t} + (\boldsymbol{U}\cdot\boldsymbol{\nabla}\boldsymbol{U})\cdot\boldsymbol{v} + \frac{1}{2}\boldsymbol{\nabla}\cdot(|\boldsymbol{v}|^2\boldsymbol{U}) + (\boldsymbol{v}\cdot\boldsymbol{\nabla}\boldsymbol{U})\cdot\boldsymbol{v} + \frac{1}{2}\cdot\boldsymbol{\nabla}(|\boldsymbol{v}|^2\boldsymbol{v})$$
$$= -\frac{1}{\rho}\boldsymbol{\nabla}\cdot(p\boldsymbol{v}) + \frac{\nu}{2}\Delta|\boldsymbol{v}|^2 - \nu|\boldsymbol{\nabla}\boldsymbol{v}|^2 + \nu\boldsymbol{\nabla}\cdot(\boldsymbol{v}\cdot\boldsymbol{\nabla}\boldsymbol{U}^T) - \nu\boldsymbol{\nabla}\boldsymbol{U}:\boldsymbol{\nabla}\boldsymbol{v}. \tag{2.11}$$

In the index notation,

$$(\boldsymbol{v}\cdot\boldsymbol{\nabla}\boldsymbol{U}^T)_i = v_j\partial_i U_j \qquad \text{and} \qquad \boldsymbol{\nabla}\boldsymbol{U}:\boldsymbol{\nabla}\boldsymbol{v} = \partial_i v_j \partial_i U_j. \tag{2.12}$$

Next, we use the identity

$$|\boldsymbol{\nabla}\boldsymbol{u}|^2 = |\boldsymbol{\nabla}\boldsymbol{U}|^2 + 2\boldsymbol{\nabla}\boldsymbol{U}:\boldsymbol{\nabla}\boldsymbol{v} + |\boldsymbol{\nabla}\boldsymbol{v}|^2, \tag{2.13}$$

in (2.11), to obtain

$$\frac{1}{2}\frac{\partial|\boldsymbol{v}|^2}{\partial t} + (\boldsymbol{U}\cdot\boldsymbol{\nabla}\boldsymbol{U})\cdot\boldsymbol{v} + \frac{1}{2}\boldsymbol{\nabla}\cdot(|\boldsymbol{v}|^2\boldsymbol{U}) + (\boldsymbol{v}\cdot\boldsymbol{\nabla}\boldsymbol{U})\cdot\boldsymbol{v} + \frac{1}{2}\cdot\boldsymbol{\nabla}(|\boldsymbol{v}|^2\boldsymbol{v}) + \frac{\nu}{2}|\boldsymbol{\nabla}\boldsymbol{u}|^2$$
$$= -\frac{1}{\rho}\boldsymbol{\nabla}\cdot(p\boldsymbol{v}) + \frac{\nu}{2}\Delta|\boldsymbol{v}|^2 - \frac{\nu}{2}|\boldsymbol{\nabla}\boldsymbol{v}|^2 + \nu\boldsymbol{\nabla}\cdot(\boldsymbol{v}\cdot\boldsymbol{\nabla}\boldsymbol{U}^T) + \frac{\nu}{2}|\boldsymbol{\nabla}\boldsymbol{U}|^2. \tag{2.14}$$

We then perform the volume average and a finite time average (from $t = 0$ to T) of (2.14), which leads to

$$\frac{1}{2T}\left[\frac{1}{|\Omega|}\int_\Omega |\boldsymbol{v}|^2\,\mathrm{d}\boldsymbol{x}\right]_{t=T} + \frac{\nu}{2}\langle|\boldsymbol{\nabla}\boldsymbol{u}|^2\rangle_T = \frac{1}{2T}\left[\frac{1}{|\Omega|}\int_\Omega |\boldsymbol{v}|^2\,\mathrm{d}\boldsymbol{x}\right]_{t=0} +$$
$$\frac{\nu}{2}\frac{1}{|\Omega|}\int_\Omega |\boldsymbol{\nabla}\boldsymbol{U}|^2\,\mathrm{d}\boldsymbol{x} - \left\langle\frac{\nu}{2}|\boldsymbol{\nabla}\boldsymbol{v}|^2 + (\boldsymbol{U}\cdot\boldsymbol{\nabla}\boldsymbol{U})\cdot\boldsymbol{v} + (\boldsymbol{v}\cdot\boldsymbol{\nabla}\boldsymbol{U})\cdot\boldsymbol{v}\right\rangle_T. \tag{2.15}$$

Here, $\langle\ \cdot\ \rangle_T$ denotes the finite-time volume average. Taking the limit $T \to \infty$

yields

$$\frac{\nu}{2}\langle|\boldsymbol{\nabla u}|^2\rangle \leq \frac{\nu}{2}\frac{1}{|\Omega|}\int_\Omega |\boldsymbol{\nabla U}|^2\,\mathrm{d}\boldsymbol{x} - \left\langle \frac{\nu}{2}|\boldsymbol{\nabla v}|^2 + (\boldsymbol{U}\cdot\boldsymbol{\nabla U})\cdot\boldsymbol{v} + (\boldsymbol{v}\cdot\boldsymbol{\nabla U})\cdot\boldsymbol{v}\right\rangle. \tag{2.16}$$

Finally, taking $\boldsymbol{v}$ to be any divergence-free vector field that satisfies homogeneous boundary conditions and taking the supremum of the right-hand side leads to

$$\begin{aligned}\varepsilon_\nu \leq & \\ &\sup_{\substack{\boldsymbol{v}(\boldsymbol{x})\\ \boldsymbol{\nabla}\cdot\boldsymbol{v}=0,\\ \boldsymbol{v}|_{\partial\Omega}=\boldsymbol{0}}} \Big(\nu\fint_\Omega |\boldsymbol{\nabla U}|^2\,\mathrm{d}\boldsymbol{x} - \nu\fint_\Omega |\boldsymbol{\nabla v}|^2\,\mathrm{d}\boldsymbol{x} - 2\fint_\Omega (\boldsymbol{U}\cdot\boldsymbol{\nabla U})\cdot\boldsymbol{v}\,\mathrm{d}\boldsymbol{x} \\ &\qquad\qquad -2\fint_\Omega (\boldsymbol{v}\cdot\boldsymbol{\nabla U})\cdot\boldsymbol{v}\,\mathrm{d}\boldsymbol{x}\Big) \\ &= \nu\fint_\Omega |\boldsymbol{\nabla U}|^2\,\mathrm{d}\boldsymbol{x} - \inf_{\substack{\boldsymbol{v}(\boldsymbol{x})\\ \boldsymbol{\nabla}\cdot\boldsymbol{v}=0,\\ \boldsymbol{v}|_{\partial\Omega}=\boldsymbol{0}}} \mathcal{H}_{\boldsymbol{U}}(\boldsymbol{v}),\end{aligned} \tag{2.17}$$

where $\mathcal{H}_{\boldsymbol{U}}$ is given by

$$\mathcal{H}_{\boldsymbol{U}} \coloneqq \underbrace{\nu\fint_\Omega |\boldsymbol{\nabla v}|^2\,\mathrm{d}\boldsymbol{x}}_{I} + \underbrace{2\fint_\Omega (\boldsymbol{U}\cdot\boldsymbol{\nabla U})\cdot\boldsymbol{v}\,\mathrm{d}\boldsymbol{x}}_{II} + \underbrace{2\fint_\Omega (\boldsymbol{v}\cdot\boldsymbol{\nabla U})\cdot\boldsymbol{v}\,\mathrm{d}\boldsymbol{x}}_{III}. \tag{2.18}$$

The goal at this point is to choose a background flow $\boldsymbol{U}$ such that the functional $\mathcal{H}_{\boldsymbol{U}}$ is positive semi definite (i.e., $\mathcal{H}_{\boldsymbol{U}}(\boldsymbol{v}) \geq 0$ for any divergence-free $\boldsymbol{v}$ that satisfies homogeneous boundary conditions), which would then imply a bound on the rate of energy dissipation:

$$\varepsilon_\nu \leq \nu\fint_\Omega |\boldsymbol{\nabla U}|^2\,\mathrm{d}\boldsymbol{x}. \tag{2.19}$$

A simple, traditional choice is to select a background flow that is unidirectional:

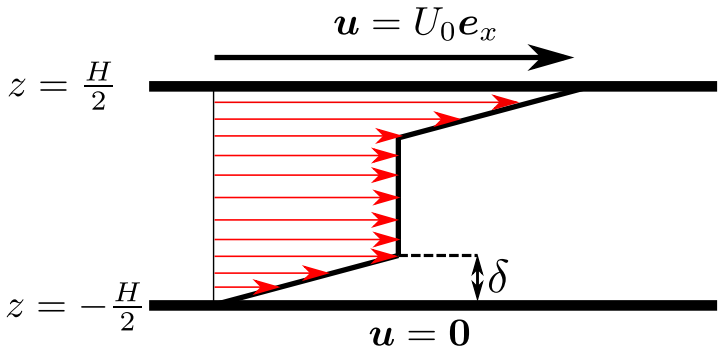

Figure 2.2: shows the one-dimensional background flow profile as defined in (2.20)

.

$\boldsymbol{U} = (U_x(z), 0, 0)$. Furthermore, we choose $U_x(z)$ so that the background flow gradient is non-zero only in thin boundary layers of thickness δ next to the boundaries. The reason for choosing such a background flow is that it allows us to bound sign indefinite terms II and III in (2.18) by the only positive term, I. In particular, we choose

$$U_x(z) = \begin{cases} \frac{U_0 H}{4\delta}\left(1 + \frac{2z}{H}\right) & \text{if} \quad -\frac{H}{2} < z \leq -\frac{H}{2} + \delta, \\ \frac{U_0}{2} & \text{if} \quad -\frac{H}{2} + \delta < z < \frac{H}{2} - \delta, \\ U_0 - \frac{U_0 H}{4\delta}\left(1 - \frac{2z}{H}\right) & \text{if} \quad \frac{H}{2} - \delta \leq z < \frac{H}{2}, \end{cases} \tag{2.20}$$

where the boundary layer thickness δ is a free parameter at this point. Figure 2.2 shows the selected background profile. For this choice of background flow, the functional $\mathcal{H}_{\boldsymbol{U}}$ simplifies to

$$\mathcal{H}_{\boldsymbol{U}} = \frac{1}{HL_xL_y}\int_0^{L_x}\int_0^{L_y}\left[\nu\int_{-\frac{H}{2}}^{\frac{H}{2}}|\boldsymbol{\nabla v}|^2 dz + \frac{U_0}{\delta}\int_{-\frac{H}{2}}^{-\frac{H}{2}+\delta} v_x v_z\, dz + \frac{U_0}{\delta}\int_{\frac{H}{2}-\delta}^{\frac{H}{2}} v_x v_z\, dz\right] dxdy. \tag{2.21}$$

Next, using a simple application of the Cauchy–Schwarz and Young's inequality, we see that

$$\begin{aligned}\left|\int_{-\frac{H}{2}}^{-\frac{H}{2}+\delta} v_x v_z \, dz\right| &\leq \left(\int_{-\frac{H}{2}}^{-\frac{H}{2}+\delta} v_x^2 \, dz\right)^{\frac{1}{2}} \left(\int_{-\frac{H}{2}}^{-\frac{H}{2}+\delta} v_z^2 \, dz\right)^{\frac{1}{2}}, \\ &\leq \frac{1}{2}\int_{-\frac{H}{2}}^{-\frac{H}{2}+\delta} v_x^2 \, dz + \frac{1}{2}\int_{-\frac{H}{2}}^{-\frac{H}{2}+\delta} v_z^2 \, dz. \end{aligned} \tag{2.22}$$

We then use the fundamental theorem of Calculus to write

$$v_x = \int_{-\frac{H}{2}}^{z} \frac{\partial v_x}{\partial z} \mathrm{d}z', \tag{2.23}$$

which implies, for any $z \in (-\frac{H}{2}, -\frac{H}{2}+\delta]$, that

$$\begin{aligned}|v_x| &\leq \int_{-\frac{H}{2}}^{z} \left|\frac{\partial v_x}{\partial z}\right| \mathrm{d}z' \\ &\leq \left(\int_{-\frac{H}{2}}^{z} \left|\frac{\partial v_x}{\partial z}\right|^2 \mathrm{d}z'\right)^{\frac{1}{2}} \left(\int_{-\frac{H}{2}}^{z} 1 \mathrm{d}z'\right)^{\frac{1}{2}} \\ &\leq \sqrt{z+\frac{H}{2}} \left(\int_{-\frac{H}{2}}^{-\frac{H}{2}+\delta} \left|\frac{\partial v_x}{\partial z}\right|^2 \mathrm{d}z'\right)^{\frac{1}{2}}. \end{aligned} \tag{2.24}$$

Squaring both sides, and integrating in z leads to

$$\int_{-\frac{H}{2}}^{-\frac{H}{2}+\delta} v_x^2 \, dz \leq \frac{\delta^2}{2} \int_{-\frac{H}{2}}^{-\frac{H}{2}+\delta} \left|\frac{\partial v_x}{\partial z}\right|^2 \mathrm{d}z'. \tag{2.25}$$

In a similar way, we can also find that

$$\int_{-\frac{H}{2}}^{-\frac{H}{2}+\delta} v_z^2 \, dz \leq \frac{\delta^2}{2} \int_{-\frac{H}{2}}^{-\frac{H}{2}+\delta} \left|\frac{\partial v_z}{\partial z}\right|^2 \mathrm{d}z'. \tag{2.26}$$

Using (2.25) and (2.26) in (2.22), we obtain

$$\left|\int_{-\frac{H}{2}}^{-\frac{H}{2}+\delta} v_x v_z \, dz\right| \leq \frac{\delta^2}{4} \int_{-\frac{H}{2}}^{-\frac{H}{2}+\delta} \left[\left|\frac{\partial v_x}{\partial z}\right|^2 + \left|\frac{\partial v_z}{\partial z}\right|^2\right] \mathrm{d}z' \leq \frac{\delta^2}{4} \int_{-\frac{H}{2}}^{-\frac{H}{2}+\delta} |\boldsymbol{\nabla v}|^2 \mathrm{d}z'. \tag{2.27}$$

In a similar way, one can show

$$\left|\int_{\frac{H}{2}-\delta}^{\frac{H}{2}} v_x v_z \, dz\right| \leq \frac{\delta^2}{4} \int_{\frac{H}{2}-\delta}^{\frac{H}{2}} |\boldsymbol{\nabla v}|^2 \mathrm{d}z'. \tag{2.28}$$

Finally, using (2.27) and (2.28) in (2.21) gives

$$\mathcal{H}_{\boldsymbol{U}} \geq \left(\nu - \frac{\delta}{4} U_0\right) \fint_{\Omega} |\boldsymbol{\nabla v}|^2 \, \mathrm{d}\boldsymbol{x}. \tag{2.29}$$

This expression immediately shows that as long as we choose

$$\delta \leq \frac{4\nu}{U_0}, \tag{2.30}$$

then the functional $\mathcal{H}_{\boldsymbol{U}}$ is positive semi definite. At the same time, the bound on the rate of energy dissipation can be calculated to be

$$\varepsilon_\nu \leq \frac{\nu U_0^2}{2\delta H}. \tag{2.31}$$

Therefore, we choose $\delta = 4\nu/U_0$ to lower this bound as much as possible, which gives

$$\varepsilon_\nu \leq \frac{1}{8} \frac{U_0^3}{H}. \tag{2.32}$$

The bound obtained by (Doering and Constantin, 1994)

$$\varepsilon_\nu \leq \frac{1}{8\sqrt{2}} \frac{U_0^3}{H}, \tag{2.33}$$

is slightly better than the one derived here. In obtaining their bound, Doering and Constantin made partial use of the incompressibility condition satisfied by the perturbed flow, which we did not do here. An even smaller prefactor, corresponding to the best possible bound in the framework of the background method, can be obtained numerically by setting up an optimization problem and solving the corresponding Euler–Lagrange equations numerically. This was done by (Plasting and Kerswell, 2003) (see also (Kumar, 2022a)), who showed that

$$\varepsilon_\nu \leq 0.008553 \frac{U_0^3}{H}. \tag{2.34}$$

2.3 Applications of the background method

Since its initial introduction, there have been several studies carried out using the background method. In this section, we discuss many important examples of fluid systems where the background method has found application. We also note that an excellent review concerning the background method was recently published by (Fantuzzi et al., 2022).

2.3.1 Surface-velocity driven flows

As the name suggests, a surface-velocity-driven flow is a fluid flow in a domain with impermeable boundaries with prescribed tangential velocity conditions. The Couette flow example given above falls under this category.

Another example of a surface-velocity-driven system is the Taylor–Couette flow, which is the flow of fluid between two independently rotating cylinders. (Constantin, 1994) first looked at this problem and obtained a bound on the energy dissipation and the mean torque on the inner cylinder. More recently, (Ding and Marensi, 2019) and (Kumar, 2022a) studied Taylor–Couette flow (where only the inner cylinder rotates) from the perspective of optimal bounds. Using a combination of numerical and analytical computations, we derived an expression that captures how the optimal bound on the energy dissipation rate depends on the radius-ratio η (a parameter that governs the geometry of the domain), (Kumar, 2022a, see). The optimal bound from this paper is

$$\varepsilon \leq 0.0677 \frac{\eta}{(1+\eta)(1+\eta^2)^2}. \tag{2.35}$$

Conveniently, this bound approaches the best bound obtained by (Plasting and Kerswell, 2003) in the limit $\eta \to 1$ (the Couette flow limit).

(Wang, 1997) has previously obtained a bound on the energy dissipation rate for a surface-driven flow in an arbitrary domain with smooth boundaries. However, he did not study this problem from the point-of-view of optimal bounds, as his goal was just to show that the rate of energy dissipation remains bounded in the limit viscosity going to zero.

Recently, (Fan et al., 2021) studied yet another interesting flow setup. They studied the plane Couette flow setup described above but used a mean tangential velocity with added stochastic noise at the top boundary. By modeling the noise using an Ornstein–Uhlenbeck process, (Fan et al., 2021) obtained a bound on the first two moments of the energy dissipation rate as a function of the mean velocity and the variance.

2.3.2 Pressure driven flow in a conduit

There are three studies of pressure-driven conduit flows that derive bounds on the turbulent friction factor, or equivalently on the volume flow rate, using the background method. The first study is due to (Constantin and Doering, 1995), who derived a bound on the friction factor for pressure-driven flow in a plane channel (Poiseuille flow). The friction factor is defined as

$$C_f := \frac{\Delta P}{\Delta L} \frac{h}{\overline{U}^2}, \tag{2.36}$$

where $\Delta P/\Delta L$ is the applied pressure gradient, $\overline{U}$ is the mean velocity field through the conduit and h is a characteristic length, in this case, the channel width. (Constantin and Doering, 1995) showed that the friction factor is bounded from above by a constant. Later, (Plasting and Kerswell, 2005) studied pressure-driven flow in a straight pipe with a circular cross-section. They examined this problem from the point-of-view of optimal bounds by solving the Euler–Lagrange equation arising in the background method framework numerically. They showed that the coefficient of friction for pipe flow is bounded above by a constant, $C_f \leq 0.27$, in this case as well.

In (Kumar, 2020), we investigated pressure-driven flow in toroidal and helical pipes. We obtained bounds on the friction factor as a function of the pipe geometry: its curvature κ and torsion τ. This study is presented in Chapter 4 of this thesis. Similar to (Constantin and Doering, 1995) and (Plasting and Kerswell, 2005), we obtained a bound on the friction factor that is independent of the applied pressure gradient but has a nontrivial geometric dependence. The expression derived is potentially useful in engineering applications and provides the behavior of friction factor in extreme limits of curvature and torsion, which otherwise

would be difficult to obtain. In (Kumar, 2020), we also provided a simple criterion for identifying flow systems (surface-velocity-driven or pressure-driven) where the background method can be successfully applied. This finding demonstrates that it ought to be relatively easy to further study pressure-driven flows, for example, in axially twisted pipes or straight pipes with elliptical cross-sections.

2.3.3 External flows

An important class of problems in fluid mechanics concerns external flows, i.e., flow past an object. This class is directly relevant to many engineering applications, such as flow past an aircraft or a ship. Canonical configurations include: flow past a flat plate, cylinder, sphere or airfoil. Ideally, we would like to apply the background method to these problems and show that the coefficient of friction remains bounded in the limit of high Reynolds numbers. Unfortunately, for most of these flow configurations, no bounds have ever been derived using the background method (or any other rigorous mathematical technique) in the limit of a high Reynolds number. However, there is one external flow problem where the background method can be successfully applied. It is the classical problem of flow past a finite length flat plate kept at zero incidence. For uniform flow past a flat plated, we showed (Kumar and Garaud, 2020, see chapter 3) that the coefficient of friction, $C_D \leq 295.49$.

2.3.4 Rayleigh–Bénard convection

Rayleigh–Bénard convection describes the buoyancy-driven motion of fluid between two horizontal differentially heated parallel plates, where the bottom plate is hot and the top plate is cold. Rayleigh–Bénard convection is arguably the

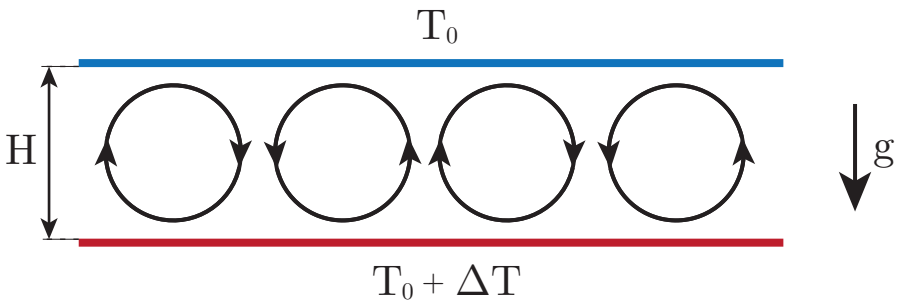

Figure 2.3: depicts convection between two differentially heated walls driven by buoyancy.

most studied fluid configuration using the background method. In the nondimensional form, the governing equations (incompressible Navier–Stokes equation under Boussinesq approximation coupled with an advection-diffusion equation) are given by

$$\nabla \cdot \boldsymbol{u} = 0, \tag{2.37a}$$

$$\frac{\partial \boldsymbol{u}}{\partial t} + \boldsymbol{u} \cdot \boldsymbol{\nabla} \boldsymbol{u} = -\nabla p + Pr \Delta \boldsymbol{u} + RaPrT\boldsymbol{e}_z, \tag{2.37b}$$

$$\frac{\partial T}{\partial t} + \boldsymbol{u} \cdot \nabla T = \Delta T. \tag{2.37c}$$

The two nondimensional parameters are the Prandtl number

$$Pr = \frac{\nu}{\kappa},$$

which is the ratio of viscosity ν to thermal diffusivity κ, and the Rayleigh number

$$Ra = \frac{g\alpha \Delta T H^3}{\nu \kappa},$$

which is the ratio of the buoyancy force to the viscous damping force, and thus governs the intensity of the convection. Here, g is the acceleration of gravity, α is

the coefficient of linear thermal expansion, $\Delta T = T_{bottom} - T_{top}$ is the temperature difference of the bottom and top boundary and H is the distance between the plates. Figure 2.37 shows a schematic of the Rayleigh–Bénard setup. The quantity of interest in Rayleigh–Bénard convection is the nondimensional heat transfer known as the Nusselt number, given by

$$Nu = 1 + \langle u_z T \rangle, \tag{2.38}$$

where the angle brackets denote the long-time volume average and u_z is the vertical component of the velocity field.

The standard Rayleigh–Bénard convection setup

In the standard Rayleigh–Bénard convection setup, the governing equations (2.37) are supplemented with no-slip boundary conditions on the top and the bottom walls:

$$\boldsymbol{u} = \mathbf{0} \quad \text{at} \quad z = 0, 1,$$

and the temperature boundary conditions:

$$T = 1 \quad \text{at} \quad z = 0, \qquad \text{and} \qquad T = 0 \quad \text{at} \quad z = 1.$$

(Doering and Constantin, 1996) derived an upper bound on the Nusselt number as a function of the Rayleigh number and the Prandtl number in that configuration. They showed that the Nusselt number is bounded by the square root of the Rayleigh number, a bound that is uniform in the Prandtl number. In particular,

they obtained

$$Nu - 1 \leq \frac{1}{6} Ra^{\frac{1}{2}}. \tag{2.39}$$

The optimal prefactor, in the framework of the background method, was found by (Plasting and Kerswell, 2003) to be

$$Nu - 1 \leq 0.02634 Ra^{\frac{1}{2}}. \tag{2.40}$$

Rayleigh–Bénard convection at high Prandtl number

In the limit of high Prandtl number, $Pr \to \infty$, the viscous forces dominate over the inertial forces. In this limit, the momentum equation (2.37b) can be approximated by the simplified linear equation:

$$0 = -\nabla p + Pr \Delta \boldsymbol{u} + RaPrT\boldsymbol{e}_z. \tag{2.41}$$

Furthermore, in two dimensions, using the incompressibility condition, (2.41) can be recast as a fourth-order elliptic equation:

$$\Delta^2 u_z = -Ra \Delta_{\|} T, \tag{2.42}$$

where $\Delta_{\|} = \partial_x^2 + \partial_y^2$. The boundary conditions accompanying (2.42) are

$$u_z = 0, \partial_z u_z = 0 \qquad \text{at} \quad z = 0, 1. \tag{2.43}$$

Using a typical background temperature profile (with a vertical varying temperature profile that is flat in the bulk and has steep gradients in boundary layers

of thickness δ) along with a few improved estimates on the vertical component of the velocity field u_z, (Doering and Constantin, 2001) proved the following bound on the Nusselt number:

$$Nu \leq 0.2545 Ra^{\frac{2}{5}}.$$

Later, using a logarithmic background profile, (Doering et al., 2006) improved this bound to

$$Nu \leq 0.64366 Ra^{\frac{1}{3}} (\log Ra)^{\frac{1}{3}},$$

which was subsequently improved further to

$$Nu \lesssim Ra^{\frac{1}{3}} (\log Ra)^{\frac{1}{15}}$$

by (Otto and Seis, 2011) using a few finer estimates. Using a slightly approach method (by combining a maximum principle for the temperature field with the background method) (Otto and Seis, 2011) further brought this bound closer to a $Ra^{\frac{1}{3}}$ scaling, showing that

$$Nu \lesssim Ra^{\frac{1}{3}} (\log \log Ra)^{\frac{1}{3}}.$$

Two dimensional Rayleigh–Bénard convection between stress free boundaries

For finite Pr, it is also possible to improve the bound on the Nusselt number in two dimensions over the one given in (2.39) when the no-slip boundary condition

on the velocity field is replaced with stress-free boundary conditions:

$$\partial_z u_x = 0, \; u_z = 0 \quad \text{at} \quad z = 0, 1. \tag{2.44}$$

The improvement in the bound comes from taking advantage of an integral constraint extracted from the vorticity equation. Numerical investigations of (Otero et al., 2002) provided earlier evidence that the upper bound on the Nusselt number, in this case, scales as $Ra^{\frac{5}{12}}$ rather than $Ra^{\frac{1}{2}}$. Later, (Whitehead and Doering, 2011b) rigorously showed that

$$Nu \leq 0.2891 Ra^{\frac{5}{12}}.$$

For convection in a box with an aspect ratio (horizontal to vertical) $2\sqrt{2}$, (Wen et al., 2015) calculated the optimal prefactor and obtained the bound

$$Nu \leq 0.106 Ra^{\frac{5}{12}}.$$

In Rayleigh–Bénard convection, the ultimate scaling theory ($Nu \sim Ra^{\frac{1}{2}}$) is based on the idea that the primary mode of heat transfer is convection. Furthermore, this theory does not distinguish between different boundary conditions or spatial dimensions. The fact that the formal $Nu \lesssim Ra^{\frac{5}{12}}$ bound obtained in the case of 2D, stress-free boundaries, therefore indicates that molecular transport cannot generally be neglected, contrary to the predictions of the ultimate scaling, (Whitehead and Doering, 2011b, see).

More recently, (Drivas et al., 2022b) considered Rayleigh–Bénard convection in two dimensions with a Naiver-slip boundary condition. They obtained a bound on the Nusselt number as a function of the Rayleigh number and the Navier–

slip. Their bound tends to $Ra^{\frac{1}{2}}$ in the no-slip case and $Ra^{\frac{5}{12}}$ in the infinite-slip (stress-free) case, and therefore, connects the two limits.

Rayleigh–Bénard convection between rough boundaries

A bound on heat transfer for Rayleigh–Bénard convection has been obtained in the case of rough boundaries as well. (Goluskin and Doering, 2016) considered a model setup in which the hot and cold boundaries, $h^B(x,y)$ and $h^T(x,y)$ are taken to be graphs of continuous function such that the gradients of these graphs are square integrable, i.e., $\left\|\nabla h^B\right\|_2, \left\|\nabla h^T\right\|_2 < \infty$. They derived a bound that is

$$Nu \leq (0.242 + \|\nabla h\|_2^2) Ra^{\frac{1}{2}}, \tag{2.45}$$

valid at high Rayleigh number. The scaling in Ra is therefore the same as in the case of smooth boundaries. However, the importance of this bound comes from the fact that the scaling $Nu \sim Ra^{\frac{1}{2}}$ is indeed observed in numerical simulations of the Rayleigh–Bénard convection with rough boundaries (Toppaladoddi et al., 2017; Zhu et al., 2017) (Toppaladoddi et al., 2021), which establishes the sharpness of the result in that case.

2.3.5 Internally heated convection

Internally heated convection is similar to the Rayleigh–Bénard convection, except that the convection is driven by volumetric heating instead of a temperature differential imposed at between two boundaries. Therefore, the equation (2.37c) is replaced with

$$\frac{\partial T}{\partial t} + \boldsymbol{u} \cdot \nabla T = \Delta T + 1, \tag{2.46}$$

and the definition of the Rayleigh number becomes

$$Ra = \frac{g\alpha H^5 Q^*}{\rho c_p \kappa \nu^2}, \tag{2.47}$$

where Q^* is a constant volumetric heating rate and c_p is the specific heat capacity of the fluid. The velocity field satisfies a no-slip condition on the boundaries. Depending on the boundary condition for the temperature field, there are three configuration that are typically studied, defined as IH1, IH2 and IH3 in (Goluskin, 2016):

$$\begin{aligned} T(x,y,0,t) = T(x,y,1,t) = 0 \quad &\text{for} \quad \text{IH1}, \\ \partial_z T(x,y,0,t) = 0,\ \partial_z T(x,y,1,t) = -1 \quad &\text{for} \quad \text{IH2}, \\ \partial_z T(x,y,0,t) = T(x,y,1,t) = 0 \quad &\text{for} \quad \text{IH3}. \end{aligned}$$

An important nondimensional quantity that is often looked at in internally heated convection is the mean vertical heat flux $\langle u_z T \rangle$. In the IH1 configuration, the mean vertical heat flux quantifies the asymmetry of the heat fluxes through top and bottom boundary. In these two cases, the mean vertical heat flux is related to the difference of the horizontally-averaged temperature between the top and the bottom wall. In IH2 and IH3 configuration, the mean vertical heat flux is also linked to the Nusselt number as

$$Nu = \frac{1}{1 - 2\langle u_z T \rangle}. \tag{2.48}$$

For the IH1 case, using a minimum principle for the temperature field, (Arslan et al., 2021b) provided the initial numerical indication that the vertical heat flux

$\langle u_z T \rangle$ is smaller than $1/2$ and the difference $1/2 - \langle u_z T \rangle$ appears to decrease faster than any power law in Rayleigh number. We later rigorously established a rigorous bound

$$\langle u_z T \rangle \leq \frac{1}{2} - c_1 Ra^{\frac{1}{5}} \exp\left(-c_2 Ra^{\frac{3}{5}}\right), \tag{2.49}$$

where c_1 and c_2 are positive constants (Kumar et al., 2022). For the IH2 case, the best known bound is

$$\langle u_z T \rangle \leq \frac{1}{2}\left(\frac{1}{2} + \frac{1}{\sqrt{3}}\right) - 1.6552 Ra^{-\frac{1}{3}}, \tag{2.50}$$

which was obtained by (Arslan et al., 2021a). For the IH3 configuration, a bound on the vertical heat flux was obtained by (Kumar et al., 2022):

$$\langle u_z T \rangle \leq \frac{1}{2} - \frac{c_3}{Ra^{\frac{1}{5}}} \exp\left(-c_4 Ra^{\frac{3}{5}}\right), \tag{2.51}$$

which also gives an upper bound on the Nusselt number as

$$Nu \leq \frac{1}{2c_3} Ra^{\frac{1}{5}} \exp\left(-c_4 Ra^{\frac{3}{5}}\right). \tag{2.52}$$

More recently, (Arslan et al., 2023) also studied internally heated convection in the high Prandtl number limit and obtained bounds on the vertical heat flux in that case as well.

Chapter 3

Bound on the drag coefficient for a flat plate in a uniform flow

This chapter is based on the paper Kumar and Garaud (2020) published in the Journal of Fluid Mechanics, Volume 900, 10 October 2020, A6.

3.1 Introduction

The idea of obtaining bounds on mean quantities using analysis techniques goes back to Howard (1963), who was interested in deriving an upper bound on the heat transfer in Rayleigh–Bénard convection, and inspired by Malkus' maximal transport hypothesis (Malkus, 1954). With the help of variational techniques, Howard (1963) obtained a formal bound on the heat transfer for solutions satisfying two integral constraints derived from the governing equations. Busse (1969, 1970) subsequently improved and extended Howard's technique to obtain bounds on the rate of energy dissipation in plane Couette flow and Poiseuille flow. Later, in a series of papers (Doering and Constantin, 1992, 1994; Constantin and Doering,

1995; Doering and Constantin, 1996), Doering and Constantin laid the foundation of a new bounding method called 'the background method'. This method also requires certain integral constraints to be satisfied with the help of trial functions to obtain a bound on the desired quantity. The freedom of choice of trial functions makes the Doering–Constantin technique relatively easier to implement than the Howard–Busse technique. Kerswell (1997, 1998) showed that the best bounds obtained using the Howard–Busse technique and the Doering–Constantin technique are the same for turbulent shear flows, thereby establishing the link between the two approaches.

Until now, all the applications of the background method have focused on flows confined between solid boundaries. Examples include bounds on the rate of energy dissipation in surface-velocity-driven flows (Doering and Constantin, 1992, 1994; Marchioro, 1994; Nicodemus et al., 1997; Wang, 1997; Hoffmann and Vitanov, 1999; Plasting and Kerswell, 2003), pressure-driven flows (Constantin and Doering, 1995), and surface-stress-driven flows (Tang et al., 2004; Hagstrom and Doering, 2014); bounds on the heat transfer in Rayleigh–Bénard convection in various settings (Doering and Constantin, 1996, 2001; Otero et al., 2002; Plasting and Ierley, 2005; Wittenberg, 2010; Whitehead and Doering, 2011b; Whitehead and Wittenberg, 2014; Goluskin, 2015; Goluskin and Doering, 2016; Fantuzzi, 2018) and Bénard–Marangoni convection (Hagstrom and Doering, 2010; Fantuzzi et al., 2018, 2020); bounds on buoyancy flux in stably stratified shear flows (Caulfield and Kerswell, 2001; Caulfield, 2005).

Despite the tremendous success of the background method to confined flows, however, there has been no application to external flows, such as flows past a streamlined or bluff body. Studying external flow problems is crucial because of the numerous potential applications in aerospace and naval engineering, including

the design of airfoils, turbine blades, ship hulls, and submarines, to name a few. An important question of investigation in all these cases is that of the dependence of the drag coefficient on the Reynolds number. In general, this dependence can be quite complex. For example, in a uniform flow past a cylinder, the flow dynamics undergo several transitions, which leads to a complex dependence of the drag coefficient on the Reynolds number (see Williamson, 1996). Ideally, one would like to construct a theory to explain and quantify this complex dependence; however, this task is too ambitious. As pointed out by Roshko (1993), there is no theory to predict the drag coefficient associated with the flow past a cylinder at moderate or large Reynolds numbers, a statement that still holds today. As such, obtaining instead a strict upper bound on the drag coefficient that has the same scaling with Reynolds number as the observations would be a significant and useful first step in the right direction. Howard (1972) and Doering and Constantin (1994) have also previously raised the question of the extensibility of bounding techniques to external flows, specifically for a flow past a sphere. However, this extension has remained elusive due to various mathematical difficulties. Proving bounds on the drag coefficient for flow past an object therefore remains an open problem. As we shall demonstrate in this work, the case of flow past a flat plate avoids these difficulties, enabling us to apply the background method to an external flow problem for the first time.

The flow past a flat plate is a classical fluid problem that has served as a benchmark for aerodynamicists for over a century. The first breakthrough towards obtaining an analytical result was due to Prandtl (1904). He postulated that the effect of viscosity would only be significant in a thin layer close to the surface of the body. This approximation led to a reduction of the equations that were subsequently solved by Blasius (1908) for a semi-infinite plate in the lami-

nar regime using the similarity technique. The problem considered in this paper, which is more relevant to engineering applications, is the problem of a finite length plate. Based on Blasius's solution, the drag coefficient for a finite length plate in the laminar regime decreases as $O(Re^{-\frac{1}{2}})$ (see Schlichting and Gersten, 2016, p. 160), where $Re = U_\infty L/\nu$ is the Reynolds number based on the free stream velocity U_∞, the length of the plate L, and the kinematic viscosity ν. Wake formation behind the plate leads to a higher-order correction to the Blasius solution, which is quite complicated to obtain (see Stewartson, 1969; Messiter, 1970; Jobe and Burggraf, 1974). In the turbulent regime no exact analytical solutions exist, and one must rely on empirical formulae for the drag coefficient obtained from experimental measurements. One of the standard empirical formulae (see Schlichting and Gersten, 2016, p. 583) suggests that the drag coefficient for the flat plate decreases as $O((\ln Re)^{-2})$ at high Reynolds number, when the flow is turbulent. As we shall demonstrate in this manuscript, it is possible to obtain a bound on the drag coefficient for a flat plate. This bound is independent of the Reynolds number, and therefore only a logarithmic factor away from the experimental measurements at high Reynolds number.

The rest of the paper is arranged as follows. In §3.2, we describe the flow configuration and define the drag coefficient. In §3.3, we describe the background method in the context of a flat plate. In §3.4, we divide our domain into subdomains for the purpose of defining the background flow. We then obtain bounds on quantities in different subdomains and combine them to obtain a bound on the drag coefficient. Finally, we conclude in §3.5.

3.2 Flow configuration

Consider a plate of zero thickness and length L kept at zero incidence in a uniform flow of an incompressible Newtonian fluid with flow speed U_∞ and far-field pressure p_∞. The extent of the plate is infinite in the spanwise direction. Let ρ and ν, respectively, be the density and kinematic viscosity of the fluid. The equations governing the flow are the incompressible Navier–Stokes equations and in the non-dimensional form are given by

$$\begin{aligned} &\boldsymbol{\nabla} \cdot \boldsymbol{u} = 0, \\ &\frac{\partial \boldsymbol{u}}{\partial t} + \boldsymbol{u} \cdot \boldsymbol{\nabla} \boldsymbol{u} = -\boldsymbol{\nabla} p + \frac{1}{Re} \nabla^2 \boldsymbol{u}, \end{aligned} \tag{3.1}$$

where we have used the following non-dimensionalization:

$$\boldsymbol{u} = \frac{\boldsymbol{u}^*}{U_\infty},\ p = \frac{p^* - p_\infty}{\rho U_\infty^2},\ t = \frac{U_\infty t^*}{L},\ \boldsymbol{x} = \frac{\boldsymbol{x}^*}{L}. \tag{3.2}$$

Here, $\boldsymbol{u}$, p, t, and $\boldsymbol{x}$ are the non-dimensional velocity field, pressure field, time and spatial coordinates, respectively, and $Re = U_\infty L/\nu$ is the Reynolds number for the flow. The quantities with a star in superscript are the dimensional quantities. The flow configuration can be best described in a Cartesian coordinate system $\boldsymbol{x} = (x_1, x_2, x_3)$. We fix the origin of the coordinate system at the leading edge of the plate, with x_1 pointing in the downstream direction, x_2 pointing upward, normal to the plate, and x_3 being the spanwise direction. The boundary condition on the surface of the plate is no-slip, i.e.,

$$\boldsymbol{u} = \boldsymbol{0} \quad \text{if} \quad x_2 = 0 \text{ and } 0 \leq x_1 \leq 1. \tag{3.3}$$

Far away from the plate, the flow is uniform, and the pressure is constant. This condition in non-dimensional variables can be written as

$$\boldsymbol{u} \to \boldsymbol{e}_{x_1},\ p \to 0 \quad \text{as} \quad x_1,\ x_2 \to \pm\infty, \tag{3.4}$$

where, $\boldsymbol{e}_{x_1}$ denotes the unit vector in the streamwise direction. Finally, we also assume that the flow is periodic in the spanwise direction (x_3), with a non-dimensional period L_s. The domain of interest therefore is

$$\Omega = \{(x_1, x_2, x_3) | x_3 \in [0, L_s]\} \setminus \{(x_1, 0, x_3) | x_1 \in [0, 1], x_3 \in [0, L_s]\}. \tag{3.5}$$

3.2.1 Drag coefficient

Let F^* denote the long-time-averaged dimensional drag force on a section of the plate with dimensional length L_s^* in the spanwise direction, where $L_s^* = LL_s$. For a flat plate in a uniform flow at zero incidence, the drag force is entirely due to skin friction, so we can obtain F^* in terms of the shear-stress integrated over the top and bottom surface of the plate. We define the drag coefficient to be the non-dimensional force per unit area:

$$C_D = \frac{F^*}{(2LL_s^*)} \Big/ \frac{1}{2}\rho U_\infty^2. \tag{3.6}$$

In terms of non-dimensional variables, the drag coefficient is given by

$$C_D = \frac{F}{ReL_s}, \tag{3.7}$$

where $F = F^*/\rho\nu U_\infty L$ is the non-dimensional force that can be written as

$$F = \frac{F^*}{\rho\nu U_\infty L} = \int_0^{L_s}\int_0^1 \overline{\tau_t}\, dx_1 dx_3 + \int_0^{L_s}\int_0^1 \overline{\tau_b}\, dx_1 dx_3, \tag{3.8}$$

where τ_t and τ_b are the non-dimensional shear-stresses on the top and bottom surfaces of the plate at point $(x_1, 0, x_3)$:

$$\tau_t = \left.\frac{\partial u_1}{\partial x_2}\right|_{x_2\to 0^+} \qquad \tau_b = -\left.\frac{\partial u_1}{\partial x_2}\right|_{x_2\to 0^-}, \tag{3.9}$$

and the overbar denotes the long-time average given as

$$\overline{[\,\cdot\,]} = \lim_{T\to\infty}\langle[\,\cdot\,]\rangle_T, \quad \text{where } \langle[\,\cdot\,]\rangle_T = \frac{1}{T}\int_0^T [\,\cdot\,]\, dt. \tag{3.10}$$

3.2.2 The relationship between drag coefficient and non-dimensional dissipation

Let $\tilde{\boldsymbol{u}}$ denote the perturbation from the uniform flow, mathematically expressed as

$$\tilde{\boldsymbol{u}} = \boldsymbol{u} - \boldsymbol{e}_{x_1}. \tag{3.11}$$

The governing equations for $\tilde{\boldsymbol{u}}$ are given by

$$\boldsymbol{\nabla}\cdot\tilde{\boldsymbol{u}} = 0, \tag{3.12}$$

$$\frac{\partial\tilde{\boldsymbol{u}}}{\partial t} + (\boldsymbol{e}_{x_1} + \tilde{\boldsymbol{u}})\cdot\boldsymbol{\nabla}\tilde{\boldsymbol{u}} = -\boldsymbol{\nabla}p + \frac{1}{Re}\nabla^2\tilde{\boldsymbol{u}}, \tag{3.13}$$

along with the boundary and the far-field conditions:

$$\tilde{\boldsymbol{u}} = -\boldsymbol{e}_{x_1} \quad \text{if} \quad x_2 = 0 \text{ and } 0 \leq x_1 \leq 1. \tag{3.14}$$

$$\tilde{\boldsymbol{u}} \to \boldsymbol{0},\ p \to 0 \quad \text{as} \quad x_1,\ x_2 \to \pm\infty. \tag{3.15}$$

The energy equation for $\tilde{\boldsymbol{u}}$ can be obtained by taking the dot product of equation (3.13) with $\tilde{\boldsymbol{u}}$ and using the divergence-free condition (3.12), and is given by

$$\frac{1}{2}\frac{\partial|\tilde{\boldsymbol{u}}|^2}{\partial t} + \frac{1}{2}\boldsymbol{\nabla}\cdot\left[(\boldsymbol{e}_{x_1}+\tilde{\boldsymbol{u}})|\tilde{\boldsymbol{u}}|^2\right] = -\boldsymbol{\nabla}\cdot(\tilde{\boldsymbol{u}}\,p) + \frac{1}{2Re}\nabla^2|\tilde{\boldsymbol{u}}|^2 - \frac{1}{Re}|\boldsymbol{\nabla}\tilde{\boldsymbol{u}}|^2. \tag{3.16}$$

We define a domain Ω_R as

$$\Omega_R = \{(x_1, x_2, x_3) | x_3 \in [0, L_s], x_1^2 + x_2^2 \leq R^2\} \cap \Omega, \tag{3.17}$$

and we integrate equation (3.16) over Ω_R with $R > 1$. After using the divergence theorem (see Folland, 2003, pp. 240) and the boundary condition on the surface of the plate, this results in

$$\begin{aligned}\frac{1}{2}\frac{d}{dt}\int_{\Omega_R}|\tilde{\boldsymbol{u}}|^2\,d\boldsymbol{x} + \frac{1}{2}\int_{S_R}|\tilde{\boldsymbol{u}}|^2\,(\boldsymbol{e}_{x_1}+\tilde{\boldsymbol{u}})\cdot\boldsymbol{n}\,d\boldsymbol{s} = \\ -\int_{S_R} p\,\tilde{\boldsymbol{u}}\cdot\boldsymbol{n}\,d\boldsymbol{s} + \frac{1}{2Re}\int_{S_R}\boldsymbol{\nabla}|\tilde{\boldsymbol{u}}|^2\cdot\boldsymbol{n}\,d\boldsymbol{s} - \frac{1}{Re}\int_{\Omega_R}|\boldsymbol{\nabla}\tilde{\boldsymbol{u}}|^2 d\boldsymbol{x} \\ +\frac{1}{2Re}\int_0^{L_s}\int_0^1\left[(\boldsymbol{\nabla}|\tilde{\boldsymbol{u}}|^2)|_{x_2\to 0^-} - (\boldsymbol{\nabla}|\tilde{\boldsymbol{u}}|^2)|_{x_2\to 0^+}\right]\cdot\boldsymbol{e}_{x_1}\,dx_1 dx_3,\end{aligned} \tag{3.18}$$

where S_R is the outer boundary of Ω_R, and $\boldsymbol{n}$ denotes the unit normal vector on the boundary. At this point, we make two assumptions. We consider only those solutions for which the decay rate of the flow variables $\tilde{\boldsymbol{u}}$ and p far from the plate

is sufficient to conclude that in equation (3.18) terms with an integral over S_R vanish, while terms with a volume integral over Ω_R converge as $R \to \infty$ uniformly in time $t \in [0, T]$ for any T. We also assume that the flow achieves a statistically steady-state. Next, we perform the following sequence of steps on equation (3.18):

(i) We take the time average of the equation from $t = 0$ to $t = T$.

(ii) We take the limit $R \to \infty$.

(iii) We take the limit $T \to \infty$.

We obtain the following result:

$$C_D = \frac{1}{ReL_s} \overline{||\boldsymbol{\nabla} \tilde{\boldsymbol{u}}||_2^2}. \tag{3.19}$$

where $||\cdot||_2$ denotes the L^2-norm defined as

$$||\cdot||_2 = \left(\int_\Omega |\cdot|^2 d\boldsymbol{x} \right)^{\frac{1}{2}}. \tag{3.20}$$

Now $\boldsymbol{u} = \tilde{\boldsymbol{u}} + \boldsymbol{e}_{x_1}$, which implies $\boldsymbol{\nabla} \boldsymbol{u} = \boldsymbol{\nabla} \tilde{\boldsymbol{u}}$. Therefore, in terms of the total velocity field, the drag coefficient is

$$C_D = \frac{1}{ReL_s} \overline{||\boldsymbol{\nabla} \boldsymbol{u}||_2^2}. \tag{3.21}$$

This type of relation is commonly used in calculations of the drag force on bubbles and drops (Moore, 1963; Harper and Moore, 1968; Leal, 2007, pp. 747-748) where it is possible to calculate the dissipation in the flow field with higher order of accuracy than the stresses on the surface.

3.3 Background method formulation

The background method formulation used here is the same as given in Doering and Constantin (1994). The background method proceeds by decomposing the total flow ($\boldsymbol{u}$) into a divergence-free background flow ($\boldsymbol{U}$) and a perturbed flow ($\boldsymbol{v}$), i.e., $\boldsymbol{u} = \boldsymbol{U} + \boldsymbol{v}$ with the condition that $\boldsymbol{\nabla} \cdot \boldsymbol{U} = 0$ and $\boldsymbol{\nabla} \cdot \boldsymbol{v} = 0$. We require that the background flow $\boldsymbol{U}$ satisfies the no-slip boundary condition at the surface of the plate, and that far away from the surface, $\boldsymbol{U}$ approaches $\boldsymbol{e}_{x_1}$ sufficiently quickly so that the far-field decay rate of perturbations $\boldsymbol{v} = \boldsymbol{u} - \boldsymbol{U}$ is comparable to that of $\tilde{\boldsymbol{u}}$ in the previous section. After some of the usual algebraic manipulations, we obtain the energy equation of the perturbed flow as

$$\begin{aligned}\frac{1}{2}\frac{\partial|\boldsymbol{v}|^2}{\partial t} + \frac{1}{2}\boldsymbol{\nabla}\cdot(\boldsymbol{v}|\boldsymbol{v}|^2) + \frac{1}{2}\boldsymbol{\nabla}\cdot(\boldsymbol{U}|\boldsymbol{v}|^2) + (\boldsymbol{v}\cdot\boldsymbol{\nabla}\boldsymbol{U})\cdot\boldsymbol{v} + (\boldsymbol{U}\cdot\boldsymbol{\nabla}\boldsymbol{U})\cdot\boldsymbol{v} \\ = -\boldsymbol{\nabla}\cdot(p\boldsymbol{v}) + \frac{1}{Re}\boldsymbol{\nabla}\cdot(\boldsymbol{v}\cdot\boldsymbol{\nabla}\boldsymbol{U}^T) - \frac{1}{Re}\boldsymbol{\nabla}\boldsymbol{U}:\boldsymbol{\nabla}\boldsymbol{v} \\ + \frac{1}{2Re}\nabla^2|\boldsymbol{v}|^2 - \frac{1}{Re}|\boldsymbol{\nabla}\boldsymbol{v}|^2, \quad (3.22)\end{aligned}$$

where, in index notation,

$$(\boldsymbol{v}\cdot\boldsymbol{\nabla}\boldsymbol{U}^T)_i = v_j\partial_i U_j, \qquad \text{and} \qquad \boldsymbol{\nabla}\boldsymbol{U}:\boldsymbol{\nabla}\boldsymbol{v} = \partial_i v_j \partial_i U_j. \quad (3.23)$$

Using the following identity

$$\boldsymbol{\nabla}\boldsymbol{u}:\boldsymbol{\nabla}\boldsymbol{u} = \boldsymbol{\nabla}\boldsymbol{U}:\boldsymbol{\nabla}\boldsymbol{U} + \boldsymbol{\nabla}\boldsymbol{v}:\boldsymbol{\nabla}\boldsymbol{v} + 2\boldsymbol{\nabla}\boldsymbol{U}:\boldsymbol{\nabla}\boldsymbol{v} \quad (3.24)$$

in (3.22), we obtain

$$\frac{1}{2}\frac{\partial|\boldsymbol{v}|^2}{\partial t}+\frac{1}{2}\boldsymbol{\nabla}\cdot(\boldsymbol{v}|\boldsymbol{v}|^2)+\frac{1}{2}\boldsymbol{\nabla}\cdot(\boldsymbol{U}|\boldsymbol{v}|^2)+(\boldsymbol{v}\cdot\boldsymbol{\nabla}\boldsymbol{U})\cdot\boldsymbol{v}+(\boldsymbol{U}\cdot\boldsymbol{\nabla}\boldsymbol{U})\cdot\boldsymbol{v}$$
$$+\frac{1}{2Re}|\boldsymbol{\nabla}\boldsymbol{u}|^2=-\boldsymbol{\nabla}\cdot(p\boldsymbol{v})+\frac{1}{Re}\boldsymbol{\nabla}\cdot(\boldsymbol{v}\cdot\boldsymbol{\nabla}\boldsymbol{U}^T)+\frac{1}{2Re}\nabla^2|\boldsymbol{v}|^2$$
$$+\frac{1}{2Re}|\boldsymbol{\nabla}\boldsymbol{U}|^2-\frac{1}{2Re}|\boldsymbol{\nabla}\boldsymbol{v}|^2. \tag{3.25}$$

Next, we perform the following sequence of steps on equation (3.25):

(i) We integrate it over Ω_R for $R>1$.

(ii) We take the time average of the equation from $t=0$ to $t=T$.

(iii) We take the limit $R\to\infty$.

(iv) We take the limit $T\to\infty$.

and obtain the following result:

$$\frac{1}{2Re}\overline{||\boldsymbol{\nabla}\boldsymbol{u}||_2^2}=\frac{1}{2Re}||\boldsymbol{\nabla}\boldsymbol{U}||_2^2$$
$$-\lim_{T\to\infty}\left\langle\frac{1}{2Re}||\boldsymbol{\nabla}\boldsymbol{v}||_2^2+\int_\Omega(\boldsymbol{v}\cdot\boldsymbol{\nabla}\boldsymbol{U})\cdot\boldsymbol{v}\,d\boldsymbol{x}+\int_\Omega(\boldsymbol{U}\cdot\boldsymbol{\nabla}\boldsymbol{U})\cdot\boldsymbol{v}\,d\boldsymbol{x}\right\rangle_T. \tag{3.26}$$

In obtaining the above equation, we have used the assumption of a statistically steady-state and appropriate far-field decay rates for the flow variables, as in §3.2.2. Next, we define the functional $\mathcal{H}(\boldsymbol{v})$ as follows:

$$\mathcal{H}(\boldsymbol{v})=\underbrace{\int_\Omega(\boldsymbol{v}\cdot\boldsymbol{\nabla}\boldsymbol{U})\cdot\boldsymbol{v}\,d\boldsymbol{x}}_{I}+\underbrace{\int_\Omega(\boldsymbol{U}\cdot\boldsymbol{\nabla}\boldsymbol{U})\cdot\boldsymbol{v}\,d\boldsymbol{x}}_{II}+\underbrace{\frac{1}{2Re}||\boldsymbol{\nabla}\boldsymbol{v}||_2^2}_{III}. \tag{3.27}$$

The key to the background method is to find a constant γ and an incompressible background flow $\boldsymbol{U}$, with $\boldsymbol{U}\to\boldsymbol{e}_{x_1}$ as $|\boldsymbol{x}|\to\infty$ and satisfying the no-slip boundary condition at the surface of the plate, such that $\mathcal{H}(\boldsymbol{v})+\gamma$ is nonnegative for all

time-independent incompressible vector fields $\boldsymbol{v}$ that decay to zero at infinity. This ensures that $\mathcal{H}(\boldsymbol{v}) + \gamma \geq 0$ also for time-dependent velocity fields $\boldsymbol{v}$ satisfying the flow's equations of motion. If we can find such $\boldsymbol{U}$ and γ, then (3.26) yields a bound

$$\overline{||\boldsymbol{\nabla u}||_2^2} \leq ||\boldsymbol{\nabla U}||_2^2 + 2Re\gamma. \tag{3.28}$$

Combining this with (3.21) gives an upper bound on the drag coefficient,

$$C_D \leq \frac{1}{Re\ L_s}||\boldsymbol{\nabla U}||_2^2 + \frac{2}{L_s}\gamma. \tag{3.29}$$

3.4 Upper bound on drag coefficient

Obtaining the *best* upper bound on the drag coefficient using the background method requires finding the optimal background flow that would minimize the right-hand side of (3.29). However, it is not possible to find this optimal background flow analytically for our problem, and even with the help of numerical methods this task is quite challenging (Plasting and Kerswell, 2003; Wen et al., 2013, 2015; Fantuzzi and Wynn, 2015, 2016; Fantuzzi, 2018; Tilgner, 2017, 2019) and is a study in its own right. Therefore, in this paper, we restrict the analysis to a simple family of background flow fields, involving a single free parameter, for which the algebra remains tractable. In the next subsections, we will therefore have the following tasks at hand: (1) to define the background flow, (2) to obtain bounds on terms I and II in (3.27), and (3) using these results, to obtain a bound on the drag coefficient.

3.4.1 Background flow construction

In section §3.3, the calculations merely required that $\boldsymbol{U}$ goes sufficiently quickly to $\boldsymbol{e}_{x_1}$ as $|\boldsymbol{x}| \to \infty$. However, to simplify the algebra, in this paper we choose a $\boldsymbol{U}$ that is actually equal to $\boldsymbol{e}_{x_1}$ outside a rectangular box Γ centered around the plate (see figures 3.1 and 3.2). This ensures that $\boldsymbol{\nabla U}$ is zero outside of Γ, so that any nonzero contribution to terms I and II in (3.27) can only come from within the domain Γ. As a result, we only have to estimate terms I and II inside Γ, which makes the forthcoming analysis easier to perform. The rectangular box Γ is formally given by

$$\Gamma = \{(x_1, x_2, x_3) | -\delta \leq x_1 \leq 1 + \delta,\ -\delta \leq x_2 \leq \delta,\ 0 \leq x_3 \leq L_s\} \cap \Omega. \quad (3.30)$$

The width of Γ in the spanwise direction is L_s which is the same as the periodicity of the flow in that direction. Γ encloses the plate on all sides with a margin of length δ (see figure 3.1), which we call the boundary layer thickness. For now, $\delta > 0$ is an unknown quantity, which will be adjusted later to make $\mathcal{H}(\boldsymbol{v}) + \gamma$ positive semi-definite for some constant γ. For the purpose of defining the background flow, we then partition Γ into eight subdomains, also shown in figure 3.1. These

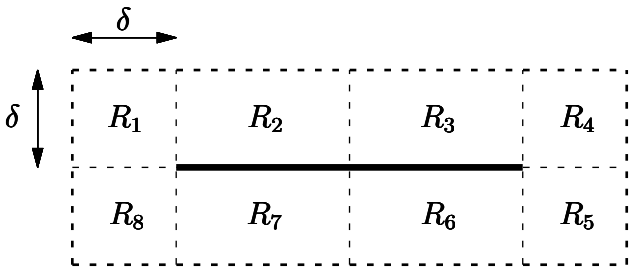

Figure 3.1: The solid line in the middle represents the plate. Γ is the domain enclosed between the plate and the thick dashed rectangular envelope (the spanwise direction is not visible in this figure). Also shown is the division of Γ into the eight subdomains R_1 through R_8.

can be mathematically written as

$$
\begin{aligned}
R_1 &= \{(x_1, x_2, x_3) \mid -\delta \le x_1 < 0,\ 0 \le x_2 \le \delta,\ 0 \le x_3 \le L_s\},\\
R_2 &= \{(x_1, x_2, x_3) \mid 0 \le x_1 \le 1/2,\ 0 < x_2 \le \delta,\ 0 \le x_3 \le L_s\},\\
R_3 &= \{(x_1, x_2, x_3) \mid 1/2 \le x_1 \le 1,\ 0 < x_2 \le \delta,\ 0 \le x_3 \le L_s\},\\
R_4 &= \{(x_1, x_2, x_3) \mid 1 < x_1 \le 1+\delta,\ 0 \le x_2 \le \delta,\ 0 \le x_3 \le L_s\},\\
R_5 &= \{(x_1, x_2, x_3) \mid 1 < x_1 \le 1+\delta,\ -\delta \le x_2 \le 0,\ 0 \le x_3 \le L_s\},\\
R_6 &= \{(x_1, x_2, x_3) \mid 1/2 \le x_1 \le 1,\ -\delta \le x_2 < 0,\ 0 \le x_3 \le L_s\},\\
R_7 &= \{(x_1, x_2, x_3) \mid 0 \le x_1 \le 1/2,\ -\delta \le x_2 < 0,\ 0 \le x_3 \le L_s\},\\
R_8 &= \{(x_1, x_2, x_3) \mid -\delta \le x_1 < 0,\ -\delta \le x_2 \le 0,\ 0 \le x_3 \le L_s\}. \qquad (3.31)
\end{aligned}
$$

For convenience, we choose the background flow $\boldsymbol{U}$ to be spanwise invariant. We note that this choice may not be possible in general. For example, for a flat plate with an irregular leading edge (see figure 3.5b), we may have to use a background flow which is three-dimensional. We define two functions, $f : [0, \delta] \to \mathbb{R}$ and

$g : [-\delta, 0] \to \mathbb{R}$ as follows:

$$f(x) = \begin{cases} \left(\frac{1+\sqrt{2}}{2\delta}\right) x^2 & 0 \le x \le \frac{\delta}{\sqrt{2}} \\ (\sqrt{2}+2)x - \frac{1+\sqrt{2}}{2\delta}\left(x^2+\delta^2\right) & \frac{\delta}{\sqrt{2}} < x \le \delta, \end{cases} \tag{3.32}$$

$$g(x) = \left(1+\frac{x}{\delta}\right)^2 \left(1-\frac{2x}{\delta}\right) \qquad -\delta \le x \le 0. \tag{3.33}$$

With these definitions, we are equipped to construct the streamfunction, $\Psi : \Omega \to \mathbb{R}$, for our background flow:

$$\Psi(x_1, x_2, x_3) = \begin{cases} (f(x_2) - x_2)g(x_1) + x_2 & (x_1, x_2, x_3) \in R_1 \\ f(x_2) & (x_1, x_2, x_3) \in R_2 \cup R_3 \\ (f(x_2) - x_2)g(1 - x_1) + x_2 & (x_1, x_2, x_3) \in R_4 \\ (-f(-x_2) - x_2)g(1 - x_1) + x_2 & (x_1, x_2, x_3) \in R_5 \\ -f(-x_2) & (x_1, x_2, x_3) \in R_6 \cup R_7 \\ (-f(-x_2) - x_2)g(x_1) + x_2 & (x_1, x_2, x_3) \in R_8 \\ x_2 & (x_1, x_2, x_3) \in \Omega \setminus \bigcup_{i=1}^{8} R_i \end{cases} . \tag{3.34}$$

The background velocity field is defined based on the streamfunction (3.34) as

$$\boldsymbol{U} = (U_1, U_2, U_3) = \left(\frac{\partial \Psi}{\partial x_2}, -\frac{\partial \Psi}{\partial x_1}, 0\right). \tag{3.35}$$

See Appendix 3.B for a sketch of the construction this background flow. It can be shown that this flow is piecewise differentiable in Ω. Figure 3.2 shows the streamwise component of $\boldsymbol{U}$ as a function of x_2 at different positions x_1 as well as lines of constant Ψ which are streamlines of $\boldsymbol{U}$. Outside Γ, the background flow is

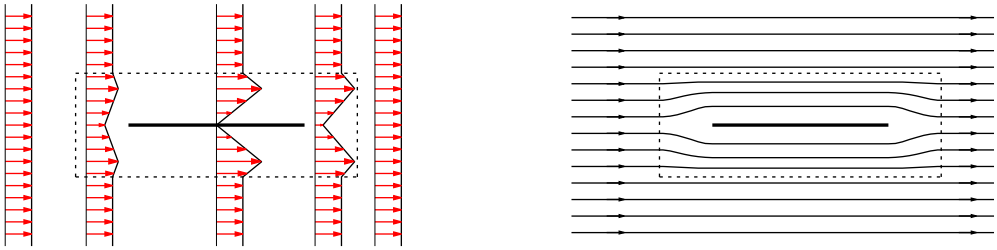

Figure 3.2: a) Streamwise velocity profile at different positions x_1. b) Streamlines of the background flow field given by (3.35). In both panels, the dashed line marks the boundary of Γ.

uniform. It then enters from the left side of Γ, rearranges itself to satisfy the no-slip boundary condition on the surface of the plate, and leaves Γ in the exact same manner as it entered. The imposed divergence free condition on the background flow explains the observed bulge in the streamwise velocity profile. Note that this background flow is a purely mathematical construct and is different from the mean flow that would be obtained in the standard Reynolds decomposition.

3.4.2 Bounds in subdomain R_1

In what follows, we will be making frequent use of two inequalities, which are stated as lemmas below. Their proof can be found in Appendix 3.A.

Lemma 3.4.1. *If $w : R_2 \to \mathbb{R}$ is a square integrable scalar function with $w(x_1, 0, x_3) = 0$ for $0 \le x_1 \le 1/2$ and $0 \le x_3 \le L_s$ then*

$$\int_{R_2} w^2 \, d\boldsymbol{x} \le \frac{\delta^2}{2} \int_{R_2} |\boldsymbol{\nabla} w|^2 \, d\boldsymbol{x}. \tag{3.36}$$

Lemma 3.4.2. *Let $w : R_1 \cup R_2 \to \mathbb{R}$ be a square integrable scalar function such*

that $w(x_1, 0, x_3) = 0$ *for* $x_1 \in [0, \delta]$ *and* $x_3 \in [0, L_s]$. *If* $\delta \leq 1/2$ *then the following inequality holds:*

$$\int_{R_1} w^2 d\boldsymbol{x} \leq 4\delta^2 \int_{R_1 \cup R_2} |\boldsymbol{\nabla} w|^2 d\boldsymbol{x}. \tag{3.37}$$

For the chosen background flow, the integrands of I and II in (3.27) are non-zero only inside Γ. Also, the fore-aft and top-bottom symmetry of the background flow ensures that bounds on I and II restricted to R_1, R_4, R_5, and R_8 are identical. We first obtain a bound on I restricted to R_1 and denote it by I_{R_1}.

$$\begin{aligned}
|I_{R_1}| = \left| \int_{R_1} (\boldsymbol{v} \cdot \boldsymbol{\nabla} \boldsymbol{U}) \cdot \boldsymbol{v} \, d\boldsymbol{x} \right| &= \left| \int_{R_1} \left[v_1^2 \frac{\partial U_1}{\partial x_1} + v_1 v_2 \left(\frac{\partial U_1}{\partial x_2} + \frac{\partial U_2}{\partial x_1} \right) + v_2^2 \frac{\partial U_2}{\partial x_2} \right] d\boldsymbol{x} \right| \\
&\leq \frac{K_1}{\delta} \int_{R_1} v_1^2 \, d\boldsymbol{x} + \frac{K_2}{\delta} \int_{R_1} |v_1||v_2| \, d\boldsymbol{x} + \frac{K_3}{\delta} \int_{R_1} v_2^2 \, d\boldsymbol{x} \\
&\leq \frac{1}{\delta}(K_1 + K_2 c_1) \int_{R_1} v_1^2 \, d\boldsymbol{x} \\
&+ \frac{1}{\delta} \left(K_3 + \frac{1}{4c_1} K_2 \right) \int_{R_1} v_2^2 \, d\boldsymbol{x} \\
&\leq 4\delta(K_1 + K_2 c_1) \int_{R_1 \cup R_2} |\boldsymbol{\nabla} v_1|^2 \, d\boldsymbol{x} \\
&+ 4\delta \left(K_3 + \frac{1}{4c_1} K_2 \right) \int_{R_1 \cup R_2} |\boldsymbol{\nabla} v_2|^2 \, d\boldsymbol{x}
\end{aligned} \tag{3.38}$$

where

$$\begin{aligned}
K_1 &= \operatorname*{ess\,sup}_{(x_1,x_2,x_3) \in R_1} \delta \left| \frac{\partial U_1}{\partial x_1} \right| = \frac{3}{2} \qquad \text{achieved as } x_1 \to -\frac{\delta}{2}, x_2 \to 0, \\
K_2 &= \operatorname*{ess\,sup}_{(x_1,x_2,x_3) \in R_1} \delta \left| \frac{\partial U_1}{\partial x_2} + \frac{\partial U_2}{\partial x_1} \right| = \frac{5}{\sqrt{2}} - \frac{1}{2} \qquad \text{achieved as } x_1 \to 0, x_2 \to \frac{\delta}{\sqrt{2}}, \\
K_3 &= \operatorname*{ess\,sup}_{(x_1,x_2,x_3) \in R_1} \delta \left| \frac{\partial U_2}{\partial x_2} \right| = \frac{3}{2} \qquad \text{achieved as } x_1 \to -\frac{\delta}{2}, x_2 \to 0,
\end{aligned} \tag{3.39}$$

and c_1 is some positive constant. In (3.39) "ess sup" denotes the essential supremum. We have used Young's inequality to obtain line three in (3.38). We then used Lemma 3.4.2 to get the last inequality in (3.38).

A bound on II restricted to subdomain R_1 is given by

$$\begin{aligned} |II_{R_1}| = \left| \int_{R_1} (\boldsymbol{U} \cdot \boldsymbol{\nabla} \boldsymbol{U}) \cdot \boldsymbol{v} \, d\boldsymbol{x} \right| \quad &\leq \int_{R_1} \frac{K_4}{\delta} |\boldsymbol{v}| \, d\boldsymbol{x} \\ &\leq \int_{R_1} \delta^{-\frac{1}{2}} |\boldsymbol{v}|^2 \, d\boldsymbol{x} + \frac{K_4^2 \delta^{\frac{1}{2}} L_s}{4} \\ &\leq 4\delta^{\frac{3}{2}} \int_{R_1 \cup R_2} |\boldsymbol{\nabla} \boldsymbol{v}|^2 \, d\boldsymbol{x} + \frac{K_4^2 \delta^{\frac{1}{2}} L_s}{4}, \end{aligned} \tag{3.40}$$

where

$$\begin{aligned} K_4 = \operatorname*{ess\,sup}_{(x_1,x_2,x_3) \in R_1} \delta |\boldsymbol{U}| \, |\boldsymbol{\nabla} \boldsymbol{U}| = \frac{1+\sqrt{2}}{2\sqrt{2}} \sqrt{39 - 10\sqrt{2}} \approx 4.2556, \\ \text{which is achieved as } x_1 \to -\frac{\delta}{2}, x_2 \to 0. \end{aligned} \tag{3.41}$$

As before, we have used Young's inequality to obtain line two and then Lemma 3.4.2 to obtain line three in (3.40). Later, we will see that the contribution of II is of higher order in δ compared with that of I, and therefore will not participate in the leading term of the final bound.

3.4.3 Bounds in subdomain R_2

We first note that bounds on I and II restricted to subdomains R_2, R_3, R_6, and R_7 will be identical. A bound on I restricted to subdomain R_2 can be obtained as follows:

$$
\begin{aligned}
|I_{R_2}| = \left| \int_{R_2} (\boldsymbol{v} \cdot \boldsymbol{\nabla} \boldsymbol{U}) \cdot \boldsymbol{v} \, d\boldsymbol{x} \right| \quad &= \left| \int_{R_2} v_1 \frac{dU_1}{dx_2} v_2 \, d\boldsymbol{x} \right| \\
&\leq \frac{K_5}{\delta} \int_{R_2} |v_1||v_2| \, d\boldsymbol{x} \\
&\leq \frac{K_5 c_2}{\delta} \int_{R_2} v_1^2 \, d\boldsymbol{x} + \frac{K_5}{4c_2\delta} \int_{R_2} v_2^2 \, d\boldsymbol{x} \\
&\leq \frac{K_5 c_2}{2} \delta \int_{R_2} |\boldsymbol{\nabla} v_1|^2 \, d\boldsymbol{x} + \frac{K_5}{8c_2} \delta \int_{R_2} |\boldsymbol{\nabla} v_2|^2 \, d\boldsymbol{x},
\end{aligned} \tag{3.42}
$$

where

$$
K_5 = \operatorname*{ess\,sup}_{(x_1,x_2,x_3)\in R_2} \delta \left| \frac{dU_1}{dx_2} \right| = 1 + \sqrt{2}
$$

$$
\text{which is achieved when } x_2 \in \left(0, \frac{\delta}{\sqrt{2}}\right) \cup \left(\frac{\delta}{\sqrt{2}}, \delta\right), \tag{3.43}
$$

and c_2 is some positive constant. We have used Young's inequality to obtain line three in (3.42). To obtain line four, we used Lemma 3.4.1.

Finally, since $\boldsymbol{U}$ is unidirectional in R_2, we have

$$
|II_{R_2}| = \left| \int_{R_2} (\boldsymbol{U} \cdot \boldsymbol{\nabla} \boldsymbol{U}) \cdot \boldsymbol{v} \, d\boldsymbol{x} \right| = 0. \tag{3.44}
$$

3.4.4 Bound on drag coefficient

In this subsection, we combine the bounds obtained from §3.4.2 and §3.4.3 to obtain a bound on the sum of the absolute value of I and II. We then optimize the size of the boundary layer (δ) to ensure that $\mathcal{H}(\boldsymbol{v}) + \gamma$ is positive semi-definite for some constant γ and simultaneously obtain a best possible bound on the drag coefficient compatible with our estimates. From the bounds obtained in R_1 and

R_2, we first note that

$$\sum_{i=1}^{2}\left|\int_{R_i}(\boldsymbol{v}\cdot\boldsymbol{\nabla}\boldsymbol{U})\cdot\boldsymbol{v}\;d\boldsymbol{x}\right| \leq \quad \delta\left(4K_1+4K_2c_1+\frac{K_5c_2}{2}\right)\int_{R_1\cup R_2}|\boldsymbol{\nabla}v_1|^2d\boldsymbol{x} \\ +\delta\left(4K_3+\frac{K_2}{c_1}+\frac{K_5}{8c_2}\right)\int_{R_1\cup R_2}|\boldsymbol{\nabla}v_2|^2d\boldsymbol{x}. \quad (3.45)$$

A similar type of calculation can be performed for terms

$$\sum_{i=3}^{4}\left|\int_{R_i}(\boldsymbol{v}\cdot\boldsymbol{\nabla}\boldsymbol{U})\cdot\boldsymbol{v}\;d\boldsymbol{x}\right|,\ \sum_{i=5}^{6}\left|\int_{R_i}(\boldsymbol{v}\cdot\boldsymbol{\nabla}\boldsymbol{U})\cdot\boldsymbol{v}\;d\boldsymbol{x}\right|,\ \text{and}\ \sum_{i=7}^{8}\left|\int_{R_i}(\boldsymbol{v}\cdot\boldsymbol{\nabla}\boldsymbol{U})\cdot\boldsymbol{v}\;d\boldsymbol{x}\right|.$$

Combining these estimates yields a bound on I as

$$\begin{aligned}|I| \quad &= \left|\int_{\Omega}(\boldsymbol{v}\cdot\boldsymbol{\nabla}\boldsymbol{U})\cdot\boldsymbol{v}\;d\boldsymbol{x}\right| \leq \sum_{i=1}^{8}\left|\int_{R_i}(\boldsymbol{v}\cdot\boldsymbol{\nabla}\boldsymbol{U})\cdot\boldsymbol{v}\;d\boldsymbol{x}\right| \\ &\leq \delta\left(4K_1+4K_2c_1+\frac{K_5c_2}{2}\right)\int_{\bigcup_{i=1}^{8}R_i}|\boldsymbol{\nabla}v_1|^2d\boldsymbol{x} \\ &\qquad +\delta\left(4K_3+\frac{K_2}{c_1}+\frac{K_5}{8c_2}\right)\int_{\bigcup_{i=1}^{8}R_i}|\boldsymbol{\nabla}v_2|^2d\boldsymbol{x} \\ &\leq \delta M\int_{\Omega}|\boldsymbol{\nabla}\boldsymbol{v}|^2d\boldsymbol{x}, \end{aligned} \quad (3.46)$$

where

$$\begin{aligned}M \quad &= \inf_{c_1,c_2>0}\max\left\{4K_1+4K_2c_1+\frac{K_5c_2}{2},4K_3+\frac{K_2}{c_1}+\frac{K_5}{8c_2}\right\} \\ &= \frac{21}{4}(1+\sqrt{2})\approx 12.6746. \end{aligned} \quad (3.47)$$

Note that the infimum is achieved when

$$c_1=c_2=\frac{1}{2}. \quad (3.48)$$

Using the results from §3.4.2 and §3.4.3, a bound on II is given by

$$|II| = \left| \int_\Omega (\boldsymbol{U} \cdot \boldsymbol{\nabla} \boldsymbol{U}) \cdot \boldsymbol{v} \, d\boldsymbol{x} \right| \leq 4\delta^{\frac{3}{2}} \int_\Omega |\boldsymbol{\nabla} \boldsymbol{v}|^2 \, d\boldsymbol{x} + K_4^2 \delta^{\frac{1}{2}} L_s. \tag{3.49}$$

From section §3.3, we note that our goal is to make $\mathcal{H}(\boldsymbol{v}) + \gamma$ nonnegative for some constant γ. Using the estimates obtained on I in (3.46) and II in (3.49) along with the triangle inequality, we get a bound on $\mathcal{H}(\boldsymbol{v})$ as

$$\mathcal{H}(\boldsymbol{v}) \geq \left(\frac{1}{2Re} - \delta M - 4\delta^{\frac{3}{2}} \right) ||\boldsymbol{\nabla} \boldsymbol{v}||_2^2 - K_4^2 \delta^{\frac{1}{2}} L_s. \tag{3.50}$$

If we define $\gamma = K_4^2 \delta^{\frac{1}{2}} L_s$, then choosing δ such that

$$\delta(M + 4\delta^{\frac{1}{2}}) \leq \frac{1}{2Re} \tag{3.51}$$

ensures that $\mathcal{H}(\boldsymbol{v}) + \gamma$ is positive semi-definite. Another constraint on δ comes from the applicability of Lemma 3.4.2, which requires

$$\delta \leq \frac{1}{2}. \tag{3.52}$$

Once γ is fixed, we can obtain the desired bound on the drag coefficient by substituting the background flow (3.35) in (3.29). This yields

$$C_D = \frac{1}{Re \; L_s} \overline{||\boldsymbol{\nabla} \boldsymbol{u}||_2^2} \leq \frac{4B_1}{ReL_s} + \frac{4B_2}{ReL_s} + 2K_4^2 \delta^{\frac{1}{2}}, \tag{3.53}$$

where

$$B_1 = \int_{R_1} |\boldsymbol{\nabla} \boldsymbol{U}|^2 \, d\boldsymbol{x} \approx 2.96 L_s \text{ and } \quad B_2 = \int_{R_2} |\boldsymbol{\nabla} \boldsymbol{U}|^2 \, d\boldsymbol{x} = \frac{(1+\sqrt{2})^2}{2} \frac{L_s}{\delta}. \tag{3.54}$$

The value of B_1 is calculated numerically. Inserting (3.54), along with the value of K_4 from (3.41) into (3.53), leads to

$$C_D \leq \frac{2(1+\sqrt{2})^2}{Re\delta} + \left(12\sqrt{2} + \frac{77}{4}\right)\delta^{\frac{1}{2}} + \frac{11.84}{Re}, \tag{3.55}$$

where δ satisfies the constraints (3.51) and (3.52). For $Re > 0.0645$, the optimal bound is obtained when δ satisfies

$$\delta(M + 4\delta^{\frac{1}{2}}) = \frac{1}{2Re}, \tag{3.56}$$

(see Appendix 3.C for more detail). In the limit of high Reynolds number, we can solve (3.56) for δ to get

$$\delta = \frac{1}{2\ M\ Re} + O(Re^{-\frac{3}{2}}). \tag{3.57}$$

Combining (3.47) and (3.57) with (3.55) yields a bound on the drag coefficient for sufficiently high Re as

$$C_D \leq 21 \times (1+\sqrt{2})^3 + O(Re^{-\frac{1}{2}}) \approx 295.49 + O(Re^{-\frac{1}{2}}). \tag{3.58}$$

3.4.5 Comparison with observations

We now compare our findings with existing theoretical and experimental results on the drag coefficient for flow past a flat plate. The drag coefficient for a laminar flow past a flat plate was obtained using the triple-deck theory (see

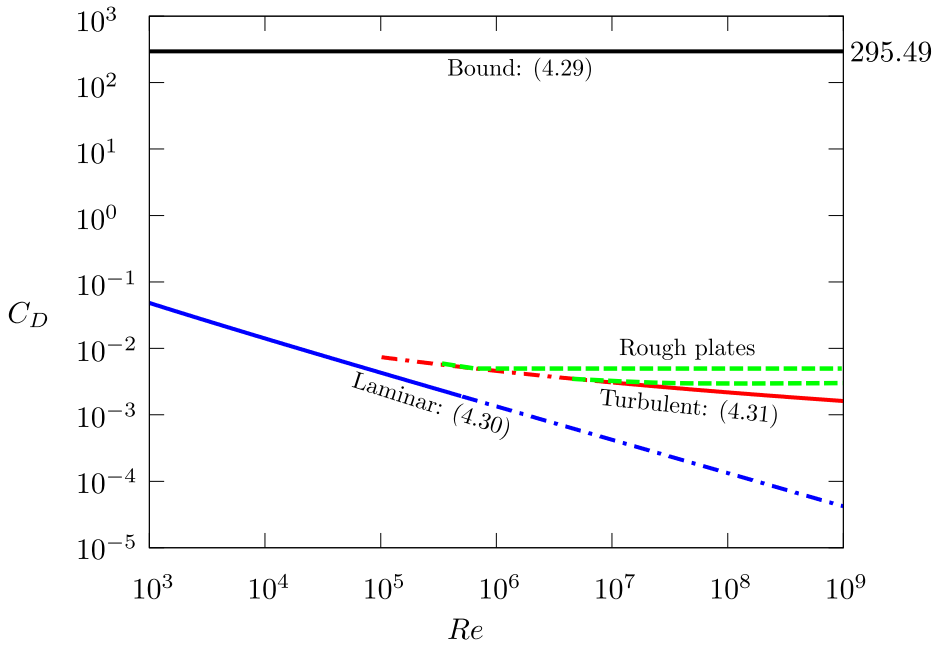

Figure 3.3: The solid black line is the leading order term in the bound (3.58) on the drag coefficient. For the range of Reynolds number considered in this figure, a bound obtained by solving (3.55) and (3.56) would differ only by 0.3% from this leading term at most. The blue line shows the analytical expression for the drag coefficient in the laminar regime given by (3.59). The red line shows the empirical formula for the drag coefficient in the turbulent regime for a smooth plate given by (3.60). In both of these cases a solid line denotes the region of validity of the formulae. For $5 \cdot 10^5 \lesssim Re \lesssim 10^7$ the experimental data seems to fall in between these two lines (see Schlichting and Gersten, 2016, p. 10). The green dashed lines show the drag coefficient variation for two rough plates with different roughnesses (see Schlichting and Gersten, 2016, p. 584).

Stewartson, 1969; Messiter, 1970; Jobe and Burggraf, 1974), and is given by

$$C_D = \frac{1.328}{\sqrt{Re}} + \frac{2.67}{Re^{7/8}} + O(Re^{-1}) \quad \text{for } 100 \lesssim Re \lesssim 5 \cdot 10^5. \tag{3.59}$$

In the turbulent regime, an empirical formula for the drag coefficient based on the law of the wall for a smooth plate (see Schlichting and Gersten, 2016, p. 583) is given by

$$C_D = 2\left[\frac{\kappa}{\ln Re}\mathrm{G}(\Lambda; D)\right]^2 \quad \text{for } Re \gtrsim 10^7, \tag{3.60}$$

where $\kappa = 0.41$ is the von Kármán constant,

$$\Lambda = \ln Re, \quad D = 2\ln\kappa + 2\kappa, \tag{3.61}$$

and G is the solution of the following equation:

$$\frac{\Lambda}{\mathrm{G}} + 2\ln\frac{\Lambda}{\mathrm{G}} - D = \Lambda. \tag{3.62}$$

This function has the property that

$$\lim_{\Lambda\to\infty} \mathrm{G}(\Lambda; D) = 1, \tag{3.63}$$

which implies that at very high Reynolds number

$$C_D \sim \frac{0.34}{\ln^2 Re}. \tag{3.64}$$

In terms of scaling, our upper bound therefore overestimates the drag coefficient by the square of the logarithm of the Reynolds number for sufficiently large Re.

Figure 3.3 compares the bound (3.58) with the analytical result (3.59) in the laminar regime and with empirical formula (3.60) in the turbulent regime. Although our theory only applies to a smooth flat plate, we also show for comparison empirical results on the drag coefficients for a flow past rough plates (see Schlichting and Gersten, 2016, p. 584). It is interesting to note that the drag coefficient does tend to a constant at high Reynolds number in these cases, which is the same scaling as our bound. We also note that in many scenarios, it has been possible to produce simple power-law bounds with logarithms (Doering et al., 2006; Otto and Seis, 2011; Whitehead and Doering, 2011a; Whitehead and Wittenberg, 2014; Fantuzzi et al., 2020). Whether there exists a more careful construction of the background flow for the flat plate, which may produce the logarithmic correction needed to match empirical observations, remains to be seen.

3.5 Discussion and Concluding Remarks

In this paper, we presented the first application of the background method to an external flow problem. Using this method, we were able to obtain an upper bound on the drag coefficient for a flat plate in a uniform flow kept at zero incidence. In particular, we showed that the drag coefficient is bounded by a constant at high Reynolds number (see 3.58).

In obtaining this bound, we considered a fairly simple family of background flows that involves only one free parameter δ, and used relatively crude estimates derived from standard inequalities. We acknowledge that a better bound can most likely be obtained using more refined analysis techniques, and with a *better* background flow. For example, by choosing a family of background flows which involves additional free parameters, we can in principle improve the bound.

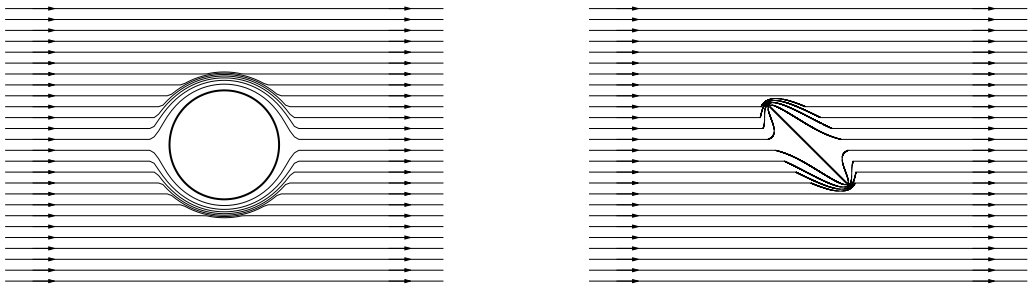

(a) **(b)**

Figure 3.4: An elementary choice of the background flow ($\boldsymbol{U}$): (a) case of flow past a cylinder and (b) case of flow past a flat plate with nonzero angle of attack. In both cases the streamlines have to squeezee around the body because of the incompressiblity of the background flow. As a result, $|\boldsymbol{\nabla U}| = O(\delta^{-2})$ as opposed to the present case where $|\boldsymbol{\nabla U}| = O(\delta^{-1})$ inside the boundary layer.

However, such considerations will almost certainly come at the expense of complicated algebraic manipulations. It is worth noting that in other studies involving the background method, such as those concerned with plane Couette flow (Doering and Constantin, 1992, 1994), it is possible to obtain a constant bound on the drag coefficient that is relatively close to the empirically determined values even with crude estimates. The reason behind this disparity between our study and that of plane Couette flow lies in the fact that in the case of a flat plate, the no-slip boundaries have lower-dimensional boundaries of their own, namely, the plate's leading and trailing edges. This fact makes it challenging to obtain good analytical bounds in the regions R_1, R_4, R_5, and R_8 which are not immediately adjacent to no-slip boundaries (see Appendix 3.A, Lemma 3.4.2). Regardless of this difficulty, we did not do any worse in terms of scalings of the bound: as in the case of Couette flow, we obtain a bound which is within a logarithmic factor of the observations.

As noted early on (Doering and Constantin, 1994; Plasting and Kerswell, 2003), the background flow is different from the mean flow that one would ob-

tain from the Reynolds decomposition. However, it is worth mentioning that for plane Couette flow, the optimal background profile does bear some resemblance to the mean flow. In particular, Plasting and Kerswell (2003) found that it has steep gradients near the wall, and is flat in the bulk, even though this optimal background flow does not capture the logarithmic layer. For the case of a flat plate, experiments at high Reynolds numbers show the development of a laminar boundary layer near the leading edge, followed by a transition to relatively thicker turbulent boundary layer further downstream. Behind the plate, a wake forms which gradually dissipates far away from the plate. Since the family of background flows that we consider here does not have these features, it would be interesting to determine whether the optimal background flow for the flat plate problem bears any similarity with the mean flow, and whether the corresponding optimal bound would improve on the scaling with Re that we have obtained. To answer these questions would require finding the optimal background flow, using techniques similar to the study of Plasting and Kerswell (2003); Wen et al. (2013, 2015); Fantuzzi and Wynn (2015, 2016); Fantuzzi (2018); Tilgner (2017, 2019). However, this will be substantially more complicated in the case of the flat plate owing to the fully two-dimensional nature of the background flow.

In this paper, we chose to obtain a bound on the drag coefficient for a flat plate because of the fundamental nature of the problem. Unfortunately, this analysis cannot be directly extended to the problem of a flow past a bluff body, or flow past a flat plate at a non-zero angle of attack (see figure 3.4). Indeed, while in the present case $|\boldsymbol{\nabla U}| = O(\delta^{-1})$ in the boundary layer, for these problems an *elementary* choice of the background flow $\boldsymbol{U}$, where $\boldsymbol{\nabla U}$ is nonzero only in a thin boundary layer of thickness δ near the body, would have $|\boldsymbol{\nabla U}| = O(\delta^{-2})$ because of the divergence-free condition on $\boldsymbol{U}$. As a result, the equivalent bound on I,

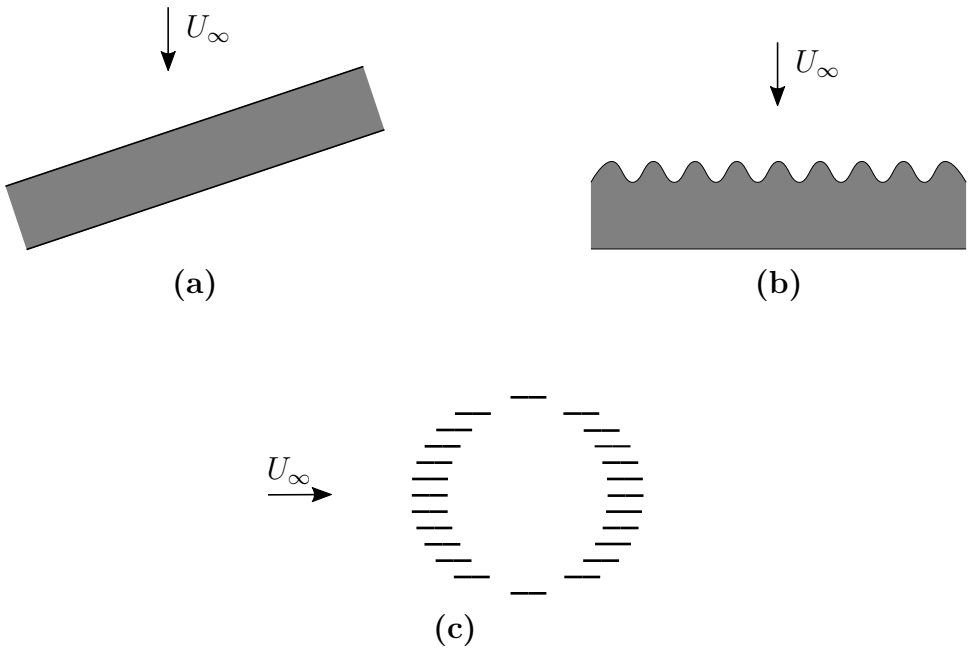

Figure 3.5: This figure shows a few flow configurations where the present analysis can be generalized. The arrow shows the direction of the uniform flow, and in all the above configurations, the objects are kept at zero incidence and are of zero thickness. These configurations are: (a) a yawed flat plate (top view), (b) a flat plate with irregular leading edge (top view), and (c) a group of flat plates (side view).

obtained from arguments similar to the ones given in §3.4, would be

$$|I| \leq C \int_{\Omega} |\boldsymbol{\nabla v}|^2 d\boldsymbol{x} = 2C \cdot Re \cdot III, \tag{3.65}$$

where C is some positive constant independent of δ. Because the factor multiplying III in (3.65) is independent of δ, it is not possible to choose δ to ensure that $\mathcal{H}(\boldsymbol{v})+\gamma$ be positive semi-definite. Hence, with the naive choice of background flow considered in figure 3.4, it is impossible to obtain a bound on the drag coefficient. It remains to be determined whether there exists a smarter choice of background flow for these cases, that would allow the analysis to proceed, or whether it is impossible to obtain a bound without invoking additional dynamical constraints.

Nevertheless the procedure developed in this paper can be generalized to other interesting scenarios with applications in engineering. For example, we can obtain a similar type of bound for a yawed flat pate, a flat plate with irregular leading edge, or a group of flat plates, see figure 3.5. Interestingly, some of these scenarios can be quite challenging to simulate numerically at high Reynolds numbers. It would be interesting to find out if, in reality, the drag coefficient tends to a constant at high enough Reynolds number for these problems.

Acknowledgement

We thank C.R. Doering and D. Goluskin for their encouragements and helpful comments on the manuscript. We also thank anonymous referees for their comments, which helped improve the quality of the manuscript. A.K. acknowledges the support from the Dean's fellowship and Regents' fellowship from the Baskin School of Engineering at UC Santa Cruz, from the GFD fellowship program 2019

at the Woods Hole Oceanographic Institution, and from NSF AST 1814327.

Appendix 3.A Proof of Lemma 3.4.1 and 3.4.2

In this appendix, we first state the two lemmas used in the main text in their full form and then prove them.

Lemma 1. *Let $w : [0, \delta] \to \mathbb{R}$ be a square integrable function such that $w(0) = 0$ for $x = 0$, then the following inequality holds:*

$$\int_0^\delta w^2 dx \leq \frac{\delta^2}{2} \int_0^\delta \left(\frac{dw}{dx}\right)^2 dx. \tag{3.66}$$

As a result, if $w : R_2 \to \mathbb{R}$ is a square integrable function with $w(x_1, 0, x_3) = 0$ for $0 \leq x_1 \leq 1/2$ and $0 \leq x_3 \leq L_s$ then

$$\int_{R_2} w^2 \, d\boldsymbol{x} \leq \frac{\delta^2}{2} \int_{R_2} \left(\frac{\partial w}{\partial x_2}\right)^2 d\boldsymbol{x} \leq \frac{\delta^2}{2} \int_{R_2} |\boldsymbol{\nabla} w|^2 \, d\boldsymbol{x}. \tag{3.67}$$

Proof. For $y \in [0, \delta]$, using the fundamental theorem of Calculus and the Cauchy–Schwarz inequality, we can prove the following estimate:

$$\begin{aligned} w^2(y) &= \left| \int_0^y \frac{dw}{dx} dx \right|^2 \\ &\leq \left(\int_0^y 1^2 dy \right) \left(\int_0^\delta \left(\frac{dw}{dx}\right)^2 dx \right) = y \int_0^\delta \left(\frac{dw}{dx}\right)^2 dx. \end{aligned} \tag{3.68}$$

Integrating in y from 0 to δ gives the desired result (3.66). The inequality such as in this Lemma has been frequently used in previous studies involving the background method going back to Doering and Constantin (1992). □

Lemma 2. *Let $w : R_1 \cup R_T \to \mathbb{R}$ be a square integrable function such that*

$w(x_1, 0, x_3) = 0$ for $x_1 \in [0, \delta]$ and $x_3 \in [0, L_s]$, then the following inequality holds:

$$\int_{R_1} w^2 d\boldsymbol{x} \leq 4\delta^2 \int_{R_T} \left[\left(\frac{\partial w}{\partial x_1} \right)^2 + \left(\frac{\partial w}{\partial x_2} \right)^2 \right] d\boldsymbol{x} + \delta^2 \int_{R_1} \left(\frac{\partial w}{\partial x_1} \right)^2 d\boldsymbol{x}, \tag{3.69}$$

where

$$R_T = \{(x_1, x_2, x_3) | x_1 \geq 0,\ x_2 > 0,\ x_1 + x_2 \leq \delta,\ 0 \leq x_3 \leq L_s\}. \tag{3.70}$$

Note that if $\delta \leq 1/2$ then $R_T \subseteq R_2$ and therefore we also have

$$\begin{aligned} \int_{R_1} w^2 d\boldsymbol{x} \quad &\leq 4\delta^2 \int_{R_2} \left[\left(\frac{\partial w}{\partial x_1} \right)^2 + \left(\frac{\partial w}{\partial x_2} \right)^2 \right] d\boldsymbol{x} + \delta^2 \int_{R_1} \left(\frac{\partial w}{\partial x_1} \right)^2 d\boldsymbol{x} \\ &\leq 4\delta^2 \int_{R_1 \cup R_2} |\boldsymbol{\nabla} w|^2 d\boldsymbol{x}. \end{aligned} \tag{3.71}$$

Proof. The proof of this inequality roughly works as follows. We first control the value of w at point p_2 (see figure 3.6) using the gradient of w along the line $p_2 p_3$, similar to the proof of Lemma 3.4.1. We then control the value of w at point p_1 using the gradient of w along the line $p_1 p_2$, again similar to the proof of Lemma 3.4.1. For $(0, y_2, y_3) \in \overline{R_1} \cap R_T$, using the fundamental theorem of Calculus and the Cauchy–Schwarz inequality, we can prove the following estimate:

$$\begin{aligned} |w(0, y_2, y_3)| \quad &= \left| \int_{-y_2}^{y_2} \frac{\partial}{\partial \eta} w \left(\frac{y_2 - \eta}{2}, \frac{y_2 + \eta}{2}, y_3 \right) d\eta \right| \\ &\leq \left(\int_{-y_2}^{y_2} 1^2 \, d\eta \right)^{1/2} \left(\int_{-y_2}^{y_2} \left[\frac{\partial}{\partial \eta} w \left(\frac{y_2 - \eta}{2}, \frac{y_2 + \eta}{2}, y_3 \right) \right]^2 d\eta \right)^{1/2} \\ &\leq (2\delta)^{1/2} \left(\int_{-y_2}^{y_2} \left[\frac{\partial}{\partial \eta} w \left(\frac{y_2 - \eta}{2}, \frac{y_2 + \eta}{2}, y_3 \right) \right]^2 d\eta \right)^{1/2}. \end{aligned} \tag{3.72}$$

This implies,

$$\int_0^{L_s}\int_0^{\delta} w^2(0,y_2,y_3)dy_2dy_3 \leq \\ 2\delta\int_0^{L_s}\int_0^{\delta}\int_{-y_2}^{y_2}\left[\frac{\partial}{\partial\eta}w\left(\frac{y_2-\eta}{2},\frac{y_2+\eta}{2},y_3\right)\right]^2 d\eta dy_2 dy_3. \quad (3.73)$$

We use the following change of variables on the right-hand side of (3.73)

$$(\eta,y_2,y_3)\mapsto(x_2-x_1,x_1+x_2,x_3). \quad (3.74)$$

The region of integration for the integral on the right-hand side of (3.73) in the old coordinates is

$$\{(\eta,y_2,y_3)|-y_2\leq\eta\leq y_2,\ 0\leq y_2\leq\delta,\ 0\leq y_3\leq L_s\}. \quad (3.75)$$

In the new coordinates, it is easy to show that this corresponds to

$$\{(x_1,x_2,x_3)|0\leq x_1,\ 0\leq x_2,\ x_1+x_2\leq\delta,\ 0\leq x_3\leq L_s\}. \quad (3.76)$$

The Jacobian for the coordinate transformation (3.74) is given by

$$\left|\frac{\partial(\eta,y_2,y_3)}{\partial(x_1,x_2,x_3)}\right|=2, \quad (3.77)$$

and the partial derivative of a quantity with η in the new coordinates is

$$\frac{\partial[\,\cdot\,]}{\partial\eta}=\frac{1}{2}\frac{\partial[\,\cdot\,]}{\partial x_2}-\frac{1}{2}\frac{\partial[\,\cdot\,]}{\partial x_1}. \quad (3.78)$$

Using these pieces of information, we rewrite (3.73) in the new coordinates

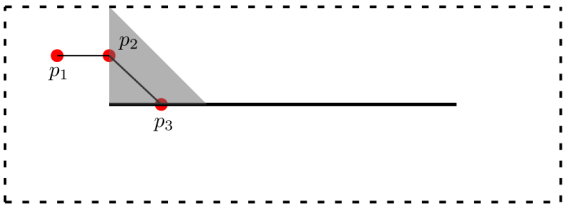

Figure 3.6: The thick line in the middle is the plate. Γ is the domain enclosed between the plate and the dashed rectangle (the spanwise direction is not visible in this figure). The shaded triangular region is R_T as defined in (3.70). Here, p_1, p_2, and p_3 are the points (x_1, x_2, x_3), $(0, x_2, x_3)$, and $(x_2, 0, x_3)$. The point p_1 belongs to R_1.

(x_1, x_2, x_3) as

$$\begin{aligned}
&\int_0^{L_s}\int_0^{\delta} w^2(0,y_2,y_3)dy_2dy_3 \leq \\
&\delta\int_0^{L_s}\int_0^{\delta}\int_0^{\delta-x_2}\left[\frac{\partial}{\partial x_2}w(x_1,x_2,x_3)-\frac{\partial}{\partial x_1}w(x_1,x_2,x_3)\right]^2 dx_1dx_2dx_3, \\
&\implies \int_0^{L_s}\int_0^{\delta} w^2(0,y_2,y_3)dy_2dy_3 \leq \\
&2\delta\int_0^{L_s}\int_0^{\delta}\int_0^{\delta-x_2}\left[\frac{\partial}{\partial x_1}w(x_1,x_2,x_3)\right]^2+\left[\frac{\partial}{\partial x_2}w(x_1,x_2,x_3)\right]^2 dx_1dx_2dx_3.
\end{aligned} \tag{3.79}$$

We also have, for any $(y_1, y_2, y_3) \in R_1$,

$$\begin{aligned}
w(y_1,y_2,y_3) &= w(0,y_2,y_3)+\int_0^{y_1}\frac{\partial}{\partial\eta}w(\eta,y_2,y_3)\,d\eta, \\
\implies w^2(y_1,y_2,y_3) &\leq 2w^2(0,y_2,y_3)+2\left(\int_0^{y_1}\frac{\partial}{\partial\eta}w(\eta,y_2,y_3)\,d\eta\right)^2 \\
&\leq 2w^2(0,y_2,y_3)+2(-y_1)\int_{y_1}^{0}\left[\frac{\partial}{\partial\eta}w(\eta,y_2,y_3)\right]^2 d\eta.
\end{aligned} \tag{3.80}$$

Note that we have obtained the second line using the Young's inequality and last

line using the Cauchy–Schwarz inequality.

$$\implies \int_0^{L_s}\int_0^{\delta}\int_{-\delta}^{0} w^2(y_1,y_2,y_3)dy_1dy_2dy_3 \leq 2\delta\int_0^{L_s}\int_0^{\delta} w^2(0,y_2,y_3)dy_2dy_3 + \delta^2\int_0^{L_s}\int_0^{\delta}\int_{-\delta}^{0}\left[\frac{\partial}{\partial\eta}w(\eta,y_2,y_3)\right]^2 d\eta dy_2dy_3. \quad (3.81)$$

Renaming the variables in the second integral of the above inequality from (η, y_2, y_3) to (x_1, x_2, x_3) and using (3.79) gives

$$\begin{aligned}&\int_0^{L_s}\int_0^{\delta}\int_{-\delta}^{0} w^2(y_1,y_2,y_3)dy_1dy_2dy_3 \leq \\ &4\delta^2\int_0^{L_s}\int_0^{\delta}\int_0^{\delta-x_2}\left[\frac{\partial}{\partial x_2}w(x_1,x_2,x_3)\right]^2+\left[\frac{\partial}{\partial x_1}w(x_1,x_2,x_3)\right]^2 dx_1dx_2dx_3 \\ &+\delta^2\int_0^{L_s}\int_0^{\delta}\int_{-\delta}^{0}\left[\frac{\partial}{\partial x_1}w(x_1,x_2,x_3)\right]^2 dx_1dx_2dx_3, \end{aligned} \quad (3.82)$$

which is the desired result. □

Appendix 3.B Sketch of the construction of the background flow (3.35)

The choice of a background flow, which leads to a constant bound on the drag coefficient, is not unique. Beyond the fact that the background flow ($\boldsymbol{U}$) should be divergence-free and should satisfy the inhomogenous boundary conditions, the principle that guides our choice of background flow is the simplification of the algebra. We start by restricting $\boldsymbol{U}$ to be spanwise invariant. Next, we choose this $\boldsymbol{U}$ to be $\boldsymbol{e}_{x_1}$ outside a bounded domain Γ enclosing the plate. Therefore $\boldsymbol{\nabla U} = 0$ outside Γ, which makes the terms I and II in (3.27) vanish outside Γ. Undoubtedly, the most straightforward choice of Γ is a rectangular box. We

choose this box to be centered around the plate with a margin of δ (see figure 3.1). At this stage, the goal is to construct a divergence-free background flow $\boldsymbol{U}$ satisfying the no-slip boundary condition on the plate surface, which is equal to $\boldsymbol{e}_{x_1}$ outside this rectangular box. Within Γ, we select for simplicity a flow that is symmetric about the plane $x_2 = 0$, which leaves the problem of defining the background flow $\boldsymbol{U}$ to regions R_1, R_2, R_3 and R_4 in figure 3.1. In regions R_2 and R_3, we choose $\boldsymbol{U}$ to be unidirectional (so the streamwise component is non-zero) which drops to zero on the surface. Its value should reach $\boldsymbol{e}_{x_1}$ at a height δ from the surface, i.e., at the edge of Γ. The most straightforward choice of $\boldsymbol{U}$ would be a velocity profile which linearly varies from $\boldsymbol{0}$ to $\boldsymbol{e}_{x_1}$, a choice which is usually made in the study of confined flows between planar boundaries (see for instance, Doering and Constantin, 1992; Hagstrom and Doering, 2014). However, in the present case, this choice would not preserve the mass flux that enters from the left side of the box. The next simplest choice of $\boldsymbol{U}$ is a piecewise linear function with two pieces, as shown in figure 3.7a and given as follows

$$\boldsymbol{U}|_{R_2 \cup R_3}(\boldsymbol{x}) = \begin{cases} U_p \frac{x_2}{\delta_p} \boldsymbol{e}_{x_1} & 0 \leq x_2 \leq \delta_p \\ \left(U_p \frac{\delta - x_2}{\delta - \delta_p} + \frac{x_2 - \delta_p}{\delta - \delta_p} \right) \boldsymbol{e}_{x_1} & \delta_p < x_2 \leq \delta, \end{cases} \tag{3.83}$$

where U_p denotes the maximum value of the streamwise component of $\boldsymbol{U}$, and δ_p is the height at which this maximum value is achieved. Along with balancing the mass flux, we choose (again for simplicity) the quantities U_p and δ_p such that the magnitude of the gradient of $\boldsymbol{U}$ is equal above and below the height $x_2 = \delta_p$. In

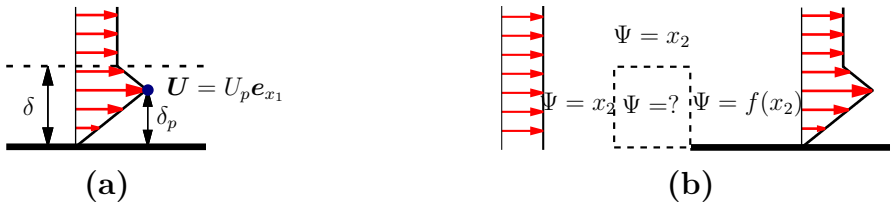

Figure 3.7: (a) Illustration of the piecewise linear choice of background flow on top of the plate. Here, U_p, the maximum value of the streamwise component of $\boldsymbol{U}$ and δ_p denotes the height from the plate where this value is achieved. (b) Illustration of the region R_1, where the streamfunction Ψ of the background flow $\boldsymbol{U}$ remains to be determined once the Ψ is constructed on top of the plate.

total, we require the following two conditions to be satisfied:

$$\int_{x_3=0}^{L_s}\int_{x_2=0}^{\delta} \boldsymbol{U}|_{R_2\cup R_3}\, dx_2 dx_3 = \int_{x_3=0}^{L_s}\int_{x_2=0}^{\delta} \boldsymbol{e}_{x_1}\, dx_2 dx_3, \quad \left|\frac{U_p}{\delta_p}\right| = \left|\frac{1-U_p}{\delta-\delta_p}\right|$$
$$\implies U_p = 1+\frac{1}{\sqrt{2}}, \quad \delta_p = \frac{1}{\sqrt{2}}. \tag{3.84}$$

Once $\boldsymbol{U}$ is fully constructed on the top and bottom of the plate, we focus on the region R_1, which is not immediately adjacent to the plate. This is the region where the streamlines shift upward, which implies that the vertical component of $\boldsymbol{U}$ is also non-zero. In order to satisfy the divergence-free condition, it is convenient to work with the streamfunction Ψ to construct $\boldsymbol{U}$. First, note that the expression for the streamfunction Ψ corresponding to the velocity field on top of the plate is

$$\Psi|_{R_2\cup R_3}(\boldsymbol{x}) = f(x_2) = \begin{cases} \left(\frac{1+\sqrt{2}}{2\delta}\right) x_2^2 & 0 \le x_2 \le \frac{\delta}{\sqrt{2}} \\ (\sqrt{2}+2)x_2 - \frac{1+\sqrt{2}}{2\delta}\left(x_2^2+\delta^2\right) & \frac{\delta}{\sqrt{2}} < x_2 \le \delta, \end{cases} \tag{3.85}$$

where f is the same as defined in (3.32). Inside the region R_1, the streamfunction Ψ must smoothly change from $\Psi(\boldsymbol{x}) = x_2$ on the left side of R_1 (at $x_1 = -\delta$) to $\Psi(\boldsymbol{x}) = f(x_2)$ on the right side of R_1 (at $x_1 = 0$), as shown in figure 3.7b.

Imposing the condition of mirror symmetry about $x_2 = 0$ also requires the vertical component of $\boldsymbol{U}$ to be zero at $x_2 = 0$, which implies that $\partial\Psi/\partial x_1 = 0$ at $x_2 = 0$. One way of defining the streamfunction in the region R_1, which obeys these conditions, is as follows

$$\Psi|_{R_1}(\boldsymbol{x}) = (f(x_2) - x_2)g(x_1) + x_2, \tag{3.86}$$

where we require the function g to satisfy the boundary conditions $g(-\delta) = 0$ and $g(0) = 1$. Now to ensure the continuity of $\boldsymbol{U}$ the function g should be smooth enough and a choice of g that suffices for our purpose is

$$g(x_1) = \left(1 + \frac{x_1}{\delta}\right)^2 \left(1 - \frac{2x_1}{\delta}\right) \qquad -\delta \leq x_1 \leq 0. \tag{3.87}$$

This function g is the same as defined in (3.33). Finally, we define the streamfunction Ψ in region R_4 so that the resultant flow goes back to being uniform on the right edge of R_4, in a manner which is the inversion of flow in the region R_1 and, therefore, can be obtained after appropriate translation and reflection of Ψ defined in R_1 (see (3.34)).

Appendix 3.C Optimal condition for the bound (3.55)

Recall from (3.51) and (3.52) that the two constraints on δ are

$$\delta(M + 4\delta^{\frac{1}{2}}) \leq \frac{1}{2Re} \quad \text{and} \quad \delta \leq \frac{1}{2}. \tag{3.88}$$

The left-hand side of the first constraint is a monotonically increasing function of δ, therefore it possible to combine these two constraints as follows

$$\delta \leq \min\left\{\delta_*, \frac{1}{2}\right\} \quad \text{where } \delta_* \text{ satisfies} \quad \delta_*(M + 4\delta_*^{\frac{1}{2}}) = \frac{1}{2Re}. \tag{3.89}$$

Given the bound (3.55) on the drag coefficient,

$$C_D \leq \frac{2(1+\sqrt{2})^2}{Re\delta} + \left(12\sqrt{2} + \frac{77}{4}\right)\delta^{\frac{1}{2}} + \frac{11.84}{Re}, \tag{3.90}$$

our goal is to minimize the right-hand side under the constraint (3.89). This right-hand side is a convex function of δ, whose minimum is achieved when

$$\delta = \delta_c = \left(\frac{16(1+\sqrt{2})^2}{(48\sqrt{2}+77)Re}\right)^{2/3}. \tag{3.91}$$

This critical value δ_c, however, does not satisfy the constraint (3.89). As the right-hand side of (3.90) is a convex function of δ, to minimize the bound under the given constraints, we simply choose a value of δ that satisfies (3.89) and is as close as possible to the critical value δ_c. The bound is therefore optimized when we choose

$$\delta = \min\left\{\delta_*, \frac{1}{2}\right\}. \tag{3.92}$$

Using the equation of δ_* from (3.89), we see that

$$\delta_* < \frac{1}{2} \quad \text{when} \quad Re > \frac{4\sqrt{2}}{58 + 21\sqrt{2}} \approx 0.0645. \tag{3.93}$$

Therefore, the optimal strategy is to choose

$$\delta = \delta_* \quad \text{when} \quad Re > 0.0645. \tag{3.94}$$

Chapter 4

Pressure-driven flows in helical pipes: bounds on flow rate and friction factor

This chapter is based on the paper Kumar (2020) published in the Journal of Fluid Mechanics, Volume 904 , 10 December 2020 , A5.

4.1 Introduction

Curved pipes have a wide range of applications in the industry because of their enhanced mixing properties, high heat transfer coefficient, and compact structure. Examples of application include, but are not limited to, heat exchangers, air-conditioning systems, chemical reactors, and steam generators (see the review by Vashisth et al., 2008; Naphon and Wongwises, 2006). One of the crucial questions in the study of turbulent flows in curved pipes is the accurate determination of the dependence of the flow rate and friction factor on the applied pressure difference

between the two ends of the pipe, and its dependence on geometrical parameters such as the pipe's curvature and torsion. The extensive usage of curved pipes in the industry has motivated many studies to characterize this dependence (see Itō, 1959; Liu and Masliyah, 1993; Yamamoto et al., 1994, 1995; Cioncolini and Santini, 2006). However, only a few of these studies consider the high Reynolds number limit, which is the objective of this paper.

The flow structure inside a curved pipe can vary substantially with Reynolds number and pipe geometry, which leads to a number of different regimes, each with its own distinct functional dependence of the flow rate and friction factor on these parameters. As such, quantifying this dependence becomes difficult even for the laminar flow, unlike the case of a straight pipe. Indeed, at low Reynolds number, an imbalance between centrifugal force and cross-stream pressure leads to the onset of secondary counter-rotating vortices known as Dean's vortices, which were first experimentally observed by Eustice (1910, 1911). Dean (1927, 1928) confirmed this observation analytically in the low curvature limit by computing the flow velocity as a perturbation of the well-known laminar Poiseuille flow solution. Dean (1928) showed that the effect of curvature is to decrease the flow rate and that this effect is of second-order, i.e. quadratic in curvature. Several other studies were performed in the limit of small curvature to obtain a steady-state flow solution in a toroidal pipe, see for example, McConalogue and Srivastava (1968); Van Dyke (1978); Dennis (1980). For a comprehensive review of the topic, the reader is referred to Berger et al. (1983). Germano (1982) further extended Dean's result to a helical pipe with small torsion and Tuttle (1990) showed that small torsion leads to a second-order decrease in the flow rate. However, no analytical result exists for the steady flow in a pipe with a finite radius of curvature or torsion. Therefore, even in the laminar regime, one has to rely on empirical formulae to

quantify the flow rate.

The transition to turbulence in curved pipes also differs substantially from the case of a straight pipe. Taylor (1929) and White (1929) found that flow in a curved pipe is more stable than in a straight pipe. Notably, they saw that the critical Reynolds number for the transition is twice as large as in the straight pipe case. Inspired by this observation, Sreenivasan and Strykowski (1983) conducted experiments in a straight tube followed by a helical tube with curvature $\kappa = 0.058$. They noticed an oscillating behavior near the inner wall of the helical tube at a moderate Reynolds number, which Webster and Humphrey (1993, 1997) attributed to the presence of traveling wave perturbations to the Dean's vortices. Recent years have witnessed a resurgence in carefully conducted studies to quantify the effect of curvature on the stability of flow in a torus. Kühnen et al. (2015) studied this problem using a novel experimental setup where a magnetically controlled steel sphere drives the flow in a torus. They conjectured that the transition switches from subcritical to supercritical for a critical torus curvature $\kappa \simeq 0.028$. Soon after that, Canton et al. (2016) performed an in-depth linear stability analysis, covering the entire curvature range, and obtained the critical Reynolds number as a function of the curvature. More recently, Canton et al. (2020) have shed light on the complexity of transition for flow in a torus, demonstrating in particular that for $\kappa \simeq 0.025$, two branches of solution can coexist at the same Reynolds number: one with subcritically-excited sustained turbulence, and the other consisting of a low-amplitude travelling wave originating from a supercritical Hopf bifurcation.

The incredible complexity of curved pipe flows makes it impossible to obtain the precise dependence of mean quantities such as flow rate or friction factor on model parameters. This is especially true at high Reynolds number, where both laboratory experiments and numerical computations are extremely challenging

and must be repeated for different pipe geometries. As noted by Vester et al. (2016), the determination of the friction factor (or equivalently the flow rate) for turbulent flows in curved pipes has generally been neglected, with only a few exceptions (Itō, 1959; Cioncolini and Santini, 2006). However, as we shall demonstrate in this paper, it is possible to obtain bounds on these mean quantities as explicit functions of flow and geometric variables, in the high Reynolds number limit.

Obtaining bounds on mean quantities in fluid mechanics goes back to the classical technique of Howard (1963), which was further developed by Busse (1969, 1970). In the 1990s, Doering and Constantin (Doering and Constantin, 1992, 1994; Constantin and Doering, 1995; Doering and Constantin, 1996), based on the ideas from Hopf (1955), developed a new technique known as the background method to bound mean quantities. This method requires a careful choice of a trial function (the background field) to satisfy a spectral constraint in order to obtain a bound on the desired quantity. Since the work of Doering and Constantin, this method has been applied to a wide variety of problems in fluid dynamics. Examples include upper bounds on the rate of energy dissipation in surface-velocity-driven flows (Doering and Constantin, 1992, 1994; Marchioro, 1994; Wang, 1997; Plasting and Kerswell, 2003), pressure-driven flows (Constantin and Doering, 1995), and surface-stress-driven flows (Tang et al., 2004; Hagstrom and Doering, 2014); upper bounds on the heat transfer in different configurations of Rayleigh–Bénard convection (Doering and Constantin, 1996, 2001; Otero et al., 2002; Plasting and Ierley, 2005; Wittenberg, 2010; Whitehead and Doering, 2011b; Whitehead and Wittenberg, 2014; Goluskin, 2015; Goluskin and Doering, 2016; Fantuzzi, 2018) and Bénard–Marangoni convection (Hagstrom and Doering, 2010; Fantuzzi et al., 2018, 2020); upper bounds on buoyancy flux in stably stratified shear flows (Caulfield

and Kerswell, 2001; Caulfield, 2005).

In this paper, we use this background method to obtain a lower bound on the flow rate and an equivalent upper bound on friction factor for flows in helical pipes. The novelty in this paper is the use of a two-dimensional background flow in contrast with most previous applications of the background method, where the geometry was simple enough to use a one-dimensional background flow to suffice the desired purpose. We start by setting up the problem in §4.2, where we describe the flow configuration and the coordinate system used to solve the problem. In §4.3, we formulate the background method in the context of pressure-driven flows in helical pipes. In §4.4, we choose the background flow and obtain bounds on the flow rate and friction factor. Finally, in §4.5, we compare our findings with available experimental data and make a few remarks about the applicability of the background method to other interesting problems in engineering.

4.2 Problem Setup

4.2.1 Flow configuration

We consider the flow of an incompressible fluid with density ρ and kinematic viscosity ν in a helical pipe. The radius of the pipe is denoted as R_p, the radius of the centerline helix R_h, and the pitch of the centerline helix is $2\pi l$ (see figure 4.1a). Here, the centerline helix refers to the locus of the center of the pipe. The flow is driven by a body force $\boldsymbol{f}^*$, which has dimensional amplitude F. The choice of forcing is described in §4.2.3. We non-dimensionalize the variables as follows

$$\boldsymbol{f} = \frac{\boldsymbol{f}^*}{F}, \quad \boldsymbol{u} = \left(\frac{\rho}{FR_p}\right)^{\frac{1}{2}} \boldsymbol{u}^*, \quad p = \frac{p^* - p_a}{FR_p}, \quad \boldsymbol{x} = \frac{\boldsymbol{x}^*}{R_p}, \quad t = \left(\frac{F}{\rho R_p}\right)^{\frac{1}{2}} t^*. \quad (4.1)$$

Here, p_a is the ambient pressure, whereas $\boldsymbol{f}$, $\boldsymbol{u}$, p, $\boldsymbol{x}$, and t denote the non-dimensional forcing, velocity, pressure, position, and time, respectively. Quantities with a star in superscript are dimensional. The equations governing the flow in non-dimensional form are as follows

$$\begin{aligned} &\boldsymbol{\nabla} \cdot \boldsymbol{u} = 0, \\ &\frac{\partial \boldsymbol{u}}{\partial t} + \boldsymbol{u} \cdot \boldsymbol{\nabla} \boldsymbol{u} = -\boldsymbol{\nabla} p + \frac{1}{Re} \nabla^2 \boldsymbol{u} + \boldsymbol{f}, \end{aligned} \tag{4.2}$$

where

$$Re = \frac{R_p}{\nu} \left(\frac{F R_p}{\rho} \right)^{\frac{1}{2}}$$

is the Reynolds number. The boundary conditions at the surface of the pipe are no-slip and impermeable.

4.2.2 Coordinate system

In this subsection, we construct an orthogonal coordinate system that is well-suited for our problem. This coordinate system was first introduced by Germano (1982), who was interested in the effect of small torsion on Dean's solution. The coordinate system has been extensively used since then in both analytical and computational studies of flows in helical pipes (Kao, 1987; Germano, 1989; Tuttle, 1990; Liu and Masliyah, 1993; Yamamoto et al., 1994; Hüttl and Friedrich, 2001; Gammack and Hydon, 2001). For clarity and self-consistency, we repeat its construction below.

Let a and $2\pi b$ be the non-dimensional centerline helix radius and pitch, where $a = R_h/R_p$ and $b = l/R_p$. The equation of this helix parameterized with arc

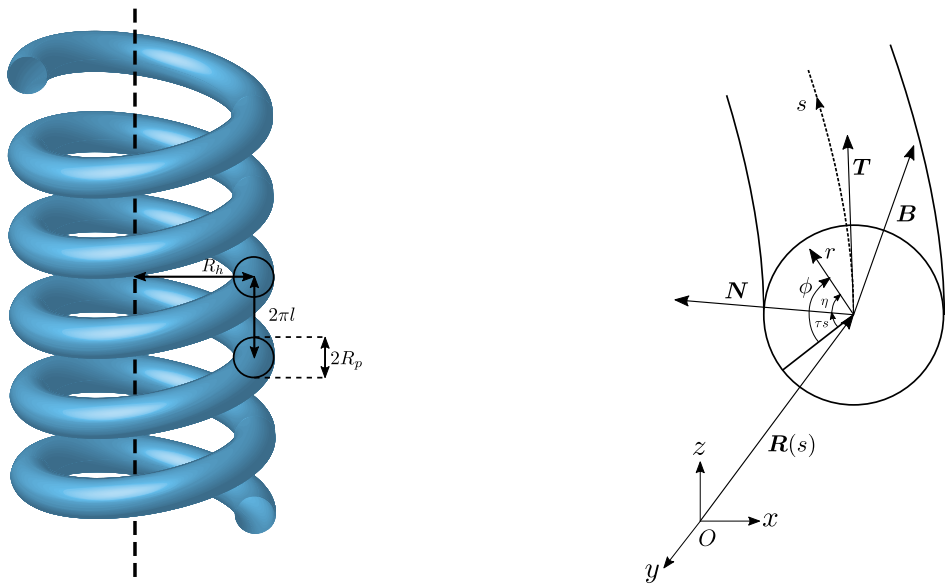

Figure 4.1: (a) Schematic diagram of a helical pipe with radius R_p, radius of the centerline helix R_h, and pitch of the centerline helix $2\pi l$. The dashed line is the axis of rotation of the helical pipe. (b) Illustration of the coordinate system (s, r, ϕ) used in this paper.

length s in a Cartesian coordinate system (x, y, z) is given by

$$(x(s), y(s), z(s)) = \left(a\cos\left(\frac{s}{\sqrt{a^2+b^2}}\right), a\sin\left(\frac{s}{\sqrt{a^2+b^2}}\right), \frac{bs}{\sqrt{a^2+b^2}} \right). \quad (4.3)$$

Let $\boldsymbol{R}(s) = (x(s), y(s), z(s))$ be the position vector and let $\boldsymbol{T}(s)$, $\boldsymbol{N}(s)$, and $\boldsymbol{B}(s)$ be the tangent, normal, and binormal to the centerline helix, which are given by

$$\boldsymbol{T} = \frac{d\boldsymbol{R}}{ds}, \quad \boldsymbol{N} = \frac{1}{\kappa}\frac{d\boldsymbol{T}}{ds}, \quad \boldsymbol{B} = \boldsymbol{T} \times \boldsymbol{N}. \quad (4.4)$$

The relations among the tangent, normal, and binormal are given by the Frenet–Serret formulae, which are

$$\frac{d\boldsymbol{N}}{ds} = \tau\boldsymbol{B} - \kappa\boldsymbol{T}, \quad \frac{d\boldsymbol{B}}{ds} = -\tau\boldsymbol{N}, \quad (4.5)$$

where

$$\kappa = \frac{a}{a^2+b^2}, \quad \text{and} \quad \tau = \frac{b}{a^2+b^2} \quad (4.6)$$

are the non-dimensional curvature and torsion of the helix. The curvature is considered smaller than one ($\kappa < 1$) in this paper. We now construct a coordinate system (s, r, η) such that any Cartesian position vector $\boldsymbol{x}$ can be expressed as

$$\boldsymbol{x} = \boldsymbol{R} + r\cos\eta\boldsymbol{N} + r\sin\eta\boldsymbol{B}. \quad (4.7)$$

With the use of (4.4) and (4.5),

$$d\boldsymbol{x} \cdot d\boldsymbol{x} = \left[(1 - r\kappa\cos\eta)^2 + \tau^2 r^2\right] ds^2 + dr^2 + r^2 d\eta^2 + 2\tau r^2 ds d\eta. \quad (4.8)$$

Therefore, the resulting coordinate system is non-orthogonal. However, using the transformation $\eta = \phi - \tau s$ in (4.8), we obtain

$$d\boldsymbol{x} \cdot d\boldsymbol{x} = (1 - r\kappa \cos(\phi - \tau s))^2 ds^2 + dr^2 + r^2 d\phi^2. \tag{4.9}$$

The coordinate system (s, r, ϕ) is orthogonal, and will be used to perform calculations in the rest of the paper. The scale factors for this coordinate system are defined as

$$h_s = (1 - r\kappa \cos(\phi - \tau s)), \quad h_r = 1, \quad h_\phi = r. \tag{4.10}$$

The impermeability and no-slip condition at the surface of the pipe in the (s, r, ϕ) coordinate system translate to

$$\boldsymbol{u} = (u_s, u_r, u_\phi) = \boldsymbol{0} \text{ at } r = 1. \tag{4.11}$$

In this paper, we assume that the flow is periodic in the streamwise direction s with period s_p. Hence, the domain of interest in the (s, r, ϕ) coordinate system is

$$\Omega = [0, s_p] \times [0, 1] \times [0, 2\pi]. \tag{4.12}$$

4.2.3 Choice of forcing

We choose to drive the flow with a dimensional forcing

$$\boldsymbol{f}^* = -\frac{1}{1 - r^*\kappa^* \cos(\phi^* - \tau^* s^*)} \times \frac{dP}{ds^*} \boldsymbol{e}_s \quad \text{for } 0 \leq r^* \leq R_p. \tag{4.13}$$

Here, $-dP/ds^*$ is a constant and can be thought of as the applied pressure gradient. Note how this streamwise directed forcing varies across the cross-section. The reason for this choice of forcing over a conventional forcing, which would be constant across the cross-section, is that the line integral along the streamwise direction for this forcing is independent of the position on the pipe cross-section and depends only on the difference of streamwise coordinates, i.e.

$$\int_{s^*=s_1^*}^{s_2^*} \boldsymbol{f}^* \cdot \boldsymbol{e}_s \, dl = \int_{s^*=s_1^*}^{s_2^*} -\frac{dP}{ds^*} \, ds^* = -\frac{dP}{ds^*}(s_2^* - s_1^*), \tag{4.14}$$

where $dl = h_s^* ds^*$ is the line element with $h_s^* = 1 - r^*\kappa^* \cos(\phi^* - \tau^* s^*)$. By contrast, for the conventional forcing, the value of this line integral would also depend on the position on the cross-section. Hence, we believe that our choice of forcing is good for modeling a flow driven by constant pressure boundary conditions. More detail on this choice of forcing in the context of flow in a torus can be found in Canton et al. (2016, 2017); Rinaldi et al. (2019). Note that in the limit of vanishing curvature ($\kappa \to 0$), our choice does reduce to constant forcing in the streamwise direction and therefore is consistent with the usual modeling of pressure-driven flow in a straight pipe. Based on (4.13), we define the forcing scale as

$$F = -\frac{dP}{ds^*}.$$

This implies that the non-dimensional forcing is given by

$$\boldsymbol{f} = \frac{1}{1 - r\kappa \cos(\phi - \tau s)} \boldsymbol{e}_s \quad \text{for } 0 \leq r \leq 1. \tag{4.15}$$

4.2.4 Quantities of interest

We are interested in obtaining a lower bound on the average non-dimensional flow rate Q, which we simply call flow rate, and an equivalent upper bound on the friction factor λ in the limit of high Reynolds number. As we are concerned with the high Reynolds number limit, so we use an inertial scaling to define the non-dimensional flow rate Q as

$$Q = \frac{1}{R_p^2}\left(\frac{\rho}{FR_p}\right)^{\frac{1}{2}} Q^* = \left\langle \int_{\phi=0}^{2\pi}\int_{r=0}^{1} u_s r dr d\phi \right\rangle, \tag{4.16}$$

where Q^* is the long-time average of the dimensional flow rate, u_s is the streamwise component of the non-dimensional velocity field $\boldsymbol{u}$ and

$$\langle [\,\cdot\,] \rangle = \lim_{T\to\infty} \frac{1}{T}\int_{t=0}^{T} [\,\cdot\,]\, dt \tag{4.17}$$

denotes the long-time average of a quantity. The Darcy–Weisbach friction factor λ, which is four times the Fanning friction factor, is defined as

$$\lambda = -\frac{dP}{ds^*}\,\frac{4R_p}{\rho u_m^{*2}}, \tag{4.18}$$

where u_m^* is the dimensional streamwise mean velocity given by

$$u_m^* = \frac{Q^*}{\pi R_p^2}. \tag{4.19}$$

When expressed in non-dimensional variables, the friction factor is

$$\lambda = \frac{4\pi^2}{Q^2}. \tag{4.20}$$

From (4.20), we notice that a lower bound on the flow rate Q will provide an upper bound on the friction factor λ.

4.3 The background method formulation

In this section, we describe the general approach of the background method applied to our problem. The formulation that we develop here is for any general background flow field and is similar to the one given in Constantin and Doering (1995) for pressure-driven channel flow.

The background method, in essence, works as follows. We first derive time-averaged integral identities from the governing equations (4.2) (using the fact that the long-time averages of certain time derivatives vanish) in order to rewrite the quantity of interest Q given by (4.16) as an equivalent long-time averaged expression that is easier to bound using analysis techniques. To that end, we begin by establishing a time-averaged total energy equation, by taking the dot product of equation (4.2) with $\boldsymbol{u}$ and then by performing a volume integration on the resulting equation. The result is

$$\frac{1}{2}\frac{d||\boldsymbol{u}||_2^2}{dt} = -\frac{1}{Re}||\boldsymbol{\nabla u}||_2^2 + \int_\Omega \boldsymbol{f}\cdot\boldsymbol{u}\, d\boldsymbol{x}, \tag{4.21}$$

where $||\cdot||_2$ denotes the L^2-norm, which is given by

$$||\cdot||_2 = \left(\int_\Omega |\cdot|^2\, d\boldsymbol{x}\right)^{\frac{1}{2}}, \tag{4.22}$$

and where the volume integral in (s, r, ϕ) coordinates is written as

$$\int_\Omega [\ \cdot\ ]\ d\boldsymbol{x} = \int_{s=0}^{s_p} \int_{\phi=0}^{2\pi} \int_{r=0}^{1} [\ \cdot\ ]\ h_s h_r h_\phi dr d\phi ds. \tag{4.23}$$

The quantity $||\boldsymbol{u}||_2^2(t)$ can be shown to be uniformly bounded in time within the framework of the background method (see Doering and Constantin, 1992; Constantin and Doering, 1995, for example). Therefore, the long-time average of the time derivative of $||\boldsymbol{u}||_2^2(t)$ vanishes. As a result, taking the long-time average of equation (4.21) leads to

$$\left\langle \int_\Omega \boldsymbol{f} \cdot \boldsymbol{u}\ d\boldsymbol{x} \right\rangle = \frac{1}{Re} \langle ||\boldsymbol{\nabla u}||_2^2 \rangle. \tag{4.24}$$

The second step of the method is to perform the background decomposition. We start by writing the total velocity $\boldsymbol{u}$ as the sum of two divergence-free velocity fields $\boldsymbol{u} = \boldsymbol{U} + \boldsymbol{v}$, where $\boldsymbol{\nabla \cdot U} = 0$ and $\boldsymbol{\nabla \cdot v} = 0$. We call $\boldsymbol{U}$ the background flow, which is steady and satisfies the same boundary conditions as the full flow $\boldsymbol{u}$, while the perturbation $\boldsymbol{v}$ satisfies the homogeneous version of the boundary conditions. The equation governing the evolution of $\boldsymbol{v}$ is given by

$$\begin{aligned} \frac{\partial \boldsymbol{v}}{\partial t} + \boldsymbol{U \cdot \nabla U} + \boldsymbol{U \cdot \nabla v} + \boldsymbol{v \cdot \nabla U} + \boldsymbol{v \cdot \nabla v} \\ = -\boldsymbol{\nabla} p + \frac{1}{Re} \nabla^2 \boldsymbol{U} + \frac{1}{Re} \nabla^2 \boldsymbol{v} + \boldsymbol{f}. \end{aligned} \tag{4.25}$$

Taking the dot product of the above equation with $\boldsymbol{v}$ and performing a volume integration, followed by taking the long-time average, results in

$$\left\langle \int_\Omega \boldsymbol{f} \cdot \boldsymbol{v}\ d\boldsymbol{x} \right\rangle = \frac{1}{2Re} \left\langle ||\boldsymbol{\nabla u}||_2^2 \right\rangle - \frac{1}{2Re} ||\boldsymbol{\nabla U}||_2^2 + \langle \mathcal{H}(\boldsymbol{v}) \rangle\,, \tag{4.26}$$

where

$$\mathcal{H}(\boldsymbol{v}) = \underbrace{\int_\Omega (\boldsymbol{v}\cdot\boldsymbol{\nabla}\boldsymbol{U}_{\text{sym}})\cdot\boldsymbol{v}\; d\boldsymbol{x}}_{I} + \underbrace{\int_\Omega (\boldsymbol{U}\cdot\boldsymbol{\nabla}\boldsymbol{U})\cdot\boldsymbol{v}\; d\boldsymbol{x}}_{II} + \underbrace{\frac{1}{2Re}||\boldsymbol{\nabla}\boldsymbol{v}||_2^2}_{III}, \tag{4.27}$$

and $\boldsymbol{\nabla}\boldsymbol{U}_{\text{sym}}$ is the symmetric part of $\boldsymbol{\nabla}\boldsymbol{U}$, i.e.

$$\boldsymbol{\nabla}\boldsymbol{U}_{\text{sym}} = \frac{\boldsymbol{\nabla}\boldsymbol{U} + \boldsymbol{\nabla}\boldsymbol{U}^\intercal}{2}. \tag{4.28}$$

We have used the following identity in deriving the equation (4.26)

$$|\boldsymbol{\nabla}\boldsymbol{u}|^2 = |\boldsymbol{\nabla}\boldsymbol{U}|^2 + |\boldsymbol{\nabla}\boldsymbol{v}|^2 + 2\boldsymbol{\nabla}\boldsymbol{U}:\boldsymbol{\nabla}\boldsymbol{v}, \tag{4.29}$$

where, in index notation,

$$\boldsymbol{\nabla}\boldsymbol{U}:\boldsymbol{\nabla}\boldsymbol{v} = \partial_i v_j \partial_i U_j. \tag{4.30}$$

Multiplying (4.26) by two and subtracting (4.24) yields

$$2\left\langle \int_\Omega \boldsymbol{f}\cdot\boldsymbol{v}\; d\boldsymbol{x}\right\rangle - \left\langle \int_\Omega \boldsymbol{f}\cdot\boldsymbol{u}\; d\boldsymbol{x}\right\rangle = -\frac{1}{Re}||\boldsymbol{\nabla}\boldsymbol{U}||_2^2 + 2\left\langle \mathcal{H}(\boldsymbol{v})\right\rangle. \tag{4.31}$$

The left-hand side of (4.31) can be simplified as follows

$$\begin{aligned}
&2\left\langle \int_\Omega \boldsymbol{f}\cdot\boldsymbol{v}\; d\boldsymbol{x}\right\rangle - \left\langle \int_\Omega \boldsymbol{f}\cdot\boldsymbol{u}\; d\boldsymbol{x}\right\rangle = \left\langle \int_\Omega \boldsymbol{f}\cdot\boldsymbol{u}\; d\boldsymbol{x}\right\rangle - 2\left\langle \int_\Omega \boldsymbol{f}\cdot\boldsymbol{U}\; d\boldsymbol{x}\right\rangle \\
&= \left\langle \int_{s=0}^{s_p}\left[\int_{\phi=0}^{2\pi}\int_{r=0}^{1} u_s r dr d\phi\right] ds\right\rangle - 2\int_{s=0}^{s_p}\left[\int_{\phi=0}^{2\pi}\int_{r=0}^{1} U_s r dr d\phi\right] ds \\
&= s_p\left\langle \int_{\phi=0}^{2\pi}\int_{r=0}^{1} u_s r dr d\phi\right\rangle - 2s_p\int_{\phi=0}^{2\pi}\int_{r=0}^{1} U_s r dr d\phi.
\end{aligned} \tag{4.32}$$

Note that we used $\boldsymbol{v} = \boldsymbol{u} - \boldsymbol{U}$ in the first line, then substituted the expression

for $\boldsymbol{f}$ from (4.15) and used the time independence of $\boldsymbol{U}$ to obtain the second line. The terms in the square brackets in the second line represent the flow of $\boldsymbol{u}$ and $\boldsymbol{U}$ through a cross-section of pipe and therefore are independent of the streamwise direction s because of the incompressibility of $\boldsymbol{u}$ and $\boldsymbol{U}$. Hence, we can easily integrate these expressions with respect to s, which leads to the third line. Using (4.32) in (4.31) and dividing by s_p on both sides gives

$$Q = \left\langle \int_{\phi=0}^{2\pi} \int_{r=0}^{1} u_s r dr d\phi \right\rangle = 2 \int_{\phi=0}^{2\pi} \int_{r=0}^{1} U_s r dr d\phi - \frac{1}{s_p Re} ||\boldsymbol{\nabla U}||_2^2 + \frac{2}{s_p} \left\langle \mathcal{H}(\boldsymbol{v}) \right\rangle . \tag{4.33}$$

If one can prove that

$$\mathcal{H}(\boldsymbol{v}) + \gamma \geq 0 \quad \forall\, \boldsymbol{v} \tag{4.34}$$

for a background flow $\boldsymbol{U}$ and some constant γ, then we have the following bound on the flow rate

$$Q \geq 2 \int_{\phi=0}^{2\pi} \int_{r=0}^{1} U_s r \; dr d\phi - \frac{1}{s_p Re} ||\boldsymbol{\nabla U}||_2^2 - \frac{2\gamma}{s_p}. \tag{4.35}$$

Following the convention (Doering and Constantin, 1994; Constantin and Doering, 1995), we call (4.34) the spectral constraint.

Note that the background method formulation given in Constantin and Doering (1995) for pressure-driven channel flows assumes that the background flow $\boldsymbol{U}$ is unidirectional and planar (a choice that is only suitable for planar geometries). As a result, the term II in (4.27) is zero and therefore the functional $\mathcal{H}(\boldsymbol{v})$ is homogenous in their work. Here, we have given the background method formulation for a general background flow $\boldsymbol{U}$. Also, as we shall see, the choice of

the background flow which works in the present case, is two-dimensional which leads to a nonzero term II in (4.27) and therefore the resultant functional $\mathcal{H}(\boldsymbol{v})$ is inhomogenous.

4.4 Bounds on flow rate and friction factor

In this section, we obtain a lower bound on the flow rate and an equivalent upper bound on the friction factor. We choose a family of background flows with varying boundary layer thickness along the circumference of the pipe. This variation of the boundary layer thickness will be carefully selected so that the spectral constraint (4.34) is satisfied while optimizing the bound (4.35) simultaneously for different values of curvature κ and torsion τ, thereby obtaining a geometrical dependence on these parameters. Note that in this paper, the *boundary layer* refers to the term boundary layer used in the context of the background method (see for instance, Doering and Constantin, 1994; Goluskin and Doering, 2016) and is not the conventional viscous boundary layer.

4.4.1 Choice of background flow

We make the following choice of background flow

$$\boldsymbol{U}(s,r,\phi) = \begin{cases} (\Lambda(1-r\kappa\cos(\phi-\tau s)),\ 0,\ \Lambda\tau r) \\ \qquad\qquad\qquad \text{if} \quad 0 \le r < 1-\delta g(s,\phi) \\ \left(\Lambda(1-r\kappa\cos(\phi-\tau s))\left(\frac{1-r}{\delta g(s,\phi)}\right),\ 0,\ \Lambda\tau r\left(\frac{1-r}{\delta g(s,\phi)}\right)\right) \\ \qquad\qquad\qquad \text{if} \quad 1-\delta g(s,\phi) \le r \le 1. \end{cases} \tag{4.36}$$

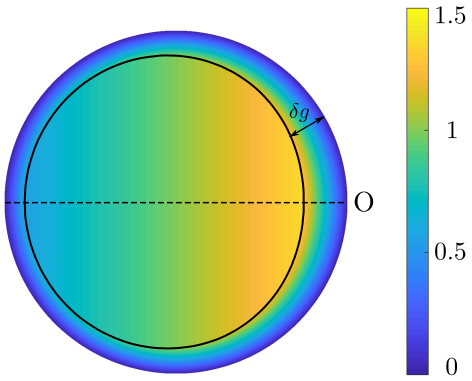

Figure 4.2: Variation of the streamwise component U_s of the background flow (4.36) across a cross-section of the pipe. In this example, the pipe's curvature is $\kappa = 0.5$ and torsion is $\tau = 0.25$. The solid black curve shows the edge of the boundary layer with variable thickness $\delta g(s, \phi)$. The point O denotes the outer edge of the pipe, i.e., the point on the cross-section, which is farthest from the axis of rotation of the helical pipe. The background flow in this figure corresponds to $\Lambda = 1$, and the boundary layer shape $g(s, \phi)$ is given by (4.56), which is the shape obtained in the process of optimizing the bound.

Here, Λ is a constant that will be adjusted later to optimize the bound,

$$\delta = \frac{1}{Re}, \tag{4.37}$$

and $g(s, \phi)$ is a non-zero bounded differentiable function of s and ϕ, that satisfies

$$0 < g_l \leq g(s, \phi) \leq g_u \quad \text{and} \quad \left|\frac{\partial g}{\partial s}\right|, \left|\frac{\partial g}{\partial \phi}\right| \leq g_u' \quad \forall\, s \in [0, s_p], \phi \in [0, 2\pi], \tag{4.38}$$

where g_l, g_u, and g_u' are constants independent of Re. The region $1 - \delta g(s, \phi) \leq r \leq 1$ is the boundary layer denoted as

$$\Omega_\delta = \{(s, r, \phi) | s \in [0, s_p], \phi \in [0, 2\pi], 1 - \delta g(s, \phi) \leq r \leq 1\}, \tag{4.39}$$

and the function $g(s, \phi)$ represents the shape of the boundary layer which will be determined later as part of the analysis to optimize the bound. Physically,

(4.38) means that the thickness of the boundary layer is everywhere non-zero and finite, and it varies smoothly. Figure (4.2) shows a color map of the streamwise component U_s of the background flow (4.36). It can be easily verified that the background flow field (4.36) satisfies the no-slip and impermeable boundary conditions on the pipe surface. Meanwhile, the divergence-free condition on the background flow enforces

$$g(s, \phi) = g(\phi - \tau s), \tag{4.40}$$

which constrains the choice of g. See Appendix 4.A for the calculation of divergence of a vector in the (s, r, ϕ) coordinate system. Also, note that for this choice of $\boldsymbol{U}$, in the bulk region $(0 \leq r \leq 1 - \delta g(s, \phi))$, we have

$$\boldsymbol{\nabla} \boldsymbol{U}_{\text{sym}} = \boldsymbol{0} \tag{4.41}$$

(see Appendix 4.C) the reason being is that in this region $\boldsymbol{U}$ is really a rigid body flow as viewed from some inertial frame of reference (see §4.5 Discussion and Concluding Remarks). Although we can obtain a bound on the flow rate with a constant boundary layer thickness, this choice does not provide the optimal bound as a function of the pipe's curvature κ and torsion τ. Unlike the case of planar geometries, the choice of the background flow (4.36) is not uniform in the bulk region. As can be seen in figure (4.2), the magnitude of the streamwise component U_s of the background flow in the bulk region varies and is higher towards the outer edge O of the pipe than the inner edge. As such, a constant boundary layer thickness is not necessarily the optimal choice for every κ and τ. Therefore, it is natural to choose a variable boundary layer thickness (which

is more general than the choice of constant boundary layer thickness) since our goal is to optimize bounds simultaneously for different curvature and torsion. Furthermore, in the process of obtaining bounds, we complement this choice of variable boundary layer thickness with inequalities suitably constructed (from standard analysis inequalities) to achieve this goal. In the forthcoming analysis, we will be interested in obtaining a bound in the limit of high Reynolds number and therefore will be frequently making use of the fact that $Re \gg 1$ or $\delta \ll 1$ to retain only the leading order terms.

4.4.2 The spectral constraint

In this subsection, we use analysis techniques to obtain a condition under which the spectral constraint (4.34) is satisfied. In what follows, we shall make use of a crucial inequality, whose proof is given in Appendix 4.B.

Lemma 1. *Let $w : \Omega_\delta \to \mathbb{R}$ be a square integrable function such that $w(s, 1, \phi) = 0$ for all $0 \leq s \leq s_p$ and $0 \leq \theta \leq 2\pi$, then the following statement is true*

$$\int_{\Omega_\delta} \sigma w^2 \, d\boldsymbol{x} \;\leq\; \frac{\delta^2}{2} \int_{\Omega_\delta} \sigma(s,1,\phi) g^2(s,\phi) \left(\frac{\partial w}{\partial r}\right)^2 \, d\boldsymbol{x} + O(\delta^3) \, ||\boldsymbol{\nabla} w||_2^2. \tag{4.42}$$

Here, $\sigma : \Omega_\delta \to \mathbb{R}$ is a positive bounded $O(1)$ function that satisfies

$$|\sigma(s,r,\phi) - \sigma(s,1,\phi)| = O(\delta) \quad \textit{for } (s,r,\phi) \in \Omega_\delta. \tag{4.43}$$

For convenience, we make use of the big O notation $O(\cdot)$. Let m and n be two functions, then in this notation, writing $m(\delta) = O(n(\delta))$ means that there exists two positive constants $C > 0$ and $\delta_0 > 0$ such that $|m(\delta)| \leq C|n(\delta)|$ whenever $0 \leq \delta < \delta_0$.

We start by obtaining a bound on I as defined in (4.27). Making use of (4.41) leads to

$$I = \int_{\Omega} (\boldsymbol{v} \cdot \boldsymbol{\nabla} \boldsymbol{U}_{\text{sym}}) \cdot \boldsymbol{v} \, d\boldsymbol{x} = \int_{\Omega_\delta} (\boldsymbol{v} \cdot \boldsymbol{\nabla} \boldsymbol{U}_{\text{sym}}) \cdot \boldsymbol{v} \, d\boldsymbol{x}. \tag{4.44}$$

The following inequality is obtained by substituting $\boldsymbol{\nabla} \boldsymbol{U}_{\text{sym}}$ (use (4.89) from Appendix 4.C for the calculation of $\boldsymbol{\nabla} \boldsymbol{U}_{\text{sym}}$) into (4.44)

$$\begin{aligned} |I| \leq \quad & \int_{\Omega_\delta} \xi_1(s,r,\phi)|v_s||v_r| \, d\boldsymbol{x} + \int_{\Omega_\delta} \xi_2(s,r,\phi)|v_\phi||v_r| \, d\boldsymbol{x} \\ & + \int_{\Omega_\delta} \xi_3 v_s^2 d\boldsymbol{x} + \int_{\Omega_\delta} \xi_4 v_\phi^2 \, d\boldsymbol{x} + \int_{\Omega_\delta} \xi_5 |v_s||v_\phi| \, d\boldsymbol{x}, \end{aligned} \tag{4.45}$$

where

$$\begin{aligned} \xi_1(s,r,\phi) &= \frac{\Lambda(1 - r\kappa\cos(\phi - \tau s))}{\delta g}, \qquad \xi_2(s,r,\phi) = \frac{\Lambda \tau r}{\delta g}, \\ \xi_3 &= \max_{(s,r,\phi)\in\Omega_\delta} \frac{\Lambda(1-r)}{\delta g^2} \left| \frac{\partial g}{\partial s} \right|, \qquad \xi_4 = \max_{(s,r,\phi)\in\Omega_\delta} \frac{\Lambda\tau(1-r)}{\delta g^2} \left| \frac{\partial g}{\partial \phi} \right|, \\ \xi_5 = \max_{(s,r,\phi)\in\Omega_\delta} \frac{\Lambda(1-r)}{\delta g^2} & \left[\frac{\tau r}{(1 - r\kappa\cos(\phi - \tau s))} \left| \frac{\partial g}{\partial s} \right| \right. \\ & \left. + \frac{(1 - r\kappa\cos(\phi - \tau s))}{r} \left| \frac{\partial g}{\partial \phi} \right| \right]. \end{aligned} \tag{4.46}$$

Given that $1 - r$ is $O(\delta)$ in the boundary layer, and using the constraints on g and its derivatives from (4.38), implies that ξ_3, ξ_4, and ξ_5 are $O(1)$ constants. Using Young's inequality $|v_s||v_\phi| \leq (|v_s|^2 + |v_\phi|^2)/2$, the last three integrals in (4.45) can be replaced by

$$\int_{\Omega_\delta} \left(\xi_3 + \frac{\xi_5}{2} \right) v_s^2 d\boldsymbol{x} + \int_{\Omega_\delta} \left(\xi_4 + \frac{\xi_5}{2} \right) v_\phi^2 \, d\boldsymbol{x}. \tag{4.47}$$

An application of Inequality 1 to these two integrals with $w = v_s$ in the first integral, $w = v_\phi$ in the second integral and taking σ to be an $O(1)$ constant in both cases results a bound on I as

$$|I| \leq \int_{\Omega_\delta} \xi_1(s,r,\phi)|v_s||v_r| \, d\boldsymbol{x} + \int_{\Omega_\delta} \xi_2(s,r,\phi)|v_\phi||v_r| \, d\boldsymbol{x} + O(\delta^2)||\boldsymbol{\nabla v}||_2^2. \tag{4.48}$$

In a similar manner, we obtain bounds on the remaining two integrals in (4.48). These bounds contribute to the leading order term of the bound on $|I|$; therefore, this time we perform the computation wisely with the intent of optimizing the bound on $|I|$ simultaneously in κ and τ. Using the following inequalities (based on Young's inequality) in (4.48)

$$|v_s||v_r| \leq \frac{c_1(s,\phi)|v_s|^2}{2} + \frac{|v_r|^2}{2c_1(s,\phi)}, \quad |v_\phi||v_r| \leq \frac{c_2(s,\phi)|v_\phi|^2}{2} + \frac{|v_r|^2}{2c_2(s,\phi)}, \tag{4.49}$$

where

$$0 < c_1(s,\phi) \quad \text{and} \quad 0 < c_2(s,\phi), \tag{4.50}$$

results in

$$\begin{aligned} |I| \leq \int_{\Omega_\delta} \left[\frac{c_1(s,\phi)\xi_1(s,r,\phi)}{2}\right] |v_s|^2 \, d\boldsymbol{x} + \int_{\Omega_\delta} \left[\frac{\xi_1(s,r,\phi)}{2c_1(s,\phi)} + \frac{\xi_2(s,r,\phi)}{2c_2(s,\phi)}\right] |v_r|^2 \, d\boldsymbol{x} \\ + \int_{\Omega_\delta} \left[\frac{c_2(s,\phi)\xi_2(s,r,\phi)}{2}\right] |v_\phi|^2 \, d\boldsymbol{x} + O(\delta^2)||\boldsymbol{\nabla v}||_2^2. \end{aligned} \tag{4.51}$$

We apply the Inequality 1 to the three integrals in (4.51) with $w = v_s, v_r$, and v_ϕ

and taking σ to be the corresponding terms in the square brackets times δ, which results in

$$|I| \leq \frac{\Lambda\delta}{4}\left[\int_{\Omega_\delta} p_1\left(\frac{\partial v_s}{\partial r}\right)^2 d\boldsymbol{x} + \int_{\Omega_\delta} p_2\left(\frac{\partial v_r}{\partial r}\right)^2 d\boldsymbol{x} + \int_{\Omega_\delta} p_3\left(\frac{\partial v_\phi}{\partial r}\right)^2 d\boldsymbol{x}\right] + O(\delta^2)||\boldsymbol{\nabla v}||_2^2, \tag{4.52}$$

where

$$\begin{aligned} p_1 &= (1-\kappa\cos(\phi-\tau s))g(s,\phi)c_1(s,\phi), \\ p_2 &= \frac{(1-\kappa\cos(\phi-\tau s))g(s,\phi)}{c_1(s,\phi)} + \frac{\tau g(s,\phi)}{c_2(s,\phi)}, \\ p_3 &= \tau g(s,\phi)c_2(s,\phi). \end{aligned} \tag{4.53}$$

We now choose the functions $g(s,\phi)$, $c_1(s,\phi)$, and $c_2(s,\phi)$ so that p_1, p_2, and p_3 are constants. For this choice, the bound on I can be written as

$$|I| \quad \leq \frac{\Lambda\delta}{4}\max\{p_1,p_2,p_3\}\ ||\boldsymbol{\nabla v}||_2^2 + O(\delta^2)||\boldsymbol{\nabla v}||_2^2. \tag{4.54}$$

To optimize the bound, we need

$$p_1 = p_2 = p_3, \tag{4.55}$$

as shown in Appendix 4.C. Combining this condition with the requirement that

p_1, p_2, and p_3 should be constants leads to

$$g(s,\phi) = \frac{g_c}{\sqrt{(1-\kappa\cos(\phi-\tau s))^2+\tau^2}}$$
$$c_1(s,\phi) = \sqrt{1+\frac{\tau^2}{(1-\kappa\cos(\phi-\tau s))^2}}, \quad c_2(s,\phi) = \sqrt{1+\frac{(1-\kappa\cos(\phi-\tau s))^2}{\tau^2}} \tag{4.56}$$

with g_c being an $O(1)$ positive constant. Note that the function $g(s,\phi)$ satisfies the constraints (4.38) and (4.40), where the constants g_l, g_u, g'_u in (4.38) can be chosen as

$$g_l = \frac{g_c}{\sqrt{(1+\kappa)^2+\tau^2}}, \quad g_u = \frac{g_c}{\sqrt{(1-\kappa)^2+\tau^2}}, \quad \text{and } g'_u = \frac{2g_c}{[(1-\kappa)^2+\tau^2]^{3/2}}. \tag{4.57}$$

Combining (4.53), (4.54), and (4.56) gives a bound on I as

$$|I| \leq \left|\int_\Omega \boldsymbol{v}\cdot\boldsymbol{\nabla U}\cdot\boldsymbol{v}\, d\boldsymbol{x}\right| \leq \left(\frac{\Lambda g_c \delta}{4} + O(\delta^2)\right)||\boldsymbol{\nabla v}||_2^2. \tag{4.58}$$

Next, we show that the contribution of term II, as defined in (4.27), is of higher order in δ compared to term I. First note that for any scalar function Ψ

$$II = \int_\Omega \boldsymbol{U}\cdot\boldsymbol{\nabla U}\cdot\boldsymbol{v}\, d\boldsymbol{x} = \int_\Omega (\boldsymbol{U}\cdot\boldsymbol{\nabla U} - \boldsymbol{\nabla}\Psi)\cdot\boldsymbol{v}\, d\boldsymbol{x} \tag{4.59}$$

using the incompressibility of $\boldsymbol{v}$, together with the fact that $\boldsymbol{v}$ satisfies the homogenous boundary conditions. Then, if we choose Ψ such that $\boldsymbol{U}\cdot\boldsymbol{\nabla U} = \boldsymbol{\nabla}\Psi$

in $\Omega \setminus \Omega_\delta$, namely,

$$\Psi(s, r, \phi) = \Lambda^2 \kappa \cos(\phi - \tau s) \left(r - \frac{r^2}{2} \kappa \cos(\phi - \tau s) \right) - \frac{\Lambda^2 \tau^2 r^2}{2}, \tag{4.60}$$

then one can readily check that

$$|(\boldsymbol{U} \cdot \boldsymbol{\nabla} \boldsymbol{U} - \boldsymbol{\nabla} \Psi)|(\boldsymbol{x}) = \begin{cases} 0 & \text{if } \boldsymbol{x} \in \Omega \setminus \Omega_\delta \\ O(1) & \text{if } \boldsymbol{x} \in \Omega_\delta \end{cases}. \tag{4.61}$$

See Appendix 4.C for the calculation of $\boldsymbol{\nabla U}$. Using (4.61), we can finally obtain a bound on II as

$$\begin{aligned} |II| \quad &= \left| \int_\Omega \boldsymbol{U} \cdot \boldsymbol{\nabla} \boldsymbol{U} \cdot \boldsymbol{v} \, d\boldsymbol{x} \right| = \left| \int_\Omega (\boldsymbol{U} \cdot \boldsymbol{\nabla} \boldsymbol{U} - \boldsymbol{\nabla} \Psi) \cdot \boldsymbol{v} \, d\boldsymbol{x} \right| \\ \implies |II| \quad &\leq O(1) \int_{\Omega_\delta} |\boldsymbol{v}| \, d\boldsymbol{x} \\ &\leq O(1) \int_{\Omega_\delta} |\boldsymbol{v}|^2 \, d\boldsymbol{x} + O(1) \int_{\Omega_\delta} 1 \, d\boldsymbol{x} \\ &\leq O(\delta^2) ||\boldsymbol{\nabla v}||_2^2 + s_p O(\delta). \end{aligned} \tag{4.62}$$

We have used Young's inequality to obtain the third line and Inequality 1 to obtain the last line. Finally,we obtain a bound on $\mathcal{H}(\boldsymbol{v})$ defined in (4.27) using the triangle inequality and the bounds derived on I and II as

$$\mathcal{H}(\boldsymbol{v}) \geq \frac{1}{2Re} ||\boldsymbol{\nabla v}||_2^2 - \left(\frac{\Lambda g_c \delta}{4} + O(\delta^2) \right) ||\boldsymbol{\nabla v}||_2^2 - s_p O(\delta), \tag{4.63}$$

which implies

$$\mathcal{H}(\boldsymbol{v}) + \gamma \geq 0 \tag{4.64}$$

as long as

$$g_c \leq \frac{2}{\Lambda} + O(\delta) \quad \text{and} \quad \gamma = s_p O(\delta). \tag{4.65}$$

4.4.3 Bound on mean quantities

We are now ready to compute the bound on the flow rate. We begin by evaluating the first term on the right-hand-side of (4.35) as

$$\begin{aligned}
\int_{\phi=0}^{2\pi}\int_{r=0}^{1} U_s r dr d\phi \quad &= \int_{\phi=0}^{2\pi}\int_{r=0}^{1-\delta g(s,\phi)} \Lambda(1 - r\kappa\cos(\phi - \tau s)) r dr d\phi \\
&+ \int_{\phi=0}^{2\pi}\int_{1-\delta g(s,\phi)}^{1} \Lambda(1 - r\kappa\cos(\phi - \tau s))\frac{(1-r)}{\delta g} r dr d\phi \\
&= \int_{\phi=0}^{2\pi}\int_{r=0}^{1} \Lambda(1 - r\kappa\cos(\phi - \tau s)) r dr d\phi + O(\delta) \\
&= \pi\Lambda + O(\delta).
\end{aligned} \tag{4.66}$$

Similarly, the second term on the right-hand-side of (4.35) is as follows

$$\begin{aligned}
||\boldsymbol{\nabla U}||_2^2 \quad &= \int_{\Omega_\delta} |\boldsymbol{\nabla U}|^2 \, d\boldsymbol{x} + \int_{\Omega\setminus\Omega_\delta} |\boldsymbol{\nabla U}|^2 \, d\boldsymbol{x} \\
&= \int_{s=0}^{s_p}\int_{\phi=0}^{2\pi}\int_{1-\delta g(s,\phi)}^{1} |\boldsymbol{\nabla U}|^2 \, h_s h_r h_\phi dr d\phi ds + s_p O(1) \\
&= \frac{2\pi\Lambda^2 s_p}{\delta \, g_c} I(\kappa,\tau) + s_p O(1),
\end{aligned} \tag{4.67}$$

where

$$I(\kappa,\tau) = \frac{1}{2\pi}\int_0^{2\pi} \left((1-\kappa\cos\alpha)^2 + \tau^2\right)^{3/2} (1 - \kappa\cos\alpha) \, d\alpha. \tag{4.68}$$

The integrand in the second line of (4.67) is explicitly calculated in (4.91), see Appendix 4.C. Using (4.66) and (4.67) in (4.35), we obtain a bound on the flow

rate Q as

$$Q \geq 2\pi\Lambda - \frac{2\pi\Lambda^2}{g_c} I(\kappa, \tau) + O(\delta). \tag{4.69}$$

We see that choosing a small value of g_c will make the bound on Q worse. Therefore, to obtain the best possible bound, we choose the largest possible value of g_c which satisfies the constraint (4.65), i.e.,

$$g_c = \frac{2}{\Lambda} + O(\delta). \tag{4.70}$$

The bound on Q then reads

$$Q \geq 2\pi\Lambda - \pi\Lambda^3 I(\kappa, \tau) + O(\delta). \tag{4.71}$$

All that remains is to choose Λ to maximize this lower bound. The optimal value of Λ is given by

$$\Lambda = \sqrt{\frac{2}{3I(\kappa, \tau)}}. \tag{4.72}$$

Substituting (4.72) into (4.71) and using $\delta = 1/Re$ as defined earlier in (4.37), gives a bound on the flow rate as

$$Q \geq \sqrt{\frac{32\pi^2}{27I(\kappa, \tau)}} + O(Re^{-1}). \tag{4.73}$$

Using this lower bound, together with the definition (4.20) of the friction factor

Pipe	Flow rate Q (lower bound)	Friction factor λ (upper bound)
Straight	$\mathscr{C}$	$\mathscr{D}$
Helical	$\mathscr{C}/\sqrt{I(\kappa,\tau)}$	$\mathscr{D}I(\kappa,\tau)$
Toroidal	$\mathscr{C}\left(1+3\kappa^2+\frac{3}{8}\kappa^4\right)^{-\frac{1}{2}}$	$\mathscr{D}\left(1+3\kappa^2+\frac{3}{8}\kappa^4\right)$
Helical ($\tau \ll 1$)	$\mathscr{C}\left(1+3\kappa^2+\frac{3}{8}\kappa^4\right)^{-\frac{1}{2}}\left(1-\frac{3(2+\kappa^2)\tau^2}{8+24\kappa^2+3\kappa^4}\right)$	$\mathscr{D}\left(1+3\kappa^2+\frac{3}{8}\kappa^4\right)\left(1+\frac{6(2+\kappa^2)\tau^2}{8+24\kappa^2+3\kappa^4}\right)$

Table 4.1: The first column shows the pipe type, the second column shows the lower bound on the flow rate Q (4.73) and the third column shows the upper bound on the friction factor λ (4.74) in different limits of curvature κ and torsion τ. In the table $\mathscr{C} = (32\pi^2/27)^{\frac{1}{2}}$ and $\mathscr{D} = 27/8$.

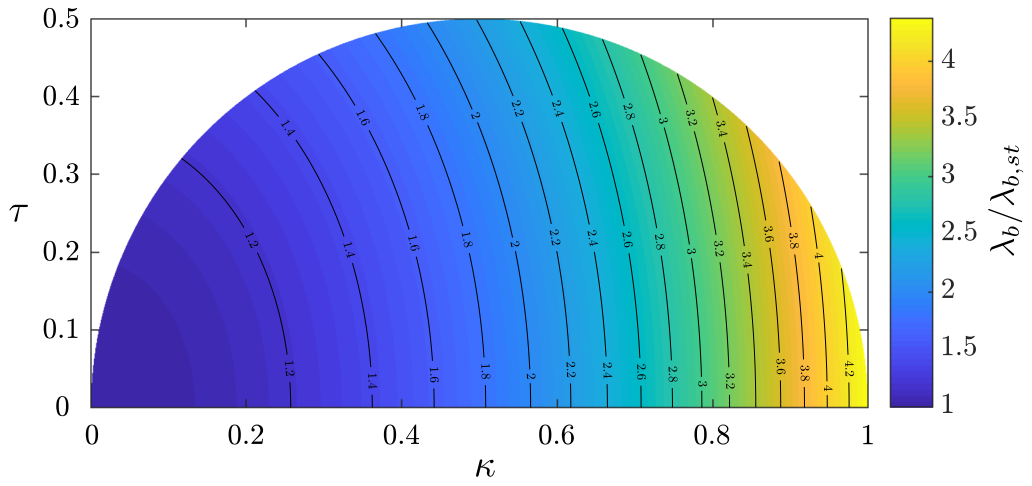

Figure 4.3: Ratio of the bound on the friction factor for a helical pipe as compared to a straight pipe ($\lambda_b/\lambda_{b,st}$), as a function of curvature κ and torsion τ. Here, λ_b is given by (4.74) and $\lambda_{b,st} = 27/8$.

λ in terms of Q, we finally obtain an upper bound on the friction factor as

$$\lambda \leq \lambda_b = \frac{27}{8} I(\kappa, \tau) + O(Re^{-1}). \tag{4.74}$$

These bounds on the flow rate (4.73) and friction factor (4.74) are also valid for a toroidal ($\kappa \neq 0, \tau = 0$) or a straight ($\kappa = 0, \tau = 0$) pipe. In general, the integral $I(\kappa, \tau)$ cannot be obtained analytically except when τ is zero or small. Table 4.1 summarizes the bounds derived on the flow rate and friction factor in different limits of curvature and torsion. For a toroidal pipe, a small radius of curvature has a second-order effect on the bounds (see table 4.1), which is also the case in the exact solution for the flow at low Reynolds number (see Dean, 1928). Similarly, for a helical pipe, the effect of a small torsion is of second-order on our bounds, and as before, this is the case for the steady-state solution at low Reynolds number (see Tuttle, 1990). More generally, the effect of increasing curvature and torsion is always to decrease the lower bound on the volume flow rate and to increase

the upper bound on the friction factor. For a straight pipe, the bound on the friction factor reduces to $\lambda_{b,st} = 27/8$ which is 12.5 times larger than the bound 0.27 (Plasting and Kerswell, 2005) obtained by solving the variational problem numerically. Figures 4.3 and 4.4 show a color map of the ratio of the bound on the friction factor for a helical pipe λ_b to the bound on the friction factor $\lambda_{b,st}$ for a straight pipe, as a function of κ, τ (figure 4.3) and a, b (figure 4.4). To avoid a self-intersecting geometry, we restrict to $1 < a < \infty$ and $0 \leq b < \infty$, which corresponds to a semicircular region in κ, τ space (see figure 4.3). The maximum increase in the bound on the friction factor is when the pipe approaches a horn torus ($\kappa = 1, \tau = 0$), which is a factor $35/8 = 4.375$ larger than for the straight pipe. From figure 4.4, we see that with the increase of the non-dimensional helix radius a or pitch $2\pi b$, the bound on the friction factor approaches that of a straight pipe, as expected.

4.5 Discussion and Concluding Remarks

In this paper, we used the background method to obtain bounds on the flow rate and friction factor in helical pipe flows. The bounds that we obtained are also valid for toroidal and straight pipes as limiting cases. By choosing a boundary layer whose thickness varies along the circumference of the pipe, we were able to obtain these bounds as a function of pipe geometry. In particular, we found that the bound on the friction factor varies with curvature κ and torsion τ according to the integral $I(\kappa, \tau)$, defined in (4.68), whose value is one for the straight pipe, i.e. $I(0, 0) = 1$.

The bound that we obtained on the friction factor is independent of the Reynolds number. However, it is a known property of wall-bounded flows in

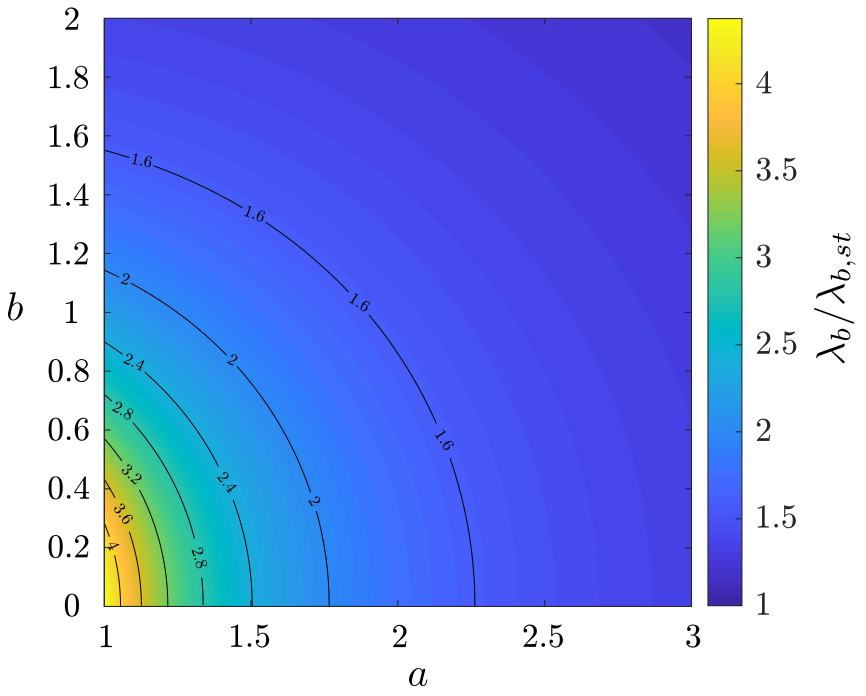

Figure 4.4: Ratio of the bound on the friction factor for a helical pipe as compared to a straight pipe ($\lambda_b/\lambda_{b,st}$), as a function of the non-dimensional geometric parameters a and b as defined earlier.

smooth geometries that the friction factor decreases as $(\log Re)^2$, as predicted using the logarithmic friction law (Tennekes and Lumley, 1972). Therefore, it appears that our bound, in terms of Reynolds number scaling is off by factor of $(\log Re)^2$, a situation similar to previous applications of the background method to shear and pressure-driven flows (Doering and Constantin, 1992, 1994; Constantin and Doering, 1995; Plasting and Kerswell, 2003). Despite being unable to capture the correct scaling in terms of Reynolds number, one may ask whether the geometrical scaling $I(\kappa, \tau)$ in the bound on the friction factor (4.74) correctly captures the variation of λ on the pipe geometry, as observed in the experiments. Assuming that is the case, then one would expect that the experimental data for the friction factor (λ_{exp}), when scaled with the integral $I(\kappa, \tau)$, should only be a function of the Reynolds number. Here, we test this hypothesis on data from carefully conducted experiments by Cioncolini and Santini (2006) for flows in helical pipes with negligible torsion. The results are shown in figure 4.5. In reporting these results, we have used the Reynolds number based on the pipe diameter ($Re_D = 2Re$), to be consistent with the literature. From figure 4.5, we see that our scaling, being second-order in the curvature κ, has a negligible effect on the pipes with small curvature ratios $\kappa = 0.028, 0.042, 0.059$. As such, the rescaled data $\lambda_{exp}/I(\kappa, \tau)$ looks almost identical to the original data, and does not collapse on a universal curve, contrary to our expectation. It thus appears that, for the range of Reynolds number considered in figure 4.5, the curvature has a first-order effect on the friction factor in the experiments, as opposed to the second-order effect predicted by our bound (see table 4.1). On a more positive note, the effect becomes qualitatively noticeable for $\kappa = 0.143$, and the rescaled data is more compact than the original data, suggesting that the dependence on the curvature κ given by the scaling $I(\kappa, \tau)$ at least has the right sign.

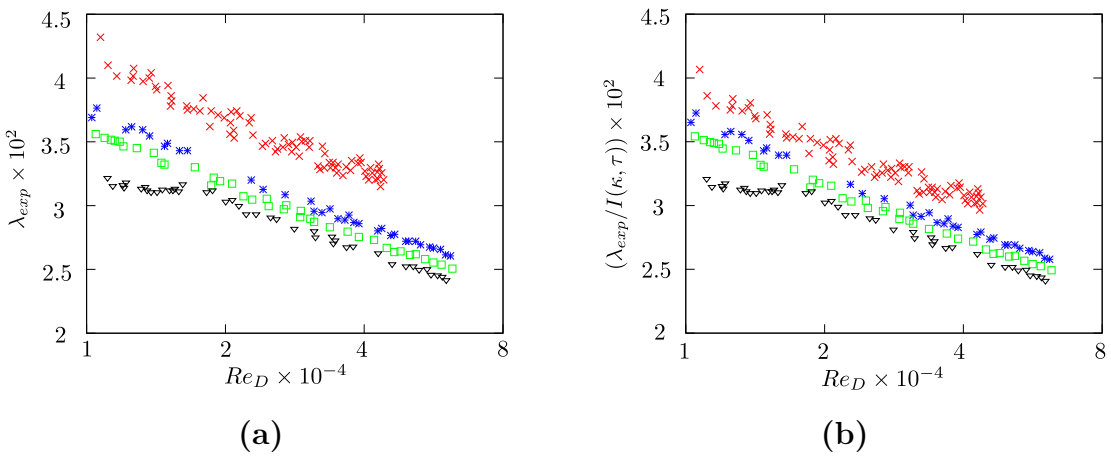

Figure 4.5: (a) Data from Cioncolini and Santini (2006), showing the friction factor (λ_{exp}) as a function of Reynolds number for four different helical pipes: (i) $\kappa = 0.028$, $\tau = 0.49 \times 10^{-3}$ (∇), (ii) $\kappa = 0.042$, $\tau = 1.87 \times 10^{-3}$($\square$), (iii) $\kappa = 0.059$, $\tau = 2.97 \times 10^{-3}$ ($*$), and (iv) $\kappa = 0.143$, $\tau = 11.4 \times 10^{-3}$ ($\times$). (b) Scaled friction factor ($\lambda_{exp}/I(\kappa,\tau)$) as a function of Reynolds number for the same four helical pipes.

There could be several possible reasons for the discrepancy between the data and the theoretical bound. First, there is further improvement possible in our analysis to capture the geometrical dependence of the friction factor better. One way to find that out would be to compute numerically the optimal bound on, e.g. the friction factor, similar to other studies of the background method (Plasting and Kerswell, 2003; Wen et al., 2013, 2015; Fantuzzi and Wynn, 2015, 2016; Fantuzzi, 2018; Tilgner, 2017, 2019) and then see if this optimal bound better accounts for the experimental data. The second possible reason for the discrepancy is that the Reynolds numbers achieved in the experiments are not high enough for our scalings to apply yet. Indeed, the critical Reynolds number for instability for a torus with curvature ratio $\kappa \approx 0.1$ is $Re_{D,c} \approx 3500$ (Canton et al., 2016), which is higher than that of a straight pipe $Re_{D,c} \approx 2040$ (Avila et al., 2011). Also, the transition for $\kappa \gtrapprox 0.028$ is supercritical (Kühnen et al., 2015), suggesting that the

flow structure slowly becomes more complex with increasing Reynolds number, only becoming fully developed turbulence at much higher Reynolds number. As a result, we believe that the maximum Reynolds number achieved by Cioncolini and Santini (2006) ($Re_D \approx 6 \times 10^4$), may not be high enough for our scalings to apply.

Beyond the fact that the bounds and the data do not agree as well as we could have hoped for, the technique used in this paper to derive formal bounds for such complex geometry deserves to be discussed. The feasibility of the background method relies on the existence of a divergence-free background flow field $\boldsymbol{U}$, which satisfies the same boundary conditions as the full flow $\boldsymbol{u}$ and for which $\mathcal{H}(\boldsymbol{v}) + \gamma$ is positive semi-definite, i.e. the spectral constraint (4.34) is satisfied. The situation becomes particularly difficult at high Reynolds number when the only undoubtedly positive term in $\mathcal{H}(\boldsymbol{v})$ (see term III in equation 4.27) becomes small. However, for an $O(1)$ background flow $\boldsymbol{U}$ for which $\boldsymbol{\nabla U}_{\text{sym}}$ is zero in bulk and is of $O(\delta^{-1})$ in a $O(\delta)$ thick boundary layer near the surface, it is possible to show that $\mathcal{H}(\boldsymbol{v}) + \gamma$ is positive semi-definite, as done in the present study and in several other studies of the background method (Doering and Constantin, 1994; Marchioro, 1994; Constantin and Doering, 1995; Wang, 1997). One may therefore generally ask under which circumstances can such a background flow $\boldsymbol{U}$ exist. We start by making two observations. First, that an $O(1)$ change in the velocity field in a boundary layer of thickness δ leads to $|\boldsymbol{\nabla U}_{\text{sym}}| = O(\delta^{-1})$ in the boundary layer. Second, that a divergence-free flow field $\boldsymbol{V}$ for which $\boldsymbol{\nabla V}_{\text{sym}} = \boldsymbol{0}$ is given by

$$\boldsymbol{V}(\boldsymbol{x}) = \boldsymbol{A}\boldsymbol{x} + \boldsymbol{V}_0, \tag{4.75}$$

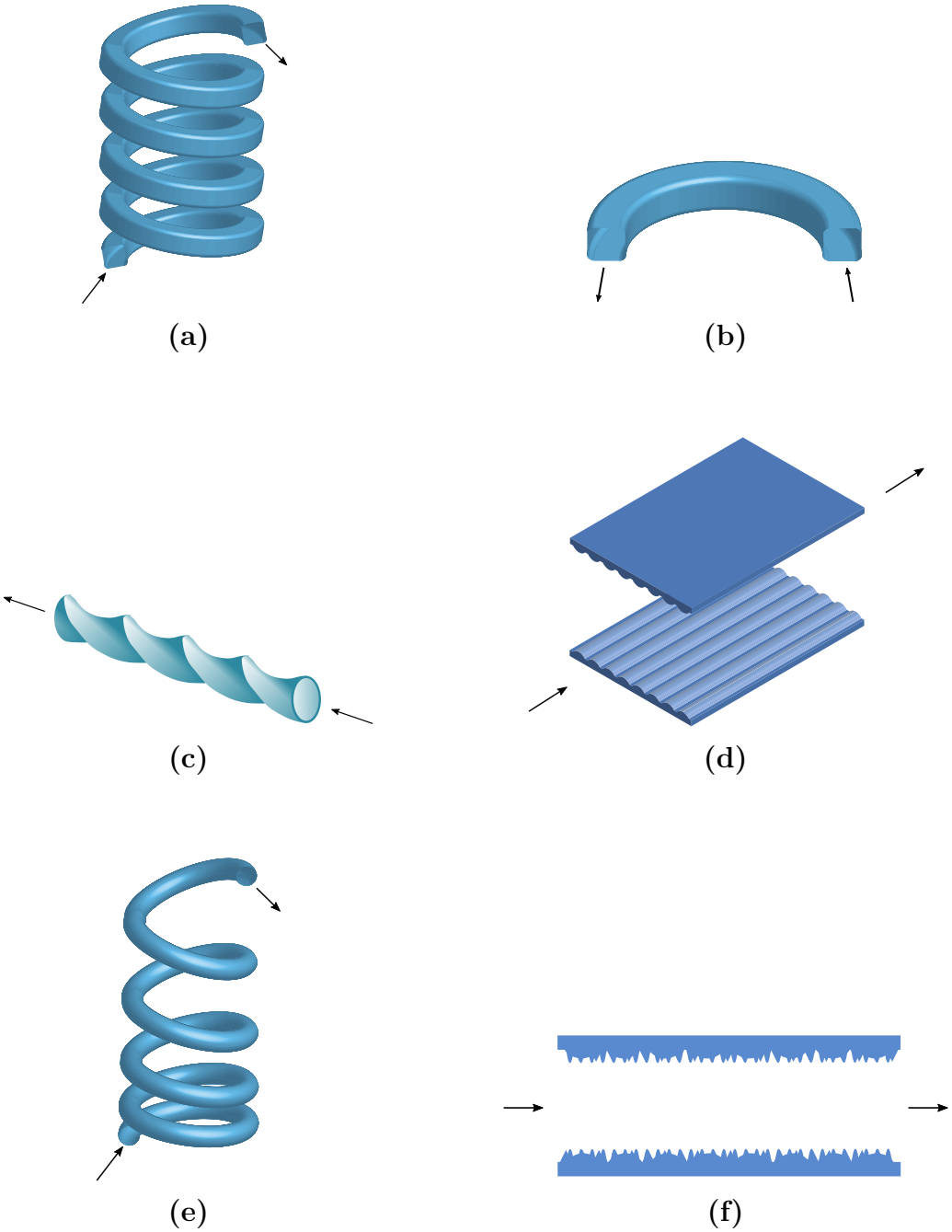

Figure 4.6: Pressure driven flow (a) through a helical pipe with a square cross-section, (b) through a toroidal pipe with a square cross-section, (c) through an axially twisted pipe with an elliptical cross-section, (d) between grooved walls where the grooves are aligned in the direction of the pressure gradient, (e) through a helical pipe with varying pitch, and (f) between rough walls (two-dimensional view). Arrows indicate the direction of the mean flow.

where $\boldsymbol{A}$ is a constant skew-symmetric tensor and $\boldsymbol{V}_0$ is a constant velocity field. The flows given by (4.75) include uniform flow, and rigid body flow. These two observations tell us that for a problem with prescribed tangential-velocity boundary conditions at impermeable boundaries where the boundaries have the shape of streamtubes of the flow field given by (4.75), it is always possible to find a background flow $\boldsymbol{U}$ for which $\boldsymbol{\nabla U}_{\text{sym}} = \boldsymbol{0}$ in the bulk and is $O(\delta^{-1})$ in a $O(\delta)$ thick boundary layer near the surface. Indeed, this is done by choosing $\boldsymbol{U} = \boldsymbol{V}$ in the bulk and by adjusting the tangential component of $\boldsymbol{U}$ by an $O(1)$ in the $O(\delta)$ boundary layer to satisfy the prescribed tangential-velocity boundary conditions. Note that these arguments apply to both pressure-driven flow and surface-velocity-driven flow problems, as they both involve the same spectral constraint (4.27). Wang (1997) considered the general problem of bounding the energy dissipation for a flow driven by an imposed tangential velocity at the boundaries in an arbitrary bounded domain when $\boldsymbol{A} = \boldsymbol{0}$ and $\boldsymbol{V}_0 = \boldsymbol{0}$. Considering the more general cases where $\boldsymbol{A}$ and $\boldsymbol{V}_0$ are non-zero enables us to extend the class of problems, as demonstrated in this paper.

Figure 4.6 shows some examples of pressure-driven flows where the criterion mentioned in the last paragraph can or cannot be applied. Although we considered the cross-section of the pipe to be circular in this paper, in general, a bound can be obtained on the friction factor for a helical, toroidal, or a straight pipe of any cross-section. Figure 4.6a and figure 4.6b, for example, show a helical pipe and a toroidal pipe with a square cross-section. These two cases fall under the case when $\boldsymbol{A} \neq \boldsymbol{0}, \boldsymbol{V}_0 \neq \boldsymbol{0}$ and $\boldsymbol{A} \neq \boldsymbol{0}, \boldsymbol{V}_0 = \boldsymbol{0}$, respectively. Figure 4.6c shows a pressure-driven flow through an axially twisted pipe with an elliptical cross-section. According to the criterion mentioned in the last paragraph, the background method can be applied to this example with $\boldsymbol{A} \neq \boldsymbol{0}, \boldsymbol{V}_0 \neq \boldsymbol{0}$. Further,

we can use the background method with $\boldsymbol{A} = \boldsymbol{0}, \boldsymbol{V}_0 \neq \boldsymbol{0}$ in case of pressure-driven flow between grooved walls (figure 4.6d) as long as the grooves are aligned in the direction of the pressure gradient. However, for pressure-driven flow through a helical pipe with varying pitch (figure 4.6e) or pressure-driven flow between rough walls (figure 4.6f), there is no choice of $\boldsymbol{A}$ and $\boldsymbol{V}_0$ which works.

The criterion we have mentioned is, so far, a sufficient criterion for the applicability of the background method. Whether this criterion is also a necessary one remains to be determined. The answer to that question is fundamental since it would provide definite guidance about which problems can and cannot be tackled using the background method.

Acknowledgement

A.K. acknowledges the support from the Dean's fellowship and Regents' fellowship from the Baskin School of Engineering at UC Santa Cruz, from the GFD fellowship program 2019 at the Woods Hole Oceanographic Institution, and from NSF AST 1814327. Many thanks to P. Garaud and anonymous referees for providing useful comments, which helped to improve the quality of the paper.

Appendix 4.A The (s, r, ϕ) coordinate system

An infinitesimal displacement $d\boldsymbol{x}$ in the (s, r, ϕ) coordinate system can be written as

$$d\boldsymbol{x} = h_s ds\ \boldsymbol{e}_s + h_r dr\ \boldsymbol{e}_r + h_\phi d\phi\ \boldsymbol{e}_\phi, \tag{4.76}$$

where the scale factors are

$$h_s = (1 - r\kappa\cos(\phi - \tau s)), \quad h_r = 1, \quad h_\phi = r. \tag{4.77}$$

The gradient of a scalar field Ψ in the (s, r, ϕ) coordinate system is given by

$$\boldsymbol{\nabla}\Psi = \frac{1}{h_s}\frac{\partial\Psi}{\partial s}\boldsymbol{e}_s + \frac{1}{h_r}\frac{\partial\Psi}{\partial r}\boldsymbol{e}_r + \frac{1}{h_\phi}\frac{\partial\Psi}{\partial\phi}\boldsymbol{e}_\phi. \tag{4.78}$$

The divergence of a vector field $\boldsymbol{q} = (q_s, q_r, q_\phi)$ in the (s, r, ϕ) coordinate system is

$$\boldsymbol{\nabla}\cdot\boldsymbol{q} = \frac{1}{h_s h_r h_\phi}\left[\frac{\partial h_r h_\phi q_s}{\partial s} + \frac{\partial h_\phi h_s q_r}{\partial r} + \frac{\partial h_s h_r q_\phi}{\partial\phi}\right]. \tag{4.79}$$

Finally, the gradient of a vector $\boldsymbol{q} = (q_s, q_r, q_\phi)$ in the (s, r, ϕ) coordinate system is written as

$$\begin{aligned}
\boldsymbol{\nabla}\boldsymbol{q} = \quad & \left(\frac{1}{h_s}\frac{\partial q_s}{\partial s} + \frac{q_r}{h_s h_r}\frac{\partial h_s}{\partial r} + \frac{q_\phi}{h_s h_\phi}\frac{\partial h_s}{\partial\phi}\right)\boldsymbol{e}_s\boldsymbol{e}_s + \left(\frac{1}{h_s}\frac{\partial q_r}{\partial s} - \frac{q_s}{h_s h_r}\frac{\partial h_s}{\partial r}\right)\boldsymbol{e}_s\boldsymbol{e}_r \\
& + \left(\frac{1}{h_s}\frac{\partial q_\phi}{\partial s} - \frac{q_s}{h_s h_\phi}\frac{\partial h_s}{\partial\phi}\right)\boldsymbol{e}_s\boldsymbol{e}_\phi + \left(\frac{1}{h_r}\frac{\partial q_s}{\partial r} - \frac{q_r}{h_r h_s}\frac{\partial h_r}{\partial s}\right)\boldsymbol{e}_r\boldsymbol{e}_s \\
& + \left(\frac{1}{h_r}\frac{\partial q_r}{\partial r} + \frac{q_s}{h_r h_s}\frac{\partial h_r}{\partial s} + \frac{q_\phi}{h_r h_\phi}\frac{\partial h_r}{\partial\phi}\right)\boldsymbol{e}_r\boldsymbol{e}_r + \left(\frac{1}{h_r}\frac{\partial q_\phi}{\partial r} - \frac{q_r}{h_r h_\phi}\frac{\partial h_r}{\partial\phi}\right)\boldsymbol{e}_r\boldsymbol{e}_\phi \\
& + \left(\frac{1}{h_\phi}\frac{\partial q_s}{\partial\phi} - \frac{q_\phi}{h_\phi h_s}\frac{\partial h_\phi}{\partial s}\right)\boldsymbol{e}_\phi\boldsymbol{e}_s + \left(\frac{1}{h_\phi}\frac{\partial q_r}{\partial\phi} - \frac{q_\phi}{h_\phi h_r}\frac{\partial h_\phi}{\partial r}\right)\boldsymbol{e}_\phi\boldsymbol{e}_r \\
& + \left(\frac{1}{h_\phi}\frac{\partial q_\phi}{\partial\phi} + \frac{q_r}{h_\phi h_r}\frac{\partial h_\phi}{\partial r} + \frac{q_s}{h_\phi h_s}\frac{\partial h_\phi}{\partial s}\right)\boldsymbol{e}_\phi\boldsymbol{e}_\phi.
\end{aligned} \tag{4.80}$$

Appendix 4.B A few useful inequalities

Lemma 0. *Let $w : [1-\delta g(s,\phi), 1] \to \mathbb{R}$ be a square integrable function such that $w(1) = 0$, then the following inequality holds*

$$w^2(r) \leq \left(\frac{1-r}{1-\kappa\cos(\phi-\tau s)} + O(\delta^2)\right) \times \int_{1-\delta g(s,\phi)}^{1} \left(\frac{\partial w}{\partial r'}\right)^2 (1 - r'\kappa\cos(\phi-\tau s))r'dr' \tag{4.81}$$

for given s, and ϕ. Here, $r \in [1-\delta g(s,\phi), 1]$.

Proof. For $r \in [1-\delta g(s,\phi), 1]$, using the fundamental theorem of calculus and the Cauchy–Schwarz inequality, the following inequality holds

$$\begin{aligned} w^2(r) &= \left|\int_1^r \frac{dw}{dr'}dr'\right|^2 \\ &\leq \left(\int_r^1 \frac{1}{(1-r'\kappa\cos(\phi-\tau s))r'}dr'\right) \times \\ &\qquad \left(\int_{1-\delta g(s,\phi)}^{1} \left(\frac{dw}{dr'}\right)^2 (1-r'\kappa\cos(\phi-\tau s))r'dr'\right). \end{aligned} \tag{4.82}$$

As mentioned earlier, the curvature satisfies $\kappa < 1$ and since $r' \leq 1$ in the above expression, we have $(1 - r'\kappa\cos(\phi-\tau s)) < 1$. Therefore, the integrands in both integrals are positive. Finally, using the fact that

$$\left|\frac{1}{(1-r'\kappa\cos(\phi-\tau s))r'} - \frac{1}{1-\kappa\cos(\phi-\tau s)}\right| = O(\delta)$$

when $r' \in [1-\delta g(s,\phi), 1]$ completes the proof. □

Lemma 1. *Let $w : \Omega_\delta \to \mathbb{R}$ be a square integrable function such that $w(s,1,\phi) = 0$*

for all $0 \leq s \leq s_p$ *and* $0 \leq \theta \leq 2\pi$*, then the following statement is true*

$$\int_{\Omega_\delta} \sigma w^2 \, d\boldsymbol{x} \;\leq\; \frac{\delta^2}{2} \int_{\Omega_\delta} \sigma(s,1,\phi) g^2(s,\phi) \left(\frac{\partial w}{\partial r}\right)^2 \, d\boldsymbol{x} + O(\delta^3) \, ||\boldsymbol{\nabla} w||_2^2. \tag{4.83}$$

Here, $\sigma : \Omega_\delta \to \mathbb{R}$ *is a positive bounded* $O(1)$ *function that satisfies*

$$|\sigma(s,r,\phi) - \sigma(s,1,\phi)| = O(\delta) \quad \textit{for } (s,r,\phi) \in \Omega_\delta. \tag{4.84}$$

Proof. The calculation is as follows:

$$\begin{aligned}
\int_{\Omega_\delta} \sigma w^2 \, d\boldsymbol{x} \quad &= \int_{s=0}^{s_p} \int_{\phi=0}^{2\pi} \int_{r=1-\delta g(s,\phi)}^{1} \sigma w^2 \, h_s h_r h_\phi \, dr d\phi ds \\
&\leq \int_{s=0}^{s_p} \int_{\phi=0}^{2\pi} \int_{r=1-\delta g(s,\phi)}^{1} \sigma \left[\left(\frac{1-r}{1-\kappa\cos(\phi-\tau s)} + O(\delta^2) \right) \right. \\
&\quad \left. \times \int_{1-\delta g(s,\phi)}^{1} \left(\frac{\partial w}{\partial r'}\right)^2 (1 - r'\kappa\cos(\phi-\tau s)) r' dr' \right] h_s h_r h_\phi \, dr d\phi ds.
\end{aligned} \tag{4.85}$$

Note that Inequality 0 was used in the second line. For $(s,r,\phi) \in \Omega_\delta$, with an application of the triangle inequality we have

$$\begin{aligned}
&|\sigma h_s h_r h_\phi - (1 - \kappa\cos(\phi-\tau s))\sigma(s,1,\phi)| \\
&\leq |\sigma(s,r,\phi) - \sigma(s,1,\phi)| \max_{(s,r,\phi)\in\Omega_\delta} (h_s h_r h_\phi) \\
&\qquad + |h_s h_r h_\phi - (1 - \kappa\cos(\phi-\tau s))| \sigma(s,1,\phi).
\end{aligned} \tag{4.86}$$

Noting that

$$|\sigma(s,r,\phi) - \sigma(s,1,\phi)| = O(\delta) \quad \text{and} \quad |h_s h_r h_\phi - (1 - \kappa\cos(\phi-\tau s))| = O(\delta),$$

when $(s, r, \phi) \in \Omega_\delta$, and

$$\max_{(s,r,\phi)\in\Omega_\delta} (h_s h_r h_\phi) = O(1) \quad \text{and} \quad \sigma(s, 1, \phi) = O(1),$$

leads to

$$|\sigma h_s h_r h_\phi - (1 - \kappa\cos(\phi - \tau s))\sigma(s, 1, \phi)| = O(\delta) \quad \text{for } (s, r, \phi) \in \Omega_\delta. \tag{4.87}$$

Using (4.87) in (4.85) and performing the integration in r leads to the desired result. □

Appendix 4.C Some useful calculations

4.C.1 Calculation of $\boldsymbol{\nabla U}$

For the background flow given by (4.36), for $\boldsymbol{x} \in \Omega \setminus \Omega_\delta$, we have

$$\begin{aligned}\boldsymbol{\nabla U} = \Lambda\kappa\cos(\phi - \tau s)\boldsymbol{e}_s\boldsymbol{e}_r - \Lambda\kappa\sin(\phi - \tau s)\boldsymbol{e}_s\boldsymbol{e}_\phi - \Lambda\kappa\cos(\phi - \tau s)\boldsymbol{e}_r\boldsymbol{e}_s \\ +\Lambda\tau\boldsymbol{e}_r\boldsymbol{e}_\phi + \Lambda\kappa\sin(\phi - \tau s)\boldsymbol{e}_\phi\boldsymbol{e}_s - \Lambda\tau\boldsymbol{e}_\phi\boldsymbol{e}_r.\end{aligned} \tag{4.88}$$

It is clear that $\boldsymbol{\nabla U}_{\text{sym}} = \mathbf{0}$ in $\Omega \setminus \Omega_\delta$. For, $\boldsymbol{x} \in \Omega_\delta$, we have

$$\begin{aligned}
\boldsymbol{\nabla U} = &-\frac{\Lambda(1-r)}{\delta g^2}\frac{\partial g}{\partial s}\boldsymbol{e}_s\boldsymbol{e}_s + \frac{\Lambda\kappa(1-r)\cos(\phi-\tau s)}{\delta g}\boldsymbol{e}_s\boldsymbol{e}_r \\
&- \left[\frac{\Lambda\tau r(1-r)}{\delta(1-r\kappa\cos(\phi-\tau s))g^2}\frac{\partial g}{\partial s} + \frac{\Lambda\kappa\sin(\phi-\tau s)(1-r)}{\delta g}\right]\boldsymbol{e}_s\boldsymbol{e}_\phi \\
&- \left[\frac{\Lambda(1-r\kappa\cos(\phi-\tau s))}{\delta g} + \frac{\Lambda\kappa\cos(\phi-\tau s)(1-r)}{\delta g}\right]\boldsymbol{e}_r\boldsymbol{e}_s \\
&+ \left[\frac{\Lambda\tau(1-r)}{\delta g} - \frac{\Lambda\tau r}{\delta g}\right]\boldsymbol{e}_r\boldsymbol{e}_\phi - \frac{\Lambda\tau(1-r)}{\delta g}\boldsymbol{e}_\phi\boldsymbol{e}_r - \frac{\Lambda\tau(1-r)}{\delta g^2}\frac{\partial g}{\partial\phi}\boldsymbol{e}_\phi\boldsymbol{e}_\phi \\
&+ \left[\frac{\Lambda\kappa\sin(\phi-\tau s)(1-r)}{\delta g} - \frac{\Lambda(1-r\kappa\cos(\phi-\tau s))(1-r)}{\delta r g^2}\frac{\partial g}{\partial\phi}\right]\boldsymbol{e}_\phi\boldsymbol{e}_s. \qquad (4.89)
\end{aligned}$$

Given that $1-r$ is $O(\delta)$ in the boundary layer, calculation of $|\boldsymbol{\nabla U}|^2$ up to leading order terms is

$$|\boldsymbol{\nabla U}|^2 = \frac{\Lambda^2(1-\kappa\cos(\phi-\tau s))^2}{\delta^2 g^2} + \frac{\Lambda^2\tau^2}{\delta^2 g^2} + O(\delta^{-1}), \qquad (4.90)$$

and

$$|\boldsymbol{\nabla U}|^2 h_s h_r h_\phi = \frac{\Lambda^2(1-\kappa\cos(\phi-\tau s))}{\delta^2 g^2}\left[(1-\kappa\cos(\phi-\tau s))^2 + \tau^2\right] + O(\delta^{-1}). \qquad (4.91)$$

We use this result in (4.67) for the calculation of $||\boldsymbol{\nabla U}||^2$. With the use of (4.38), we see that the only two terms that are $O(\delta^{-1})$ in (4.89) are the terms involving $\boldsymbol{e}_r\boldsymbol{e}_s$ and $\boldsymbol{e}_r\boldsymbol{e}_\phi$. However, these terms do not contribute to the calculation of $\boldsymbol{U}\cdot\boldsymbol{\nabla U}$, as they are multiplied with U_r (the r component of $\boldsymbol{U}$) which is zero. Therefore, $\boldsymbol{U}\cdot\boldsymbol{\nabla U}$ is $O(1)$ in Ω_δ. This result is useful in showing (4.61).

4.C.2 Reason behind choice 4.55

In the analysis done in the main text, if we had just assumed that p_1, p_2, and p_3 are constant functions but not necessarily equal, then a similar calculation would have led to

$$\begin{aligned} g(s,\phi) &= \sqrt{\frac{p_1 p_2 p_3}{p_3(1-\kappa\cos(\phi-\tau s))^2 + p_1\tau^2}} \\ c_1(s,\phi) &= \sqrt{\frac{p_1}{p_2} + \frac{p_1^2\tau^2}{p_2 p_3(1-\kappa\cos(\phi-\tau s))^2}}, \\ c_2(s,\phi) &= \sqrt{\frac{p_3}{p_2} + \frac{p_3^2(1-\kappa\cos(\phi-\tau s))^2}{p_1 p_2\tau^2}}. \end{aligned} \tag{4.92}$$

With this choice, we could have obtained the same bounds on the flow rate and the friction factor, namely

$$Q \geq \sqrt{\frac{32\pi^2}{27 I(\kappa,\tau)}} + O(Re^{-1}) \qquad \lambda \leq \lambda_b = \frac{27}{8} I(\kappa,\tau) + O(Re^{-1}). \tag{4.93}$$

However, this time

$$I(\kappa,\tau) = \frac{1}{2\pi}\int_0^{2\pi} (1-\kappa\cos\alpha)\left((1-\kappa\cos\alpha)^2+\tau^2\right)\sqrt{\frac{M^2(1-\kappa\cos\alpha)^2}{p_1'} + \frac{M^2\tau^2}{p_3'}}\, d\alpha, \tag{4.94}$$

where

$$M = \max\{p_1', 1, p_3'\}, \quad p_1' = \frac{p_1}{p_2}, \quad p_3' = \frac{p_3}{p_2}. \tag{4.95}$$

To optimize the bound, we need to minimize $I(\kappa, \tau)$ and that clearly happens when

$$p_1' = p_3' = 1 \quad \Longrightarrow \; p_1 = p_2 = p_3. \tag{4.96}$$

Chapter 5

Geometrical dependence of optimal bounds in Taylor–Couette flow

This chapter is based on the paper Kumar (2022a) published in the Journal of Fluid Mechanics, Volume 948, 10 October 2022, A11.

5.1 Introduction

An important problem in the study of turbulent flows is to estimate the functional dependence of global properties (such as energy dissipation, drag force, heat and mass transport, and mixing efficiency) on input parameters. The lack of analytical solutions of the Navier–Stokes equations in the fully turbulent regime has forced the scientific community to adopt a multi-faceted approach to this problem, in which simple physical theories and reduced models are proposed, and then corroborated by direct numerical simulations (DNS) and/or results from labora-

tory experiments. However, the inability to perform simulations and experiments in the extreme parameter regimes that often concern atmospheric, oceanic and astrophysical flows and engineering applications leaves these theories unsubstantiated.

In these extreme parameter regimes, an alternative approach that can provide meaningful information is to obtain rigorous bounds on the aforementioned global properties. The first method to obtain bounds was developed by Howard (1963) and Busse (1969), but it was not until the 1990s that bounding techniques gained general popularity, with the introduction of the so-called "Background Method" by Doering and Constantin (Doering and Constantin, 1992, 1994; Constantin and Doering, 1995; Doering and Constantin, 1996). The background method is based on ideas from Hopf to produce *a priori* estimates for the solutions of the Navier–Stokes equations with inhomogeneous boundary conditions (Hopf, 1955). It has so far been applied to many different fluid mechanics problems (Doering and Constantin, 1992; Constantin and Doering, 1995; Doering and Constantin, 1996; Caulfield and Kerswell, 2001; Tang et al., 2004; Whitehead and Doering, 2011b; Goluskin and Doering, 2016; Fantuzzi et al., 2018; Fantuzzi, 2018; Kumar and Garaud, 2020; Arslan et al., 2021b; Fan et al., 2021; Arslan et al., 2021a; Kumar et al., 2022). See Fantuzzi et al. (2022) for a recent review.

In the background method, we write the total flow field as a sum of two flow fields: the background flow and the perturbed flow. To obtain a bound on the desired bulk quantity requires choosing a background field that satisfies a certain integral constraint (extracted from the governing equations of the perturbed flow). Generally, one takes one of the two following routes. The first route is to specify a functional form of the background flow and then use standard inequalities. This route leads to an analytical but suboptimal bound on the bulk quantity as a

function of system parameters. The second route is to find the *best* possible bound (optimal bound) through a variational formulation of the background method in which one solves the corresponding Euler–Lagrange equations usually numerically. Numerous studies pertaining to the background flow have concentrated on the scaling of optimal bounds as a function of the principal flow parameter, such as the Reynolds number and the Rayleigh number. However, only a handful of them studied the variation of these bounds with the shape of the domain. One such study is by Wen et al. (2013), where the authors were interested in determining the dependence on aspect ratio of the optimal bound on heat transfer in porous medium convection.

In this paper, we are concerned with the question of whether it is possible to obtain the analytical expression for the dependence of optimal bounds on the geometrical parameters of the system. Indeed, while the numerically obtained optimal bounds usually follow an easily-identifiable simple power-law in the principal flow parameter, the variation of the optimal bounds with geometrical parameters, however, is not so readily apparent. Furthermore, we also aim to determine whether this analytical form bears any resemblance to the actual dependence of the corresponding bulk quantity on system geometry in fully turbulent flows. This question is motivated by engineering applications where the geometry plays an important role.

In a recent study, we attempted to provide bounds on the friction factor in the context of pressure driven helical pipe flows (Kumar, 2020). We focussed in particular on the dependence of this bound on the geometrical parameters: the curvature and torsion of the pipe. We took the first route described above, and used standard functional inequalities to find a suboptimal bound on the friction factor. In order to account for the geometry, we constructed a background flow

in which we allowed for a boundary layer thickness that varies along the circumference of the pipe, and optimized the shape of that boundary layer to find the best possible bound for any curvature and torsion. Without giving any further evidence, we hypothesized that the suboptimal bound thus produced might have the same geometrical dependence as the optimal bound.

This paper demonstrates that this hypothesis holds true for Taylor–Couette flow; i.e., the analytical geometrical dependence of the suboptimal bound obtained using traditional functional inequalities (but with a definition of the background flow with optimized boundary layer thickness) is the same as for the optimal bounds obtained using the variational approach.

There are several reasons why we choose to work with the Taylor–Couette flow to test this hypothesis. The Taylor–Couette flow is one of the most extensively investigated problems in fluid mechanics, going back to the seminal paper of Taylor (Taylor, 1923) and laboratory experiments of Wendt (Wendt, 1933), which are one of the early major contributions to the field. It is known that the Taylor–Couette system exhibits rich flow structures and complex fluid dynamical phenomena and has served as a testing ground for the theories of turbulent flows. The simplicity of the Taylor–Couette setup makes it amenable to conduct direct numerical simulations and experiments with high precision at high Reynolds numbers. As a result, starting with the work of Lathrop et al. (1992a,b), the last two decades have seen a tremendous activity in the study of high Reynolds number Taylor–Couette flow from the computational and experimental point of view (see a review by Grossmann et al. (2016)).

Concurrently, progress has also been made on obtaining rigorous bounds in Taylor–Couette flow. Nickerson (1969) was the first to derive an upper bound on the torque in Taylor–Couette flow using the technique developed by Howard

(1963) and Busse (1969). Constantin (1994) later revisited the problem using the background method of Doering and Constantin, and also derived an analytical upper bound on the torque. More recently, Ding and Marensi (2019) computed the corresponding optimal bounds numerically for systems where the ratio of the inner to outer cylinder radii, called the radius ratio hereafter, is 0.5, 0.714 and 0.909. Note that these three studies concentrated on the dependence of the bounds on the Reynolds number.

The primary goal of this paper is to obtain the correct functional dependence of the optimal bounds on the torque with respect to the radius ratio. To do so, we shall begin by obtaining an analytical bound using standard inequalities, with the aim of optimizing this bound simultaneously for all values of the radius ratio. Subsequently, we obtain numerical optimal bounds for several values of the radius ratio considering three different scenarios for the perturbations, which are the following:

case 1: The perturbations that satisfy the homogeneous boundary conditions but are not necessarily incompressible;

case 2: Additionally, the perturbations are three-dimensional and incompressible;

case 3: The perturbations, along with satisfying the boundary conditions and being incompressible, are only two-dimensional (invariant in the axial direction).

We note that while formulating the background method, we do use the incompressibility condition on the perturbed flow. These three separate cases are considered once the background method has been formulated. These scenarios impose increasingly stringent constraints on the type of admissible perturbations and allow us to systematically test the hypothesis described above. We shall demonstrate

that the optimal bounds computed in each case not only have the same dependence in the radius ratio in all scenarios as the Reynolds number tends to infinity, but also that this dependence is the same as the one obtained from the suboptimal analytical bound.

The arrangement of the paper is as follows. We begin by describing the problem configuration, the definitions of the relevant mean quantities and the relations between those quantities in §5.2. In §5.3, we perform the energy stability analysis of the laminar flow. In §5.4, we obtain analytical bounds on the mean quantities. §5.5 presents optimal bounds obtained in the three cases listed above and compares the results with the analytical bounds from §5.4. In §5.6, we show that the background method cannot be applied to certain flow problems past certain Reynolds numbers. Finally, §5.7 presents a discussion, comparison with DNS results, the broad applicability of the present study and open problems.

5.2 Problem setup

Consider the flow of an incompressible Newtonian fluid of density ρ and kinematic viscosity ν between two coaxial circular cylinders, where the inner cylinder rotates with a constant angular velocity Ω and the outer cylinder is stationary. The radius of the inner cylinder is R_i and the radius of the outer cylinder is R_o. The quantity $\eta = R_i/R_o$ is referred to as the radius ratio hereafter, and $d = R_o - R_i$ is the gap width. We non-dimensionalize the variables as follows:

$$\boldsymbol{x} = \frac{\boldsymbol{x}^*}{d}, \quad \boldsymbol{u} = \frac{\boldsymbol{u}^*}{\Omega R_i}, \quad t = \frac{t^*}{d/(\Omega R_i)}, \quad p = \frac{p^* - p_0}{\rho \Omega^2 R_i^2}, \tag{5.1}$$

where p_0 is the reference pressure and $\boldsymbol{x}$, $\boldsymbol{u}$, t and p denote the non-dimensional position, velocity, time and pressure, respectively. The starred variables are the corresponding dimensional quantities. In non-dimensional form, the governing equations are

$$\boldsymbol{\nabla} \cdot \boldsymbol{u} = 0, \tag{5.2}$$

$$\frac{\partial \boldsymbol{u}}{\partial t} + \boldsymbol{u} \cdot \boldsymbol{\nabla} \boldsymbol{u} = -\boldsymbol{\nabla} p + \frac{1}{Re} \nabla^2 \boldsymbol{u}, \tag{5.3}$$

where

$$Re = \frac{\Omega R_i d}{\nu} \tag{5.4}$$

is the Reynolds numbers which, along with the radius ratio η, fully characterizes the flow field. Note that instead of the Reynolds number, one can also use the Taylor number

$$Ta = \frac{(1+\eta)^4}{64\eta^2} \frac{d^2 (R_i + R_o)^2 \Omega^2}{\nu^2} = \frac{(1+\eta)^6}{64\eta^4} Re^2, \tag{5.5}$$

to characterize the flow field. We use a cylindrical coordinate system (r, θ, z). The boundary conditions are

$$(u_r, u_\theta, u_z) = (0, 1, 0) \quad \text{at} \quad r = r_i, \tag{5.6}$$

$$(u_r, u_\theta, u_z) = (0, 0, 0) \quad \text{at} \quad r = r_o, \tag{5.7}$$

where r_i and r_o are the non-dimensional inner and outer cylinder radii. In this paper, we will assume that the flow is periodic in the spanwise direction z with non-dimensional length L. The domain of interest, denoted by V, is therefore

given by

$$V = \{(r, \theta, z) | r_i \leq r \leq r_o, 0 \leq \theta < 2\pi, 0 \leq z < L\}. \tag{5.8}$$

At sufficiently small Reynolds numbers, or equivalently, at small Taylor numbers, the flow is laminar and can be expressed as

$$\boldsymbol{u}_{lam} = \frac{1}{1-\eta^2}\left(\frac{r_i}{r} - \frac{r r_i}{r_o^2}\right)\boldsymbol{e}_\theta. \tag{5.9}$$

Before proceeding further, it is useful to introduce a few convenient notations. We use angle brackets for the volume integration and overbar for the long-time average of a quantity:

$$\langle [\,\cdot\,] \rangle = \int_V [\,\cdot\,]\, d\boldsymbol{x}, \quad \overline{[\,\cdot\,]} = \lim_{T\to\infty} \frac{1}{T}\int_{t=0}^{T} [\,\cdot\,]\, dt. \tag{5.10}$$

The L^2-norm of a quantity is henceforth denoted as

$$\|[\,\cdot\,]\|_2 = \left\langle [\,\cdot\,]^2 \right\rangle^{\frac{1}{2}}. \tag{5.11}$$

In what follows, the three quantities that we are interested in bounding are the energy dissipation rate, the torque and the equivalent of a Nusselt number (defined based on the transverse current of azimuthal velocity). These quantities are not independent, as we now demonstrate. We start by writing the dimensional expression of the time-averaged torque required to rotate the inner cylinder:

$$G^* = -R_i \times \int_0^{L^*}\int_0^{2\pi} \overline{\tau^*_{r\theta}}\,\Big|_{r^*=R_i}\; R_i d\theta^* dz^*, \tag{5.12}$$

where $\tau^*_{r\theta}$ denotes the shear-stress. In non-dimensional form the torque is given by

$$G = \frac{G^*}{\rho\nu^2 L^*} = -\frac{Re r_i^2}{L}\int_0^L \int_0^{2\pi} \left[\overline{\frac{1}{r}\frac{\partial u_r}{\partial \theta} + \frac{\partial u_\theta}{\partial r} - \frac{u_\theta}{r}} \right]_{r=r_i} d\theta dz. \tag{5.13}$$

In a statistically stationary state, the work done by the torque to rotate the inner cylinder eventually dissipates in the fluid, i.e.,

$$G^*\Omega = \varepsilon^*, \tag{5.14}$$

where ε^* is the time-averaged total dissipation given by

$$\varepsilon^* = 2\rho\nu \int_{V^*} \overline{\boldsymbol{\nabla}^*\boldsymbol{u}^* : \boldsymbol{\nabla}^*\boldsymbol{u}^*}_{sym} \; d\boldsymbol{x}^*, \tag{5.15}$$

where

$$\boldsymbol{\nabla}^*\boldsymbol{u}^*_{sym} = \frac{\boldsymbol{\nabla}^*\boldsymbol{u}^* + \boldsymbol{\nabla}^*\boldsymbol{u}^{*T}}{2}. \tag{5.16}$$

The total kinetic energy of the fluid can be shown to be uniformly bounded in time within the framework of the background method (see Doering and Constantin, 1992, for example). The identity (5.14) can therefore be obtained by taking the long-time average of the evolution equation of the total kinetic energy. The dissipation per unit mass non-dimensionalized by $\Omega^3 R_i^3/d$ is given by

$$\varepsilon = \frac{\varepsilon^*}{\Omega^3 R_i^3/d} = \frac{2}{(\pi r_o^2 - \pi r_i^2) L \; Re} \overline{\langle \boldsymbol{\nabla}\boldsymbol{u} : \boldsymbol{\nabla}\boldsymbol{u}_{sym} \rangle}. \tag{5.17}$$

From the divergence-free condition (5.2), the boundary conditions (5.6) and (5.7)

along with the use of the divergence theorem, one finds that

$$\left\langle \boldsymbol{\nabla u} : \boldsymbol{\nabla u}^T \right\rangle = \langle \boldsymbol{\nabla} \cdot \boldsymbol{\nabla} \cdot (\boldsymbol{u} \otimes \boldsymbol{u}) \rangle = 2\pi L. \tag{5.18}$$

As a result, the non-dimensional dissipation can also be written as

$$\varepsilon = \frac{1}{(\pi r_o^2 - \pi r_i^2) Re} \left[\frac{1}{L} \overline{\|\boldsymbol{\nabla u}\|_2^2} + 2\pi \right]. \tag{5.19}$$

Using (5.13), (5.14) and (5.17), we finally obtain a relation between the non-dimensional torque and the non-dimensional dissipation as

$$G = \pi (r_i + r_o) r_i Re^2 \varepsilon. \tag{5.20}$$

which is the non-dimensional version of (5.14).

Another quantity of interest is the transverse current of azimuthal velocity as defined in Eckhardt et al. (2007) and is given by

$$J^{\omega *} = \frac{1}{2\pi L^*} \int_0^{L^*} \int_0^{2\pi} r^{*3} \left[\overline{u_r^* \omega^*} - \nu \partial_{r^*} \overline{\omega^*} \right] \, r^* d\theta^* dz^*, \tag{5.21}$$

where $\omega^* = u_\theta^*/r^*$ is the local angular velocity. As shown by Eckhardt et al. (2007), $J^{\omega *}$ is independent of the radial direction. In an analogy with Rayleigh–Bénard convection, one defines the Nusselt number as the ratio of the transverse current of azimuthal velocity to its corresponding value in the laminar regime, i.e.

$$Nu = \frac{J^{\omega *}}{J_{lam}^{\omega *}}. \tag{5.22}$$

Substituting $r^* = R_i$ in the right-hand-side of (5.21), one obtains the following

relation between the torque and the transverse current of azimuthal velocity:

$$J^{\omega *} = \frac{G^*}{2\pi L^* \rho}, \tag{5.23}$$

implying that the Nusselt number can also be written as

$$Nu = \frac{G}{G_{lam}} = \frac{\varepsilon}{\varepsilon_{lam}}, \tag{5.24}$$

where G_{lam} and ε_{lam} are the values of the non-dimensional torque and dissipation in the laminar regime, respectively.

5.3 Energy stability analysis

We begin by discussing the energy stability of the laminar flow $\boldsymbol{u}_{lam}$. The importance of energy stability analysis in the context of bounding theories comes from the fact that bounds on mean quantities introduced in the last section are by definition saturated by the laminar state below the energy stability threshold. The energy stability of the laminar Taylor–Couette flow has been studied before both theoretically and numerically, by e.g. Serrin (1959) and Joseph (1976). In these studies, the general conclusion was that at the energy stability threshold, the least stable perturbations are axisymmetric Taylor vortices. However, as we shall demonstrate in this section, this commonly accepted result does not hold below a certain radius ratio ($\eta < 0.0556$). Instead, we find that the least stable perturbations at the energy stability threshold in that case are fully three-dimensional.

We begin by defining the functional

$$\mathcal{H}(\tilde{\boldsymbol{v}}) = \left[\frac{1}{2Re} \|\boldsymbol{\nabla} \tilde{\boldsymbol{v}}\|_2^2 + \int_V \tilde{\boldsymbol{v}} \cdot (\boldsymbol{\nabla} \boldsymbol{u}_{lam})_{sym} \cdot \tilde{\boldsymbol{v}} \, d\boldsymbol{x} \right], \tag{5.25}$$

where $\tilde{\boldsymbol{v}}$ is a perturbation over the laminar flow which satisfies the homogeneous boundary conditions at the inner and outer cylinders . From the governing equations, one can show that the laminar flow $\boldsymbol{u}_{lam}$ is energy stable when $\mathcal{H}(\tilde{\boldsymbol{v}})$ is nonnegative (see, for example, Serrin, 1959; Ding and Marensi, 2019). We shall consider three types of constraints on the perturbations $\tilde{\boldsymbol{v}}$: no constraints, other than the homogeneous boundary conditions (case 1), 3D incompressible perturbations (case 2) and 2D (z-invariant) incompressible perturbations (case 3). We perform an energy stability analysis for each of these cases, and present the results as a function of the radius ratio. We note that recently Ding and Marensi (2019) also studied the energy stability of the laminar state in Taylor–Couette flow but only for the axisymmetric perturbations.

The critical Taylor number Ta_c defining the energy stability threshold is the largest Taylor number for which the functional $\mathcal{H}(\tilde{\boldsymbol{v}})$ is nonnegative. For clarity, we add superscripts and use the notation Ta_c^{nc}, Ta_c^{3D} and Ta_c^{2D} when referring to case 1, case 2 and case 3, respectively. The statement of the nonnegativity of the functional $\mathcal{H}(\tilde{\boldsymbol{v}})$ can be posed as a convex optimization problem, where we require that the minimum value of $\mathcal{H}$ to be nonnegative. Then , it can be shown using the corresponding Euler–Lagrange equations that the nonnegativity of the functional $\mathcal{H}(\tilde{\boldsymbol{v}})$ is equivalent to the nonnegativity of the smallest eigenvalue in the eigenvalue problem

$$\boldsymbol{\nabla} \cdot \tilde{\boldsymbol{v}} = 0, \tag{5.26a}$$

$$2\lambda \tilde{\boldsymbol{v}} = \frac{1}{Re}\nabla^2 \tilde{\boldsymbol{v}} - 2\tilde{\boldsymbol{v}} \cdot \boldsymbol{\nabla}(\boldsymbol{u}_{lam})_{sym} - \boldsymbol{\nabla}\tilde{p}. \tag{5.26b}$$

Note that for case 1, the eigenvalue problem corresponds just to equation (5.26b) without the pressure term. The eigenvalue problem (5.26) is standard in the

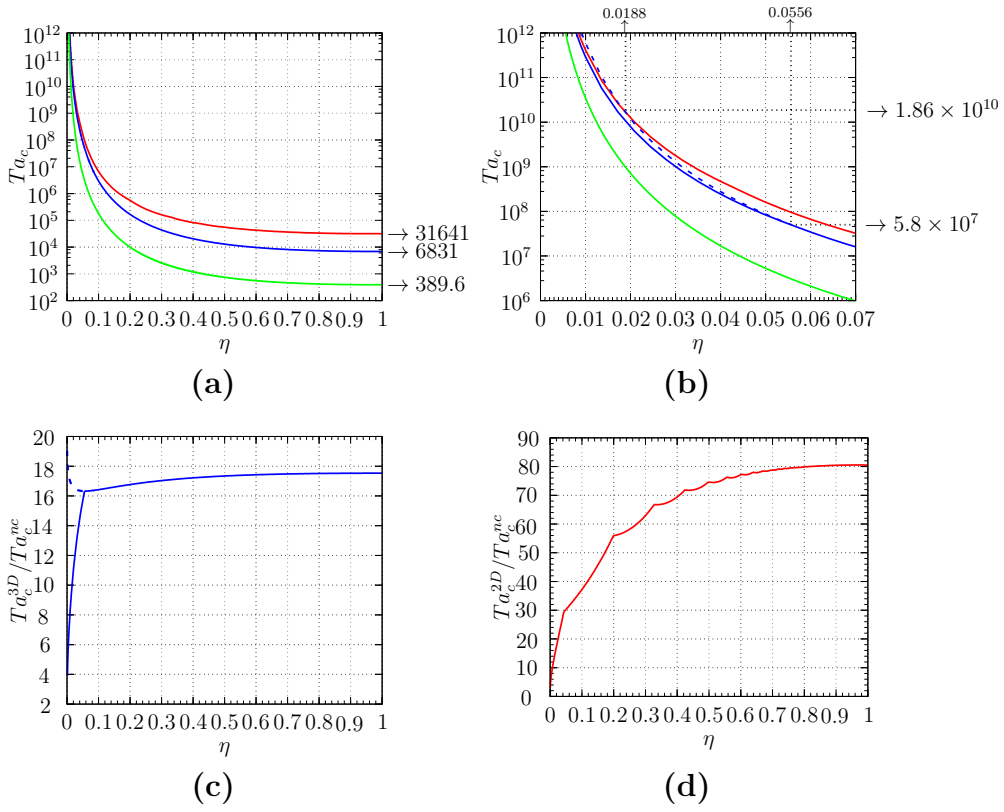

Figure 5.1: Panel (a) shows the critical Taylor number Ta_c^{nc} (green line), Ta_c^{3D} (blue line) and Ta_c^{2D} (red line) as a function of the radius ratio η and (b) shows a close-up view of the same plot for small η. The dashed blue line corresponds to the marginally stable axisymmetric Taylor vortices, while Ta_c^{3D} is continued to be shown with the solid blue line. Panels (c) and (d) shows the critical Taylor number Ta_c^{3D} and Ta_c^{2D} normalized by Ta_c^{nc} as a function of η.

energy stability analysis (see, for example, Serrin, 1959; Ding and Marensi, 2019).

We can actually obtain the critical Taylor number analytically for case 1. Indeed, in this case, we first simplify the eigenvalue problem using two pieces of information. From lemma 5.B.1 (see appendix 5.B), we note that the least stable perturbed flow (which optimizes $\mathcal{H}$) is a function of the radial direction only. Furthermore, the laminar flow $\boldsymbol{u}_{lam}$ satisfies the required condition in lemma 5.B.1, therefore, the least stable perturbation also satisfies $\tilde{v}_r = \tilde{v}_\theta$. Using these two facts, we find that the marginally stable solution of (5.26b) which satisfies the

homogeneous boundary condition at $r = r_i$ is given by

$$\tilde{v}_r = \tilde{v}_\theta = c \sin\left(\xi \log \frac{r}{r_i}\right), \qquad \xi = \sqrt{\frac{\eta}{(1+\eta)(1-\eta)^2} Re + 1}. \tag{5.27}$$

The critical Reynolds number for energy stability is the smallest value of Re for which this solution also satisfies the homogeneous boundary condition at $r = r_o$. We then obtain the critical Taylor number using (5.5), which leads to

$$Ta_c^{nc} = \frac{(1+\eta)^8 (1-\eta)^4}{64\eta^6} \left(1 + \frac{\pi^2}{\log^2 \eta}\right)^2. \tag{5.28}$$

In case 2 (3D incompressible $\tilde{\boldsymbol{v}}$) and case 3 (2D (z-invariant) incompressible $\tilde{\boldsymbol{v}}$), we must turn to numerical computations to calculate the critical Taylor number. To find the eigenvalues of the equations (5.26), we first transform the equations into a generalized eigenvalue problem using the spatial discretization described in §5.5 and then use the DGGEV routine by Lapack for the computation. Let's call the critical wavenumbers of the least stable perturbation at the energy stability threshold $2\pi/L_c$ (where L_c would then be known as the critical aspect ratio) in the z-direction and m_c in the θ-direction. We use the bisection algorithm in the Taylor number and the ternary search algorithm in aspect ratio or azimuthal wavenumber (depending on the case at hand) to accurately determine Ta_c, L_c and m_c.

The dependence of the critical Taylor number for energy stability on the radius-ratio η is shown in figure 5.1 for all 3 cases. The critical axial wavenumber ($2\pi/L_c$) and the critical azimuthal wavenumber (m_c) of the corresponding perturbations in case 2 and case 3 are shown in figure 5.2. From figure 5.1a, we see that the critical Taylor number increases as we go from case 1 (green line) to case 3 (red

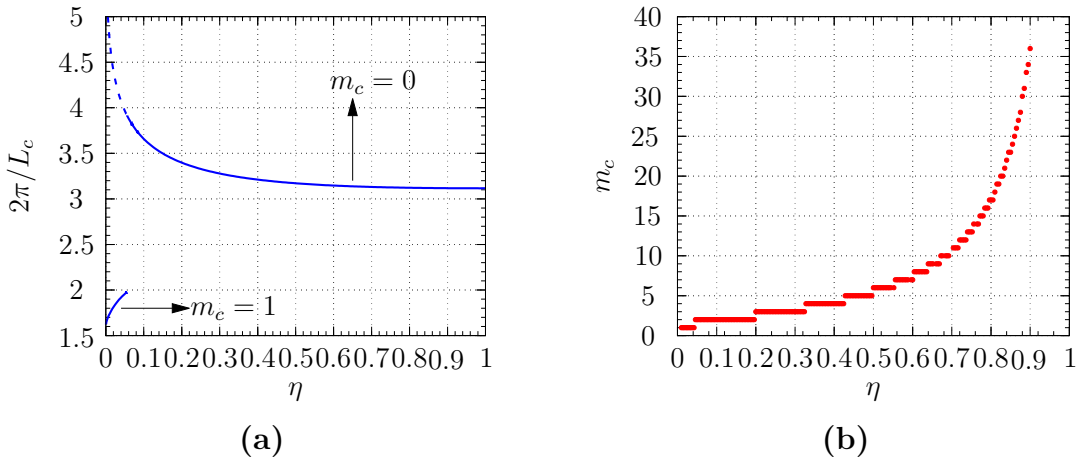

Figure 5.2: Variation of the critical axial wavenumber $2\pi/L_c$ and critical azimuthal wavenumber m_c with radius ratio η for (a) case 2 and (b) case 3. In panel (a), the critical azimuthal wavenumber changes from $m_c = 0$ above $\eta = \eta_s = 0.0556$ to $m_c = 1$ below η_s, as discussed in the main text.

line), which is not surprising since we correspondingly increase the number of constraints on the perturbations. In all three cases, the critical Taylor number monotonically increases with decreasing η and tends to infinity as $\eta \to 0$. By contrast, the critical Taylor number tends to a constant in the small gap width limit ($\eta \to 1$): in case 1 $Ta_c^{nc} \to 4\pi^4 \approx 389.6364$, whereas, in case 2 and case 3, $Ta_c^{3D} \to 6831$ and $Ta_c^{2D} \to 31641$, which are, respectively, 17.5 and 81.2 times larger than in case 1. In this limit, the marginally stable perturbation in case 2 recovers the well-known axisymmetric Taylor vortices (Serrin, 1959; Joseph, 1976). In case 3, the marginally stable perturbation is composed of vortices whose axis is parallel to the cylinder axis (Harrison, 1921).

Figure 5.1b shows a zoomed-in version of figure 5.1a for small values of η. We also show, for case 2 (blue line), a separate curve that assumes that perturbations are axially symmetric (dashed blue line). For large radius ratio, the two are identical, confirming that the axisymmetric Taylor vortices are indeed the least

stable perturbations. However, we note that below radius ratio $\eta_s = 0.0556$, the marginally stable perturbation switches from the axisymmetric Taylor vortices to being fully three-dimensional.

Figure 5.3 shows the marginally stable 3D flow and Taylor vortices at $\eta = \eta_s$. A distinctive feature of the marginally stable 3D flow, compared to marginally stable axisymmetric Taylor vortices, is that one end of a typical vortex lies near the outer cylinder but the other end lies at one of the two lines that are offset from the inner cylinder. Also, the critical aspect ratio corresponding to marginally stable 3D flow is larger than the one corresponding to the Taylor vortices. In fact, with further decrease in the radius-ratio, the axisymmetric critical aspect-ratio corresponding to the marginally stable 3D flow grows, whereas the one corresponding to Taylor vortices shrinks, as can been seen from figure 5.2a. The decrease of the aspect ratio of the critical perturbations implies that the term $\|\boldsymbol{\nabla}\tilde{\boldsymbol{v}}\|_2^2$ increases rapidly as $\eta \to 0$, which causes the corresponding critical Taylor number for axisymmetric flows to do the same. This explains why the axisymmetric perturbations are no longer preferred for very low η. At $\eta = 0.0188$, the critical Taylor number for the marginally stable Taylor vortices becomes even larger than the one corresponding to the two-dimensional flow (Ta_c^{2D}).

Given that we were able to compute the critical Taylor number in case 1 analytically as a function of η, it is worth investigating whether the dependence of Ta_c on η in cases 2 and 3 is similar to that of case 1. To do so, we look at the figures 5.1c and 5.1d, which show the ratios Ta_c^{3D}/Ta_c^{nc} and Ta_c^{2D}/Ta_c^{nc} respectively. One striking observation is that Ta_c^{3D}/Ta_c^{nc} remains within 3.6% of 16.92 for a fairly large range of radius ratio $0.0556 \leq \eta \leq 1$. So, for this range of

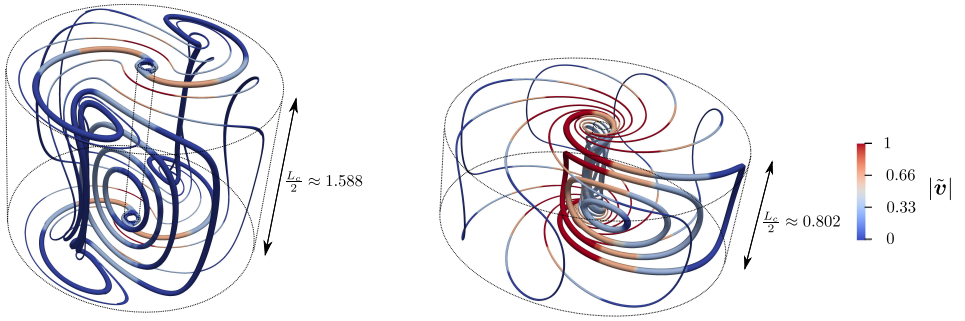

(a) **(b)**

Figure 5.3: Panel (a) shows selected streamlines of the marginally stable 3D flow and panel (b) shows selected streamlines of the marginally stable axisymmetric Taylor vortices, in both cases at a radius ratio ($\eta_s = 0.0556$). The corresponding critical Taylor numbers in both cases are equal. The streamlines are colored according to the magnitude of the velocity. In both the cases the velocity field has been scaled such that the maximum magnitude is 1. A typical vortex is shown using relatively thicker lines in both cases. Note that only half the vortex is shown in the axial direction.

η

$$Ta_c^{3D} \approx \frac{16.92(1+\eta)^8(1-\eta)^4}{64\eta^6}\left(1+\frac{\pi^2}{\log^2\eta}\right)^2. \tag{5.29}$$

However, the same is not valid for case 3, where Ta_c^{2D}/Ta_c^{nc} varies substantially with η. The spikes in figure 5.1d, which are not visible in figure 5.1a, correspond to the discrete change in critical azimuthal wavenumber when η varies, shown in figure 5.2b.

For small radius ratio it is possible to predict the asymptotic behavior of Ta_c^{3D} and Ta_c^{2D}. We find that both Ta_c^{3D}/Ta_c^{nc} and Ta_c^{2D}/Ta_c^{nc} decrease as $\eta \to 0$ as can be seen in 5.1c and 5.1d. By construction, the asymptotic value of the ratios have to be larger than 1. Therefore, in the small radius ratio limit, we can obtain

the asymptotic behavior of Ta_c^{3D} and Ta_c^{2D} as

$$Ta_c^{3D} = C_0^{3D} \lim_{\eta\to 0} Ta_c^{nc} = \frac{C_0^{3D}\pi^4}{\eta^6 \log^4 \eta},\ Ta_c^{2D} = C_0^{2D} \lim_{\eta\to 0} Ta_c^{nc} = \frac{C_0^{2D}\pi^4}{\eta^6 \log^4 \eta} \text{ as } \eta \to 0, \tag{5.30}$$

where $1 \leq C_0^{3D}, C_0^{2D} < \infty$ are two constants.

5.4 An analytical bound

In this section, we obtain a simple, suboptimal, analytical bound on the torque, the rate of energy dissipation and the Nusselt number defined in §5.2. We use the well-known background method (Doering and Constantin, 1992, 1994) whose exact formulation in the context of the present problem is given in appendix 5.A. As usual, we define $\boldsymbol{U}$ to be the background flow and $\boldsymbol{v}$ to be the perturbed flow such that the total flow is $\boldsymbol{u} = \boldsymbol{U} + \boldsymbol{v}$. The background flow $\boldsymbol{U}$ is divergence-free and satisfies the same boundary conditions as $\boldsymbol{u}$, so the perturbed flow $\boldsymbol{v}$ satisfies the homogeneous version of the boundary conditions. For mathematical convenience (see appendix 5.A) we further define the so-called "shifted perturbation" $\tilde{\boldsymbol{v}} = \boldsymbol{v} - \boldsymbol{\phi}$ (see equation 5.98) and we simply refer to $\tilde{\boldsymbol{v}}$ as the perturbation from here onward. As shown in appendix 5.A, a bound on the rate of energy dissipation,

$$\varepsilon \leq \frac{1}{(\pi r_o^2 - \pi r_i^2)ReL}\left[\frac{1}{a(2-a)}\|\boldsymbol{\nabla U}\|_2^2 - \frac{(1-a)^2}{a(2-a)}\|\boldsymbol{\nabla u}_{lam}\|_2^2 + 2\pi L\right], \tag{5.31}$$

can be obtained for any choice of the background flow for which the functional

$$\mathcal{H}(\tilde{\boldsymbol{v}}) = \frac{2-a}{2Re}\|\boldsymbol{\nabla}\tilde{\boldsymbol{v}}\|_2^2 + \underbrace{\int_V \tilde{\boldsymbol{v}} \cdot \boldsymbol{\nabla} \boldsymbol{U}_{sym} \cdot \tilde{\boldsymbol{v}}\, d\boldsymbol{x}}_{II}, \tag{5.32}$$

(see 5.103) is positive semi-definite. In (5.31), the constant a is a balance parameter that takes values between 0 and 2. This bound is identical to the one obtained by Ding and Marensi (2019), after noting that they used a different non-dimensionalization. While showing $\mathcal{H}(\tilde{\boldsymbol{v}})$ is nonnegative, we do not impose the incompressibility constraint on the perturbations $\tilde{\boldsymbol{v}}$ and only assume $\tilde{\boldsymbol{v}}$ satisfies the homogeneous boundary conditions. We make a choice of the background flow $\boldsymbol{U}$ for which

$$\boldsymbol{\nabla U}_{sym} = \frac{\boldsymbol{\nabla U} + \boldsymbol{\nabla U}^T}{2}$$

is non-zero only in boundary layers, which are assumed to have thicknesses δ_i and δ_o near the inner and the outer cylinder, respectively. In particular, the selected background flow $\boldsymbol{U}$ is then

$$\boldsymbol{U}(r,\theta,z) = U(r)\boldsymbol{e}_\theta = \begin{cases} \frac{\Lambda(r_i+\delta_i)(r-r_i)-(r-r_i-\delta_i)}{\delta_i}\boldsymbol{e}_\theta & \text{if} \quad r_i \le r \le r_i+\delta_i, \\ \Lambda r \boldsymbol{e}_\theta & \text{if} \quad r_i+\delta_i < r \le r_o-\delta_o, \\ \frac{\Lambda(r_o-\delta_o)(r_o-r)}{\delta_o}\boldsymbol{e}_\theta & \text{if} \quad r_o-\delta_o < r \le r_o, \end{cases} \tag{5.33}$$

where Λ is an $O(1)$ constant, i.e., independent of Re. The decision to allow for different boundary layer thicknesses is inspired from the work of Kumar (2020), who speculated in the context of helical pipe flows that by doing so, it is possible to capture important geometrical aspects of problem that would otherwise not appear. As we are primarily interested in deriving bounds at asymptotically high Reynolds numbers, for convenience, we define rescaled boundary layer thicknesses as

$$h_i = \frac{\delta_i}{\delta} \quad \text{and} \quad h_o = \frac{\delta_o}{\delta} \qquad \text{where} \quad \delta = \frac{1}{Re}, \tag{5.34}$$

where, by construction, $h_i, h_o > 0$ and are $O(1)$. Our goal in this section is to adjust the relative size of the boundary layers (h_i/h_o) to optimize the bound (5.31) simultaneously for different values of η in the limit of high Reynolds number.

We start by obtaining a simple estimate for the quantity

$$\begin{aligned}
\int_{r_i}^{r_i+\delta_i} |\tilde{v}_r|\,|\tilde{v}_\theta| dr &= \int_{r_i}^{r_i+\delta_i} \left|\int_{r_i}^{r} \frac{\partial \tilde{v}_r}{\partial r'} dr'\right| \left|\int_{r_i}^{r} \frac{\partial \tilde{v}_\theta}{\partial r'} dr'\right| dr \\
&\leq \int_{r_i}^{r_i+\delta_i} (r-r_i) \left[\int_{r_i}^{r_i+\delta_i} \left(\frac{\partial \tilde{v}_r}{\partial r'}\right)^2 dr'\right]^{\frac{1}{2}} \left[\int_{r_i}^{r_i+\delta_i} \left(\frac{\partial \tilde{v}_\theta}{\partial r'}\right)^2 dr'\right]^{\frac{1}{2}} dr \\
&= \frac{\delta_i^2}{2} \left[\int_{r_i}^{r_i+\delta_i} \left(\frac{\partial \tilde{v}_r}{\partial r'}\right)^2 dr'\right]^{1/2} \left[\int_{r_i}^{r_i+\delta_i} \left(\frac{\partial \tilde{v}_\theta}{\partial r'}\right)^2 dr'\right]^{1/2} \\
&\leq \frac{\delta_i^2}{4} \int_{r_i}^{r_i+\delta_i} \left(\frac{\partial \tilde{v}_r}{\partial r'}\right)^2 dr' + \frac{\delta_i^2}{4} \int_{r_i}^{r_i+\delta_i} \left(\frac{\partial \tilde{v}_\theta}{\partial r'}\right)^2 dr'. \qquad (5.35)
\end{aligned}$$

In deriving the result, we have used the fundamental theorem of calculus in the first line, Hölder's inequality in the second line followed by an integration in r to obtain the third line. Finally, we used Young's inequality to obtain the last line. In a similar manner, one can also show that

$$\int_{r_o-\delta_o}^{r_o} |\tilde{v}_r|\,|\tilde{v}_\theta| dr \leq \frac{\delta_o^2}{4} \int_{r_o-\delta_o}^{r_o} \left(\frac{\partial \tilde{v}_r}{\partial r'}\right)^2 dr' + \frac{\delta_o^2}{4} \int_{r_o-\delta_o}^{r_o} \left(\frac{\partial \tilde{v}_\theta}{\partial r'}\right)^2 dr'. \qquad (5.36)$$

Next, we note that

$$\left|\int_{r=r_i}^{r_i+\delta_i} \tilde{v}_r \tilde{v}_\theta \left(\frac{dU}{dr} - \frac{U}{r}\right) r dr\right| \leq \max_{r_i<r<r_i+\delta_i} \left|\frac{dU}{dr} - \frac{U}{r}\right| (r_i+\delta_i) \int_{r=r_i}^{r_i+\delta_i} |\tilde{v}_r||\tilde{v}_\theta| dr, \qquad (5.37)$$

and

$$\left|\int_{r=r_o-\delta_o}^{r_o} \tilde{v}_r \tilde{v}_\theta \left(\frac{dU}{dr} - \frac{U}{r}\right) r dr\right| \leq \max_{r_o-\delta_o<r<r_o} \left|\frac{dU}{dr} - \frac{U}{r}\right| r_o \int_{r=r_o-\delta_o}^{r_o} |\tilde{v}_r|\,|\tilde{v}_\theta| dr. \qquad (5.38)$$

Using estimates (5.35)-(5.38) along with the expression of the background flow (5.33), we finally obtain a simple bound on term II in (5.32) as

$$|II| \leq \frac{M}{Re}\|\boldsymbol{\nabla}\tilde{\boldsymbol{v}}\|_2^2, \tag{5.39}$$

where

$$M = \max\left\{\frac{h_i}{4}|1-\Lambda r_i|,\ \frac{h_o}{4}|\Lambda| r_o\right\} + O(\delta). \tag{5.40}$$

This shows that the functional $\mathcal{H}$ is positive semi-definite as long as

$$M \leq 1 - \frac{a}{2}. \tag{5.41}$$

Using (5.9) and (5.33) in (5.31), we then obtain an upper bound on the dissipation as follows

$$\varepsilon \leq \varepsilon_b^a = \frac{2}{a(2-a)(r_o^2 - r_i^2)}\left(\frac{(1-\Lambda r_i)^2 r_i}{h_i} + \frac{\Lambda^2 r_o^3}{h_o}\right) + O(\delta). \tag{5.42}$$

The upper bound obtained is called ε_b^a, and we use 'b' in the subscript to signify that it is a bound and use 'a' in the superscript to signify that it is obtained analytically. In final step of the procedure, we adjust the values of the unknown parameters h_i, h_o, Λ and a to optimize the bound (5.42) while satisfying the constraint (5.41). The optimal values of the parameters, in the limit of high Reynolds number are,

$$\Lambda = \frac{r_i}{r_i^2 + r_o^2}, \quad a = \frac{2}{3}, \quad h_o = \frac{8}{3\Lambda r_o} \quad \text{and} \quad \frac{h_i}{h_o} = \eta. \tag{5.43}$$

Using (5.34) and (5.5), we can now write the optimal choice of boundary layer thicknesses δ_i and δ_o in the limit of $Re \to \infty$ (or equivalently $Ta \to \infty$) as

$$\delta_i = \frac{8(1+\eta^2)}{3\,Re} = \frac{(1+\eta^2)(1+\eta)^3}{3\,\eta^2\,Ta^{\frac{1}{2}}}, \qquad \delta_o = \frac{8(1+\eta^2)}{3\,\eta\,Re} = \frac{(1+\eta^2)(1+\eta)^3}{3\,\eta^3\,Ta^{\frac{1}{2}}}. \tag{5.44}$$

The corresponding bound on the dissipation in the limit of $Re \to \infty$ is then given by

$$\varepsilon^a_{b,\infty} = \frac{27}{32}\frac{\eta}{(1+\eta)(1+\eta^2)^2}. \tag{5.45}$$

Here, we added '∞' in the subscript to indicate that it is the main term of the bound in the limit $Re \to \infty$. Using the relationship (5.24), we obtain an equivalent upper bound on the Nusselt number in the high Reynolds number limit as

$$Nu^a_{b,\infty} = \frac{27}{16}\frac{\eta^3}{(1+\eta)^2(1+\eta^2)^2}Ta^{1/2}. \tag{5.46}$$

This expression contains a dependence on both the Taylor number (the principal flow parameter) as well as the radius ratio (the geometrical parameter). To separate out the geometrical dependence in (5.46), we define

$$\chi(\eta) = \frac{16\eta^3}{(1+\eta)^2(1+\eta^2)^2}, \tag{5.47}$$

and call it the geometrical scaling of the bound on Nu. This geometrical scaling is defined in such a way that $\chi(1) = 1$ (the relevance of $\eta = 1$ being that it corresponds to the plane Couette flow case).

Finally, by combining (5.45) with the relation (5.20), we obtain an upper bound

on the torque as a function of the Reynolds number

$$G^a_{b,\infty} = \frac{27\pi}{32}\frac{\eta^2(1+\eta)^2}{(1-\eta^4)^2}Re^2. \tag{5.48}$$

Constantin (1994) had previously obtained a bound on the torque in Taylor–Couette flows by considering a background flow with a single boundary layer. The bound obtained by Constantin is also proportional to Re^2, as in (5.48). But, the coefficient in front has a different dependence on the radius ratio η. The reason for this difference is that we chose a background flow with two boundary layers and adjusted their relative thicknesses to optimize the bound. We shall see later that this optimization procedure enables us to capture the actual dependence of optimal bounds on the radius ratio.

5.5 Optimal bounds

In this section, we now proceed to obtain optimal bounds on the bulk quantities, i.e., the best possible bounds within the framework of the background method. As described in §5.1, we consider three scenarios, 'case 1', 'case 2' and 'case 3', in which we incrementally impose constraints on the perturbed flow field and numerically obtain the optimal bounds in each case, which allow us to systematically examine the hypothesis stated in the introduction.

The general development of the background method for Taylor–Couette flow is presented in appendix 5.A. In what follows, we first describe our numerical algorithm, then proceed to present the results.

5.5.1 Numerical Algorithm

Here, we first describe the general numerical framework used to compute the optimal bounds, and then provide further details of the algorithm in each of the specific cases. Finding the optimal bound begins with the same background method applied to the Taylor–Couette flow as in §5.4, which is described in appendix 5.A. However, instead of using functional inequalities, we now follow the standard route toward optimal bounds, and derive a set of Euler–Lagrange equations that optimal solutions satisfy, given specific constraints in each case. The derivation is presented in appendix 5.A, and the equations are given in (5.109a-d). In general, the Euler–Lagrange equations can have multiple solutions. However, we are interested in finding the unique solution that also satisfies the spectral constraint (5.104). To find this particular solution, we use the two-step algorithm first introduced by Wen et al. (2013) in the context of porous medium convection. A remarkable property of this algorithm is that it eliminates the requirement of numerical continuation (Plasting and Kerswell, 2003). As the two-step algorithm can be implemented at any value of the flow parameter, this flexibility has led to wider usage in several other studies of the background method to obtain the optimal bound numerically (Wen et al., 2015; Wen and Chini, 2018; Lee et al., 2019; Ding and Marensi, 2019; Souza et al., 2020). The first step of the algorithm uses a pseudo-time stepping scheme in which the Euler–Lagrange equations (5.109a-d) are converted into a time-dependent system of partial differential equations(PDEs) as follows

$$\frac{\partial \tilde{\boldsymbol{v}}_i}{\partial t} = \frac{a}{2(2-a)}\frac{\delta \mathcal{L}}{\delta \tilde{\boldsymbol{v}}_i}, \quad \frac{\partial U_\theta}{\partial t} = -\frac{a(2-a)}{4\pi L}\frac{1}{r}\frac{\delta \mathcal{L}}{\delta U_\theta}, \quad \frac{\partial a}{\partial t} = -\frac{\delta \mathcal{L}}{\delta a}, \quad \boldsymbol{\nabla}\cdot\tilde{\boldsymbol{v}} = 0, \tag{5.49}$$

where the index i ranges over the r, θ and z components of $\tilde{\boldsymbol{v}}$. Steady-state solutions of (5.49) are equivalently solutions of the Euler–Lagrange equations (5.109a-d). Note that we multiply the Frechet derivatives with certain coefficients before introducing the time derivatives on the left-hand side. This makes the coefficient of the linear term (the Laplacian) a constant in the resultant time-dependent PDEs. Also, note that the coefficient in front of the Frechet derivative with respect to $\tilde{\boldsymbol{v}}$ is positive, while the coefficients in front of the Frechet derivatives with respect to U_θ and a are negative. The reason is that we are maximizing the bound with respect to $\tilde{\boldsymbol{v}}$ while minimizing it with respect to U_θ and a.

Ding and Marensi (2019) proved that if the pseudo-time stepping scheme leads to a steady-state solution then that solution must be the globally optimal solution of the Euler–Lagrange equations (5.109a-d), i.e., the one that leads to optimal bounds. Conveniently, the same proof extends to the case where the perturbed flow only satisfies the homogeneous boundary conditions and to the case where the perturbed flow is two-dimensional and incompressible. The proof of Ding and Marensi (2019) does not guarantee the existence of a steady-state solution to (5.49). But in all the cases that we investigated, the pseudo-time stepping scheme did relax to a steady-state solution.

The second step of the two-step algorithm is a Newton iteration (see Wen et al., 2015) which has a faster convergence rate than the pseudo-time stepping scheme but requires a good initial guess. Naturally, we use the solutions obtained at the end of the pseudo-time stepping scheme as the initial guess.

Solving the Euler–Lagrange equations in case 1 comes with two major simplifications. First, the pressure gradient term in (5.109a) disappears, as we do not impose the incompressibility constraint on the perturbation. Second, it can be shown that the optimal perturbation depends only on the radial direction

(see appendix 5.B). With these simplifications, the convergence of the pseudo-time stepping scheme is so rapid that the subsequent Newton iteration is not needed. Therefore, we only use the first step of the two-step algorithm described above. Furthermore, we found that it is also possible to solve the simplified Euler–Lagrange equations analytically in the limit $Re \to \infty$ using the method of matched asymptotics (solutions are presented in appendix 5.B).

In case 2 it is also possible to make a simplification. Indeed, Ding and Marensi (2019) presented numerical evidence that the optimal solution does not depend on θ when the aspect ratio L(i.e. the height of the cylinder) is large enough. Therefore, we choose $L = 20$, which is sufficiently large to guarantee that the optimal flow is axisymmetric. To solve the system of time-dependent PDEs (5.49), we consider the following Fourier decomposition in the z direction

$$\tilde{\boldsymbol{v}} = \sum_{n=1}^{N} \begin{bmatrix} \tilde{v}_{r,n}(r,t)\cos(k_n z) \\ \tilde{v}_{\theta,n}(r,t)\cos(k_n z) \\ \tilde{v}_{z,n}(r,t)\sin(k_n z) \end{bmatrix}, \quad \tilde{p} = \sum_{n=1}^{N} \tilde{p}_n(r,t)\cos(k_n z) \quad \text{where} \quad k_n = \frac{2\pi n}{L}. \tag{5.50}$$

The radial direction is further discretized using the Chebyshev collocation method. We use a semi-implicit Crank–Nicolson scheme for the time integration where we treat the linear terms implicitly and use the second-order Adams–Bashforth extrapolation for the nonlinear terms. We use an influence matrix method to solve for the pressure at each time step (see Peyret, 2013, p. 236). The code is parallelized using MPI. Note that the pressure $\tilde{p}$ in (5.50), as compared to the one in appendix 5.A, has been multiplied with an appropriate factor such that it is precisely the gradient of $\tilde{p}$ that appears in the time-evolving PDEs (5.49).

Depending on the radius ratio and Taylor number considered, we vary the number modes in the z direction from $N = 200$ to $N = 6000$ and the number collocation points in the r direction from 120 to 320.

The numerical strategy for solving the Euler–Lagrange equations in case 3 is similar to case 2 described above. The only difference is that for the 2D incompressible perturbations, the flow quantities depend on the θ direction but are independent of z. Therefore, we consider the following decomposition instead

$$\tilde{\boldsymbol{v}} = \sum_{\substack{m=-M \\ m\neq 0}}^{M} \begin{bmatrix} \tilde{v}_{r,m}(r,t)e^{im\theta} \\ \tilde{v}_{\theta,m}(r,t)e^{im\theta} \end{bmatrix}, \quad \tilde{p} = \sum_{\substack{m=-M \\ m\neq 0}}^{M} \tilde{p}_m(r,t)e^{im\theta}. \tag{5.51}$$

In this case, depending on the radius ratio and Taylor number considered, we vary the number modes in the θ direction from $M = 40$ to $M = 3000$ and the number collocation points in the r direction from 120 to 320.

5.5.2 Optimal bound results

In this subsection, we present the optimal bounds obtained using the numerical schemes described above for each of the three different sets of constraints on the perturbations. We begin by showing a typical optimal background flow profiles at $\eta = 0.6$ and $Ta = 10^6$ in each case in figure 5.4. For comparison, we have also included the background flow profile constructed in (5.33) to derive the original analytical bound. As can be seen in figure 5.4, all four background flow profiles vary as cr, for some constant c, in the bulk region. This is intuitively expected as this type of background profile makes the sign-indefinite term (which is, in a loose sense, the hardest to control in the bulk region) in the spectral constraint (5.104) zero. Near the cylinders, the background flows consist of two thin boundary

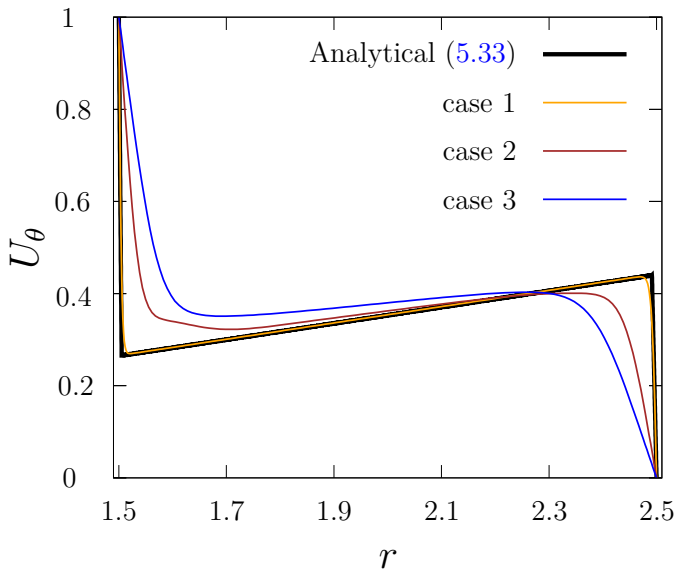

Figure 5.4: The optimal background flow $U_\theta(r)$ at parameter values $Ta = 10^6$ and $\eta = 0.6$. The orange color is used for case 1, brown color for case 2 and blue color for case 3. Also, shown as a black thick line is the background flow (5.33) used to construct the analytical bound in §5.4, with the values of Λ, δ_i and δ_o given by (5.43) in definition (5.33).

layers. In order to meet the prescribed boundary conditions, the gradients in these thin layers are large, which makes the sign-indefinite term nonzero. However, as the perturbation has to satisfy the homogeneous boundary conditions, the net contribution from this term will still be smaller than the positive term in (5.104) as long as the boundary layer thickness is small enough. In the optimal state, the boundary layers are of just the right size so that the positive term and the sign-indefinite term balance each other out and the spectral constraint is marginally satisfied. When moving from case 1 to case 3, the restrictions on the perturbations increase, and this decreases the possibilities in which the sign-indefinite term can be negative. Therefore, the boundary layers become thicker, protruding more into the bulk region.

Figure 5.5 shows the optimal bounds on the Nusselt number, Nu_b, as a function

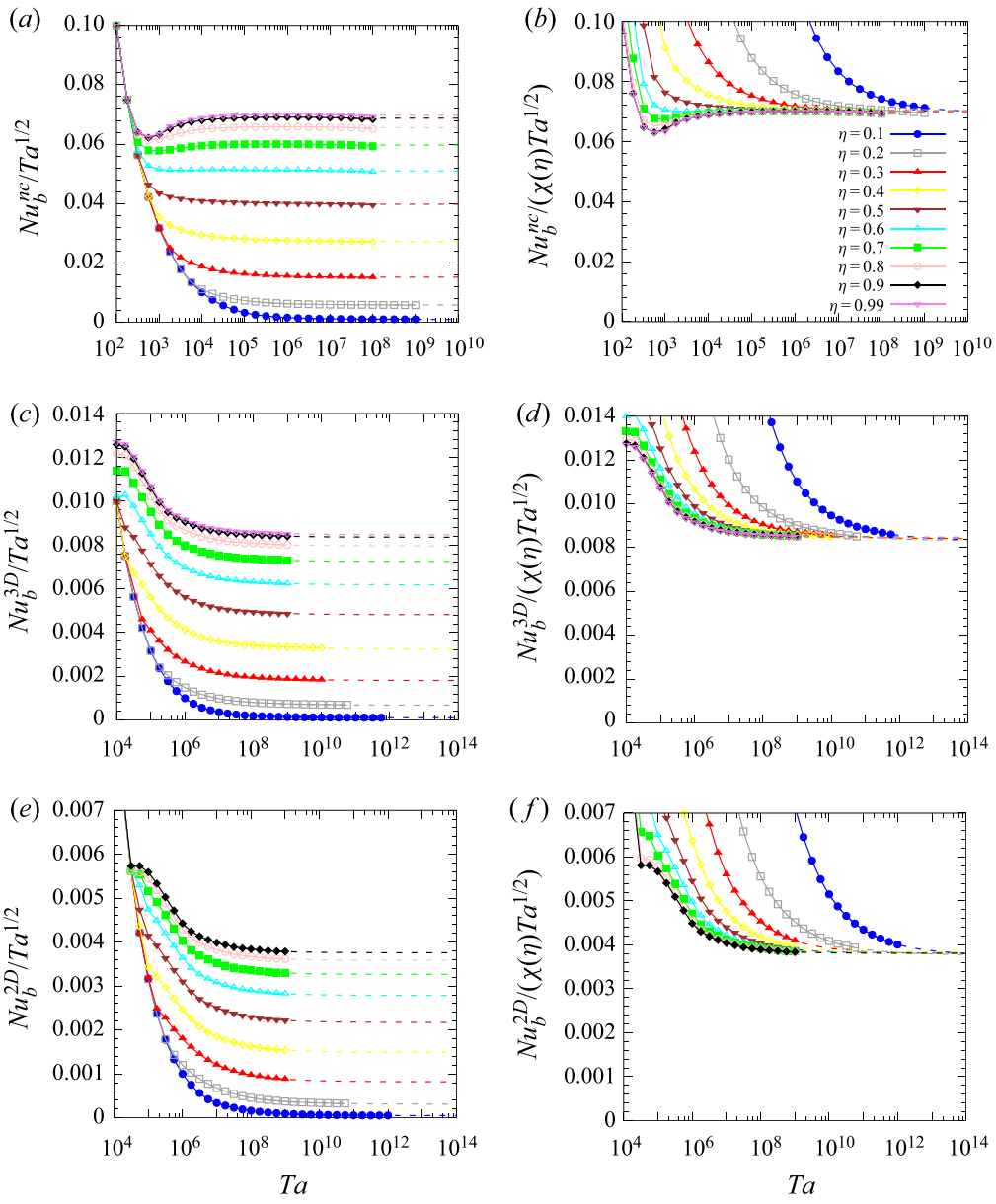

Figure 5.5: The left column shows the optimal bound Nu_b compensated with $Ta^{\frac{1}{2}}$ in case 1, case 2 and case 3 (top to bottom) as a function of the Taylor number for a wide range of radius ratios. The right column shows the same plots but further scaled with the analytical geometrical scaling $\chi(\eta)$ given by (5.47). The collapse of the curves at high Taylor numbers suggests that the bound on Nusselt number Nu_b asymptotes to $c\chi(\eta)Ta^{\frac{1}{2}}$ in all three cases where the unknown constant c is given in (5.53a-c)

η	$A^{nc}(\eta)/\chi(\eta)$	$A^{3D}(\eta)/\chi(\eta)$	$A^{2D}(\eta)/\chi(\eta)$
0.1	0.0694315	0.00832565	0.00376439
0.2	0.0700607	0.00830294	0.00377039
0.3	0.0702631	0.00840836	0.0038083
0.4	0.0699845	0.00843543	0.0038438
0.5	0.0698495	0.00846619	0.00381451
0.6	0.0697773	0.00847018	0.0038186
0.7	0.0697175	0.00847478	0.00381908
0.8	0.069738	0.00846118	0.00381454
0.9	0.0697065	0.00846983	0.00380973
0.99	0.0697082	0.0084623	–

Table 5.1: Variation of the ratio $A(\eta)/\chi(\eta)$, where $A(\eta)$ is from the relation (5.52) and $\chi(\eta)$ is given in (5.47), in case 1, case 2 and case 3 where we have respectively added 'nc', '$3D$' and '$2D$' in the superscript to signify the case. Notice that $A(\eta)$ when scaled with $\chi(\eta)$ becomes almost invariant in η.

of the Taylor number Ta. We denote the bounds as Nu_b^{nc} for case 1, Nu_b^{3D} for case 2, and Nu_b^{2D} for case 3, and these are shown in the top, middle and bottom rows, respectively. We cover a wide range of parameters both in radius ratio (from $\eta = 0.1$ to $\eta = 0.99$) and in Taylor number. In figures 5.5a, 5.5c and 5.5e the bound Nu_b has been scaled with its expected asymptotic dependence on Ta, namely $Ta^{\frac{1}{2}}$. The color and shape of the symbols each correspond to a different radius ratio, as shown in the legend. The symbols in the plots in figure 5.5 correspond to data points computed using the numerical algorithm from the previous subsection, whereas the solid lines connecting the data points are calculated using interpolation, providing a guide to the eye. For every radius ratio value, the solid line is extended up to the highest Taylor number for which the computation is performed. Beyond this point, we extrapolate using a best fit

of the form

$$f(\eta) = A(\eta) + \frac{B(\eta)}{Ta^{\alpha(\eta)}} \tag{5.52}$$

applied to the data of $Nu_b/Ta^{\frac{1}{2}}$ computed from the last two decades in Ta. For each value of η, we thus define $A(\eta)$ as the asymptotic limit of $Nu_b/Ta^{\frac{1}{2}}$ as $Ta \to \infty$. Table 5.1 summarizes the values of $A(\eta)$ obtained from this fitting procedure for different radius ratios. We have added appropriate abbreviations in the superscript of $A(\eta)$ to signify the case at hand. We remark that these extrapolations were necessary, especially for the small radius ratios, where the bound on the Nusselt number Nu_b converges slowly to its asymptotic scaling in the Taylor number Ta.

In figures 5.5b, 5.5d and 5.5f the bound Nu_b has been scaled by $Ta^{\frac{1}{2}}$ as well as the geometrical scaling $\chi(\eta)$ obtained in (5.47). Note the striking collapse of the different radius ratio curves at high Taylor numbers in all three cases. Correspondingly, we also see from table 5.1 that the ratio $A(\eta)/\chi(\eta)$ is nearly independent of η with less than 1.1% variation in the average between the largest and smallest values. This suggests that the geometrical dependence of the bound on the Nusselt number at high Taylor number is $\chi(\eta)$ irrespective of the case considered. In case 1, the value of $A^{nc}(\eta)/\chi(\eta)$ is close to 9/128 which is the exact asymptotic result we obtained from the method of matched asymptotics in appendix 5.C. We also observe from table 5.1 that the value of $A/\chi(\eta)$ in case 2 and case 3 is very close to a constant for $\eta > 0.5$, but varies a little more for $\eta < 0.5$. This is likely due to the fact that the extrapolation is less accurate at small radius ratio because the computed data is further from being in the asymptotic regime compared with the case when the radius ratio is not small.

For this reason, we assume that the average of $A(\eta)$ calculated for $\eta \geq 0.5$ is the correct asymptotic limit of $Nu_b/Ta^{\frac{1}{2}}$ as $Ta \to \infty$ and obtain

$$Nu_{b,\infty}^{nc} = \frac{9}{8}\frac{\eta^3}{(1+\eta)^2(1+\eta^2)^2}Ta^{\frac{1}{2}}, \tag{5.53a}$$

$$Nu_{b,\infty}^{3D} = \frac{0.1354\,\eta^3}{(1+\eta)^2(1+\eta^2)^2}Ta^{\frac{1}{2}}, \tag{5.53b}$$

$$Nu_{b,\infty}^{2D} = \frac{0.0610\,\eta^3}{(1+\eta)^2(1+\eta^2)^2}Ta^{\frac{1}{2}}. \tag{5.53c}$$

Here, we have added '∞' in the subscript to point out that these are the main terms of the optimal bounds in the limit $Ta \to \infty$.

In summary, we have shown that for case 1, case 2 and case 3, the optimal bounds are respectively a factor of 1.5, 12.46 and 27.66 better than the suboptimal bound (5.46) in the high Taylor number limit. Crucially, this improvement is uniform in the radius ratio η. We had obtained the analytical expression for the geometrical scaling $\chi(\eta)$ from a fairly simple suboptimal analytical bound calculated using a choice of background flow with two boundary layers whose thicknesses were adjusted to optimize the bound. During this procedure, we had not applied any constraint on the perturbed flow $\tilde{\boldsymbol{v}}$ (other than the homogeneous boundary conditions) and further used standard calculus inequalities which are known to overestimate the bound on Nu_b. Consequently, it is not at all self-evident why the optimal bounds should have the same geometrical scaling. The fact that the optimal bounds (5.53a-c), which are up to an order of magnitude better than the suboptimal bound (5.46), preserve the same geometrical dependence on radius ratio is therefore a simple yet remarkable result.

5.5.3 Wavenumber spectrum of perturbation

In this subsection, we investigate the wavenumber spectrum of the perturbed flow $\tilde{\boldsymbol{v}}$ with a particular focus on the small scale structures present in $\tilde{\boldsymbol{v}}$. In the optimal state, $\tilde{\boldsymbol{v}}$ contains only a finite number of modes, called the critical modes, either in the z or θ direction, depending on the case considered, i.e.,

$$\tilde{\boldsymbol{v}} = \sum_{n \in K_2} \begin{bmatrix} \tilde{v}_{r,n}(r)\cos(k_n z) \\ \tilde{v}_{\theta,n}(r)\cos(k_n z) \\ \tilde{v}_{z,n}(r)\sin(k_n z) \end{bmatrix} \text{ in case 2} \quad \tilde{\boldsymbol{v}} = \sum_{m \in K_3} \begin{bmatrix} \tilde{v}_{r,m}(r)e^{im\theta} \\ \tilde{v}_{\theta,m}(r)e^{im\theta} \end{bmatrix} \text{ in case 3} \tag{5.54}$$

where $K_2 \subset \mathbb{N}$ and $K_3 \subset \mathbb{Z} \setminus \{0\}$ are finite sets. Moreover, as we shall demonstrate below, the smallest scales in the perturbation are present only near the boundaries. It is thus reasonable to hypothesize that the smallest length scale in the perturbation $\tilde{\boldsymbol{v}}$ is similar to the boundary layer thickness of the background flow $\boldsymbol{U}$. To further pursue this idea, we divide the critical modes present in the perturbation into four different categories. If, for a given critical mode, more than 90% of the contribution to its $L^1(dr)$ norm comes from the region

$$S_{in} \coloneqq \left\{ r \mid r_i \leq r \leq r_i + \frac{r_o - r_i}{3} \right\}$$

then we say that mode is active only near the inner cylinder. Similarly, if it comes from the region

$$S_{out} \coloneqq \left\{ r \mid r_o - \frac{r_o - r_i}{3} \leq r \leq r_o \right\}$$

then we say it is active only near the outer cylinder. Finally, if more than 90% of the contribution comes from region S_{in} and S_{out} together then we say the mode is active near both the cylinders, otherwise we say the mode is active in the bulk.

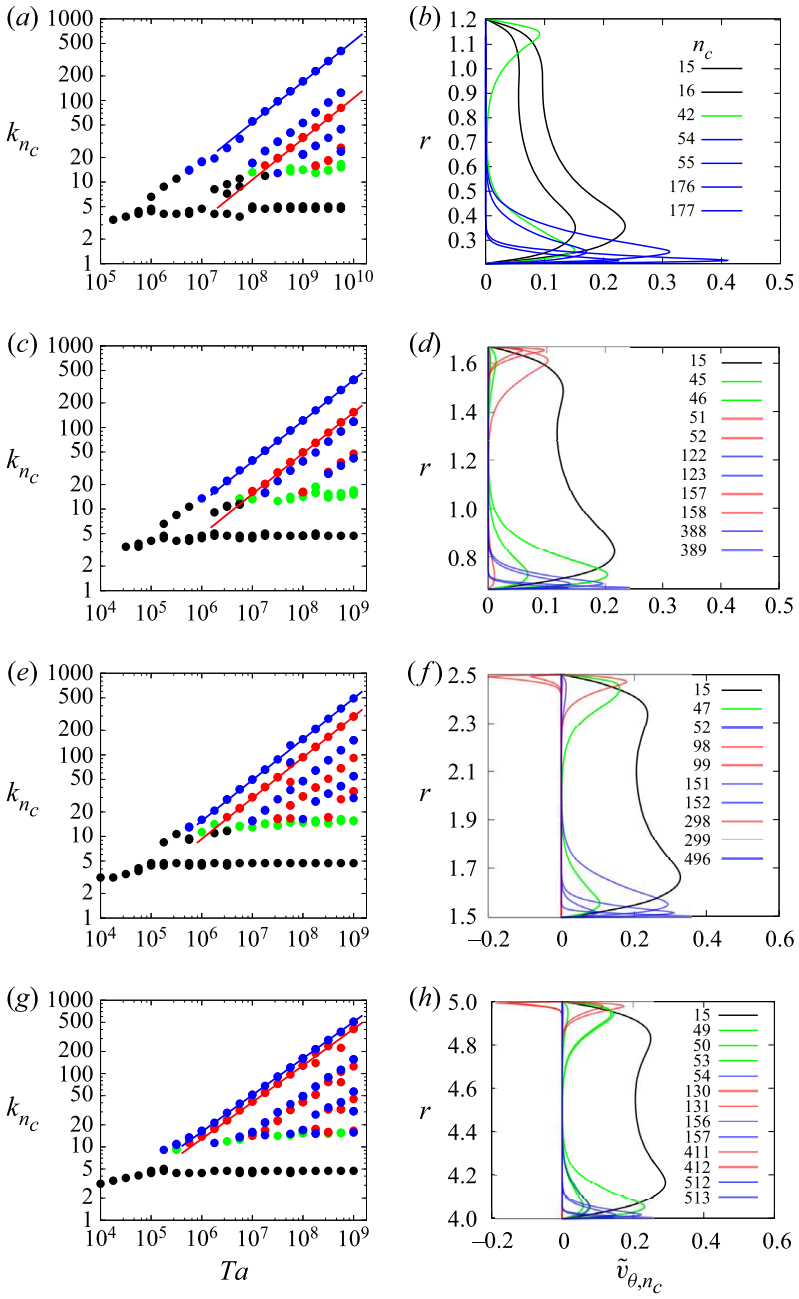

Figure 5.6: The left column shows the wavenumbers of the critical modes in the optimal perturbation as a function of Ta at $\eta = 0.2, 0.4, 0.6$ and 0.8 (top to bottom). The color indicates if the critical mode is active near the inner cylinder (blue), outer cylinder (red), both cylinders (green) and in the bulk (black), according to the classification given in the main text. The blue and red solid lines are the theoretical predictions for the critical mode with the largest wavenumber active near the inner and the outer cylinder, (see equation (5.57)), respectively. The right column shows the corresponding azimuthal component $\tilde{v}_{\theta,n_c}(r)$ of critical modes at the same radius ratios, at $Ta = 10^8$.

This way of categorizing the modes may seem somewhat arbitrary at first, but looking at the shape of different critical modes, it becomes readily apparent that any other appropriate definition would have led to the same conclusion. We use the following color scheme to differentiate modes according to our classification: blue for the modes that are active near the inner cylinder, red for the modes that are active near the outer cylinder, green for the modes that are active near both the cylinders and black for the modes that are active in bulk. The right column in figure 5.6 shows the plots of $\tilde{v}_{\theta,n_c}(r)$ for critical modes at $Ta = 10^8$ and for radius ratios $\eta = 0.2, 0.4, 0.6$ and 0.8. We now see that the plots of $\tilde{v}_{\theta,n_c}(r)$ provide an unambiguous visual justification of our earlier classification of critical modes into four categories, and therefore, our classification is robust.

We first apply this categorization to the optimal perturbations found in case 2 and denote the wavenumber of the critical mode with smallest length scale that is active near the inner cylinder as k^s_{in} and the one that is active near the outer cylinder as k^s_{out}. Assuming that our hypothesis about the similarity of the boundary layer thickness in the background flow and the smallest length scale in the perturbation made above is correct, then we may expect

$$k^s_{in} \propto \frac{1}{\delta_i}, \qquad k^s_{out} \propto \frac{1}{\delta_o}, \tag{5.55}$$

where δ_i and δ_o are given by (5.44). Substituting their expressions in above relation leads to

$$k^s_{in} \propto \frac{\eta^2}{(1+\eta^2)(1+\eta)^3} Ta^{\frac{1}{2}}, \qquad k^s_{out} \propto \frac{\eta^3}{(1+\eta^2)(1+\eta)^3} Ta^{\frac{1}{2}}. \tag{5.56}$$

From these relations, we not only obtain the dependence of k^s_{in} and k^s_{out} on Ta,

but also on the radius ratio η. In particular, we predict that the smallest length scales in the perturbation should become larger as $\eta \to 0$. Furthermore, at a given η, the small scale structures near the outer cylinder are predicted to be $1/\eta$ times larger than the ones near the inner cylinder.

The left column in figure 5.6 shows the wavenumbers of the critical modes in the optimal perturbations as a function of the Taylor number for four different radius ratio values $\eta = 0.2, 0.4, 0.6$ and 0.8 (top to bottom row). By fitting these plots, we find that the constant of proportionality in (5.56) that best fists the data at high Taylor numbers is $C = 0.244$, therefore we expect

$$k_{in}^s = 0.244 \frac{\eta^2}{(1+\eta^2)(1+\eta)^3} Ta^{\frac{1}{2}}, \qquad k_{out}^s = 0.244 \frac{\eta^3}{(1+\eta^2)(1+\eta)^3} Ta^{\frac{1}{2}}. \quad (5.57)$$

These two relations are plotted in figures 5.6a, 5.6c, 5.6e and 5.6g with solid blue and red lines, respectively. We see that smallest length scales in the critical perturbation near the inner and outer boundaries, respectively, indeed follow the relations (5.57). Furthermore, these smallest scales achieve their asymptotic scaling in Taylor number quicker than the corresponding optimal bounds on Nusselt number shown in figure 5.5, without any need for extrapolation of the data. We therefore argue that (5.57) and figure 5.6 together provide a strong validation of the analytical predictions from §5.4.

We can use similar ideas to predict the scaling of the smallest length scales in optimal perturbations in case 3. Using (5.43), one would anticipate $m_i^s \propto r_i/\delta_i$ and $m_o^s \propto r_o/\delta_o$, where m_i^s is the largest wavenumber of a critical mode active near the inner cylinder and m_o^s is the largest wavenumber of a critical mode active near the outer cylinder. The plots on the left-hand side column in figure 5.7 shows the wavenumbers of critical modes in the 2D optimal perturbations as a function of

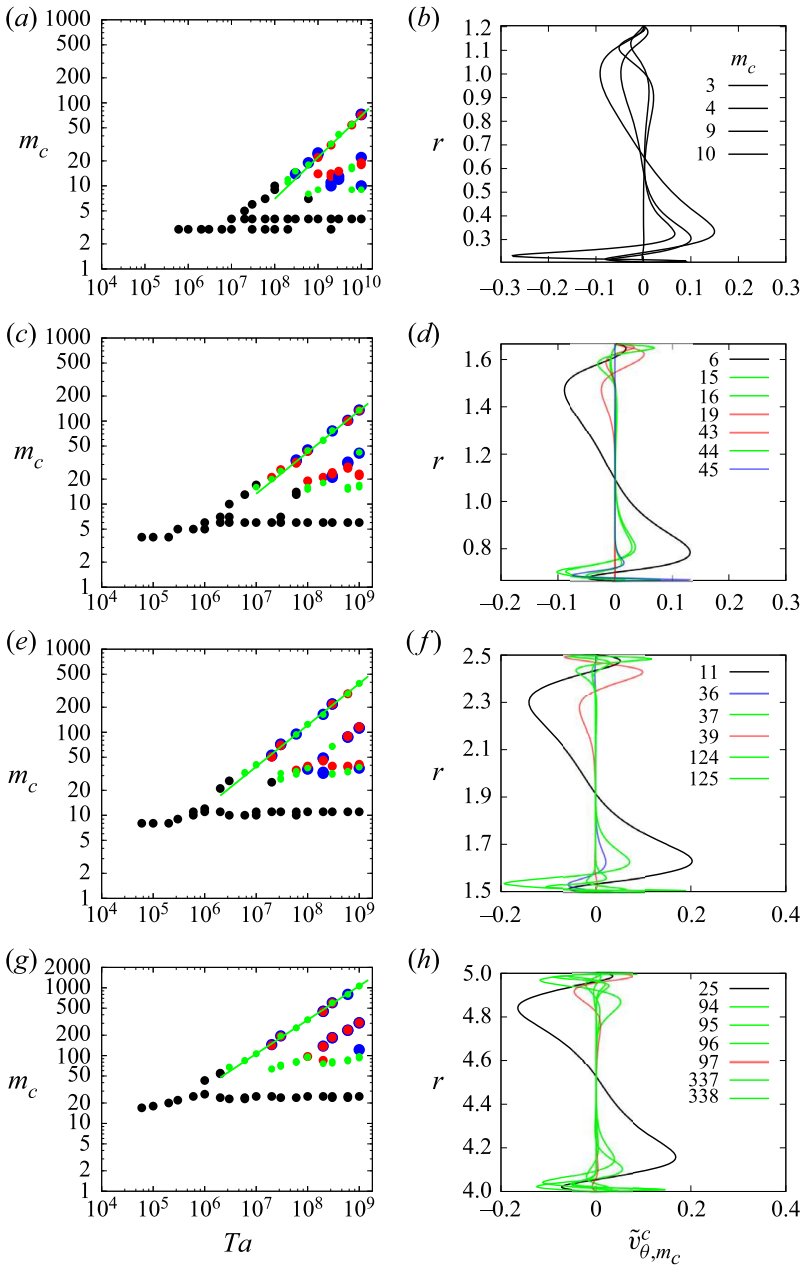

Figure 5.7: The plots in the left column shows the wavenumber m_c of the critical modes that constitutes the two dimensional optimal perturbation as a function of the Taylor number for radius ratios $\eta = 0.2, 0.4, 0.6$ and 0.8 (top to bottom). We use the same color scheme as in figure 5.6 to distinguish different critical modes. The solid green line is the relation (5.58) which predicts the largest critical wavenumber. The right column shows the plots of $\tilde{v}^c_{\theta,m_c}$, the coefficient of $\cos m_c\theta$ in the azimuthal component of the velocity, at $Ta = 10^8$ and the same radius ratios as the left-hand side plots.

the Taylor number at radius ratios $0.2, 0.4, 0.6$ and 0.8. We apply the same mode identification method, and use the same color scheme to differentiate the critical modes as before. From these plots, we can fit the data at high Taylor numbers, to measure the constant of proportionality in the expressions for m_i^s and m_o^s, leading to

$$m_i^s = m_o^s = \frac{0.126\eta^3}{(1-\eta^4)(1+\eta)^2} Ta^{\frac{1}{2}}. \tag{5.58}$$

We see that the wavenumber of the critical mode with smallest length scale that is active near the inner cylinder and outer cylinder are equal. The relation (5.58), shown as a solid green line on the left-hand side of figure 5.7, does seem to predict the largest wavenumbers at high Taylor numbers correctly.

As in figure 5.6, the right-hand side column of figure 5.7 shows the function $v^c_{\theta,m_c}(r)$, defined as the coefficient of $\cos m_c\theta$ in the expression

$$\tilde{v}_{\theta,m_c}(r)e^{im_c\theta} + \tilde{v}_{\theta,-m_c}(r)e^{-im_c\theta},$$

where m_c refers to a critical mode. The main difference between the shape of modes $\tilde{v}_{\theta,n_c}(r)$ in figure 5.6 compared with $v^c_{\theta,m_c}(r)$ in figure 5.7, is that the mean of $\tilde{v}^c_{\theta,m_c}(r)$ is zero, i.e.,

$$\int_{r_i}^{r_o} \tilde{v}^c_{\theta,m_c}(r)dr = 0. \tag{5.59}$$

This condition comes from incompressibility, which leads to (5.59) in 2D, but does not in 3D because the z-component, $\tilde{v}_z$, is nonzero. As a result, in 2D, modes which are active solely near the cylinders oscillates in the boundary layer to ensure that (5.59) is satisfied.

5.6 A note on the applicability of the background method

In one of our previous studies (Kumar, 2020), we presented a sufficient criterion to determine when the background method can be applied, for a given flow geometry and boundary conditions. We demonstrated that it can be used with any flow problem (tangential-velocity-driven or pressure-driven) with impermeable boundaries, provided the boundaries have the shape of streamtubes of the following flow

$$\boldsymbol{V} = \boldsymbol{A}\boldsymbol{x} + \boldsymbol{V}_0. \tag{5.60}$$

Here, $\boldsymbol{A}$ is a constant skew-symmetric tensor, $\boldsymbol{V}_0$ is a constant vector and $\boldsymbol{x}$ is the position vector. For these types of problems, one can further show that the upper bound on the dissipation becomes independent of viscosity at high Reynolds numbers. In this section, we explore the complementary question of whether there exist flow configurations for which the background method *cannot* be applied.

Indeed, the applicability of the background method depends on the existence of an incompressible background flow (which also satisfies the inhomogeneous boundary conditions) such that the following functional is positive semi-definite

$$\mathcal{H}(\boldsymbol{v}) = \left[\frac{1}{2Re}\|\boldsymbol{\nabla}\tilde{\boldsymbol{v}}\|_2^2 + \int_V \tilde{\boldsymbol{v}}\cdot\boldsymbol{\nabla}\boldsymbol{U}_{sym}\cdot\tilde{\boldsymbol{v}}\;d\boldsymbol{x} + \int_V \boldsymbol{U}\cdot\boldsymbol{\nabla}\boldsymbol{U}\cdot\tilde{\boldsymbol{v}}\;d\boldsymbol{x}\right], \tag{5.61}$$

for any perturbations $\tilde{\boldsymbol{v}}$ that satisfies the homogeneous boundary conditions. Consequently, proving that the background method *cannot* be applied reduces to the problem of finding a perturbation or a family of perturbations such that there is

no background flow $\boldsymbol{U}$ for which $\mathcal{H}$ is positive semi-definite.

We start by giving a few examples where the applicability of the background flow can be rigorously dismissed. We first consider the case of Taylor–Couette flow with suction at the inner cylinder. The energy stability analysis of this problem was considered by Gallet et al. (2010). The boundary conditions for this problem are:

$$\boldsymbol{u} = -\boldsymbol{e}_r + \omega_i r_i \boldsymbol{e}_\theta \quad \text{at} \quad r = r_i, \qquad \boldsymbol{u} = -\frac{r_i}{r_o}\boldsymbol{e}_r + \omega_o r_o \boldsymbol{e}_\theta \quad \text{at} \quad r = r_o, \tag{5.62}$$

where the Reynolds number Re is defined such that $\boldsymbol{u} \cdot \boldsymbol{e}_r = -1$ at the inner cylinder. The non-dimensional angular velocities of the inner and outer cylinder are ω_i and ω_o, respectively. In this problem, the flow is constricted to a narrow area as it moves from the outer cylinder (inlet) to the inner cylinder (outlet). We restrict ourselves to two dimensions but the arguments given below are valid in three dimensions as well. The domain of interest is $V = [r_i, r_o] \times [0, 2\pi]$.

We consider a perturbation $\tilde{\boldsymbol{v}}$ of the form

$$\tilde{\boldsymbol{v}} = (\tilde{v}_r, \tilde{v}_\theta) = (0,\ v_0 r(r - r_i)(r - r_o))\,, \tag{5.63}$$

whose amplitude is v_0. Note that $\tilde{\boldsymbol{v}}$ satisfies the homogeneous boundary conditions and is incompressible. We now demonstrate that for this perturbation, the spectral constraint can never be satisfied above a certain Reynolds number regardless of the choice of background flow $\boldsymbol{U}$.

To show that the spectral constraint (5.61) is not satisfied, we have to show that the second term is negative and that its absolute value is larger than the first term. Being linear in $\tilde{\boldsymbol{v}}$, the last term can be made arbitrarily small compared

with the first two terms by choosing v_0 in (5.63) to be large enough for any given background flow $\boldsymbol{U}$. As such, it does not play any role in the following argument.

The calculation of the first term is straightforward:

$$\frac{1}{2Re}\|\boldsymbol{\nabla}\tilde{\boldsymbol{v}}\|_2^2 = \frac{\pi}{60Re}(r_i + r_o)(5r_i^2 + 5r_o^2 + 2)v_0^2. \tag{5.64}$$

In the calculation of the second term, we take advantage of the fact that the chosen perturbation (5.63) is independent of θ, so

$$\int_V \tilde{\boldsymbol{v}} \cdot \boldsymbol{\nabla}\boldsymbol{U} \cdot \tilde{\boldsymbol{v}}\, d\boldsymbol{x} = \int_{r_i}^{r_o} \tilde{v}_\theta^2 \left[\int_0^{2\pi} \left(\frac{1}{r}\frac{\partial U_\theta}{\partial \theta} + \frac{U_r}{r}\right) d\theta\right] r dr. \tag{5.65}$$

Now, using periodicity as well as the incompressibility condition satisfied by the background flow $\boldsymbol{U}$, the following holds

$$\int_0^{2\pi} \frac{\partial U_\theta}{\partial \theta} d\theta = 0, \qquad \int_0^{2\pi} U_r d\theta = -\frac{2\pi r_i}{r}. \tag{5.66}$$

Using (5.63) and (5.66) in (5.65) gives

$$\int_V \tilde{\boldsymbol{v}} \cdot \boldsymbol{\nabla}\boldsymbol{U} \cdot \tilde{\boldsymbol{v}}\, d\boldsymbol{x} = -\frac{\pi}{30}(r_i^2 + r_i r_o)v_0^2. \tag{5.67}$$

From (5.64) and (5.67), we deduce that the spectral constraint (5.61) will not be satisfied if

$$Re > \frac{5r_i^2 + 5r_o^2 + 2}{2r_i}, \tag{5.68}$$

a condition that is, remarkably, independent of the choice of $\boldsymbol{U}$. Note that in the limit of $r_i/r_o \to 1$, the Reynolds number beyond which the method fails goes to

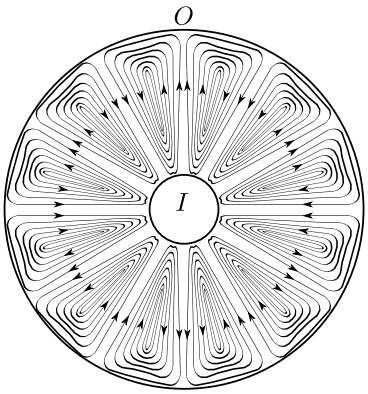

Figure 5.8: A cartoon of the streamlines of the flow field given by (5.72).

infinity. This limit recovers the case of a plane Couette flow with suction and injection at the walls (Doering et al., 2000), where the background method can indeed be applied, so (5.68) is consistent with these results.

A similar type of condition on the Reynolds number can be derived in the problem of the Taylor–Couette flow with injection at the inner cylinder, i.e.,

$$\boldsymbol{u} = \boldsymbol{e}_r + \omega_i r_i \boldsymbol{e}_\theta \quad \text{at} \quad r = r_i, \qquad \boldsymbol{u} = \frac{r_i}{r_o}\boldsymbol{e}_r + \omega_o r_o \boldsymbol{e}_\theta \quad \text{at} \quad r = r_o. \tag{5.69}$$

In this problem, the flow overall expands into a larger area as it moves from the inner cylinder (inlet) to the outer cylinder (outlet). For this case, we can use similar arguments but with the new perturbed flow

$$\tilde{\boldsymbol{v}} = (\tilde{v}_r, \tilde{v}_\theta) = (v_0 r(r - r_i)(r - r_o),\ 0)\,. \tag{5.70}$$

The perturbation this time is not incompressible but can be shown to yield a negative $\mathcal{H}(\tilde{\boldsymbol{v}})$ regardless of the background flow $\boldsymbol{U}$, for sufficiently large Reynolds number. However, noting that the perturbation (5.70) is radial, one may then expect that an incompressible perturbation, which is composed of vortices stretched

in the radial direction will also yield a negative $\mathcal{H}(\tilde{\boldsymbol{v}})$. This observation led us to consider the following streamfunction:

$$\psi_v = v_0 r^2 (r - r_i)^2 (r - r_o)^2 \sin m\theta \quad \text{where } m \in \mathbb{N}. \tag{5.71}$$

We define the corresponding velocity field $\tilde{\boldsymbol{v}} = (\tilde{v}_r, \tilde{v}_\theta)$ as

$$\tilde{v}_r = \frac{1}{r}\frac{\partial \psi_v}{\partial \theta}, \quad \tilde{v}_\theta = -\frac{\partial \psi_v}{\partial r}. \tag{5.72}$$

This velocity field is divergence free and satisfies the homogeneous boundary conditions at the surface of the cylinders. The streamlines of $\tilde{\boldsymbol{v}}$ are depicted in figure 5.8. Next define a family of rotation operators $\mathcal{Q}_\varphi : \mathcal{D}_\sigma(V) \to \mathcal{D}_\sigma(V)$, indexed with φ, on the space of divergence-free vector fields that satisfies the homogeneous boundary conditions at ∂V as

$$\mathcal{Q}_\varphi(\tilde{\boldsymbol{v}})(r, \theta) = \tilde{\boldsymbol{v}}(r, \theta + \varphi) \quad \forall (r, \theta) \in V. \tag{5.73}$$

A tedious calculation, first involving an integration in φ and then using the arguments similar to the suction problem above, shows

$$\int_0^{2\pi} \mathcal{H}(\mathcal{Q}_\varphi(\tilde{\boldsymbol{v}}))d\varphi = \frac{\pi(r_i + r_o)}{1260}\left[\frac{246r_i^4 + 138r_o^4 + 108r_o^3 + 120r_i^2 r_o^2 + 108r_i^2 r_o + 8m^2(r_o^3 - r_i^3) + m^4}{2Re} - r_i(m^2 - 6(r_i^2 + r_o^2))\right]. \tag{5.74}$$

This calculation implies that if

$$m > \left\lceil \sqrt{6r_i^2 + 6r_o^2} \right\rceil, \tag{5.75}$$

where $\lceil \cdot \rceil$ is the ceiling function, then for

$$Re > \frac{246r_i^4 + 138r_o^4 + 108r_o^3 + 120r_i^2r_o^2 + 108r_i^2r_o + 8m^2(r_o^3 - r_i^3) + m^4}{2r_i\left(m^2 - 6r_i^2 - 6r_o^2\right)} \tag{5.76}$$

the integral (5.74) is negative, which implies there is at least one $\varphi \in [0, 2\pi]$ such that $\mathcal{H}(\mathcal{Q}_\varphi(\tilde{\boldsymbol{v}})) < 0$. More generally, there exist a set $S \subset [0, 2\pi]$, depending on the background flow $\boldsymbol{U}$, of positive measure ($\mu(S) > 0$) such that $\mathcal{H}(\mathcal{Q}_\varphi(\tilde{\boldsymbol{v}})) < 0$ for any $\varphi \in S$, i.e., the spectral constraint is not satisfied. Note that the condition (5.75) is basically saying that the vortices in the incompressible perturbed flow field (5.72) should be stretched in the radial direction, which we expected from the example of the compressible perturbed flow (5.70).

The key message from these two problems is that if there is a converging flow, then one can rule out the applicability of the background method by creating a perturbation whose streamlines are perpendicular to the direction of the mean flow, while in the case of a diverging flow, one can use a perturbation whose streamlines are parallel to the direction of the mean flow instead. Of course, in both the cases, we need to make sure that the perturbation satisfies the homogeneous boundary conditions.

Combining these ideas suggests that one cannot apply the background method to flows in a converging-diverging nozzle, either because one can choose the perturbation to be composed of vortices that stretch in the perpendicular direction to the flow in the converging section or parallel to the flow in the diverging section.

Using the same arguments, one would then also conjecture that the background method can in general not be applied to flows between rough walls. Indeed, in this case, one can always find vertical sections where the flow expands or compresses and then one could use the same strategy to choose perturbations for which $\mathcal{H}(\tilde{\boldsymbol{v}}) < 0$. However, note that, in this case, the compression or expansion is small, i.e., the gap width on averages decreases only by a factor of $(1 - \epsilon)$ in the converging part or increases by a factor of $(1 + \epsilon)$ in the diverging part, where ϵ is the non-dimensional roughness scale. This problem is analogous to the converging-diverging nozzle if the Reynolds number is based on the surface roughness ϵ. Therefore, for the Reynolds number based on the average gap width, we expect that the spectral constraint (5.61) will not be satisfied if $Re \gtrsim \epsilon^{-1}$.

This still leaves the problem open for the flow systems which do not have a converging or diverging section, for example, flow in tortuous channels. We believe that even for these problems the spectral constraint will fail to hold past a certain Reynolds number for any background flow. Therefore, we conjecture that the sufficient condition for the applicability of the background method mentioned in the beginning of this section is also a necessary condition.

5.7 Discussion and conclusion

5.7.1 Summary and implications

In this paper, we computed optimal bounds on mean quantities in the Taylor–Couette flow problem with a stationary outer cylinder, with particular focus on the dependence of these bounds on the system geometry. Along the way, we studied the energy stability of the laminar flow in §5.3. The main finding of this section

was that for a value of radius ratio r_i/r_o below 0.0556, the marginally stable flow at the energy stability threshold is not composed of the well-known axisymmetric Taylor vortices but is instead a fully three-dimensional flow field.

To uncover the functional dependence of the optimal bounds on the radius ratio at large Taylor number, we began by deriving a suboptimal but analytical bound with the use of standard inequalities and a choice of background flow with two boundary layers (one near the inner cylinder and one near the outer cylinder) whose thicknesses were then adjusted to optimize the bound. We then argued that the dependence on the radius ratio captured by this analytical bound should also be the same for the optimal bounds at large Taylor numbers. We systematically verified this statement by obtaining distinct optimal bounds under three circumstances. In the first case, we imposed no constraints on the perturbation other than the homogeneous boundary conditions (case 1). Next, we allowed for three-dimensional incompressible perturbations (case 2), and finally, we considered two-dimensional incompressible perturbations (case 3). In the high Taylor number limit, we see an improvement of 1.5, 12.46 and 27.66, respectively, over the analytical bound as we move from case 1 to case 3, and that improvement is the same for all radius ratios. This result is striking and non-trivial because there is no known transformation of variables which makes the Euler–Lagrange equations (5.109a-d) of the optimal bounds independent of the radius ratio.

In §5.6, we rigorously dismissed the applicability of the background method for two flow problems. The limitation of the background method is previously known in the context of Rayleigh–Bénard convection at infinite Prandtl number (Nobili and Otto, 2017), where it was shown that using a different method a tighter bound can be obtained as compared to the background method. Here, we have shown that past a certain Reynolds number, no bound can be obtained

using the background method applied to Taylor–Couette flow with suction or injection at the inner cylinder, i.e., there is no background flow that satisfies the spectral constraint even when the incompressibility condition on the perturbation is imposed. Generalizing these results then suggests that the spectral condition may not be satisfied for flow problems that contain converging or diverging sections, such as flow in a converging-diverging nozzle or flow between the rough walls. The auxiliary functional method (Chernyshenko et al., 2014) could possibly be a way forward to obtain bounds for such problems. The current best-known implementation of this auxiliary functional method to obtain a bound on energy dissipation in flow problems uses only quadratic functionals, in which case it has been shown to be equivalent to the background method (Chernyshenko, 2022). However, Chernyshenko (2022) also proposed potential ways to implement nonquadratic functionals, which might be able to produce a finite bound on the energy dissipation in the problems stated above. Another possible approach, this time numerical, is to consider finite-dimensional truncated models of the actual flow problem, where there is a systematic way to use higher-than-quadratic auxiliary polynomials with the help of the sum-of-squares method (Goulart and Chernyshenko, 2012; Huang et al., 2015; Fantuzzi et al., 2016; Goluskin, 2018; Kumar, 2019; Olson et al., 2021).

Our study brings into light the significance (or lack of significance, to be more precise) of the incompressibility constraint on the perturbation while calculating optimal bounds, especially in the limit of high Reynolds number, which is generally of interest in turbulent flows. As we showed in the present study, dropping the incompressibility constraint on the perturbations altogether (case 1) still recovers the correct dependence of the bounds on both the principal flow parameter (Ta, or equivalently Re) and on the domain geometry (through the radius ra-

tio). One cannot help but wonder whether the same holds true for other flow problems, including for instance the case of convection. It is a fundamental question of concern, as not imposing the incompressibility constraint tremendously decreases the computational cost of the optimal bound calculation. In the particular example studied here, in fact, not imposing the incompressibility condition allowed us to solve the Euler–Lagrange equations analytically using the method of matched asymptotic. This could also be potentially helpful in other studies involving the background method where it is relatively difficult to establish the scaling of the optimal bound even numerically, perhaps because the bounds involve logarithms (Fantuzzi et al., 2018, 2020) or a scaling other than a simple power-law (Kumar et al., 2022). In such situations, from an analysis point of view, it is usually challenging to decide what combination of the background field and calculus inequalities might be required to obtain the correct asymptotic scaling of the optimal bound. When the bound is obtained numerically instead, it can be difficult to establish its actual functional dependence of the principal flow parameter. Therefore, in these situations, considering case 1 can be very useful as one can try solving the Euler–Lagrange equations analytically using the method of matched asymptotics. These ideas can also be of relevance to other variational approaches such as the wall-to-wall transport problem (Hassanzadeh et al., 2014; Tobasco and Doering, 2017; Motoki et al., 2018b,a; Doering and Tobasco, 2019; Souza et al., 2020; Tobasco, 2022; Kumar, 2022b) which asks the question of what is the maximum heat transfer for a fixed energy or enstrophy budget.

Finally, assuming that the conclusions of this study apply more broadly, case 3 is also relevant to flow problems which are frequently investigated not just in three dimensions but in two dimensions as well, such as Rayleigh–Bénard convection or internally heated convection. For example, it could be interesting to determine

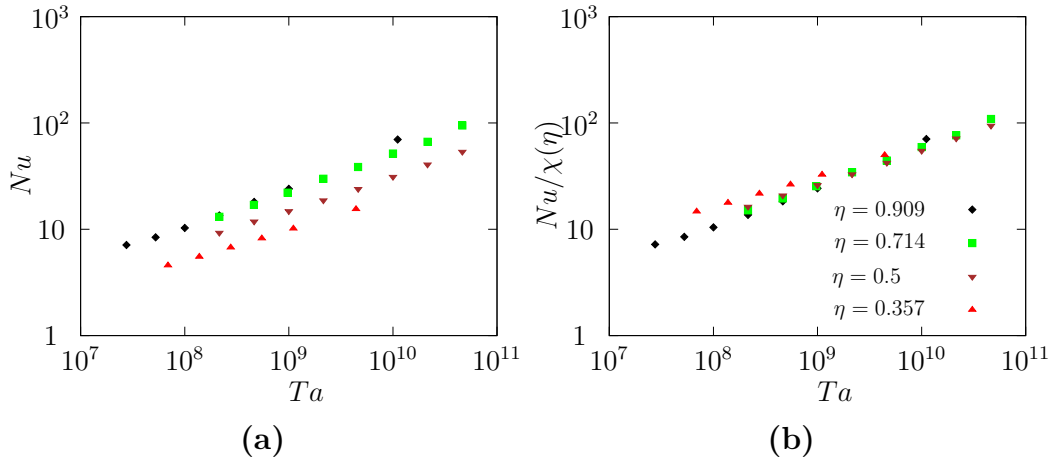

Figure 5.9: (a) The Nusselt number (Nu) from DNS as a function of the Taylor number (Ta). (b) The Nusselt number (Nu) scaled with the geometrical scaling $X(\eta)$ given by (5.47) as a function of Taylor number (Ta). In these figures the DNS results are taken from (Ostilla-Mónico et al., 2014) for $\eta = 0.5, 0.714$ and 0.909 and from (Froitzheim et al., 2019) for $\eta = 0.357$.

how the optimal bounds depends on the shape of the roughness of the wall in two dimensional Rayleigh–Bénard convection with rough boundaries, a problem previously investigated by Goluskin and Doering (2016) using the background method.

Before proceeding further, we note that one can also use the direct method of Seis (2015) to derive an upper bound on the Nusselt number with the same Taylor number dependence as in this paper. However, a question of interest could be if a bound with the same geometrical scaling can also be derived. We would expect that if one makes estimates near both the cylinders in Seis's approach and uses an analogous optimization procedure (similar to this paper), one may be able to derive a suboptimal bound with the same geometrical scaling as in this paper.

5.7.2 Comparison with the DNS

We now briefly analyze our results from a more practical point of view and ask the question of whether the dependence of the Nusselt number on the radius ratio obtained in this paper bears any relationship with that of the actual turbulent flow. Note that the asymptotic dependence of the optimal bound on the Taylor number is known to overestimate the actual Nusselt number in turbulent Taylor Couette flows by a logarithmic factor in Ta (Grossmann et al., 2016). As such, we cannot directly compare our results to the data, but instead merely ask the question of whether the geometric prefactor $g(\eta)$ in the expression $Nu(\eta, Ta) = g(\eta)f(Ta)$ measured in turbulent Taylor–Couette flows bears any resemblance with the prefactor $\chi(\eta)$ obtained in our optimal bound calculation, see equation (5.47).

We first test this idea on the direct numerical simulations (DNS) data from Ostilla-Mónico et al. (2014) and Froitzheim et al. (2019). On the left-hand panel in figure 5.9, we have plotted Nu vs Ta from these DNS, and on the right-hand panel, we show the same data divided by $\chi(\eta)$. We see that the rescaled data does become more compact and appears to fall on a single curve. This observation gives us confidence that the geometrical dependence of the bound $\chi(\eta)$ obtained in this paper is a good approximation to that of the actual Nusselt number Nu measured in turbulent Taylor Couette flows. However, we note that the data has not yet reached the asymptotic scaling corresponding to the high Ta regime, so the comparison at this point remains tentative. We also note that a different prediction for $Nu(\eta, Ta)$ has recently been obtained by Berghout et al. (2020) using the idea of Monin–Obukhov theory for thermally stratified turbulent boundary layers. Their

scaling the asymptotic limit of high Ta number is given as

$$Nu \sim 4\kappa^2 \frac{\eta^3}{(1+\eta)^2} \frac{Ta^{\frac{1}{2}}}{\log^2 Ta} = 0.6084 \frac{\eta^3}{(1+\eta)^2} \frac{Ta^{\frac{1}{2}}}{\log^2 Ta}, \tag{5.77}$$

where $\kappa = 0.39$ is the von Kármán constant. The geometrical dependence in (5.77) differs from $\chi(\eta)$ by a factor of $(1+\eta^2)^2$. However, it is reassuring to see that both expressions are proportional to η^3 in the limit of small radius ratio. A definitive answer to the question of whether the geometrical scaling $\chi(\eta)$ given by our bound is exact or just an approximation would require a precise comparison with the turbulent data at very high Taylor numbers collected for a range of radius ratios spanning the entire interval $(0, 1)$, which is at present a challenge for the numerical computations.

5.7.3 Further generalizations

We end this paper by discussing a few important consequences and generalizations of our study as well as future outlooks. The first one of these consequences concerns the bound on dissipation. The optimal bound on the Nusselt number for case 2 (3D incompressible perturbations) combined with the relations (5.24) and (5.5) gives us the optimal bound on the dissipation

$$\varepsilon_{b,\infty}^{3D} = 0.0677 \frac{\eta}{(1+\eta)(1+\eta^2)^2}. \tag{5.78}$$

This bound tends to 0.00846 in the limit $\eta \to 1$, which is within 1% of the optimal bound obtained by Plasting and Kerswell (2003) for the plane Couette flow, namely 0.008553. The consistency between the two results shows that our work can, in retrospect, be viewed as a generalization of the result of Plasting and

Kerswell (2003) to Taylor–Couette flow for an arbitrary radius ratio.

The second item is related to our previous work (Kumar, 2020) on the dependence of the bound on the friction factor λ on the radius of curvature κ and torsion τ for a pressure-driven flow in a helical pipe. We were able to employ a similar boundary layer optimization technique together with standard inequalities as we did here to obtain the following analytical bound on the friction factor in high Re limit

$$\lambda^{a}_{b,\infty} = \frac{27}{8} I(\kappa, \tau), \tag{5.79}$$

where

$$I(\kappa, \tau) = \frac{1}{2\pi} \int_0^{2\pi} ((1 - \kappa \cos\alpha)^2 + \tau^2)^{3/2} (1 - \kappa \cos\alpha)\, d\alpha. \tag{5.80}$$

However, the complexity of the helical pipe geometry makes it impossible in practice to compute the corresponding optimal bound. Nevertheless, in the light of results from the present study, and assuming that we captured the geometrical dependence correctly, one can in principle compute the prefactor in a limit where the optimal bound *can* be computed, namely the case of a straight pipe, for which $\kappa = \tau = 0$. This bound was computed by Plasting and Kerswell (2005) to be $\lambda^{3D}_{b,\infty}(0, 0) = 0.27$, and using this result we then expect that the optimal bound for helical pipes in the limit of high Reynolds number is

$$\lambda^{3D}_{b,\infty} = 0.27 I(\kappa, \tau). \tag{5.81}$$

Finally, the results presented in this paper potentially open the door to solving many important outstanding problems in engineering. Indeed, within that

context we are often interested in finding the optimal geometry of the system or the object involved that minimizes or maximizes a certain flow quantity subject to some physical constraint. These types of problems therefore, demand a careful study of the effect of the domain shape on a flow quantity. From this perspective, our study has broader implications. Even though we ruled out the applicability of the background method to a large class of problems (see §5.6), this still leaves a number of interesting problems open for analysis. For example, two problems which have been investigated using direct numerical simulations before but where an application of the background method can provide further insights are the Taylor–Couette flow with axisymmetric grooved walls (Zhu et al., 2016) and pressure-driven flow in a pipe with an elliptic cross-section (Nikitin and Yakhot, 2005). Another problem where the background method has previously been used but capturing the exact domain shape dependence in the bounds were not the primary focus are the flow of fluid in an arbitrary domain driven by moving boundaries (Wang, 1997). Our study suggests an interesting avenue towards solving these problems, by using the background method, together with perturbations that are not assumed to be incompressible, which, as we demonstrated here, can greatly simplify the calculation.

Acknowledgement

This paper is dedicated to Charlie Doering, whose work has been instrumental in motivating the author's research. A.K. thanks P. Garaud for a careful read of the paper and for providing comments that improved the quality of the paper. A.K. acknowledges use of the lux supercomputer at UC Santa Cruz, funded by NSF MRI grant AST 1828315.

Appendix 5.A The background method

In this section, we formulate the background method to obtain an upper bound on the quantity

$$\frac{1}{Re}\overline{\|\boldsymbol{\nabla u}\|_2^2}, \tag{5.82}$$

in Taylor–Couette flow. It is clear from (5.19) that an upper bound on this quantity immediately provides an upper bound on the dissipation ε.

We begin by writing the total flow field $\boldsymbol{u}$ as a sum of two divergence-free flow fields,

$$\boldsymbol{u} = \boldsymbol{U} + \boldsymbol{v}. \tag{5.83}$$

We call $\boldsymbol{U}$ the background flow, and require that it satisfies same boundary conditions as $\boldsymbol{u}$ and is only a function of space. We call $\boldsymbol{v}$, the perturbation, or perturbed flow, which satisfies homogeneous boundary conditions. The governing equation for the perturbation, obtained by substituting (5.83) in (5.3), is given by

$$\frac{\partial \boldsymbol{v}}{\partial t} + \boldsymbol{U}\cdot\boldsymbol{\nabla U} + \boldsymbol{U}\cdot\boldsymbol{\nabla v} + \boldsymbol{v}\cdot\boldsymbol{\nabla U} + \boldsymbol{v}\cdot\boldsymbol{\nabla v} = -\boldsymbol{\nabla} p + \frac{1}{Re}\nabla^2\boldsymbol{U} + \frac{1}{Re}\nabla^2\boldsymbol{v}. \tag{5.84}$$

We then obtain the evolution equation of the energy in the perturbed flow by taking the dot product of (5.84) with $\boldsymbol{v}$ and integrating over the volume,

$$\frac{d\|\boldsymbol{v}\|_2^2}{dt} = \frac{1}{Re}\int_V \nabla^2\boldsymbol{U}\cdot\boldsymbol{v}\, d\boldsymbol{x} - \frac{1}{Re}\|\boldsymbol{\nabla v}\|_2^2 - \int_V \boldsymbol{v}\cdot\boldsymbol{\nabla U}\cdot\boldsymbol{v}\, d\boldsymbol{x} - \int_V \boldsymbol{U}\cdot\boldsymbol{\nabla U}\cdot\boldsymbol{v}\, d\boldsymbol{x}, \tag{5.85}$$

Now using integration by parts, we can write

$$\int_V \nabla^2 \boldsymbol{U} \cdot \boldsymbol{v}\, d\boldsymbol{x} = -a \int_V \boldsymbol{\nabla U} : \boldsymbol{\nabla v}\, d\boldsymbol{x} + (1-a) \int_V \nabla^2 \boldsymbol{U} \cdot \boldsymbol{v}\, d\boldsymbol{x}. \tag{5.86}$$

where, in the index notation,

$$\boldsymbol{\nabla U} : \boldsymbol{\nabla v} = \partial_i \boldsymbol{v}_j \partial_i \boldsymbol{U}_j. \tag{5.87}$$

At the same time, one also has the following identity

$$\boldsymbol{\nabla U} : \boldsymbol{\nabla v} = \frac{|\boldsymbol{\nabla u}|^2 - |\boldsymbol{\nabla U}|^2 - |\boldsymbol{\nabla v}|^2}{2}. \tag{5.88}$$

Using (5.86) and (5.88) in (5.85) leads to

$$\frac{d\|\boldsymbol{v}\|_2^2}{dt} + \frac{a\|\boldsymbol{\nabla u}\|_2^2}{2Re} = \frac{a\|\boldsymbol{\nabla U}\|_2^2}{2Re} - \frac{(2-a)}{2Re}\|\boldsymbol{\nabla v}\|_2^2 + \frac{(1-a)}{Re}\int_V \nabla^2 \boldsymbol{U} \cdot \boldsymbol{v}\, d\boldsymbol{x} - \int_V \boldsymbol{v} \cdot \boldsymbol{\nabla U} \cdot \boldsymbol{v}\, d\boldsymbol{x} - \int_V \boldsymbol{U} \cdot \boldsymbol{\nabla U} \cdot \boldsymbol{v}\, d\boldsymbol{x}. \tag{5.89}$$

The introduction of a balance parameter 'a' in the background formulation goes back to Nicodemus et al. (1997). Now it can be shown within the framework of the background method that the quantity $\|\boldsymbol{v}\|_2^2$ is uniformly bounded in time (see Doering and Constantin, 1992, for example). As a result, the long-time average of the time derivative of $\|\boldsymbol{v}\|_2^2$ vanishes. Therefore, taking the long-time average of the equation (5.89) leads to the following bound

$$\frac{1}{Re}\overline{\|\boldsymbol{\nabla u}\|_2^2} \leq \frac{1}{Re}\|\boldsymbol{\nabla U}\|_2^2 - \frac{2}{a}\overline{\mathcal{F}(\boldsymbol{v})}, \tag{5.90}$$

where

$$\mathcal{F}(\boldsymbol{v}) = \left[\frac{2-a}{2Re}\|\boldsymbol{\nabla v}\|_2^2 - \frac{(1-a)}{Re}\int_V \nabla^2 \boldsymbol{U}\cdot\boldsymbol{v}\; d\boldsymbol{x} + \int_V \boldsymbol{v}\cdot\boldsymbol{\nabla U}\cdot\boldsymbol{v}\; d\boldsymbol{x} + \int_V \boldsymbol{U}\cdot\boldsymbol{\nabla U}\cdot\boldsymbol{v}\; d\boldsymbol{x}\right]. \quad (5.91)$$

This formulation of the background method is general, until this point. From here onward, we restrict the background flow $\boldsymbol{U}$ to be unidirectional, of the form

$$\boldsymbol{U} = U_\theta(r)\boldsymbol{e}_\theta. \quad (5.92)$$

At this point, we give proof of a straightforward but important lemma.

Lemma 5.A.1. *Let the domain V be given by (5.8). Then for a continuous function $f : [r_i, r_o] \to \mathbb{R}$ and a divergence-free vector field $\boldsymbol{w} : V \to \mathbb{R}^3$ such that $\boldsymbol{w}|_{r=r_i} = \boldsymbol{w}|_{r=r_o} = \boldsymbol{0}$ and periodic in the z direction, the following holds:*

$$\int_V f(r) w_r\; d\boldsymbol{x} = 0, \quad (5.93)$$

where, w_r is the radial component of $\boldsymbol{w}$.

Proof. Let

$$F(r,\theta,z) = \int_{r'=r_i}^{r} f(r')\; dr'. \quad (5.94)$$

Then we can write

$$\int_V f(r) w_r d\boldsymbol{x} = \int_V \boldsymbol{\nabla} F\cdot\boldsymbol{w}\; d\boldsymbol{x} = \int_V \boldsymbol{\nabla}\cdot(F\boldsymbol{w}) d\boldsymbol{x} = 0 \quad (5.95)$$

where we used the divergence theorem and the boundary conditions on $\boldsymbol{w}$ to

obtain the last equality. □

The assumption (5.92) combined with lemma 5.A.1 implies

$$\int_V \boldsymbol{U}\cdot\boldsymbol{\nabla}\boldsymbol{U}\cdot\boldsymbol{v}\,d\boldsymbol{x}=0. \tag{5.96}$$

The functional $\mathcal{F}$ therefore takes the following form

$$\mathcal{F}(\boldsymbol{v})=\left[\frac{2-a}{2Re}\|\boldsymbol{\nabla}\boldsymbol{v}\|_2^2+\int_V \boldsymbol{v}\cdot\boldsymbol{\nabla}\boldsymbol{U}\cdot\boldsymbol{v}\,d\boldsymbol{x}-\frac{(1-a)}{Re}\int_V \nabla^2\boldsymbol{U}\cdot\boldsymbol{v}\,d\boldsymbol{x}\right]. \tag{5.97}$$

If the infimum of this functional $\mathcal{F}$ over all the divergence-free vector fields $\boldsymbol{v}$ is finite then it may not be zero as $\mathcal{F}$ is not homogeneous due the presence of a linear term. Therefore, similar to Doering and Constantin (1998a) and Plasting and Kerswell (2003), we define a shifted perturbation as

$$\tilde{\boldsymbol{v}}=\boldsymbol{v}-\boldsymbol{\phi}, \tag{5.98}$$

where both $\tilde{\boldsymbol{v}}$ and $\boldsymbol{\phi}$ are divergence-free and satisfy homogeneous boundary conditions at the surface of the cylinders, and select $\boldsymbol{\phi}$ to eliminate the linear term when the bound (5.90) is written in terms of $\tilde{\boldsymbol{v}}$.

We substitute (5.98) in (5.90) and use (5.92) and lemma 5.A.1 whenever required. We obtain the following linear term in $\tilde{\boldsymbol{v}}$:

$$\frac{2}{aRe}\int_V\left[(2-a)\nabla^2\boldsymbol{\phi}+(1-a)\nabla^2\boldsymbol{U}\right]\cdot\tilde{\boldsymbol{v}}\,d\boldsymbol{x}. \tag{5.99}$$

Therefore, for this linear term to be zero, we require

$$(2-a)\nabla^2\boldsymbol{\phi}+(1-a)\nabla^2\boldsymbol{U}=0. \tag{5.100}$$

Without loss of generality, we can select the unidirectional solution

$$\boldsymbol{\phi} = -\frac{1-a}{2-a}\left[U_\theta - u_{lam,\theta}\right]\boldsymbol{e}_\theta. \tag{5.101}$$

Using this expression for $\boldsymbol{\phi}$, the bound in terms of $\tilde{\boldsymbol{v}}$ now reads

$$\frac{1}{Re}\overline{\|\boldsymbol{\nabla u}\|_2^2} \leq \frac{1}{a(2-a)Re}\|\boldsymbol{\nabla U}\|_2^2 - \frac{(1-a)^2}{a(2-a)Re}\|\boldsymbol{\nabla u}_{lam}\|_2^2 - \frac{2}{a}\mathcal{H}(\tilde{\boldsymbol{v}}), \tag{5.102}$$

where

$$\mathcal{H}(\tilde{\boldsymbol{v}}) = \left[\frac{2-a}{2Re}\|\boldsymbol{\nabla}\tilde{\boldsymbol{v}}\|_2^2 + \int_V \tilde{\boldsymbol{v}}\cdot\boldsymbol{\nabla U}\cdot\tilde{\boldsymbol{v}}\;d\boldsymbol{x}\right]. \tag{5.103}$$

If we choose a background flow $\boldsymbol{U}$ such that the functional $\mathcal{H}$ is positive semi-definite on the space of divergence-free vector field $\tilde{\boldsymbol{v}}$, i.e.

$$\inf_{\substack{\tilde{\boldsymbol{v}}\\ \boldsymbol{\nabla}\cdot\tilde{\boldsymbol{v}}=0}} \mathcal{H}(\tilde{\boldsymbol{v}}) \geq 0, \tag{5.104}$$

then the bound (5.102) simply is

$$\frac{1}{Re}\overline{\|\boldsymbol{\nabla u}\|_2^2} \leq \frac{1}{a(2-a)Re}\|\boldsymbol{\nabla U}\|_2^2 - \frac{(1-a)^2}{a(2-a)Re}\|\boldsymbol{\nabla u}_{lam}\|_2^2. \tag{5.105}$$

The positive semi-definite condition (5.104) on $\mathcal{H}$ is referred to as the spectral constraint. Since the functional $\mathcal{H}$ is quadratic and homogeneous, we can rewrite the spectral constraint as

$$\mathcal{H}(\tilde{\boldsymbol{v}}) \geq 0 \quad \forall\tilde{\boldsymbol{v}} \quad \text{such that} \quad \boldsymbol{\nabla}\cdot\tilde{\boldsymbol{v}} = 0 \quad \text{and} \quad \|\tilde{\boldsymbol{v}}\|_2 = 1. \tag{5.106}$$

Using the Euler–Lagrange equations, the spectral constraint (5.106) is equivalent

to the non-negativity of the smallest eigenvalue λ of the following self-adjoint spectral problem

$$\boldsymbol{\nabla} \cdot \tilde{\boldsymbol{v}} = 0, \tag{5.107a}$$

$$2\lambda \tilde{\boldsymbol{v}} = \frac{(2-a)}{Re} \nabla^2 \tilde{\boldsymbol{v}} - 2\tilde{\boldsymbol{v}} \cdot \boldsymbol{\nabla} \boldsymbol{U}_{sym} - \boldsymbol{\nabla} \tilde{p}. \tag{5.107b}$$

Here, $\tilde{p}$ and λ are the Lagrange multipliers for the constraints $\boldsymbol{\nabla} \cdot \tilde{\boldsymbol{v}} = 0$ and $1 - \|\tilde{\boldsymbol{v}}\|_2^2 = 0$.

Now, to optimize the bound (5.102) under the incompressibility constraint on $\tilde{\boldsymbol{v}}$, we write the following Lagrangian

$$\mathcal{L} = \frac{1}{a(2-a)Re} \|\boldsymbol{\nabla} \boldsymbol{U}\|_2^2 - \frac{(1-a)^2}{a(2-a)Re} \|\boldsymbol{\nabla} \boldsymbol{u}_{lam}\|_2^2 - \frac{2}{a} \mathcal{H}(\tilde{\boldsymbol{v}}) + \int_V \tilde{p}\, \boldsymbol{\nabla} \cdot \tilde{\boldsymbol{v}}\, d\boldsymbol{x}. \tag{5.108}$$

Letting the first variation (the Frechet derivative) of this functional with respective

to $\tilde{\boldsymbol{v}}$, $\tilde{p}$, $\boldsymbol{U}$ and a to zero, leads to

$$\frac{\delta \mathcal{L}}{\delta \tilde{\boldsymbol{v}}} = \frac{2(2-a)}{aRe}\nabla^2 \tilde{\boldsymbol{v}} - \frac{4}{a}\tilde{\boldsymbol{v}} \cdot \boldsymbol{\nabla} \boldsymbol{U}_{sym} - \boldsymbol{\nabla}\tilde{p} = 0, \tag{5.109a}$$

$$\frac{\delta \mathcal{L}}{\delta \tilde{p}} = \boldsymbol{\nabla} \cdot \tilde{\boldsymbol{v}} = 0, \tag{5.109b}$$

$$\frac{\delta \mathcal{L}}{\delta U_\theta} = -\frac{4\pi L}{a(2-a)Re}\left(r\frac{d^2 U_\theta}{dr^2} + \frac{dU_\theta}{dr} - \frac{U_\theta}{r}\right) + \frac{1}{r}\frac{d}{dr}\left(\frac{2r^2}{a}\int_{\theta=0}^{2\pi}\int_{z=0}^{L} \tilde{v}_r \tilde{v}_\theta d\theta dz\right) = 0, \tag{5.109c}$$

$$\frac{\delta \mathcal{L}}{\delta a} = \frac{2(a-1)}{a^2(2-a)^2 Re}\left(\|\boldsymbol{\nabla}\boldsymbol{U}\|_2^2 - \|\boldsymbol{\nabla}\boldsymbol{u}_{lam}\|_2^2\right) + \frac{2}{a^2}\left(\frac{1}{Re}\|\boldsymbol{\nabla}\tilde{\boldsymbol{v}}\|_2^2 + \int_V \tilde{\boldsymbol{v}} \cdot \boldsymbol{\nabla}\boldsymbol{U} \cdot \tilde{\boldsymbol{v}}\, d\boldsymbol{x}\right) = 0. \tag{5.109d}$$

In general, these equations do not have a unique solution. However, the solution to these equations for which the background flow also satisfies the spectral constraint (5.104), or equivalently, all the eigenvalues of the eigenvalue problem (5.107 a,b) are non-negative, is unique.

Appendix 5.B A useful lemma

Here we prove that the marginally stable perturbations in the energy stability analysis §5.3 or optimal perturbations in §5.5 only depend on radius when they are not required to be incompressible.

Lemma 5.B.1. *Let $\mathcal{D}(V)$ be the set of smooth velocity fields (not necessarily incompressible) that satisfy the homogeneous boundary conditions. For a given choice of the balance parameter $0 < a < 2$ and of the unidirectional background*

flow $\boldsymbol{U} = U_\theta(r)\boldsymbol{e}_\theta$*, the functional* $\mathcal{H}(\tilde{\boldsymbol{v}})$ *(given by (5.103)) achieves a minimum when* $\tilde{\boldsymbol{v}}$ *is a function of the radial direction only. Furthermore, if the background flow satisfies* $(dU_\theta/dr - U_\theta/r) \leq 0$ *then the optimal perturbed flow corresponds to* $\tilde{v}_r = \tilde{v}_\theta$*.*

Remark 5.B.1. *Although we do not prove that the optimal background flow satisfies* $(dU_\theta/dr - U_\theta/r) \leq 0$*, this condition was found to hold in every numerical computations of optimal bounds in all the three cases considered in our paper as well as for the choice of the background flow in analytical construction presented in §5.4. Therefore, it is natural to make the assumption that* $(dU_\theta/dr - U_\theta/r) \leq 0$*.*

Proof. In the first part of the lemma, it is sufficient to show that for every $\tilde{\boldsymbol{v}} \in \mathcal{D}(V)$ there exist $\tilde{\boldsymbol{v}}_0 \in \mathcal{D}(V)$ with $\tilde{\boldsymbol{v}}_0(\boldsymbol{x}) = \tilde{\boldsymbol{v}}_0(r)$ such that $\mathcal{H}(\tilde{\boldsymbol{v}}_0) \leq \mathcal{H}(\tilde{\boldsymbol{v}})$.

$$\begin{aligned}
\mathcal{H}(\tilde{\boldsymbol{v}}) &= \left[\frac{2-a}{2Re}\|\boldsymbol{\nabla}\tilde{\boldsymbol{v}}\|_2^2 + \int_V \tilde{\boldsymbol{v}}\cdot\boldsymbol{\nabla}\boldsymbol{U}\cdot\tilde{\boldsymbol{v}}\; d\boldsymbol{x}\right] \\
&= \left[\int_{z=0}^{L}\int_{\theta=0}^{2\pi}\left(\int_{r=r_i}^{r_o}\frac{2-a}{2Re}|\boldsymbol{\nabla}\tilde{\boldsymbol{v}}|^2 + \tilde{\boldsymbol{v}}\cdot\boldsymbol{\nabla}\boldsymbol{U}\cdot\tilde{\boldsymbol{v}}\;\; r dr\right)\;\; d\theta dz\right] \\
&\geq \left[\int_{z=0}^{L}\int_{\theta=0}^{2\pi}\inf_{\substack{0\leq\theta\leq 2\pi\\ 0\leq z\leq L}}\left(\int_{r=r_i}^{r_o}\frac{2-a}{2Re}|\boldsymbol{\nabla}\tilde{\boldsymbol{v}}|^2 + \tilde{\boldsymbol{v}}\cdot\boldsymbol{\nabla}\boldsymbol{U}\cdot\tilde{\boldsymbol{v}}\;\; r dr\right)\;\; d\theta dz\right] \\
&= \mathcal{H}(\tilde{\boldsymbol{v}}_0),
\end{aligned} \tag{5.110}$$

where $\tilde{\boldsymbol{v}}_0(\boldsymbol{x}) = \tilde{\boldsymbol{v}}(r,\theta_0,z_0)$ and θ_0, z_0 corresponds to the values for which the infimum in third line is achieved.

In the second part, for every perturbation $\tilde{\boldsymbol{v}} = (\tilde{v}_r, \tilde{v}_\theta)$, we define a modified perturbation

$$\hat{\boldsymbol{v}} = \left(\frac{\sqrt{\tilde{v}_r^2 + \tilde{v}_\theta^2}}{\sqrt{2}}, \frac{\sqrt{\tilde{v}_r^2 + \tilde{v}_\theta^2}}{\sqrt{2}}\right). \tag{5.111}$$

So, if the initial perturbations $\tilde{\boldsymbol{v}}$ are weakly differentiable in space then so is the modified perturbation $\hat{\boldsymbol{v}}$. Therefore, all the operations below apply. For this modified perturbation, we have

$$\begin{aligned}\|\boldsymbol{\nabla}\hat{\boldsymbol{v}}\|_2^2 &= \frac{\tilde{v}_r^2}{\tilde{v}_r^2+\tilde{v}_\theta^2}\left(\frac{\partial\tilde{v}_r}{\partial r}\right)^2 + \frac{\tilde{v}_\theta^2}{\tilde{v}_r^2+\tilde{v}_\theta^2}\left(\frac{\partial\tilde{v}_\theta}{\partial r}\right)^2 + \frac{\tilde{v}_r\tilde{v}_\theta}{\tilde{v}_r^2+\tilde{v}_\theta^2}\frac{\partial\tilde{v}_r}{\partial r}\frac{\partial\tilde{v}_\theta}{\partial r} + \frac{\tilde{v}_r^2+\tilde{v}_\theta^2}{r} \\ &\leq \left(\frac{\partial\tilde{v}_r}{\partial r}\right)^2 + \left(\frac{\partial\tilde{v}_\theta}{\partial r}\right)^2 + \frac{\tilde{v}_r^2+\tilde{v}_\theta^2}{r} = \|\boldsymbol{\nabla}\tilde{\boldsymbol{v}}\|_2^2, \end{aligned} \tag{5.112}$$

where we used Young's inequality on the third term on the right-hand side in the first line to obtain the second line. Now the assumption on U_θ implies

$$\frac{\tilde{v}_r^2+\tilde{v}_\theta^2}{2}\left(\frac{dU_\theta}{dr}-\frac{U_\theta}{r}\right) \leq \tilde{v}_r\tilde{v}_\theta\left(\frac{dU_\theta}{dr}-\frac{U_\theta}{r}\right), \tag{5.113}$$

again through the use of Young's inequality. Combining (5.112) and (5.113) with the definition of $\mathcal{H}(\boldsymbol{v})$, leads to

$$\mathcal{H}(\hat{\boldsymbol{v}}) \leq \mathcal{H}(\tilde{\boldsymbol{v}}). \tag{5.114}$$

Finally, noting that $\hat{v}_r = \hat{v}_\theta$ proves the lemma. □

Appendix 5.C Analytical solution of the Euler–Lagrange equations in case 1 at high Reynolds number

Before writing the Euler–Lagrange equations, we recall the simplifications pertaining to case 1. From lemma 5.B.1, we note that the optimal perturbations depends only on the radial direction and that $\tilde{v}_r = \tilde{v}_\theta$. Finally, noting that the Lagrangian $\mathcal{L}$ in case 1 does not involve the pressure term, as we do not impose the incompressibility condition, therefore the simplified Euler–Lagrange equations (5.109a-d) in case 1 are given by

$$\frac{(2-a)}{Re}\left(\frac{d^2\tilde{v}_r}{dr^2} + \frac{1}{r}\frac{d\tilde{v}_r}{dr} - \frac{\tilde{v}_r}{r^2}\right) - \tilde{v}_r\left(\frac{dU_\theta}{dr} - \frac{U_\theta}{r}\right) = 0, \tag{5.115a}$$

$$-\frac{1}{(2-a)Re}\left(r\frac{d^2U_\theta}{dr^2} + \frac{dU_\theta}{dr} - \frac{U_\theta}{r}\right) + \frac{1}{r}\frac{d(r^2\tilde{v}_r^2)}{dr} = 0, \tag{5.115b}$$

$$\frac{(a-1)}{(2-a)^2Re}\left(\|\boldsymbol{\nabla U}\|_2^2 - \|\boldsymbol{\nabla u}_{lam}\|_2^2\right) + \frac{1}{Re}\|\boldsymbol{\nabla}\tilde{\boldsymbol{v}}\|_2^2 + \int_V \tilde{\boldsymbol{v}}\cdot\boldsymbol{\nabla U}\cdot\tilde{\boldsymbol{v}}\; d\boldsymbol{x} = 0. \tag{5.115c}$$

These equations need to be solved with boundary conditions

$$U_\theta = 1, \quad \tilde{v}_r = 0 \qquad \text{at} \quad r = r_i, \tag{5.116a}$$

$$U_\theta = 0, \quad \tilde{v}_r = 0 \qquad \text{at} \quad r = r_o. \tag{5.116b}$$

As $\tilde{v}_z$ does not enter into the computations, it can be taken to be zero; as such $\tilde{\boldsymbol{v}}$ here should be understood as $(\tilde{v}_r, \tilde{v}_r, 0)$.

These equations can be solved using the method of matched asymptotics as described below. We consider three different regions: the inner boundary layer, the bulk and the outer boundary layer. We use the following scaled coordinates

for the inner and outer boundary layer, respectively:

$$s_i = \frac{r - r_i}{\delta}, \qquad s_o = \frac{r_o - r}{\delta}, \tag{5.117}$$

where

$$\delta = \frac{1}{Re}. \tag{5.118}$$

We will use *in*, *bulk* and *out* in the superscript of the variables to indicate in which region the variable is being considered. Before proceeding further, we make the following change of variables

$$U = \frac{U_\theta}{r}, \quad \tilde{v} = r\tilde{v}_r. \tag{5.119}$$

Next, we write separate expansions for the variables in each of the three different regions as

$$\tilde{v}^{in}(s_i) = \tilde{v}_0^{in}(s_i) + \delta\ \tilde{v}_1^{in}(s_i) + \delta^2\ \tilde{v}_2^{in}(s_i) + \ldots, \tag{5.120a}$$

$$\tilde{v}^{bulk}(r) = \tilde{v}_0^{bulk}(r) + \delta\ \tilde{v}_1^{bulk}(r) + \delta^2\ \tilde{v}_2^{bulk}(r) + \ldots, \tag{5.120b}$$

$$\tilde{v}^{in}(s_o) = \tilde{v}_0^{out}(s_o) + \delta\ \tilde{v}_1^{out}(s_o) + \delta^2\ \tilde{v}_2^{out}(s_o) + \ldots. \tag{5.120c}$$

A similar expansion can be written for U. Finally, we also use a simple expansion for the balance parameter

$$a = a_0 + \delta a_1 + \delta^2 a_2 + \ldots. \tag{5.121}$$

Substituting the change of variables (5.119) and the series expansions of these new

variables in (5.115a-c), one can find out the leading order equations in different regions which then need to be solved with the boundary conditions (5.116a-b) and the following matching conditions

$$U_0^{in}(s_i \to \infty) = U_0^{bulk}(r = r_i), \quad U_0^{bulk}(r = r_o) = U_0^{out}(s_o \to \infty), \tag{5.122a}$$

$$\tilde{v}_0^{in}(s_i \to \infty) = \tilde{v}_0^{bulk}(r = r_i), \quad \tilde{v}_0^{bulk}(r = r_o) = \tilde{v}_0^{out}(s_o \to \infty). \tag{5.122b}$$

Upon solving the resultant set of equations, we find that the leading order term in the background flow in the three different regions is given by

$$U_\theta^{in} = \frac{r}{r_i}\left(1 - \frac{4\sqrt{2}}{3}\alpha \tanh\left(\frac{\alpha s_i}{\sqrt{2}}\right)\right) + O(\delta), \tag{5.123a}$$

$$U_\theta^{bulk} = \frac{r_i r}{r_i^2 + r_o^2} + O(\delta), \tag{5.123b}$$

$$U_\theta^{out} = \frac{r}{r_o}\left(\frac{4\sqrt{2}}{3}\beta \tanh\left(\frac{\beta s_o}{\sqrt{2}}\right)\right) + O(\delta), \tag{5.123c}$$

whereas the perturbed flow field is given by

$$\tilde{v}_r^{in} = \tilde{v}_\theta^{in} = \frac{\alpha r_i}{r} \tanh\left(\frac{\alpha s_i}{\sqrt{2}}\right) + O(\delta), \tag{5.124a}$$

$$\tilde{v}_r^{out} = \tilde{v}_\theta^{out} = \frac{\beta r_o}{r} \tanh\left(\frac{\beta s_o}{\sqrt{2}}\right) + O(\delta), \tag{5.124b}$$

$$\tilde{v}_r^{bulk} = \tilde{v}_\theta^{bulk} = \left(\frac{3 r_i r_o^2}{4\sqrt{2}(r_i^2 + r_o^2)}\right)\frac{1}{r} + O(\delta), \tag{5.124c}$$

where α and β depend on η and are given by

$$\alpha = \frac{3}{4\sqrt{2}}\frac{1}{1+\eta^2}, \quad \beta = \frac{3}{4\sqrt{2}}\frac{\eta}{1+\eta^2}. \tag{5.125}$$

The balance parameter takes the value $a = 2/3 + O(\delta)$. This optimal value $a = 2/3$

of the balance parameter, in the limit of large Re, is also observed numerically by Ding and Marensi (2019) (and corresponds to 3/2 in their nondimensionalization) as well as in case 2 and case 3 in our study. Using the expression of the background flow (5.123a-c) in (5.105) and the relationships between different mean quantities (5.19) and (5.24), the leading order term in the bound on the Nusselt number in the limit of high Reynolds number (or equivalently high Taylor number), is given by

$$Nu_b^{nc} = \frac{9}{8}\frac{\eta^3}{(1+\eta)^2(1+\eta^2)^2}Ta^{1/2}. \tag{5.126}$$

This bound is 2/3 of the bound (5.46) obtained using standard inequalities. This improvement has also been confirmed from the numerical results.

Chapter 6

Analytical bounds on the heat transport in internally heated convection

This chapter is based on the paper Kumar, Arslan, Fantuzzi, Craske and Wynn(2022) published in the Journal of Fluid Mechanics, Volume 938, 10 May 2022, A26.

6.1 Introduction

Convection driven by buoyancy is abundant in geophysical and astrophysical flows, from atmospheric convection driving ocean currents to solar convection transporting heat in stars. The prototypical setup for studying these flows is that of Rayleigh–Bénard convection, where flow in a layer of fluid is driven by the temperature differential across the boundaries. In reality, convection in many natural or engineering situations is at least partially driven by an internal heating

source. Examples include convection in the Earth's mantle due to radiogenic heat (Davies and Richards, 1992; Schubert et al., 2001; Mulyukova and Bercovici, 2020), convection in radiative planet atmospheres (Seager, 2010; Pierrehumbert, 2010; Guervilly et al., 2019), and engineering flows where exothermic chemical or nuclear reactions drive the convection (Tran and Dinh, 2009). Gaining insights into these physical and practical scenarios requires a thorough understanding of internally heated (IH) convection, and yet studies in this direction are relatively few.

Following the early investigations by Roberts (1967) and Tritton (1975), research into IH convection has recently gained renewed momentum through computational analysis (Goluskin and Spiegel, 2012; Goluskin, 2015; Goluskin and van der Poel, 2016) and experiments (Lepot et al., 2018; Bouillaut et al., 2019; Limare et al., 2019, 2021). However, a comprehensive understanding of flows driven by internal heating is far from complete and the behaviour of such flows in the limiting regime of extreme heating remains unknown.

Here, we probe this regime using rigorous upper bounding theory. Specifically, we bound the mean vertical convective heat flux in two configurations of IH convection, one where the fluid is bounded between horizontal plates held at the same temperature and one where the bottom plate is replaced by a perfect insulator. These two configurations, which we refer to as IH1 and IH3 following the terminology introduced by Goluskin (2016), are illustrated schematically in panels (a) and (b) of figure 6.1.

The mean vertical convective heat flux $\langle wT \rangle$, where w and T are the nondimensional vertical velocity and temperature and angled brackets denote space-time averages, has a slightly different physical interpretation in the two configurations. For the IH1 case, $\langle wT \rangle$ is related to the asymmetry in the heat fluxes $\mathcal{F}_T$ and $\mathcal{F}_B$

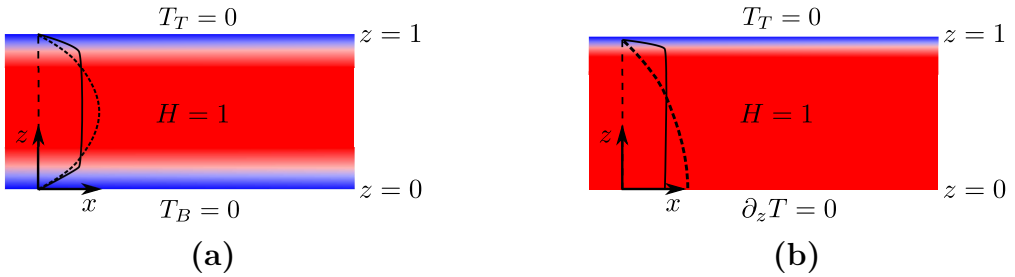

Figure 6.1: The two configurations considered in this paper. (a) IH1: Isothermal boundaries, (b) IH3: Isothermal top boundary and insulating bottom boundary. In both configurations the heating is uniform, so the non-dimensional thermal source term is $H = 1$. Dashed lines show the temperature profiles in the pure conduction state, while solid lines sketch the temporally- and horizontally-averaged temperature profiles in a typical turbulent state (also shown using the color plot).

through the top and the bottom boundaries. Specifically, space-time averaging the dimensionless transport equation for temperature (see (6.6c) in §6.2) multiplied by the wall-normal coordinate z yields

$$\mathcal{F}_T = \frac{1}{2} + \langle wT \rangle, \qquad \mathcal{F}_B = \frac{1}{2} - \langle wT \rangle. \tag{6.1}$$

In the purely conductive state, the heat generated inside the domain leaves equally between the two boundaries, hence $\mathcal{F}_T = \mathcal{F}_B = 1/2$. In the convective state, instead, the asymmetry of buoyancy combines with the uniform heat source to create boundary layers with different characteristics near the top and bottom boundaries, as illustrated in figure 6.1(a). The bottom boundary layer is stably stratified, whereas the top boundary layer is unstably stratified. Convective heat transport ($\langle wT \rangle > 0$) makes the top boundary layer thinner than the bottom one, so in any convective state one has $\mathcal{F}_T > \mathcal{F}_B$. Since the boundary temperature is fixed and the fluid is internally heated, one also expects the boundary flux $\mathcal{F}_B$ to remain non-negative, meaning that heat can escape from the bottom boundary but not enter through it. This fact can be proved rigorously (Goluskin and Spiegel,

2012, Appendix A.1; Arslan et al., 2021b, Appendix A) and translates into the following upper bounds on the vertical heat transport (Goluskin and Spiegel, 2012):

$$\langle wT \rangle \leq \frac{1}{2} \quad \text{in IH1.} \tag{6.2}$$

For the IH3 configuration, instead, the mean vertical flux $\langle wT \rangle$ is related to the difference of the horizontally-averaged temperature between the top $\overline{T}_T$ and the bottom wall $\overline{T}_B$. Indeed, upon multiplying the dimensionless evolution equation for the temperature (see (6.6c) in §6.2) with the wall-normal coordinate z and space-time averaging one obtains

$$\langle wT \rangle = \overline{T}_T - \overline{T}_B + \frac{1}{2}. \tag{6.3}$$

The isothermal boundary condition implies that the temperature T_T at the top boundary is in fact constant, so $\overline{T}_T = T_T$, and we take it be zero without loss of generality in our nondimensionalization. Since the nondimensional internal heating rate is positive, one expects the mean bottom temperature $\overline{T}_B$ to be non-negative. As before, this fact can be proved rigorously and results in the upper bound (Goluskin, 2016, Chapter 1)

$$\langle wT \rangle \leq \frac{1}{2} \quad \text{in IH3.} \tag{6.4}$$

For the IH1 configuration, Arslan et al. (2021b) recently proved that $\langle wT \rangle \leq 2^{-21/5} R^{1/5}$, where R is a nondimensional parameter that measures the strength of the internal heating and may be interpreted as a Rayleigh number. This result, which is independent of the Prandtl number Pr, fails to improve the uniform bound in (6.2) for $R > 2^{16} = 65536$. However, numerical evidence by the

same authors suggests that an upper bound on $\langle wT \rangle$ approaching $1/2$ from below monotonically as R is increased may be provable when the background method by Doering & Constantin (Doering and Constantin, 1992, 1994, 1996; Constantin and Doering, 1995) is augmented with a minimum principle stating that the fluid's temperature cannot be smaller than that the top boundary. Unfortunately, they also provided a rather tantalizing proof that such a bound cannot be obtained using typical analytical constructions.

In this paper we overcome this barrier and show that R-dependent bounds on $\langle wT \rangle$ strictly smaller than $1/2$ can be obtained analytically not only in the IH1 case, but also for the IH3 configuration. Precisely, we prove that

$$\langle wT \rangle \leq \frac{1}{2} - c_1 R^{\frac{1}{5}} \exp\left(-c_2 R^{\frac{3}{5}}\right) \qquad \text{in IH1,} \tag{6.5a}$$

$$\langle wT \rangle \leq \frac{1}{2} - \frac{c_3}{R^{\frac{1}{5}}} \exp\left(-c_4 R^{\frac{3}{5}}\right) \qquad \text{in IH3,} \tag{6.5b}$$

where c_1, c_2, c_3 and c_4 are constants (independent of both R and Pr). To establish these results, we formulate a bounding principle for $\langle wT \rangle$ using the auxiliary functional method (Chernyshenko et al., 2014; Fantuzzi et al., 2016; Tobasco et al., 2018; Chernyshenko, 2022). This method is a generalization of the background method of Doering and Constantin, which has successfully been applied to several fluid dynamical problems (Doering and Constantin, 1992; Constantin and Doering, 1995; Doering and Constantin, 1996; Caulfield and Kerswell, 2001; Tang et al., 2004; Whitehead and Doering, 2011b; Goluskin and Doering, 2016; Fantuzzi et al., 2018; Fantuzzi, 2018; Kumar and Garaud, 2020; Kumar, 2020; Fan et al., 2021; Arslan et al., 2021a,b; Kumar, 2022a). The auxiliary functional method, as implemented in this paper, also has an equivalent formulation using the background method.

The novelty aspects in our arguments are the use of a background temperature field with a lower boundary layer growing as z^{-1}, motivated by the numerical results by Arslan et al. (2021b), and the application of Hardy inequalities (IH1) and Rellich inequalities (IH3). Such inequalities have already been employed to prove bounds on convective flows at infinite Prandtl number (Doering et al., 2006; Whitehead and Doering, 2011a) but, to the best of our knowledge, their use at finite Prandtl number is new.

The rest of this work is organized as follows. We start by describing the problem setup in §2. In §3, we apply the auxiliary function method formulate upper bounding principles for $\langle wT \rangle$ in both IH1 and IH3 configurations. We then prove the upper bound (6.5a) in §4 and the upper bound (6.5b) in §5. Finally, §6, discusses our method of proof, compares our results with available phenomenological theories, and offers concluding remarks.

6.2 Problem setup

We consider the flow of a Newtonian fluid of density ρ, viscosity ν, thermal diffusivity κ and specific heat capacity c_p driven by buoyancy forces resulting from internal heating. The fluid is confined between two horizontal no-slip plates with a gap of width d and the heat is produced at a constant volumetric rate of H^* (with units $\mathrm{W/m^3} = \mathrm{kg/ms^3}$). We consider the two configurations sketched in figure 6.1, one where both plates are kept at constant temperature T_0^* (IH1) and one where the top plate is kept at a constant temperature T_0^* while the bottom plate is insulating (IH3). We assume that the fluid properties are a weak function of the temperature and use the Naiver–Stokes equations under the Boussinesq approximation to model the problem. Various justifications have been put forward for

the Boussinesq approximation; see, for example, Spiegel and Veronis (1960) and Rajagopal et al. (1996). In their non-dimensional form, the governing equations are

$$\boldsymbol{\nabla} \cdot \boldsymbol{u} = 0, \tag{6.6a}$$

$$\partial_t \boldsymbol{u} + \boldsymbol{u} \cdot \boldsymbol{\nabla} \boldsymbol{u} + \boldsymbol{\nabla} p = Pr \nabla^2 \boldsymbol{u} + PrRT \boldsymbol{e}_z, \tag{6.6b}$$

$$\partial_t T + \boldsymbol{u} \cdot \boldsymbol{\nabla} T = \boldsymbol{\nabla}^2 T + 1, \tag{6.6c}$$

where we have used the following non-dimensionalization for the variables:

$$\boldsymbol{x} = \frac{\boldsymbol{x}^*}{d}, \quad t = \frac{t^*}{d^2/\kappa}, \quad \boldsymbol{u} = \frac{\boldsymbol{u}^*}{\kappa/d}, \quad p = \frac{p^* - p_0}{\rho\kappa^2/d^2}, \quad T = \frac{T^* - T_0^*}{d^2 H^*/(\kappa \rho c_p)}. \tag{6.7}$$

Here, $\boldsymbol{x}$, t, $\boldsymbol{u}$, p and T denote the non-dimensional position, time, velocity, pressure and temperature, respectively, whereas p_0 is the dimensional hydrostatic ambient pressure. The quantities with a star in superscript are dimensional. The non-dimensional governing parameters of the flow are the Prandtl number and the Rayleigh number, given by

$$Pr = \frac{\nu}{\kappa} \qquad \text{and} \qquad R = \frac{g\alpha d^5 H^*}{\rho c_p \nu \kappa^2}, \tag{6.8}$$

where α is the coefficient of thermal expansion. Our choice of nondimensionalization implies that the heating source appears as a unit force in (6.6c).

We use the Cartesian coordinates $\boldsymbol{x} = (x, y, z)$ and place the origin of the coordinate system at the bottom plate. The z-direction points vertically upward and the x and y directions are horizontal. In this coordinate system, we write the velocity vector as $\boldsymbol{u} = (u, v, w)$ where u, v and w are the velocity components in

the x, y and z directions respectively. In this coordinate system, the boundary conditions at the top and bottom plates for velocity and temperature can be written as

$$\boldsymbol{u}(x,y,0,t) = \boldsymbol{u}(x,y,1,t) = \boldsymbol{0}, \tag{6.9a}$$

$$T(x,y,0,t) = T(x,y,1,t) = 0 \qquad \text{for IH1}, \tag{6.9b}$$

$$\partial_z T(x,y,0,t) = T(x,y,1,t) = 0 \qquad \text{for IH3}. \tag{6.9c}$$

We further assume that the fluid layer is periodic in the horizontal directions x and y with length L_x and L_y, meaning that the domain of interest is $\Omega = \mathbb{T}_{[0,L_x]} \times \mathbb{T}_{[0,L_y]} \times [0,1]$.

Throughout the paper, spatial averages, long-time horizontal averages and long-time volume averages will be denoted, respectively, by

$$\fint_\Omega [\,\cdot\,]\,\mathrm{d}\boldsymbol{x} = \frac{1}{L_x L_y}\int_0^1\int_0^{L_y}\int_0^{L_x} [\,\cdot\,]\,\mathrm{d}x\mathrm{d}y\mathrm{d}z, \tag{6.10a}$$

$$\overline{[\,\cdot\,]} = \lim_{\tau\to\infty}\frac{1}{\tau L_x L_y}\int_0^\tau\int_0^{L_y}\int_0^{L_x} [\,\cdot\,]\,\mathrm{d}x\mathrm{d}y\mathrm{d}t, \tag{6.10b}$$

$$\langle [\,\cdot\,] \rangle = \lim_{\tau\to\infty}\frac{1}{\tau}\int_0^\tau \fint_\Omega [\,\cdot\,]\,\mathrm{d}\boldsymbol{x}\mathrm{d}t. \tag{6.10c}$$

6.3 The auxiliary functional method

A bound on the mean vertical heat flux can be derived using the auxiliary function method. The formulation of the method given here is very similar to the one given by Arslan et al. (2021b) for isothermal boundaries, but we repeat it to make the paper self-contained and highlight the changes required when the lower

boundary is insulating.

Let $\mathcal{V}\{\boldsymbol{u}, T\}$ be a functional that is uniformly bounded in time along solutions $\boldsymbol{u}(t)$ and $T(t)$ of the governing equations (6.6a-c). Further, let $\mathcal{L}\{\boldsymbol{u}, T\}$ be the Lie derivative of $\mathcal{V}\{\boldsymbol{u}, T\}$, meaning a functional such that

$$\mathcal{L}\{\boldsymbol{u}(t), T(t)\} = \frac{\mathrm{d}}{\mathrm{d}t}\mathcal{V}\{\boldsymbol{u}(t), T(t)\} \tag{6.11}$$

when $\boldsymbol{u}(t)$ and $T(t)$ solve the governing equations. Then, a simple calculation shows that the long-time average of $\mathcal{L}\{\boldsymbol{u}(t), T(t)\}$ vanishes and, given any constant B, we can rewrite the mean vertical heat flux as

$$\begin{aligned} \langle wT \rangle \quad &= \lim_{\tau\to\infty} \frac{1}{\tau}\int_0^\tau \left[\fint_\Omega wT \,\mathrm{d}\boldsymbol{x} + \mathcal{L}\{\boldsymbol{u}(t), T(t)\}\right] \,\mathrm{d}t, \\ &= B + \lim_{\tau\to\infty} \frac{1}{\tau}\int_0^\tau \left[\fint_\Omega wT \,\mathrm{d}\boldsymbol{x} + \mathcal{L}\{\boldsymbol{u}(t), T(t)\} - B\right] \,\mathrm{d}t. \end{aligned} \tag{6.12}$$

If the functional $\mathcal{V}$ can be chosen such that

$$\mathcal{S}^*\{\boldsymbol{u}, T\} \coloneqq \fint_\Omega wT \,\mathrm{d}\boldsymbol{x} + \mathcal{L}\{\boldsymbol{u}, T\} - B \leq 0 \tag{6.13}$$

for any solution of the governing equations, then it follows that $\langle wT \rangle \leq B$. Of course, it is intractable to impose (6.13) only over the set of solutions of the governing equation, because they are not known explicitly. However, to obtain a (possibly conservative) bound it suffices to enforce the stronger condition that (6.13) holds for all pairs of divergence-free velocity fields $\boldsymbol{u}$ and temperature fields T that satisfy the boundary conditions (6.9a-c).

Following Arslan et al. (2021b), we choose the functional $\mathcal{V}$ to be

$$\mathcal{V}\{\boldsymbol{u}, T\} = \fint_\Omega \left[\frac{a}{2PrR}|\boldsymbol{u}|^2 + \frac{b}{2}|T|^2 - (\psi(z) + z - 1)T\right] \mathrm{d}\boldsymbol{x}, \tag{6.14}$$

where the function $\psi(z)$ and the nonnegative scalars a and b are to be optimised to obtain the best possible bound. The profile $[\psi(z) + z - 1]/b$ corresponds exactly to the background temperature field. Differentiating this functional in time along solutions of the governing equations, followed by standard integrations by parts using the divergence-free and boundary conditions, yields an expression for $\mathcal{L}\{\boldsymbol{u}, T\}$ that can be substituted into (6.13) to obtain

$$\begin{aligned}\mathcal{S}^*\{\boldsymbol{u}, T\} = \fint_\Omega \left[\frac{a}{R}|\boldsymbol{\nabla u}|^2 + b|\boldsymbol{\nabla} T|^2 - (a - \psi')wT + (bz - \psi')\frac{\partial T}{\partial z} + \psi\right] \mathrm{d}\boldsymbol{x} \\ + T(0) - T(1) + \psi(1)\left.\overline{\frac{\partial T}{\partial z}}\right|_{z=1} - (\psi(0) - 1)\left.\overline{\frac{\partial T}{\partial z}}\right|_{z=0} + B - \frac{1}{2} \geq 0.\end{aligned} \tag{6.15}$$

This inequality needs to be satisfied for all $\boldsymbol{u}$ and T satisfying (6.6a), (6.9a) and either (6.9b) for IH1 or (6.9c) for IH3.

A crucial improvement to the best upper bound B implied by (6.15) can be achieved by imposing the minimum principle, which says that $T \geq 0$ at all times if it is so initially, and that any negative component decays exponentially quickly (Arslan et al., 2021b). We may therefore restrict the attention to nonnegative temperature fields, thereby relaxing inequality (6.15). As explained by Arslan et al. (2021b), the constraint can be enforced with the help of a nondecreasing Lagrange multiplier function $q(z)$ by adding the term

$$\fint_\Omega q'(z)T \mathrm{d}\boldsymbol{x} \tag{6.16}$$

to the right-hand side of (6.15). Integrating by parts and rearranging leads to the weaker constraint

$$\mathcal{S}\{\boldsymbol{u}, T\} \coloneqq \mathcal{S}^*\{\boldsymbol{u}, T\} + \fint_\Omega q(z)\frac{\partial T}{\partial z}\mathrm{d}\boldsymbol{x} + q(0)T(0) - q(1)T(1) \geq 0, \tag{6.17}$$

and the best upper bound on $\langle wT \rangle$ implied by this inequality is

$$\langle wT \rangle \leq \inf_{B,\psi(z),q(z),a,b} \Bigg\{ B : \quad q(z) \text{ non-decreasing}, \\ \mathcal{S}\{\boldsymbol{u}, T\} \geq 0 \quad \forall (\boldsymbol{u}, T) \text{ satisfying (6.6a) and (6.9)} \Bigg\}. \tag{6.18}$$

Moreover, since no derivatives of the Lagrange multiplier $q(z)$ appear in inequality (6.17), one can perform the optimization over nondecreasing Lagrange multipliers that are not necessarily differentiable everywhere and may even be discontinuous. A rigorous justification of this statement is given by Arslan et al. (2021b).

To prove an explicit rigorous bound on $\langle wT \rangle$, it is convenient to replace inequality (6.17) with a stronger condition that is more amenable to analytical treatment. To achieve this, we introduce the following Fourier series decomposition of the variables in the x and y directions:

$$\begin{bmatrix} \boldsymbol{u}(\boldsymbol{x}) \\ T(\boldsymbol{x}) \end{bmatrix} = \sum_{\boldsymbol{k} \in K} \begin{bmatrix} \hat{\boldsymbol{u}}_{\boldsymbol{k}}(z) \\ \hat{T}_{\boldsymbol{k}}(z) \end{bmatrix} e^{ik_x x + ik_y y}, \tag{6.19}$$

where

$$K \equiv \left\{ (k_x, k_y) = \left(\frac{2m\pi}{L_x}, \frac{2n\pi}{L_y} \right) \middle| \, (m, n) \in \mathbb{Z}^2 \right\}. \tag{6.20}$$

Since $\boldsymbol{u}$ and T in (6.19) are real-valued, the Fourier expansion coefficients satisfy $\hat{w}_{\boldsymbol{k}}^* = \hat{w}_{-\boldsymbol{k}}$ and $\hat{T}_{\boldsymbol{k}}^* = \hat{T}_{-\boldsymbol{k}}$ for all $\boldsymbol{k} \in K$, subject to the boundary conditions

$$\hat{w}_{\boldsymbol{k}}(0) = \hat{w}'_{\boldsymbol{k}}(0) = \hat{w}_{\boldsymbol{k}}(1) = \hat{w}'_{\boldsymbol{k}}(1) = 0, \tag{6.21a}$$

$$\hat{T}_{\boldsymbol{k}}(0) = \hat{T}_{\boldsymbol{k}}(1) = 0, \qquad \text{IH1}, \tag{6.21b}$$

$$\hat{T}'_{\boldsymbol{k}}(0) = \hat{T}_{\boldsymbol{k}}(1) = 0, \qquad \text{IH3}. \tag{6.21c}$$

Substituting (6.19) in (6.17), using the incompressiblity condition on $\boldsymbol{u}$, applying the inequality of arithmetic and geometric means (AM–GM inequality), and dropping positive terms in $\hat{u}_{\boldsymbol{k}}$ and $\hat{v}_{\boldsymbol{k}}$, we can estimate

$$\mathcal{S}\{\boldsymbol{u}, T\} \geq \mathcal{S}_{\boldsymbol{0}}\{\hat{T}_{\boldsymbol{0}}\} + \sum_{\boldsymbol{k} \neq \boldsymbol{0}} \mathcal{S}_{\boldsymbol{k}}\{\hat{w}_{\boldsymbol{k}}, \hat{T}_{\boldsymbol{k}}\}, \tag{6.22}$$

where

$$\begin{aligned}\mathcal{S}_{\boldsymbol{0}}\{\hat{T}_{\boldsymbol{0}}\} \coloneqq \int_0^1 \left[b|\hat{T}'_{\boldsymbol{0}}|^2 + (bz - \psi' + q)\hat{T}'_{\boldsymbol{0}} + \psi\right] \mathrm{d}z + (q(0)+1)\hat{T}_{\boldsymbol{0}}(0) \\ - (q(1)+1)\hat{T}_{\boldsymbol{0}}(1) + \psi(1)\hat{T}'_{\boldsymbol{0}}(1) - (\psi(0)-1)\hat{T}'_{\boldsymbol{0}}(0) + B - \frac{1}{2},\end{aligned} \tag{6.23}$$

and

$$\begin{aligned}\mathcal{S}_{\boldsymbol{k}}\{\hat{w}_{\boldsymbol{k}}, \hat{T}_{\boldsymbol{k}}\} \coloneqq \int_0^1 \left[\frac{a}{R}\left(\frac{1}{k^2}|\hat{w}''_{\boldsymbol{k}}|^2 + 2|\hat{w}'_{\boldsymbol{k}}|^2 + k^2|\hat{w}_{\boldsymbol{k}}|^2\right)\right. \\ \left. + b|\hat{T}'_{\boldsymbol{k}}|^2 + bk^2|\hat{T}_{\boldsymbol{k}}|^2 - (a - \psi')\hat{w}_{\boldsymbol{k}}\hat{T}^*_{\boldsymbol{k}}\right] \mathrm{d}z.\end{aligned} \tag{6.24}$$

In the last expression, $k = \sqrt{k_x^2 + k_y^2}$.

To establish inequality (6.17), therefore, it suffices to check the nonnegativity of the right-hand side of (6.22). As all the different Fourier modes $\hat{w}_{\boldsymbol{k}}$ and $\hat{T}_{\boldsymbol{k}}$ can

be chosen independently, this requires $\mathcal{S}_{\boldsymbol{k}}\{\hat{w}_{\boldsymbol{k}}, \hat{T}_{\boldsymbol{k}}\} + \mathcal{S}_{-\boldsymbol{k}}\{\hat{w}_{-\boldsymbol{k}}, \hat{T}_{-\boldsymbol{k}}\} \geq 0$ for all wavevectors $\boldsymbol{k} \in K$, which in turn holds true if and only if $\mathcal{S}_{\boldsymbol{k}}\{\mathrm{Re}\{\hat{w}_{\boldsymbol{k}}\}, \mathrm{Re}\{\hat{T}_{\boldsymbol{k}}\}\} \geq 0$ and $\mathcal{S}_{\boldsymbol{k}}\{\mathrm{Im}\{\hat{w}_{\boldsymbol{k}}\}, \mathrm{Im}\{\hat{T}_{\boldsymbol{k}}\}\} \geq 0$ for all wavevectors $\boldsymbol{k} \in K$. This, combined with the fact that the real and imaginary parts of $\hat{w}_{\boldsymbol{k}}$ and $\hat{T}_{\boldsymbol{k}}$ can be chosen independently, implies that we may take $\hat{w}_{\boldsymbol{k}}$ and $\hat{T}_{\boldsymbol{k}}$ to be real-valued without loss of generality and impose

$$\mathcal{S}_{\boldsymbol{0}}\{\hat{T}_{\boldsymbol{0}}\} \geq 0, \tag{6.25a}$$

$$\mathcal{S}_{\boldsymbol{k}}\{\hat{w}_{\boldsymbol{k}}, \hat{T}_{\boldsymbol{k}}\} \geq 0 \quad \forall \boldsymbol{k} \in K,\, \boldsymbol{k} \neq \boldsymbol{0}. \tag{6.25b}$$

From the nonnegativity condition on $\mathcal{S}_{\boldsymbol{0}}\{\hat{T}_{\boldsymbol{0}}\}$, it is possible to extract the bound B explicitly. First of all, the nonnegativity of $\mathcal{S}_{\boldsymbol{0}}\{\hat{T}_{\boldsymbol{0}}\}$ requires

$$\psi(0) = 1, \qquad \psi(1) = 0 \qquad \text{for IH1}, \tag{6.26a}$$

$$q(0) = -1, \qquad \psi(1) = 0 \qquad \text{for IH3}, \tag{6.26b}$$

otherwise it is possible to choose a profile $\hat{T}_{\boldsymbol{0}}(z)$ that is non-zero only near the boundaries and for which $\mathcal{S}_{\boldsymbol{0}}\{\hat{T}_{\boldsymbol{0}}\} \leq 0$. With these simplifications, one can write

$$\mathcal{S}_{\boldsymbol{0}}\{\hat{T}_{\boldsymbol{0}}\} = \int_0^1 \left[\sqrt{b}\hat{T}_{\boldsymbol{0}}' + \frac{(bz - \psi' + q)}{2\sqrt{b}}\right]^2 \mathrm{d}z + B - \frac{1}{4b}\int_0^1 (bz - \psi' + q)^2 \mathrm{d}z + \int_0^1 \psi(z)\mathrm{d}z - \frac{1}{2}. \tag{6.27}$$

Therefore, $\mathcal{S}_{\boldsymbol{0}}\{\hat{T}_{\boldsymbol{0}}\}$ is nonnegative if we choose B to cancel the negative and sign-indefinite terms. After gathering (6.18), (6.19), (6.21), (6.25b) and (6.26) we

conclude that

$$\langle wT \rangle \leq \inf_{a,b,\psi(z),q(z)} \left\{ \frac{1}{2} + \frac{1}{4b} \int_0^1 (bz - \psi' + q)^2 \mathrm{d}z - \int_0^1 \psi(z) \mathrm{d}z \right\}, \tag{6.28}$$

provided

$$q(z) \text{ is a nondecreasing function,} \tag{6.29a}$$

$$\psi(0) = 1, \quad \psi(1) = 0 \quad \text{for IH1,} \tag{6.29b}$$

$$q(0) = -1, \quad \psi(1) = 0 \quad \text{for IH3,} \tag{6.29c}$$

$$\mathcal{S}_{\boldsymbol{k}}\{\hat{w}_{\boldsymbol{k}}, \hat{T}_{\boldsymbol{k}}\} \geq 0 \quad \forall \hat{w}_{\boldsymbol{k}}, \hat{T}_{\boldsymbol{k}} : (6.21), \ \forall \boldsymbol{k} \neq \boldsymbol{0} \tag{6.29d}$$

Explicit constructions for which the right-hand side of (6.28) is strictly less than 1/2 at all Rayleigh numbers are given in §6.4 and §6.5 for the IH1 and IH3 configurations, respectively. First, however, we summarize our proof strategy to explain the intuition behind our constructions. From (6.28), we see that the competition between the second term (which is always positive) and the third term will decide if $\langle wT \rangle$ can be less than 1/2 as long as we are able to enforce that $\mathcal{S}_{\boldsymbol{k}}\{\hat{w}_{\boldsymbol{k}}, \hat{T}_{\boldsymbol{k}}\} \geq 0$. For previous studies using the background method, the standard approach has been to choose a profile $\psi(z)$ that is linear in boundary layers near the walls, whereas in the bulk region $\psi(z)$ is chosen such that the sign indefinite term in $\mathcal{S}_{\boldsymbol{k}}$ is zero. Unfortunately, in the present case, for a profile of $\psi(z)$ which is linear in the boundary layers, we are unable to show that the magnitude of the second term in (6.28) is smaller than the third term unless we violate the constraint (6.25b). However, if we use a z^{-1} profile in $\psi(z)$ in the outer layer of a two-layer lower boundary layer we gain an extra factor of a logarithm in the

integral of ψ. Such a boundary layer structure, along with the choice $q(z) = \psi'(z)$ in the bottom boundary layer to cancel the otherwise large contribution of this layer to the quadratic term in (6.28), matches the numerically optimal profiles computed by Arslan et al. (2021b, Fig. 7). This makes it possible to show that sum of the last two terms in (6.28) is negative without violating $\mathcal{S}_{\boldsymbol{k}}\{\hat{w}_{\boldsymbol{k}}, \hat{T}_{\boldsymbol{k}}\} \geq 0$. To establish this nontrivial result we rely on the following Hardy and Rellich inequalities, proofs of which are provided for completeness in Appendix 6.A.

Lemma 6.3.1 (Hardy inequality)**.** *Let $f : [0, \infty) \to \mathbb{R}$ be a function such that $f, f' \in L^2(0, \infty)$ and such that $f(0) = 0$. Then, for any $\epsilon > 0$ and any $\alpha \geq 0$,*

$$\int_0^\alpha \frac{|f|^2}{(z+\epsilon)^2} \mathrm{d}z \leq 4 \int_0^\alpha |f'|^2 \mathrm{d}z. \tag{6.30}$$

Lemma 6.3.2 (Rellich inequality)**.** *Let $f : [0, \infty) \to \mathbb{R}$ be function such that $f, f', f'' \in L^2(0, \infty)$ and such that $f(0) = f'(0) = 0$. Then, for any $\epsilon > 0$ and any $\alpha \geq 0$,*

$$\int_0^\alpha \frac{|f|^2}{(z+\epsilon)^4} \mathrm{d}z \leq \frac{16}{9} \int_0^\alpha |f''|^2 \mathrm{d}z. \tag{6.31}$$

We now present detailed proofs of the main results. Our emphasis is on the steps necessary to obtain an R-dependent bound on $\langle wT \rangle$, and we do not attempt to optimize the constants appearing in our estimates.

6.4 Bound on heat flux in IH1 configuration

To prove the bound in (6.5a), we start by setting

$$\psi(z) = \begin{cases} 1 - \frac{z}{4\sigma\delta} & 0 \le z \le 2\sigma\delta, \\ \frac{\sigma\delta}{z} & 2\sigma\delta \le z \le \delta, \\ \sigma + a(z-\delta) & \delta \le z \le 1-\gamma, \\ (1-z)\frac{\sigma + a(1-\gamma-\delta)}{\gamma} & 1-\gamma \le z \le 1, \end{cases} \qquad q(z) = \begin{cases} -\frac{1}{4\sigma\delta} & 0 \le z \le 2\sigma\delta, \\ -\frac{\sigma\delta}{z^2} & 2\sigma\delta \le z \le \delta, \\ 0 & \delta \le z \le 1. \end{cases} \tag{6.32}$$

These functions are sketched in figure 6.2. In the definition of ψ, the parameter δ denotes the thickness of the boundary layer near the bottom plate. The parameter σ is the value of ψ taken at the edge of lower boundary layer ($z = \delta$). The lower boundary layer itself is divided into two parts, an inner sublayer where ψ is linear and an outer sublayer where $\psi \sim z^{-1}$. These sublayers meet at an intermediate point ($z = 2\sigma\delta$) where both the value and slope of ψ are equal. The inverse-z scaling of ψ in the outer part of the lower boundary layer is one of the key ingredients in proving (6.5a). The linear inner sublayer, instead, is used to satisfy the boundary condition $\psi(0) = 1$ from (6.29b). In the bulk of the layer ($\delta \le z \le 1-\gamma$) we have $\psi' = a$, so the indefinite sign term in (6.24) is zero. Thus, we only need to control the indefinite sign term in the boundary layers. The parameter γ is the thickness of the boundary layer near the upper boundary in which the profile of ψ is linear.

The sole purpose behind the choice of the function $q(z)$ is to ensure $\psi' - q = 0$ in the lower boundary layer, thereby making the positive contribution from the second term in the bound (6.28) small in this layer. All parameters are taken to

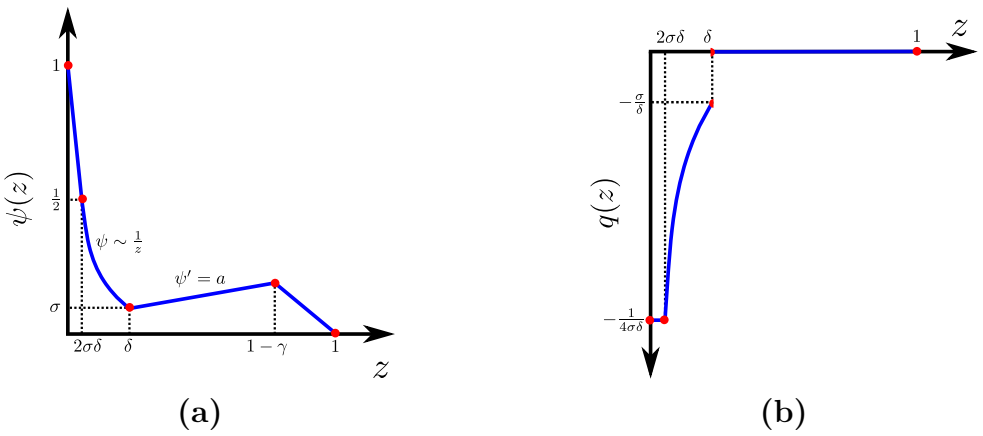

Figure 6.2: Sketch of the functions $\psi(z)$ and $q(z)$ from (6.32), used to obtain a bound on the heat flux $\langle wT \rangle$ in the IH1 configuration.

satisfy

$$a, b, \sigma, \delta, \gamma \leq 1 \tag{6.33}$$

and this assumption will be implicit in the proof below.

The goal now is to adjust the free parameters a, b, σ, δ and γ such that the spectral constraint (6.29d) is satisfied and, at the same time, the bound (6.28) is as small as possible. We begin by estimating from above the second term in the bound (6.28):

$$\begin{aligned}
\frac{1}{4b}\int_0^1 (bz - \psi' + q)^2 \mathrm{d}z \quad &\leq \frac{1}{2b}\int_0^1 b^2 z^2 \, \mathrm{d}z + \frac{1}{2b}\left\|\psi'(z) - q(z)\right\|_2^2 \\
&= \frac{b}{6} + \frac{1}{2b}\int_\delta^1 |\psi'(z) - q(z)|^2 \, \mathrm{d}z \\
&\leq \frac{b}{6} + \frac{1}{b}\int_\delta^1 |\psi'(z)|^2 \, \mathrm{d}z + \frac{1}{b}\int_\delta^1 |q(z)|^2 \, \mathrm{d}z \\
&\leq \frac{b}{6} + \frac{(\sigma + a)^2}{b\gamma} + \frac{a^2}{b} \\
&\leq \frac{b}{6} + \frac{2(\sigma + a)^2}{b\gamma}.
\end{aligned} \tag{6.34}$$

Next, we estimate from below the last term in the bound (6.28):

$$\begin{aligned}\int_0^1 \psi \,\mathrm{d}z \quad &= \frac{3\sigma\delta}{2} - \sigma\delta\log(2\sigma) + \frac{(2\sigma + a(1-\gamma-\delta))}{2} + \frac{(\sigma + a(1-\gamma-\delta))\gamma}{2} \\ &\geq -\sigma\delta\log(\sigma). \end{aligned} \tag{6.35}$$

Combining (6.34) and (6.35) with (6.28), we obtain

$$\langle wT\rangle \leq \frac{1}{2} + \frac{b}{6} + \frac{2(\sigma+a)^2}{b\gamma} + \sigma\delta\log(\sigma). \tag{6.36}$$

Assuming that

$$\frac{b}{6} \leq -\frac{1}{4}\sigma\delta\log(\sigma), \qquad \frac{2(\sigma+a)^2}{b\gamma} \leq -\frac{1}{4}\sigma\delta\log(\sigma), \tag{6.37a,b}$$

which will be the case for the choices of a, b, σ, δ, γ made below, the right-hand side of (6.36) can be further estimated from above to obtain

$$\langle wT\rangle \leq \frac{1}{2} + \frac{1}{2}\sigma\delta\log(\sigma). \tag{6.38}$$

We now shift our focus to the constraint (6.29d). Dropping the positive terms proportional to $|\hat{w}_{\boldsymbol{k}}|^2$, $|\hat{w}''_{\boldsymbol{k}}|^2$ and $|\hat{T}_{\boldsymbol{k}}|^2$, it is enough to verify that

$$\widetilde{\mathcal{S}}(\hat{w},\hat{T}) := \int_0^1 \left[\frac{2a}{R}|\hat{w}'|^2 + b|\hat{T}'|^2 - (a-\psi')\hat{w}\hat{T}\right]\mathrm{d}z \geq 0. \tag{6.39}$$

Here, $\hat{w}$ and $\hat{T}$ satisfy the boundary conditions

$$\hat{w}(0) = \hat{w}'(0) = \hat{T}(0) = 0, \tag{6.40a}$$

$$\hat{w}(1) = \hat{w}'(1) = \hat{T}(1) = 0, \tag{6.40b}$$

where $\hat{w}'(0) = \hat{w}'(1) = 0$ is a result of the no-slip boundary condition and the incompressibility of the flow field. For brevity, we have dropped $\boldsymbol{k}$ from the subscript. The positive terms we have dropped could be retained, at the expense of a more complicated algebra, in order to improve various prefactors in the eventual bounds. Since this is not our primary goal and the functional form of the bound one obtains does not change, we work with the stronger constraint (6.39) to ease the presentation.

Substituting the expression of ψ from (6.32) into (6.39) gives

$$\begin{aligned}\widetilde{S}(\hat{w},\hat{T}) = \quad & \int_0^{2\sigma\delta}\left[\frac{2a}{R}|\hat{w}'|^2 + b|\hat{T}'|^2 - \left(a+\frac{1}{4\sigma\delta}\right)\hat{w}\hat{T}\right]\,\mathrm{d}z \\ & + \int_{2\sigma\delta}^{\delta}\left[\frac{2a}{R}|\hat{w}'|^2 + b|\hat{T}'|^2 - \left(a+\frac{\sigma\delta}{z^2}\right)\hat{w}\hat{T}\right]\,\mathrm{d}z \\ & + \int_{1-\gamma}^{1}\left[\frac{2a}{R}|\hat{w}'|^2 + b|\hat{T}'|^2 - \left(\frac{\sigma+a(1-\delta)}{\gamma}\right)\hat{w}\hat{T}\right]\,\mathrm{d}z. \quad (6.41)\end{aligned}$$

Since $\widetilde{S}(\hat{w},\hat{T}) \geq \widetilde{S}(|\hat{w}|,|\hat{T}|)$ with equality when w and T are nonnegative, we shall assume without loss of generality that $\hat{w},\hat{T} \geq 0$. We further observe that, if

$$8a\delta \leq \sigma, \quad (6.42)$$

then

$$\begin{aligned}&\frac{9}{2}\frac{\sigma\delta}{(z+\sigma\delta)^2} \geq a + \frac{1}{4\sigma\delta} \quad \text{when} \quad 0 \leq z \leq 2\sigma\delta, \\ &\frac{9}{2}\frac{\sigma\delta}{(z+\sigma\delta)^2} \geq a + \frac{\sigma\delta}{z^2} \quad \text{when} \quad 2\sigma\delta \leq z \leq \delta. \quad (6.43)\end{aligned}$$

Assuming that $8a\delta \leq \sigma$, therefore, we can combine the first two terms in (6.41)

to conclude

$$\widetilde{S}(\hat{w},\hat{T}) \geq \widetilde{S}_B(\hat{w},\hat{T}) + \widetilde{S}_T(\hat{w},\hat{T}) \tag{6.44}$$

where

$$\widetilde{S}_B(\hat{w},\hat{T}) = \int_0^{\delta} \left[\frac{2a}{R}|\hat{w}'|^2 + b|\hat{T}'|^2 - \frac{9}{2}\frac{\sigma\delta}{(z+\sigma\delta)^2}\hat{w}\hat{T} \right] \mathrm{d}z, \tag{6.45a}$$

$$\widetilde{S}_T(\hat{w},\hat{T}) = \int_{1-\gamma}^{1} \left[\frac{2a}{R}|\hat{w}'|^2 + b|\hat{T}'|^2 - \frac{(\sigma+a)}{\gamma}\hat{w}\hat{T} \right] \mathrm{d}z. \tag{6.45b}$$

Next, we derive conditions that ensure $\widetilde{S}_B(\hat{w},\hat{T})$ and $\widetilde{S}_T(\hat{w},\hat{T})$ are individually nonnegative, thereby implying the nonnegativity of $\widetilde{S}(\hat{w},\hat{T})$.

First, we deal with $\widetilde{S}_T(\hat{w},\hat{T})$. Using the boundary conditions (6.40b) along with the fundamental theorem of calculus and the Cauchy–Schwarz inequality leads to

$$|\hat{w}|^2 \leq (1-z)\int_{1-\gamma}^{1} |\hat{w}'|^2 \mathrm{d}z, \qquad |\hat{T}|^2 \leq (1-z)\int_{1-\gamma}^{1} |\hat{T}'|^2 \mathrm{d}z. \tag{6.46a,b}$$

Using (6.46a,b) in the expression (6.45b) of $\widetilde{S}_T$, along with the AM–GM inequality, implies that $\widetilde{S}_T \geq 0$ if

$$\gamma(\sigma+a) \leq 4\sqrt{\frac{2ab}{R}}. \tag{6.47}$$

A condition for the nonnegativity of $\widetilde{S}_B(\hat{w},\hat{T})$, instead, can be derived using the Hardy inequality given in Lemma 6.3.1. First, using the AM-GM inequality,

we write

$$\widetilde{S}_B(\hat{w},\hat{T}) \geq \int_0^\delta \left[\frac{2a}{R}|\hat{w}'|^2 + b|\hat{T}'|^2 - \frac{9}{4}\frac{\sigma\delta\beta}{(z+\sigma\delta)^2}|\hat{w}|^2 - \frac{9}{4}\frac{\sigma\delta}{(z+\sigma\delta)^2\beta}|\hat{T}|^2\right] \mathrm{d}z \quad (6.48)$$

for some constant $\beta > 0$ to be specified later. Then, we can apply Lemma 6.3.1 to estimate

$$\int_0^\delta \frac{|\hat{w}|^2}{(z+\sigma\delta)^2}\mathrm{d}z \leq 4\int_0^\delta |\hat{w}'|^2\mathrm{d}z, \qquad \int_0^\delta \frac{|\hat{T}|^2}{(z+\sigma\delta)^2}\mathrm{d}z \leq 4\int_0^\delta |\hat{T}'|^2\mathrm{d}z. \quad (6.49a,b)$$

Using (6.49*a,b*), (6.48), and choosing

$$\beta = \sqrt{\frac{2a}{bR}}, \quad (6.50)$$

we conclude that $\widetilde{S}_B(\hat{w},\hat{T})$ is nonnegative if

$$\sigma\delta \leq \frac{1}{9}\sqrt{\frac{2ab}{R}}. \quad (6.51)$$

Given (6.47) and (6.51), and the functional forms of (6.37*a,b*) with respect to the variables, one can show that the bound (6.38) is optimized when a is proportional to σ and δ is proportional to γ. For simplicity, therefore, we take $a = \sigma$ and $\delta = \gamma$; we expect that different choices affect only the value of various prefactors appearing in the final bound, but not its functional form or the powers of R. With these additional simplifications, the constraints (6.47), (6.51) and

(6.37*a*,*b*) are satisfied if we take

$$a = \sigma = \exp\left(-2^{\frac{8}{5}}3^{\frac{8}{5}}R^{\frac{3}{5}}\right), \tag{6.52a}$$

$$b = 2^{\frac{7}{5}}3^{\frac{6}{5}}R^{\frac{1}{5}}\exp\left(-2^{\frac{8}{5}}3^{\frac{8}{5}}R^{\frac{3}{5}}\right), \tag{6.52b}$$

$$\delta = \gamma = 2^{\frac{6}{5}}3^{-\frac{7}{5}}R^{-\frac{2}{5}}. \tag{6.52c}$$

These choices satisfy the inequalities (6.33) and (6.42) assumed in our derivation provided that $R \geq 2^{\frac{21}{2}}3^{-\frac{7}{2}} \approx 30.97$. We therefore conclude from (6.38) that

$$\langle wT \rangle \leq \frac{1}{2} - 2^{\frac{7}{5}}3^{\frac{1}{5}}R^{\frac{1}{5}}\exp\left(-2^{\frac{8}{5}}3^{\frac{8}{5}}R^{\frac{3}{5}}\right) \qquad \forall R \geq 2^{\frac{21}{2}}3^{-\frac{7}{2}}. \tag{6.53}$$

We end this section with two remarks. First, the scaling of the upper boundary layer thickness given by (6.52c) is stronger (i.e. the boundary layer is thinner) than the scalings $\gamma \sim R^{-1/4}$ and $\gamma \sim R^{-1/3}$ implied by classical (Malkus, 1954; Priestley, 1954) and ultimate (Spiegel, 1963) scaling arguments for Rayleigh-Bérnard convection, respectively (for further details see §3 in Arslan et al., 2021b). Second, if instead of using the Hardy inequality in (6.45) we had used the Cauchy–Schwarz and AM–GM inequalities, as we did in the upper boundary layer, then we would have obtained the condition

$$-\frac{9}{2}\sigma\delta\left(\frac{1}{1+\sigma} + \log\left(\frac{\sigma}{1+\sigma}\right)\right) \leq \frac{1}{2}\sqrt{\frac{2ab}{R}}, \tag{6.54}$$

and therefore $\sigma\delta\log\sigma \lesssim \sqrt{ab/R}$. This is worse than condition (6.51) by a factor of $\log\sigma^{-1}$ and, as a result, no bound on $\langle wT \rangle$ strictly smaller than $1/2$ can be obtained beyond a certain Rayleigh number.

6.5 Bound on heat flux in IH3

We now prove the bound (6.5b) for the IH3 configuration. Similar to the previous section, the key ingredients of the proof are (i) a profile of ψ proportional to $1/z$ near the bottom boundary, and (ii) the use of a nonstandard Rellich inequality.

We start by choosing the functions $\psi(z)$ and $q(z)$:

$$\psi(z) = \begin{cases} 2\sqrt{\sigma\delta} - z & 0 \le z \le \sqrt{\sigma\delta}, \\ \frac{\sigma\delta}{z} & \sqrt{\sigma\delta} \le z \le \delta, \\ \sigma + a(z-\delta) & \delta \le z \le 1-\gamma, \\ (1-z)\frac{\sigma + a(1-\gamma-\delta)}{\gamma} & 1-\gamma \le z \le 1. \end{cases} \qquad q(z) = \begin{cases} -1 & 0 \le z \le \sqrt{\sigma\delta}, \\ -\frac{\sigma\delta}{z^2} & \sqrt{\sigma\delta} \le z \le \delta, \\ 0 & \delta \le z \le 1. \end{cases} \tag{6.55}$$

These choices are sketched in figure 6.3 and the parameters σ, δ and γ have the same purpose as in the last section. The difference between these profiles and those used for the IH1 configuration in §6.4 is in the bottom boundary layer ($0 \le z \le \delta$). Here, we require $q(0) = -1$ and at the same time want $q - \psi' = 0$ in the lower boundary. To satisfy these requirements we take the linear boundary sublayer of ψ near the bottom boundary ($0 \le z \le \sqrt{\sigma\delta}$) to have slope equal to -1. As before, in the outer part of bottom boundary layer ($\sqrt{\sigma\delta} \le z \le \delta$), ψ behaves like z^{-1} and matches smoothly with inner part up to the first derivative. At the edge of the bottom boundary layer ($z = \delta$), the value of ψ is σ. In the proof below, we assume

$$a, b, \sigma, \delta, \gamma \le 1 \tag{6.56}$$

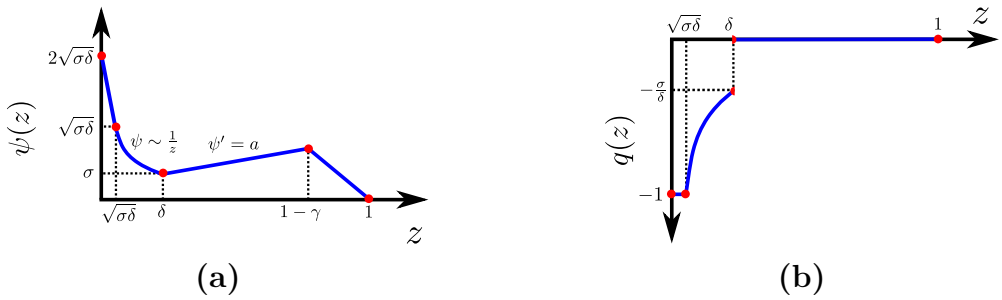

Figure 6.3: Sketch of the functions $\psi(z)$ and $q(z)$ from (6.55), used to obtain bound on the heat flux $\langle wT \rangle$ in the IH3 configuration.

Estimating the second term in the bound (6.28) from above gives

$$\frac{1}{4b}\int_0^1 (bz - \psi' + q)^2 \mathrm{d}z \qquad \leq \frac{b}{6} + \frac{2(\sigma+a)^2}{b\gamma}, \tag{6.57}$$

while the last term can be estimated from below as

$$\int_0^1 \psi \, \mathrm{d}z \qquad \geq -\frac{1}{2}\sigma\delta \log\left(\frac{\sigma}{\delta}\right). \tag{6.58}$$

Combining (6.57) and (6.58) with (6.28), we obtain

$$\langle wT \rangle \leq \frac{1}{2} + \frac{b}{6} + \frac{2(\sigma+a)^2}{b\gamma} + \frac{1}{2}\sigma\delta \log\left(\frac{\sigma}{\delta}\right). \tag{6.59}$$

Finally, we assume that

$$\frac{b}{6} \leq -\frac{1}{8}\sigma\delta \log\left(\frac{\sigma}{\delta}\right), \qquad \frac{2(\sigma+a)^2}{b\gamma} \leq -\frac{1}{8}\sigma\delta \log\left(\frac{\sigma}{\delta}\right) \tag{6.60}$$

(these constraints will be verified later) and estimate the right-hand side of (6.59) to arrive at the simpler bound

$$\langle wT \rangle \leq \frac{1}{2} + \frac{1}{4}\sigma\delta \log\left(\frac{\sigma}{\delta}\right). \tag{6.61}$$

For this bound to be valid, we need to adjust the parameters a, b, δ, γ and σ such that the spectral condition (6.29d) is satisfied. Dropping the positive terms proportional to $|\hat{w}_{\boldsymbol{k}}|^2$, $|\hat{w}'_{\boldsymbol{k}}|^2$ and $|\hat{T}'_{\boldsymbol{k}}|^2$, we will verify the stronger inequality

$$\widetilde{\mathcal{S}}(\hat{w},\hat{T}) := \int_0^1 \left[\frac{a}{Rk^2}|\hat{w}''|^2 + bk^2|\hat{T}|^2 - (a-\psi')\hat{w}\hat{T}\right] \mathrm{d}z \geq 0 \tag{6.62}$$

for all z-dependent functions $\hat{w}$ and $\hat{T}$ satisfying the boundary conditions

$$\hat{w}(0) = \hat{w}'(0) = \hat{T}'(0) = 0, \tag{6.63a}$$

$$\hat{w}(1) = \hat{w}'(1) = \hat{T}(1) = 0. \tag{6.63b}$$

Again, we have dropped the subscript $\boldsymbol{k}$ to lighten the notation.

Using arguments similar to those used in §6.4 and noticing that if

$$8a\delta \leq \sigma \tag{6.64}$$

then

$$\frac{9}{2}\frac{\sigma\delta}{(z+\sqrt{\sigma\delta})^2} \geq a+1 \quad \text{when} \quad 0 \leq z \leq \sqrt{\sigma\delta}, \tag{6.65}$$

$$\frac{9}{2}\frac{\sigma\delta}{(z+\sqrt{\sigma\delta})^2} \geq a+\frac{\sigma\delta}{z^2} \quad \text{when} \quad \sqrt{\sigma\delta} \leq z \leq \delta, \tag{6.66}$$

we can write

$$\widetilde{S}(\hat{w},\hat{T}) \geq \widetilde{S}_B(\hat{w},\hat{T}) + \widetilde{S}_T(\hat{w},\hat{T}), \tag{6.67}$$

where

$$\widetilde{S}_B(\hat{w},\hat{T}) = \int_0^{\delta} \left[\frac{a}{Rk^2}|\hat{w}''|^2 + bk^2|\hat{T}|^2 - \frac{9}{2}\frac{\sigma\delta}{(z+\sqrt{\sigma\delta})^2}\hat{w}\hat{T} \right] \mathrm{d}z, \tag{6.68a}$$

$$\widetilde{S}_T(\hat{w},\hat{T}) = \int_{1-\gamma}^{1} \left[\frac{a}{Rk^2}|\hat{w}''|^2 + bk^2|\hat{T}|^2 - \frac{(\sigma+a)}{\gamma}\hat{w}\hat{T} \right] \mathrm{d}z. \tag{6.68b}$$

Finding a condition under which $\widetilde{S}_T(\hat{w},\hat{T}) \geq 0$ is straightforward. Using the fundamental theorem of calculus, the boundary conditions on $\hat{w}$ and Cauchy–Schwarz inequality, we obtain

$$|\hat{w}|^2 \leq \frac{4(1-z)^3}{9}\int_{1-\gamma}^{1} |\hat{w}''|^2 \mathrm{d}z. \tag{6.69}$$

Then, substituting (6.69) in (6.68b) and using the AM-GM inequality shows that $\widetilde{S}_T(\hat{w},\hat{T})$ is nonnegative as long as

$$(\sigma+a)\gamma \leq 6\sqrt{\frac{ab}{R}}. \tag{6.70}$$

To show that $\widetilde{S}_B(\hat{w},\hat{T})$ is nonnegative, instead, we rely on the Rellich inequality stated in Lemma 6.3.2. First, using the AM-GM inequality we estimate

$$\widetilde{S}_B(\hat{w},\hat{T}) \geq \int_0^{\delta} \left[\frac{a}{Rk^2}|\hat{w}''|^2 + bk^2|\hat{T}|^2 - \frac{9}{4}\frac{\sigma\delta\beta}{(z+\sqrt{\sigma\delta})^4}|\hat{w}|^2 - \frac{9}{4}\frac{\sigma\delta}{\beta}|\hat{T}|^2 \right] \mathrm{d}z, \tag{6.71}$$

for a the positive constant β to be specified below. Next, using Lemma 6.3.2 we obtain

$$\int_0^{\delta} \frac{|\hat{w}|^2}{(z+\sqrt{\sigma\delta})^4}\mathrm{d}z \leq \frac{16}{9}\int_0^{\delta} |\hat{w}''|^2 \mathrm{d}z. \tag{6.72}$$

Combining (6.72) in (6.71) and setting

$$\beta = \frac{3}{4k^2}\sqrt{\frac{a}{bR}} \tag{6.73}$$

we conclude that $\widetilde{S}_B(\hat{w}, \hat{T})$ is nonnegative if

$$\sigma\delta \leq \frac{1}{3}\sqrt{\frac{ab}{R}}. \tag{6.74}$$

At this stage, all that remains is to choose values for a, b, δ, γ and σ such that (6.60), (6.70) and (6.74) hold, at least for sufficiently large Rayleigh numbers, while minimizing the right-hand side of (6.61). For the same reasons explained at the end of §6.4, we simplify the algebra by choosing $a = \sigma$ and $\delta = \gamma$. Then, optimizing the bound (6.61) subject to (6.70) and (6.74) leads to

$$a = \sigma = \frac{2^{\frac{4}{5}}}{3^{\frac{3}{5}}}\frac{1}{R^{\frac{2}{5}}}\exp\left(-2^{\frac{14}{5}}3^{\frac{2}{5}}R^{\frac{3}{5}}\right), \tag{6.75a}$$

$$b = \frac{2^{\frac{12}{5}}3^{\frac{1}{5}}}{R^{\frac{1}{5}}}\exp\left(-2^{\frac{14}{5}}3^{\frac{2}{5}}R^{\frac{3}{5}}\right), \tag{6.75b}$$

$$\delta = \gamma = \frac{2^{\frac{4}{5}}}{3^{\frac{3}{5}}}\frac{1}{R^{\frac{2}{5}}}. \tag{6.75c}$$

These choices satisfy the constraints in(6.60) assumed in our proof for all $R \geq 2^{\frac{19}{2}}3^{-\frac{3}{2}} \approx 139.35$. Thus, from (6.61) we obtain

$$\langle wT\rangle \leq \frac{1}{2} - \frac{2^{\frac{12}{5}}}{3^{\frac{4}{5}}}\frac{1}{R^{\frac{1}{5}}}\exp\left(-2^{\frac{14}{5}}3^{\frac{2}{5}}R^{\frac{3}{5}}\right) \quad \forall R \geq 2^{\frac{19}{2}}3^{-\frac{3}{2}}. \tag{6.76}$$

It is interesting to note that only the boundary layer thicknesses δ and γ have the same $O(R^{-\frac{2}{5}})$ scaling as for the IH1 configuration. The parameters σ, a, b and the correction to $1/2$ in the bound (6.76), instead, are all $O(R^{\frac{2}{5}})$ smaller than their

corresponding values for the IH1 case.

6.6 Discussion and concluding remarks

We considered the problem of uniform internally heated convection between two parallel boundaries where either both the boundaries are held at the same constant temperature (IH1 configuration) or the temperature at the top boundary is fixed and the bottom boundary is insulating (IH3 configuration). For both configurations we obtained rigorous R-dependent bounds on the heat flux using the background method, which we formulated in terms of a quadratic auxiliary function and augmented with a minimum principle that enables one to consider only nonnegative temperature fields in the optimization problem for the bound. In each configuration, we were able to prove that $\langle wT \rangle < 1/2$ with exponentially decaying corrections. The two essential ingredients in our proofs were a boundary layer with inverse-z scaling in the background field and the use of Hardy and Rellich inequalities, which allow for a refined analysis of the spectral constraint compared to standard Cauchy–Schwarz inequalities. Without any of these two components, the proof breaks down and it appears impossible to obtain R-dependent corrections to the uniform $\langle wT \rangle \leq 1/2$ at arbitrarily large Rayleigh numbers.

The exponential rate at which our analytical bounds (6.53) and (6.76) approach $1/2$ is not inconsistent with the numerically optimal bounds computed by Arslan et al. (2021b) for the IH1 configuration. These numerical bounds also approach $1/2$ from below rapidly as $R \to \infty$ and appear to do so faster than any power law, suggesting that the best possible bounds provable with the background

method may indeed have the functional form

$$\langle wT \rangle \leq \frac{1}{2} - c_1 R^{\alpha} \exp\left(-c_2 R^{\beta}\right) \quad \text{in IH1,} \tag{6.77a}$$

$$\langle wT \rangle \leq \frac{1}{2} - \frac{c_3}{R^{\alpha}} \exp\left(-c_4 R^{\beta}\right) \quad \text{in IH3} \tag{6.77b}$$

for some positive exponents α, β and positive constants c_1, c_2, c_3, c_4. Unfortunately, the limited range of Rayleigh numbers spanned by the available numerical results does not permit a confident estimation of these parameters, so we cannot say whether the exponents $\alpha = 1/5$ and $\beta = 3/5$ of our analytical bounds are optimal or not. Nevertheless, as illustrated in figure 6.4, the numerically optimal profiles for the functions $\psi(z)$ and $q(z)$ computed by Arslan et al. (2021a) in the IH1 case exhibit the same inverse-z behaviour in the outer part of the bottom boundary layer as the suboptimal profiles used in our analysis. We expect the same to be true for the IH3 configuration even though we have not optimized ψ and q numerically in this case due to the computational challenges of accurately resolving the nonsmooth bottom boundary layers, which our present analysis suggest will be much thinner that those observed in the IH1 computations by Arslan et al. (2021a). If the exponents α and β can be improved at all, such improvements must come either from improved estimates, or from different choices for ψ and q in other parts of the fluid layer.

In the case of IH3, if (6.77b) is the correct scaling of the optimal bound in the framework of quadratic auxiliary functions, then we note that it will not be trivial to prove the conjecture (Goluskin, 2016, p. 17)

$$\langle wT \rangle \leq \frac{1}{2} - \frac{C}{R^{1/3}}. \tag{6.78}$$

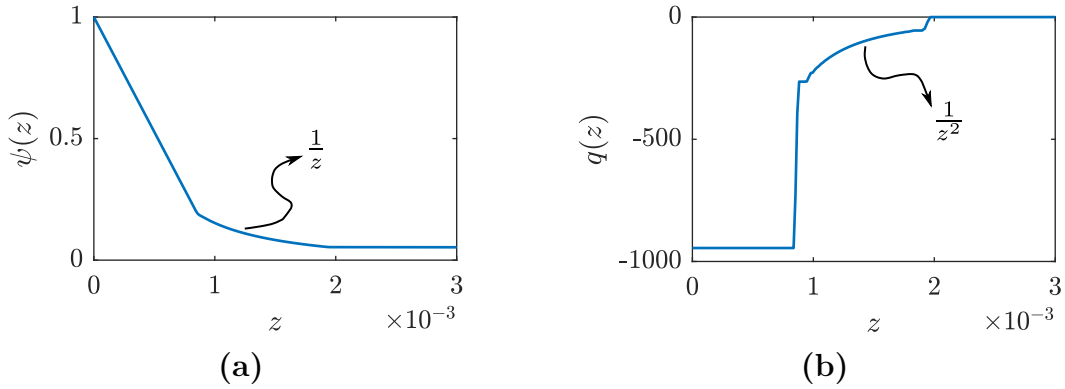

Figure 6.4: Bottom boundary layer structure of the numerically optimal functions $\psi(z)$ and $q(z)$ computed by Arslan et al. (2021b) for the IH1 configuration. The results shown are for $R = 2.67 \times 10^5$ but are typical of the behaviour observed at all sufficiently large R values. The boundary layer in $\psi(z)$ has an approximately linear inner sublayer ($0 \leq z \lessapprox 0.001$) followed by an outer sublayer where $\psi(z) \sim z^{-1}$ ($0.001 \leq z \lessapprox 0.002$). The transition between the two is nonsmooth. The optimal q approximately satisfies $q(z) = \psi'(z)$ in the boundary layer. This boundary layer structure is modelled similar to the analytical ψ and q sketched in Figure 6.2.

It seems reasonable to expect that progress can be made by considering further constraints derived from the governing equations, which go beyond the energy balances encoded by the auxiliary function $\mathcal{V}$ in (6.14) and the minimum principle. However, it is presently unclear if this can be done within an analytically tractable framework.

For the IH3 configuration, moreover, any bound on $\langle wT \rangle$ can be translated into a bound on the Nusselt number—defined as the ratio of the mean total heat flux to the conductive heat flux—via the identity

$$Nu = \frac{1}{1 - 2\langle wT \rangle}. \tag{6.79}$$

In particular, (6.76) implies

$$Nu \leq \frac{3^{\frac{4}{5}}}{2^{\frac{17}{5}}} R^{\frac{1}{5}} \exp\left(2^{\frac{14}{5}} 3^{\frac{2}{5}} R^{\frac{3}{5}}\right). \tag{6.80}$$

The exponential growth of this bound is in stark contrast with the power-law bounds available for Raleigh-Bénard convection, most of which can be obtained with much simpler arguments that those used here for IH3.

In the case of IH1, we can compare our bound on $\langle wT \rangle$ with 3D direct numerical simulations by (Goluskin and van der Poel, 2016), which suggest

$$\langle wT \rangle \sim \frac{1}{2} - \frac{0.8}{R^{0.055}}. \tag{6.81}$$

Again, this slow power-law correction to the asymptotic value of $1/2$ contrasts the exponential behaviour of our bound (6.77a). It remains to be seen if this result is truly overly conservative, as one may expect based on phenomenological arguments (Arslan et al., 2021b), or if there exist solutions of the governing equations (6.6) that saturate it. In that regard, there are two approaches generally used in the Rayleigh–Bénard convection. The first one is the study of bulk properties of steady-state solutions bifurcating from the pure conduction state has attracted growing interest in recent years (Waleffe et al., 2015; Sondak et al., 2015; Miquel et al., 2019; Wen et al., 2020, 2022; Kooloth et al., 2021; Motoki et al., 2021), and it has been shown that they can transport more heat than turbulence (Wen et al., 2022). The second one is the optimal wall-to-wall approach (Hassanzadeh et al., 2014; Tobasco and Doering, 2017; Motoki et al., 2018b; Doering and Tobasco, 2019; Souza et al., 2020; Tobasco, 2022), which concerns designing incompressible flows with a constraint on the kinetic energy or enstrophy that leads to optimal

heat transfer. It would be interesting to conduct similar studies for the two cases of internally heated convection studied in this work.

Acknowledgement

A.K. thanks D. Goluskin for a discussion and providing comments on the paper. A.A. acknowledges funding by the EPSRC Centre for Doctoral Training in Fluid Dynamics across Scales (award number EP/L016230/1). G.F. was supported by an Imperial College Research Fellowship.

Appendix 6.A Proof of Hardy and Rellich inequalities

6.A.1 Proof of the Hardy inequality in Lemma 6.3.1

Set $f(z) = g(z)\sqrt{z+\epsilon}$ for a suitable function $g(z)$ satisfying $g(0) = 0$, and estimate

$$\begin{aligned} |f'|^2 &= (z+\epsilon)|g'|^2 + \left(\frac{1}{2}g^2\right)' + \frac{1}{4}(z+\epsilon)^{-1}|g|^2 \\ &= (z+\epsilon)|g'|^2 + \left(\frac{1}{2}g^2\right)' + \frac{1}{4}(z+\epsilon)^{-2}|f|^2 \\ &\geq \left(\frac{1}{2}g^2\right)' + \frac{1}{4}(z+\epsilon)^{-2}|f|^2. \end{aligned} \tag{6.82}$$

Upon integrating this inequality in z from 0 to α and using the boundary condition $g(0) = 0$, we find

$$\begin{aligned}\int_0^\alpha |f'(z)|^2 \,\mathrm{d}z &\geq \frac{1}{2}g(\alpha)^2 + \frac{1}{4}\int_0^\alpha (z+\epsilon)^{-2}|f(z)|^2 \,\mathrm{d}z \\ &\geq \frac{1}{4}\int_0^\alpha (z+\epsilon)^{-2}|f(z)|^2 \,\mathrm{d}z, \end{aligned} \tag{6.83}$$

which is the desired inequality.

6.A.2 Proof of the Rellich inequality in Lemma 6.3.2

Write $f'(z) = \sqrt{z+\epsilon}g(z)$ and $f(z) = (z+\epsilon)^{3/2}h(z)$ for suitable functions g and h satisfying $g(0) = 0 = h(0)$. Then,

$$\begin{aligned}|f''|^2 &= (z+\epsilon)|g'|^2 + \frac{g^2}{4(z+\epsilon)} + \left(\frac{1}{2}g^2\right)' \\ &= (z+\epsilon)|g'|^2 + \frac{|f'|^2}{4(z+\epsilon)^2} + \left(\frac{1}{2}g^2\right)' \\ &\geq \frac{|f'|^2}{4(z+\epsilon)^2} + \left(\frac{1}{2}g^2\right)' \end{aligned} \tag{6.84a}$$

and

$$\begin{aligned}|f'|^2 &= (z+\epsilon)^3|h'|^2 + \frac{9}{4}(z+\epsilon)h^2 + (z+\epsilon)^2\left(\frac{3}{2}h^2\right)' \\ &= (z+\epsilon)^3|h'|^2 + \frac{9}{4}\frac{|f|^2}{(z+\epsilon)^2} + (z+\epsilon)^2\left(\frac{3}{2}h^2\right)' \\ &\geq \frac{9}{4}\frac{|f|^2}{(z+\epsilon)^2} + (z+\epsilon)^2\left(\frac{3}{2}h^2\right)' \end{aligned} \tag{6.84b}$$

Combining (6.84b) and (6.84a) and then integrating in z from 0 to α yields

$$\begin{aligned}\int_0^\alpha |f''|^2 \mathrm{d}z &\geq \int_0^\alpha \frac{9|f|^2}{16(z+\epsilon)^4} + \left(\frac{3}{8}h^2\right)' + \left(\frac{1}{2}g^2\right)' \mathrm{d}z \\ &= \int_0^\alpha \frac{9|f|^2}{16(z+\epsilon)^4}\,\mathrm{d}z + \frac{3}{8}h(\alpha)^2 + \frac{1}{2}g(\alpha)^2 \\ &\geq \int_0^\alpha \frac{9|f|^2}{16(z+\epsilon)^4}\mathrm{d}z, \end{aligned} \tag{6.85}$$

which completes the proof. □

Chapter 7

Three dimensional branching pipe flows for optimal scalar transport between walls

This chapter is based on the paper Kumar (2022b) (to be submitted soon). A preprint is available at arXiv:2205.03367.

7.1 Introduction

7.1.1 Motivation

An important subdiscipline of thermal engineering is devoted to the design of heat exchangers, ventilation systems, air-conditioning systems, refrigeration systems, boilers, and chemical reactors (Arora, 2000; Jakobsen, 2008; Thulukkanam, 2013; Alam and Kim, 2018). A fundamental challenge in this field is how to transport heat from a hot surface to a cold surface by moving the fluid using actuators

such as fans or pumps, which can advect heat at a quicker rate than pure conduction. For most practical purposes, one would of course like to do so in the most economical way, minimizing the power supplied to the actuators. In the design of the systems described above, we would therefore like to know the answers to the following questions:

(A) What is the optimal heat transfer rate as a function of the power supplied?

(B) What is the corresponding placement of fans/pumps which maximizes the heat transfer for a given amount of power supplied?

In this paper, we are able to provide a definitive answer to a mathematical idealization of this problem and thus gain insight into possible practical engineering solutions.

To model the problem mathematically, we use the forced Navier–Stokes equation to describe the flow of an incompressible fluid:

$$\partial_t \boldsymbol{u} + \boldsymbol{u} \cdot \nabla \boldsymbol{u} = -\nabla p + \nu \Delta \boldsymbol{u} + \boldsymbol{f} \quad \text{in } \Omega,$$

where Ω is a bounded domain with smooth boundaries and ν is the viscosity of the fluid. We assume that the fluid satisfies a no-slip boundary condition on the surface, i.e., $\boldsymbol{u}|_{\partial\Omega} = \boldsymbol{0}$. In this mathematical formulation of the problem, the question of interest now involves finding the optimal design for the force $\boldsymbol{f}$ that maximizes the heat transfer with a given finite mean power supply $\mathscr{P}^*$. Denoting the volume average and the long-time volume average, respectively, as

$$\fint_\Omega [\,\cdot\,]\,\mathrm{d}\boldsymbol{x} = \frac{1}{|\Omega|}\int_\Omega [\,\cdot\,]\,\mathrm{d}\boldsymbol{x} \qquad \text{and} \qquad \langle [\,\cdot\,] \rangle = \limsup_{\tau\to\infty} \frac{1}{\tau}\int_0^\tau \fint_\Omega [\,\cdot\,]\,\mathrm{d}\boldsymbol{x}\mathrm{d}t,$$

we can express the constraint on the mean power supply as $\langle \boldsymbol{f} \cdot \boldsymbol{u} \rangle \le \mathscr{P}^*$.

Assuming the velocity field stays smooth and the kinetic energy of flow stays bounded in time, then the long-time spatial average of the energy equation leads to

$$\langle \boldsymbol{f} \cdot \boldsymbol{u} \rangle = \nu \langle |\nabla \boldsymbol{u}|^2 \rangle.$$

Physically, this means that the work done by the force $\boldsymbol{f}$ to move the fluid is eventually dissipated viscously. It also shows that instead fixing the power supply, one can equivalently impose a constraint on the enstrophy of the flow, i.e., $\langle |\nabla \boldsymbol{u}|^2 \rangle \leq \nu^{-1} \mathscr{P}^*$.

The advantage of formulating the constraint in terms of the enstrophy is that we can from here on ignore the momentum equation entirely. We can simply ask, what is the flow $\boldsymbol{u}$ that maximizes the heat transfer, for a given bound on the enstrophy ($\langle |\nabla \boldsymbol{u}|^2 \rangle \leq \nu^{-1} \mathscr{P}^*$). Once that flow $\boldsymbol{u}$ is found, the corresponding forcing $\boldsymbol{f}$ can then be computed from (7.1). Whether the optimal flow $\boldsymbol{u}$ obtained in this manner is dynamically stable is a separate question that we will not address in this paper.

Beyond the primary engineering motivation, the optimal heat transport problem considered in this paper is also inspired by two problems: (1) anomalous dissipation in a passive scalar, (2) Rayleigh–Bénard convection. These problems, and their relationship with the optimal transport problem investigated here, will be discussed in section 7.5.

7.1.2 Problem setup

Although the problem discussed above is very general, we now focus on a special case in the simplest possible geometry namely the transport of a passive scalar T (which we refer to as temperature) by a flow field $\boldsymbol{u}$ between two parallel

walls held at different constant values of T. We assume that the flow field $\boldsymbol{u}$ is incompressible and satisfies no-slip boundary conditions at the walls, which in the wall-normal coordinates are located at $z = -H/2$ and $z = H/2$, where H denotes the distance between the walls. The temperature field evolves according to the advection-diffusion equation

$$\partial_t T + \boldsymbol{u} \cdot \nabla T - \kappa \Delta T = 0, \tag{7.1}$$

and satisfies Dirichlet boundary conditions

$$T = T_B \ \text{ at } \ z = -H/2, \quad T = T_T \ \text{ at } \ z = H/2. \tag{7.2}$$

In (7.1), κ is the thermal diffusivity, and without loss of generality, we choose $T_B > T_T$ in (7.2). For simplicity, we consider the horizontal directions x and y to be periodic with length l_x and l_y. The domain of interest is thus given by $\Omega \coloneqq \mathbb{T}_{l_x} \times \mathbb{T}_{l_y} \times (-H/2, H/2)$.

For a given flow field $\boldsymbol{u}$, we define the corresponding rate of heat transfer as

$$Q(\boldsymbol{u}) \coloneqq \left\langle u_z T - \kappa \frac{\partial T}{\partial z} \right\rangle = \langle u_z T \rangle + \frac{\kappa (T_B - T_T)}{H}.$$

By performing the long-time horizontal average of equation (7.1), one can show that $Q(\boldsymbol{u})$ is equal to the heat flux at the top or the bottom boundary, hence the definition. Furthermore, by multiplying (7.1) with T and performing the long-time volume average, one can alternatively express the rate of heat transfer $Q(\boldsymbol{u})$ as

$$Q(\boldsymbol{u}) = \frac{\kappa H}{T_B - T_T} \langle |\nabla T|^2 \rangle.$$

The question of optimal heat transport described in the previous subsection seeks to find the maximum possible value of Q over all incompressible flow fields satisfying the no-slip boundary condition and the enstrophy constraint:

$$Q_{\max}(\mathscr{P}^*) := \sup_{\substack{\boldsymbol{u}(t,\boldsymbol{x}) \\ \nabla\cdot\boldsymbol{u}=0,\ \boldsymbol{u}|_{\partial\Omega}=\boldsymbol{0} \\ \langle|\nabla\boldsymbol{u}|^2\rangle\leq\nu^{-1}\mathscr{P}^*}} Q(\boldsymbol{u}).$$

Before we proceed further, we nondimensionalize the problem by making the following transformations, respectively, for the position, time, velocity field, temperature and the heat transfer:

$$\begin{aligned} &\boldsymbol{x}\to H\boldsymbol{x}, \quad t\to\frac{H^2}{\kappa}t, \quad \boldsymbol{u}\to\frac{\kappa}{H}\boldsymbol{u}, \\ &T\to(T_B-T_T)T+T_T, \quad Q\to\frac{\kappa(T_B-T_T)}{H}Q. \end{aligned} \tag{7.3}$$

We continue to denote the nondimensional horizontal periodic lengths with l_x and l_y. After the rescaling (7.3), a single nondimensional parameter remains, namely the nondimensional power given by

$$\mathscr{P} = \mathscr{P}^*\frac{H^4}{\nu\kappa^2}$$

which can be increased by either increasing the dimensional power supply $\mathscr{P}^*$ and the domain size H or by decreasing the thermal diffusivity κ and viscosity ν of the fluid. After the nondimensionalization the enstrophy constraint becomes $\langle|\nabla\boldsymbol{u}|^2\rangle \leq \mathscr{P}$.

As the problem of optimal heat transport can be considered both in two and

three dimensions, let us define

$$\Omega^{2D} \coloneqq \mathbb{T}_{l_x} \times (-1/2, 1/2), \qquad \Omega^{3D} \coloneqq \mathbb{T}_{l_x} \times \mathbb{T}_{l_x} \times (-1/2, 1/2). \quad (7.4\text{a-b})$$

In the introduction, Ω is used to mean either Ω^{2D} or Ω^{3D} except in places where the distinction is required, in which case we will make the reference explicit. In rest of the paper Ω will only mean Ω^{3D}. Without loss of generality, we assume that the aspect ratio of the domain satisfies $l_x \leq l_y$. Next, we explicitly formulate the steady and unsteady versions of the optimal heat transport problem.

Steady case

In the steady case, we seek

$$Q^s_{\max}(\mathscr{P}) = \sup_{\substack{\boldsymbol{u}\in L^\infty(\Omega) \\ \nabla\cdot\boldsymbol{u}=0,\ \boldsymbol{u}|_{\partial\Omega}=\boldsymbol{0} \\ \fint_\Omega |\nabla\boldsymbol{u}|^2 \,\mathrm{d}\boldsymbol{x}\leq\mathscr{P}}} Q(\boldsymbol{u}) \qquad \text{where} \qquad Q(\boldsymbol{u}) = \fint_\Omega |\nabla T|^2 \,\mathrm{d}\boldsymbol{x}, \quad (7.5)$$

and T solves the steady advection-diffusion equation with Dirichlet boundary conditions

$$\left.\begin{gathered} \boldsymbol{u}\cdot\nabla T - \Delta T = 0, \\ T = 1 \ \text{ at } \ z = -1/2, \quad T = 0 \ \text{ at } \ z = 1/2. \end{gathered}\right\} \quad (7.6)$$

Unsteady case

In the unsteady case, we seek

$$Q^u_{\max}(\mathscr{P}) = \sup_{\substack{\boldsymbol{u}\in L^\infty([0,\infty)\times\Omega) \\ \nabla\cdot\boldsymbol{u}=0,\ \boldsymbol{u}|_{\partial\Omega}=\boldsymbol{0} \\ \langle|\nabla\boldsymbol{u}|^2\rangle\leq\mathscr{P}}} Q(\boldsymbol{u}) \qquad \text{where} \qquad Q(\boldsymbol{u}) = \langle|\nabla T|^2\rangle, \quad (7.7)$$

and T solves the unsteady advection-diffusion equation with Dirichlet boundary conditions

$$\left.\begin{aligned} \partial_t T + \boldsymbol{u} \cdot \nabla T - \Delta T = 0, \\ T = T_0 \in L^2(\Omega) \ \text{ at } \ t = 0, \\ T = 1 \ \text{ at } \ z = -1/2, \quad T = 0 \ \text{ at } \ z = 1/2 \quad \forall\, t \in (0, \infty). \end{aligned}\right\} \tag{7.8}$$

Remark 7.1.1. *It is clear that for every $\mathscr{P}$, we have the inequality $Q^s_{\max} \leq Q^u_{\max}$. Therefore, any upper bound on $Q^u_{\max}$ provides an upper bound on $Q^s_{\max}$. Similarly, any lower bound on $Q^s_{\max}$ is also a lower bound on $Q^u_{\max}$.*

Remark 7.1.2. *The values of $Q^s_{\max}$ and $Q^u_{\max}$ for the three-dimensional problem are larger than their corresponding values for the two-dimensional problem. This is because any two-dimensional solution of the advection-diffusion equation is also a solution in three dimensions by an extension that is invariant in the third direction.*

Remark 7.1.3. *In the unsteady case, the quantity $Q(\boldsymbol{u})$ does not depend on the initial condition T_0 as long as this initial condition belongs to $L^2(\Omega)$. Physically, this means that the dependence of the solution T on the initial data is lost at long times because of the presence of diffusion.*

For both the steady and unsteady cases, in their two- and three-dimensional versions, the questions of prime importance are:

(A) How do the maximum heat fluxes $Q^s_{\max}$ and $Q^u_{\max}$ scale with the input power $\mathscr{P}$ for asymptotically large values of $\mathscr{P}$?

(B) What does the structure of the flow fields that transfer heat "most efficiently" look like?

In this paper, we investigate these questions for the steady case only. The unsteady case is also of great importance and will be considered in a future study.

7.1.3 Previous work and the present results

The problem of optimal heat transport between parallel walls, as described above, was first introduced in the work of Hassanzadeh et al. (2014) whose motivation was to improve previously known upper bounds on heat transfer in porous medium convection (Doering and Constantin, 1998b) and Rayleigh–Bénard convection (Doering and Constantin, 1996; Plasting and Kerswell, 2003; Whitehead and Doering, 2011b; Wen et al., 2015). They studied the problem in two dimensions, with stress-free boundary conditions. Using a combination of numerical techniques and matched asymptotic analysis, they were able to establish distinct upper bounds on the heat transport for fixed energy, as well as for fixed enstrophy.

Their initial investigation has since inspired several studies of optimal heat transport between differentially heated plates (Tobasco and Doering, 2017; Motoki et al., 2018b; Doering and Tobasco, 2019; Souza et al., 2020) and the slightly different problem of optimal cooling of a fluid subjected to a given volumetric heating (Marcotte et al., 2018; Iyer and Van, 2022; Tobasco, 2022). Of all these studies, the three of particular interest to the current paper are (Tobasco and Doering, 2017), (Motoki et al., 2018b) and (Doering and Tobasco, 2019). They all investigate the same problem considered in this paper, i.e., optimal heat transport between parallel boundaries by incompressible flows satisfying no-slip boundary conditions with an enstrophy constraint. Doering and Tobasco (2019) derived an upper bound on the maximum possible heat transfer, and showed that flows satisfying the required constraint cannot transport heat faster than a rate proportional

to the enstrophy to the power of 1/3, i.e.,

$$Q^u_{\max}(\mathscr{P}) \le C' \mathscr{P}^{1/3} \qquad \text{for} \quad \mathscr{P} \ge C'', \tag{7.9}$$

where C' is a universal constant but C'' depends on the aspect ratio. This upper bound is valid both in two and three dimensions and applies to $Q^s_{\max}(\mathscr{P})$ as well (see Remark 7.1.1). The same bound had been proved before in the context of Rayleigh–Bénard convection in at least three different ways: using the variational principle of Howard (Howard, 1963; Busse, 1969), the background method of Doering & Constantin (Doering and Constantin, 1996; Plasting and Kerswell, 2003) and more recently by Seis (Seis, 2015).

Complementary to their upper bound, Tobasco and Doering (2017) and Doering and Tobasco (2019) constructed two-dimensional steady branching flows (in which the flow structures have increasingly fine scales as one approaches the boundary, see figure 7.2b) and showed that the upper bound (7.9) could be attained up to an unknown logarithmic correction. More specifically, they showed

$$\frac{\mathscr{P}^{1/3}}{\log^{4/3} \mathscr{P}} \lesssim Q^s_{\max}(\mathscr{P}).$$

Soon after the work of Tobasco and Doering (2017), Motoki et al. (2018b), through a numerical optimization procedure, discovered complicated but rather beautiful three-dimensional steady branching flows (depending on $\mathscr{P}$) that appear to display a heat transfer rate $Q^s_{\max}(\mathscr{P}) \sim \mathscr{P}^{1/3}$.

In this paper, we rigorously prove the empirical results of Motoki et al. (2018b) and show that $\mathscr{P}^{1/3} \lesssim Q^s_{\max}(\mathscr{P})$ by constructing three-dimensional steady branching pipe flows. Our main result is:

Theorem 7.1.4 (Steady three-dimensional case)**.** *Let* Ω *be* Ω^{3D} *as defined in (7.4a-b). Then there exists two positive constants* $\mathscr{P}_0$ *and* C *such that* $Q^s_{\max}$*, as defined in (7.5), obeys the following lower bound:*

$$C\mathscr{P}^{1/3} \leq Q^s_{\max}(\mathscr{P})$$

for $\mathscr{P}_0 \leq \mathscr{P}$*. The constants* $\mathscr{P}_0$ *and* C *depends on* l_x *as follows:*

$$\mathscr{P}_0(l_x) = \frac{1+l_x^2}{l_x^2}\mathscr{P}'_0, \quad C(l_x) = \frac{l_x^{8/3}}{1+l_x^{8/3}}C',$$

where $\mathscr{P}'_0, C' > 0$ *are two universal constants.*

Remark 7.1.5. *Combining the result of Theorem 7.1.4 with the upper bound (7.9) and Remark 7.1.1, we fully characterize the exact behavior of maximum heat transfer in three dimensions. In particular, we have* $Q^s_{\max} \sim \mathscr{P}^{1/3}$ *(as a result* $Q^u_{\max} \sim \mathscr{P}^{1/3}$*) in three dimensions. Whether* $Q^s_{\max} \sim \mathscr{P}^{1/3}$ *in two dimensions as well as an open problem (see Conjecture 7.1.9).*

Remark 7.1.6. *It is clear that if* $l_x \geq 1$*, then* $\mathscr{P}_0$ *and* C *are bounded from below by two positive constants independent of* l_x*. Therefore, assuming* $l_x \geq 1$*, i.e., for sufficiently wide domains, we can also restate the above theorem where* $\mathscr{P}_0$ *and* C *are two positive constants independent of any parameter.*

Remark 7.1.7. *We consider here a periodic setting in the* x *and* y *directions. As the flows that we construct to prove the theorem have a compact support in space, the theorem remains true if* Ω *is a closed box of size* l_x *and* l_y *with insulating and no-slip side walls.*

7.1.4 Overview and philosophy of the proof

The variational principle

The proof of Theorem 7.1.4 relies on a variational principle for the heat transfer derived by Doering and Tobasco (2019), which was inspired by the work in homogenization theory such as of Avellaneda and Majda (1991); Fannjiang and Papanicolaou (1994) about estimating the effective diffusivity in a random or periodic array of vortices. To state the result, we start by defining two admissible sets:

$$\mathcal{A}^s \coloneqq L^\infty(\Omega;\mathbb{R}^3) \cap H^1_0(\Omega;\mathbb{R}^3), \tag{7.10a}$$

$$\mathcal{X}^s \coloneqq H^1_0(\Omega). \tag{7.10b}$$

For steady velocity fields, the variational principle associated with the maximization of heat transfer can be stated as

Proposition 7.1.8 (Doering and Tobasco (2019))**.** *For $Q^s_{\max}$ given by (7.5), we have*

$$Q^s_{\max}(\mathscr{P}) - 1 = \sup_{\substack{\boldsymbol{u}\in\mathcal{A}^s \\ \nabla\cdot\boldsymbol{u}=0}} \sup_{\substack{\xi\in\mathcal{X}^s \\ \xi\not\equiv 0}} \frac{\left(\fint_\Omega u_z \xi \,\mathrm{d}\boldsymbol{x}\right)^2}{\fint_\Omega |\nabla\Delta^{-1}(\boldsymbol{u}\cdot\nabla\xi)|^2 \,\mathrm{d}\boldsymbol{x} + \frac{1}{\mathscr{P}}\fint_\Omega |\nabla\boldsymbol{u}|^2 \,\mathrm{d}\boldsymbol{x} \fint_\Omega |\nabla\xi|^2 \,\mathrm{d}\boldsymbol{x}}. \tag{7.11}$$

In (7.11), Δ^{-1} denotes the inverse Laplacian operator in Ω corresponding to the homogeneous Dirichlet boundary conditions. For completeness, we provide a derivation of this variation principle in Appendix 7.B, which is adapted from Doering and Tobasco (2019).

From the variational principles (7.11), we see that any choice of admissible

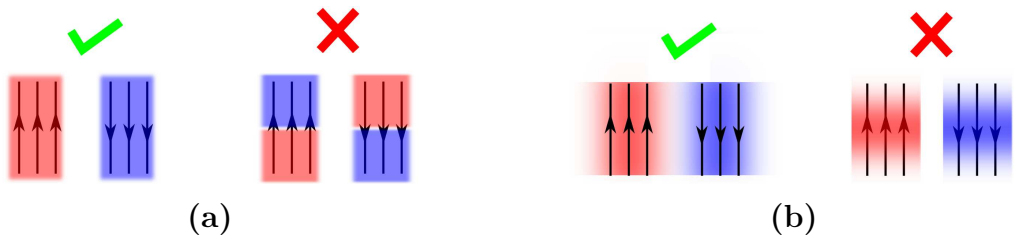

Figure 7.1: Panel (a) illustrates good and bad strategies to maximize term I defined in (7.12a-c). In the good scenario, ξ is positive (indicated by red color) where the flow is moving upward (positive z-direction) and is negative (blue color) where the flow is moving downward. Therefore, u_z and ξ are positively correlated. This is not the case in the bad scenario. Panel (b) illustrates good and bad strategies to minimize term II. In the good scenario, $\nabla\xi$ is perpendicular to $\boldsymbol{u}$, hence $\boldsymbol{u}\cdot\nabla\xi \equiv 0$, i.e., ξ is constant along the streamlines and therefore the term II zero. In the bad scenario, $\nabla\xi$ is parallel to $\boldsymbol{u}$, so the term II is nonzero.

velocity field $\boldsymbol{u}$ and scalar field ξ provides a lower bound on the heat transfer. Our goal, therefore, is to find a "good" flow field $\boldsymbol{u}$ (depending on $\mathscr{P}$), and a corresponding ξ, for which the dependence on $\mathscr{P}$ of the lower bound obtained matches that of the theoretical upper bound (7.9), namely, $\mathscr{P}^{1/3}$.

We closely analyze each term involved in the right-hand side of (7.11). We label them

$$I = \left(\fint_\Omega u_z\xi \,\mathrm{d}\boldsymbol{x}\right)^2, \qquad II = \fint_\Omega |\nabla\Delta^{-1}(\boldsymbol{u}\cdot\nabla\xi)|^2 \,\mathrm{d}\boldsymbol{x},$$
$$III = \frac{1}{\mathscr{P}}\fint_\Omega |\nabla\boldsymbol{u}|^2 \,\mathrm{d}\boldsymbol{x}\fint_\Omega |\nabla\xi|^2 \,\mathrm{d}\boldsymbol{x}, \qquad \text{(7.12a-c)}$$

and henceforth refer to them as the transport term (I), the nonlocal term (II) and the dissipation term (III), respectively.

In order to obtain a good lower bound, we would ideally like to choose $\boldsymbol{u}$ and ξ to maximize the right-hand side of (7.11) as much as possible. This, in turn, means we should aim to maximize I and minimize II and III.

To maximize I, we should choose a flow field $\boldsymbol{u}$ such that its z-component is

"positively correlated" with the ξ field. Figure 7.1a shows examples of a good and a bad scenario. To minimize II, we should choose $\boldsymbol{u}$ to be perpendicular to $\nabla\xi$ in most of the domain, which can alternatively be stated as ξ should be constant along the streamlines of the flow $\boldsymbol{u}$. Figure 7.1b shows examples of a good and a bad scenario.

Our aim at this point is to provide heuristic but compelling arguments why trial velocity profiles such as (i) standard convection rolls and (ii) the two-dimensional steady branching flows considered by Tobasco and Doering (2017); Doering and Tobasco (2019) are not sufficient to prove Theorem 7.1.4. By diligently inspecting the limitations of these trial flow fields, we are then naturally led to propose three-dimensional branching pipe flows as the optimal solution.

Convection rolls

The first choice of a trial velocity profile $\boldsymbol{u}$ that comes to mind is the one associated with planar convection rolls, as this is one of the simplest incompressible flow fields capable of transporting heat by advection. Figure 7.2a shows the streamlines of typical convection rolls. In the bulk region, far from the horizontal walls, the flow either moves up or down. To maintain the incompressibility constraint, the flow must turn around in a boundary layer near the walls. We then select a ξ field accordingly, in an attempt to maximize I and minimize II (see figure 7.1).

The advantage of this configuration is that it is possible to restrict the region where $\boldsymbol{u}\cdot\nabla\xi$ is non-zero (which eventually contributes toward II) to the boundary layer only. However, this choice turns out to be particularly bad with respect to the term III. Indeed, assuming the flow velocity $|\boldsymbol{u}| \sim 1$ in the bulk region, then we must have a "large" fluid velocity $|\boldsymbol{u}| \sim \ell/\delta$ in the boundary layer because

of the incompressibility condition, where ℓ is the width of a single convection roll. Consequently, $\nabla \boldsymbol{u} \sim \ell/\delta^2$, which essentially becomes "very large" for small boundary layer thickness δ. Performing a formal scaling analysis of each individual terms in the variational principle (7.11) yields

$$Q^s_{\max} \gtrsim \frac{1}{\delta + \frac{1}{\mathscr{P}}\left(\frac{\ell^2}{\delta^4} + \frac{1}{\ell^4}\right)}.$$

The right-hand side is optimized by choosing $\delta \sim \mathscr{P}^{-3/11}$ and $\ell \sim \mathscr{P}^{-2/11}$, which leads to

$$Q^s_{\max} \gtrsim \mathscr{P}^{3/11}.$$

This scaling recovers the result of Souza et al. (2020), who rigorously showed that $Q^s(\boldsymbol{u}) \sim \mathscr{P}^{3/11}$ for a particular choice of convective rolls, as well as the results of Howard (1963); Doering and Constantin (1996) who found the same scaling in the context of Rayleigh–Bénard convection. The exponent 3/11 is clearly less than 1/3, suggesting that the convection rolls may not be the most efficient way of transporting heat at high $\mathscr{P}$.

Two-dimensional steady branching flows

One way to improve the heat transport is to consider a flow field with a branching structure, i.e., where the scale of flow patterns becomes smaller (possibly in a self-similar manner) as one approaches the walls, an idea that goes back to Busse (Busse, 1969). The branching ends after a finite number of steps N, which depends on $\mathscr{P}$. The idea behind the branching is to continue dividing the flow into "multiple channels" as it moves towards the wall, which helps maintain the typical magnitude of the velocity field to be order unity throughout the domain. Letting

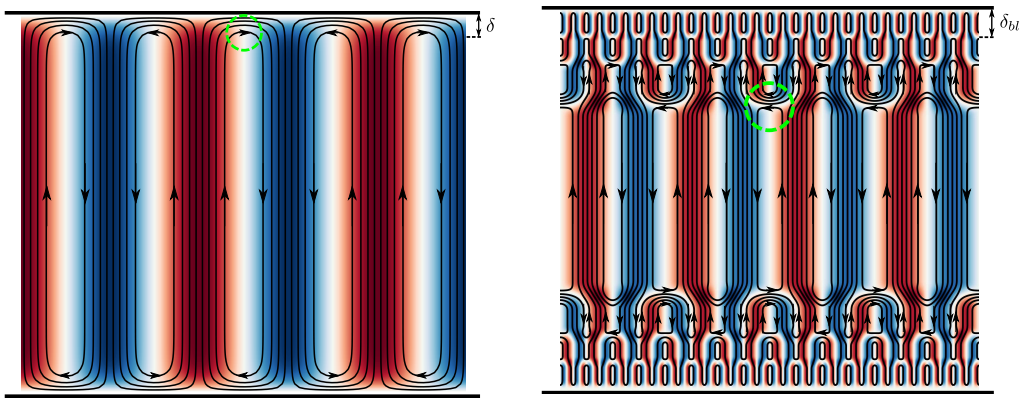

Figure 7.2: Panel (a) shows the streamlines of a set of typical convective rolls. Panel (b) shows the streamlines of a steady two dimensional branching flow. In both figures, the streamlines have been overlayed with a ξ field according to the good scenario described in figure 7.1a (i.e. ξ is positive whenever u_z is positive, and ξ is negative whenever u_z is negative). The red color indicates a positive value of ξ, whereas the blue color indicates a negative value. The dashed circles in both figures show regions where $\boldsymbol{u} \cdot \nabla \xi$ is nonzero.

δ_{bl} be the vertical thickness of the last branching level (namely, the boundary layer), then such branching flows have $\nabla \boldsymbol{u} \sim \delta_{bl}^{-1}$ in the boundary layer, which is significantly smaller than $\nabla \boldsymbol{u} \sim \delta_{bl}^{-2}$ in the case of convection rolls. As a result, branching greatly helps minimize term III compared with a flow without branching.

A replica of the two-dimensional steady branching flow structure constructed by Tobasco and Doering (2017); Doering and Tobasco (2019) is shown in figure 7.2b and we have overlaid the streamlines with a ξ field according to the good scenario shown in figure 7.1a. Branching in two dimensions requires some part of the flow to fold back at every branching level. Although this solves the problem regarding the size of term III, it creates a different topological issue. From figure 7.2b, it becomes clear that $\nabla \xi$ is parallel to $\boldsymbol{u}$ not just in the boundary layer but also in the bulk at every branching level. A typical region is shown in the dashed

circle in figure 7.2b. As a result, $\boldsymbol{u}\cdot\nabla\xi$ is nonzero (which ultimately increases term II) in a significant portion of the domain compared with the case of convection rolls where this term was nonzero only in the boundary layer. Furthermore, there does not appear to be a way around this topological obstruction by simply choosing a different ξ field. This is because the streamlines of the flow $\boldsymbol{u}$ continually fold back throughout the branching structure, from the bulk to the boundary layer, (see figure 7.2b) and leaving only very few streamlines to continue towards the boundary layer. It therefore appears that the 'good' strategy of figure 7.1a (which chooses ξ positive wherever u_z is positive), is not compatible with maintaining ξ constant along streamlines (even in the bulk). In other words, it does not seem to be possible to maximize I and minimize II at the same time in two dimensions. However, it turns out the situation is still much better than the convection rolls and a formal scaling analysis (see Doering and Tobasco, 2019) shows that

$$Q^s_{\max} \gtrsim \frac{1}{\ell_{bl} + \int_{\frac{1}{2}}^{1-\delta_{bl}} (\ell')^2 \,\mathrm{d}z + \frac{1}{\mathscr{P}} \left(\frac{1}{\ell^2_{bulk}} + \int_{\frac{1}{2}}^{1-\delta_{bl}} \frac{1}{\ell^2} \,\mathrm{d}z + \frac{1}{\ell_{bl}} \right)^2},$$

where ℓ_{bulk} and ℓ_{bl} denote the horizontal width of a typical roll in the bulk region and in the boundary layer region, respectively, while the function $\ell(z)$ captures the change of the roll width as a function of the z coordinate. After optimizing the unknown parameters ($\delta_{bl}, l_{bulk}, l_{bl}$ and $l(z)$), one can at best show

$$Q^s_{\max} \gtrsim \frac{\mathscr{P}^{1/3}}{\log^{4/3} \mathscr{P}},$$

which is result of Tobasco and Doering (2017); Doering and Tobasco (2019).

Whether there exists a two-dimensional steady flow that can overcome the topological obstruction elaborated above to show $\mathscr{P}^{1/3} \lesssim Q^s_{\max}$ remains an open

question. Based on the heuristic reasons given previously, we believe that there are no such flows and therefore conjecture the following:

Conjecture 7.1.9 (Weak)**.** *Let* Ω *be* Ω^{2D} *given by (7.4a-b). Then the heat transfer defined in (7.5) obeys*

$$Q^s_{\max} = o(\mathscr{P}^{1/3})$$

for large $\mathscr{P}$*, where 'o' denotes the little-o.*

The weak conjecture states that $Q^s_{\max}$ is asymptotically smaller than $\mathscr{P}^{1/3}$ but does not identify the correct asymptotic scaling of $Q^s_{\max}$ at large $\mathscr{P}$. It is reasonable to assume that the lower bound estimate of Tobasco and Doering (2017); Doering and Tobasco (2019) could be sharp. We therefore also conjecture:

Conjecture 7.1.10 (Strong)**.** *Let* Ω *be* Ω^{2D} *given by (7.4a-b). Then the heat transfer defined in (7.5) obeys*

$$Q^s_{\max} \sim \frac{\mathscr{P}^{1/3}}{\log^{4/3} \mathscr{P}},$$

for large $\mathscr{P}$*.*

We strongly believe that the weak conjecture is true but have somewhat less confidence that the strong conjecture is also true.

Three-dimensional steady branching pipe flows

The novelty of this work comes from the realization that the topological obstruction discussed above can be overcome by taking advantage of the third dimension. Indeed, in three dimensions, it is possible to construct flows with a branching structure that continues all the way to the wall without the need to

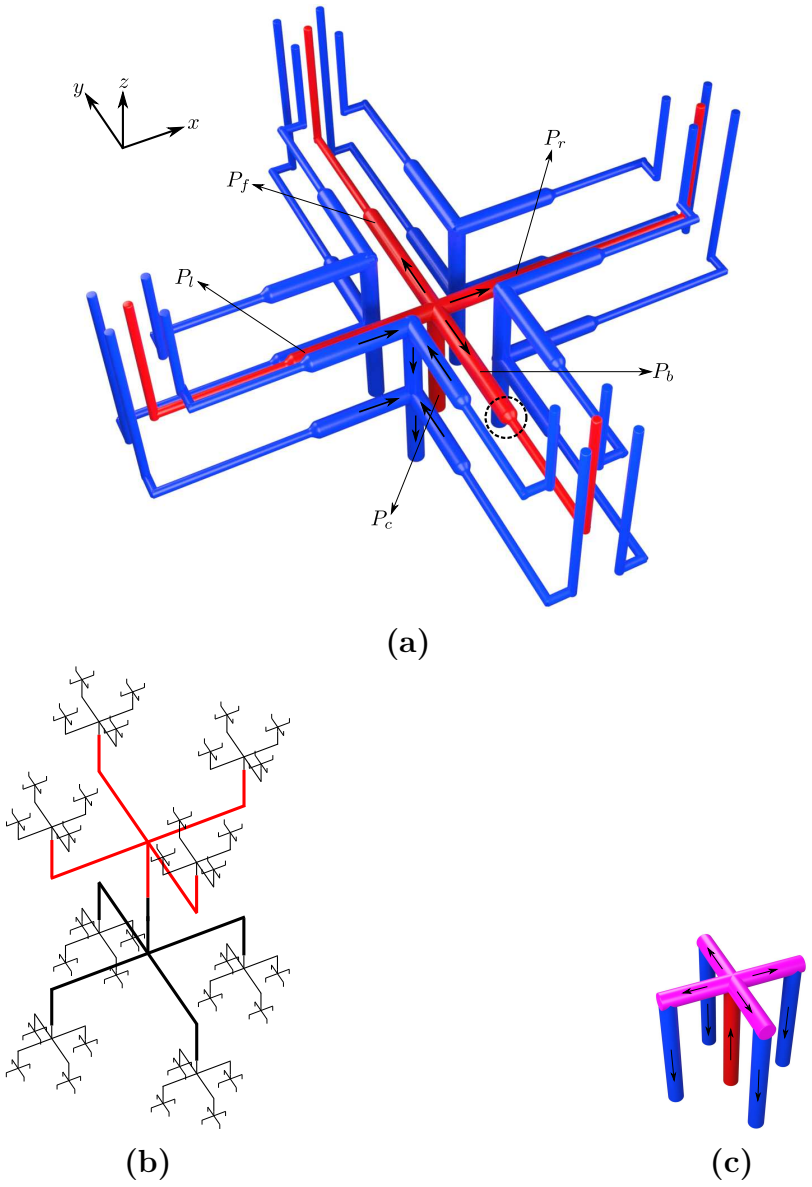

Figure 7.3: Illustration of the branching pipe flow. Panel (a): the parent construct $\overline{\boldsymbol{u}}$. It consists of red and blue pipes which are the part of pipelines $\boldsymbol{P}_{up}$ and $\boldsymbol{P}_{down}$, respectively. In panel (a), arrows are used in some pipes to show the direction of the flow. The reducer region of a pipe, in which the radius of the pipe decreases by a factor of half to ensure that the velocity remains, is also shown using a dashed circle. Panel (b): the branching skeleton. To build the main copy $\overline{\boldsymbol{u}}_N$ away from the boundary layer, we place the appropriately dilated version of the parent construct $\overline{\boldsymbol{u}}$ along the skeleton up to N levels. Panel (c): the parent construct $\overline{\boldsymbol{u}}_b$, used in the boundary layer. In the construct $\overline{\boldsymbol{u}}_b$, the flow from red pipes turn back to blue pipes (shown in the pink color). A 2D cartoon of the resultant pipe flow is shown in figure 7.4.

fold back as in the two-dimensional case. Therefore, in three dimensions, it is possible to construct a flow field $\boldsymbol{u}$ that has a branching structure that ensures $|\boldsymbol{u}| \sim 1$ everywhere, and a scalar field ξ such that u_z and ξ always have the same sign and $\boldsymbol{u} \cdot \nabla \xi = 0$ everywhere except in the boundary layer. The construction of the flow field $\boldsymbol{u}$ is both self-similar, and has finite support, so it looks like a branching pipe flow.

The parent construct used to generate the self-similar flow $\boldsymbol{u}$ and scalar field ξ is shown in figure 7.3a. It consists of two different types of pipes, one in which the flow moves up (shown in red), so we choose ξ positive in this region, and one in which the flow moves down (shown in blue), so we choose ξ negative in this region. By placing appropriately scaled copies of this parent construct along the tree structure shown in figure 7.3b, we obtain the desired self-similar branching flow field. The self-similar construction does not continue forever, however, it truncates after a finite number of levels N that depends on the value of $\mathscr{P}$. After N branching levels, the flow finally folds back in the boundary layer, according to the construct shown in figure 7.3c. This is the region where the hot and cold pipelines finally merge and where $\boldsymbol{u} \cdot \nabla \xi$ is nonzero. A two-dimensional cartoon projection of this three-dimensional branching pipe structure is shown in figure 7.4. This projection also illustrates the appearance of the topological obstruction in two dimensions which informally can be expressed as "it is not possible to build two branching channels, one hot (in which the flow moves up) and other one cold (in which the flow moves down), in two-dimensions without having them intersect."

Using this choice of flow $\boldsymbol{u}$ and scalar field ξ, we demonstrate in section 7.3 that a formal scaling analysis of the various terms in the variational principle

stated in Proposition (7.1.8) yields

$$Q^s_{\max} \gtrsim \frac{1}{2^{-N} + \frac{4^N}{\mathscr{P}}}. \tag{7.13}$$

The right-hand-side of this equation is optimized by choosing $N = \lceil \log_2 \mathscr{P}^{1/3} \rceil$, so we find that $Q^s_{\max} \gtrsim \mathscr{P}^{1/3}$. Theorem 7.1.4 is the rigorous result of this statement, which will be proved in the subsequent sections. The construction carried out in this paper can thus be summarized in three steps.

- Step I: Creating the parent constructs (the building blocks)

  The velocity fields from this step form the basis for the self-similar construction in the second step. In this step, we construct (i) $\overline{\boldsymbol{u}}$ (figure 7.3a), which is used to build branching flow away from the boundary layer. (ii) $\overline{\boldsymbol{u}}_b$ (figure 7.3c), which is used in the boundary layer to truncate the branching structure.

- Step II: Construction of the main copy (a single tree)

  In this step, we assemble the appropriately dilated copies of the parent constructs from the previous step to build the flow field $\overline{\boldsymbol{u}}_N$ (a 2D cartoon is shown in figure 7.4). Here, N denotes the number of branching levels which depends on $\mathscr{P}$. We also refer to this main copy as a single tree.

- Step III: Construction of the final flow field (a forest)

  The flow field constructed in the last step is enough to capture the correct dependence of $Q^s_{\max}$ on $\mathscr{P}$. However, to capture the correct dependence on the domain length and width l_x and l_y, we build the final flow field $\boldsymbol{u}$ by placing several copies of the tree side-by-side to fill the whole domain, which then looks like a forest.

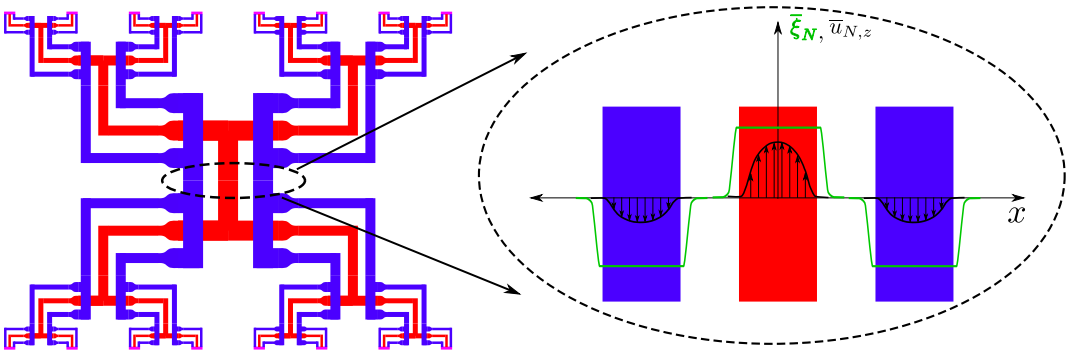

Figure 7.4: shows a 2D cartoon of the main copy $\overline{\boldsymbol{u}}_N$. The pipeline $\boldsymbol{P}_{up}$ is shown in red color and the pipeline $\boldsymbol{P}_{down}$ is shown in blue color. In the blow-up figure of a section of the pipeline, the graph of $\overline{\xi}_N$ is also shown. Notice is that $\overline{\xi}_N$ is constant in the support of $\overline{\boldsymbol{u}}_N$.

7.1.5 Organization of the paper

The rest of paper is organized as follows. In section 7.2, we introduce a few notations and preliminaries that will be frequently used throughout the paper. In section 7.3, we perform Step III of the construction and prove the main theorem. We provide a detailed sketch of the parent constructs in section 7.4. We then carry out Step I and Step II. We provide a proof of Proposition 7.3.2 (essential for the analysis of the nonlocal term defined in (7.12a-c)) in section 7.A. We close by discussing implications of our results in section 7.5. A few of the more cumbersome but trivial calculations required to finish the proofs are carried out in appendices.

Acknowledgement

A.K. thanks P. Garaud for a careful read of the paper and providing comments. A.K. also thanks I. Tobasco for providing comments, an invitation to visit University of Illinois Chicago and for several useful discussions.

7.2 Notation and preliminaries

The three domains we will be frequently using in this paper are: $\mathbb{R}^3$, Ω and D, where

$$\Omega \coloneqq \mathbb{T}_{l_x} \times \mathbb{T}_{l_y} \times (-1/2, 1/2), \qquad D \coloneqq \mathbb{R}^2 \times (-1/2, 1/2). \tag{7.14a-b}$$

Here, for some $l > 0$, $\mathbb{T}_l \coloneqq (\mathbb{R}/l\mathbb{Z})$ and $\mathbb{T}_l$ is identified with $[-l/2, l/2)$ in the usual way. In the rest of this section, V will denote either of these three domains: $\mathbb{R}^3$, Ω and D, whereas $\widetilde{V}$ will denote either $\mathbb{R}^3$ or D. Let $\boldsymbol{x}, \boldsymbol{x}' \in \widetilde{V}$, for which we denote

$$\boldsymbol{x}_\parallel \coloneqq (x, y, 0), \qquad \text{and} \qquad |\boldsymbol{x} - \boldsymbol{x}'|_\parallel \coloneqq |\boldsymbol{x}_\parallel - \boldsymbol{x}'_\parallel|, \tag{7.15a-b}$$

where $|\cdot|$ denotes the Euclidean distance. Let $S \subseteq V$, we will use $\mathbf{1}_S$ to denote the indicator function corresponding to the set S.

We define the support of a scalar or a vector-valued function f on V as

$$\operatorname{supp} f \coloneqq \overline{\{\boldsymbol{x} \in V \,|\, f(\boldsymbol{x}) \neq 0\}}, \tag{7.16}$$

and the support only in the z variable as

$$\operatorname{supp}_z f \coloneqq \overline{\{z \in \mathbb{R} \,|\, (x, y, z) \in V, f(x, y, z) \neq 0\}}. \tag{7.17}$$

For a given $\boldsymbol{p} \in \mathbb{R}^3$, we define a translation map $T^{\boldsymbol{p}} : \mathbb{R}^3 \to \mathbb{R}^3$ as $T^{\boldsymbol{p}}(\boldsymbol{x}) = \boldsymbol{x} + \boldsymbol{p}$. The inverse map is therefore denoted as $T^{-\boldsymbol{p}}$. Then, if f is a scalar function or a vector-valued function on $\mathbb{R}^3$, we define the corresponding translated function

$T^{\boldsymbol{p}} f$ as

$$(T^{\boldsymbol{p}} f)(\boldsymbol{x}) = f(T^{-\boldsymbol{p}}(\boldsymbol{x})), \quad \text{where} \quad \boldsymbol{x} \in \mathbb{R}^3. \tag{7.18}$$

Similarly, for a given $\theta \in [0, 2\pi]$, we define a rotation map $\rho_\theta : \widetilde{V} \to \widetilde{V}$, which performs a counterclockwise rotation in the xy-plane by an angle θ. We denote the inverse map by $\rho_{-\theta}$. Then, if ζ is a scalar function on $\widetilde{V}$, we define the corresponding rotated scalar function $\rho_\theta \zeta$ on $\widetilde{V}$ as

$$(\rho_\theta \zeta)(\boldsymbol{x}) = \zeta(\rho_{-\theta}(\boldsymbol{x})), \quad \text{where} \quad \boldsymbol{x} \in \widetilde{V}. \tag{7.19}$$

Furthermore, if $\boldsymbol{v}$ is a vector-valued function defined on $\widetilde{V}$, we define the corresponding rotated vector-valued function $\rho_\theta \boldsymbol{v}$ on $\widetilde{V}$ as

$$(\rho_\theta \boldsymbol{v})(\boldsymbol{x}) = \rho_\theta \left(\boldsymbol{v}(\rho_{-\theta}(\boldsymbol{x})) \right), \quad \text{where} \quad \boldsymbol{x} \in \widetilde{V}. \tag{7.20}$$

Let us denote the $\sigma-$algebra of Borel sets by $\mathcal{B}(\mathbb{R}^3)$. Given a Radon measure $\mu : \mathcal{B}(\mathbb{R}^3) \to \mathbb{R}$ and a vector field $\boldsymbol{u} \in L^1_{loc}(\mathbb{R}^3; \mathbb{R}^3, \mu)$, the set function $\nu : \mathcal{B}(\mathbb{R}^3) \to \mathbb{R}^3$

$$\nu := (\nu_x, \nu_y, \nu_z) := (u_x \mu, u_y \mu, u_z \mu) \tag{7.21}$$

is called a vector-valued Radon measure. In what follows, we will also use the alternate notation $\nu = \boldsymbol{u}\mu$. The Riesz's theorem ensures that the space of vector-valued Radon measure $\mathcal{M}$ is dual to the space of compactly supported continuous vector fields $C_c(\mathbb{R}^3; \mathbb{R}^3)$ (Giaquinta et al., 1998; Maggi, 2012). Given a function $f \in C_c(\mathbb{R}^3)$ and $\nu \in \mathcal{M}$ as defined in (7.21), the integration of f with respect to

the measure ν is a vector in $\mathbb{R}^3$ and is given by

$$\int_{\mathbb{R}^3} f \,\mathrm{d}\nu = \left(\int_{\mathbb{R}^3} f u_x \,\mathrm{d}\mu, \int_{\mathbb{R}^3} f u_y \,\mathrm{d}\mu, \int_{\mathbb{R}^3} f u_z \,\mathrm{d}\mu \right), \tag{7.22}$$

and the convolution is given by

$$(f * \nu)(\boldsymbol{x}) = \int_{\mathbb{R}^3} f(\boldsymbol{x} - \boldsymbol{x}') \,\mathrm{d}\nu(\boldsymbol{x}'). \tag{7.23}$$

7.3 Step III of the construction: Proof of Theorem 7.1.4

In this section, we begin by performing Step III of the construction of the full flow field $\boldsymbol{u}$ and scalar function ξ. We assume the existence of main copies $\overline{\boldsymbol{u}}_N$ and $\overline{\xi}_N$ with properties stated in the proposition below. Then we place several of these copies together in Ω, to build the flow field $\boldsymbol{u}$ and scalar field ξ, which we then use in the variational principle (7.11) to prove Theorem 7.1.4.

Proposition 7.3.1. *For every positive integer N, there exist $\overline{\boldsymbol{u}}_N \in C_c^\infty(D;\mathbb{R}^3)$ and $\overline{\xi}_N \in C_c^\infty(D)$ such that*

(i) $\nabla \cdot \overline{\boldsymbol{u}}_N \equiv 0$,

(ii) $\operatorname{supp} \overline{\boldsymbol{u}}_N \cup \operatorname{supp} \overline{\xi}_N \Subset (-1/2,1/2) \times (-1/2,1/2) \times (-1/2,1/2)$,

(iii) $\operatorname{supp}_z(\overline{\boldsymbol{u}}_N \cdot \nabla \overline{\xi}_N) \Subset (1/2 - c_1 2^{-N}, 1/2 - c_2 2^{-N}) \cup (-1/2 + c_2 2^{-N}, -1/2 + c_1 2^{-N})$,

(iv) $\left\| \overline{\boldsymbol{u}}_N \cdot \nabla \overline{\xi}_N \right\|_{L^\infty(D)} \lesssim 2^N$,

(v) $\int_D |\nabla \overline{\boldsymbol{u}}_N|^2 \,\mathrm{d}\boldsymbol{x} + \int_D |\nabla \overline{\xi}_N|^2 \,\mathrm{d}\boldsymbol{x} \lesssim 2^N$,

(vi) $\int_D \overline{u}_{N,z} \overline{\xi}_N \,\mathrm{d}\boldsymbol{x} \geq c_3 > 0$,

Here, $0 < c_2 < c_1 < 1$ and c_3 are constants independent of N and $\overline{u}_{N,z}$ is the z-component of $\overline{\boldsymbol{u}}_N$.

Proof of Theorem 7.1.4. We construct $\boldsymbol{u}$ (and ξ) by appropriately placing several horizontally scaled copies of $\overline{\boldsymbol{u}}_N$ (and $\overline{\xi}_N$) from Proposition 7.3.1 side-by-side (see below for details). Specifically, let n_x and n_y be two positive integers, then we place $n_x n_y$ copies of $\overline{\boldsymbol{u}}_N$ (and $\overline{\xi}_N$) in a two-dimensional rectangular horizontal array. Then from the conditions on $\overline{\boldsymbol{u}}_N$ and $\overline{\xi}_N$ given in Proposition 7.3.1, we can obtain estimates on the various terms in the expression (7.11) and show that the desired lower bound on $Q^s_{\max}$, stated in Theorem 7.1.4.

More specifically, given $n_x, n_y \in \mathbb{N}$, we define two lengths d_x and d_y as follows:

$$d_x = \frac{l_x}{n_x} \quad \text{and} \quad d_y = \frac{l_y}{n_y}.$$

Next, we define $\boldsymbol{u} : D \to \mathbb{R}^3$ and $\xi : D \to \mathbb{R}$ as

$$\begin{aligned}
\boldsymbol{u}\left(xd_x - \frac{l_x}{2} + \frac{2i-1}{2}d_x, yd_y - \frac{l_y}{2} + \frac{2j-1}{2}d_y, z\right) &\coloneqq \overline{\boldsymbol{u}}_N(x,y,z) \\
\xi\left(xd_x - \frac{l_x}{2} + \frac{2i-1}{2}d_x, yd_y - \frac{l_y}{2} + \frac{2j-1}{2}d_y, z\right) &\coloneqq \overline{\xi}_N(x,y,z)
\end{aligned}$$

for all $i, j \in \mathbb{Z}$ and $(x, y, z) \in (-1/2, 1/2) \times (-1/2, 1/2) \times (-1/2, 1/2)$, otherwise, $\boldsymbol{u} \coloneqq \boldsymbol{0}$ and $\xi \coloneqq 0$. It is clear that $\boldsymbol{u}$ and ξ are $l_x - l_y-$periodic functions. It is the identification of these $l_x - l_y-$periodic functions with functions on $\Omega = \mathbb{T}_{l_x} \times \mathbb{T}_{l_y} \times (-1/2, 1/2)$, which we continue to denote as $\boldsymbol{u}$ and ξ, that we use throughout.

By construction, $\boldsymbol{u} \in C^\infty_c(\Omega; \mathbb{R}^3)$ and $\xi \in C^\infty_c(\Omega)$ and therefore belongs to the admissible sets $\mathcal{A}^s$ and $\mathcal{X}^s$ defined in (7.10a) and (7.10b), respectively. Having constructed these functions, we can now estimate the important terms in the

variational formula (7.11). Let's start with the following:

$$\fint_\Omega |\nabla \boldsymbol{u}|^2 \,\mathrm{d}\boldsymbol{x} = \frac{1}{l_x l_y}\int_\Omega |\nabla \boldsymbol{u}|^2 \,\mathrm{d}\boldsymbol{x} = \frac{n_x n_y}{l_x l_y}\int_{-\frac{l_x}{2}}^{-\frac{l_x}{2}+d_x}\int_{-\frac{l_y}{2}}^{-\frac{l_y}{2}+d_y}\int_{-\frac{1}{2}}^{\frac{1}{2}} |\nabla \boldsymbol{u}|^2 \,\mathrm{d}\boldsymbol{x}$$
$$\lesssim \frac{n_x n_y d_x d_y}{l_x l_y \min\{d_x^2, d_y^2, 1\}}\int_D |\nabla \overline{\boldsymbol{u}}_N|^2 \,\mathrm{d}\boldsymbol{x} \lesssim \frac{n_x n_y d_x d_y}{l_x l_y \min\{d_x^2, d_y^2, 1\}} 2^N. \quad (7.25)$$

Similarly, we have

$$\fint_\Omega |\nabla \xi|^2 \,\mathrm{d}\boldsymbol{x} \lesssim \frac{n_x n_y d_x d_y}{l_x l_y \min\{d_x^2, d_y^2, 1\}}\int_D |\nabla \overline{\xi}_N|^2 \,\mathrm{d}\boldsymbol{x} \lesssim \frac{n_x n_y d_x d_y}{l_x l_y \min\{d_x^2, d_y^2, 1\}} 2^N. \quad (7.26)$$

and

$$\fint_\Omega u_z \xi \,\mathrm{d}\boldsymbol{x} = \frac{n_x n_y d_x d_y}{l_x l_y}\int_D \overline{u}_{N,z}\,\overline{\xi}_N \,\mathrm{d}\boldsymbol{x} \geq \frac{n_x n_y d_x d_y c_3}{l_x l_y}, \quad (7.27)$$

Finally, we have

$$\|\boldsymbol{u}\cdot\nabla\xi\|_{L^\infty(\Omega)} \lesssim \frac{2^N}{\min\{d_x, d_y, 1\}}, \quad (7.28)$$

with

$$\mathrm{supp}_z(\boldsymbol{u}\cdot\nabla\xi) \Subset$$
$$(1/2 - c_1 2^{-N}, 1/2 - c_2 2^{-N}) \cup (-1/2 + c_2 2^{-N}, -1/2 + c_1 2^{-N}). \quad (7.29)$$

Provided $N \geq 3$, we obtain

$$\fint_\Omega |\nabla \Delta^{-1}\,\mathrm{div}(\boldsymbol{u}\xi)|^2 \,\mathrm{d}\boldsymbol{x} \lesssim \frac{1}{2^N \min\{d_x^2, d_y^2, 1\}}, \quad (7.30)$$

using the following proposition.

Proposition 7.3.2. *Let $f \in L^\infty(\Omega)$ such that $\operatorname{supp}_z f \subseteq (1/2 - c_1\varepsilon, 1/2 - c_2\varepsilon) \cup (-1/2 + c_2\varepsilon, -1/2 + c_1\varepsilon)$, where $0 < c_2 < c_1 < 1$ and $\varepsilon < 1/4$ are three constants, then we have*

$$\fint_\Omega |\nabla \Delta^{-1} f|^2 \, \mathrm{d}\boldsymbol{x} \lesssim \varepsilon^3 \, \|f\|^2_{L^\infty(\Omega)} \,. \tag{7.31}$$

Proof of the Proposition 7.3.2 is provided in section 7.A.

At this point, we prescribe n_x and n_y. As stated in the introduction, we have chosen $l_x \leq l_y$ without loss of generality. We divide the proof of the theorem into two parts: (i) when $l_x \geq 1$, (ii) when $l_x < 1$.

In the first case ($l_x \geq 1$), we choose

$$n_x = \lceil l_x \rceil \quad \text{and} \quad n_y = \lceil l_y \rceil \,, \tag{7.32}$$

where $\lceil \cdot \rceil$ is the ceiling function. Then from the definitions of d_x and d_y, we have

$$\frac{1}{2} \leq d_x, d_y \leq 1. \tag{7.33}$$

Noting this and using the estimates (7.25), (7.26), (7.27) and (7.28) in (7.11) gives

$$\frac{1}{c_5 \frac{1}{2^N} + c_6 \frac{4^N}{\mathscr{P}}} \lesssim Q_{\max}(\mathscr{P}), \tag{7.34}$$

where c_5 and c_6 are two constants independent of any parameter. Choosing the value of N as

$$N = \left\lceil \frac{1}{3} \log_2 \frac{c_5 \mathscr{P}}{2c_6} \right\rceil, \tag{7.35}$$

we can show

$$\mathscr{P}^{1/3} \lesssim Q_{\max}(\mathscr{P}) \tag{7.36}$$

provided

$$\mathscr{P} \gtrsim \frac{2c_6}{c_5}. \tag{7.37}$$

In the second case, when $l_x < 1$, we choose

$$n_x = 1 \quad \text{and} \quad n_y = \left\lceil \frac{l_y}{l_x} \right\rceil, \tag{7.38}$$

then we have

$$d_x = l_x \quad \text{and} \quad \frac{l_x}{2} \leq d_y \leq l_x. \tag{7.39}$$

The estimates (7.25), (7.26), (7.27) and (7.28) then imply

$$\frac{1}{c_7 \frac{1}{2^N l_x^2} + c_8 \frac{4^N}{\mathscr{P} l_x^4}} \lesssim Q_{\max}(\mathscr{P}), \tag{7.40}$$

for some positive constants c_7 and c_8 independent of any parameter. Now choosing the following value of N

$$N = \left\lceil \frac{1}{3} \log_2 \frac{c_7 \mathscr{P} l_x^2}{2c_8} \right\rceil, \tag{7.41}$$

we obtain

$$\mathscr{P}^{1/3} l_x^{8/3} \lesssim Q_{\max}(\mathscr{P}), \tag{7.42}$$

provided

$$\mathscr{P} \gtrsim \frac{2c_8}{c_7 l_x^2}, \tag{7.43}$$

which then completes the proof of the Theorem 7.1.4. □

7.4 Construction of three-dimensional branching pipe flow: Step I and Step II

Having established that if Proposition 7.3.1 holds, then we can prove Theorem 7.1.4, we now turn to the more delicate question of how to prove Proposition 7.3.1. In other words, the goal of this section is to perform Step I, which is to build the parent constructs $\overline{\boldsymbol{u}}$, $\overline{\boldsymbol{u}}_b$, $\overline{\xi}$ and $\overline{\xi}_b$, followed by Step II, which is to create the main copies $\overline{\boldsymbol{u}}_N$ and $\overline{\xi}_N$. We start by giving a sketch of the parent copies and how to assemble their dilated versions to create the main copies, which is then followed by the actual construction in Step I and Step II.

7.4.1 An overivew of the construction

As the support of the velocity field $\overline{\boldsymbol{u}}_N$ looks like a pipe network (see figure 7.4) and the flow field itself is similar to flow in pipes, we use words such as pipe, pipe network or pipeline for ease of exposition below.

The main copy $\overline{\boldsymbol{u}}_N$ consists of two "pipelines": one in which the flow goes upward (the positive z-direction) in a branching fashion, $\boldsymbol{P}_{up}$ (shown in red in figure 7.4) and one in which the flow goes downward (the negative z-direction), again in a branching fashion, $\boldsymbol{P}_{down}$ (shown in blue). The part of the pipelines

$\boldsymbol{P}_{up}$ and $\boldsymbol{P}_{down}$ that resides in the parent construct $\overline{\boldsymbol{u}}$ is also shown in red and blue, in figure 7.3.

The volume flow rate through both of these pipelines is the same. In what follows, we describe the pipeline design only for $z \geq 0$ and simply use mirror symmetry to construct the pipeline for $z \leq 0$. In the parent construct, $\boldsymbol{P}_{up}$ starts from a center pipe, denoted by P_c in figure 7.3a. The center pipe goes up vertically, until a first junction at $z = 1/8$, where it splits into four pipes going right (positive x-direction) P_r, left (negative x-direction) P_l, front (positive y-direction) P_f and back (negative y-direction) P_b. In plumbing terms, the junction of these pipes would be known as a 5-way cross. The horizontal extent of these pipes is $1/4$. Near the junction, each of the four horizontal pipes has a radius equal to that of P_c. Therefore, because of incompressibility condition, the speed of the flow goes down by a factor of four as the flow enters from P_c to P_r, P_l, P_f and P_b. However, away from the junction (midway), a constriction is added to reduce the radii of these four pipes by a factor of half after which the speed of the flow regains its original value (again because of incompressibility). In plumbing terms, the region where the radius of the pipe decreases is known as a reducer. Finally, these horizontal pipes bend upward up to a level $z = 1/4$. With this construction, the pipeline $\boldsymbol{P}_{up}$ near $z = 1/4$ consists of four pipes whose radius is half that of the pipe P_c near $z = 0$ but all of them with same magnitude of velocity. We can then continue the pipeline from $z = 1/4$ to $z = 1/4+1/8$ by adding four half-sized copies of the original one. In a similar way, the pipeline can be further continued up to any number of levels N.

The pipeline P_{down} in which the flow goes down, consists of four pipes surrounding P_c, each with radii equal to that of P_c. The speed of the flow in one of these four pipes is $1/4$ the speed of the flow in P_c, ensuring that the total volume

flow going upward and downward are the same. The flow in these four pipes come from the horizontally placed pipes that are similarly surrounding the pipes P_r, P_l, P_f and P_b as shown in figure 7.3a. The radii of these horizontal pipes, similar to the case of the previous pipeline, changes by a factor of two to ensure that the flow velocity in the vertical pipes that they connect remains the same. Finally, before bending in the upward direction, the horizontal pipes, in this pipeline, close their distance to the horizontal pipes from pipeline $\boldsymbol{P}_{up}$ to make sure that we can glue a self-similar parent copy of half-the-size to continue the pipeline.

The self-similar continuation of both pipelines truncates after a fixed number of levels N (depending on $\mathscr{P}$). In the last level (closest to the wall), the two pipelines merge, i.e., the flow from the pipeline $\boldsymbol{P}_{up}$ goes to the pipeline $\boldsymbol{P}_{down}$. This done by gluing an appropriately scaled parent construct $\overline{\boldsymbol{u}}_b$ as shown in figure 7.3c.

Once we have the main copy $\overline{\boldsymbol{u}}_N$ ready, we can select $\overline{\xi}_N$. We choose $\overline{\xi}_N$ (everywhere except in the boundary layers where the pipelines truncate) to be such that its value is a positive constant ξ_0 in the region where the pipeline $\boldsymbol{P}_{up}$ lies and is $-\xi_0$ in the region where the pipeline $\boldsymbol{P}_{down}$ lies and decays to zero rapidly away from these pipelines (see figure 7.4). There are two advantages with this choice:

(i) The quantity $\overline{\boldsymbol{u}}_N \cdot \nabla\overline{\xi}_N$ is identically zero except in the last level of construction where the branching structure truncates. Therefore, it is possible to restrict the support of $\overline{\boldsymbol{u}}_N \cdot \nabla\overline{\xi}_N$ to a thin horizontal layer close to the wall, which helps in obtaining a good estimate on the nonlocal term in (7.12a-c).

(ii) The transport term simplifies as follows.

$$\int \overline{u}_{N,z}\, \overline{\xi}_N \, \mathrm{d}\boldsymbol{x} \approx \xi_0 \int_{\boldsymbol{P}_{up}} \overline{u}_{N,z} \, \mathrm{d}\boldsymbol{x} - \xi_0 \int_{\boldsymbol{P}_{down}} \overline{u}_{N,z} \, \mathrm{d}\boldsymbol{x} \approx 2\xi_0 V_0,$$

where $V_0 > 0$ is the total flow (constant volume flux through any horizontal section) going upward in pipeline $\boldsymbol{P}_{up}$ or downward in pipeline $\boldsymbol{P}_{down}$. There will be minor corrections in the region where the pipelines truncate, which is why we use the approximate symbol.

In summary, we built two pipelines with a self-similar "tree-like" branching structure. The first one, $\boldsymbol{P}_{up}$, is "hot" (as $\overline{\xi}_N$ is positive in that region) in which the flow goes up and the second one, $\boldsymbol{P}_{down}$, is "cold" (as $\overline{\xi}_N$ is negative) and surrounds (without touching) the hot pipeline $\boldsymbol{P}_{up}$. This type of "disentanglement" of the hot pipeline from the cold one is possible in three dimensions but not in two dimensions and is the main reason behind the proof of Theorem 7.1.4.

7.4.2 Step I: Construction of the parent copies

The purpose of this subsection is to build the parent constructs: $\overline{\boldsymbol{u}}$, $\overline{\boldsymbol{u}}_b$ and the trial ξ-field: $\overline{\xi}$, $\overline{\xi}_b$. Let us define a few parameters that will be frequently used in this section:

$$\gamma = \frac{1}{500}, \qquad \lambda = \frac{1}{100}, \qquad \delta = \frac{1}{20}. \tag{7.44}$$

These parameters can roughly be understood as follows. The parameter γ can be thought of as the radius of pipes in which the flow field is supported, whereas λ is the radius of pipes in which the $\xi-$field is supported and δ denotes the distance between pipeline $\boldsymbol{P}_{up}$ and $\boldsymbol{P}_{down}$ in the parent copy $\overline{\boldsymbol{u}}$.

The flow field $\overline{\boldsymbol{u}}$ and $\overline{\boldsymbol{u}}_b$

To construct the flow field, the basic idea is to define an appropriate vector-valued Radon measure supported on a set. This set is a collection of line segments and rays, which, in a loose sense, form the skeleton of the pipelines whose sketch is described in subsection 7.4.1. Most of the desired flow field will then be created by regularizing the Radon measure using a convolution with a mollifier, except in the reducer region of the pipelines. The flow field in the reducer region will be designed separately with the help of an axisymmetric streamfuction.

We start by defining a few important points in $\mathbb{R}^3$, which will be helpful in creating the "skeleton" of the pipelines. We define

$$\boldsymbol{p}_1 \coloneqq (0,0,0), \quad \boldsymbol{p}_2 \coloneqq (0,0,1/8), \quad \boldsymbol{p}_3 \coloneqq (1/4,0,1/8), \quad \boldsymbol{p}_4 \coloneqq (1/4,0,1/4),$$

and

$$\boldsymbol{q}_1^{i,j} \coloneqq (\delta,\, j\delta,\, 0)\,, \quad \boldsymbol{q}_2^{i,j} \coloneqq (\delta,\, j\delta,\, 1/8 - i\delta)\,, \quad \boldsymbol{q}_3^{i,j} \coloneqq \left(\frac{1}{4} + \frac{i\delta}{2},\, j\delta,\, 1/8 - i\delta\right),$$
$$\boldsymbol{q}_4^{i,j} \coloneqq \left(\frac{1}{4} + \frac{i\delta}{2},\, \frac{j\delta}{2},\, 1/8 - i\delta\right), \quad \boldsymbol{q}_5^{i,j} \coloneqq \left(\frac{1}{4} + \frac{i\delta}{2},\, \frac{j\delta}{2},\, \frac{1}{4}\right),$$

where $i, j \in \mathbb{Z}$. Next, we define a family of points, obtained by horizontal rotation of the points defined above. Let $\theta \in [0, 2\pi]$, we define

$$\begin{aligned} \boldsymbol{p}_{k,\theta} &\coloneqq \rho_\theta(\boldsymbol{p}_k) \qquad \text{for} \quad k \in \{1,2,3,4\}; \\ \boldsymbol{q}_{k,\theta}^{i,j} &\coloneqq \rho_\theta(\boldsymbol{q}_k^{i,j}) \qquad \text{for} \quad k \in \{1,2,3,4,5\}. \end{aligned} \tag{7.45}$$

We recall that the transformation ρ_θ, defined in section 7.2, is a counterclockwise horizontal rotation by an angle θ.

We define two sets:

$$J \coloneqq \{-1, 1\} \qquad \text{and} \qquad \Theta \coloneqq \left\{0, \frac{\pi}{2}, \pi, \frac{3\pi}{2}\right\}.$$

Before defining the appropriate vector-valued Radon measures, we set a few notations. Given two points $\boldsymbol{a}_1, \boldsymbol{a}_2 \in \mathbb{R}^3$, where $\boldsymbol{a}_1 \neq \boldsymbol{a}_2$, we denote the line segment whose end points are $\boldsymbol{a}_1$ and $\boldsymbol{a}_2$ as

$$\overline{\boldsymbol{a}_1\boldsymbol{a}_2} \coloneqq \{(1-t)\boldsymbol{a}_1 + t\boldsymbol{a}_2 |\ t \in [0,1]\}, \tag{7.46}$$

whereas to denote the ray that starts at $\boldsymbol{a}_1$ and goes all the way up to infinity, passing through the point $\boldsymbol{a}_2$ as

$$\overrightarrow{\boldsymbol{a}_1\boldsymbol{a}_2} \coloneqq \{(1-t)\boldsymbol{a}_1 + t\boldsymbol{a}_2 |\ t \in [0,\infty)\}. \tag{7.47}$$

For a given $S \subseteq \mathbb{R}^3$ and $\varepsilon > 0$, we denote the $\varepsilon-$neighborhood of the set S by

$$S^{\varepsilon} \coloneqq \{\boldsymbol{x} \in \mathbb{R}^3 \mid \operatorname{dist}(\boldsymbol{x}, S) \leq \varepsilon\}. \tag{7.48}$$

Finally, $\mathcal{H}^1$ denotes the Hausdorff measure of dimension one.

Using Table 7.1, we now define a few vector-valued measures as

$$\nu^u \coloneqq \nu_0 + \nu_1 + \nu_2, \tag{7.50a}$$

$$\nu^d \coloneqq \nu_3 + \nu_4 + \nu_5 + \nu_6 + \nu_7, \tag{7.50b}$$

$$\nu_b \coloneqq \nu_0 + \nu_8 + \nu_9. \tag{7.50c}$$

The measure ν^u will be used in constructing the upward moving part of the flow

$\ell_0 \coloneqq \overrightarrow{\boldsymbol{p}_2\boldsymbol{p}_1}$	$\boldsymbol{e}_0 \coloneqq \boldsymbol{e}_z$	$\nu_0 \coloneqq \boldsymbol{e}_0\mathcal{H}^1 \llcorner \ell_0$	(7.49a)
$\ell_{1,\theta} \coloneqq \overline{\boldsymbol{p}_{2,\theta}\,\boldsymbol{p}_{3,\theta}}$	$\boldsymbol{e}_{1,\theta} \coloneqq \frac{1}{4}\frac{\boldsymbol{p}_{3,\theta}-\boldsymbol{p}_{2,\theta}}{\lvert\boldsymbol{p}_{3,\theta}-\boldsymbol{p}_{2,\theta}\rvert}$	$\nu_1 \coloneqq \sum_{\theta\in\Theta} \boldsymbol{e}_{1,\theta}\mathcal{H}^1 \llcorner \ell_{1,\theta}$	(7.49b)
$\ell_{2,\theta} \coloneqq \overrightarrow{\boldsymbol{p}_{3,\theta}\,\boldsymbol{p}_{4,\theta}}$	$\boldsymbol{e}_{2,\theta} \coloneqq \frac{\boldsymbol{e}_z}{4}$	$\nu_2 \coloneqq \sum_{\theta\in\Theta} \boldsymbol{e}_{2,\theta}\mathcal{H}^1 \llcorner \ell_{2,\theta}$	(7.49c)
$\ell_{3,\theta} \coloneqq \overrightarrow{\boldsymbol{q}_{2,\theta}^{1,1}\,\boldsymbol{q}_{1,\theta}^{0,1}}$	$\boldsymbol{e}_{3,\theta} \coloneqq -\frac{\boldsymbol{e}_z}{4}$	$\nu_3 \coloneqq \sum_{\theta\in\Theta} \boldsymbol{e}_{3,\theta}\mathcal{H}^1 \llcorner \ell_{3,\theta}$	(7.49d)
$\ell_{4,\theta} \coloneqq \overline{\boldsymbol{q}_{2,\theta}^{-1,1}\,\boldsymbol{q}_{2,\theta}^{1,1}}$	$\boldsymbol{e}_{4,\theta} \coloneqq -\frac{\boldsymbol{e}_z}{8}$	$\nu_4 \coloneqq \sum_{\theta\in\Theta} \boldsymbol{e}_{4,\theta}\mathcal{H}^1 \llcorner \ell_{4,\theta}$	(7.49e)
$\ell_{5,\theta}^{i,j} \coloneqq \overline{\boldsymbol{q}_{2,\theta}^{i,j}\,\boldsymbol{q}_{3,\theta}^{i,j}}$	$\boldsymbol{e}_{5,\theta}^{i,j} \coloneqq \frac{1}{16}\frac{\boldsymbol{q}_{2,\theta}^{i,j}-\boldsymbol{q}_{3,\theta}^{i,j}}{\lvert\boldsymbol{q}_{2,\theta}^{i,j}-\boldsymbol{q}_{3,\theta}^{i,j}\rvert}$	$\nu_5 \coloneqq \sum_{\theta\in\Theta}\sum_{i,j\in J} \boldsymbol{e}_{5,\theta}^{i,j}\mathcal{H}^1 \llcorner \ell_{5,\theta}^{i,j}$	(7.49f)
$\ell_{6,\theta}^{i,j} \coloneqq \overline{\boldsymbol{q}_{3,\theta}^{i,j}\,\boldsymbol{q}_{4,\theta}^{i,j}}$	$\boldsymbol{e}_{6,\theta}^{i,j} \coloneqq \frac{1}{16}\frac{\boldsymbol{q}_{3,\theta}^{i,j}-\boldsymbol{q}_{4,\theta}^{i,j}}{\lvert\boldsymbol{q}_{3,\theta}^{i,j}-\boldsymbol{q}_{4,\theta}^{i,j}\rvert}$	$\nu_6 \coloneqq \sum_{\theta\in\Theta}\sum_{i,j\in J} \boldsymbol{e}_{6,\theta}^{i,j}\mathcal{H}^1 \llcorner \ell_{6,\theta}^{i,j}$	(7.49g)
$\ell_{7,\theta}^{i,j} \coloneqq \overrightarrow{\boldsymbol{q}_{4,\theta}^{i,j}\,\boldsymbol{q}_{5,\theta}^{i,j}}$	$\boldsymbol{e}_{7,\theta}^{i,j} \coloneqq -\frac{\boldsymbol{e}_z}{16}$	$\nu_7 \coloneqq \sum_{\theta\in\Theta}\sum_{i,j\in J} \boldsymbol{e}_{7,\theta}^{i,j}\mathcal{H}^1 \llcorner \ell_{7,\theta}^{i,j}$	(7.49h)
$\ell_{8,\theta} \coloneqq \overrightarrow{\boldsymbol{q}_{2,\theta}^{0,1}\,\boldsymbol{q}_{1,\theta}^{0,1}}$	$\boldsymbol{e}_{8,\theta} \coloneqq -\frac{\boldsymbol{e}_z}{4}$	$\nu_8 \coloneqq \sum_{\theta\in\Theta} \boldsymbol{e}_{8,\theta}\mathcal{H}^1 \llcorner \ell_{8,\theta}$	(7.49i)
$\ell_{9,\theta} \coloneqq \overline{\boldsymbol{p}_2\,\boldsymbol{q}_{2,\theta}^{0,1}}$	$\boldsymbol{e}_{9,\theta} \coloneqq \frac{1}{4}\frac{\boldsymbol{q}_{2,\theta}^{0,1}-\boldsymbol{p}_2}{\lvert\boldsymbol{q}_{2,\theta}^{0,1}-\boldsymbol{p}_2\rvert}$	$\nu_9 \coloneqq \sum_{\theta\in\Theta} \boldsymbol{e}_{9,\theta}\mathcal{H}^1 \llcorner \ell_{9,\theta}$	(7.49j)

Table 7.1: A few useful definitions: line segments or rays (column one), vectors in $\mathbb{R}^3$ (column two) and vector-valued measures (column three).

field $\overline{\boldsymbol{u}}$ and ν^d will be used for constructing the downward moving part of the flow field, whereas, ν_b will be useful in constructing the flow field $\overline{\boldsymbol{u}}_b$. We also define a

few useful sets as

$$S^u \coloneqq \ell_0 \cup \bigcup_{\theta\in\Theta} \ell_{1,\theta} \cup \ell_{2,\theta}, \tag{7.51a}$$

$$S^d \coloneqq \bigcup_{\theta\in\Theta} \left(\ell_{3,\theta} \cup \ell_{4,\theta} \cup \bigcup_{i,j\in J} \ell^{i,j}_{5,\theta} \cup \ell^{i,j}_{6,\theta} \cup \ell^{i,j}_{7,\theta} \right), \tag{7.51b}$$

$$S \coloneqq S^u \cup S^d, \tag{7.51c}$$

$$S_b \coloneqq \ell_0 \cup \bigcup_{\theta\in\Theta} \ell_{8,\theta} \cup \ell_{9,\theta}. \tag{7.51d}$$

To regularize the measures, we define a family of mollifiers. Let $\varphi \in C_c^\infty(\mathbb{R}^3)$ be any radial bump function whose support lies in $|\boldsymbol{x}| \leq 1$, such as

$$\varphi(\boldsymbol{x}) \coloneqq \overline{\varphi}(|\boldsymbol{x}|), \tag{7.52}$$

where $\overline{\varphi} : \mathbb{R} \to \mathbb{R}$ is defined as

$$\overline{\varphi}(r) \coloneqq \begin{cases} c \exp\left(\frac{1}{r^2-1}\right) & \text{if} \quad |r| < 1, \\ 0 \quad \text{if} \quad |r| \geq 1, \end{cases} \tag{7.53}$$

and c is chosen such that $\int_{\mathbb{R}^3} \varphi(\boldsymbol{x})\, \mathrm{d}\boldsymbol{x} = 1$. For any $\varepsilon > 0$, we then define a standard mollifier as

$$\varphi_\varepsilon(\boldsymbol{x}) \coloneqq \frac{1}{\varepsilon^3} \varphi\left(\frac{\boldsymbol{x}}{\varepsilon}\right). \tag{7.54}$$

We use this definition of mollifier and the measures (7.50a-d) to define the velocity

fields

$$\left.\begin{aligned} \overline{\boldsymbol{u}}_1^u &:= \varphi_\gamma * \nu^u, & \overline{\boldsymbol{u}}_2^u &:= \varphi_{\frac{\gamma}{2}} * \nu^u, \\ \overline{\boldsymbol{u}}_1^d &:= \varphi_\gamma * \nu^d, & \overline{\boldsymbol{u}}_2^d &:= \varphi_{\frac{\gamma}{2}} * \nu^d, \\ \overline{\boldsymbol{u}}_b &:= \varphi_\gamma * \nu_b. \end{aligned}\right\} \tag{7.55a-e}$$

From the definition of φ_ε in (7.54) and the definition of the velocity fields (7.55a-e), we see that

$$\left.\begin{aligned} &\operatorname{supp} \overline{\boldsymbol{u}}_1^u \cup \operatorname{supp} \overline{\boldsymbol{u}}_2^u \subseteq S^{u,\gamma}, && \operatorname{supp} \overline{\boldsymbol{u}}_1^d \cup \operatorname{supp} \overline{\boldsymbol{u}}_2^d \subseteq S^{d,\gamma}, \\ &\operatorname{supp} \overline{\boldsymbol{u}}_b \subseteq S_b^\gamma. \end{aligned}\right\} \tag{7.56a-c}$$

Here, we added γ in the superscripts to mean γ-neighborhood of the sets (see definition (7.48)). Also, from the definition (7.55a-e), we see that all the velocity fields belong to $L^\infty(\mathbb{R}^3;\mathbb{R}^3)$.

Our next task is to show that the velocity fields as defined in (7.55a-e) belong to $C^\infty(\mathbb{R}^3;\mathbb{R}^3)$ and are divergence free. We start with the following definition.

Definition 7.4.1 (Kirchhoff's junction)**.** *Let $\widehat{\boldsymbol{p}} \in \mathbb{R}^3$ be a point and $\widehat{\boldsymbol{e}}_j \in \mathbb{R}^3$, for $j = 1$ to $n \in \mathbb{N}$, be different non-zero vectors. Also, let $o_j \in \{-1, 1\}$, for $j \in \{1, \dots n\}$, be n numbers. We say $\widehat{\boldsymbol{p}}$ together with the set of pairs $\widehat{\boldsymbol{e}}_j$ and o_j forms a Kirchhoff's junction if*

$$\sum_{j=1}^{n} o_j |\widehat{\boldsymbol{e}}_j| = 0. \tag{7.57}$$

For every Kirchhoff's junction defined above, we can associate a vector-valued Radon measure $\widehat{\nu}$. First define n rays emanating from $\widehat{\boldsymbol{p}}$ as $\widehat{\ell}_j := \{\boldsymbol{y}_j(t) \,|\, t \in [0, \infty)\}$, where $\boldsymbol{y}_j : \mathbb{R} \to \mathbb{R}^3$ are curves which in the parametric form are given by

$\boldsymbol{y}_j(t) \coloneqq \widehat{\boldsymbol{p}} + t\widehat{\boldsymbol{e}}_j/|\widehat{\boldsymbol{e}}_j|$, for $t \in [0,\infty)$. Consider the vector-valued Radon measures supported on these rays as $\widehat{\nu}_j \coloneqq o_j \widehat{\boldsymbol{e}}_j \mathcal{H}^1 \llcorner \widehat{\ell}_j$. Using these measures, we define a measure corresponding to the Kirchhoff's junction as

$$\widehat{\nu} \coloneqq \sum_{j=1}^{n} \widehat{\nu}_j. \tag{7.58}$$

Next, we state an important lemma.

Lemma 7.4.1. *Let $\psi \in C_c^\infty(\mathbb{R}^3)$ be a radially symmetric mollifier such that the support of ψ lies in $|\boldsymbol{x}| \leq \varepsilon$, for some $\varepsilon > 0$. Assume that $\widehat{\boldsymbol{p}} \in \mathbb{R}^3$ and a set of n pairs, $\widehat{\boldsymbol{e}}_j \in \mathbb{R}^3$ and $o_j \in \{-1, 1\}$, for $j = 1$ to $n \in \mathbb{N}$, forms a Kirchhoff's junction. Let $\widehat{\nu}$ be the associated vector-valued Radon measure to this junction. Then the velocity field given by $\widehat{\boldsymbol{u}} \coloneqq \psi * \widehat{\nu}$ belongs to $C^\infty(\mathbb{R}^3;\mathbb{R}^3)$ and is divergence-free.*

Proof of Lemma 7.4.1. By differentiating under the integral sign in the expression of $\widehat{\boldsymbol{u}}$, we immediately see that $\widehat{\boldsymbol{u}} \in C^\infty(\mathbb{R}^3;\mathbb{R}^3)$. Next, for any $\boldsymbol{x}_0 \in \mathbb{R}^3$, the following calculation holds

$$\begin{aligned}
(\nabla \cdot \widehat{\boldsymbol{u}})(\boldsymbol{x}_0) \quad &= \sum_{j=1}^{n} o_j \int_{\mathbb{R}^3} \widehat{\boldsymbol{e}}_j \cdot \nabla\psi(\boldsymbol{x}_0 - \boldsymbol{y}) \, \mathrm{d}\mathcal{H}^1 \llcorner \widehat{\ell}_j(\boldsymbol{y}) \\
&= \sum_{j=1}^{n} o_j \int_0^\infty \widehat{\boldsymbol{e}}_j \cdot \nabla\psi(\boldsymbol{x}_0 - \boldsymbol{y}_j(t_j)) \, \mathrm{d}t_j \\
&= -\sum_{j=1}^{n} o_j |\widehat{\boldsymbol{e}}_j| \int_0^\infty \frac{\partial \psi(\boldsymbol{x}_0 - \boldsymbol{y}_j(t_j))}{\partial t_j} \, \mathrm{d}t_j \\
&= -\sum_{j=1}^{n} o_j |\widehat{\boldsymbol{e}}_j| \, \psi(\boldsymbol{x}_0 - \boldsymbol{y}_j(t_j))\Big|_0^\infty \\
&= \psi(\widehat{\boldsymbol{p}}) \sum_{j=1}^{n} o_j |\widehat{\boldsymbol{e}}_j|.
\end{aligned}$$

Finally, using the assumption of the Kirchhoff's junction, implies $\nabla \cdot \widehat{\boldsymbol{u}} \equiv 0$. $\square$

Corollary 7.4.1. *Let $\psi \in C_c^\infty(\mathbb{R}^3)$ be a radially symmetric mollifier such that the support of ψ lies in $|\boldsymbol{x}| \leq \varepsilon$, for some $\varepsilon > 0$. Let $\widehat{\boldsymbol{p}}_i \in \mathbb{R}^3$, where $i \in \{1, \dots m\}$, be m points which are part of m different Kirchhoff's junctions and let $\widehat{\nu}_i$ be the vector-valued Radon measures associated to each of the Kirchhoff's junction. Then for the vector-valued Radon measure defined as $\breve{\nu} \coloneqq \sum_{i=1}^m \widehat{\nu}_i$, the velocity field given by $\breve{\boldsymbol{u}} \coloneqq \psi * \breve{\nu}$ belongs to $C^\infty(\mathbb{R}^3; \mathbb{R}^3)$ and is divergence-free.*

Lemma 7.4.2. *Let $\widehat{\boldsymbol{p}}_1$ and $\widehat{\boldsymbol{p}}_2$ be two different points in $\mathbb{R}^3$. Let $\widehat{\ell}_{12} = \overline{\widehat{\boldsymbol{p}}_1 \widehat{\boldsymbol{p}}_2}$ and $\widehat{\boldsymbol{e}}_{12} = c(\widehat{\boldsymbol{p}}_2 - \widehat{\boldsymbol{p}}_1)$ for some $c > 0$. Then a vector-valued measure defined as $\widehat{\nu}_{12} \coloneqq \widehat{\boldsymbol{e}}_{12} \mathcal{H}^1 \llcorner \widehat{\ell}_{12}$ can also be written as $\widehat{\nu}_{12} = \widehat{\nu}_{in} + \widehat{\nu}_{out}$, where $\widehat{\nu}_{in} = (-\widehat{\boldsymbol{e}}_{12}) \mathcal{H}^1 \llcorner \widehat{\ell}_{in}$, $\widehat{\nu}_{out} = \widehat{\boldsymbol{e}}_{12} \mathcal{H}^1 \llcorner \widehat{\ell}_{out}$, $\widehat{\ell}_{in} = \{\widehat{\boldsymbol{p}}_2 + t\boldsymbol{e}_{12} \,|\, t \in [0, \infty)\}$, and $\widehat{\ell}_{out} = \{\widehat{\boldsymbol{p}}_1 + t\boldsymbol{e}_{12} \,|\, t \in [0, \infty)\}$.*

Proof of 7.4.2. We can write $\widehat{\nu}_{out} = \widehat{\nu}_{out} \llcorner \widehat{\ell}_{12} + \widehat{\nu}_{out} \llcorner \widehat{\ell}_{in}$. Now $\widehat{\nu}_{out} \llcorner \widehat{\ell}_{12}$ coincides with $\widehat{\nu}_{12}$ in $\mathbb{R}^3$, whereas $\widehat{\nu}_{in} + \widehat{\nu}_{out} \llcorner \widehat{\ell}_{in}$ is a zero measure, which then finishes the proof. □

A tedious verification shows that using Lemma 7.4.2, the vector-valued measures (7.50a-c) can be written as a sum of vector-valued measures associated with different Kirchhoff's junctions. Therefore, the velocity fields as defined in (7.55a-e) belong to $C^\infty(\mathbb{R}^3; \mathbb{R}^3)$ and are divergence free. Here, we write down the Kirchhoff's junctions such that the sum of associated vector-valued measures is ν^u:

Junction No.	The point $\widehat{\boldsymbol{p}}$	The set of pairs of $\widehat{\boldsymbol{e}}_j$ and o_j
1	$\boldsymbol{p}_2$	$\{(\boldsymbol{e}_z, 1), (\frac{\boldsymbol{e}_x}{4}, -1), (\frac{\boldsymbol{e}_y}{4}, -1), (-\frac{\boldsymbol{e}_x}{4}, -1), (-\frac{\boldsymbol{e}_y}{4}, -1)\}$
2	$\boldsymbol{p}_{3,0}$	$\left\{\left(-\frac{\boldsymbol{e}_x}{4}, 1\right), \left(\frac{\boldsymbol{e}_z}{4}, -1\right)\right\}$
3	$\boldsymbol{p}_{3,\frac{\pi}{2}}$	$\left\{\left(-\frac{\boldsymbol{e}_y}{4}, 1\right), \left(\frac{\boldsymbol{e}_z}{4}, -1\right)\right\}$
4	$\boldsymbol{p}_{3,\pi}$	$\left\{\left(\frac{\boldsymbol{e}_x}{4}, 1\right), \left(\frac{\boldsymbol{e}_z}{4}, -1\right)\right\}$
5	$\boldsymbol{p}_{3,\frac{3\pi}{2}}$	$\left\{\left(\frac{\boldsymbol{e}_y}{4}, 1\right), \left(\frac{\boldsymbol{e}_z}{4}, -1\right)\right\}$

It can be shown that a similar decomposition exists for the other three measures defined in (7.50).

Patching up $\overline{\boldsymbol{u}}_1$ and $\overline{\boldsymbol{u}}_2$: Construction in the reducer region

To design the velocity field $\overline{\boldsymbol{u}}$, we need to patch the velocity fields $\overline{\boldsymbol{u}}_1$ and $\overline{\boldsymbol{u}}_2$ by defining an appropriate velocity field in the reducer region. Therefore, at this point, we shift our focus to designing velocity field in the reducer region.

We start by considering a simple example of one reducer, where we design such a velocity field. Let's define a function $m : \mathbb{R} \to \mathbb{R}$ as

$$m(r) \coloneqq \frac{1}{\gamma^3} \int_{-\infty}^{\infty} \overline{\varphi}\left(\frac{\sqrt{x'^2 + r^2}}{\gamma}\right) \mathrm{d}x', \tag{7.59}$$

where $\overline{\varphi}$ is defined in (7.53). In what follows, we will use

$$\varrho \text{ as a placeholder for } \sqrt{y^2 + z^2}$$

in rest of the section. With these definitions in hand, we define two velocity fields $\overline{\boldsymbol{u}}_s, \overline{\boldsymbol{u}}_e : \mathbb{R}^3 \to \mathbb{R}^3$ as

$$\begin{aligned} \overline{\boldsymbol{u}}_s(\boldsymbol{x}) &\coloneqq (\overline{u}_{x,s}, \overline{u}_{y,s}, \overline{u}_{z,s}) \coloneqq (m(\varrho), 0, 0), \\ \overline{\boldsymbol{u}}_e(\boldsymbol{x}) &\coloneqq (\overline{u}_{x,e}, \overline{u}_{y,e}, \overline{u}_{z,e}) \coloneqq (4m(2\varrho), 0, 0) \quad \text{for} \quad \boldsymbol{x} \in \mathbb{R}^3. \end{aligned} \tag{7.60}$$

As $\overline{\varphi}$ has a compact support, therefore, $\overline{\boldsymbol{u}}_s, \overline{\boldsymbol{u}}_e \in L^\infty(\mathbb{R}^3, \mathbb{R}^3)$. The arguments given in Appendix 7.D show that both of these velocity fields also belong to $C^\infty(\mathbb{R}^3, \mathbb{R}^3)$. Furthermore, it is clear that both the velocity fields are divergence free. Finally,

one can verify that the volume flux through any plane parallel to the yz-plane is same for both the velocity fields.

The task at hand is to come up with a divergence free velocity field $\overline{\boldsymbol{u}}_c$ such that it coincides with $\boldsymbol{u}_s$ in the region $x \leq 0$ and it coincides with $\boldsymbol{u}_e$ in the region $\gamma \leq x$, and it belongs to $L^\infty(\mathbb{R}^3;\mathbb{R}^3) \cap C^\infty(\mathbb{R}^3,\mathbb{R}^3)$. To ensure the required velocity field is divergence free, we work with streamfunctions. The strategy is to define the velocity field in the reducer region ($0 < x < \gamma$) based on a streamfunction which smoothly matches with streamfunction corresponding to the velocity field $\boldsymbol{u}_s$ for $x \leq 0$ and with streamfunction corresponding to the velocity field $\boldsymbol{u}_e$ for $x \geq \gamma$. To pursue this idea, we define two functions $\Psi_s, \Psi_e : \mathbb{R} \to \mathbb{R}$ as

$$\Psi_s(r) \coloneqq \int_0^{|r|} r' m(r') \, \mathrm{d}r', \qquad \Psi_e(r) \coloneqq 4 \int_0^{|r|} r' m(2r') \, \mathrm{d}r'.$$

Next, we define $\Psi_c : \mathbb{R}^2 \to \mathbb{R}$ as

$$\Psi_c(x,r) \coloneqq (1 - \eta_\gamma(x))\Psi_s(r) + \eta_\gamma(x)\Psi_e(r),$$

where $\eta_\varepsilon = \eta(x/\varepsilon)$ and η is a smooth cut-off function such that $\eta \equiv 0$ for $x \leq 0$ and $\eta \equiv 1$ for $x \geq 1$.

The function $\Psi_c(x,r)$ may be understood as the axisymmetric streamfunction of the desired velocity field. With the help of $\Psi_c(x,r)$, we are ready to define the

components of the velocity field that we wish to construct as

$$\overline{u}_{x,c}(\boldsymbol{x}) \coloneqq (1-\eta_\gamma(x))m(\varrho) + 4m(2\varrho)\eta_\gamma(x)$$
$$\overline{u}_{y,c}(\boldsymbol{x}) \coloneqq \begin{cases} y\frac{d\eta_\gamma}{dx}\frac{1}{\varrho^2}(\Psi_s(\varrho)-\Psi_e(\varrho)) & \text{if} \quad \varrho \neq 0, \\ 0 \quad \text{if} \quad y,z=0. \end{cases}$$
$$\overline{u}_{z,c}(\boldsymbol{x}) \coloneqq \begin{cases} z\frac{d\eta_\gamma}{dx}\frac{1}{\varrho^2}(\Psi_s(\varrho)-\Psi_e(\varrho)) & \text{if} \quad \varrho \neq 0, \\ 0 \quad \text{if} \quad y,z=0. \end{cases}$$

where $\boldsymbol{x} \in \mathbb{R}^3$. The velocity field is then given by

$$\overline{\boldsymbol{u}}_c \coloneqq (\overline{u}_{x,c}, \overline{u}_{y,c}, \overline{u}_{z,c}). \tag{7.61}$$

With this definition, we state the following lemma.

Lemma 7.4.3. *Let the velocity field $\overline{\boldsymbol{u}}_c$ be as defined in (7.61). Then it coincides with $\overline{\boldsymbol{u}}_s$ when $x \leq 0$ and with $\overline{\boldsymbol{u}}_e$ when $\gamma \leq x$. Furthermore, $\overline{\boldsymbol{u}}_c \in L^\infty(\mathbb{R}^3;\mathbb{R}^3) \cap C^\infty(\mathbb{R}^3;\mathbb{R}^3)$ and is divergence free with*

$$\operatorname{supp} \overline{\boldsymbol{u}}_c \subseteq \{(x,y,z) \,|\, y^2+z^2 \leq \gamma^2\}. \tag{7.62}$$

Proof. With the definition of function m (7.59) and noting that $\Psi_s(\varrho) = \Psi_e(\varrho)$ when $\varrho > \gamma$, we obtain (7.62). It is clear by construction that $\overline{\boldsymbol{u}}_c$ coincides with $\overline{\boldsymbol{u}}_s$ when $x \leq 0$ and with $\overline{\boldsymbol{u}}_e$ when $\gamma \leq x$ and therefore it is also infinite differentiable in these regions. To see the infinite differentiability in the region $0 < x < \gamma$, we use Lemma 7.4.3 given in Appendix 7.D. Finally, as the velocity field $\overline{\boldsymbol{u}}_c$ is defined based on a streamfunction, it is necessarily divergence-free. □

With this lemma in hand, we are ready to patch $\overline{\boldsymbol{u}}_1$ and $\overline{\boldsymbol{u}}_2$ using $\overline{\boldsymbol{u}}_c$ to construct the velocity field $\overline{\boldsymbol{u}}$. For this purpose, we define a few points in $\mathbb{R}^3$ as

$$\boldsymbol{s}_0 = (1/8, 0, 0), \qquad \boldsymbol{s}_1^{i,j} = (1/8, j\delta, -i\delta) \quad \text{for} \quad i, j \in J. \tag{7.63}$$

We also define two velocity field as

$$\overline{\boldsymbol{u}}_{red}^{\,u} \coloneqq \frac{1}{4} T^{\boldsymbol{s}_0} \overline{\boldsymbol{u}}_c, \qquad \overline{\boldsymbol{u}}_{red}^{\,d} \coloneqq -\frac{1}{16} \sum_{i,j \in J} T^{\boldsymbol{s}_1^{i,j}} \overline{\boldsymbol{u}}_c.$$

As a result of Lemma 7.4.3, the velocity fields

$$\begin{aligned}
\overline{\boldsymbol{u}}^{\,u} &\coloneqq \overline{\boldsymbol{u}}_1^{\,u} \mathbf{1}_{\{|x|,|y| \le 1/8\}} + \overline{\boldsymbol{u}}_2^{\,u} \mathbf{1}_{\{|x| \ge 1/8+\gamma\} \cup \{|y| \ge 1/8+\gamma\}} + \sum_{\theta \in \Theta} \rho_\theta \, \overline{\boldsymbol{u}}_{red}^{\,u} \mathbf{1}_{\{1/8 < x < 1/8+\gamma\}}, \\
\overline{\boldsymbol{u}}^{\,d} &\coloneqq \overline{\boldsymbol{u}}_1^{\,d} \mathbf{1}_{\{|x|,|y| \le 1/8\}} + \overline{\boldsymbol{u}}_2^{\,d} \mathbf{1}_{\{|x| \ge 1/8+\gamma\} \cup \{|y| \ge 1/8+\gamma\}} + \sum_{\theta \in \Theta} \rho_\theta \, \overline{\boldsymbol{u}}_{red}^{\,d} \mathbf{1}_{\{1/8 < x < 1/8+\gamma\}},
\end{aligned}$$

are uniformly bounded, infinitely differentiable, divergence free with $\operatorname{supp} \overline{\boldsymbol{u}}^{\,u} \subseteq S^{\,u,\gamma}$ and $\operatorname{supp} \overline{\boldsymbol{u}}^{\,d} \subseteq S^{\,d,\gamma}$. Finally, we arrive at the definition of the parent construct

$$\overline{\boldsymbol{u}} \coloneqq \overline{\boldsymbol{u}}^u + \overline{\boldsymbol{u}}^b. \tag{7.64}$$

Summarizing the properties of the parent constructs $\overline{\boldsymbol{u}}$ and $\overline{\boldsymbol{u}}_b$ (from (7.55a-e)), we have $\overline{\boldsymbol{u}}, \overline{\boldsymbol{u}}_b \in C^\infty(\mathbb{R}^3; \mathbb{R}^3) \cap L^\infty(\mathbb{R}^3; \mathbb{R}^3)$, both obeying $\nabla \cdot \overline{\boldsymbol{u}} \equiv 0$ and $\nabla \cdot \overline{\boldsymbol{u}}_b \equiv 0$ with

$$\operatorname{supp} \overline{\boldsymbol{u}} \subseteq S^{\,\gamma}, \qquad \operatorname{supp} \overline{\boldsymbol{u}}_b \subseteq S_b^{\,\gamma}. \tag{7.65}$$

Next, define a few points in $\mathbb{R}^3$ as

$$\boldsymbol{\tau}_\theta \coloneqq \left(\frac{\cos\theta}{4}, \frac{\sin\theta}{4}, -\frac{1}{4}\right) \quad \text{for} \quad \theta \in \Theta.$$

We now gather an important property of the parent constructs $\overline{\boldsymbol{u}}$ and $\overline{\boldsymbol{u}}_b$, which is that the velocity fields defined as

$$\widetilde{\boldsymbol{u}} \coloneqq \overline{\boldsymbol{u}}(\boldsymbol{x})\mathbf{1}_{\{z<1/4\}} + \left(\sum_{\theta\in\Theta} T^{\boldsymbol{\tau}_\theta}\overline{\boldsymbol{u}}(2\boldsymbol{x})\right)\mathbf{1}_{\{z\geq 1/4\}}, \tag{7.66a}$$

$$\widetilde{\boldsymbol{u}}_b \coloneqq \overline{\boldsymbol{u}}(\boldsymbol{x})\mathbf{1}_{\{z<1/4\}} + \left(\sum_{\theta\in\Theta} T^{\boldsymbol{\tau}_\theta}\overline{\boldsymbol{u}}_b(2\boldsymbol{x})\right)\mathbf{1}_{\{z\geq 1/4\}}, \tag{7.66b}$$

$$\widetilde{\boldsymbol{u}}_r \coloneqq \overline{\boldsymbol{u}}(\boldsymbol{x})\,\mathbf{1}_{z\geq 0} + (-\overline{u}_x(x,y,-z), -\overline{u}_y(x,y,-z), \overline{u}_z(x,y,-z))\;\mathbf{1}_{z<0}, \tag{7.66c}$$

all belong to $C^\infty(\mathbb{R}^3;\mathbb{R}^3)$. For example, let's look at $\widetilde{\boldsymbol{u}}$. The infinite differentiability away from $z = 1/4$ is clear by definition. However, the velocity fields $\overline{\boldsymbol{u}}$ and

$$\sum_{\theta\in\Theta} T^{\boldsymbol{\tau}_\theta}\overline{\boldsymbol{u}}(2\boldsymbol{x})$$

are identical when $7/32 < z < 9/32$, which can be shown by writing down their explicit expressions in this region. Therefore, $\widetilde{\boldsymbol{u}}$ is infinitely differentiable at $z = 1/4$ as well. Similar arguments apply for $\widetilde{\boldsymbol{u}}_b$ and $\widetilde{\boldsymbol{u}}_r$.

The scalar fields $\overline{\xi}$ and $\overline{\xi}_b$

The construction of $\overline{\xi}$ and $\overline{\xi}_b$ is relatively simple but somewhat different from that of $\overline{\boldsymbol{u}}$ and $\overline{\boldsymbol{u}}_b$. Recall from the detailed sketch given in section 7.4.1, we want to create a scalar field ξ that is constant in the support of the velocity field $\boldsymbol{u}$ (with the exception of the boundary layer). To that end, we first define a few sets consisting of line segments and rays, which in a sense form the skeleton. This step is the

same as in the previous subsection. We then consider a λ-neighborhood of this skeleton for sufficiently small positive λ. Next, we mollify the indicator function of this λ-neighborhood set. If the mollification parameter, which we choose to be γ, is small compared with λ, we will have designed a smooth function supported in tubes of radius $\lambda + \gamma$ and constant in tubes of radius $\lambda - \gamma$ enveloping the skeleton. This strategy works everywhere except in the reducer region, where we design the scalar field using a cut-off function similar to the case of the velocity field. We now begin our construction.

In addition to (7.45), we define a few extra points in $\mathbb{R}^3$ as

$$\boldsymbol{p}_5 \coloneqq (0, 0, h), \qquad \boldsymbol{q}_6 \coloneqq (\delta, \delta, h),$$

and a few rays

$$\ell_{10} \coloneqq \overrightarrow{\boldsymbol{p}_5 \boldsymbol{p}_1}, \qquad \ell_{11,\theta} \coloneqq \overrightarrow{\boldsymbol{q}_{6,\theta} \boldsymbol{q}_{1,\theta}^{0,1}},$$

where $\boldsymbol{q}_{6,\theta} = \rho_\theta(\boldsymbol{q}_6)$. Here, we choose

$$h \coloneqq \frac{1}{16}.$$

To complement (7.51), we also define

$$\widetilde{S}_b^u \coloneqq \ell_{10}, \qquad \widetilde{S}_b^d \coloneqq \bigcup_{\theta \in \Theta} \ell_{11,\theta}.$$

Remember, we chose $\lambda = 1/100$ and $\gamma = 1/500$ (see (7.44)). Now using the

definition of ε-neighborhood of a set (7.48), we define the following scalar fields:

$$\left.\begin{aligned} \overline{\xi}_1^u &:= \varphi_\gamma * \mathbf{1}_{S^{u,\lambda}} \ , & \overline{\xi}_1^d &:= -\varphi_\gamma * \mathbf{1}_{S^{d,\lambda}} \ , \\ \overline{\xi}_2^u &:= \varphi_{\gamma/2} * \mathbf{1}_{S^{u,\lambda/2}} \ , & \overline{\xi}_2^d &:= -\varphi_{\gamma/2} * \mathbf{1}_{S^{d,\lambda/2}} \ , \\ \overline{\xi}_b^u &:= \varphi_\gamma * \mathbf{1}_{\widetilde{S}_b^{u,\lambda}} \ , & \overline{\xi}_b^d &:= -\varphi_\gamma * \mathbf{1}_{\widetilde{S}_b^{d,\lambda}} \ , \end{aligned}\right\} \tag{7.67a-f}$$

which belong to $C^\infty(\mathbb{R}^3)$ as a result of the following lemma.

Lemma 7.4.4. *Let $f : \mathbb{R}^3 \to \mathbb{R}$ be a locally integrable function and let $\psi \in C_c^\infty(\mathbb{R}^3)$ be a radially symmetric mollifier such that the support of ψ lies in $|\boldsymbol{x}| \leq \epsilon$. Then the function given by $g = \psi * f$ belongs to $C^\infty(\mathbb{R}^3)$.*

Proof. By differentiating under the integral sign in the expression of g, one can finish the proof. □

From the definitions (7.67a-f), we notice

$$\left.\begin{aligned} &\operatorname{supp} \overline{\xi}_1^{\,u} \cup \operatorname{supp} \overline{\xi}_2^{\,u} \subseteq S^{u,\,\lambda+\gamma}, & &\operatorname{supp} \overline{\xi}_1^{\,d} \cup \operatorname{supp} \overline{\xi}_2^{\,d} \subseteq S^{d,\,\lambda+\gamma}, \\ &\operatorname{supp} \overline{\xi}_b^{\,u} \subseteq \widetilde{S}_b^{u,\lambda+\gamma}, & &\operatorname{supp} \overline{\xi}_b^{\,d} \subseteq \widetilde{S}_b^{d,\lambda+\gamma}. \end{aligned}\right\} \tag{7.68a-d}$$

Moreover,

$$\left.\begin{aligned} &\overline{\xi}_1^{\,u}(\boldsymbol{x}) = \overline{\xi}_2^{\,u}(\boldsymbol{x}) = 1 \quad \text{when} \quad \boldsymbol{x} \in S^{u,\,\frac{\lambda-\gamma}{2}}, \\ &\overline{\xi}_1^{\,d}(\boldsymbol{x}) = \overline{\xi}_2^{\,d}(\boldsymbol{x}) = -1 \quad \text{when} \quad \boldsymbol{x} \in S^{d,\,\frac{\lambda-\gamma}{2}} \\ &\overline{\xi}_b^{\,u}(\boldsymbol{x}) = 1 \quad \text{when} \quad \boldsymbol{x} \in \widetilde{S}_b^{u,\,\lambda-\gamma}, \\ &\overline{\xi}_b^{\,d}(\boldsymbol{x}) = -1 \quad \text{when} \quad \boldsymbol{x} \in \widetilde{S}_b^{d,\,\lambda-\gamma}. \end{aligned}\right\} \tag{7.69a-d}$$

Next, let's define two scalar fields for the construction in the reducer region

$$\overline{\xi}^{u}_{red}(\boldsymbol{x}) \coloneqq \overline{\xi}^{u}_{1}(\boldsymbol{x})\,(1-\eta_\gamma(x-1/8)) + \overline{\xi}^{u}_{2}(\boldsymbol{x})\,\eta_\gamma(x-1/8) \quad \text{for} \quad \boldsymbol{x}\in\mathbb{R}^3,$$
$$\overline{\xi}^{d}_{red}(\boldsymbol{x}) \coloneqq \overline{\xi}^{d}_{1}(\boldsymbol{x})\,(1-\eta_\gamma(x-1/8)) + \overline{\xi}^{d}_{2}(\boldsymbol{x})\,\eta_\gamma(x-1/8) \quad \text{for} \quad \boldsymbol{x}\in\mathbb{R}^3.$$

We can use them to define

$$\overline{\xi}^{\,u} \coloneqq \overline{\xi}^{u}_{1}\mathbf{1}_{\{|x|,|y|\le 1/8\}} + \overline{\xi}^{u}_{2}\mathbf{1}_{\{|x|,|y|\ge 1/8+\gamma\}} + \sum_{\theta\in\Theta}\rho_\theta\,\overline{\xi}^{u}_{red}\mathbf{1}_{\{1/8<x<1/8+\gamma\}},$$
$$\overline{\xi}^{\,d} \coloneqq \overline{\xi}^{d}_{1}\mathbf{1}_{\{|x|,|y|\le 1/8\}} + \overline{\xi}^{d}_{2}\mathbf{1}_{\{|x|,|y|\ge 1/8+\gamma\}} + \sum_{\theta\in\Theta}\rho_\theta\,\overline{\xi}^{d}_{red}\mathbf{1}_{\{1/8<x<1/8+\gamma\}}.$$

It can be easily verified that $\overline{\xi}^{\,u}$ is infinitely differentiable, that its support lies in $S^{u,\,\lambda+\gamma}$ and that its value is 1 when $\boldsymbol{x}\in S^{u,\,\frac{\lambda-\gamma}{2}}$. Similarly, $\overline{\xi}^{\,d}$ is infinitely differentiable has a support that lies in $S^{d,\,\lambda+\gamma}$ and its value is -1 when $\boldsymbol{x}\in S^{d,\,\frac{\lambda-\gamma}{2}}$. We finally define the parent copies for the scalar field as

$$\overline{\xi} \coloneqq \overline{\xi}^{\,u} + \overline{\xi}^{\,d}, \qquad \overline{\xi}_b \coloneqq \overline{\xi}^{u}_{b} + \overline{\xi}^{d}_{b}. \tag{7.72a-b}$$

In summary, $\overline{\xi},\overline{\xi}_b \in L^\infty(\mathbb{R}^3)\cap C^\infty(\mathbb{R}^3)$, $\operatorname{supp}\overline{\xi}\subseteq S^{u,\,\lambda+\gamma}\cup S^{d,\,\lambda+\gamma}$ and $\operatorname{supp}\overline{\xi}_b \subseteq \widetilde{S}^{u,\,\lambda+\gamma}_{b}\cup\widetilde{S}^{d,\,\lambda+\gamma}_{b}$

Similar to the case of velocity field, an important outcome of our construction is that scalar fields

$$\widetilde{\xi}(\boldsymbol{x}) \coloneqq \overline{\xi}(\boldsymbol{x})\,\mathbf{1}_{z<1/4} + \sum_{\theta\in\Theta} T^{\boldsymbol{\tau}_\theta}(\overline{\xi}(2\boldsymbol{x}))\,\mathbf{1}_{z\ge 1/4}, \tag{7.73a}$$
$$\widetilde{\xi}_b(\boldsymbol{x}) \coloneqq \overline{\xi}(\boldsymbol{x})\,\mathbf{1}_{z<1/4} + \sum_{\theta\in\Theta} T^{\boldsymbol{\tau}_\theta}(\overline{\xi}_b(2\boldsymbol{x}))\,\mathbf{1}_{z\ge 1/4}, \tag{7.73b}$$
$$\widetilde{\xi}_r(\boldsymbol{x}) \coloneqq \overline{\xi}(\boldsymbol{x})\,\mathbf{1}_{z\ge 0} + \overline{\xi}(x,y,-z)\,\mathbf{1}_{z<0}, \tag{7.73c}$$

all belong to $C^\infty(\mathbb{R}^3)$.

Let's now gather some of the important properties of the parent constructs of the velocity field and the scalar field in the following proposition.

Proposition 7.4.2. *In the definitions (7.64, 7.55a-e) and (7.72a-b) the two velocity fields $\overline{\boldsymbol{u}}, \overline{\boldsymbol{u}}_b \in C^\infty(\mathbb{R}^3, \mathbb{R}^3) \cap L^\infty(\mathbb{R}^3, \mathbb{R}^3)$ and the scalar fields $\overline{\xi}, \overline{\xi}_b \in C^\infty(\mathbb{R}^3) \cap L^\infty(\mathbb{R}^3)$ are such that the following statements are true.*

(i) $\nabla \cdot \overline{\boldsymbol{u}} \equiv 0$ *and* $\nabla \cdot \overline{\boldsymbol{u}}_b \equiv 0$,

(ii) $\operatorname{supp} \overline{\boldsymbol{u}} \cup \operatorname{supp} \overline{\xi} \subseteq (-1/3, 1/3) \times (-1/3, 1/3) \times \mathbb{R}$,

(iii) $\operatorname{supp} \overline{\boldsymbol{u}}_b \cup \operatorname{supp} \overline{\xi}_b \subseteq (-1/3, 1/3) \times (-1/3, 1/3) \times (-\infty, 1/4)$,

(iv) $\overline{\boldsymbol{u}} \cdot \nabla \overline{\xi} \equiv 0$, *while* $\operatorname{supp}_z(\overline{\boldsymbol{u}}_b \cdot \nabla \overline{\xi}_b) \Subset (1/32, 5/64)$,

(v) $\int_{\mathbb{R}^2} \int_{z=0}^{1/4} \overline{u}_z \overline{\xi} \, \mathrm{d}\boldsymbol{x} \geq c_3 > 0$ *and* $\int_{\mathbb{R}^2} \int_{z=0}^{1/8} \overline{u}_{b,z} \overline{\xi}_b \, \mathrm{d}\boldsymbol{x} \geq 0$.

Here, c_3 is a positive constant independent of any parameter. Furthermore, the velocity fields $\widetilde{\boldsymbol{u}}, \widetilde{\boldsymbol{u}}_b, \widetilde{\boldsymbol{u}}_r$ as defined in (7.66) and the scalar fields $\widetilde{\xi}, \widetilde{\xi}_b, \widetilde{\xi}_r$ defined in (7.73), respectively belong to $C^\infty(\mathbb{R}^3, \mathbb{R}^3)$ and $C^\infty(\mathbb{R}^3)$.

Proof of Proposition 7.4.2. We already proved all the points except (iv) and (v), which we prove now.

We first focus on point (iv). We note that: (1) $\operatorname{supp} \overline{\boldsymbol{u}} = \operatorname{supp} \overline{\boldsymbol{u}}^u \cup \operatorname{supp} \overline{\boldsymbol{u}}^d$, (2) $\operatorname{supp} \overline{\boldsymbol{u}}^u \subseteq S^{u,\gamma} \subset S^{u,\frac{\lambda-\gamma}{2}}$, (3) $\operatorname{supp} \overline{\boldsymbol{u}}^d \subseteq S^{d,\gamma} \subset S^{d,\frac{\lambda-\gamma}{2}}$. Furthermore, because of our choices of δ, γ and λ, we see that $S^{u,\frac{\lambda-\gamma}{2}} \cap S^{d,\frac{\lambda-\gamma}{2}} = \emptyset$. Now, if $\boldsymbol{x} \notin S^{u,\frac{\lambda-\gamma}{2}} \cup S^{d,\frac{\lambda-\gamma}{2}}$, it clear that $(\overline{\boldsymbol{u}} \cdot \nabla \overline{\xi})(\boldsymbol{x}) = 0$, as for this case $\boldsymbol{x} \notin \operatorname{supp} \overline{\boldsymbol{u}}$. In the next case, when $\boldsymbol{x} \in S^{u,\frac{\lambda-\gamma}{2}}$, we have $\overline{\xi} \equiv 1$ which implies $(\overline{\boldsymbol{u}} \cdot \nabla \overline{\xi})(\boldsymbol{x}) = 0$. In a similar manner, one can show $(\overline{\boldsymbol{u}} \cdot \nabla \overline{\xi})(\boldsymbol{x}) = 0$ when $\boldsymbol{x} \in S^{d,\frac{\lambda-\gamma}{2}}$.

Next, we show that $\operatorname{supp}_z \overline{\boldsymbol{u}}_b \cdot \nabla \overline{\xi}_b \Subset (1/32, 5/64)$. We first note that

$$\{z < h\} \cap \operatorname{supp} \overline{\boldsymbol{u}}_b \subset \widetilde{S}_b^{u,\lambda-\gamma} \cup \widetilde{S}_b^{d,\lambda-\gamma},$$

and that $\widetilde{S}_b^{u,\lambda-\gamma} \cap \widetilde{S}_b^{d,\lambda-\gamma} = \emptyset$. For $z < h$, we proceed as in the last paragraph to show $(\overline{\boldsymbol{u}}_b \cdot \nabla \overline{\xi}_b)(\boldsymbol{x}) = 0$. When $z > h + \lambda + \gamma$, from the definition of $\widetilde{S}_b^u$ and $\widetilde{S}_u^d$, we see that $\overline{\xi}_b \equiv 0$, therefore, $(\overline{\boldsymbol{u}}_b \cdot \nabla \overline{\xi}_b)(\boldsymbol{x}) = 0$ in this region as well. To summarize, $\operatorname{supp}_z \overline{\boldsymbol{u}}_b \cdot \nabla \overline{\xi}_b \subseteq [h, h + \gamma + \lambda] \Subset (1/32, 5/64)$.

Now we move to point (v) of Proposition 7.4.2. From a straightforward calculation, we see that

$$\begin{aligned}
\int_{\mathbb{R}^3 \cap \{0<z<1/4\}} \overline{u}_z \overline{\xi} \, \mathrm{d}\boldsymbol{x} \quad &= \int_{(\operatorname{supp} \overline{\boldsymbol{u}}^u \cup \operatorname{supp} \overline{\boldsymbol{u}}^d) \cap \{0<z<1/4\}} \overline{u}_z \overline{\xi} \, \mathrm{d}\boldsymbol{x} \\
&= \int_{\operatorname{supp} \overline{\boldsymbol{u}}^u \cap \{0<z<1/4\}} \overline{u}_z \overline{\xi} \, \mathrm{d}\boldsymbol{x} + \int_{\operatorname{supp} \overline{\boldsymbol{u}}^d \cap \{0<z<1/4\}} \overline{u}_z \overline{\xi} \, \mathrm{d}\boldsymbol{x} \\
&= \int_{\operatorname{supp} \overline{\boldsymbol{u}}^u \cap \{0<z<1/4\}} \overline{u}_z^u \overline{\xi} \, \mathrm{d}\boldsymbol{x} + \int_{\operatorname{supp} \overline{\boldsymbol{u}}^d \cap \{0<z<1/4\}} \overline{u}_z^d \overline{\xi} \, \mathrm{d}\boldsymbol{x} \\
&= \int_{\operatorname{supp} \overline{\boldsymbol{u}}^u \cap \{0<z<1/4\}} \overline{u}_z^u \, \mathrm{d}\boldsymbol{x} - \int_{\operatorname{supp} \overline{\boldsymbol{u}}^d \cap \{0<z<1/4\}} \overline{u}_z^d \, \mathrm{d}\boldsymbol{x} \\
&= \int_{\mathbb{R}^3 \cap \{0<z<1/4\}} \overline{u}_z^u \, \mathrm{d}\boldsymbol{x} - \int_{\mathbb{R}^3 \cap \{0<z<1/4\}} \overline{u}_z^d \, \mathrm{d}\boldsymbol{x} \\
&= \frac{1}{4} \int_{\mathbb{R}^2} \overline{u}_z^u(\cdot, 0) \, \mathrm{d}x\mathrm{d}y - \frac{1}{4} \int_{\mathbb{R}^2} \overline{u}_z^d(\cdot, 0) \, \mathrm{d}x\mathrm{d}y \\
&= c_3 > 0, \qquad (7.74)
\end{aligned}$$

where c_3 is some constant. To obtain the fourth line, we used the fact that $\xi(\boldsymbol{x}) = 1$ when $\boldsymbol{x} \in \operatorname{supp} \overline{\boldsymbol{u}}^u$ and $\xi(\boldsymbol{x}) = -1$ when $\boldsymbol{x} \in \operatorname{supp} \overline{\boldsymbol{u}}^d$. To obtain the sixth line, we used the fact that $\overline{\boldsymbol{u}}^u$ and $\overline{\boldsymbol{u}}^d$ are divergence-free and that their support is bounded in the xy-plane, which in turn implies that the volume flux through any horizontal section is the same, i.e.,

$$\begin{aligned}
\int_{\mathbb{R}^2} \overline{u}_z^u(\cdot, z) \, \mathrm{d}x\mathrm{d}y &= \int_{\mathbb{R}^2} \overline{u}_z^u(\cdot, 0) \, \mathrm{d}x\mathrm{d}y \quad \text{and} \\
\int_{\mathbb{R}^2} \overline{u}_z^d(\cdot, z) \, \mathrm{d}x\mathrm{d}y &= \int_{\mathbb{R}^2} \overline{u}_z^d(\cdot, 0) \, \mathrm{d}x\mathrm{d}y \quad \text{for any} \quad z.
\end{aligned}$$

To show

$$\int_{\mathbb{R}^3\cap\{0<z<1/4\}} \overline{u}_{b,z}\overline{\xi}_b \,\mathrm{d}\boldsymbol{x} \geq 0,$$

we simply note that $\overline{\xi}_b \equiv 0$ when $z \geq h+\lambda+\gamma$ and for $z < h+\lambda+\gamma$, the velocity $\overline{\boldsymbol{u}}_b$ is unidirectional (only the z-component is non-zero). Furthermore, in this region, wherever $\overline{u}_{b,z} > 0$, we have $\overline{\xi}_b \geq 0$ and wherever $\overline{u}_{b,z} < 0$, we have $\overline{\xi}_b \leq 0$. □

7.4.3 Main copies $\overline{\boldsymbol{u}}_N$ and $\overline{\xi}_N$: Proof of Proposition 7.3.1

Let's begin with a few useful definitions. First, let

$$z_i \coloneqq \frac{1}{2} - \frac{1}{2^{i+1}} \quad \text{for} \quad i \in \mathbb{Z}_{\geq 0},$$

mark the vertical positions of the interfaces of different layers, while the intervals

$$Z_i \coloneqq [z_{i-1}, z_i) \quad \text{for} \quad i \in \mathbb{N}, \tag{7.75}$$

denote the different layers. We define the set

$$F \coloneqq \{(1,0),(-1,0),(0,1),(0,-1)\}$$

which we use to define sets of nodal points as

$$\mathcal{N}_i = \left\{ (x,y,z_i) \,\middle|\, x = \sum_{j=1}^{|i|} \frac{\alpha_j}{2^{j+1}},\ y = \sum_{j=1}^{|i|} \frac{\beta_j}{2^{j+1}},\ (\alpha_j,\beta_j) \in F \right\} \quad \text{for} \quad i \in \mathbb{N}. \tag{7.76}$$

Proof of Proposition 7.3.1. For a given integer $N \geq 1$, we need to construct a velocity field $\overline{\boldsymbol{u}}_N$ and a scalar field $\overline{\xi}_N$ in the domain D such that they satisfy

the properties specified in Proposition 7.3.1. To that end, we start by creating an intermediate flow field $\overline{\boldsymbol{u}}_{int,1} : \mathbb{R}^3 \to \mathbb{R}^3$, whose support lies in $z \geq 0$ and is defined as follows:

$$\overline{\boldsymbol{u}}_{int,1}(\boldsymbol{x}) \coloneqq \overline{\boldsymbol{u}}(\boldsymbol{x})\, \mathbf{1}_{Z_1} + \sum_{i=1}^{N-1} \sum_{\boldsymbol{p} \in \mathcal{N}_i} T^{\boldsymbol{p}}(\overline{\boldsymbol{u}}(2^i \boldsymbol{x})) \mathbf{1}_{Z_{i+1}} + \sum_{\boldsymbol{p} \in \mathcal{N}_N} T^{\boldsymbol{p}}(\overline{\boldsymbol{u}}_b(2^N \boldsymbol{x}))\, \mathbf{1}_{Z_{N+1}} \quad \text{for} \quad \boldsymbol{x} \in \mathbb{R}^3. \tag{7.77}$$

To create $\overline{\boldsymbol{u}}_N$, we glue $\overline{\boldsymbol{u}}_{int,1}$ and its mirror reflection about $z = 0$. Let

$$\overline{\boldsymbol{u}}_{int,2}(\boldsymbol{x}) \coloneqq (-\overline{u}_{x,int,1}(x, y, -z), -\overline{u}_{y,int,1}(x, y, -z), \overline{u}_{z,int,1}(x, y, -z))\, \mathbf{1}_{z<0} \quad \text{for} \quad \boldsymbol{x} \in \mathbb{R}^3. \tag{7.78}$$

Notice that the signs of x and y components are flipped to maintain the divergence-free condition. We finally define $\overline{\boldsymbol{u}}_N$ as

$$\overline{\boldsymbol{u}}_N(\boldsymbol{x}) \coloneqq \overline{\boldsymbol{u}}_{int,1}(\boldsymbol{x}) + \overline{\boldsymbol{u}}_{int,2}(\boldsymbol{x}). \tag{7.79}$$

Note that $\operatorname{supp} \overline{\boldsymbol{u}}_N \Subset D$ and it is really the restriction of $\overline{\boldsymbol{u}}_N$ to D, which we continue to call $\overline{\boldsymbol{u}}_N$, that we use in the proof of Proposition 7.3.1. We then define $\overline{\xi}_N$ in a similar way. First, we define an intermediate scalar field $\overline{\xi}_{int,1} : \mathbb{R}^3 \to \mathbb{R}$ as

$$\overline{\xi}_{int,1}(\boldsymbol{x}) \coloneqq \overline{\xi}(\boldsymbol{x})\, \mathbf{1}_{Z_1} + \sum_{i=1}^{N-1} \sum_{\boldsymbol{p} \in \mathcal{N}_i} T^{\boldsymbol{p}}(\overline{\xi}(2^i \boldsymbol{x})) \mathbf{1}_{Z_{i+1}} + \sum_{\boldsymbol{p} \in \mathcal{N}_N} T^{\boldsymbol{p}}(\overline{\xi}_b(2^N \boldsymbol{x}))\, \mathbf{1}_{Z_{N+1}} \quad \text{for} \quad \boldsymbol{x} \in \mathbb{R}^3,$$

and its reflection about $z = 0$ as

$$\overline{\xi}_{int,2}(\boldsymbol{x}) = \overline{\xi}_{int,1}(x, y, -z)\mathbf{1}_{z<0} \quad \text{for} \quad \boldsymbol{x} \in \mathbb{R}^3,$$

using which we define

$$\overline{\xi}_N(\boldsymbol{x}) \coloneqq \overline{\xi}_{int,1}(\boldsymbol{x}) + \overline{\xi}_{int,2}(\boldsymbol{x}) \quad \text{for} \quad \boldsymbol{x} \in \mathbb{R}^3. \tag{7.80}$$

As before, $\operatorname{supp} \overline{\xi}_N \Subset D$ and it is the restriction of $\overline{\xi}_N$ to D, which we continue to denote as $\overline{\xi}_N$, that we use in Proposition 7.3.1. We claim that the velocity field $\overline{\boldsymbol{u}}_N$ and the scalar field $\overline{\xi}_N$ defined here satisfy all the requirements stated in Proposition 7.3.1.

We first show that $\operatorname{supp} \overline{\boldsymbol{u}}_N \Subset (-1/2, 1/2) \times (-1/2, 1/2) \times (-z_{N+2}, z_{N+2}) \Subset D$. It is clear from the definition of $\overline{\boldsymbol{u}}_N$ given in (7.79) along with (7.77), (7.78) and the definition of Z_i in (7.75) that if $\widehat{\boldsymbol{x}} \in \operatorname{supp} \overline{\boldsymbol{u}}_N$ then

$$\widehat{z} \in [-z_{N+1}, z_{N+1}] \subset (-z_{N+2}, z_{N+2}). \tag{7.81}$$

Next from the statement (ii) in Proposition 7.4.2, we note that if $\widehat{\boldsymbol{x}} \in \operatorname{supp} \overline{\boldsymbol{u}}(2^i \boldsymbol{x})$ then

$$\widehat{x}, \widehat{y} \in \left(-\frac{1}{3 \cdot 2^i}, \frac{1}{3 \cdot 2^i} \right).$$

Also, note that if $\boldsymbol{p} \in \mathcal{N}_i$ for $i \in \mathbb{N}$, then

$$|p_x|, |p_y| \leq \frac{1}{2} - \frac{1}{2^{i-1}},$$

Combining these two pieces of information tells us that if $\widehat{\boldsymbol{x}} \in \operatorname{supp} T^{\boldsymbol{p}} \overline{\boldsymbol{u}}(2^i \boldsymbol{x})$

then

$$\widehat{x}, \widehat{y} \in \left(-\frac{1}{2} + \frac{1}{3 \cdot 2^i}, \frac{1}{2} - \frac{1}{3 \cdot 2^i}\right) \subset \left(-\frac{1}{2}, \frac{1}{2}\right). \tag{7.82}$$

Finally, combining (7.81) and (7.82) with the definition (7.79) gives

$$\operatorname{supp} \overline{\boldsymbol{u}}_N \Subset (-1/2, 1/2) \times (-1/2, 1/2) \times (-z_{N+2}, z_{N+2}) \Subset D. \tag{7.83}$$

We now show that $\overline{\boldsymbol{u}}_N$ is infinitely differentiable, which together with (7.83) will imply $\overline{\boldsymbol{u}}_N \in C_c^\infty(D; \mathbb{R}^3)$. Let's first define two sets

$$\Lambda \coloneqq \left(\bigcup_{0 \le i \le N-1} (z_i, z_{i+1})\right) \cup \left(\bigcup_{0 \le i \le N-1} (-z_{i+1}, -z_i)\right) \cup (z_N, 1/2) \cup (-1/2, -z_N),$$
$$\Gamma \coloneqq \{z_0, z_1, -z_1, \dots z_N, -z_N\}.$$

It is easy to see from (7.77), (7.78), (7.79) and from the infinite differentiability of $\overline{\boldsymbol{u}}$ and $\overline{\boldsymbol{u}}_b$ in Proposition 7.4.2 that $\overline{\boldsymbol{u}}_N(\boldsymbol{x})$ is infinitely differentiable when $z \in \Lambda$. Therefore, the only thing we still need to show is that $\overline{\boldsymbol{u}}_N(\boldsymbol{x})$ is infinitely differentiable when $z \in \Gamma$, i.e., at the interfaces.

The fact $\widetilde{\boldsymbol{u}}_r$ in Proposition 7.4.2 belongs to $C^\infty(\mathbb{R}^3, \mathbb{R}^3)$ and $\overline{\boldsymbol{u}}_N$ coincides with $\widetilde{\boldsymbol{u}}_r$ when $z \in (-z_1, z_1)$, implies $\overline{\boldsymbol{u}}_N(\boldsymbol{x})$ is infinite differentiable when $z = z_0$. Now if $\boldsymbol{x}$ is such that $z \in (z_0, z_2)$ then $\overline{\boldsymbol{u}}_N(\boldsymbol{x})$ coincides with $\widetilde{\boldsymbol{u}}_b(\boldsymbol{x})$ when $N = 1$ or it coincides with $\widetilde{\boldsymbol{u}}(\boldsymbol{x})$ when $N > 1$, which then concludes the infinite differentiability of $\overline{\boldsymbol{u}}_N$ at $z = z_1$. A similar argument can be applied to conclude the infinite differentiability at $z = -z_1$. In the last case, when $N > 1$ and $i \in \{2, \dots N-1\}$,

then one can show

$$\begin{aligned}\overline{\boldsymbol{u}}_N(\boldsymbol{x}) &= \sum_{\boldsymbol{p}\in\mathcal{N}_{i-1}} T^{\boldsymbol{p}}(\overline{\boldsymbol{u}}(2^{i-1}\boldsymbol{x}))\mathbf{1}_{Z_i} + \sum_{\boldsymbol{p}\in\mathcal{N}_i} T^{\boldsymbol{p}}(\overline{\boldsymbol{u}}(2^i\boldsymbol{x}))\mathbf{1}_{Z_{i+1}} \\ &= \sum_{\boldsymbol{p}\in\mathcal{N}_{i-1}} T^{\boldsymbol{p}}\left(\left(\overline{\boldsymbol{u}} + \sum_{\boldsymbol{p}'\in\mathcal{N}_1} T^{\boldsymbol{p}'}\overline{\boldsymbol{u}}\right)(2^{i-1}\boldsymbol{x})\right) \\ &= \sum_{\boldsymbol{p}\in\mathcal{N}_{i-1}} T^{\boldsymbol{p}}(\widetilde{\boldsymbol{u}}(2^{i-1}\boldsymbol{x})) \quad \text{when} \quad \boldsymbol{x}\in(z_{i-1},z_{i+1}),\end{aligned}$$

or when $i = N$, then

$$\overline{\boldsymbol{u}}_N(\boldsymbol{x}) = \sum_{\boldsymbol{p}\in\mathcal{N}_{i-1}} T^{\boldsymbol{p}}(\widetilde{\boldsymbol{u}}_b(2^{i-1}\boldsymbol{x})) \quad \text{when} \quad \boldsymbol{x}\in(z_{i-1},z_{i+1}),$$

which then establishes that $\overline{\boldsymbol{u}}_N(\boldsymbol{x})$ is infinitely differentiable when $z = z_i$ for $2 \le i \le N$. A similar argument applies when $z = -z_i$ for $2 \le i \le N$, which finishes the proof of $\overline{\boldsymbol{u}}_N \in C_c^\infty(D;\mathbb{R}^3)$. We note similar arguments will also work to show $\overline{\xi}_N \in C_c^\infty(D)$.

It is now fairly easy prove (i) in Proposition 7.3.1. It is trivial to see that $\nabla\cdot\overline{\boldsymbol{u}}_N = 0$ when $z\in\Lambda$. As $\overline{\boldsymbol{u}}_N \in C_c^\infty(D;\mathbb{R}^3)$, the derivatives of $\overline{\boldsymbol{u}}_N$ are continuous in D, which leads us to conclude that $\nabla\cdot\overline{\boldsymbol{u}}_N = 0$ everywhere in D.

Next, we see that (7.83) and a similar conclusion derived for $\overline{\xi}_N$ proves (ii) in Proposition 7.3.1.

To prove (iii) in Proposition 7.3.1, we need the following simple lemma.

Lemma 7.4.5. *For $i\in\mathbb{N}$, let $\boldsymbol{p}_1,\boldsymbol{p}_2\in\mathcal{N}_i$ such that $\boldsymbol{p}_1\neq\boldsymbol{p}_2$, then*

$$\Big(\operatorname{supp} T^{\boldsymbol{p}_1}\overline{\boldsymbol{u}}(2^i\boldsymbol{x}) \cup \operatorname{supp} T^{\boldsymbol{p}_1}\overline{\xi}(2^i\boldsymbol{x})\Big) \bigcap \Big(\operatorname{supp} T^{\boldsymbol{p}_2}\overline{\boldsymbol{u}}(2^i\boldsymbol{x}) \cup \operatorname{supp} T^{\boldsymbol{p}_2}\overline{\xi}(2^i\boldsymbol{x})\Big) = \emptyset,$$

$$\Big(\operatorname{supp} T^{\boldsymbol{p}_1}\overline{\boldsymbol{u}}_b(2^i\boldsymbol{x}) \cup \operatorname{supp} T^{\boldsymbol{p}_1}\overline{\xi}_b(2^i\boldsymbol{x})\Big) \bigcap \Big(\operatorname{supp} T^{\boldsymbol{p}_2}\overline{\boldsymbol{u}}_b(2^i\boldsymbol{x}) \cup \operatorname{supp} T^{\boldsymbol{p}_2}\overline{\xi}_b(2^i\boldsymbol{x})\Big) = \emptyset.$$

Proof of Lemma 7.4.5. As $\boldsymbol{p}_1 \neq \boldsymbol{p}_2$, from the definition (7.76) of $\mathcal{N}_i$, we note the following lower bound on the absolute difference of x and y coordinates of $\boldsymbol{p}_1$ and $\boldsymbol{p}_2$:

$$|\boldsymbol{p}_{1,x} - \boldsymbol{p}_{2,x}| \geq \frac{1}{2^i} \quad \text{and} \quad |\boldsymbol{p}_{1,y} - \boldsymbol{p}_{2,y}| \geq \frac{1}{2^i},$$

which implies

$$|\boldsymbol{p}_1 - \boldsymbol{p}_2|_{\|} \geq \frac{\sqrt{2}}{2^i}.$$

Now, if $\boldsymbol{x}_1 \in \left(\operatorname{supp} T^{\boldsymbol{p}_1}\overline{\boldsymbol{u}}(2^i\boldsymbol{x}) \cup \operatorname{supp} T^{\boldsymbol{p}_1}\overline{\xi}(2^i\boldsymbol{x})\right)$ or $\boldsymbol{x}_1 \in \left(\operatorname{supp} T^{\boldsymbol{p}_1}\overline{\boldsymbol{u}}_b(2^i\boldsymbol{x}) \cup \operatorname{supp} T^{\boldsymbol{p}_1}\overline{\xi}_b(2^i\boldsymbol{x})\right)$ and if $\boldsymbol{x}_2 \in \left(\operatorname{supp} T^{\boldsymbol{p}_2}\overline{\boldsymbol{u}}(2^i\boldsymbol{x}) \cup \operatorname{supp} T^{\boldsymbol{p}_2}\overline{\xi}(2^i\boldsymbol{x})\right)$ or $\boldsymbol{x}_2 \in \left(\operatorname{supp} T^{\boldsymbol{p}_2}\overline{\boldsymbol{u}}_b(2^i\boldsymbol{x}) \cup \operatorname{supp} T^{\boldsymbol{p}_2}\overline{\xi}_b(2^i\boldsymbol{x})\right)$, then using the statements (ii) and (iii) from Proposition 7.4.2, we see that

$$|\boldsymbol{x}_1 - \boldsymbol{p}_1|_{\|} \leq \frac{\sqrt{2}}{3 \cdot 2^i} \quad \text{and} \quad |\boldsymbol{x}_2 - \boldsymbol{p}_2|_{\|} \leq \frac{\sqrt{2}}{3 \cdot 2^i}.$$

We can now finish the proof with a simple application of the triangle inequality as

$$|\boldsymbol{x}_1 - \boldsymbol{x}_2| \geq |\boldsymbol{p}_1 - \boldsymbol{p}_2|_{\|} - |\boldsymbol{x}_1 - \boldsymbol{p}_1|_{\|} - |\boldsymbol{x}_2 - \boldsymbol{p}_2|_{\|} \geq \frac{\sqrt{2}}{3 \cdot 2^i}.$$

□

Using the lemma, we can write

$$(\overline{\boldsymbol{u}}_{int,1}\cdot\nabla\overline{\xi}_{int,1})(\boldsymbol{x})=\overline{\boldsymbol{u}}(\boldsymbol{x})\cdot\nabla\overline{\xi}(\boldsymbol{x})\,\mathbf{1}_{Z_1}+\sum_{i=1}^{N-1}\sum_{\boldsymbol{p}\in\mathcal{N}_i}T^{\boldsymbol{p}}(\overline{\boldsymbol{u}}(2^i\boldsymbol{x}))\cdot\nabla T^{\boldsymbol{p}}(\overline{\xi}(2^i\boldsymbol{x}))\mathbf{1}_{Z_{i+1}}$$
$$+\sum_{\boldsymbol{p}\in\mathcal{N}_N}T^{\boldsymbol{p}}(\overline{\boldsymbol{u}}_b(2^N\boldsymbol{x}))\cdot\nabla T^{\boldsymbol{p}}(\overline{\xi}_b(2^N\boldsymbol{x}))\,\mathbf{1}_{Z_{N+1}}\quad\text{for}\quad z\in\Lambda,$$

which implies

$$(\overline{\boldsymbol{u}}_{int,1}\cdot\nabla\overline{\xi}_{int,1})(\boldsymbol{x})=\overline{\boldsymbol{u}}(\boldsymbol{x})\cdot\nabla\overline{\xi}(\boldsymbol{x})\,\mathbf{1}_{Z_1}+\sum_{i=1}^{N-1}\sum_{\boldsymbol{p}\in\mathcal{N}_i}T^{\boldsymbol{p}}\left(\overline{\boldsymbol{u}}(2^i\boldsymbol{x})\cdot\nabla\overline{\xi}(2^i\boldsymbol{x})\right)\mathbf{1}_{Z_{i+1}}$$
$$+\sum_{\boldsymbol{p}\in\mathcal{N}_N}T^{\boldsymbol{p}}\left(\overline{\boldsymbol{u}}_b(2^N\boldsymbol{x})\cdot\nabla\overline{\xi}_b(2^N\boldsymbol{x})\right)\mathbf{1}_{Z_{N+1}}\quad\text{for}\quad z\in\Lambda.\tag{7.85}$$

Using (7.85) and point (iv) from Proposition 7.4.2, we conclude

$$(\overline{\boldsymbol{u}}_{int,1}\cdot\nabla\overline{\xi}_{int,1})(\boldsymbol{x})=0\quad\text{when}\quad z\in\Lambda\setminus\left(\frac{1}{2}-\frac{15}{32\cdot2^N},\frac{1}{2}-\frac{27}{64\cdot2^N}\right)\tag{7.86}$$

A simple calculation then shows that

$$(\overline{\boldsymbol{u}}_N\cdot\nabla\overline{\xi}_N)(x,y,z)=-(\overline{\boldsymbol{u}}_N\cdot\nabla\overline{\xi}_N)(x,y,-z)\quad\text{when}\quad z\in\Lambda\tag{7.87}$$

which, combined with the result (7.86) and the fact that $\overline{\boldsymbol{u}}_N$ and the derivatives of $\overline{\xi}_N$ are continuous when $z\in\Gamma$, help us conclude

$$(\overline{\boldsymbol{u}}_N\cdot\nabla\overline{\xi}_N)(\boldsymbol{x})=0\quad\text{when}\quad\boldsymbol{x}\in\Gamma.$$

In total, we then have

$$\operatorname{supp}_z(\overline{\boldsymbol{u}}_N\cdot\nabla\overline{\xi}_N)\Subset\left(\frac{1}{2}-\frac{15}{32\cdot2^N},\frac{1}{2}-\frac{27}{64\cdot2^N}\right)\cup\left(-\frac{1}{2}+\frac{27}{64\cdot2^N},-\frac{1}{2}+\frac{15}{32\cdot2^N}\right).$$

To prove (iv) in Proposition 7.3.1, we note from (7.85) and point (iv) in Proposition 7.4.2 that

$$(\overline{\boldsymbol{u}}_{int,1} \cdot \nabla \overline{\xi}_{int,1})(\boldsymbol{x}) = \sum_{\boldsymbol{p} \in \mathcal{N}_N} 2^N T^{\boldsymbol{p}} \left((\overline{\boldsymbol{u}}_b \cdot \nabla \overline{\xi}_b)(2^N \boldsymbol{x}) \right) \mathbf{1}_{Z_{N+1}} \quad \text{for} \quad z \in \Lambda,$$

which when combined with Lemma 7.4.5, implies

$$\left\| \overline{\boldsymbol{u}}_{int,1} \cdot \nabla \overline{\xi}_{int,1} \right\|_{L^\infty(D)} \leq 2^N \left\| \overline{\boldsymbol{u}}_b \cdot \nabla \overline{\xi}_b \right\|_{L^\infty(\mathbb{R}^3)}.$$

Noting (7.87) and that $\overline{\boldsymbol{u}}_N \cdot \nabla \overline{\xi}_N$ coincides with $\overline{\boldsymbol{u}}_{int,1} \cdot \nabla \overline{\xi}_{int,1}$ when $z > 0$, we have

$$\left\| \overline{\boldsymbol{u}}_N \cdot \nabla \overline{\xi}_N \right\|_{L^\infty(D)} \leq 2^N \left\| \overline{\boldsymbol{u}}_b \cdot \nabla \overline{\xi}_b \right\|_{L^\infty(\mathbb{R}^3)}.$$

Now $\overline{\boldsymbol{u}}_b \cdot \nabla \overline{\xi}_b$ is an infinite differentiable function and its support lies in a bounded set from (iii) and (iv) in Proposition 7.4.2, therefore $\left\| \overline{\boldsymbol{u}}_b \cdot \nabla \overline{\xi}_b \right\|_{L^\infty(\mathbb{R}^3)}$ is bounded and we can conclude that

$$\left\| \overline{\boldsymbol{u}}_N \cdot \nabla \overline{\xi}_N \right\|_{L^\infty(D)} \lesssim 2^N.$$

Proof of (v) in Proposition 7.3.1 is a simple computation. Once again using Lemma 7.4.5, one can write the following

$$\begin{aligned} \int_D |\nabla \overline{\boldsymbol{u}}_N|^2 \, \mathrm{d}\boldsymbol{x} \quad &= 2 \int_{\{0<z<1/2\}} |\nabla \overline{\boldsymbol{u}}_{int,1}|^2 \, \mathrm{d}\boldsymbol{x} \\ &= 2 \int_{\{z \in Z_1\}} |\nabla \overline{\boldsymbol{u}}(\boldsymbol{x})|^2 \, \mathrm{d}\boldsymbol{x} + 2 \sum_{i=1}^{N-1} \sum_{\boldsymbol{p} \in \mathcal{N}_i} \int_{\{z \in Z_{i+1}\}} |\nabla T^{\boldsymbol{p}}(\overline{\boldsymbol{u}}(2^i \boldsymbol{x}))|^2 \, \mathrm{d}\boldsymbol{x} \\ &\quad + 2 \sum_{\boldsymbol{p} \in \mathcal{N}_N} \int_{\{z \in Z_{N+1}\}} |\nabla T^{\boldsymbol{p}}(\overline{\boldsymbol{u}}_b(2^N \boldsymbol{x}))|^2 \, \mathrm{d}\boldsymbol{x}. \end{aligned}$$

After an appropriate translation and dilation of the coordinate variables and noting that $|\mathcal{N}_i| = 4^i$, one can show that

$$\begin{aligned}\int_D |\nabla \overline{\boldsymbol{u}}_N|^2 \,\mathrm{d}\boldsymbol{x} &= \left(\sum_{i=0}^{N-1} 2^{i+1}\right) \int_{Z_1} |\nabla \overline{\boldsymbol{u}}(\boldsymbol{x})|^2 \,\mathrm{d}\boldsymbol{x} + 2^{N+1} \int_{\{z\in Z_1\}} |\nabla \overline{\boldsymbol{u}}_b(\boldsymbol{x})|^2 \,\mathrm{d}\boldsymbol{x} \\ &= 2^{N+1} \max\left\{ \int_{\{z\in Z_1\}} |\nabla \overline{\boldsymbol{u}}(\boldsymbol{x})|^2 \,\mathrm{d}\boldsymbol{x}, \int_{\{z\in Z_1\}} |\nabla \overline{\boldsymbol{u}}_b(\boldsymbol{x})|^2 \,\mathrm{d}\boldsymbol{x} \right\} \lesssim 2^N.\end{aligned}$$

Similarly, one can also conclude

$$\int_D |\nabla \overline{\xi}_N|^2 \,\mathrm{d}\boldsymbol{x} \lesssim 2^N,$$

which then proves (v).

The proof of (vi) in Proposition 7.3.1 is also very similar to that of (v). We first write

$$\begin{aligned}\int_D \overline{u}_{N,z}\, \overline{\xi}_N \,\mathrm{d}\boldsymbol{x} \quad &= 2 \int_{\{0<z<1/2\}} \overline{u}_{int,1,z}\, \overline{\xi}_{int,1} \,\mathrm{d}\boldsymbol{x} \\ &= 2 \int_{\{z\in Z_1\}} \overline{u}_z\, \overline{\xi} \,\mathrm{d}\boldsymbol{x} \\ &\quad + 2 \sum_{i=1}^{N-1} \sum_{\boldsymbol{p}\in\mathcal{N}_i} \int_{\{z\in Z_{i+1}\}} T^{\boldsymbol{p}}\left(\overline{u}_z(2^i\boldsymbol{x})\right)\, T^{\boldsymbol{p}}\left(\overline{\xi}(2^i\boldsymbol{x})\right) \,\mathrm{d}\boldsymbol{x} \\ &\quad + 2 \sum_{\boldsymbol{p}\in\mathcal{N}_N} \int_{\{z\in Z_{N+1}\}} T^{\boldsymbol{p}}\left(\overline{u}_{b,z}(2^i\boldsymbol{x})\right)\, T^{\boldsymbol{p}}\left(\overline{\xi}_b(2^i\boldsymbol{x})\right) \,\mathrm{d}\boldsymbol{x}.\end{aligned}$$

After an appropriate translation and dilation of the coordinate variables and noting that $|\mathcal{N}_i| = 4^i$, we obtain

$$\int_D \overline{u}_{N,z}\, \overline{\xi}_N \,\mathrm{d}\boldsymbol{x} = \left(\sum_{i=0}^{N-1} 2^{-i+1}\right) \int_{\{z\in Z_1\}} \overline{u}_z\, \overline{\xi} \,\mathrm{d}\boldsymbol{x} + 2^{-N+1} \int_{\{z\in Z_1\}} \overline{u}_{b,z}\, \overline{\xi}_b \,\mathrm{d}\boldsymbol{x} \geq 2c_3 > 0,$$

where c_3 is a strictly positive constant independent of N. □

7.5 Discussion

In this paper, we studied the problem of optimizing the heat transfer between two differentially heated parallel plates by incompressible flows that satisfy an enstrophy constraint ($\langle|\nabla \boldsymbol{u}|^2\rangle \leq \mathscr{P}$) and no-slip boundary conditions. The main result of this paper was to show that the previously derived upper bound on the heat transfer are sharp in the scaling with $\mathscr{P}$, which we demonstrated by constructing an explicit example of three-dimensional branching pipe flows. In this section, we discuss the implications of our result in the context of (1) anomalous dissipation in a passive scalar and (2) Rayleigh–Bénard convection.

7.5.1 Anomalous dissipation in a passive scalar

The initial motivation for our study was a result by Drivas et al. (2022a), regarding the anomalous dissipation in a passive scalar transport. They constructed a velocity field $\boldsymbol{u} \in C^\infty([0,\tau)\times\mathbb{T}^d)\cap L^1([0,\tau];C^\alpha(\mathbb{T}^d))$, where $d\geq 2$, τ is a fixed time and $\alpha<1$, such that the solution of the advection-diffusion equation

$$\partial_t T^\kappa + \boldsymbol{u}\cdot\nabla T^\kappa = \kappa\Delta T^\kappa$$

follows

$$\liminf_{\kappa\to 0}\kappa\int_0^\tau\int_{\mathbb{T}^d}|\nabla T^\kappa|^2\,d\boldsymbol{x}\,dt\geq\chi>0,$$

where χ may depend on the initial data. While this result was obtained for a periodic domain, we were inspired by the possibility of proving such a result in a domain with boundaries. After appropriately rescaling the velocity fields that we created to prove Theorem 7.1.4, we can state a weak result in this direction.

Corollary 7.5.1. *For a constant $\kappa_0 > 0$, there exist velocity fields $\boldsymbol{u}^\kappa$, for every $0 < \kappa < \kappa_0$, such that $\|\boldsymbol{u}^\kappa\|_{H^1_0(\Omega)} \leq 1$ and the solution of the steady advection diffusion equation: $\boldsymbol{u}^\kappa \cdot \nabla T^\kappa = \kappa \Delta T^\kappa$ in Ω with boundary conditions $T^\kappa = 1$ at $z = -1/2$ and $T^\kappa = 0$ at $z = 1/2$ obeys*

$$\liminf_{\kappa \to 0} \kappa^{2/3} \fint_\Omega |\nabla T^\kappa|^2 \, d\boldsymbol{x} \geq \chi_0 > 0. \tag{7.88}$$

for a constant χ_0.

We see from (7.88) that the exponent for κ is $2/3$, which is less than one. Therefore this corrolary is not as strong as the statement we would have hoped to prove. However, the a priori upper bound (7.9) also shows that this is the best result one can achieve in the setting considered in Corollary 7.5.1. However, if we allow the velocity field to be less smooth, in particular, we allow $\boldsymbol{u}^\kappa$ to be only uniformly bounded in the L^2 norm, then we can indeed prove

$$\liminf_{\kappa \to 0} \kappa \fint_\Omega |\nabla T^\kappa|^2 \, d\boldsymbol{x} \geq \chi_0 > 0. \tag{7.89}$$

This can be shown after appropriately rescaling the velocity fields of Doering and Tobasco (2019) used to prove Theorem 1.1 in their paper. Another possibility is to allow the walls to be rough. This has not yet, to our knowledge, been investigated, which raises the following question: if we allow the boundary of the domain, which locally is the graph of functions that are α–Hölder continuous with exponent $\alpha < 1$, can one also prove (7.89) in that case? Physically, it would mean that we are increasing the heat transfer by letting the area of walls go to infinity. Indeed, it is known in the literature that fractal boundaries tend to enhance heat transfer (Toppaladoddi et al., 2021). Answer to such a question will, therefore,

help in understanding the role played by rough boundaries in increasing the heat transfer. Along the same line, it would also be interesting to investigate the role played by a slip boundary condition for the velocity field (see (Drivas et al., 2022b) and a recent review by Nobili (2021)).

7.5.2 Rayleigh–Bénard convection

Rayleigh–Bénard convection is the flow of fluid between two differentially heated parallel plates driven by buoyancy force. The flow is traditionally modeled by the Navier–Stokes equations under the Boussinesq approximation, written here in nondimensional form as

$$\partial_t \boldsymbol{u} + \boldsymbol{u} \cdot \nabla \boldsymbol{u} = -\nabla p + Pr \Delta \boldsymbol{u} + PrRaT\boldsymbol{e}_z, \tag{7.90a}$$

$$\partial_t T + \boldsymbol{u} \cdot \nabla T = \Delta T, \tag{7.90b}$$

where Ra is the Rayleigh number and Pr is the Prandtl number, respectively given by

$$Ra = \frac{g\alpha H^3 (T_B - T_T)}{\kappa \nu}, \qquad Pr = \frac{\nu}{\kappa}.$$

In these above expressions, ν is the kinematic viscosity, κ is the thermal diffusivity, α is the coefficient of thermal expansion, H is the height of the domain, $T_B - T_T$ is the temperature difference and g is the magnitude of the gravitational acceleration acting in $-\boldsymbol{e}_z$ direction.

We solve the nondimensional governing equations (7.90a-b) in domain Ω with

boundary conditions

$$\boldsymbol{u} = \mathbf{0}, \quad T = 1 \quad \text{at } z = -1/2 \qquad \text{and} \qquad \boldsymbol{u} = \mathbf{0}, \quad T = 0 \quad \text{at } z = 1/2.$$

The quantity of interest is the nondimensional heat transfer known as the Nusselt number Nu given by

$$Nu = 1 + \langle u_z T \rangle.$$

The angle brackets denote the long-time volume average and u_z is the component of the velocity in the z direction. Of course, Nu depends on the initial condition. However, Doering and Constantin (1996) using the background method (see Fantuzzi et al. (2022) for a survey), proved the following a priori bound for any initial condition when $Ra \gg 1$:

$$Nu \lesssim Ra^{\frac{1}{2}}.$$

This bound is uniform in the Prandtl number Pr. To date, the best known upper bound, namely $Nu \leq 0.02634 Ra^{\frac{1}{2}}$, was obtained by Plasting and Kerswell (2003).

An important question is whether the scaling of this bound with respect to the Rayleigh number is sharp. Our result, in this context, proves that this scaling is indeed sharp if one replaces the momentum equation with a simple enstrophy condition.

$$\langle |\nabla \boldsymbol{u}|^2 \rangle = Ra(Nu - 1). \tag{7.91}$$

In other words Theorem 7.1.4 proves that, for large enough Rayleigh number, there exists velocity fields (depending on Ra) such that the solution of the advection-

diffusion equation (7.90b) satisfies the relation (7.91) and for which

$$Nu \sim Ra^{\frac{1}{2}}.$$

Appendix 7.A A useful estimate for the solution of the Poisson's equation: Proof of Proposition 7.3.2

The aim of this section is to give an estimate on the solution of Poisson's equation $\Delta\varphi = f$ solved between parallel boundaries with homogeneous Dirichlet boundary conditions imposed on φ. In particular, we are interested in obtaining bounds on the L^2 norm of $\nabla\varphi$ for a given specific form of the function f. The calculations done in this section will be helpful in establishing an upper bound on the nonlocal term $⨍_\Omega |\nabla\Delta^{-1}\operatorname{div}(\boldsymbol{u}\xi)|^2$ from the section 7.3 (see calculation (7.30)). The basic idea is to write down the solution of Poisson's equation using the Green's function method and then obtain estimates on the derivative of the Green's function to achieve our goal.

The domain of interest for this section is

$$D \coloneqq \mathbb{R} \times \mathbb{R} \times (-1/2, 1/2),$$

as defined in section 7.2 with boundary

$$\partial D \coloneqq \partial D_+ \cup \partial D_- \coloneqq \mathbb{R} \times \mathbb{R} \times \{1/2\} \cup \mathbb{R} \times \mathbb{R} \times \{-1/2\}.$$

Now, suppose φ solves Poisson's equation

$$\Delta\varphi = f \quad \text{in } D, \tag{7.92}$$

with boundary condition

$$\varphi = 0 \quad \text{on} \quad \partial D. \tag{7.93}$$

Then for a sufficiently smooth function f, we can write the solution of Poisson's equation using a Green's function

$$\varphi(\boldsymbol{x}) = \int_D G(\boldsymbol{x}, \boldsymbol{x}') f(\boldsymbol{x}') \, \mathrm{d}\boldsymbol{x}, \tag{7.94}$$

where $G : D \times D \to [-\infty, \infty]$ is given by

$$G(\boldsymbol{x}, \boldsymbol{x}') \coloneqq K(|\boldsymbol{x} - \boldsymbol{x}'|_{\|}, z, z') \tag{7.95}$$

and

$$K(\sigma, z, z') \coloneqq \int_1^\infty I(\sigma, z, z', \tau) \, \frac{\mathrm{d}\tau}{\sqrt{\tau^2 - 1}}, \tag{7.96}$$

$$I(\sigma, z, z', \tau) \coloneqq \frac{\cos(\pi z) \cos(\pi z') \sinh(\pi\tau\sigma)}{2\pi \left[\cosh(\pi\tau\sigma) + \cos\pi(z' + z)\right] \left[\cosh(\pi\tau\sigma) - \cos\pi(z' - z)\right]}. \tag{7.97}$$

In particular, we have the following theorem

Theorem 7.A.1 (Solution of the Poisson's equation)**.** *Let $f \in C^2(D) \cap L^\infty(D)$ whose is support lies a finite distance away from the boundary, i.e.,* $\operatorname{supp} f \subseteq \mathbb{R} \times \mathbb{R} \times (-1/2 + \beta, 1/2 - \beta)$ *for some $\beta \in (0, 1/2)$. Then φ given by (7.94) belongs*

to $C^2(D)$ and solves the Poisson's equation (7.92) with boundary condition (7.93).

Proof. The proof of the theorem is a standard one and is therefore omitted from the paper. The proof relies on the method of images to write the desired Green's function between parallel boundaries as a sum of appropriately translated Green's functions corresponding to the whole space $\mathbb{R}^3$, where the summation is then performed using Cauchy's residue theorem. □

Once we know that the solution φ of the Poisson's equation is given by (7.94), we can use it to calculate $\nabla\varphi$. If $f \in L^\infty(D)$ then by an application of the mean value theorem and the dominated convergence theorem, we can perform differentiation under the integral sign in (7.94), which leads to

$$\nabla\varphi = \int_D \nabla_{\boldsymbol{x}} G(\boldsymbol{x}, \boldsymbol{x}') f(\boldsymbol{x}') \, \mathrm{d}\boldsymbol{x}. \tag{7.98}$$

From (7.98), we see that estimates on $\nabla_{\boldsymbol{x}} G(\boldsymbol{x}, \boldsymbol{x}')$ can provide an upper bound on $|\nabla\varphi|$. Next, we state our result in that direction, but first, we note the following.

For clarity, we use a and b as placeholders for

$$\left|\frac{2}{\pi}\sin\left(\frac{\pi(z-z')}{2}\right)\right| \quad \text{and} \quad \left|\frac{2}{\pi}\cos\left(\frac{\pi(z+z')}{2}\right)\right| \tag{7.99}$$

respectively in the rest of this section and we will use the fact that

$$b^2 - a^2 = \frac{4}{\pi^2}\cos\pi z \cos\pi z' \geq 0 \quad \text{when} \quad z, z' \in (-1/2, 1/2) \tag{7.100}$$

in several places. We will use c for a positive constant (not necessarily the same in all places) independent of any parameters.

Proposition 7.A.2. *Let $f \in L^\infty(D)$ and let φ be defined by the formula (7.94), then the following holds:*

$$|\nabla\varphi|(\boldsymbol{x}) \leq \|f\|_{L^\infty(D)} \int_{\mathrm{supp}_z f} g(z, z')\,\mathrm{d}z'$$

where

$$g(z, z') = c\left(\log\left(1 + \frac{(b^2 - a^2)}{a^2}\right) + \frac{\cos \pi z'}{b}\right) \tag{7.101}$$

and $c > 0$ is a positive constant.

The functions f that are of special interests to us are those which are supported in a "thin layers" close to the boundaries. From Proposition 7.A.2, we can derive the following result for such functions.

Corollary 7.A.3. *Let $f \in L^\infty(D)$ such that $\mathrm{supp}\, f \subseteq \mathbb{R} \times \mathbb{R} \times (1/2 - c_1\varepsilon, 1/2 - c_2\varepsilon) \cup \mathbb{R} \times \mathbb{R} \times (-1/2 + c_2\varepsilon, -1/2 + c_1\varepsilon)$, where $0 < c_2 < c_1 < 1$ and $\varepsilon < 1/4$ are three constants. If φ is defined by the formula (7.94), then the following holds*

$$\frac{1}{l_x l_y} \int_{-l_x/2}^{l_x/2} \int_{-l_y/2}^{l_y/2} \int_{-1/2}^{1/2} |\nabla\varphi|^2 \,\mathrm{d}z\mathrm{d}y\mathrm{d}x \lesssim \varepsilon^3 \|f\|^2_{L^\infty(D)}\,. \tag{7.102}$$

Proof of Proposition 7.3.2. We identify a $l_x - l_y-$periodic function on D with the function f. Then using Corollary 7.A.3, we can finish the proof. □

Proof of Corollary 7.A.3. We note from Proposition 7.A.2

$$\begin{aligned}\frac{1}{l_x l_y}\int_{-l_y/2}^{l_y/2}\int_{-l_x/2}^{l_x/2}\int_{-1/2}^{1/2}|\nabla\varphi|^2\,\mathrm{d}z\mathrm{d}x\mathrm{d}y \leq \\ \|f\|_{L^\infty(D)}^2\int_{-1/2}^{1/2}\left(\int_{\mathrm{supp}_z f} g(z,z')\,\mathrm{d}z'\right)^2\mathrm{d}z \\ = \|f\|_{L^\infty(D)}^2\int_{0}^{1/2}\left(\int_{\mathrm{supp}_z f} g(z,z')\,\mathrm{d}z'\right)^2\mathrm{d}z+ \\ \|f\|_{L^\infty(D)}^2\int_{-1/2}^{0}\left(\int_{\mathrm{supp}_z f} g(z,z')\,\mathrm{d}z'\right)^2\mathrm{d}z. \end{aligned} \tag{7.103}$$

We focus on obtaining a bound on the first term (where the integral is carried from $z = 0$ to $z = 1/2$) in (7.103), as the calculation for the other integral is identical.

When $z' \in (1/2 - c_1\varepsilon, 1/2 - c_2\varepsilon) \cup (-1/2 + c_2\varepsilon, -1/2 + c_1\varepsilon)$ and $z \geq 0$, the following simple succession of inequalities hold:

$$b \geq \frac{1}{\pi}\max\{\cos\pi z, \cos\pi z'\} \tag{7.104a}$$

$$b \geq \frac{1}{2\pi}(\cos\pi z + \cos\pi z') \geq \frac{1}{4}\left(\frac{1}{2} - z + c_2\varepsilon\right) \tag{7.104b}$$

$$\frac{\pi c_2\varepsilon}{2} \leq \cos\pi z' \leq \pi c_1\varepsilon \tag{7.104c}$$

$$\frac{\pi}{4} - \frac{\pi z}{2} \leq \cos\pi z \leq \frac{\pi}{2} - \pi z \tag{7.104d}$$

$$a \geq \frac{1}{2}\left(\frac{1}{2} - c_1\varepsilon - z\right) \quad \text{when} \quad \frac{1}{2} - 2c_1\varepsilon \geq z \geq 0 \tag{7.104e}$$

$$a \geq \frac{1}{2}|z - z'| \quad \text{when} \quad \frac{1}{2} \geq z \geq \frac{1}{2} - 2c_1\varepsilon \tag{7.104f}$$

$$a \geq \frac{1}{5} \quad \text{when} \quad z' \in (-1/2 + c_2\varepsilon, -1/2 + c_1\varepsilon) \tag{7.104g}$$

$$\log(1+\alpha) \leq \alpha \quad \text{when} \quad \alpha \geq 0 \tag{7.104h}$$

Here, (7.104c), (7.104d), (7.104e) and (7.104f) are a simple consequence of the inequality $z/2 \leq \sin z \leq z$ when $z \in [0, \pi/2]$, whereas (7.104a) is obtained by

simple applications of trigonometric identities and (7.104b) is a result of (7.104a), (7.104c) and (7.104d). The result (7.104g) is a consequence of the assumption $0 < c_2 < c_1 < 1$. Finally, (7.104h) can be derived using a Taylor series expansion.

Next, using (7.101) and the Young's inequality, we can write

$$\begin{aligned}\left(\int_{\mathrm{supp}_z f} g(z,z')\,\mathrm{d}z'\right)^2 \lesssim & \left(\int_{\mathrm{supp}_z f\cap\mathbb{R}_+} \log\left(1+\frac{(b^2-a^2)}{a^2}\right)\,\mathrm{d}z'\right)^2 \\ & + \left(\int_{\mathrm{supp}_z f\cap\mathbb{R}_-} \log\left(1+\frac{(b^2-a^2)}{a^2}\right)\,\mathrm{d}z'\right)^2 \\ & + \left(\int_{\mathrm{supp}_z f} \frac{\cos\pi z'}{b}\,\mathrm{d}z'\right)^2. \end{aligned} \tag{7.105}$$

Using (7.104b) and (7.104c), the last term in (7.105) can be bounded from above by

$$\lesssim \frac{\varepsilon^4}{\left(\frac{1}{2}-z+c_2\varepsilon\right)^2}, \tag{7.106}$$

Using (7.100), (7.104c), (7.104g) and (7.104h), the second term in (7.105) satisfies the bound

$$\lesssim \varepsilon^4. \tag{7.107}$$

We divide the calculation of the first term in (7.105) into two cases, when $0 \le z \le 1/2 - 2c_1\varepsilon$ and when $1/2 - 2c_1\varepsilon \le z \le 1/2$. In the first case, using (7.100), (7.104c), (7.104d), (7.104e) and (7.104h), we conclude the first term is

$$\lesssim \frac{\varepsilon^4}{\left(\frac{1}{2}-z-c_1\varepsilon\right)^2}. \tag{7.108}$$

In the second case, when $1/2-2c_1\varepsilon \le z \le 1/2$, we use (7.100), (7.104c), (7.104d),

(7.104f), which gives

$$\lesssim \varepsilon^2. \tag{7.109}$$

Note that in this calculation we do not use the estimate (7.104h). After using (7.104f), we have a logarithmic singularity in the integrand but it is integrable.

Finally, collecting the results (7.106), (7.107), (7.108) and (7.109), and carrying out an integration in z from 0 to 1/2, one can bound the first term in (7.103) as

$$\lesssim \varepsilon^3 \left\| f \right\|^2_{L^\infty(D)}.$$

A similar calculation can be performed for the second term in (7.103) and the same result can be derived which then finishes the proof. □

7.A.1 Proof of Proposition 7.A.2

To prove Proposition 7.A.2, we need to obtain estimates on $\nabla_{\boldsymbol{x}} G(\boldsymbol{x}, \boldsymbol{x}')$. From (7.95), we notice that the derivative of $G(\boldsymbol{x}, \boldsymbol{x}')$ with respect to x can be written as

$$\begin{aligned}\frac{\partial}{\partial x} G(\boldsymbol{x}, \boldsymbol{x}') &= \frac{\partial |\boldsymbol{x} - \boldsymbol{x}'|_{\|}}{\partial x} \cdot \frac{\partial}{\partial \sigma} K(\sigma, z, z') \bigg|_{\sigma = |\boldsymbol{x} - \boldsymbol{x}'|_{\|}} \\ &= \frac{(x - x')}{|\boldsymbol{x} - \boldsymbol{x}'|_{\|}} \cdot \frac{\partial}{\partial \sigma} K(\sigma, z, z') \bigg|_{\sigma = |\boldsymbol{x} - \boldsymbol{x}'|_{\|}},\end{aligned}$$

which leads to the following estimate

$$\left| \frac{\partial}{\partial x} G(\boldsymbol{x}, \boldsymbol{x}') \right| \leq \left(\left| \frac{\partial}{\partial \sigma} K(\sigma, z, z') \right| \right) \bigg|_{\sigma = |\boldsymbol{x} - \boldsymbol{x}'|_{\|}}. \tag{7.110}$$

A similar calculation for the y-derivative of $G(\boldsymbol{x}, \boldsymbol{x}')$ leads to

$$\left|\frac{\partial}{\partial y} G(\boldsymbol{x}, \boldsymbol{x}')\right| \leq \left(\left|\frac{\partial}{\partial \sigma} K(\sigma, z, z')\right|\right)\Big|_{\sigma=|\boldsymbol{x}-\boldsymbol{x}'|_{\|}}, \tag{7.111}$$

while the estimate for the z-derivative of $G(\boldsymbol{x}, \boldsymbol{x}')$ simply is

$$\left|\frac{\partial}{\partial z} G(\boldsymbol{x}, \boldsymbol{x}')\right| \leq \left(\left|\frac{\partial}{\partial z} K(\sigma, z, z')\right|\right)\Big|_{\sigma=|\boldsymbol{x}-\boldsymbol{x}'|_{\|}}. \tag{7.112}$$

Using (7.110), (7.111) and (7.112), we conclude that

$$\begin{aligned}
|\nabla_{\boldsymbol{x}} G(\boldsymbol{x}, \boldsymbol{x}')| &\leq \left|\frac{\partial}{\partial x} G(\boldsymbol{x}, \boldsymbol{x}')\right| + \left|\frac{\partial}{\partial y} G(\boldsymbol{x}, \boldsymbol{x}')\right| + \left|\frac{\partial}{\partial z} G(\boldsymbol{x}, \boldsymbol{x}')\right| \\
&\leq 2\left(\left|\frac{\partial}{\partial \sigma} K(\sigma, z, z')\right|\right)\Big|_{\sigma=|\boldsymbol{x}-\boldsymbol{x}'|_{\|}} + \left(\left|\frac{\partial}{\partial z} K(\sigma, z, z')\right|\right)\Big|_{\sigma=|\boldsymbol{x}-\boldsymbol{x}'|_{\|}} \\
&\leq H(|\boldsymbol{x}-\boldsymbol{x}'|_{\|}, z, z'),
\end{aligned} \tag{7.113}$$

for some suitable $H : \mathbb{R}_+ \times (-1/2, 1/2) \times (-1/2, 1/2) \to [0, +\infty]$. It then follows that

$$\begin{aligned}
|\nabla \varphi(\boldsymbol{x})| &\leq \|f\|_{L^\infty(D)} \int_{-\infty}^{\infty} \int_{-\infty}^{\infty} \int_{\operatorname{supp}_z f} H(|\boldsymbol{x}-\boldsymbol{x}'|_{\|}, z, z')\, \mathrm{d}z' \mathrm{d}x' \mathrm{d}y', \\
&= \|f\|_{L^\infty(D)} \int_{-\infty}^{\infty} \int_{-\infty}^{\infty} \int_{\operatorname{supp}_z f} H(|\boldsymbol{x}'|_{\|}, z, z')\, \mathrm{d}z' \mathrm{d}x' \mathrm{d}y'.
\end{aligned}$$

By considering a transformation from Cartesian coordinates to cylindrical coordinates

$$(x', y', z') \mapsto (\sigma, \theta, z')$$

one obtains

$$\begin{aligned} |\nabla\varphi(\boldsymbol{x})| &\leq \|f\|_{L^\infty(D)} \int_0^\infty \int_0^{2\pi} \int_{\mathrm{supp}_z f} \sigma H(\sigma, z, z')\,\mathrm{d}z'\mathrm{d}\theta\mathrm{d}\sigma, \\ &\lesssim \|f\|_{L^\infty(D)} \int_0^\infty \int_{\mathrm{supp}_z f} \sigma H(\sigma, z, z')\,\mathrm{d}z'\mathrm{d}\sigma. \end{aligned}$$

So, to prove Proposition 7.A.2, we need to find an appropriate $H(\sigma, z, z')$ and then perform the integral

$$\int_0^\infty \sigma H(\sigma, z, z')\,\mathrm{d}\sigma, \tag{7.114}$$

which is our next goal.

To calculate (7.110), (7.111) and (7.112), we need the derivative of $K(\sigma, z, z')$ with σ and z. Using (7.96) and (7.97) along with an application of the mean value theorem and the dominated convergence theorem leads to

$$\frac{\partial K}{\partial \sigma} = \int_1^\infty I_{\sigma 1} \frac{\mathrm{d}\tau}{\sqrt{\tau^2 - 1}} + \int_1^\infty I_{\sigma 2} \frac{\mathrm{d}\tau}{\sqrt{\tau^2 - 1}} + \int_1^\infty I_{\sigma 3} \frac{\mathrm{d}\tau}{\sqrt{\tau^2 - 1}}, \tag{7.115}$$

and

$$\frac{\partial K}{\partial z} = \int_1^\infty I_{z 1} \frac{\mathrm{d}\tau}{\sqrt{\tau^2 - 1}} + \int_1^\infty I_{z 2} \frac{\mathrm{d}\tau}{\sqrt{\tau^2 - 1}} + \int_1^\infty I_{z 3} \frac{\mathrm{d}\tau}{\sqrt{\tau^2 - 1}}, \tag{7.116}$$

where

$$I_{\sigma 1} \coloneqq \frac{\cos(\pi z)\,\cos(\pi z')\,\tau\cosh(\pi\tau\sigma)}{2\left[\cosh(\pi\tau\sigma)+\cos\pi(z'+z)\right]\left[\cosh(\pi\tau\sigma)-\cos\pi(z'-z)\right]}, \tag{7.117a}$$

$$I_{\sigma 2} \coloneqq -\frac{\cos(\pi z)\cos(\pi z')\tau\sinh^2(\pi\tau\sigma)}{2\left[\cosh(\pi\tau\sigma)+\cos\pi(z'+z)\right]^2\left[\cosh(\pi\tau\sigma)-\cos\pi(z'-z)\right]}, \tag{7.117b}$$

$$I_{\sigma 3} \coloneqq -\frac{\cos(\pi z)\cos(\pi z')\tau\sinh^2(\pi\tau\sigma)}{2\left[\cosh(\pi\tau\sigma)+\cos\pi(z'+z)\right]\left[\cosh(\pi\tau\sigma)-\cos\pi(z'-z)\right]^2}, \tag{7.117c}$$

$$I_{z 1} \coloneqq -\frac{\sin(\pi z)\cos(\pi z')\sinh(\pi\tau\sigma)}{2\left[\cosh(\pi\tau\sigma)+\cos\pi(z'+z)\right]\left[\cosh(\pi\tau\sigma)-\cos\pi(z'-z)\right]}, \tag{7.117d}$$

$$I_{z 2} \coloneqq \frac{\cos(\pi z)\cos(\pi z')\sin\pi(z'+z)\sinh(\pi\tau\sigma)}{2\left[\cosh(\pi\tau\sigma)+\cos\pi(z'+z)\right]^2\left[\cosh(\pi\tau\sigma)-\cos\pi(z'-z)\right]}, \tag{7.117e}$$

$$I_{z 3} \coloneqq \frac{\cos(\pi z)\cos(\pi z')\sin\pi(z'-z)\sinh(\pi\tau\sigma)}{2\left[\cosh(\pi\tau\sigma)+\cos\pi(z'+z)\right]\left[\cosh(\pi\tau\sigma)-\cos\pi(z'-z)\right]^2}. \tag{7.117f}$$

Next, we state a few important lemmas to bound the derivatives of $K(\sigma, z, z')$. We will always implicitly assume that $z, z' \in (-1/2, 1/2)$.

Lemma 7.A.1. *Let $\sigma \geq \frac{1}{2\pi}$, then we have*

(i)

$$\int_1^\infty (|I_{\sigma 1}| + |I_{\sigma 2}| + |I_{\sigma 3}|)\,\frac{\mathrm{d}\tau}{\sqrt{\tau^2-1}} \lesssim \cos(\pi z')\exp(-\pi\sigma).$$

(ii)

$$\int_1^\infty (|I_{z 1}| + |I_{z 2}| + |I_{z 3}|)\,\frac{\mathrm{d}\tau}{\sqrt{\tau^2-1}} \lesssim \cos(\pi z')\exp(-\pi\sigma).$$

Lemma 7.A.2. *Let $0 < \sigma < \frac{1}{2\pi}$, then we have*

(i)

$$\int_{\frac{1}{\pi\sigma}}^{\infty} (|I_{\sigma 1}| + |I_{\sigma 2}| + |I_{\sigma 3}|) \frac{\mathrm{d}\tau}{\sqrt{\tau^2 - 1}} \lesssim \frac{\cos(\pi z')}{\sigma}.$$

(ii)

$$\int_{\frac{1}{\pi\sigma}}^{\infty} (|I_{z1}| + |I_{z2}| + |I_{z3}|) \frac{\mathrm{d}\tau}{\sqrt{\tau^2 - 1}} \lesssim \cos(\pi z').$$

Lemma 7.A.3. *Let $0 < \sigma < \frac{1}{2\pi}$ and $z \neq z'$, then we have*

(i)

$$\int_{1}^{\frac{1}{\pi\sigma}} (|I_{\sigma 1}| + |I_{\sigma 2}| + |I_{\sigma 3}|) \frac{\mathrm{d}\tau}{\sqrt{\tau^2 - 1}} \lesssim \frac{1}{\sigma} \left[\frac{1}{\sqrt{\sigma^2 + a^2}} - \frac{1}{\sqrt{\sigma^2 + b^2}} \right].$$

(ii)

$$\int_{1}^{\frac{1}{\pi\sigma}} |I_{z1}| \frac{\mathrm{d}\tau}{\sqrt{\tau^2 - 1}} \lesssim |\tan \pi z| \left[\frac{1}{\sqrt{\sigma^2 + a^2}} - \frac{1}{\sqrt{\sigma^2 + b^2}} \right].$$

(iii)

$$\int_{1}^{\frac{1}{\pi\sigma}} |I_{z2} + I_{z3}| \frac{\mathrm{d}\tau}{\sqrt{\tau^2 - 1}} \lesssim \cos^2 \pi z \cos \pi z' \left[P_1(\sigma, z, z') + P_2(\sigma, z, z') \right].$$

Here,

$$P_1(\sigma,z,z') \coloneqq \frac{2ab\pi}{4(b^2-a^2)^3}\left[\frac{4}{\sqrt{\sigma^2+b^2}}-\frac{4}{\sqrt{\sigma^2+a^2}} \right.$$
$$\left. +(b^2-a^2)\left(\frac{1}{(\sigma^2+a^2)^{3/2}}+\frac{1}{(\sigma^2+b^2)^{3/2}}\right)\right],$$
$$P_2(\sigma,z,z') \coloneqq \frac{\pi^3}{4(b^2-a^2)^3}\left[\frac{4b^2}{\sqrt{\sigma^2+b^2}}-\frac{4a^2}{\sqrt{\sigma^2+a^2}} \right.$$
$$\left. +(b^2-a^2)\left(\frac{2\sigma^2+a^2}{(\sigma^2+a^2)^{3/2}}+\frac{2\sigma^2+b^2}{(\sigma^2+b^2)^{3/2}}\right)\right].$$

Proof of Proposition 7.A.2. Using the results from the above lemmas, a suitable function $H(\sigma,z,z')$ that works in (7.113) is

$$H(\sigma,z,z') \coloneqq c\left(\frac{1}{\sigma}\left[\frac{1}{\sqrt{\sigma^2+a^2}}-\frac{1}{\sqrt{\sigma^2+b^2}}\right]+|\tan\pi z|\left[\frac{1}{\sqrt{\sigma^2+a^2}}-\frac{1}{\sqrt{\sigma^2+b^2}}\right]\right.$$
$$\left. +\cos^2\pi z\cos\pi z'\left[P_1(\sigma,z,z')+P_2(\sigma,z,z')\right]+\frac{\cos\pi z'}{\sigma}\right),$$

when $(\sigma,z,z') \in (0,1/2\pi)\times(-1/2,1/2)\times(-1/2,1/2)$ and

$$H(\sigma,z,z') \coloneqq c\cos\pi z'\exp(-\pi\sigma),$$

when $(\sigma,z,z') \in [1/2\pi,\infty)\times(-1/2,1/2)\times(-1/2,1/2)$. Here, $c>0$ is some positive constant. With this definition of the function H and Lemma 7.C.1 from appendix 7.C, we can obtain a bound on the integral (7.114) as

$$\begin{aligned}\int_0^\infty \sigma H(\sigma,z,z')\,\mathrm{d}\sigma \quad &\lesssim \log\left(1+\frac{4(b^2-a^2)}{3a^2}\right)\\ &\quad +\frac{\cos\pi z'}{b}+\frac{\cos^2\pi z\cos\pi z'}{b^3}+\cos\pi z'\\ &\lesssim \log\left(1+\frac{(b^2-a^2)}{a^2}\right)+\frac{\cos\pi z'}{b}. \end{aligned} \tag{7.119}$$

Here, we used (7.104a) to obtain the last line. □

Proof of Lemma 7.A.1. We first note that

$$\int_1^\infty (|I_{\sigma 1}| + |I_{\sigma 2}| + |I_{\sigma 3}|) \frac{\mathrm{d}\tau}{\sqrt{\tau^2-1}} \le \int_1^2 (|I_{\sigma 1}| + |I_{\sigma 2}| + |I_{\sigma 3}|) \frac{\mathrm{d}\tau}{\sqrt{\tau^2-1}} + 2\int_2^\infty (|I_{\sigma 1}| + |I_{\sigma 2}| + |I_{\sigma 3}|) \frac{\mathrm{d}\tau}{\tau}. \quad (7.120)$$

We also have

$$\int_1^\infty (|I_{z 1}| + |I_{z 2}| + |I_{z 3}|) \frac{\mathrm{d}\tau}{\sqrt{\tau^2-1}} \le \int_1^2 (|I_{z 1}| + |I_{z 2}| + |I_{z 3}|) \frac{\mathrm{d}\tau}{\sqrt{\tau^2-1}} + \int_2^\infty (|I_{z 1}| + |I_{z 2}| + |I_{z 3}|)\, \mathrm{d}\tau. \quad (7.121)$$

Now the assumption in the lemma is $\sigma \ge 1/2\pi$. So, if $\tau \ge 1$, then

$$\cosh(\pi\tau\sigma) - 1 \ge \frac{\cosh(\pi\tau\sigma)}{8},$$

and we always have

$$\sinh(\pi\tau\sigma) \le \cosh(\pi\tau\sigma) \quad \text{and} \quad \frac{\exp(\pi\tau\sigma)}{2} \le \cosh(\pi\tau\sigma).$$

Using these relations in (7.117a-f), one can show

$$|I_{\sigma 1}| \lesssim \cos(\pi z')\tau \exp(-\pi\tau\sigma), \quad |I_{\sigma 2}| \lesssim \cos(\pi z')\tau \exp(-\pi\tau\sigma),$$
$$|I_{\sigma 3}| \lesssim \cos(\pi z')\tau \exp(-\pi\tau\sigma),$$
$$|I_{z 1}| \lesssim \cos(\pi z') \exp(-\pi\tau\sigma), \quad |I_{z 2}| \lesssim \cos(\pi z') \exp(-2\pi\tau\sigma),$$
$$|I_{z 3}| \lesssim \cos(\pi z') \exp(-2\pi\tau\sigma).$$

In total, we obtain

$$|I_{\sigma 1}| + |I_{\sigma 2}| + |I_{\sigma 3}| \lesssim \cos(\pi z')\tau \exp(-\pi\tau\sigma), \tag{7.122a}$$

$$|I_{z1}| + |I_{z2}| + |I_{z3}| \lesssim \cos(\pi z') \exp(-\pi\tau\sigma). \tag{7.122b}$$

Next, we substitute (7.122a) in (7.120) and (7.122b) in (7.121). We also use the fact $\exp(-\pi\tau\sigma) \leq \exp(-\pi\sigma)$ for the integrals carried from $\tau = 1$ to $\tau = 2$ in (7.120) and (7.121), which leads to

$$\begin{aligned}\int_1^\infty (|I_{\sigma 1}| + |I_{\sigma 2}| + |I_{\sigma 3}|) \frac{\mathrm{d}\tau}{\sqrt{\tau^2 - 1}} \quad &\lesssim \cos(\pi z') \exp(-\pi\sigma) + \cos(\pi z') \frac{\exp(-2\pi\sigma)}{\pi\sigma} \\ &\lesssim \cos(\pi z') \exp(-\pi\sigma), \end{aligned} \tag{7.123}$$

and

$$\begin{aligned}\int_1^\infty (|I_{z1}| + |I_{z2}| + |I_{z3}|) \frac{\mathrm{d}\tau}{\sqrt{\tau^2 - 1}} \quad &\lesssim \cos(\pi z') \exp(-\pi\sigma) + \cos(\pi z') \frac{\exp(-2\pi\sigma)}{\pi\sigma} \\ &\lesssim \cos(\pi z') \exp(-\pi\sigma). \end{aligned} \tag{7.124}$$

□

Proof of Lemma 7.A.2. The proof is similar to the proof of lemma 7.A.1. □

Proof of Lemma 7.A.3. First, we establish a few simple relations. The assumption in the lemma is $\sigma < \frac{1}{2\pi}$. So, if $1 \leq \tau \leq \frac{1}{\pi\sigma}$, then

$$\sinh(\pi\sigma\tau) \leq (\pi\sigma\tau)\sinh(1), \quad \cosh(\pi\sigma\tau) \leq \cosh(1),$$
$$\text{and} \quad \cosh(\pi\sigma\tau) \leq 1 + (\cosh(1) - 1)\pi^2\sigma^2\tau^2,$$

and we always have

$$\cosh(\pi\sigma\tau) \geq 1 + \frac{(\pi\sigma\tau)^2}{2}.$$

(i) We can then use the relations above to derive a simple bound on $|I_{\sigma 1}|$:

$$|I_{\sigma 1}| \leq I^b_{\sigma 1} \coloneqq \frac{2\cosh(1)\cos(\pi z)\,\cos(\pi z')\,\tau}{\pi^4\left[\sigma^2\tau^2 + a^2\right]\left[\sigma^2\tau^2 + b^2\right]}.$$

We can also obtain a simple bound on $|I_{\sigma 2}|$ as follows

$$\begin{aligned} |I_{\sigma 2}| \quad &\leq \frac{4\sinh^2(1)\cos(\pi z)\,\cos(\pi z')\,\sigma^2\tau^3}{\pi^4\left[\sigma^2\tau^2 + a^2\right]^2\left[\sigma^2\tau^2 + b^2\right]} \\ &\leq \frac{4\sinh^2(1)\cos(\pi z)\,\cos(\pi z')\,\tau}{\pi^4\left[\sigma^2\tau^2 + a^2\right]\left[\sigma^2\tau^2 + b^2\right]} = \frac{2\sinh^2(1)}{\cosh(1)} I^b_{\sigma 1}. \end{aligned}$$

With a similar calculation, we prove that the same bound also holds for $|I_{\sigma 3}|$. We can now finish the proof as given below

$$\begin{aligned} \int_1^{\frac{1}{\pi\sigma}} |I_{\sigma 1}| + |I_{\sigma 2}| + |I_{\sigma 3}| \,\frac{\mathrm{d}\tau}{\sqrt{\tau^2 - 1}} &\lesssim \int_1^{\infty} |I^b_{\sigma 1}| \,\frac{\mathrm{d}\tau}{\sqrt{\tau^2 - 1}} \\ &\lesssim \frac{1}{\sigma}\left[\frac{1}{\sqrt{\sigma^2 + a^2}} - \frac{1}{\sqrt{\sigma^2 + b^2}}\right]. \end{aligned}$$

(ii) We can obtain a following simple bound on $|I_{z1}|$ as

$$|I_{z1}| \leq \frac{2\pi\sigma\sinh(1)|\sin\pi z|\cos\pi z'\tau}{\pi^4\left[\sigma^2\tau^2 + a^2\right]\left[\sigma^2\tau^2 + b^2\right]} = (\pi\sigma)\tanh(1)|\tan(\pi z)| I^b_{\sigma 1}.$$

Performing an integration in τ as in part (i) leads to the desired result.

(iii) We first obtain a simple bound on the sum $I_{z2} + I_{z3}$ given as follows

$$I_{z2} + I_{z3} = \frac{\cos^2(\pi z)\cos(\pi z')\sinh(\pi\tau\sigma)\left[\sin\pi z'\cosh(\pi\sigma\tau) - \sin\pi z\right]}{\left[\cosh(\pi\tau\sigma) + \cos\pi(z'+z)\right]^2\left[\cosh(\pi\tau\sigma) - \cos\pi(z'-z)\right]^2},$$

$$\implies \quad |I_{z2} + I_{z3}| \leq \frac{16}{\pi^7}\cos^2(\pi z)\cos(\pi z')\frac{\sigma\tau\left[|\sin\pi z' - \sin\pi z| + \pi^2\sigma^2\tau^2\right]}{\left[\sigma^2\tau^2 + a^2\right]^2\left[\sigma^2\tau^2 + b^2\right]^2}.$$

This result, combined with the following integrals

$$\int_1^\infty \frac{\sigma\tau}{\left[\sigma^2\tau^2 + a^2\right]^2\left[\sigma^2\tau^2 + b^2\right]^2}\frac{\mathrm{d}\tau}{\sqrt{\tau^2-1}} =$$
$$\frac{\pi}{4(b^2-a^2)^3}\left[\frac{4}{\sqrt{\sigma^2+b^2}} - \frac{4}{\sqrt{\sigma^2+a^2}} + (b^2-a^2)\left(\frac{1}{(\sigma^2+a^2)^{3/2}} + \frac{1}{(\sigma^2+b^2)^{3/2}}\right)\right],$$
$$\int_1^\infty \frac{\sigma^3\tau^3}{\left[\sigma^2\tau^2 + a^2\right]^2\left[\sigma^2\tau^2 + b^2\right]^2}\frac{\mathrm{d}\tau}{\sqrt{\tau^2-1}} =$$
$$\frac{\pi}{4(b^2-a^2)^3}\left[\frac{4b^2}{\sqrt{\sigma^2+b^2}} - \frac{4a^2}{\sqrt{\sigma^2+a^2}} + (b^2-a^2)\left(\frac{2\sigma^2+a^2}{(\sigma^2+a^2)^{3/2}} + \frac{2\sigma^2+b^2}{(\sigma^2+b^2)^{3/2}}\right)\right],$$

leads to the desired result. □

Appendix 7.B Derivation of the variational principle for heat transfer (7.11)

In this appendix, we derive the variational principle given in (7.11). The proof is taken from the paper of Doering & Tobasco (Doering and Tobasco, 2019) and provided here for completeness. We begin by recalling

$$Q(\boldsymbol{u}) = \fint_\Omega |\nabla T|^2\,\mathrm{d}\boldsymbol{x} = 1 + \fint_\Omega u_z T\,\mathrm{d}\boldsymbol{x}, \tag{7.126}$$

where T solves the steady convection diffusion equation and the velocity is assumed to be in $L^\infty(\Omega;\mathbb{R}^3)$. After substituting

$$T = \theta + \frac{1}{2} - z,$$

we obtain

$$Q(\boldsymbol{u}) = 1 + \fint_\Omega |\nabla\theta|^2 \,\mathrm{d}\boldsymbol{x} = 1 + \fint_\Omega u_z\theta \,\mathrm{d}\boldsymbol{x}, \tag{7.127}$$

where $\theta \in H_0^1(\Omega)$ solves

$$\boldsymbol{u}\cdot\nabla\theta = \Delta\theta + u_z \qquad \text{in} \qquad \Omega,$$

and satisfies the homogeneous Dirichlet boundary conditions. Next, we consider a system of two PDEs.

$$\left.\begin{aligned} \boldsymbol{u}\cdot\nabla\eta_0 &= \Delta\xi_0 + u_z, \\ \boldsymbol{u}\cdot\nabla\xi_0 &= \Delta\eta_0, \end{aligned}\right\} \quad \text{in} \quad \Omega, \tag{7.128a-b}$$

where both η_0 and ξ_0 satisfy the homogeneous Dirichlet boundary conditions. Clearly then

$$\theta = \eta_0 + \xi_0. \tag{7.129}$$

By multiplying the equation (2.128b) with ξ_0 and integrating, one obtains

$$\int_\Omega \nabla\eta_0\cdot\nabla\xi_0 \,\mathrm{d}\boldsymbol{x} = 0. \tag{7.130}$$

Next, we multiply the equation (2.128a) with η_0 and integrate and use (7.130) to obtain

$$\int_\Omega u_z \eta_0 \,\mathrm{d}\boldsymbol{x} = 0. \tag{7.131}$$

Finally, we substitute (7.129) in (7.127) and use (7.130) and (7.131) to get

$$Q(\boldsymbol{u}) - 1 = \fint_\Omega |\nabla \xi_0|^2 + |\nabla \eta_0|^2 \,\mathrm{d}\boldsymbol{x} = \fint_\Omega u_z \xi_0 \,\mathrm{d}\boldsymbol{x}, \tag{7.132}$$

which after using (2.128b) can be rewritten as

$$Q(\boldsymbol{u}) - 1 = 2\fint_\Omega u_z \xi_0 \,\mathrm{d}\boldsymbol{x} - \fint_\Omega |\nabla \xi_0|^2 \,\mathrm{d}\boldsymbol{x} - \fint_\Omega |\nabla \Delta^{-1} \boldsymbol{u} \cdot \nabla \xi_0|^2 \,\mathrm{d}\boldsymbol{x}, \tag{7.133}$$

where Δ^{-1} denotes the inverse Laplacian operator in Ω corresponding to the homogeneous Dirichlet boundary conditions. We now consider the following maximization problem

$$\sup_{\xi \in H_0^1(\Omega)} 2\fint_\Omega u_z \xi \,\mathrm{d}\boldsymbol{x} - \fint_\Omega |\nabla \xi|^2 \,\mathrm{d}\boldsymbol{x} - \fint_\Omega |\nabla \Delta^{-1} \boldsymbol{u} \cdot \nabla \xi|^2 \,\mathrm{d}\boldsymbol{x}, \tag{7.134}$$

which is strictly concave, therefore, the only maximizer satisfies the Euler–Lagrange equation

$$\boldsymbol{u} \cdot \nabla \Delta^{-1} (\boldsymbol{u} \cdot \nabla \xi) = \Delta \xi + u_z.$$

We see that ξ_0 is the solution of above equation, therefore, ξ_0 maximizes (7.134), which then combined with (7.133) gives us

$$Q(\boldsymbol{u}) - 1 = \max_{\xi \in H_0^1(\Omega)} 2\fint_\Omega u_z \xi \,\mathrm{d}\boldsymbol{x} - \fint_\Omega |\nabla \xi|^2 \,\mathrm{d}\boldsymbol{x} - \fint_\Omega |\nabla \Delta^{-1} \boldsymbol{u} \cdot \nabla \xi|^2 \,\mathrm{d}\boldsymbol{x}. \tag{7.135}$$

To make this formulation homogeneous in the variable ξ, we consider the transformation $\xi \to s\xi$ and optimize in the scaling s to obtain

$$Q(\boldsymbol{u}) - 1 = \sup_{\substack{\xi \in H_0^1(\Omega) \\ \xi \not\equiv 0}} \frac{\left(\fint_\Omega u_z \xi \, \mathrm{d}\boldsymbol{x} \right)^2}{\fint_\Omega |\nabla \xi|^2 \, \mathrm{d}\boldsymbol{x} + \fint_\Omega |\nabla \Delta^{-1} \operatorname{div}(\boldsymbol{u}\xi)|^2 \, \mathrm{d}\boldsymbol{x}}. \tag{7.136}$$

Next, from the definition of $Q^s_{\max}(\mathscr{P})$ given in (7.5), we simply obtain

$$Q^s_{\max}(\boldsymbol{u}) - 1 = \sup_{\substack{\boldsymbol{u} \in L^\infty(\Omega) \\ \nabla \cdot \boldsymbol{u} = 0, \ \boldsymbol{u}|_{\partial\Omega} = \boldsymbol{0} \\ \fint_\Omega |\nabla \boldsymbol{u}|^2 \, \mathrm{d}\boldsymbol{x} \le \mathscr{P}}} \sup_{\substack{\xi \in H_0^1(\Omega) \\ \xi \not\equiv 0}} \frac{\left(\fint_\Omega u_z \xi \, \mathrm{d}\boldsymbol{x} \right)^2}{\fint_\Omega |\nabla \xi|^2 \, \mathrm{d}\boldsymbol{x} + \fint_\Omega |\nabla \Delta^{-1} \operatorname{div}(\boldsymbol{u}\xi)|^2 \, \mathrm{d}\boldsymbol{x}}. \tag{7.137}$$

Finally, considering the following transformation

$$\boldsymbol{u} \to \frac{\mathscr{P}^{\frac{1}{2}}}{\fint_\Omega |\nabla \boldsymbol{u}|^2 \, \mathrm{d}\boldsymbol{x}} \boldsymbol{u}, \qquad \xi \to \frac{\fint_\Omega |\nabla \boldsymbol{u}|^2 \, \mathrm{d}\boldsymbol{x}}{\mathscr{P}^{\frac{1}{2}}} \xi, \tag{7.138}$$

in (7.137) leads to the desired result stated in Proposition 7.11.

Appendix 7.C Bounds on a few integrals

Lemma 7.C.1. *Let a and b be as given in (7.99). Let $z, z' \in (-1/2, 1/2)$ and $z \neq z'$, then the following estimates hold*

(i)

$$\int_0^1 \left[\frac{1}{\sqrt{\sigma^2 + a^2}} - \frac{1}{\sqrt{\sigma^2 + b^2}} \right] \mathrm{d}\sigma \le \frac{1}{2} \log \left(1 + \frac{4(b^2 - a^2)}{3a^2} \right). \tag{7.139}$$

(ii)

$$\int_0^1 \left[\frac{\sigma}{\sqrt{\sigma^2+a^2}} - \frac{\sigma}{\sqrt{\sigma^2+b^2}}\right] \mathrm{d}\sigma \leq \frac{b^2-a^2}{b}. \tag{7.140}$$

(iii)

$$\int_0^1 \sigma P_1(\sigma, z, z') \,\mathrm{d}\sigma \leq \frac{\pi}{2b^3}. \tag{7.141}$$

(iv)

$$\int_0^1 \sigma P_2(\sigma, z, z') \,\mathrm{d}\sigma \leq \frac{\pi^3}{4b^3}. \tag{7.142}$$

Proof of Lemma 7.C.1.

Recall from the definition (7.99) of a and b that $a \leq b$, a fact which we will use in the proofs below.

(i)

$$\begin{aligned}
\int_0^1 \left[\frac{1}{\sqrt{\sigma^2+a^2}} - \frac{1}{\sqrt{\sigma^2+b^2}}\right] \mathrm{d}\sigma \quad &= \frac{1}{2}\log\frac{1+\sqrt{1+a^2}}{1+\sqrt{1+b^2}} + \frac{1}{2}\log\frac{\sqrt{1+b^2}-1}{\sqrt{1+a^2}-1} \\
&\leq \frac{1}{2}\log\left(1 + \frac{\sqrt{1+b^2}-\sqrt{1+a^2}}{\sqrt{1+a^2}-1}\right) \\
&\leq \frac{1}{2}\log\left(1 + \frac{8(b^2-a^2)}{3a^2\left[\sqrt{1+b^2}+\sqrt{1+a^2}\right]}\right) \\
&\leq \frac{1}{2}\log\left(1 + \frac{4(b^2-a^2)}{3a^2}\right).
\end{aligned} \tag{7.143}$$

(ii)

$$\int_0^1 \left[\frac{\sigma}{\sqrt{\sigma^2+a^2}} - \frac{\sigma}{\sqrt{\sigma^2+b^2}}\right] \mathrm{d}\sigma = \sqrt{1+a^2} - \sqrt{1+b^2} + b - a \\ \leq \frac{b^2-a^2}{b+a} \leq \frac{b^2-a^2}{b}. \tag{7.144}$$

(iii)

$$\int_0^1 \sigma P_1(\sigma, z, z') \,\mathrm{d}\sigma = \frac{\pi ab}{2}\left[\frac{1}{ab(b+a)^3} - \frac{1}{\sqrt{1+a^2}\sqrt{1+b^2}(\sqrt{1+b^2}+\sqrt{1+a^2})^3}\right] \\ \leq \frac{\pi}{2b^3}. \tag{7.145}$$

(iv)

$$\int_0^1 \sigma P_2(\sigma, z, z') \,\mathrm{d}\sigma = \frac{\pi^3}{4}\left[\frac{1}{(b+a)^3} - \frac{1}{(\sqrt{1+b^2}+\sqrt{1+a^2})^3} \right. \\ \left. - \frac{1}{\sqrt{1+a^2}\sqrt{1+b^2}(\sqrt{1+b^2}+\sqrt{1+a^2})^3}\right] \\ \leq \frac{\pi^3}{4b^3}. \tag{7.146}$$

□

Appendix 7.D A few basic lemmas

Lemma 7.D.1. *Let $f \in C^0(\mathbb{R})$ such that $f'(r)$ exists for all $r \neq 0$. Now assume that $f'(r) \to \mathfrak{f}_0'$ as $r \to 0$ for some finite $\mathfrak{f}_0'$, then $f'(0)$ exists and its value is $\mathfrak{f}_0'$.*

Proof of Lemma 7.D.1. Using the mean value theorem, we have

$$\frac{f(h)-f(0)}{h} = f'(\eta) \qquad \text{for some } \eta \in (0,h), \tag{7.147}$$

The proof of lemma follows by taking $h \to 0$. □

Definition 7.D.1. *A function $f : \mathbb{R} \to \mathbb{R}$ is said to have the property (N) if*

$$f \in C^\infty(\mathbb{R}) \qquad \text{and} \qquad \left.\frac{d^{2n-1} f(r)}{d\, r^{2n-1}}\right|_{r=0} = 0 \quad \forall\, n \in \mathbb{N}. \tag{7.148}$$

It is clear that if $f(r)$ has the property (N) then so does the $f(\alpha r)$ for any $\alpha \neq 0$. Furthermore, we have the following lemma.

Lemma 7.D.2. *If a function $f : \mathbb{R} \to \mathbb{R}$ has the property (N) then so does the function $g : \mathbb{R} \to \mathbb{R}$ defined as*

$$g(r) := \begin{cases} \frac{1}{r}\frac{df(r)}{dr} & \text{if} \quad r \neq 0, \\ f''(0) & \text{if} \quad r = 0, \end{cases} \tag{7.149}$$

has the property (N).

Proof of Lemma 7.D.2. It is clear that $g(r)$ is continuous when $r \neq 0$. Now from L'Hospital's rule we obtain

$$\lim_{r\to 0} \frac{1}{r}\frac{df(r)}{dr} = \lim_{r\to 0} \frac{d^2 f(r)}{dr^2} = f''(0), \tag{7.150}$$

therefore, using Lemma 7.D.1, $g(r)$ is continuous at $r = 0$ as well. Now, for $n \geq 1$, we have

$$\frac{d^n g(r)}{dr^n} = \frac{n!}{r^{n+1}} \sum_{i=0}^{n} \frac{(-1)^{n-i} r^i}{i!} \frac{d^{i+1} f(r)}{dr^{i+1}} \qquad \text{if} \quad r \neq 0. \tag{7.151}$$

Taking the limit $r \to 0$ and using the L'Hospital's rule, we obtain

$$\begin{aligned}\lim_{r\to 0}\frac{d^n g(r)}{dr^n} &= \lim_{r\to 0}\frac{n!}{r^{n+1}}\sum_{i=0}^{n}\frac{(-1)^{n-i}r^i}{i!}\frac{d^{i+1}f(r)}{dr^{i+1}} \\ &= \lim_{r\to 0}\frac{n!}{(n+1)r^n}\left[\sum_{i=0}^{n}\frac{(-1)^{n-i}r^i}{i!}\frac{d^{i+2}f(r)}{dr^{i+2}} - \sum_{i=1}^{n}\frac{(-1)^{n-i-1}r^{i-1}}{(i-1)!}\frac{d^{i+1}f(r)}{dr^{i+1}}\right] \\ &= \frac{1}{(n+1)}\frac{d^{i+2}f(r)}{dr^{i+2}}\bigg|_{r=0}. \end{aligned} \tag{7.152}$$

Noting that g is continuous and using Lemma 7.D.1 and the formula (7.152), for $n = 1$, we see that $g(r)$ is differentiable at $r = 0$, furthermore, $g'(r)$ is continuous everywhere. Proceeding in a similar manner, an induction argument then shows that g is infinitely differentiable. Once again, noting from the formula (7.152) that all the odd derivatives of g are zero at $r = 0$, proves the lemma. □

Lemma 7.D.3. *Let $g : \mathbb{R}^2 \to \mathbb{R}$ be given by $g(y, z) = y^{\alpha_y} z^{\alpha_z} f(\varrho)$, where α_y and α_z are nonnegative integers and ϱ is a placeholder for $\sqrt{y^2 + z^2}$. Furthermore, the function $f : \mathbb{R} \to \mathbb{R}$ has the property (N). Then the function g is infinitely differentiable.*

Proof. We can prove this lemma using an induction argument combined with Lemma 7.D.2. □

Now it is a standard exercise in classical real analysis to show that the functions $\overline{\varphi}(r)$, $h(r)$, $\Psi_s(r)$, $\Psi_e(r)$, $\frac{\Psi_s(r)}{r^2}$ and $\frac{\Psi_e(r)}{r^2}$, with relevant definitions given in (7.53), (7.59)and (7.61), have the property (N). Using Lemma 7.D.3, one can then conclude that the velocity field, as defined in (7.61), is infinitely smooth.

Chapter 8

Nonuniqueness of trajectories on a set of full measure for Sobolev vector fields

This chapter is based on the paper Kumar (2023) (to be submitted soon). A preprint is available at arXiv:2301.05185.

8.1 Introduction

In this paper, we consider the following system of ordinary differential equations (ODE)

$$\frac{d\boldsymbol{x}(t)}{dt} = \boldsymbol{u}(t, \boldsymbol{x}(t)) \qquad \text{with} \qquad \boldsymbol{x}(0) = \boldsymbol{x}_0 \in \mathbb{T}^d, \tag{8.1}$$

where $\mathbb{T}^d$ is a d-dimensional Torus and $\boldsymbol{u} : [0, T] \times \mathbb{T}^d \to \mathbb{R}^d$ is a vector field taken to be continuous for convenience. We are interested in studying an important

question regarding this ODE for the case when the vector field $\boldsymbol{u}$ has only Sobolev regularity. To describe the complete problem, let us start with a few definitions.

Definition 8.1.1 (Trajectory)**.** *We say $\gamma_{\boldsymbol{x}}^{\boldsymbol{u}} : [0,T] \to \mathbb{T}^d$ is a trajectory corresponding to the vector field $\boldsymbol{u}$ starting at $\boldsymbol{x}$ if $\gamma_{\boldsymbol{x}}^{\boldsymbol{u}}$ is absolutely continuous, $\gamma_{\boldsymbol{x}}^{\boldsymbol{u}}$ solves the ODE (8.1), i.e., $\dot{\gamma}_{\boldsymbol{x}}^{\boldsymbol{u}}(t) = \boldsymbol{u}(t, \gamma_{\boldsymbol{x}}^{\boldsymbol{u}}(t))$ $\forall t \in [0,T]$ and $\gamma_{\boldsymbol{x}}^{\boldsymbol{u}}(0) = \boldsymbol{x}$.*

For a vector field $\boldsymbol{u}$, by bundling these trajectories for $\mathscr{L}^d$-a.e. $\boldsymbol{x} \in \mathbb{T}^d$, we can define a flow map as follows.

Definition 8.1.2 (Flow map)**.** *A map $X^{\boldsymbol{u}} : [0,T] \times \mathbb{T}^d \to \mathbb{T}^d$ is called a flow map corresponding to the vector field $\boldsymbol{u}$ if, for $\mathscr{L}^d$-a.e. $\boldsymbol{x} \in \mathbb{T}^d$, $X^{\boldsymbol{u}}(\cdot, \boldsymbol{x}) : [0,T] \to \mathbb{T}^d$ is a trajectory starting from $\boldsymbol{x}$.*

With this definition, we say two flow maps $X_1^{\boldsymbol{u}}$ and $X_2^{\boldsymbol{u}}$ are the same if trajectories $X_1^{\boldsymbol{u}}(\cdot, \boldsymbol{x})$ and $X_2^{\boldsymbol{u}}(\cdot, \boldsymbol{x})$ are the same for $\mathscr{L}^d$-a.e. $\boldsymbol{x} \in \mathbb{T}^d$. A restricted class of flow maps is called *regular Lagrangian flows*, which plays an important role in DiPerna and Lions (1989) theory. The following definition is taken from a paper by Ambrosio (2004).

Definition 8.1.3 (Regular Lagrangian flow)**.** *A map $X_{RL}^{\boldsymbol{u}} : [0,T] \times \mathbb{T}^d \to \mathbb{T}^d$ is a regular Lagrangian flow if it is a flow map corresponding to the vector field $\boldsymbol{u}$. In addition, it satisfies the following condition.*

- *For any time $t \in [0,T]$, $X_{RL}^{\boldsymbol{u}}(t, \cdot)_{\#}\mathscr{L}^d \leq C\mathscr{L}^d$ for some constant $C > 0$.*

If the vector field is Lipschitz continuous, then the classical Cauchy–Lipschitz theorem guarantees the uniqueness of trajectories starting from any $\boldsymbol{x}$. Moreover, the corresponding flow map $X^{\boldsymbol{u}}$ is automatically a regular Lagrangian flow, i.e., the additional condition required in the definition (8.1.3) is a consequence in the classical theory.

In the late 1980s, DiPerna and Lions (1989), in a pioneering work, developed the theory of ODE for Sobolev vector fields with bounded divergence, where they showed the existence and uniqueness in the class of regular Lagrangian flow. The theory of DiPerna and Lions was later extended by Ambrosio (2004) to vector fields of bounded variation. Since the theory of DiPerna and Lions first came out, an interesting question remained: is it possible to show the uniqueness of a general flow map, as in definition (8.1.2), for Sobolev vector fields? In other words, is any flow map automatically a regular Lagrangian flow, just as in the classical case?

In recent years, the answer to this question has been given. Caravenna and Crippa (2021) showed that if $\boldsymbol{u} \in C([0,T]; W^{1,p}(\mathbb{T}^d, \mathbb{R}^d))$ with $p > d$, then the trajectories are unique for $\mathscr{L}^d$-a.e. $\boldsymbol{x} \in \mathbb{T}^d$. However, if $p < d$, then Brué et al. (2021) showed that there are divergence-free vector fields $\boldsymbol{u} \in C([0,T]; W^{1,p}(\mathbb{T}^d, \mathbb{R}^d) \cap L^s)$ for $s < \infty$ such that the trajectories are not unique on a set of positive measure, which also implies that there are flow maps $X^{\boldsymbol{u}}$ that are not regular Lagrangian. Their proof uses a convex integration type scheme to prove the nonuniqueness of positive solutions of the continuity equation and then uses Ambrosio's superposition principle to conclude the nonuniqueness of trajectories for the ODE. Using the same methodology, Giri and Sorella (2022); Pitcho and Sorella (2021) covered the case of autonomous vector fields. They constructed a divergence-free vector field $\boldsymbol{u} \in W^{1,p}(\mathbb{T}^d, \mathbb{R}^d)$ with $p < d-1$ and showed that the nonuniqueness of trajectories could occur on a set of positive measure. We also note that explicit examples of vector fields for which nonuniqueness happens on a set of full Hausdorff dimension but of measure zero are known (Fefferman et al., 2021).

Inspired by one of our recent studies on branching flow for optimal heat transport (Kumar, 2022b), in this paper, we give an explicit example of a vector field $\boldsymbol{u} \in C([0,T]; W^{1,p}(\mathbb{T}^d, \mathbb{R}^d)$ with $p < d$, for which we show that the set of initial

conditions for which trajectories are not unique can be of full measure. Furthermore, the vector field that we construct also possesses Hölder continuity of exponent α arbitrarily close to one. The following theorem summarizes our result for the unsteady case.

Theorem 8.1.1 (Main result: unsteady case)**.** *For every integer $d \geq 2$ and every $1 \leq p < d$, $0 < \alpha < 1$ and $T > 0$, there exists a divergence-free vector field $\boldsymbol{u} \in C([0,T]; W^{1,p}(\mathbb{T}^d, \mathbb{R}^d)) \cap C^\alpha([0,T] \times \mathbb{T}^d, \mathbb{R}^d)$ such that the set of initial conditions for which trajectories are not unique is a full measure set.*

The unsteady vector field construction to prove the above theorem can be trivially modified to produce a similar result using a steady vector field. Essentially, we trade time for one space dimension. The result is summarized in the following theorem.

Theorem 8.1.2 (Main result: steady case)**.** *For every integer $d \geq 3$ and every $1 \leq p < d-1$ and $0 < \alpha < 1$, there exists a divergence-free vector field $\boldsymbol{u}^s \in W^{1,p}(\mathbb{T}^d, \mathbb{R}^d) \cap C^\alpha(\mathbb{T}^d, \mathbb{R}^d)$ such that the set of initial conditions for which trajectories are not unique is a full measure set.*

8.1.1 Notation

In this paper, we will work with both $\mathbb{R}^d$ and a d-dimensional torus $\mathbb{T}^d = \mathbb{R}^d/\mathbb{Z}^d$. We identify point $\boldsymbol{x} \in \mathbb{R}^d$ or $\mathbb{T}^d$ through its components as $\boldsymbol{x} = (x_1, \ldots, x_d)$, where $x_i \in \mathbb{R}$ or $\mathbb{T}$ for $1 \leq i \leq d$. We will also use the notation $(\boldsymbol{x})_i$ to denote the ith component of $\boldsymbol{x}$ when it is more convenient to do so. We use $\mathscr{L}^d$ to mean the d-dimensional Lebesgue measure on $\mathbb{R}^d$ or $\mathbb{T}^d$. Given a vector

field $\boldsymbol{u}$, we define the support of $\boldsymbol{u}$ in the time variable as

$$\operatorname{supp}_t \boldsymbol{u} \coloneqq \overline{\{t \in \mathbb{R} | \boldsymbol{u}(t, \boldsymbol{x}) = \boldsymbol{0} \, \forall \, \boldsymbol{x} \in \mathbb{R}^d \text{ or } \mathbb{T}^d\}}. \tag{8.2}$$

Throughout the paper, we will use $a \lesssim b$ to mean that $a < c\, b$ for some constant $c > 0$ independent of any parameter, except we will allow this constant c to depend on the dimension d.

8.1.2 Organization of the paper

The paper is arranged as follows. As our design of vector field $\boldsymbol{u}$ will involve a Cantor set, we give the required Cantor set construction and prove a few associated basic lemmas in section 8.2. We give an overview of the design of the vector field $\boldsymbol{u}$ in section 8.3. In section 8.4, we give proof of Theorem 8.1.1 and briefly summarize the changes required to prove Theorem 8.1.2. Finally, in section 8.5, we construct a useful flow that helps translate cubes in the domain and is essential in the design of vector field $\boldsymbol{u}$.

8.2 Cantor set construction

The purpose of this section is to fix some notations and give a Cantor set construction in a way that is readily usable throughout the paper. We also state and prove a few basic lemmas required later for constructing the vector field.

Notation 1. Given a point $\boldsymbol{x}_c$ in $\mathbb{R}^d$ or $\mathbb{T}^d$ and $\ell > 0$, we define an open cube of length ℓ centered at $\boldsymbol{x}_c$ as follows

$$Q(\boldsymbol{x}_c, \ell) \coloneqq \left\{ \boldsymbol{x} \in \mathbb{R}^d \text{ or } \mathbb{T}^d \;\middle|\; |x_i - x_i^c| < \frac{\ell}{2}, \; 1 \leq i \leq d \right\}, \tag{8.3}$$

and a close cube $\overline{Q}(\boldsymbol{x}_c, \ell)$ to be the closure of $Q(\boldsymbol{x}_c, \ell)$.

Notation 2. In preparation for constructing Cantor sets, we first define a few important sets and sequences. We let,

$$\mathbb{I} \coloneqq \{1, -1\}, \qquad \text{and} \qquad \mathbb{I}^d \coloneqq \{\boldsymbol{s} = (s^1, \dots, s^d) \,|\, s^i \in \mathbb{I}\}. \tag{8.4}$$

For every $n \in \mathbb{N}$, we define a set of $n-$tuples with elements from $\mathbb{I}^d$ as

$$S_n \coloneqq \{\mathfrak{s} = (\boldsymbol{s}_1, \dots, \boldsymbol{s}_n) \,|\, \boldsymbol{s}_i \in \mathbb{I}^d, 1 \leq i \leq n\}. \tag{8.5}$$

It is clear that $|S_n| = 2^{nd}$. We define a set of sequences with elements from $\mathbb{I}^d$ as

$$\mathcal{S} \coloneqq \{\boldsymbol{\mathfrak{s}} = (\boldsymbol{s}_1, \boldsymbol{s}_2, \dots) \,|\, \boldsymbol{s}_i \in \mathbb{I}^d, i \in \mathbb{N}\}. \tag{8.6}$$

We note that we use Fraktur font to denote elements from a set S_n and *bold* Fraktur font to denote elements from the set $\mathcal{S}$. Given $\mathfrak{s} \in S_n$ with $n \geq 2$, we will denote

$$\mathfrak{s}' \coloneqq (\boldsymbol{s}_1, \dots, \boldsymbol{s}_{n-1}) \in S_{n-1}, \tag{8.7}$$

and we define $\sigma_n : \mathcal{S} \to S_n$ as follows

$$\sigma_n(\boldsymbol{\mathfrak{s}}) \coloneqq (\boldsymbol{s}_1, \dots \boldsymbol{s}_n) \qquad \text{for} \qquad \boldsymbol{\mathfrak{s}} \in \mathcal{S}. \tag{8.8}$$

Notation 3. Consider a sequence $\Psi \coloneqq \{\psi_i\}_{i=1}^{\infty}$ with elements $0 < \psi_i \leq 1$ and a

sequence of 1's

$$\Theta \coloneqq \{1, 1, \dots\}. \tag{8.9}$$

We define a few lengths corresponding to Ψ as

$$\ell_\Psi^0 = 1 \qquad \text{and} \qquad \ell_\Psi^n = \frac{\prod_{i=1}^{n} \psi_i}{2^n} \qquad \text{for} \qquad n \in \mathbb{N}. \tag{8.10}$$

With this definition and the fact that $0 < \psi_i \leq 1$, we note that

$$\ell_\Psi^n \leq \frac{\ell_\Psi^{n-1}}{2} \qquad \text{for} \qquad n \in \mathbb{N}. \tag{8.11}$$

The significance of ℓ_Ψ^n is shown in figure 8.1. The length ℓ_Ψ^n represents the size of the n-th generation cubes in the Cantor set construction process or the n-th generation dyadic cubes if Ψ is chosen to be Θ (the sequence of 1's).

Next, for a given sequence Ψ as above, we associate every element $\mathfrak{s}$ in S_n with a point $\boldsymbol{x}$ in $\mathbb{T}^d$. For every $n \in \mathbb{N}$, we define $P_\Psi^n : S_n \to \mathbb{T}^d$ as

$$P_\Psi^n(\mathfrak{s}) \coloneqq \left(\frac{1}{2} + \frac{1}{4} \sum_{i=1}^{n} s_i^1 \ell_\Psi^{i-1},\ \dots\ , \frac{1}{2} + \frac{1}{4} \sum_{i=1}^{n} s_i^d \ell_\Psi^{i-1} \right) \text{ for } \mathfrak{s} = (\boldsymbol{s}_1, \dots, \boldsymbol{s}_n) \in S_n. \tag{8.12}$$

The positions $P_\Psi^n(\mathfrak{s})$ would denote the centers of the n-th generation cubes in the Cantor set construction process (see figure 8.1), and $P_\Theta^n(\mathfrak{s})$ denote the centers of

the n-th generation dyadic cubes. We also define $\widetilde{P}^n_\Psi : S_n \to \mathbb{T}^d$ as $\widetilde{P}^1_\Psi := P^1_\Psi$ and

$$\begin{aligned}\widetilde{P}^n_\Psi(\mathfrak{s}) &:= P^n_\Psi(\mathfrak{s}) - P^{n-1}_\Psi(\mathfrak{s}') + P^{n-1}_\Theta(\mathfrak{s}') \\ &= \left(\frac{1}{2} + \frac{1}{4}\sum_{i=1}^{n-1}\frac{s^1_i}{2^{i-1}} + \frac{1}{4}s^1_n\ell^{n-1}_\Psi,\ \dots\ , \frac{1}{2} + \frac{1}{4}\sum_{i=1}^{n-1}\frac{s^d_i}{2^{i-1}} + \frac{1}{4}s^d_n\ell^{n-1}_\Psi\right) \text{ for } n \geq 2.\end{aligned} \tag{8.13}$$

We will need $\widetilde{P}^n_\Psi$ while constructing the vector field, which will be based on translating various cubes (see section 8.3). In that respect, $\widetilde{P}^n_\Psi(\mathfrak{s})$ represents the center of an n-th generation cube in the Cantor set construction process relative to the center $P^{n-1}_\Psi(\mathfrak{s}')$ of a cube from the previous generation, which is then shifted to $P^{n-1}_\Theta(\mathfrak{s}')$, the center of an $(n-1)$th-generation dyadic cube. Finally, we define $\mathcal{P}_\Psi : \mathcal{S} \to \mathbb{T}^d$ as

$$\mathcal{P}_\Psi(\mathfrak{s}) := \left(\frac{1}{2} + \frac{1}{4}\sum_{i=1}^{\infty} s^1_i\ell^{i-1}_\Psi,\ \dots\ \frac{1}{2} + \frac{1}{4}\sum_{i=1}^{\infty} s^d_i\ell^{i-1}_\Psi\right). \tag{8.14}$$

Next, we state a few useful lemmas whose proof is fairly straightforward and given here only for completeness.

Lemma 8.2.1. *Let $\Psi = \{\psi_i\}_{i=1}^\infty$ be a sequence with $0 < \psi_i < 1$ and let $\mathfrak{s}$ and $\mathfrak{r}$ be two different elements of S_n then the closed cubes $\overline{Q}(P^n_\Psi(\mathfrak{s}), \ell^n_\Psi)$ and $\overline{Q}(P^n_\Psi(\mathfrak{r}), \ell^n_\Psi)$ are disjoint.*

Proof. Since $\mathfrak{s} = (\boldsymbol{s}_1, \dots, \boldsymbol{s}_n)$ and $\mathfrak{r} = (\boldsymbol{r}_1, \dots, \boldsymbol{r}_n)$ are different, that means for some $1 \leq i \leq n$, $\boldsymbol{s}_i = (s^1_i, \dots, s^d_i)$ and $\boldsymbol{r}_i = (r^1_i, \dots, r^d_i)$ are different. This, in turn, implies that for some $1 \leq j \leq d$, s^j_i and r^j_i are different. From the definition of P^n_Ψ in (8.12), we see that

$$\left|\left(P^n_\Psi(\mathfrak{s}) - P^n_\Psi(\mathfrak{r})\right)_j\right| \geq \frac{1}{2}\ell^{n-1}_\Psi,$$

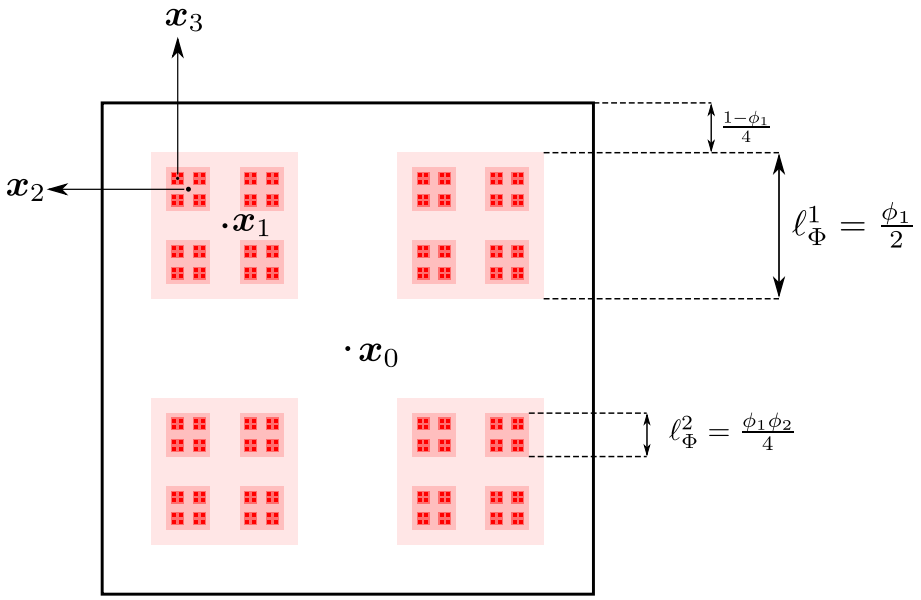

Figure 8.1: An illustration of the construction process of the Cantor set $\mathcal{C}_\Phi$ in two dimensions. The sequence Φ is given by (8.20), and we have chosen $\nu = \frac{3}{4}$. The figure shows the collection of first four generations of cubes, C^1_Φ, C^2_Φ, C^3_Φ and C^4_Φ, in increasingly less pale red color. In the figure, $\boldsymbol{x}_0 = (1/2, 1/2)$, $\boldsymbol{x}_1 = P^1_\Phi(\mathfrak{s}_1)$, $\boldsymbol{x}_2 = P^2_\Phi(\mathfrak{s}_2)$ and $\boldsymbol{x}_3 = P^3_\Phi(\mathfrak{s}_3)$. Here, $\mathfrak{s}_1$, $\mathfrak{s}_2$ and $\mathfrak{s}_3$ are the elements of S_1, S_2 and S_3, respectively, given by $\mathfrak{s}_1 = \{(-1,-1)\}$, $\mathfrak{s}_2 = \{(-1,-1),(-1,-1)\}$ and $\mathfrak{s}_3 = \{(-1,-1),(-1,-1),(-1,-1)\}$.

where $(\ \cdot\ )_j$ denotes the j-th component. Now suppose that $\boldsymbol{x} \in \overline{Q}(P^n_\Psi(\mathfrak{s}), \ell^n_\Psi)$, this means

$$\left|(P^n_\Psi(\mathfrak{s}) - \boldsymbol{x})_j\right| \le \frac{\ell^n_\Psi}{2}, \tag{8.15}$$

which implies

$$\begin{aligned}\left|(P^n_\Psi(\mathfrak{r}) - \boldsymbol{x})_j\right| &\ge \left|(P^n_\Psi(\mathfrak{s}) - P^n_\Psi(\mathfrak{r}))_j\right| - \left|(P^n_\Psi(\mathfrak{s}) - \boldsymbol{x})_j\right| \\ &\ge \frac{1}{2}\ell^{n-1}_\Psi - \frac{1}{2}\ell^n_\Psi \ge \frac{1}{\psi_i}\ell^n_\Psi - \frac{1}{2}\ell^n_\Psi > \frac{1}{2}\ell^n_\Psi.\end{aligned}$$

Therefore, $\boldsymbol{x} \notin \overline{Q}(P^n_\Psi(\mathfrak{r}), \ell^n_\Psi)$, which then completes the proof. □

Lemma 8.2.2. *Let the sequence Ψ be the same as in the previous lemma, and let $\mathfrak{s}$ and $\mathfrak{r}$ be two different elements of $\mathcal{S}$. Then $\mathcal{P}_\Psi(\mathfrak{s}) \neq \mathcal{P}_\Psi(\mathfrak{r})$.*

Proof. The proof is similar to the previous lemma. □

Lemma 8.2.3. *Let Θ be a sequence of $1's$ as defined in (8.9). Let $\mathfrak{s}$ and $\mathfrak{r}$ be two different elements of S_n then the open cubes $Q(P^n_\Theta(\mathfrak{s}), \ell^n_\Theta)$ and $Q(P^n_\Theta(\mathfrak{r}), \ell^n_\Theta)$ are disjoint.*

Proof. The proof works the same as in Lemma 8.2.1. The only difference is that instead of (8.15), for $\boldsymbol{x}$ to be in $Q(P^n_\Theta(\mathfrak{s}), \ell^n_\Theta)$, we need

$$\left|\left(P^n_\Theta(\mathfrak{s}) - \boldsymbol{x}\right)_j\right| < \frac{\ell^n_\Theta}{2}. \tag{8.16}$$

□

Lemma 8.2.4. *Let $\Psi = \{\psi_i\}_{i=1}^\infty$ be a sequence with $0 < \psi_i \leq 1$ and let $\mathfrak{s} = (\boldsymbol{s}_1, \ldots \boldsymbol{s}_n) \in S_n$ for some $n \geq 2$ and $\mathfrak{s}' = (\boldsymbol{s}_1, \ldots \boldsymbol{s}_{n-1})$. Then $\overline{Q}(P^n_\Psi(\mathfrak{s}), \ell^n_\Psi) \subset \overline{Q}(P^{n-1}_\Psi(\mathfrak{s}'), \ell^{n-1}_\Psi)$.*

Proof. Suppose $\boldsymbol{x} \in \overline{Q}(P^n_\Psi(\mathfrak{s}), \ell^n_\Psi)$. This means

$$\left|\left(P^n_\Psi(\mathfrak{s}) - \boldsymbol{x}\right)_j\right| \leq \frac{\ell^n_\Psi}{2},$$

where $(\,\cdot\,)_j$ denotes the j-th component. A straightforward calculation shows that

$$\left|\left(P^{n-1}_\Psi(\mathfrak{s}') - \boldsymbol{x}\right)_j\right| \leq \left|\left(P^{n-1}_\Psi(\mathfrak{s}') - P^n_\Psi(\mathfrak{s})\right)_j\right| + \left|\left(P^n_\Psi(\mathfrak{s}) - \boldsymbol{x}\right)_j\right| \leq \frac{\ell^{n-1}_\Psi}{4} + \frac{\ell^n_\Psi}{2} \leq \frac{\ell^{n-1}_\Psi}{2}.$$

This implies $\boldsymbol{x} \in \overline{Q}(P^{n-1}_\Psi(\mathfrak{s}'), \ell^{n-1}_\Psi)$. Hence, $\overline{Q}(P^n_\Psi(\mathfrak{s}), \ell^n_\Psi) \subset \overline{Q}(P^{n-1}_\Psi(\mathfrak{s}'), \ell^{n-1}_\Psi)$ is true. □

Lemma 8.2.5. *Let $\mathfrak{s} \in \mathcal{S}$. Then for every $n \in \mathbb{N}$, $\mathcal{P}_\Psi(\mathfrak{s}) \in \overline{Q}(P^n_\Psi(\sigma_n(\mathfrak{s})), \ell^n_\Psi)$.*

Proof. For any $j \in \{1, \dots, d\}$, we note that

$$\left|(\mathcal{P}_\Psi(\mathfrak{s}) - P^n_\Psi(\mathfrak{s}))_j\right| \leq \frac{1}{4} \sum_{i=n+1}^{\infty} \ell_\Psi^{i-1} \leq \frac{1}{4} \sum_{i=n+1}^{\infty} \frac{\ell^n_\Psi}{2^{i-n-1}} \leq \frac{\ell^n_\Psi}{2}.$$

□

Corollary 8.2.1. *Let $\mathfrak{s} \in \mathcal{S}$. Then $\mathcal{P}_\Psi(\mathfrak{s}) = \bigcap\limits_{n\in\mathbb{N}} \overline{Q}(P^n_\Psi(\sigma_n(\mathfrak{s})), \ell^n_\Psi)$.*

Proof. From Lemma 8.2.4, $\overline{Q}(P^n_\Psi(\sigma_n(\mathfrak{s})), \ell^n_\Psi)$ forms a nested sequence of cubes, i.e.,

$$\overline{Q}(P^1_\Psi(\sigma_1(\mathfrak{s})), \ell^1_\Psi) \supset \overline{Q}(P^2_\Psi(\sigma_2(\mathfrak{s})), \ell^2_\Psi) \supset \dots.$$

Also, the size of the cube $\overline{Q}(P^n_\Psi(\sigma_n(\mathfrak{s})), \ell^n_\Psi)$ goes to zero as $n \to \infty$. Therefore, $\bigcap\limits_{n\in\mathbb{N}} \overline{Q}(P^n_\Psi(\sigma_n(\mathfrak{s})), \ell^n_\Psi)$ contains only one single point from $\mathbb{T}^d$. From Lemma 8.2.5, we note that $\mathcal{P}_\Psi(\mathfrak{s}) \in \bigcap\limits_{n\in\mathbb{N}} \overline{Q}(P^n_\Psi(\sigma_n(\mathfrak{s})), \ell^n_\Psi)$, which finishes the proof. □

Lemma 8.2.6. *Let $\mathfrak{s} \in S_n$, then $\overline{Q}(P^n_\Theta(\mathfrak{s}), \ell^n_\Theta) = \bigcup\limits_{\substack{\mathfrak{r}\in S_{n+1}\\ \mathfrak{r}'=\mathfrak{s}}} \overline{Q}(P^{n+1}_\Theta(\mathfrak{r}), \ell^{n+1}_\Theta)$. Furthermore, $\mathbb{T}^d = \bigcup\limits_{\mathfrak{s}\in S_n} \overline{Q}(P^n_\Theta(\mathfrak{s}), \ell^n_\Theta)$ for any $n \in \mathbb{N}$.*

Proof. These are standard properties in a dyadic decomposition. □

Lemma 8.2.7. *For every $\boldsymbol{x} \in \mathbb{T}^d$, $\exists\, \mathfrak{s} \in \mathcal{S}$ such that $\boldsymbol{x} = \mathcal{P}_\Theta(\mathfrak{s})$.*

Proof. From Lemma 8.2.6, there exist $\mathfrak{s}_1 \in S_1$ such that $\boldsymbol{x} \in \overline{Q}(P^1_\Theta(\mathfrak{s}_1), \ell^1_\Theta)$. Having selected $\mathfrak{s}_i \in S_i$ for $i \geq 1$ such that $\boldsymbol{x} \in \overline{Q}(P^i_\Theta(\mathfrak{s}_i), \ell^i_\Theta)$, again using Lemma 8.2.6, we choose $\mathfrak{s}_{i+1} \in S_{i+1}$ such that $\mathfrak{s}'_{i+1} = \mathfrak{s}_i$ and $\boldsymbol{x} \in \overline{Q}(P^{i+1}_\Theta(\mathfrak{s}_{i+1}), \ell^{i+1}_\Theta)$. Finally, we define $\mathfrak{s} \in \mathcal{S}$ as follows. We let the nth component of $\mathfrak{s}$ to be the nth component of $\mathfrak{s}_n$, i.e., $\boldsymbol{s}_n = \boldsymbol{s}_{n,n}$. By construction $\boldsymbol{x} = \bigcap\limits_{n\in\mathbb{N}} \overline{Q}(P^n_\Psi(\sigma_n(\mathfrak{s})), \ell^n_\Psi)$. Finally, referring to Corollary 8.2.1 finishes the proof. □

Notation 4. If $\Psi = \{\psi_i\}_{i=1}^{\infty}$ is such that $0 < \psi_i < 1$, then we define

$$C_{\Psi}^{n} \coloneqq \bigcup_{\mathfrak{s} \in S_n} \overline{Q}(P_{\Psi}^{n}(\mathfrak{s}), \ell_{\Psi}^{n}). \tag{8.17}$$

The set C_{Ψ}^{n} is the union of nth generation cubes in the Cantor set construction process. From Lemma 8.2.4, we note that C_{Ψ}^{n}'s form a nested sequence of sets, i.e.,

$$C_{\Psi}^{1} \supset C_{\Psi}^{2} \supset C_{\Psi}^{3} \dots . \tag{8.18}$$

Finally, we define a Cantor set corresponding to the sequence Ψ as

$$\mathcal{C}_{\Psi} \coloneqq \bigcap_{i=1}^{\infty} C_{\Psi}^{n}. \tag{8.19}$$

From the definition (8.19) and Corollary 8.2.1, we immediately see that for any $\mathfrak{s} \in \mathcal{S}$, $\mathcal{P}_{\Psi}(\mathfrak{s}) \in \mathcal{C}_{\Psi}$. Moreover, the following lemma states that any $\boldsymbol{x} \in \mathcal{C}_{\Psi}$ can be represented this way.

Lemma 8.2.8. *Let $\Psi = \{\psi_i\}_{i=1}^{\infty}$ be a sequence with $0 < \psi_i < 1$, then for every $\boldsymbol{x} \in \mathcal{C}_{\Psi}$, $\exists! \mathfrak{s} \in \mathcal{S}$ such that $\boldsymbol{x} = \mathcal{P}_{\Psi}(\mathfrak{s})$.*

Proof. We only need to show the existence of $\mathfrak{s} \in \mathcal{S}$ as the uniqueness is clear from Lemma 8.2.2. Given $\boldsymbol{x} \in \mathcal{C}_{\Psi}$, we construct an $\mathfrak{s} = (\boldsymbol{s}_1, \boldsymbol{s}_2, \dots) \in \mathcal{S}$ as follows.

By definition of $\mathcal{C}_{\Psi}$, for every $n \in \mathbb{N}$ there is $\mathfrak{s}_n \in S_n$ such that $\boldsymbol{x} \in \overline{Q}(P_{\Psi}^{n}(\mathfrak{s}_n), \ell_{\Psi}^{n})$. Moreover, as the cubes from the nth generation in the Cantor set construction process are disjoint from Lemma 8.2.1, this $\mathfrak{s}_n$ is unique. Using (8.7) from Notation 2, this also means $\mathfrak{s}_n' = \mathfrak{s}_{n-1}$. Finally, we define the nth component of $\mathfrak{s}$ as $\boldsymbol{s}_n \coloneqq \boldsymbol{s}_{n,n}$, where $\boldsymbol{s}_{n,n}$ is the nth component of $\mathfrak{s}_n$.

By construction of $\mathfrak{s}$, we see that for every $n \in \mathbb{N}$, $\boldsymbol{x} \in \overline{Q}(P^n_\Psi(\sigma_n(\mathfrak{s})), \ell^n_\Psi)$. Finally, noting Corollary 8.2.1 implies $\boldsymbol{x} = \mathcal{P}(\mathfrak{s})$. □

An important sequence that we use for the construction of our vector field is

$$\Phi \coloneqq \{\phi_i\}_{i=1}^\infty \coloneqq \left\{\frac{1}{2^\nu}\right\}_{i=1}^\infty \qquad \text{where } \nu \in (0,1) \text{ is a constant.} \tag{8.20}$$

From this sequence Φ, we have that

$$\ell^0_\Phi = 1 \qquad \text{and} \qquad \ell^n_\Phi = \frac{1}{2^{(1+\nu)n}} \qquad \text{for} \qquad n \in \mathbb{N}. \tag{8.21}$$

Lemma 8.2.9. *Let the sequence Φ be as given in (8.20). Then the Hausdorff dimension of the corresponding Cantor set $\mathcal{C}_\Phi$ is*

$$\dim_H \mathcal{C}_\Phi = \frac{d}{1+\nu}.$$

Proof. The calculation of the Hausdorff dimension of a Cantor set is standard, see for example, (Stein and Shakarchi, 2005, ch. 7) or (Falconer, 2014, ch. 3). □

Finally, we finish this section by stating a simple lemma that will be useful in proof of Proposition 8.4.2 given in section 8.5.3. We first let

$$\vartheta = \vartheta(\nu) \coloneqq \frac{1}{8}(2^\nu - 1). \tag{8.22}$$

Lemma 8.2.10. *For any $a \in [0,1]$ and for any $\mathfrak{s} \in S_i$ for some $i \in \mathbb{N}$, let*

$\boldsymbol{x}_a = (1-a)\widetilde{P}^i_\Phi(\mathfrak{s}) + aP^i_\Theta(\mathfrak{s})$ *then*

$$\overline{Q}(\boldsymbol{x}_a, (1+\vartheta)\ell^i_\Phi) \Subset Q(P^i_\Theta(\mathfrak{s}), \ell^i_\Theta).$$

Proof. The proof is a straightforward verification of the statement. □

8.3 Overview of the approach

In order to prove Theorem 8.1.1, we aim to construct a vector field $\boldsymbol{u}$ such that there exists a flow map for which, at some time, $T > 0$, we have

$$X^{\boldsymbol{u}}(T, \mathbb{T}^d) \subseteq \mathcal{C}_\Phi. \tag{8.23}$$

From Lemma 8.2.9, we see that the Hausdorff dimension $\dim_H \mathcal{C}_\Phi < d$. Therefore, the d-dimensional Lebesgue measure of $\mathcal{C}_\Phi$ is zero. As a result, this flow map $X^{\boldsymbol{u}}$ is not a regular Lagrangian flow. However, as we shall see, the flow $\boldsymbol{u}$ possesses a Sobolev regularity and falls in the range of DiPerna and Lions theory, which then guarantees the existence of a regular Lagrangian flow $X^{\boldsymbol{u}}_{RL}$ as well. The existence of two different flow maps implies that the set of initial conditions for which the trajectories are not unique is a set of positive measure. Because the condition (8.23) holds, this set is, in fact, a full-measure set.

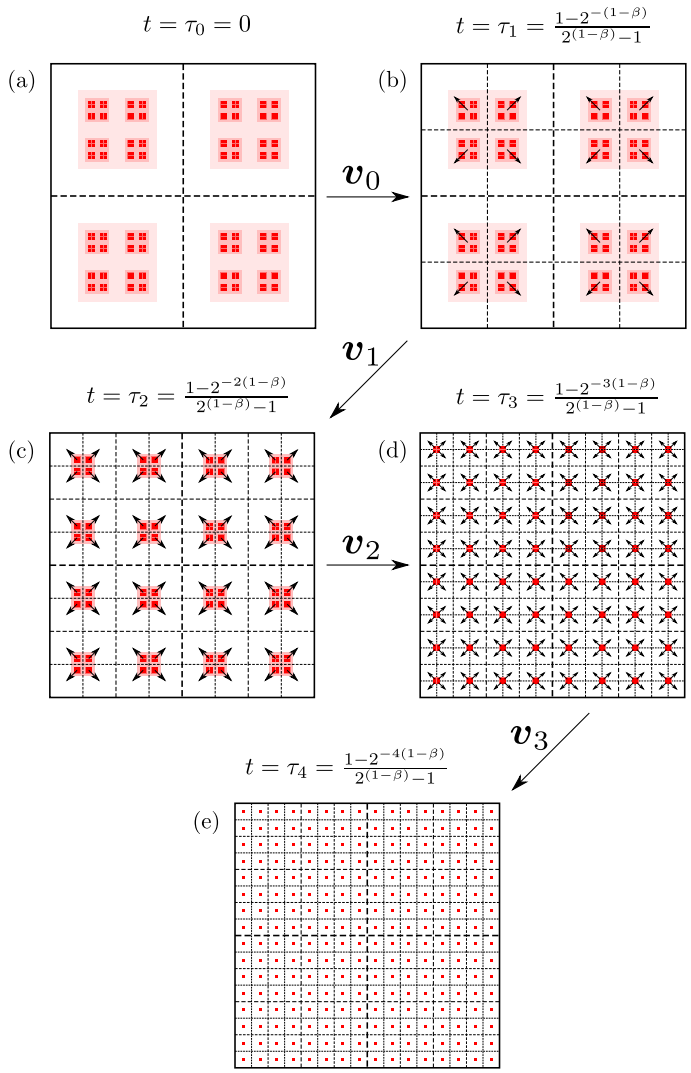

Figure 8.2: The motion of the first four generations of cubes in the Cantor set construction process under the flow of vector field $\boldsymbol{v} = \sum_{i=0}^{\infty} \boldsymbol{v}_i$. At the ith stage, the vector field $\boldsymbol{v}_i$ translates the cubes of the ith generation so that their centers align with the dyadic cubes of the ith generation. In the first step, by definition of the centers (8.12), we have this alignment at $t = \tau_0$ itself. Therefore, in the first step, we simply choose $\boldsymbol{v}_0 \equiv 0$. The arrows in the figure indicate the direction of the motion of cubes. In panels (b), (c) and (d), the tails of the arrow lie at the shifted center (see (8.13)), $\widetilde{P}^1_\Phi(\mathfrak{s}_1)$, $\widetilde{P}^2_\Phi(\mathfrak{s}_2)$ and $\widetilde{P}^3_\Phi(\mathfrak{s}_3)$, respectively, for $\mathfrak{s}_1 \in S_1$, $\mathfrak{s}_2 \in S_2$ and $\mathfrak{s}_3 \in S_3$. Finally, in our construction, the vector field $\boldsymbol{v}_{i-1}$ is supported near the ith generation cubes in the Cantor set construction process as they move around in space. The size of these ith generation cubes becomes increasingly smaller compared to ith generation dyadic cubes, as can be seen in panel (e), for example. This shrinking of the support of the vector field $\boldsymbol{v}_i$ with large i is one of the main reasons that allow us to bound the Sobolev norm of the vector field uniformly in time.

We construct the vector field $\boldsymbol{u}$ through a time reversal argument applied to a vector field $\boldsymbol{v}$, whose construction we describe next. For some $0 < \beta < 1$, let us define a sequence of times as

$$\tau_i \coloneqq \frac{1 - 2^{-(1-\beta)i}}{2^{(1-\beta)} - 1} \quad \text{for} \quad i \in \mathbb{Z}_{\geq 0} \qquad \text{and} \qquad \tau_\infty \coloneqq \frac{1}{2^{(1-\beta)} - 1}. \tag{8.24}$$

It is clear that

$$\tau_i - \tau_{i-1} = \frac{1}{2^{(1-\beta)i}} \quad \text{for} \quad i \in \mathbb{N}.$$

We design the vector field $\boldsymbol{v}$ to be such that it has a unique flow map $X^{\boldsymbol{v}}$. Moreover, at time $t = \tau_\infty$, we have

$$X^{\boldsymbol{v}}(\tau_\infty, \mathcal{C}_\Phi) = \mathbb{T}^d. \tag{8.25}$$

In our definition of the vector field $\boldsymbol{v}$, we will write $\boldsymbol{v}$ to be an infinite sum of vector fields $\boldsymbol{v}_i$'s, i.e., $\boldsymbol{v} = \sum_{i=0}^{\infty} \boldsymbol{v}_i$. Under the flow of vector field $\boldsymbol{v}$, the mapping of $\mathcal{C}_\Phi$ to $\mathbb{T}^d$ will occur in a sequence of infinite steps. The vector field $\boldsymbol{v}_{i-1}$, whose support lies in $[\tau_{i-1}, \tau_i]$, will execute the ith step in the sequence. Figure 8.2 depicts the first four steps in this infinite sequence of steps.

In the first step, the vector field $\boldsymbol{v}_0$ translates $Q(P^1_\Phi(\mathfrak{s}), \ell^1_\Phi)$ (the first-generation cubes in the Cantor set construction process) such that after the translation, the centers of these cubes align with the centers of first-generation dyadic cubes. Continuing in this way, at the ith step, the vector field $\boldsymbol{v}_{i-1}$ translates the cubes $Q(\widetilde{P}^i_\Phi(\mathfrak{s}), \ell^i_\Phi)$ (the ith generation cubes in the Cantor set construction process after translations under flow $\boldsymbol{v}_j$'s, $j < i - 1$) such that their centers align with the centers of the ith generation dyadic cubes. After performing the ith step, the

centers of the $i+1$th generation of cubes in the Cantor set construction process now shift to $\widetilde{P}_\Phi^{i+1}(\mathfrak{s})$, which we note are different from the centers $P_\Phi^{i+1}(\mathfrak{s})$ in the original configuration of the Cantor set. To translate the cubes at any step, we use what we call a "blob flow." An overview and the construction of a blob flow are given in section 8.5.

Now we quickly see why the flow of vector field $\boldsymbol{v}$ takes $\mathcal{C}_\Phi$ to $\mathbb{T}^d$. From Lemma 8.2.7, we see that for every $\boldsymbol{x}_e \in \mathbb{T}^d$, there is an element $\mathfrak{s} \in \mathcal{S}$ such that $\boldsymbol{x}_e = \mathcal{P}_\Theta(\mathfrak{s})$. But for this $\mathfrak{s}$ there is $\boldsymbol{x}_s \in \mathcal{C}_\Phi$ given by $\boldsymbol{x}_s = \mathcal{P}_\Phi(\mathfrak{s})$. From the description given above, a trajectory corresponding to vector field $\boldsymbol{v}$ starting at $\boldsymbol{x}_s$ after time τ_i is given by $\gamma^{\boldsymbol{v}}_{\boldsymbol{x}_s}(\tau_i) = \mathcal{P}_\Phi(\mathfrak{s}) - P^i_\Phi(\sigma_i(\mathfrak{s})) + P^i_\Theta(\sigma_i(\mathfrak{s}))$. Letting $i \to \infty$, we see that $\gamma^{\boldsymbol{v}}_{\boldsymbol{x}_s}(\tau_\infty) = \mathcal{P}_\Theta(\mathfrak{s})$. In conclusion, $X^{\boldsymbol{v}}(\tau_\infty, \mathcal{C}_\Phi) = \mathbb{T}^d$.

Finally, we note that the vector field $\boldsymbol{v}$ that we create lies in $C([0,\tau_\infty]; W^{1,p}(\mathbb{T}^d, \mathbb{R}^d))$, and we can do this for any $1 \le p < d$. Our vector field design has one main advantage compared to, for example, the "checkerboard" flow used in optimal mixing problems (Yao and Zlatoš, 2017; Alberti et al., 2019). For both a checkerboard flow and our vector field $\boldsymbol{v}$, the number of cubes at the ith step are the same, which is 2^{id}. However, the size of cubes that we translate at the ith step in our vector field $\boldsymbol{v}$ is $\frac{1}{2^{(1+\nu)i}}$, which is at large i substantially smaller than $\frac{1}{2^i}$, the size of cubes at the ith step in a typical checkerboard flow. This is one of the main reasons we are able to bound the Sobolev norm uniformly in time.

8.4 Proof of Theorem 8.1.1 and the design of vector field $\boldsymbol{v}$

This section will prove Theorem 8.1.1 and construct the vector field $\boldsymbol{v}$ from last section, given the properties of its components $\boldsymbol{v}_i$. Before stating the next proposition, recall the definition of Φ from (8.20), which uses a parameter ν and the definition of τ_i from (8.24), which uses a parameter β.

Proposition 8.4.1. *For every $p < d$ and $\alpha < 1$, there are two numbers, $\nu := \nu(p,\alpha) \in (0,1)$ and $\beta := 1-\nu^2$, and there exists a divergence-free vector field $\boldsymbol{v} \in C([0,\tau_\infty]; W^{1,p}(\mathbb{T}^d,\mathbb{R}^d)) \cap C^\alpha([0,\tau_\infty]\times\mathbb{T}^d,\mathbb{R}^d) \cap C^\infty([0,\tau_\infty)\times\mathbb{T}^d,\mathbb{R}^d)$ with the following two properties:*

(i) For every $\boldsymbol{x}_s \in \mathbb{T}^d$, the trajectory $\gamma^{\boldsymbol{v}}_{\boldsymbol{x}_s} : [0,\tau_\infty] \to \mathbb{T}^d$ is unique. As a result, the flow map $X^{\boldsymbol{v}}$ is also unique.

(ii) Let Φ be as in (8.20). Then given a sequence $\mathfrak{s} \in \mathcal{S}$, let $\boldsymbol{x}_s = \mathcal{P}_\Phi(\mathfrak{s})$ and $\boldsymbol{x}_e = \mathcal{P}_\Theta(\mathfrak{s})$, then $\gamma^{\boldsymbol{v}}_{\boldsymbol{x}_s}(\tau_\infty) = \boldsymbol{x}_e$.

Proof of Theorem 8.1.1. Let's define the required vector field $\boldsymbol{u} : [0,T]\times\mathbb{T}^d \to \mathbb{R}^d$ as

$$\boldsymbol{u}(t,\boldsymbol{x}) := -\frac{\tau_\infty}{T}\boldsymbol{v}\left(\tau_\infty\left(1-\frac{t}{T}\right),\boldsymbol{x}\right).$$

Clearly, $\boldsymbol{u} \in C([0,T]; W^{1,p}(\mathbb{T}^d,\mathbb{R}^d)) \cap C^\alpha([0,T]\times\mathbb{T}^d,\mathbb{R}^d)$ and is divergence-free.

Next, for every $\boldsymbol{x} \in \mathbb{T}^d$, we define a trajectory corresponding to the vector field $\boldsymbol{u}$ that starts at $\boldsymbol{x}$. From Lemma 8.2.7, for every $\boldsymbol{x}_e \in \mathbb{T}^d$, there exist an $\mathfrak{s} \in \mathcal{S}$ such that $\boldsymbol{x}_e = \mathcal{P}_\Theta(\mathfrak{s})$. After choosing such an $\mathfrak{s}$, let us assign $\boldsymbol{x}_s = \mathcal{P}_\Phi(\mathfrak{s})$. With

that, it is easy to verify that $\gamma^{\boldsymbol{u}}_{\boldsymbol{x}_e} : [0,T] \to \mathbb{T}^d$ defined as

$$\gamma^{\boldsymbol{u}}_{\boldsymbol{x}_e}(t) \coloneqq \gamma^{\boldsymbol{v}}_{\boldsymbol{x}_s}\left(\tau_\infty\left(1 - \frac{t}{T}\right)\right)$$

is a trajectory corresponding to the vector field $\boldsymbol{u}$ starting from $\boldsymbol{x}_e$.

Finally, we define a map $X^{\boldsymbol{u}} : [0,T] \times \mathbb{T}^d \to \mathbb{T}^d$ as

$$X^{\boldsymbol{u}}(t, \boldsymbol{x}) \coloneqq \gamma^{\boldsymbol{u}}_{\boldsymbol{x}}(t).$$

Clearly, $X^{\boldsymbol{u}}$ is a flow map for which

$$X^{\boldsymbol{u}}(T, \mathbb{T}^d) \subseteq \mathcal{C}_\Phi. \tag{8.26}$$

As the Hausdorff dimension $\dim_H \mathcal{C}_\Phi < d$, which means $\mathscr{L}^d(\mathcal{C}_\Phi) = 0$. Therefore, $X^{\boldsymbol{u}}$ is not a regular Lagrangian flow. As the vector field $\boldsymbol{u}$ has the required Sobolev regularity, from DiPerna–Lions theory, there is another flow map $X^{\boldsymbol{u}}_{RL}$ which is regular Lagrangian. This implies that the set of initial conditions for which the trajectories are not unique has a positive d-dimensional Lebesgue measure. Furthermore, from (8.26) and the definition of regular Lagrangian flow (8.1.3), we see that this set is, in fact, a full-measure set. □

Proposition 8.4.2. *Given $\nu \in (0,1)$ and $\beta \in (0,1)$, for every $i \in \mathbb{Z}_{\geq 0}$, there exists a vector field $\boldsymbol{v}_i : [0, \tau_\infty] \times \mathbb{T}^d \to \mathbb{R}^d$ with the following properties.*

(i) $\boldsymbol{v}_i \in C^\infty([0,\tau_\infty] \times \mathbb{T}^d, \mathbb{R}^d)$,

(ii) $\boldsymbol{v}_i$ *is divergence-free,*

(iii) $\operatorname{supp}_t \boldsymbol{v}_i \Subset (\tau_i, \tau_{i+1})$,

(iv) $\|\boldsymbol{v}_i\|_{L^\infty_{t,\boldsymbol{x}}} \lesssim \frac{1}{(2^\nu-1)}\frac{1}{2^{\beta i}}$

(v) $\|\nabla \boldsymbol{v}_i\|_{L^\infty_{t,\boldsymbol{x}}} \lesssim \frac{2^{(1+\nu-\beta)i}}{(2^\nu-1)^2}$

(vi) For a given $p \in [1,\infty)$, $\|\boldsymbol{v}_i(t,\cdot)\|_{W^{1,p}} \lesssim \frac{1}{(2^\nu-1)^2} \times 2^{\frac{[(1+\nu-\beta)p-d\nu]}{p} i}$,

(vii) $\|\partial_t \boldsymbol{v}_i\|_{L^\infty_{t,\boldsymbol{x}}} \lesssim \frac{1}{(2^\nu-1)^2}\frac{1}{2^{[2\beta-\nu-1]i}}$

(viii) For a given $\mathfrak{s} \in S_{i+1}$ *and* $\boldsymbol{x} \in \overline{Q}(\widetilde{P}^{i+1}_\Phi(\mathfrak{s}), \ell^{i+1}_\Phi)$, *we have* $\gamma^{\boldsymbol{v}_i}_{\boldsymbol{x}}(\tau_{i+1}) = \boldsymbol{x} - \widetilde{P}^{i+1}_\Phi(\mathfrak{s}) + P^{i+1}_\Theta(\mathfrak{s})$.

Proof of Proposition 8.4.1. Let us define a vector field $\boldsymbol{v} : [0,\tau_\infty] \times \mathbb{T}^d \to \mathbb{R}^d$ as follows

$$\boldsymbol{v} \coloneqq \sum_{i=0}^{\infty} \boldsymbol{v}_i, \tag{8.27}$$

where $\boldsymbol{v}_i$'s are the vector fields from Proposition 8.4.2. Next, we show that the vector field $\boldsymbol{v}$ has the properties stated in Proposition 8.4.1.

In the proof that follows, we make the following choices of parameters: ν is a sufficiently small number and $\beta = 1-\nu^2$.

- $\underline{\boldsymbol{v} \in C^\infty([0,\tau_\infty)\times\mathbb{T}^d,\mathbb{R}^d)}$: We conclude this by noting property (i) and that the support of $\boldsymbol{v}_i$'s are disjoint.

- $\underline{\boldsymbol{v} \text{ is divergence-free:}}$ As for any time $t \in [0,\tau_\infty]$, at most one of the $\boldsymbol{v}_i$ is non-zero, $\nabla\cdot\boldsymbol{v} \equiv 0$ follows from the divergence-free nature of the $\boldsymbol{v}_i$'s.

- $\underline{\boldsymbol{v} \in C([0,\tau_\infty]; W^{1,p}(\mathbb{T}^d,\mathbb{R}^d))}$: From the disjoint support of $\boldsymbol{v}_i$'s in time,

we note that

$$\|\boldsymbol{v}\|_{L_t^\infty W_{\boldsymbol{x}}^{1,p}} \leq \sup_i \|\boldsymbol{v}_i\|_{L_t^\infty W_{\boldsymbol{x}}^{1,p}}.$$

From property (vi) in Proposition 8.4.2, we see that the right-hand side is bounded if we choose

$$p < \frac{d\nu}{1+\nu-\beta}. \tag{8.28}$$

As $\boldsymbol{v} \in C^\infty([0,\tau_\infty) \times \mathbb{T}^d, \mathbb{R}^d)$, the continuity of the Sobolev norm in time is clear for any $t \in [0,\tau_\infty)$. For $t = \tau_\infty$, we simply have

$$\left\|\boldsymbol{v}(\tau_\infty,\cdot) - \boldsymbol{v}(\tilde{t},\cdot)\right\|_{W^{1,p}} = \left\|\boldsymbol{v}(\tilde{t},\cdot)\right\|_{W^{1,p}}.$$

Using the property (vi) in Proposition 8.4.2, the right-hand side decreases to zero as $\tilde{t}$ approaches τ_∞ if (8.28) holds. Finally, we note that in condition (8.28), the exponent p can be made arbitrarily close to d if we choose ν small enough and $\beta = 1-\nu^2$.

- $\underline{\boldsymbol{v} \in C^\alpha([0,\tau_\infty] \times \mathbb{T}^d, \mathbb{R}^d)}$: We start with the definition of α-Hölder norm:

$$\|\boldsymbol{v}\|_{C^\alpha_{t,\boldsymbol{x}}} = \sup_{(t_1,\boldsymbol{x}_1)\neq(t_2,\boldsymbol{x}_2)} \frac{|\boldsymbol{v}(t_1,\boldsymbol{x}_1) - \boldsymbol{v}(t_2,\boldsymbol{x}_2)|}{|(t_1,\boldsymbol{x}_1) - (t_2,\boldsymbol{x}_2)|^\alpha}. \tag{8.29}$$

If $t_1 = t_2 = \tau_\infty$, but $\boldsymbol{x}_1 \neq \boldsymbol{x}_2$, then the right-hand side in (8.29) is simply zero. If $t_1 = \tau_\infty$, but $t_2 \neq \tau_\infty$, then we have

$$\begin{aligned}\frac{|\boldsymbol{v}(t_1,\boldsymbol{x}_1) - \boldsymbol{v}(t_2,\boldsymbol{x}_2)|}{|(t_1,\boldsymbol{x}_1) - (t_2,\boldsymbol{x}_2)|^\alpha} &= \frac{|\boldsymbol{v}(t_2,\boldsymbol{x}_2)|}{|(\tau_\infty,\boldsymbol{x}_1) - (t_2,\boldsymbol{x}_2)|^\alpha} \\ &\leq \frac{|\boldsymbol{v}(t_2,\boldsymbol{x}_2)|}{|\tau_\infty - t_2|^\alpha} \lesssim \frac{1}{2^\nu - 1} \sup_i \frac{1}{2^{[\beta-\alpha(1-\beta)]i}},\end{aligned}$$

which is bounded if

$$\alpha < \frac{\beta}{1-\beta}. \tag{8.30}$$

Finally, if $t_1, t_2 \in [0, \tau_\infty)$, then we have

$$\frac{|\boldsymbol{v}(t_1, \boldsymbol{x}_1) - \boldsymbol{v}(t_2, \boldsymbol{x}_2)|}{|(t_1, \boldsymbol{x}_1) - (t_2, \boldsymbol{x}_2)|^\alpha} \leq \|\partial_t \boldsymbol{v}\|_{L^\infty_{t,\boldsymbol{x}}} |t_1 - t_2|^{1-\alpha} + \sup_t \|\boldsymbol{v}(t, \cdot)\|_{C^\alpha}.$$

Now the first term on the right-hand side is bounded if $\alpha \leq 1$ and $1 + \nu < 2\beta$, which is true for the choices we made at the beginning of the proof. For the second term, we have

$$\begin{aligned}
\sup_{\boldsymbol{x}_1 \neq \boldsymbol{x}_2} \frac{|\boldsymbol{v}(t, \boldsymbol{x}_1) - \boldsymbol{v}(t, \boldsymbol{x}_2)|}{|\boldsymbol{x}_1 - \boldsymbol{x}_2|^\alpha} &\leq 2 \min \left\{ |\boldsymbol{x}_1 - \boldsymbol{x}_2|^{1-\alpha} \|\nabla \boldsymbol{v}(t, \cdot)\|_{L^\infty}, \frac{\|\boldsymbol{v}(t, \cdot)\|_{L^\infty}}{|\boldsymbol{x}_1 - \boldsymbol{x}_2|^\alpha} \right\}, \\
&\leq 2 \|\boldsymbol{v}(t, \cdot)\|^{1-\alpha}_{L^\infty} \|\nabla \boldsymbol{v}(t, \cdot)\|^\alpha_{L^\infty}, \\
&\lesssim \left(\frac{1}{2^\nu - 1} \right)^{1+\alpha} \sup_i \; 2^{[\alpha(1+\nu) - \beta]i},
\end{aligned}$$

which is bounded if

$$\alpha < \frac{\beta}{1+\nu}. \tag{8.31}$$

As before, by choosing ν to be small enough and $\beta = 1 - \nu^2$, the exponent α can be made arbitrarily close to one.

- Uniqueness of trajectories: As the vector field $\boldsymbol{v} \in C^\infty([0, \tau_\infty) \times \mathbb{T}^d, \mathbb{R}^d)$, the existence and uniqueness of a trajectory $\gamma^{\boldsymbol{v}}_{\boldsymbol{x}}$ starting from $\boldsymbol{x} \in \mathbb{T}^d$ is clear for any time $t < \tau_\infty$. The existence and uniqueness at time $t = \tau_\infty$ are obtained from

the fact that $\|\boldsymbol{v}(t,\cdot)\|_{L^\infty} \to 0$ as $t \to \tau_\infty$.

- Trajectories starting from $\mathcal{C}_\Phi$: Let $\boldsymbol{x}_s \in \mathcal{C}_\Phi$, then from Lemma 8.2.8, there is a unique $\mathfrak{s} \in \mathcal{S}$ such that $\boldsymbol{x}_s = \mathcal{P}_\Phi(\mathfrak{s})$. We will show that $\gamma^{\boldsymbol{v}}_{\boldsymbol{x}_s}(\tau_\infty) = \boldsymbol{x}_e$, where $\boldsymbol{x}_e = \mathcal{P}_\Theta(\mathfrak{s})$, which will then imply $X^{\boldsymbol{v}}(\tau_\infty, \mathcal{C}_\Phi) = \mathbb{T}^d$ from Lemma 8.2.7. Given a $\boldsymbol{x} \in \mathbb{T}^d$, let us first define $\boldsymbol{y}_i \in \mathbb{T}^d$ for all $i \in \mathbb{Z}_{\geq 0}$ as

$$\boldsymbol{y}_0 \coloneqq \boldsymbol{x}_s, \qquad \text{and} \qquad \boldsymbol{y}_{i+1} \coloneqq \gamma^{\boldsymbol{v}_i}_{\boldsymbol{y}_i}(\tau_i) \quad \forall\, i \in \mathbb{Z}_{\geq 0}.$$

Next, let us define a trajectory $\gamma^{\boldsymbol{v}}_{\boldsymbol{x}} : [0, \tau_\infty] \to \mathbb{T}^d$ as

$$\gamma^{\boldsymbol{v}}_{\boldsymbol{x}}(t) \coloneqq \begin{cases} \gamma^{\boldsymbol{v}_i}_{\boldsymbol{y}_i}(t) & \text{for } t \in [\tau_i, \tau_{i+1}), \\ \lim\limits_{i \to \infty} \gamma^{\boldsymbol{v}_i}_{\boldsymbol{y}_i}(\tau_i) & \text{if } t = \tau_\infty. \end{cases} \tag{8.32}$$

Using property (iii) about the disjoint supports of $\boldsymbol{v}_i$'s, one can verify through an induction argument that $\gamma^{\boldsymbol{v}}_{\boldsymbol{x}}$ is indeed the unique trajectory corresponding to the flow $\boldsymbol{v}$ starting at $\boldsymbol{x}$. Next, we claim that

$$\gamma^{\boldsymbol{v}}_{\boldsymbol{x}_s}(\tau_i) = \mathcal{P}_\Phi(\mathfrak{s}) - P^i_\Phi(\sigma_i(\mathfrak{s})) + P^i_\Theta(\sigma_i(\mathfrak{s})). \tag{8.33}$$

The claim is obviously true for $i = 1$. Now suppose that the claim is true for some $i \geq 1$. We will show that it is also true for $i+1$. From Lemma 8.2.5, we know that

$$\mathcal{P}_\Phi(\mathfrak{s}) \in \overline{Q}(P^{i+1}_\Phi(\sigma_{i+1}(\mathfrak{s})), \ell^{i+1}_\Phi).$$

This implies

$$\mathcal{P}_\Phi(\mathfrak{s}) - P^i_\Phi(\sigma_i(\mathfrak{s})) + P^i_\Theta(\sigma_i(\mathfrak{s})) \in \overline{Q}(\widetilde{P}^{i+1}_\Phi(\sigma_{i+1}(\mathfrak{s})), \ell^{i+1}_\Phi), \tag{8.34}$$

after using the fact that

$$\widetilde{P}^{i+1}_\Phi(\sigma_{i+1}(\mathfrak{s})) = P^{i+1}_\Phi(\sigma_{i+1}(\mathfrak{s})) - P^i_\Phi(\sigma_i(\mathfrak{s})) + P^i_\Theta(\sigma_i(\mathfrak{s})). \tag{8.35}$$

Using (8.34), property (viii) and definition (8.32), we have that

$$\begin{aligned}\gamma^{\boldsymbol{v}}_{\boldsymbol{x}_s}(\tau_{i+1}) &= \mathcal{P}_\Phi(\mathfrak{s}) - P^i_\Phi(\sigma_i(\mathfrak{s})) + P^i_\Theta(\sigma_i(\mathfrak{s})) - \widetilde{P}^{i+1}_\Phi(\sigma_{i+1}(\mathfrak{s})) + P^{i+1}_\Theta(\sigma_{i+1}(\mathfrak{s})) \\ &= \mathcal{P}_\Phi(\mathfrak{s}) - P^{i+1}_\Phi(\sigma_{i+1}(\mathfrak{s})) + P^{i+1}_\Theta(\sigma_{i+1}(\mathfrak{s})),\end{aligned}$$

where we used (8.35) to obtain the second line. Finally, taking the limit $i \to \infty$, we see that

$$\gamma^{\boldsymbol{v}}_{\boldsymbol{x}_s}(\tau_\infty) = \mathcal{P}_\Theta(\mathfrak{s}).$$

□

8.4.1 Modifications required to prove Theorem 8.1.2

Our design of a steady vector field $\boldsymbol{u}^s : \mathbb{T}^d \to \mathbb{R}^d$ for $d \geq 3$ is based on the unsteady vector field construction of dimension $d-1$, which we denote as $\boldsymbol{u}^{d-1}$ in this subsection. Let $\boldsymbol{x} = (x_1, x_2, \ldots x_d) \in \mathbb{T}^d$, we denote $\boldsymbol{x}' = (x_1, \ldots x_{d-1}) \in \mathbb{T}^{d-1}$, and we write $\boldsymbol{x} = (\boldsymbol{x}', x_d)$. In our definition below, the coordinate x_d serves as a

function of time. Given $0 < \varepsilon < 1$, we define

$$\boldsymbol{u}^s(\boldsymbol{x}', x_d) \coloneqq \begin{cases} (0, \ldots, 0, 1) & \text{if} \quad 0 \leq x_d < 1 - \varepsilon, \\ \left(\frac{1}{\varepsilon}\boldsymbol{u}^{d-1}\left(\frac{x_d - (1-\varepsilon)}{\varepsilon}, \boldsymbol{x}'\right), 1\right) & \text{if} \quad 1 - \varepsilon \leq x_d \leq 1, \end{cases} \tag{8.36}$$

where we use final time $T = 1$ in the definition of $\boldsymbol{u}^{d-1}$. Using the properties of the unsteady vector field $\boldsymbol{u}^{d-1}$, it is not difficult to show that $\boldsymbol{u}^s$ is indeed the required vector field in Theorem 8.1.2.

8.5 Blob flow

As described in the approach, to translate a cube in the domain from a starting point $\boldsymbol{x}_s$ to an endpoint $\boldsymbol{x}_e$, we use what we call a "blob flow." A schematic of a blob flow is shown in figure 8.3. The properties of a blob flow $\widetilde{\boldsymbol{v}}$ are specified in Proposition 8.5.1. For a blob flow, the vector field $\widetilde{\boldsymbol{v}}$ is uniform inside a cube of length λ, and the support of the vector field lies in a cube of a slightly larger length $\lambda(1 + \delta)$, where δ can be understood as an offset. The vector field folds back outside the cube of length λ to maintain the divergence-free condition (see figure 8.3). Our goal now is to first construct a stationary blob flow, using which we construct the required blob flow and finally give proof of Proposition 8.4.2.

8.5.1 A stationary blob flow

Let us first define a bump function as

$$\varphi(x) \coloneqq \begin{cases} c \exp\left(\frac{1}{x^2 - \frac{1}{4}}\right) & \text{if} \quad x \in \left(-\frac{1}{2}, \frac{1}{2}\right), \\ 0 & \text{if} \quad x \in \left(-\infty, -\frac{1}{2}\right] \cup \left[\frac{1}{2}, \infty\right), \end{cases} \tag{8.37}$$

where the constant c is chosen such that $\int_{\mathbb{R}} \varphi(x')\,\mathrm{d}x' = 1$. For any $\varepsilon > 0$, we define a standard mollifier as

$$\varphi_\varepsilon(x) \coloneqq \frac{1}{\varepsilon}\varphi\left(\frac{x}{\varepsilon}\right). \tag{8.38}$$

Next, for $\delta \in (0,1)$, let $\chi_{[-\frac{1}{2}-\frac{3\delta}{8},\frac{1}{2}+\frac{3\delta}{8}]}$ be an indicator function which is 1 if $x \in [-\frac{1}{2}-\frac{3\delta}{8},\frac{1}{2}+\frac{3\delta}{8}]$ and zero otherwise. We define a function $\zeta_1 : \mathbb{R} \to \mathbb{R}$ as

$$\zeta_1 \coloneqq \varphi_{\frac{\delta}{8}} * \chi_{[-\frac{1}{2}-\frac{3\delta}{8},\frac{1}{2}+\frac{3\delta}{8}]}. \tag{8.39}$$

For $d \geq 2$, we define $\zeta_d : \mathbb{R}^d \to \mathbb{R}$ as

$$\zeta_d(\boldsymbol{x}) \coloneqq \zeta_1(x_1)\zeta_1(x_2)\ldots\zeta_1(x_d). \tag{8.40}$$

It is a standard calculation to check that $\zeta_d \in C_c^\infty(\mathbb{R}^d)$, $\operatorname{supp}\zeta_d \subseteq [-\frac{1}{2}-\frac{\delta}{2},\frac{1}{2}+\frac{\delta}{2}]^d$, $\|\zeta_d\|_{L^\infty} = 1$ and that $\zeta_d(\boldsymbol{x}) = 1$ if $\boldsymbol{x} \in [-\frac{1}{2},\frac{1}{2}]^d$. Furthermore, $\|\nabla^i\zeta_d\|_{L^\infty} \lesssim \frac{1}{\delta^i}$ for $i \in \mathbb{N}$.

Let $\boldsymbol{q} \in \mathbb{S}^{d-1}$ and $d = 2k$ or $2k+1$ for some $k \in \mathbb{N}$, we define a function $F_1 : \mathbb{R}^d \to \mathbb{R}$ as

$$F_1(\boldsymbol{x}) \coloneqq (q_1x_2 - q_2x_1 + q_3x_4 - q_4x_3 \cdots + q_{2k-1}x_{2k} - q_{2k}x_{2k-1})\,\zeta_d(\boldsymbol{x}). \tag{8.41}$$

When $d = 2k+1$, we also define a function $F_2 : \mathbb{R}^d \to \mathbb{R}$ as

$$F_2(\boldsymbol{x}) \coloneqq q_{2k+1}x_1\zeta_d(\boldsymbol{x}). \tag{8.42}$$

Finally, we define the stationary blob flow $\boldsymbol{w} : \mathbb{R}^d \to \mathbb{R}^d$. When $d = 2k$, we let

$$\begin{aligned} \boldsymbol{w} \quad &= (w_1, w_2, \dots, w_{2k}) \\ &\coloneqq \left(\partial_{x_2} F_1, -\partial_{x_1} F_1, \partial_{x_4} F_1, -\partial_{x_3} F_1, \dots, \partial_{x_{2k}} F_1, -\partial_{x_{2k-1}} F_1\right), \end{aligned} \tag{8.43}$$

and when $d = 2k + 1$, we let

$$\begin{aligned} \boldsymbol{w} \quad &= (w_1, w_2, \dots, w_{2k+1}) \\ &\coloneqq \left(\partial_{x_2} F_1 - \partial_{x_{2k+1}} F_2, -\partial_{x_1} F_1, \partial_{x_4} F_1, -\partial_{x_3} F_1, \dots, \partial_{x_{2k}} F_1, -\partial_{x_{2k-1}} F_1, \partial_{x_1} F_2\right). \end{aligned} \tag{8.44}$$

From the definition itself, it is clear that $\boldsymbol{w}$ is divergence-free. In general, we record the properties of $\boldsymbol{w}$ in the following lemma.

Lemma 8.5.1. *Depending on two parameters, $\boldsymbol{q} \in \mathbb{S}^{d-1}$ and $\delta \in (0, 1)$, there is a divergence-free vector field $\boldsymbol{w}(\cdot\,; \boldsymbol{q}, \delta) \in C_c^\infty(\mathbb{R}^d, \mathbb{R}^d)$ with the following properties.*

(i) $\operatorname{supp} \boldsymbol{w} \subseteq \overline{Q}(\mathbf{0}, 1 + \delta)$,

(ii) If $\boldsymbol{x} \in \overline{Q}(\mathbf{0}, 1)$, then $\boldsymbol{w}(\boldsymbol{x}) = \boldsymbol{q}$,

(iii) $\|\boldsymbol{w}\|_{L^\infty} \lesssim \frac{1}{\delta}$,

(iv) $\|\nabla^i \boldsymbol{w}\|_{L^\infty} \lesssim \frac{1}{\delta^{i+1}} \quad \forall\, i \in \mathbb{N}$.

8.5.2 A moving blob

Using the vector field $\boldsymbol{w}$, our goal now is to design an unsteady vector field $\widetilde{\boldsymbol{v}}$ which translates a cube centered around a starting point $\boldsymbol{x}_s$ to an endpoint $\boldsymbol{x}_e$.

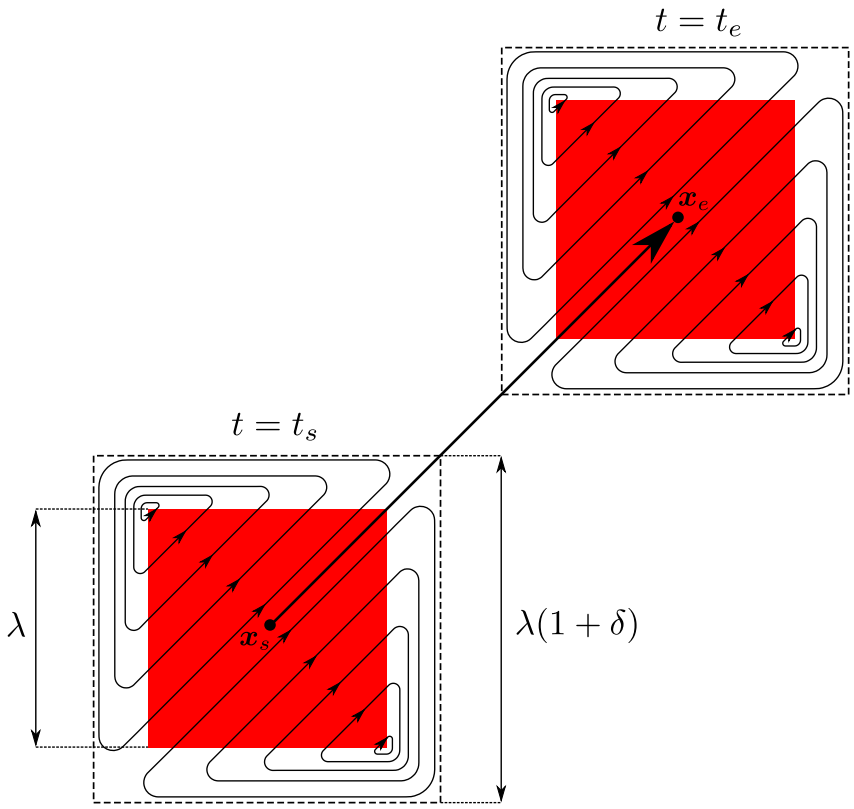

Figure 8.3: An illustration of the blob flow $\widetilde{\boldsymbol{v}}$ in two dimensions. The vector field $\widetilde{\boldsymbol{v}}$ translates a cube of length λ centered at $\boldsymbol{x}_s$ at time $t = t_s$ to a cube centered at $\boldsymbol{x}_e$ at $t = t_e$. The cube is shown in red color. As the cube moves, the vector field $\widetilde{\boldsymbol{v}}$ inside the red cube is always uniform, and the support of the vector field lies in a slightly bigger cube of length $\lambda(1+\delta)$ (shown in dashed).

We first define $\eta : \mathbb{R} \to \mathbb{R}$ as

$$\eta(x) \coloneqq \int_{-\infty}^{x-\frac{1}{2}} \varphi(x')\,\mathrm{d}x', \tag{8.45}$$

where φ is given by (8.37). It is clear that $\eta(x) = 0$ if $x \leq 0$ and $\eta(x) = 1$ if $x \geq 1$.

Given two points $\boldsymbol{x}_s, \boldsymbol{x}_e \in \mathbb{R}^d$ and time $t_s < t_e$, we define $\boldsymbol{x}_p : \mathbb{R} \to \mathbb{R}^d$ as

$$\boldsymbol{x}_p(t) \coloneqq \boldsymbol{x}_s + (\boldsymbol{x}_e - \boldsymbol{x}_s)\eta(t; t_s, t_e). \tag{8.46}$$

where we define

$$\eta(t; t_s, t_e) \coloneqq \eta\left(\frac{t - t_s}{t_e - t_s}\right). \tag{8.47}$$

Finally, given $0 < \delta < 1$ and $\lambda > 0$, we define a vector field $\widetilde{\boldsymbol{v}}(\cdot\,; \boldsymbol{x}_s, \boldsymbol{x}_e, t_s, t_e, \lambda, \delta) : \mathbb{R} \times \mathbb{R}^d \to \mathbb{R}^d$ as

$$\widetilde{\boldsymbol{v}}(t, \boldsymbol{x}) \coloneqq |\boldsymbol{x}_p'(t)| \boldsymbol{w}\left(\frac{\boldsymbol{x} - \boldsymbol{x}_p(t)}{\lambda}; \frac{\boldsymbol{x}_e - \boldsymbol{x}_s}{|\boldsymbol{x}_e - \boldsymbol{x}_s|}, \delta\right). \tag{8.48}$$

Here, $\boldsymbol{x}_p(t)$ signifies the trajectory of the center of the cube that $\widetilde{\boldsymbol{v}}$ would translate. We collect all the important properties of the vector field $\widetilde{\boldsymbol{v}}$ in the following proposition.

Proposition 8.5.1. *Given a few parameters $\boldsymbol{q} \in \mathbb{S}^{d-1}$, $\delta \in (0, 1)$, $\boldsymbol{x}_s, \boldsymbol{x}_e \in \mathbb{R}^d$ and $0 \le t_s < t_e$, then the vector field $\widetilde{\boldsymbol{v}}(\cdot\,; \boldsymbol{x}_s, \boldsymbol{x}_e, t_s, t_e, \lambda, \delta) : \mathbb{R} \times \mathbb{R}^d \to \mathbb{R}^d$ as defined in (8.48) has the following properties.*

(i) $\widetilde{\boldsymbol{v}} \in C_c^\infty(\mathbb{R} \times \mathbb{R}^d, \mathbb{R}^d)$,

(ii) $\widetilde{\boldsymbol{v}}$ *is divergence-free,*

(iii) $\operatorname{supp}_t \widetilde{\boldsymbol{v}} \subseteq [t_s, t_e]$,

(iv) $\operatorname{supp} \widetilde{\boldsymbol{v}}(t, \cdot) \subseteq \overline{Q}(\boldsymbol{x}_p(t), \lambda(1 + \delta))$,

(v) If $\boldsymbol{x} \in \overline{Q}(\boldsymbol{x}_p(t), \lambda)$ *then* $\widetilde{\boldsymbol{v}}(t, \boldsymbol{x}) = \frac{(\boldsymbol{x}_e - \boldsymbol{x}_s)}{t_e - t_s} \eta'\left(\frac{t - t_s}{t_e - t_s}\right)$,

(vi) $\|\widetilde{\boldsymbol{v}}\|_{L^\infty_{t,\boldsymbol{x}}} \lesssim \frac{|\boldsymbol{x}_e - \boldsymbol{x}_s|}{\delta(t_e - t_s)}$,

(vii) $\|\nabla^i \widetilde{\boldsymbol{v}}\|_{L^\infty_{t,\boldsymbol{x}}} \lesssim \frac{1}{\lambda^i \delta^{i+1}} \frac{|\boldsymbol{x}_e - \boldsymbol{x}_s|}{t_e - t_s} \quad \forall i \in \mathbb{N}$,

(viii) $\|\partial_t \widetilde{\boldsymbol{v}}\|_{L^\infty_{t,\boldsymbol{x}}} \lesssim \frac{|\boldsymbol{x}_e - \boldsymbol{x}_s|}{\delta(t_e - t_s)^2} + \frac{1}{\lambda\delta^2} \frac{|\boldsymbol{x}_e - \boldsymbol{x}_s|^2}{(t_e - t_s)^2}$,

(ix) If $\boldsymbol{x} \in \overline{Q}(\boldsymbol{x}_s, \lambda)$ *then* $\gamma_{\boldsymbol{x}}^{\widetilde{v}}(t_e) = \boldsymbol{x} + (\boldsymbol{x}_e - \boldsymbol{x}_s)\eta(t; t_s, t_e)$.

Proof of Proposition 8.5.1. The proof of all these properties is straightforward. Properties (i) to (v) is straight from the definition and Lemma 8.5.1.We perform a few simple computations to show properties (vi) to (viii). For the property (vi), we have

$$\begin{aligned}
\widetilde{\boldsymbol{v}} &= \frac{|\boldsymbol{x}_e - \boldsymbol{x}_s|}{t_e - t_s}\eta'\left(\frac{t - t_s}{t_e - t_s}\right)\boldsymbol{w}\left(\frac{\boldsymbol{x} - \boldsymbol{x}_p(t)}{\lambda}; \frac{\boldsymbol{x}_e - \boldsymbol{x}_s}{|\boldsymbol{x}_e - \boldsymbol{x}_s|}, \delta\right) \\
\implies \|\widetilde{\boldsymbol{v}}\|_{L^\infty_{t,\boldsymbol{x}}} &\leq \frac{|\boldsymbol{x}_e - \boldsymbol{x}_s|}{t_e - t_s}\sup_t|\eta'|\,\|\boldsymbol{w}\|_{L^\infty} \lesssim \frac{|\boldsymbol{x}_e - \boldsymbol{x}_s|}{\delta(t_e - t_s)}.
\end{aligned}$$

The property (vii) can be shown to hold as follows.

$$\begin{aligned}
\nabla^i\widetilde{\boldsymbol{v}} &= \frac{1}{\lambda^i}\frac{|\boldsymbol{x}_e - \boldsymbol{x}_s|}{t_e - t_s}\eta'\left(\frac{t - t_s}{t_e - t_s}\right)(\nabla^i\boldsymbol{w})\left(\frac{\boldsymbol{x} - \boldsymbol{x}_p(t)}{\lambda}; \frac{\boldsymbol{x}_e - \boldsymbol{x}_s}{|\boldsymbol{x}_e - \boldsymbol{x}_s|}, \delta\right) \\
\implies \left\|\nabla^i\widetilde{\boldsymbol{v}}\right\|_{L^\infty_{t,\boldsymbol{x}}} &\leq \frac{1}{\lambda^i}\frac{|\boldsymbol{x}_e - \boldsymbol{x}_s|}{t_e - t_s}\sup_t|\eta'|\left\|\nabla^i\boldsymbol{w}\right\|_{L^\infty} \lesssim \frac{1}{\lambda^i\delta^{i+1}}\frac{|\boldsymbol{x}_e - \boldsymbol{x}_s|}{t_e - t_s}.
\end{aligned}$$

The property (viii) is also proved through a simple computation.

$$\begin{aligned}
\partial_t\widetilde{\boldsymbol{v}} =& \frac{|\boldsymbol{x}_e - \boldsymbol{x}_s|}{(t_e - t_s)^2}\eta''\left(\frac{t - t_s}{t_e - t_s}\right)\boldsymbol{w}\left(\frac{\boldsymbol{x} - \boldsymbol{x}_p(t)}{\lambda}; \frac{\boldsymbol{x}_e - \boldsymbol{x}_s}{|\boldsymbol{x}_e - \boldsymbol{x}_s|}, \delta\right) \\
&+ \frac{|\boldsymbol{x}_e - \boldsymbol{x}_s|}{t_e - t_s}\eta'\left(\frac{t - t_s}{t_e - t_s}\right)\left[(\nabla\boldsymbol{w})\left(\frac{\boldsymbol{x} - \boldsymbol{x}_p(t)}{\lambda}; \frac{\boldsymbol{x}_e - \boldsymbol{x}_s}{|\boldsymbol{x}_e - \boldsymbol{x}_s|}, \delta\right)\cdot\right. \\
&\left.\left(\frac{(\boldsymbol{x_s} - \boldsymbol{x}_e)}{\lambda(t_e - t_s)}\eta'\left(\frac{t - t_s}{t_e - t_s}\right)\right)\right] \\
\implies \|\partial_t\widetilde{\boldsymbol{v}}\|_{L^\infty_{t,\boldsymbol{x}}} &\lesssim \frac{|\boldsymbol{x}_e - \boldsymbol{x}_s|}{\delta(t_e - t_s)^2} + \frac{1}{\lambda\delta^2}\frac{|\boldsymbol{x}_e - \boldsymbol{x}_s|^2}{(t_e - t_s)^2}
\end{aligned}$$

Finally, for the property (ix), we claim that

$$\gamma^{\widetilde{v}}_{\boldsymbol{x}}(t) := \boldsymbol{x} + (\boldsymbol{x}_e - \boldsymbol{x}_s)\eta\left(\frac{t - t_s}{t_e - t_s}\right) \qquad \text{for} \quad \boldsymbol{x} \in \overline{Q}(\boldsymbol{x}_s, \lambda)$$

is a trajectory starting from $\boldsymbol{x}$. It is easy to see that in the above definition

$\gamma_{\boldsymbol{x}}^{\widetilde{\boldsymbol{v}}}(t) \in \overline{Q}(\boldsymbol{x}_p(t), \lambda)$, therefore, from the property (v), we have

$$\widetilde{\boldsymbol{v}}(t, \gamma_{\boldsymbol{x}}^{\widetilde{\boldsymbol{v}}}(t)) = \frac{(\boldsymbol{x}_e - \boldsymbol{x}_s)}{t_e - t_s} \eta' \left(\frac{t - t_s}{t_e - t_s} \right).$$

Next, we simply verify that

$$\frac{d\gamma_{\boldsymbol{x}}^{\widetilde{\boldsymbol{v}}}(t)}{dt} = \widetilde{\boldsymbol{v}}(t, \gamma_{\boldsymbol{x}}^{\widetilde{\boldsymbol{v}}}(t)) \qquad \text{and} \qquad \gamma_{\boldsymbol{x}}^{\widetilde{\boldsymbol{v}}}(0) = \boldsymbol{x}.$$

□

8.5.3 Assembly of moving blobs: A proof of Proposition 8.4.2

Proof of Proposition 8.4.2. Given $\mathfrak{s} \in S_{i+1}$ for $i \in \mathbb{Z}_{\geq 0}$, let us first define $\overline{\boldsymbol{v}}_{\mathfrak{s}} : [0, \tau_\infty] \times \mathbb{T}^d \to \mathbb{R}^d$ as

$$\overline{\boldsymbol{v}}_{\mathfrak{s}}(t, \boldsymbol{x}) \coloneqq \widetilde{\boldsymbol{v}} \left(t, \boldsymbol{x}; \widetilde{P}_\Phi^{i+1}(\mathfrak{s}), P_\Theta^{i+1}(\mathfrak{s}), \frac{2\tau_i + \tau_{i+1}}{3}, \frac{\tau_i + 2\tau_{i+1}}{3}, \ell_\Phi^{i+1}, \vartheta(\nu) \right), \quad (8.49)$$

where

$$\vartheta(\nu) = \frac{2^\nu - 1}{8},$$

as defined in (8.22). In the above definition, $\widetilde{\boldsymbol{v}} : [0, \tau_\infty] \times \mathbb{T}^d \to \mathbb{R}^d$ is the $\mathbb{T}^d$-periodized version of the $\widetilde{\boldsymbol{v}}$ from Proposition 8.5.1 restricted to time 0 to τ_∞. Next, we define $\boldsymbol{v}_i : [0, \tau_\infty] \times \mathbb{T}^d \to \mathbb{R}^d$ as

$$\boldsymbol{v}_i \coloneqq \sum_{\mathfrak{s} \in S_{i+1}} \overline{\boldsymbol{v}}_{\mathfrak{s}}. \quad (8.50)$$

We claim that $\boldsymbol{v}_i$ satisfies all the properties as specified in Proposition 8.4.2. Noting properties (i) and (ii) from Proposition 8.5.1, it is clear that $\boldsymbol{v}_i \in C^\infty([0,\tau_\infty]\times\mathbb{T}^d,\mathbb{R}^d)$ and that $\boldsymbol{v}_i$ is divergence-free. Further, using property (iii) from Proposition 8.5.1, we see that

$$\operatorname{supp}_t \boldsymbol{v}_i \subseteq \left[\frac{2\tau_i+\tau_{i+1}}{3}, \frac{\tau_i+2\tau_{i+1}}{3}\right] \Subset (\tau_i,\tau_{i+1}).$$

Before proving the rest of the properties in Proposition 8.4.2, we first notice that in the definition (8.50), $\operatorname{supp}\overline{\boldsymbol{v}}_{\mathfrak{s}}(t,\cdot)$ are disjoint. Using the property (iv) in Proposition 8.5.1, for any $\mathfrak{s}\in S_{i+1}$, we note that

$$\operatorname{supp}\overline{\boldsymbol{v}}_{\mathfrak{s}}(t,\cdot) \subseteq \overline{Q}(\boldsymbol{x}_{\mathfrak{s}}(t), \ell_\Phi^{i+1}(1+\vartheta)),$$

where

$$\boldsymbol{x}_{\mathfrak{s}}(t) = \widetilde{P}_\Phi^{i+1}(\mathfrak{s})\left[1-\eta\left(\frac{3t-2\tau_i-\tau_{i+1}}{\tau_{i+1}-\tau_i}\right)\right] + P_\Theta^{i+1}(\mathfrak{s})\eta\left(\frac{3t-2\tau_i-\tau_{i+1}}{\tau_{i+1}-\tau_i}\right).$$

Next, using Lemma (8.2.10), we have that

$$\operatorname{supp}\overline{\boldsymbol{v}}_{\mathfrak{s}}(t,\cdot) \subseteq \overline{Q}(\boldsymbol{x}_{\mathfrak{s}}(t), \ell_\Phi^{i+1}(1+\vartheta)) \Subset Q(P_\Theta^{i+1}(\mathfrak{s}), \ell_\Theta^{i+1}).$$

From Lemma 8.2.3, the open cubes $Q(P_\Theta^{i+1}(\mathfrak{s}),\ell_\Theta^{i+1})$ are disjoint, which in turn implies that $\operatorname{supp}\overline{\boldsymbol{v}}_{\mathfrak{s}}(t,\cdot)$ are disjoint, an important detail we frequently use in the rest of the proof. Using property (vi) from Proposition 8.5.1, we obtain

$$\|\boldsymbol{v}_i\|_{L^\infty_{t,\boldsymbol{x}}} \le \max_{\mathfrak{s}\in S_{i+1}} \|\overline{\boldsymbol{v}}_{\mathfrak{s}}\|_{L^\infty_{t,\boldsymbol{x}}} \lesssim \frac{1}{(2^\nu-1)}\frac{\ell_\Theta^{i+1}}{(\tau_{i+1}-\tau_i)} \le \frac{1}{(2^\nu-1)}\frac{1}{2^{i\beta}}.$$

Using property (vii) from Proposition 8.5.1, we have

$$\|\nabla \boldsymbol{v}_i\|_{L^\infty_{t,\boldsymbol{x}}} \leq \max_{\mathfrak{s}\in S_{i+1}} \|\nabla \overline{\boldsymbol{v}}_{\mathfrak{s}}\|_{L^\infty_{t,\boldsymbol{x}}} \lesssim \frac{1}{\ell_\Phi^{i+1}(2^\nu-1)^2}\frac{\ell_\Theta^{i+1}}{(\tau_{i+1}-\tau_i)} \leq \frac{2^{(1+\nu-\beta)i}}{(2^\nu-1)^2}.$$

The Sobolev norm of the vector field $\boldsymbol{v}_i$ can be obtained after using properties (vi) and (vii) as

$$\begin{aligned}
\|\boldsymbol{v}_i(t,\cdot)\|_{W^{1,p}} &\leq \left(\sum_{\mathfrak{s}\in S_{i+1}} \left(\|\overline{\boldsymbol{v}}_{\mathfrak{s}}\|^p_{L^\infty_{t,\boldsymbol{x}}} + \|\nabla\overline{\boldsymbol{v}}_{\mathfrak{s}}\|^p_{L^\infty_{t,\boldsymbol{x}}}\right)\mathscr{L}^d(\operatorname{supp}\overline{\boldsymbol{v}}_{\mathfrak{s}}(t,\cdot))\right)^{\frac{1}{p}} \\
&\lesssim \left(\sum_{\mathfrak{s}\in S_{i+1}} \left(\frac{2^{(1+\nu-\beta)pi}}{(2^\nu-1)^{2p}}\,\frac{1}{2^{(1+\nu)d(i+1)}}\right)\right)^{\frac{1}{p}} \\
&\lesssim \frac{1}{(2^\nu-1)^2}\times 2^{\frac{[(1+\nu-\beta)p-d\nu]}{p}i}.
\end{aligned}$$

An upper bound on the time derivative of the vector field $\boldsymbol{v}_i$ can be obtained after using (viii) as

$$\begin{aligned}
\|\partial_t \boldsymbol{v}_i\|_{L^\infty_{t,\boldsymbol{x}}} \leq \max_{\mathfrak{s}\in S_{i+1}} \|\partial_t \overline{\boldsymbol{v}}_{\mathfrak{s}}\|_{L^\infty_{t,\boldsymbol{x}}} &\lesssim \frac{1}{(2^\nu-1)}\frac{\ell_\Theta^{i+1}}{(\tau_{i+1}-\tau_i)^2} + \frac{1}{\ell_\Phi^{i+1}(2^\nu-1)^2}\frac{(\ell_\Theta^{i+1})^2}{(\tau_{i+1}-\tau_i)^2} \\
&\lesssim \frac{1}{(2^\nu-1)^2}\frac{1}{2^{[2\beta-\nu-1]i}}.
\end{aligned}$$

Finally, using the fact that at any point in time $\operatorname{supp}\overline{\boldsymbol{v}}_{\mathfrak{s}}(t,\cdot) \Subset Q(P_\Theta^{i+1}(\mathfrak{s}), \ell_\Theta^{i+1})$ and the property (ix) in Proposition 8.5.1, we conclude that if for some $\mathfrak{s}\in S_{i+1}$, $\boldsymbol{x}\in \overline{Q}(\widetilde{P}_\Phi^{i+1}(\mathfrak{s}), \ell_\Phi^{i+1})$, then $\gamma_{\boldsymbol{x}}^{\boldsymbol{v}_i}(\tau_{i+1}) = \boldsymbol{x} - \widetilde{P}_\Phi^{i+1}(\mathfrak{s}) + P_\Theta^{i+1}(\mathfrak{s})$. □

8.6 Conclusion and Future work

In this chapter, we studied a problem related to the nonuniqueness of flow maps $X^{\boldsymbol{u}}$ in an ODE system

$$\frac{d\boldsymbol{x}(t)}{dt} = \boldsymbol{u}(t, \boldsymbol{x}(t)) \quad \text{with} \quad \boldsymbol{x}(0) = \boldsymbol{x}_0 \in \mathbb{T}^d, \tag{8.51}$$

where the vector field $\boldsymbol{u}$ is divergence-free and belongs to the Sobolev space $W^{1,p}$. We constructed an explicit example of a vector field $\boldsymbol{u}$ that is continuous in time with values in Sobolev space $W^{1,p}$, i.e., $\boldsymbol{u} \in C([0,T]; W^{1,p}(\mathbb{T}^d; \mathbb{R}^d)$, for every $p < d$ such that the flow map corresponding to the ODE (8.51) is not unique. The nonuniqueness of flow maps with vector fields in Sobolev space has previously been proven by Brué et al. (2021), but their construction was not continuous. In contrast, our construction in this paper is continuous. In particular, for every $\alpha < 1$, our example belongs to Hölder space, $\boldsymbol{u} \in C^\alpha([0,T] \times \mathbb{T}^d; \mathbb{R}^d)$.

Our construction can further be used to prove the nonuniqueness of solutions of two PDEs: the transport equation

$$\partial_t \rho + \boldsymbol{u} \cdot \nabla \rho = 0, \quad \text{on } \mathbb{T}^d \tag{8.52}$$

and the continuity equation

$$\partial_t \rho + \nabla \cdot (\boldsymbol{u}\rho) = 0, \quad \text{on } \mathbb{T}^d. \tag{8.53}$$

We note that these two equations are the same when the vector field $\boldsymbol{u}$ is divergence free. Therefore, in what follows, we discuss the nonuniqueness of solutions of the continuity equation but all of the arguments automatically apply to the transport

equation.

Consider solutions of the continuity equation (8.53) with an initial condition that is identically unity, i.e., $\rho(0,\cdot) = \rho_0 \equiv 1$. The construction proposed in this paper already produces nonuniqueness of the solution of the continuity equation in the class of measures $L^\infty([0,T],\mathcal{M})$. Note that the flow map $X^{\boldsymbol{u}}$ that we constructed maps the whole domain $\mathbb{T}^d$ to a Cantor set $\mathcal{C}_\Phi$ of measure zero. Therefore, using the pushforward formula (see, for example, (Ambrosio and Crippa, 2014)), we see that the pushforward of the density ρ_0 under the flow map $X^{\boldsymbol{u}}$, $\rho(t,\cdot) = X(t,\cdot)_{\#}\rho_0$ is a solution of the continuity equation. The support of this measure $\rho(T,\cdot)$ (at time $t = T$) is concentrated on the Cantor set $\mathcal{C}_\Phi$. In particular, it is not the d-dimensional Lebesgue measure $\mathscr{L}^d$. However, noting that a density field that is always unity in time and space is a trivial solution to the continuity equation, we prove the nonuniqueness of the solutions of (8.53) in the class of measures.

As an extension, it appears that we can further modify our construction to produce nonuniqueness of solutions in the class of integrable solutions, $\rho \in L^\infty_t L^r_x$ for $1 \leq r$ depending on the Sobolev exponent p for the vector field. We plan to work on this problem in the future.

Chapter 9

Conclusion

In this thesis, we have presented and investigated a few problems related to the study of bulk properties and flow structures in turbulence. As explained in Chapter 1, these questions are of foremost importance in the study of natural turbulent flows (e.g. to explain the transport of mass, energy or momentum for flows in rivers, oceans or accretion disks around stars), and in engineering (e.g. in the design of airfoils or heat exchangers). The "bulk" properties are spatially averaged, time-averaged emergent quantities in a flow system, such as the drag force, energy dissipation, heat, mass and momentum transport. In contrast, the study of flow structures, roughly speaking, relates to quantifying the range and the energy distribution through different flow scales. With these questions in mind, we pursued two different but complementary research directions. Accordingly, the thesis is divided into two parts.

In the first part, we were interested in estimating rigorous upper or lower bounds on bulk quantities, such as the ones mentioned above, as a function of system parameters in different flow setups. There are two advantages of these bounds: (i) the bounds are obtained directly from the governing equations, and

therefore, their derivation does not involve any unwarranted assumption, (ii) these bounds provide useful information about the bulk quantities in the extreme parameter regimes which often concerns geophysical and engineering turbulent flows. In the second part of the thesis, we were interested in problems related to the construction of incompressible flows that possess some specific properties. In this part of the thesis, we worked on two related but different problems: (i) the design of flows for optimal heat transport between two differentially heated walls and (ii) the design of "rough" vector fields in an ODE system leading to the nonuniqueness of flow maps.

The rest of this chapter summarizes the studies considered in each part of this thesis and highlights the most important findings. We also state a few open problems and future directions.

9.1 Rigorous bounds on bulk quantities

9.1.1 Summary of the thesis results

In the first part of the thesis we studied four different flow systems from the perspective of rigorous bounds on global mean quantities. In all these flow problems, we use a tool known as the background method, described in Chapter 2, to obtain the bounds. The flow setups we investigated and the corresponding important findings are as follows.

In Chapter 3, we studied uniform flow past a flat plate kept at zero incidence. We obtained a bound on the drag coefficient and showed that it stays bounded in the limit of a high Reynolds number. Although similar bounds have previously been obtained for internal flow systems (flow between boundaries), the flat plate

is the first example of an external flow problem (flow past an obstacle) where such a bound is derived.

In Chapter 4, we studied pressure-driven flow in a helical pipe. In this chapter, we were interested in obtaining a bound on the friction factor (equivalently on the volume flow rate). Our main achievement was to obtain a nontrivial dependence of this bound on the pipe's geometry (curvature and torsion of the pipe). In this chapter, we also provided a sufficient criterion for the applicability of the background method to flow problems.

In Chapter 5, we looked at Taylor–Couette flow (flow of fluid between two independently rotating concentric cylinders) with a stationary outer cylinder. We obtained bounds on the rate of energy dissipation, torque and angular momentum transport. The Taylor–Couette flow is the simplest setup with a geometrical parameter governing the dynamics, namely the radius ratio. We first derived suboptimal but analytical bounds using simple functional inequalities augmented with a boundary layer optimization procedure. We also obtained optimal bounds in the background method framework by setting up an optimization procedure and numerically solving the corresponding Euler–Lagrange equations. One of the main findings of this study was to show that the dependence of suboptimal analytical bounds on the radius ratio (the geometrical dependence) is the same as in the optimal bounds. Moreover, we demonstrated that this geometrical dependence is consistent with that obtained in the direct numerical simulations. In this chapter, we also conclusively established the limitation of the background method to two example flow setups: Taylor–Couette flow with suction and Taylor–Couette flow with injection.

In Chapter 6, we studied internally heated convection between two parallel plates with no slip boundaries in two different scenarios: (1) IH1: isothermal

boundaries, (2) IH3: isothermal top boundary and insulating bottom boundary. In both cases, we derived upper bounds on the mean vertical heat flux. The derivation of bounds in the internally heated case is substantially more complex than in its more standard counterpart, Rayleigh–Bénard convection. We used a maximum principle for the temperature and a nonstandard background field which takes the form of a vertical varying temperature profile with a two-layered boundary layer structure.

9.1.2 Open problems and future prospects

As mentioned in Chapter 2, flow setups where the background method can provide a useful bound are relatively rare. In this subsection, we list a few open problems where obtaining a bound has not been possible using the background method or any other mathematical technique. We then discuss the auxiliary functional method, a recently developed tool to obtain bounds on mean quantities, which may be helpful in making further progress.

Open problems

Despite the numerous successes of the background method, there are several important flow systems where a bound on the quantity of interest is not known. For example, an important open problem is whether the rate of energy dissipation in pressure-driven flows between non-planar walls remains bounded in the limit of vanishing viscosity. The exact mathematical formulation of this problem is as

follows: consider two non constant functions, $h_B, h_T \in C^k(\mathbb{T}_{L_x} \times \mathbb{T}_{L_y})$ such that

$$
\begin{aligned}
-\frac{H}{2} \leq \min_{x,y} h_B(x,y) < \max_{x,y} h_B(x,y) \leq -c\frac{H}{2}, \\
c\frac{H}{2} \leq \min_{x,y} h_T(x,y) < \max_{x,y} h_T(x,y) \leq \frac{H}{2},
\end{aligned}
$$

where $0 < c < 1$ is a prescribed constant. The degree of smoothness k can be chosen as large as one desires. The domain of interest Ω is

$$
\Omega \coloneqq \{(x,y,z) \,|\, h_B(x,y) < z < h_T(x,y), x \in \mathbb{T}_{L_x}, y \in \mathbb{T}_{L_y}\}. \tag{9.1}
$$

The lengths $0 < L_x, L_y$ set the periodicity of the flow in x and y directions, and the functions h_B and h_T are the graphs of the bottom and top boundaries. We are interested in solving for the velocity field $\boldsymbol{u} : [0,\infty) \times \Omega \to \mathbb{R}^3$ from equations

$$
\nabla \cdot \boldsymbol{u} = 0, \tag{9.2a}
$$

$$
\frac{\partial \boldsymbol{u}}{\partial t} + \boldsymbol{u} \cdot \boldsymbol{\nabla} \boldsymbol{u} = -\frac{1}{\rho}\nabla p + \nu \Delta \boldsymbol{u} + \frac{\Delta P}{\Delta L}\boldsymbol{e}_x, \tag{9.2b}
$$

with initial condition $\boldsymbol{u}(0,\cdot) = \boldsymbol{u}_0$ and no-slip boundary conditions

$$
\boldsymbol{u}(t,\boldsymbol{x}) = \boldsymbol{0} \qquad \text{when} \quad z = h_B(x,y) \text{ or } z = h_T(x,y) \quad \forall t > 0. \tag{9.3}
$$

In equation (9.2b), $\Delta P/\Delta L$ is the applied pressure in the x direction divided by the density. We define the rate of energy dissipation as

$$
\varepsilon_\nu \coloneqq \nu \langle |\boldsymbol{\nabla} \boldsymbol{u}|^2 \rangle \qquad \text{where} \quad \langle [\,\cdot\,] \rangle = \limsup_{T\to\infty} \frac{1}{T}\int_0^T \frac{1}{|\Omega|}\int_\Omega [\,\cdot\,]\,\mathrm{d}\boldsymbol{x}. \tag{9.4}
$$

The following is an open problem:

Problem 9.1.1. *For sufficiently small ν_0, is it true that for every $0 < \nu < \nu_0$*

$$\varepsilon_\nu < c_0 \sqrt{H} \left(\frac{\Delta P}{\Delta L} \right)^{\frac{3}{2}}, \tag{9.5}$$

where c_0 is a constant independent of ν?

Another important problem concerns the rate of energy dissipation in flow past a sphere or cylinder, as raised for instance in Doering and Constantin (1994). This problem motivated the work presented in Chapter 3 on flow past a flat plate, but to date, our work remains the only known example of bounds obtained in external flows.

The auxiliary function method

Given the limitations of the background method, new ideas or tools are needed to progress. One such tool was recently introduced by Chernyshenko et al. (2014) and is known as the auxiliary functional method. The idea of this method is quite simple and is described below (based on Chernyshenko (2022)). Consider a dynamical system, finite or infinite dimensional, as

$$\frac{d\boldsymbol{u}}{dt} = \boldsymbol{f}(\boldsymbol{u}), \qquad \text{with} \quad \boldsymbol{u}(0) = \boldsymbol{u}_0. \tag{9.6}$$

The Navier–Stokes equation, for example, can be recast in this form, where $\boldsymbol{u}$ would be an incompressible flow field. Suppose that for this dynamical system, we are interested in obtaining a bound on $\overline{F}$, the long-time average of a particular functional $F[\boldsymbol{u}]$. For the Navier–Stokes equation, $F[\boldsymbol{u}]$ could be the volume-averaged energy dissipation rate, for example. Now for a given (different)

functional $V[\boldsymbol{u}]$ (differentiable w.r.t. $\boldsymbol{u}$), let us define a functional $D_V[\boldsymbol{u}]$ as

$$D_V[\boldsymbol{u}] = \boldsymbol{f} \cdot \frac{\delta V}{\delta u}, \tag{9.7}$$

which is the Lie derivative of V with respect to $\boldsymbol{f}$. Now assuming $\boldsymbol{u}(t)$ (solution to (9.6)) stays bounded in time, then so does $V[\boldsymbol{u}(t)]$. As a result, from the long-time average of $D_V[\boldsymbol{u}]$, we get

$$\overline{D_V[\boldsymbol{u}(t)]} = \overline{\boldsymbol{f} \cdot \frac{\delta V}{\delta u}\bigg|_{\boldsymbol{u}=\boldsymbol{u}(t)}} = \lim_{t\to\infty} \frac{V[\boldsymbol{u}(t)] - V[\boldsymbol{u}(0)]}{t} = 0. \tag{9.8}$$

From these considerations, we see that if we can find a functional $V[\boldsymbol{u}]$ and a constant B such that

$$F[\boldsymbol{u}] + D_V[\boldsymbol{u}] \leq B, \tag{9.9}$$

then by taking the long-time average, we can obtain a bound on $\overline{F}$ as

$$\overline{F[\boldsymbol{u}(t)]} \leq B. \tag{9.10}$$

Furthermore, by trying all possible choices of functional V, we can obtain the optimal bound in the framework of the auxiliary functional method:

$$\overline{F[\boldsymbol{u}(t)]} \leq B_{opt} \coloneqq \inf_{V} \sup_{\boldsymbol{u}} (F[\boldsymbol{u}] + D_V[\boldsymbol{u}]). \tag{9.11}$$

The auxiliary functional method can, in principle, provide a sharp bound as shown by Tobasco et al. (2018) for finite dimensional systems (ODEs) and by Rosa and Temam (2020) for infinite dimensional systems (PDEs). In recent years, the

auxiliary functional method has become popular, and been applied to both finite dimensional systems (Fantuzzi et al., 2016; Goluskin, 2018; Fantuzzi and Goluskin, 2020; Goluskin, 2020; Kumar, 2019; Olson et al., 2021) and infinite dimensional systems, such as the Kuramoto–Sivashinsky equation (Goluskin and Fantuzzi, 2019).

As for the Navier–Stokes equations, the auxiliary functional method can, in principle, produce a bound on the energy dissipation rate for flow systems such as pressure-driven flow between nonplanar walls or uniform flow past a cylinder. The main difficulty with this method is to find a good functional $V[\boldsymbol{u}]$. For a choice of quadratic functional $V[\boldsymbol{u}]$, the background method and the auxiliary functional method are equivalent (Chernyshenko, 2022), which can be shown by choosing

$$V[\boldsymbol{u}] = \alpha \left\| \boldsymbol{u} - \boldsymbol{U} \right\|_2^2 , \tag{9.12}$$

where α is a constant and $\boldsymbol{U}$ is a background flow. However, no-one has yet found a suitable functional $V[\boldsymbol{u}]$, that can be used in the auxiliary functional method and is beyond quadratic for the Navier-Stokes equations, that would help obtain bounds in systems that cannot be treated using the background method.

To move forward, there are two potential options. One way is to extend the background method by making the background flow $\boldsymbol{U}$ depend on the flow $\boldsymbol{u}$. The idea roughly is that there may not exist a single good choice of the background flow $\boldsymbol{U}$ that works for all perturbed flow $\boldsymbol{v}$ (equivalently for all total flows $\boldsymbol{u}$) but for every total flow $\boldsymbol{u}$ we may still be able to find a good choice (not necessarily the same) of the background flow $\boldsymbol{U}$. This idea was successfully applied by Goodman (1994) in the context of Kuramoto–Sivashinsky equation. For the Navier–Stokes equations, this idea is given in Chernyshenko (2022). The strategy of choosing

the background flow $\boldsymbol{U}$ that depends on the total flow $\boldsymbol{u}$ was also independently realized by us in unpublished work. The main problem with this strategy is to identify the right dependence of $\boldsymbol{U}$ on $\boldsymbol{u}$. Another way to move forward, as suggested by Chernyshenko (2022), is to make use of the information about the total helicity in the flow (Moffatt, 1969; Moffatt and Tsinober, 1992) in designing a suitable functional $V[\boldsymbol{u}]$.

9.2 The design of incompressible flows in fluid problems

In the second part of the thesis, we investigated two problems related to the design of incompressible flows under some given constraint (which can be understood as the cost to generate the flow) such that the velocity field has some specific desired property.

In Chapter 7, we studied the problem of optimizing heat transport between two parallel walls kept at different temperatures by designing a convective velocity field $\boldsymbol{u}$ (with a given enstrophy constraint, $\langle|\nabla \boldsymbol{u}|^2\rangle \leq \mathscr{P}$) in the convection-diffusion equation. The budget on the enstrophy can also be understood as a constraint on the power supply to generate this flow using a body force in the Navier–Stokes equation. An upper bound on the maximum heat transfer is known, which says that with $\mathscr{P}$ amount of power supply budget, the heat transfer cannot scale faster than $\mathscr{P}^{1/3}$. However, it was not previously known whether velocity fields exist (under the power supply constraint) for which the corresponding heat transfer saturates this upper bound. In this chapter, we designed novel three-dimensional incompressible branching velocity fields for which the heat transfer scales precisely

as $\mathscr{P}^{1/3}$, therefore establishing the sharpness of the known upper bound. Our construction also allows us to identify the exact physical mechanism that makes these branching flows very efficient in transferring heat.

In Chapter 8, we studied a problem related to the nonuniqueness of trajectories in an ODE system where the vector field of bounded divergence belongs to the Sobolev space $W^{1,p}$, and therefore falls under Diperna–Lions theory. Recently, Brué et al. (2021) constructed a divergence-free vector field $\boldsymbol{u} \in C([0,T]; L^s(\mathbb{T}^d;\mathbb{R}^d) \cap W^{1,p}(\mathbb{T}^d;\mathbb{R}^d))$ $(s < \infty,\ p < d)$ using the method of convex integration and employing Ambrosio's superposition principle to prove that the flow map of the corresponding ODE, $\frac{d\boldsymbol{x}}{dt} = \boldsymbol{u}(\boldsymbol{x},t)$, is not unique. In this chapter, we provide an explicit construction of a divergence-free vector field $\boldsymbol{u} \in C([0,T]; W^{1,p}(\mathbb{T}^d;\mathbb{R}^d)) \cap C^\alpha([0,T]\times\mathbb{T}^d;\mathbb{R}^d)$ $(\alpha < 1,\ p < d)$ for which we show that the set of initial conditions for which the trajectories are not unique is of full measure. In particular, the flow map is not unique.

9.2.1 Open problems and future prospects

In the last fifteen years, there has been a tremendous amount of activity in the mathematical fluid dynamics community to study various turbulent flow properties, such as anomalous dissipation (De Lellis and L. Székelyhidi, 2013; Isett, 2018; Buckmaster et al., 2019; Drivas et al., 2022a; Bruè and De Lellis, 2023), enhanced dissipation (Bedrossian and Coti Zelati, 2017; Coti Zelati et al., 2020; Coti Zelati and Dolce, 2020) and mixing (Yao and Zlatoš, 2017; Alberti et al., 2019; Elgindi and Zlatoš, 2019). Arguably, one of the remarkable achievements of the last decade was the resolution of Onsager's conjecture which is related to anomalous dissipation, an intrinsic characteristic of turbulence. Anomalous dis-

sipation, as we explained in the Introduction (see Chapter 1), is the statement that the energy dissipation remains finite in the limit of viscosity going to zero, namely

$$\limsup_{\nu \to 0} \varepsilon_\nu \geq \varepsilon_0 > 0. \tag{9.13}$$

The phenomenon of anomalous dissipation is such a fundamental characteristic of turbulent flows that it is aptly called the "Zeroth law" of turbulence.

For viscous incompressible flows, the viscosity provides a route to dissipate energy; therefore, statement (9.13) is feasible. However, such a mechanism is absent for ideal fluids governed by the Euler equations:

$$\nabla \cdot \boldsymbol{u} = 0, \tag{9.14a}$$

$$\frac{\partial \boldsymbol{u}}{\partial t} + \boldsymbol{u} \cdot \boldsymbol{\nabla} \boldsymbol{u} = -\frac{1}{\rho} \nabla p, \tag{9.14b}$$

as the viscosity is zero. Indeed, by taking the dot product of equation (9.14b) with $\boldsymbol{u}$ and performing a volume and time integration, we find that the kinetic energy is conserved for the smooth Euler solutions, i.e.,

$$\frac{1}{2} \left\| \boldsymbol{u}(T) \right\|_2^2 = \frac{1}{2} \left\| \boldsymbol{u}(0) \right\|_2^2 . \tag{9.15}$$

The conservation of kinetic energy for the Euler equation seems incompatible with the phenomenon of anomalous dissipation. This, therefore, suggests that in the limit viscosity going to zero, the turbulent solutions of the Navier–Stokes equation cannot possess enough regularity to justify the derivation of (9.15) from (9.14). In fact, Onsager's conjecture quantifies this regularity of the Euler solution. Onsager conjectured the following:

- (rigidity part) if the solution of the Euler equations has at least one-third Hölder regularity, then the energy is conserved, i.e., (9.15) holds,

- (flexibility part) there are examples of solutions of the Euler equations with Hölder regularity less than one-third for which the energy dissipates.

The important consequence of this conjecture is that the turbulent velocity field cannot possess more than 1/3 Hölder regularity in the limit viscosity going to zero.

The energy conservation part of the conjecture, which is relatively more straightforward, was proved by Constantin et al. (1994), with initial partial results by Eyink (1994). The more difficult part of the conjecture is proving that for every $\alpha < 1/3$ in the class C^α, there are solutions to the Euler equations which do not conserve energy. In a pioneering work, De Lellis and L. Székelyhidi (2009, 2013) introduced the method of convex integration to the Euler equation to build precisely these types of solutions. Their work was inspired by the Nash embedding theorem and Gromov's h-principle. The initial construction of De Lellis and L. Székelyhidi (2013) did not reach the one-third limit, as conjectured by Onsager. But a series of studies after their initial construction progressively filled this gap, eventually leading to the proof of this conjecture (Isett, 2018). The construction of Isett was compactly supported in time. Buckmaster et al. (2019) then showed that in the class C^α ($\alpha < 1/3$), there are solutions for which the kinetic energy is non-increasing.

With the construction of solutions that dissipate energy for the Euler system, the next significant challenge, which is also of physical importance, is to create solutions of the Navier–Stokes which has the fundamental property of turbulence, i.e., anomalous dissipation. More precisely, the question is whether it is possible

to design with "simple" solutions of the Navier–Stokes equations (either steady or time-periodic) $\boldsymbol{u}^\nu$, which depend on viscosity, to the Navier–Stokes equations and obey the relation (9.13). Two physically important settings to consider this problem are (1) surface-velocity driven flows such as Couette flow or flow past a cylinder (2) fixed body force driven flows, where the applied body force is smooth (such as one created by combining a finite number of Fourier modes). Even though this problem is one of the most important problems in mathematical fluid dynamics, it remains (as stated) open and probably too difficult to solve with currently available tools.

Consequently, before getting into the more challenging problem of anomalous dissipation, one can consider simplified versions of the problem that are still non-trivial but are within reach of current methods and tools available to us and, therefore, can help us gain the insights needed to tackle the original problem. For example, one could instead ask the following question: is it possible to build velocity fields driven by a body forcing that is "rough" for which (9.13) holds? Indeed, this line of questioning is already considered by Bruè and De Lellis (2023) in a recent paper, where they construct a family of forcings that belongs to the class of C^α for every exponent $\alpha < 1$ and for which (9.13) is true. Their result is nontrivial in the sense that if the Navier–Stokes equations are replaced with the Stokes equations (without the nonlinear term) but same forcing, then the resultant velocity fields do not have anomalous dissipation. Therefore, along with the rough forcing, the nonlinearity plays a nontrivial role in their construction to help generate small enough scales for (9.13) to hold.

Another way to simplify the problem is first to create numerically the required velocity fields that exhibit anomalous dissipation. To date, even numerical evidence of the existence of such simple (steady or time-periodic) velocity fields is

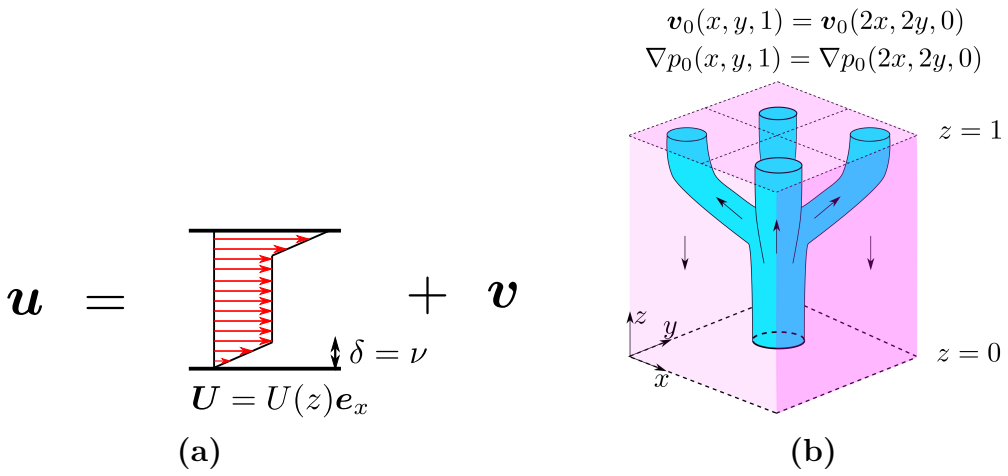

Figure 9.1: (a) A background decomposition of the flow as described in the main text. (b) One flow unit as described in the main text. The main property of this flow unit is that at level $z = 1$, the flow field is made up of four self-similar copies at level $z = 0$.

absent. A simple flow setup that comes to mind where creating the required velocity fields might be possible is Couette flow. A schematic of Couette flow is shown in Chapter 2 in Figure 2.1. For Couette flow, a formal calculation shows that one can relate the energy dissipation to the momentum transport between two walls as

$$\varepsilon_\nu = \underbrace{\frac{U_0}{H}\left[\overline{u_x u_z} - \nu\overline{\frac{\partial u_x}{\partial z}}\right]_{z=z_0}}_{\text{Momentum Transport}},$$

where the overbar denotes a long-time horizontal average. Therefore, more momentum transport implies more energy dissipation. From this identity, the problem of anomalous dissipation can therefore be posed as a problem of optimal momentum transport between two walls.

To solve this optimal momentum transport problem, we propose to combine ideas from Chapter 2 (the background method) and Chapter 7 (the design of

branching flows for optimal heat transport). We begin by splitting the total flow $\boldsymbol{u}$ as the sum of two divergence-free flow fields, the background flow $\boldsymbol{U} = U(z)\boldsymbol{e}_x$ (can be thought of as anticipated mean flow and is chosen in advance) and the perturbed flow $\boldsymbol{v}$. Figure 9.1a shows such a decomposition which is the same as the one in the background method from Chapter 2. Then, we propose to construct the perturbed flow $\boldsymbol{v}$ as a branching flow, which contains self-similarly scaled copies of a unit building block $\boldsymbol{v}_0$, specifically designed to facilitate efficient transfer of momentum. An example of such a unit $\boldsymbol{v}_0$ is shown in figure 9.1b. The idea is to find a solution to the Navier–Stokes equation such that the velocity field and the pressure gradient are periodic in the x, and y directions and, the slice at $z = 1$ level consists of four dilated (half the size) copies of the slice at $z = 0$ level as explained in figure 9.1b. This approach is different from previous computational work, as the emphasis here is on producing one single unit that can be glued with dilated copies of itself to design the perturbed flow $\boldsymbol{v}$ in whole domain. Once we have designed such a unit, a rough scaling analysis shows that by gluing self-similar copies of $\boldsymbol{v}_0$ to N branching levels and choosing N appropriately (depending on the viscosity), we should be able to get anomalous dissipation. Physically, these branching structures help carry the momentum, which is dominated by advection in the bulk of the domain (i.e., the losses to diffusion are negligible) up to very thin boundary layers near the top and bottom walls, where finally, diffusion takes over. The physical mechanism invoked here, echoes the way energy is transferred in turbulent flows from large scales to small enough scales where the viscous diffusion takes over. This is one line of research that we plan to pursue in the future.

Finally, the question of the design of velocity fields such that the evolution of passive scalar exhibits anomalous dissipation is yet another physically interesting

problem as it relates to Obukhov–Corrsin's theory but is simpler than the original problem. In fact, there has been a lot of activity recently in this direction (see, for example, Drivas et al., 2022a; Colombo et al., 2022). In the spirit of anomalous dissipation with forcing, one can ask the question about anomalous dissipation of a passive scalar in an internally heating setup. In particular, is it possible to find a smooth source of volumetric heating $H : \mathbb{T}^d \to \mathbb{R}$ which is balanced, i.e., $\int_{\mathbb{T}^d} H \, \mathrm{d}\boldsymbol{x} = 0$ and a velocity field $\boldsymbol{u} : \mathbb{T}^d \to \mathbb{R}^d$ such the evolution of the temperature field in the equation

$$\frac{\partial T}{\partial t} + \boldsymbol{u} \cdot \boldsymbol{\nabla} T = \kappa \Delta T + H \qquad \text{in} \quad \mathbb{T}^d, \tag{9.16}$$

$$\text{exhibits} \qquad \limsup_{\kappa \to 0} \int_0^\tau \int_{\mathbb{T}^d} |\nabla T|^2 \, \mathrm{d}\boldsymbol{x} \mathrm{d}t \geq c > 0, \tag{9.17}$$

for any initial condition $T(0, \cdot) = T_0 \in L^2(\mathbb{T}^d)$? The vector fields we designed in Chapter 8 or similar ideas can be instrumental in resolving this question and we are actively pursuing this line of investigation.

In conclusion, even though the original problem of producing an example of a velocity field that obeys the fundamental property of turbulent flows remains elusive, the pursuit of this problem has generated tremendous activity in the mathematical fluid dynamics community. Every month new studies are published that are related to this problem in one way or the other, and explore new ways/mechanisms to trigger anomalous dissipation for simpler or modified problems. Whether this problem of anomalous dissipation will be solved anytime soon is up for debate, but working in this direction is extremely engaging at this point in time, and the future of the field seems bright.

Bibliography

Alam, T. and Kim, M.-H. (2018). A comprehensive review on single phase heat transfer enhancement techniques in heat exchanger applications. *Renewable and Sustainable Energy Reviews*, 81:813–839.

Alberti, G., Crippa, G., and Mazzucato, A. L. (2019). Exponential self-similar mixing by incompressible flows. *J. Amer. Math. Soc.*, 32(2):445–490.

Ambrosio, L. (2004). Transport equation and Cauchy problem for BV vector fields. *Invent. Math.*, 158(2):227–260.

Ambrosio, L. and Crippa, G. (2014). Continuity equations and ODE flows with non-smooth velocity. *Proc. Roy. Soc. Edinburgh Sect. A*, 144(6):1191–1244.

Arora, C. P. (2000). *Refrigeration and air conditioning*. Tata McGraw-Hill Education.

Arslan, A., Fantuzzi, G., Craske, J., and Wynn, A. (2021a). Bounds for internally heated convection with fixed boundary heat flux. *J. Fluid Mech.*, 922:R1.

Arslan, A., Fantuzzi, G., Craske, J., and Wynn, A. (2021b). Bounds on heat transport for convection driven by internal heating. *J. Fluid Mech.*, 919:A15.

Arslan, A., Fantuzzi, G., Craske, J., and Wynn, A. (2023). Rigorous scaling laws

for internally heated convection at infinite Prandtl number. *J. Math. Phys.*, 64(2):023101.

Avellaneda, M. and Majda, A. J. (1991). An integral representation and bounds on the effective diffusivity in passive advection by laminar and turbulent flows. *Comm. Math. Phys.*, 138(2):339–391.

Avila, K., Moxey, D., de Lozar, A., Avila, M., Barkley, D., and Hof, B. (2011). The onset of turbulence in pipe flow. *Science*, 333:192–196.

Avila, M. (2012). Stability and angular-momentum transport of fluid flows between corotating cylinders. *Phys. Rev. Lett.*, 108(12):124501.

Balbus, S. A. (2017). When is high reynolds number shear flow not turbulent? *J. Fluid Mech.*, 824:1–4.

Barkley, D. (2016). Theoretical perspective on the route to turbulence in a pipe. *J. Fluid Mech.*, 803:P1.

Bedrossian, J. and Coti Zelati, M. (2017). Enhanced dissipation, hypoellipticity, and anomalous small noise inviscid limits in shear flows. *Arch. Ration. Mech. Anal.*, 224(3):1161–1204.

Berger, S. A., Talbot, L., and Yao, L. S. (1983). Flow in curved pipes. *Annu. Rev. Fluid Mech.*, 15:461–512.

Berghout, P., Verzicco, R., Stevens, R. J., Lohse, D., and Chung, D. (2020). Calculation of the mean velocity profile for strongly turbulent Taylor–Couette flow at arbitrary radius ratios. *J. Fluid Mech.*, 905.

Blasius, H. (1908). *Grenzschichten in Flüssigkeiten mit kleiner Reibung.* B.G. Teubner.

Böhm-Vitense, E. (1958). Über die wasserstoffkonvektionszone in sternen verschiedener effektivtemperaturen und leuchtkräfte. Mit 5 textabbildungen. *Zeitschrift für Astrophysik, Vol. 46, p. 108*, 46:108.

Bouillaut, V., Lepot, S., Aumaître, S., and Gallet, B. (2019). Transition to the ultimate regime in a radiatively driven convection experiment. *J. Fluid Mech.*, 861.

Brué, E., Colombo, M., and De Lellis, C. (2021). Positive solutions of transport equations and classical nonuniqueness of characteristic curves. *Arch. Ration. Mech. Anal.*, 240(2):1055–1090.

Bruè, E. and De Lellis, C. (2023). Anomalous Dissipation for the Forced 3D Navier-Stokes Equations. *Comm. Math. Phys.*, 400(3):1507–1533.

Buckmaster, T., De Lellis, C., L. Székelyhidi, J., and Vicol, V. (2019). Onsager's conjecture for admissible weak solutions. *Comm. Pure Appl. Math.*, 72(2):229–274.

Busse, F. H. (1969). On Howard's upper bound for heat transport by turbulent convection. *J. Fluid Mech.*, 37(3):457–477.

Busse, F. H. (1970). Bounds for turbulent shear flow. *J. Fluid Mech.*, 41(1):219–240.

Cadot, O., Couder, Y., Daerr, A., Douady, S., and Tsinober, A. (1997). Energy injection in closed turbulent flows: Stirring through boundary layers versus inertial stirring. *Phys. Rev. E*, 56(1):427.

Caldwell, D. R. and Mourn, J. N. (1995). Turbulence and mixing in the ocean. *Rev. Geophys.*, 33(S2):1385–1394.

Canton, J., Örlü, R., and Schlatter, P. (2017). Characterisation of the steady, laminar incompressible flow in toroidal pipes covering the entire curvature range. *Intl J. Heat Fluid Flow*, 66:95–107.

Canton, J., Rinaldi, E., Örlü, R., and Schlatter, P. (2020). Critical point for bifurcation cascades and featureless turbulence. *Phys. Rev. Lett.*, 124:014501.

Canton, J., Schlatter, P., and Örlü, R. (2016). Modal instability of the flow in a toroidal pipe. *J. Fluid Mech.*, 792:894–909.

Caravenna, L. and Crippa, G. (2021). A directional Lipschitz extension lemma, with applications to uniqueness and Lagrangianity for the continuity equation. *Comm. Partial Differential Equations*, 46(8):1488–1520.

Caulfield, C. P. (2005). Buoyancy flux bounds for surface-driven flow. *J. Fluid Mech.*, 536:367–376.

Caulfield, C. P. and Kerswell, R. R. (2001). Maximal mixing rate in turbulent stably stratified couette flow. *Phys. Fluids*, 13(4):894–900.

Chernyshenko, S. (2022). Relationship between the methods of bounding time averages. *Phil. Trans. R. Soc. Lond. A*, 380(2225):20210044.

Chernyshenko, S. I., Goulart, P., Huang, D., and Papachristodoulou, A. (2014). Polynomial sum of squares in fluid dynamics: a review with a look ahead. *Phil. Trans. R. Soc. Lond. A: Math. Phys. Eng. Sci.*, 372(2020):20130350.

Cioncolini, A. and Santini, L. (2006). An experimental investigation regarding the laminar to turbulent flow transition in helically coiled pipes. *Exp. Therm. Fluid Sci.*, 30:367–380.

Coles, D. (1965). Transition in circular Couette flow. *J. Fluid Mech.*, 21(3):385–425.

Colombo, M., Crippa, G., and Sorella, M. (2022). Anomalous dissipation and lack of selection in the Obukhov–Corrsin theory of scalar turbulence. *arXiv preprint arXiv:2207.06833*.

Constantin, P. (1994). Geometric statistics in turbulence. *SIAM Rev.*, 36(1):73–98.

Constantin, P. and Doering, C. R. (1995). Variational bounds on energy dissipation in incompressible flows. II. Channel flow. *Phys. Rev. E*, 51(4):3192–3198.

Constantin, P., E, W., and Titi, E. S. (1994). Onsager's conjecture on the energy conservation for solutions of Euler's equation. *Comm. Math. Phys.*, 165(1):207–209.

Coti Zelati, M., Delgadino, M. G., and Elgindi, T. M. (2020). On the relation between enhanced dissipation timescales and mixing rates. *Comm. Pure Appl. Math.*, 73(6):1205–1244.

Coti Zelati, M. and Dolce, M. (2020). Separation of time-scales in drift-diffusion equations on $\mathbb{R}^2$. *J. Math. Pures Appl. (9)*, 142:58–75.

Davies, G. F. and Richards, M. A. (1992). Mantle convection. *J. Geol.*, 100(2):151–206.

De Lellis, C. and L. Székelyhidi, J. (2009). The Euler equations as a differential inclusion. *Ann. of Math. (2)*, 170(3):1417–1436.

De Lellis, C. and L. Székelyhidi, J. (2013). Dissipative continuous Euler flows. *Invent. Math.*, 193(2):377–407.

Dean, W. R. (1927). Note on the motion of fluid in a curved pipe. *Phil. Mag.*, 4:208–223.

Dean, W. R. (1928). The stream-line motion of fluid in a curved pipe. *Phil. Mag.*, 5:673–695.

Dennis, S. C. R. (1980). Calculation of the steady flow through a curved tube using a new finite-difference method. *J. Fluid Mech.*, 99:449–467.

Ding, Z. and Marensi, E. (2019). Upper bound on angular momentum transport in taylor-couette flow. *Phys. Rev. E*, 100(6):063109.

DiPerna, R. J. and Lions, P.-L. (1989). Ordinary differential equations, transport theory and Sobolev spaces. *Invent. Math.*, 98(3):511–547.

DiPrima, R. C. and Swinney, H. L. (1981). *Instabilities and transition in flow between concentric rotating cylinders*. Springer.

Doering, C. R. and Constantin, P. (1992). Energy dissipation in shear driven turbulence. *Phys. Rev. Lett.*, 69(11):1648–1651.

Doering, C. R. and Constantin, P. (1994). Variational bounds on energy dissipation in incompressible flows: Shear flow. *Phys. Rev. E*, 49(5):4087–4099.

Doering, C. R. and Constantin, P. (1996). Variational bounds on energy dissipation in incompressible flows. III. Convection. *Phys. Rev. E*, 53(6):5957–5981.

Doering, C. R. and Constantin, P. (1998a). Bounds for heat transport in a porous layer. *J. Fluid Mech.*, 376(1):263–296.

Doering, C. R. and Constantin, P. (1998b). Bounds for heat transport in a porous layer. *J. Fluid Mech.*, 376:263–296.

Doering, C. R. and Constantin, P. (2001). On upper bounds for infinite Prandtl number convection with or without rotation. *J. Math. Phys.*, 42(2):784–795.

Doering, C. R., Otto, F., and Reznikoff, M. G. (2006). Bounds on vertical heat transport for infinite-prandtl-number Rayleigh–Bénard convection. *J. Fluid Mech.*, 560:229–241.

Doering, C. R., Spiegel, E. A., and Worthing, R. A. (2000). Energy dissipation in a shear layer with suction. *Phys. Fluids*, 12(8):1955–1968.

Doering, C. R. and Tobasco, I. (2019). On the optimal design of wall-to-wall heat transport. *Comm. Pure Appl. Math.*, 72(11):2385–2448.

Drivas, T. D., Elgindi, T. M., Iyer, G., and Jeong, I. (2022a). Anomalous dissipation in passive scalar transport. *Arch. Ration. Mech. Anal.*, 243(3):1151–1180.

Drivas, T. D., Nguyen, H. Q., and Nobili, C. (2022b). Bounds on heat flux for Rayleigh–Bénard convection between Navier-slip fixed-temperature boundaries. *Phil. Trans. R. Soc. Lond. A*, 380(2225):20210025.

Dryden, H. L. (1943). A review of the statistical theory of turbulence. *Q. Appl. Math.*, 1(1):7–42.

Duvigneau, R., Visonneau, M., and Deng, G. B. (2003). On the role played by turbulence closures in hull shape optimization at model and full scale. *J. Mar. Sci. Technol.*, 8:11–25.

Eckhardt, B., Grossmann, S., and Lohse, D. (2007). Torque scaling in turbulent taylor-couette flow between independently rotating cylinders. *J. Fluid Mech.*, 581:221–250.

Elgindi, T. M. and Zlatoš, A. (2019). Universal mixers in all dimensions. *Adv. Math.*, 356:106807, 33.

Eustice, J. (1910). Flow of water in curved pipes. *Proc. R. Soc. Lond. A*, 84:107–118.

Eustice, J. (1911). Experiments on streamline motion in curved pipes. *Proc. R. Soc. Lond. A*, 85:119–131.

Eyink, G. L. (1994). Energy dissipation without viscosity in ideal hydrodynamics. I. Fourier analysis and local energy transfer. *Phys. D*, 78(3-4):222–240.

Falconer, K. (2014). *Fractal geometry*. John Wiley & Sons, Ltd., Chichester, third edition. Mathematical foundations and applications.

Fan, W. L., Jolly, M., and Pakzad, A. (2021). Three-dimensional shear driven turbulence with noise at the boundary. *Nonlinearity*, 34(7):4764.

Fannjiang, A. and Papanicolaou, G. (1994). Convection enhanced diffusion for periodic flows. *SIAM J. Appl. Math.*, 54(2):333–408.

Fantuzzi, G. (2018). Bounds for Rayleigh–Bénard convection between free-slip boundaries with an imposed heat flux. *J. Fluid Mech.*, 837.

Fantuzzi, G., Arslan, A., and Wynn, A. (2022). The background method: theory and computations. *Phil. Trans. R. Soc. Lond. A*, 380(2225):20210038.

Fantuzzi, G. and Goluskin, D. (2020). Bounding extreme events in nonlinear dynamics using convex optimization. *SIAM J. Appl. Dyn. Syst.*, 19(3):1823–1864.

Fantuzzi, G., Goluskin, D., Huang, D., and Chernyshenko, S. I. (2016). Bounds for deterministic and stochastic dynamical systems using sum-of-squares optimization. *SIAM J. Appl. Dyn. Syst.*, 15(4):1962–1988.

Fantuzzi, G., Nobili, C., and Wynn, A. (2020). New bounds on the vertical heat transport for Bénard–Marangoni convection at infinite Prandtl number. *J. Fluid Mech.*, 885.

Fantuzzi, G., Pershin, A., and Wynn, A. (2018). Bounds on heat transfer for Bénard–Marangoni convection at infinite Prandtl number. *J. Fluid Mech.*, 837:562–596.

Fantuzzi, G. and Wynn, A. (2015). Construction of an optimal background profile for the Kuramoto–Sivashinsky equation using semidefinite programming. *Phys. Lett. A*, 379(1-2):23–32.

Fantuzzi, G. and Wynn, A. (2016). Optimal bounds with semidefinite programming: an application to stress-driven shear flows. *Phys. Rev. E*, 93(4):043308.

Fefferman, C. L., Pooley, B. C., and Rodrigo, J. L. (2021). Non-conservation of dimension in divergence-free solutions of passive and active scalar systems. *Arch. Ration. Mech. Anal.*, 242(3):1445–1478.

Folland, G. B. (2003). *Advanced calculus*. Pearson.

Froitzheim, A., Merbold, S., Ostilla-Mónico, R., and Egbers, C. (2019). Angular momentum transport and flow organization in Taylor–Couette flow at radius ratio of η= 0.357. *Phys. Rev. Fluids*, 4(8):084605.

Gallet, B., Doering, C. R., and Spiegel, E. A. (2010). Destabilizing Taylor–Couette flow with suction. *Phys. Fluids*, 22(3):034105.

Gammack, D. and Hydon, P. E. (2001). Flow in pipes with non-uniform curvature and torsion. *J. Fluid Mech.*, 433:357–382.

Germano, M. (1982). On the effect of torsion on a helical pipe flow. *J. Fluid Mech.*, 125:1–8.

Germano, M. (1989). The dean equations extended to a helical pipe flow. *J. Fluid Mech.*, 203:289–305.

Giaquinta, M., Modica, G., and Souček, J. (1998). *Cartesian currents in the calculus of variations. I*, volume 37 of *Ergebnisse der Mathematik und ihrer Grenzgebiete. 3. Folge. A Series of Modern Surveys in Mathematics [Results in Mathematics and Related Areas. 3rd Series. A Series of Modern Surveys in Mathematics]*. Springer-Verlag, Berlin. Cartesian currents.

Giri, V. and Sorella, M. (2022). Non-uniqueness of integral curves for autonomous Hamiltonian vector fields. *Differential Integral Equations*, 35(7-8):411–436.

Goluskin, D. (2015). Internally heated convection beneath a poor conductor. *J. Fluid Mech.*, 771:36–56.

Goluskin, D. (2016). *Internally heated convection and Rayleigh-Bénard convection*. Springer.

Goluskin, D. (2018). Bounding averages rigorously using semidefinite programming: mean moments of the Lorenz system. *J. Nonlinear Sci.*, 28(2):621–651.

Goluskin, D. (2020). Bounding extrema over global attractors using polynomial optimisation. *Nonlinearity*, 33(9):4878.

Goluskin, D. and Doering, C. R. (2016). Bounds for convection between rough boundaries. *J. Fluid Mech.*, 804:370–386.

Goluskin, D. and Fantuzzi, G. (2019). Bounds on mean energy in the Kuramoto–Sivashinsky equation computed using semidefinite programming. *Nonlinearity*, 32(5):1705.

Goluskin, D. and Spiegel, E. A. (2012). Convection driven by internal heating. *Phys. Lett. A*, 377(1-2):83–92.

Goluskin, D. and van der Poel, E. P. (2016). Penetrative internally heated convection in two and three dimensions. *J. Fluid Mech.*, 791.

Goodman, J. (1994). Stability of the Kuramoto–Sivashinsky and related systems. *Comm. Pure Appl. Math.*, 47(3):293–306.

Gough, D. (1977). The current state of stellar mixing-length theory. In Spiegel, E. A. and Zahn, J.-P., editors, *Problems of Stellar Convection*, pages 15–56, Berlin, Heidelberg. Springer Berlin Heidelberg.

Goulart, P. J. and Chernyshenko, S. (2012). Global stability analysis of fluid flows using sum-of-squares. *Physica D: Nonlinear Phenomena*, 241(6):692–704.

Grossmann, S., Lohse, D., and Sun, C. (2016). High–Reynolds number Taylor–Couette turbulence. *Annu. Rev. Fluid Mech.*, 48:53–80.

Guervilly, C., Cardin, P., and Schaeffer, N. (2019). Turbulent convective length scale in planetary cores. *Nature*, 570(7761):368–371.

Hagstrom, G. and Doering, C. R. (2010). Bounds on heat transport in Bénard–Marangoni convection. *Phys. Rev. E*, 81(4):047301.

Hagstrom, G. I. and Doering, C. R. (2014). Bounds on surface stress-driven shear flow. *J. Nonlinear Sci.*, 24(1):185–199.

Harper, J. F. and Moore, D. W. (1968). The motion of a spherical liquid drop at high Reynolds number. *J. Fluid Mech.*, 32(2):367–391.

Harrison, W. J. (1921). On the stability of the steady motion of viscous liquid contained between two rotating coaxial circular cylinders. *Proc. Camb. Phil. Soc.*, 20:455–459.

Hassanzadeh, P., Chini, G. P., and Doering, C. R. (2014). Wall to wall optimal transport. *J. Fluid Mech.*, 751:627–662.

Hoffmann, N. P. and Vitanov, N. K. (1999). Upper bounds on energy dissipation in Couette–Ekman flow. *Phys. Lett. A*, 255(4-6):277–286.

Hopf, E. (1955). Lecture series of the symposium on partial differential equations.

Howard, L. N. (1963). Heat transport by turbulent convection. *J. Fluid Mech.*, 17(3):405–432.

Howard, L. N. (1972). Bounds on flow quantities. *Annu. Rev. Fluid Mech.*, 4:473–494.

Huang, D., Chernyshenko, S., Goulart, P., Lasagna, D., Tutty, O., and Fuentes, F. (2015). Sum-of-squares of polynomials approach to nonlinear stability of fluid flows: an example of application. *Proc. R. Soc. Lond. A*, 471(2183):20150622.

Hüttl, T. J. and Friedrich, R. (2001). Direct numerical simulation of turbulent flows in curved and helically coiled pipes. *Comput. Fluids*, 30:591–605.

Isett, P. (2018). A proof of Onsager's conjecture. *Ann. of Math. (2)*, 188(3):871–963.

Itō, H. (1959). Friction factors for turbulent flow in curved pipes. *Trans. ASME J. Basic Engng*, 81:123–134.

Iyer, G. and Van, T.-S. (2022). Bounds on the heat transfer rate via passive advection. *SIAM J. Math. Anal.*, 54(2):1927–1965.

Jakobsen, H. A. (2008). *Chemical reactor modeling*. Springer.

Ji, H., Burin, M., Schartman, E., and Goodman, J. (2006). Hydrodynamic turbulence cannot transport angular momentum effectively in astrophysical disks. *Nature*, 444(7117):343–346.

Jobe, C. E. and Burggraf, O. R. (1974). The numerical solution of the asymptotic equations of trailing edge flow. *Proc. R. Soc. Lond. A*, 340(1620):91–111.

Joseph, D. D. (1976). *Stability of Fluid Motions I*. Springer.

Kaneda, Y., Ishihara, T., Yokokawa, M., Itakura, K., and Uno, A. (2003). Energy dissipation rate and energy spectrum in high resolution direct numerical simulations of turbulence in a periodic box. *Phys. Fluids*, 15(2):L21–L24.

Kao, H. C. (1987). Torsion effect on fully developed flow in a helical pipe. *J. Fluid Mech.*, 184:335–356.

Kerswell, R. R. (1997). Variational bounds on shear-driven turbulence and turbulent Boussinesq convection. *Physica D*, 100(3-4):355–376.

Kerswell, R. R. (1998). Unification of variational principles for turbulent shear flows: the background method of Doering–Constantin and the mean-fluctuation formulation of Howard–Busse. *Physica D*, 121(1-2):175–192.

Kim, K. Y. and Choi, J. Y. (2005). Shape optimization of a dimpled channel to enhance turbulent heat transfer. *Numerical Heat Transfer, Part A: Applications*, 48(9):901–915.

Kolmogorov, A. N. (1941a). *Dokl. Akad. Nauk SSSR*, 30:301–305.

Kolmogorov, A. N. (1941b). *Dokl. Akad. Nauk SSSR*, 31:538–540.

Kolmogorov, A. N. (1991). Dissipation of energy in the locally isotropic turbulence. *Proc. R. Soc. Lond. A*, 434(1890):15–17.

Kooloth, P., Sondak, D., and Smith, L. (2021). Coherent solutions and transition to turbulence in two-dimensional rayleigh-bénard convection. *Phys. Rev. Fluids*, 6(1):013501.

Kühnen, J., Braunshier, P., Schwegel, M., Kuhlmann, H. C., and Hof, B. (2015). Subcritical versus supercritical transition to turbulence in curved pipes. *J. Fluid Mech.*, 770.

Kumar, A. (2019). Maximal heat transport in Rayleigh–Bénard convection: Reduced models, birfurcations, and polynomial optimization. Technical report, Geophysical Fluid Dynamics Program of Study, Woods Hole Oceanographic Institution Technical Report (in press).

Kumar, A. (2020). Pressure-driven flows in helical pipes: bounds on flow rate and friction factor. *J. Fluid Mech.*, 904.

Kumar, A. (2022a). Geometrical dependence of optimal bounds in taylor–couette flow. *J. Fluid Mech.*, 948:A11.

Kumar, A. (2022b). Three dimensional branching pipe flows for optimal scalar transport between walls. *arXiv preprint arXiv:2205.03367*.

Kumar, A. (2023). Nonuniqueness of trajectories on a set of full measure for sobolev vector fields. *arXiv preprint arXiv:2301.05185*.

Kumar, A., Arslan, A., Fantuzzi, G., Craske, J., and Wynn, A. (2022). Analytical bounds on the heat transport in internally heated convection. *J. Fluid Mech.*, 938.

Kumar, A. and Garaud, P. (2020). Bound on the drag coefficient for a flat plate in a uniform flow. *J. Fluid Mech.*, 900.

Lathrop, D. P., Fineberg, J., and Swinney, H. L. (1992a). Transition to shear-driven turbulence in Couette–Taylor flow. *Phys. Rev. A*, 46:6390–6405.

Lathrop, D. P., Fineberg, J., and Swinney, H. L. (1992b). Turbulent flow between concentric rotating cylinders at large Reynolds number. *Phys. Rev. Lett.*, 68:1515–1518.

Leal, L. G. (2007). *Advanced Transport Phenomena: Fluid Mechanics and Convective Transport Processes*. Cambridge University Press.

Lee, H., Wen, B., and Doering, C. R. (2019). Improved upper bounds on the energy dissipation rate for shear flow with injection and suction. *Phys. Fluids*, 31(8):085102.

Lepot, S., Aumaître, S., and Gallet, B. (2018). Radiative heating achieves the ultimate regime of thermal convection. *Proc. Natl Acad. Sci.*, 115(36):8937–8941.

Limare, A., Jaupart, C., Kaminski, E., Fourel, L., and Farnetani, C. G. (2019). Convection in an internally heated stratified heterogeneous reservoir. *J. Fluid Mech.*, 870:67–105.

Limare, A., Kenda, B., Kaminski, E., Surducan, E., Surducan, V., and Neamtu, C. (2021). Transient convection experiments in internally-heated systems. *MethodsX*, 8:101224.

Liu, S. and Masliyah, J. H. (1993). Axially invariant laminar flow in helical pipes with a finite pitch. *J. Fluid Mech.*, 251:315–353.

Lumley, J. L. (1992). Some comments on turbulence. *Phys. Fluids*, 4(2):203–211.

Maggi, F. (2012). *Sets of finite perimeter and geometric variational problems*, volume 135 of *Cambridge Studies in Advanced Mathematics*. Cambridge University Press, Cambridge. An introduction to geometric measure theory.

Malkus, M. V. R. (1954). The heat transport and spectrum of thermal turbulence. *Proc. R. Soc. Lond. A*, 225(1161):196–212.

Marchioro, C. (1994). Remark on the energy dissipation in shear driven turbulence. *Physica D*, 74(3-4):395–398.

Marcotte, F., Doering, C. R., Thiffeault, J.-L., and Young, W. R. (2018). Optimal heat transfer and optimal exit times. *SIAM J. Appl. Math.*, 78(1):591–608.

McConalogue, D. J. and Srivastava, R. S. (1968). Motion of a fluid in a curved tube. *Proc. R. Soc. Lond. A*, 307:37–53.

Messiter, A. F. (1970). Boundary-layer flow near the trailing edge of a flat plate. *SIAM J. Appl. Math.*, 18(1):241–257.

Milgram, J. H. (1998). Fluid mechanics for sailing vessel design. *Annu. Rev. Fluid Mech.*, 30(1):613–653.

Miquel, B., Lepot, S., Bouillaut, V., and Gallet, B. (2019). Convection driven by internal heat sources and sinks: Heat transport beyond the mixing-length or "ultimate" scaling regime. *Phys. Rev. Fluids*, 4(12):121501.

Moffatt, H. K. (1969). The degree of knottedness of tangled vortex lines. *J. Fluid Mech.*, 35(1):117–129.

Moffatt, H. K. and Tsinober, A. (1992). Helicity in laminar and turbulent flow. *Annu. Rev. Fluid Mech.*, 24(1):281–312.

Mohammadi, B. and Pironneau, O. (1993). *Analysis of the k-epsilon turbulence model*. Editions MASSON.

Mohammadi, B. and Pironneau, O. (2009). *Applied shape optimization for fluids*. OUP Oxford.

Mooneghi, M. A. and Kargarmoakhar, R. (2016). Aerodynamic mitigation and shape optimization of buildings. *Journal of Building Engineering*, 6:225–235.

Moore, D. W. (1963). The boundary layer on a spherical gas bubble. *J. Fluid Mech.*, 16(2):161–176.

Motoki, S., Kawahara, G., and Shimizu, M. (2018a). Maximal heat transfer between two parallel plates. *J. Fluid Mech.*, 851.

Motoki, S., Kawahara, G., and Shimizu, M. (2018b). Optimal heat transfer enhancement in plane couette flow. *J. Fluid Mech.*, 835:1157–1198.

Motoki, S., Kawahara, G., and Shimizu, M. (2021). Multi-scale steady solution for Rayleigh–Bénard convection. *J. Fluid Mech.*, 914.

Mulyukova, E. and Bercovici, D. (2020). Mantle convection in terrestrial planets. *Oxford Research Encyclopedia of Planetary Science*.

Munk, W. and Wunsch, C. (1998). Abyssal recipes II: Energetics of tidal and wind mixing. *Deep Sea Research Part I: Oceanographic Research Papers*, 45(12):1977–2010.

Naphon, P. and Wongwises, S. (2006). A review of flow and heat transfer characteristics in curved tubes. *Renewable and Sustainable Energy Rev.*, 10(5):463–490.

Nickerson, E. C. (1969). Upper bounds on the torque in cylindrical Couette flow. *J. Fluid Mech.*, 38(4):807–815.

Nicodemus, R., Grossmann, S., and Holthaus, M. (1997). Improved variational principle for bounds on energy dissipation in turbulent shear flow. *Physica D*, 101(1-2):178–190.

Nikitin, N. and Yakhot, A. (2005). Direct numerical simulation of turbulent flow in elliptical ducts. *J. Fluid Mech.*, 532:141–164.

Nobili, C. (2021). The role of boundary conditions in scaling laws for turbulent heat transport. *arXiv preprint arXiv:2112.15564*.

Nobili, C. and Otto, F. (2017). Limitations of the background field method applied to Rayleigh-Bénard convection. *J. Math. Phys.*, 58(9):093102.

Olson, M. L., Goluskin, D., Schultz, W. W., and Doering, C. R. (2021). Heat transport bounds for a truncated model of Rayleigh–Bénard convection via polynomial optimization. *Physica D: Nonlinear Phenomena*, 415:132748.

Ostilla-Mónico, R., van der Poel, E. P., Verzicco, R., Grossmann, S., and Lohse, D. (2014). Exploring the phase diagram of fully turbulent Taylor–Couette flow. *J. Fluid Mech.*, 761:1–26.

Otero, J., Wittenberg, R. W., Worthing, R. A., and Doering, C. R. (2002). Bounds on Rayleigh–Bénard convection with an imposed heat flux. *J. Fluid Mech.*, 473:191–199.

Otto, F. and Seis, C. (2011). Rayleigh–Bénard convection: improved bounds on the Nusselt number. *J. Math. Phys.*, 52(8):083702.

Pearson, B. R., Krogstad, P.-Å., and van de Water, W. (2002). Measurements of the turbulent energy dissipation rate. *Phys. Fluids*, 14(3):1288–1290.

Pena, B. and Huang, L. (2021). A review on the turbulence modelling strategy for ship hydrodynamic simulations. *Ocean Eng.*, 241:110082.

Peyret, R. (2013). *Spectral methods for incompressible viscous flow*, volume 148. Springer Science & Business Media.

Pierrehumbert, R. T. (2010). *Principles of planetary climate*. Cambridge University Press.

Pitcho, J. and Sorella, M. (2021). Almost everywhere non-uniqueness of integral curves for divergence-free sobolev vector fields. *arXiv preprint arXiv:2108.03194*.

Plasting, S. C. and Ierley, G. R. (2005). Infinite-Prandtl-number convection. Part 1. Conservative bounds. *J. Fluid Mech.*, 542:343–363.

Plasting, S. C. and Kerswell, R. R. (2003). Improved upper bound on the energy dissipation rate in plane Couette flow: the full solution to Busse's problem and

the Constantin–Doering–Hopf problem with one-dimensional background field. *J. Fluid Mech.*, 477:363–379.

Plasting, S. C. and Kerswell, R. R. (2005). A friction factor bound for transitional pipe flow. *Phys. Fluids*, 17(1):011706.

Pope, S. B. (2000). *Turbulent flows*. Cambridge university press.

Prandtl, L. (1904). Über Flüssigkeitsbewegung bei sehr kleiner Reibung. *Verhandlungen des dritten internationalen Mathematiker-Kongresses in Heidelberg*.

Priestley, C. (1954). Vertical heat transfer from impressed temperature fluctuations. *Austral. J. Phys.*, 7(1):202–209.

Pringle, J. E. (1981). Accretion discs in astrophysics. *Annu. Rev. Astron. Astrophys.*, 19(1):137–160.

Rajagopal, K. R., Ruzicka, M., and Srinivasa, A. (1996). On the Oberbeck–Boussinesq approximation. *Math. Models Methods Appl. Sci.*, 6(08):1157–1167.

Rinaldi, E., Canton, J., and Schlatter, P. (2019). The vanishing of strong turbulent fronts in bent pipes. *J. Fluid Mech.*, 866:487–502.

Roberts, P. (1967). Convection in horizontal layers with internal heat generation. theory. *J. Fluid Mech.*, 30(1):33–49.

Rosa, R. and Temam, R. M. (2020). Optimal minimax bounds for time and ensemble averages of dissipative infinite-dimensional systems with applications to the incompressible Navier–Stokes equations. *arXiv preprint arXiv:2010.06730*.

Roshko, A. (1961). Experiments on the flow past a circular cylinder at very high reynolds number. *J. Fluid Mech.*, 10(3):345–356.

Roshko, A. (1993). Perspectives on bluff body aerodynamics. *J. Wind Engng Ind. Aerodyn.*, 49(1-3):79–100.

Schlichting, H. and Gersten, K. (2016). *Boundary-layer theory*. Springer, 9 edition.

Schubert, G., Turcotte, D. L., and Olson, P. (2001). *Mantle convection in the Earth and planets*. Cambridge University Press.

Seager, S. (2010). *Exoplanet Atmospheres: Physical Processes*. Princeton Series in Astrophysics. Princeton University Press.

Seis, C. (2015). Scaling bounds on dissipation in turbulent flows. *J. Fluid Mech.*, 777:591–603.

Serrin, J. (1959). On the stability of viscous fluid motions. *Arch. Rat. Mech. Anal.*, 3(1):1–13.

Shakura, N. I. and Sunyaev, R. A. (1973). Black holes in binary systems. observational appearance. *Astron. Astrophys.*, 24:337–355.

Sondak, D., Smith, L. M., and Waleffe, F. (2015). Optimal heat transport solutions for Rayleigh–Bénard convection. *J. Fluid Mech.*, 784:565–595.

Souza, A. N., Tobasco, I., and Doering, C. R. (2020). Wall-to-wall optimal transport in two dimensions. *J. Fluid Mech.*, 889.

Spiegel, E. A. (1963). A generalization of the mixing-length theory of turbulent convection. *Astrophys. J.*, 138:216.

Spiegel, E. A. and Veronis, G. (1960). On the Boussinesq approximation for a compressible fluid. *Astrophys. J.*, 131:442.

Spruit, H. C., Nordlund, A., and Title, A. M. (1990). Solar convection. *Annu. Rev. Astron. Astrophys.*, 28(1):263–303.

Sreenivasan, K. R. (1984). On the scaling of the turbulence energy dissipation rate. *Phys. Fluids*, 27(5):1048–1051.

Sreenivasan, K. R. (1998). An update on the energy dissipation rate in isotropic turbulence. *Phys. Fluids*, 10(2):528–529.

Sreenivasan, K. R. and Antonia, R. A. (1997). The phenomenology of small-scale turbulence. *Annu. Rev. Fluid Mech.*, 29(1):435–472.

Sreenivasan, K. R. and Strykowski, P. J. (1983). Stabilization effects in flow through helically coiled pipes. *Exp. Fluids*, 1(1):31–36.

Stein, E. M. and Shakarchi, R. (2005). *Real analysis*, volume 3 of *Princeton Lectures in Analysis*. Princeton University Press, Princeton, NJ. Measure theory, integration, and Hilbert spaces.

Stewartson, K. (1969). On the flow near the trailing edge of a flat plate II. *Mathematika*, 16(1):106–121.

Tang, W., Caulfield, C. P., and Young, W. R. (2004). Bounds on dissipation in stress-driven flow. *J. Fluid Mech.*, 510:333–352.

Taylor, G. I. (1923). Stability of a viscous liquid contained between two rotating cylinders. *Phi. Trans. R. Soc. Lond.*, 223(605-615):289–343.

Taylor, G. I. (1929). The criterion for turbulence in curved pipes. *Proc. R. Soc. Lond. A*, 124:243–249.

Tennekes, H. and Lumley, J. L. (1972). *A first course in turbulence*. MIT press.

Thulukkanam, K. (2013). *Heat Exchanger Design Handbook, Second Edition*. Mechanical Engineering. Taylor & Francis.

Tilgner, A. (2017). Bounds on poloidal kinetic energy in plane layer convection. *Phys. Rev. Fluids*, 2(12):123502.

Tilgner, A. (2019). Time evolution equation for advective heat transport as a constraint for optimal bounds in Rayleigh–Bénard convection. *Phys. Rev. Fluids*, 4(1):014601.

Tobasco, I. (2022). Optimal cooling of an internally heated disc. *Phil. Trans. R. Soc. Lond. A*, 380(2225):20210040.

Tobasco, I. and Doering, C. R. (2017). Optimal wall-to-wall transport by incompressible flows. *Phys. Rev. Lett.*, 118(26):264502.

Tobasco, I., Goluskin, D., and Doering, C. R. (2018). Optimal bounds and extremal trajectories for time averages in nonlinear dynamical systems. *Phys. Lett. A*, 382(6):382–386.

Toppaladoddi, S., Succi, S., and Wettlaufer, J. S. (2017). Roughness as a route to the ultimate regime of thermal convection. *Phys. Rev. Lett.*, 118(7):074503.

Toppaladoddi, S., Wells, A. J., Doering, C. R., and Wettlaufer, J. S. (2021). Thermal convection over fractal surfaces. *J. Fluid Mech.*, 907:A12.

Tran, C. T. and Dinh, T. N. (2009). The effective convectivity model for simulation of melt pool heat transfer in a light water reactor pressure vessel lower head. Part I: Physical processes, modeling and model implementation. *Prog. Nucl. Energy*, 51(8):849–859.

Tritton, D. J. (1975). Internally heated convection in the atmosphere of venus and in the laboratory. *Nature*, 257(5522):110–112.

Tuttle, E. R. (1990). Laminar flow in twisted pipes. *J. Fluid Mech.*, 219:545–570.

Van Dyke, M. (1978). Extended stokes series: laminar flow through a loosely coiled pipe. *J. Fluid Mech.*, 86:129–145.

Vashisth, S., Kumar, V., and Nigam, K. (2008). A review on the potential applications of curved geometries in process industry. *Ind. Engng Chem. Res.*, 47(10):3291–3337.

Vassilicos, J. C. (2015). Dissipation in turbulent flows. *Annu. Rev. Fluid Mech.*, 47:95–114.

Vester, A. K., Örlü, R., and Alfredsson, P. H. (2016). Turbulent flows in curved pipes: recent advances in experiments and simulations. *Appl. Mech. Rev.*, 68.

Vitense, E. (1953). Die wasserstoffkonvektionszone der sonne. Mit 11 textabbildungen. *Zeitschrift fur Astrophysik*, 32:135.

Waleffe, F., Boonkasame, A., and Smith, L. M. (2015). Heat transport by coherent Rayleigh–Bénard convection. *Phys. Fluids*, 27(5):051702.

Wang, X. (1997). Time averaged energy dissipation rate for shear driven flows in $\mathbb{R}^n$. *Physica D*, 99(4):555–563.

Webster, D. R. and Humphrey, J. A. C. (1993). Experimental observations of flow instability in a helical coil (Data bank contribution). *Trans. ASME J. Fluids Engng*, 115:436–443.

Webster, D. R. and Humphrey, J. A. C. (1997). Traveling wave instability in helical coil flow. *Phys. Fluids*, 9:407–418.

Wen, B. and Chini, G. (2018). Reduced modeling of porous media convection in a minimal flow unit at large Rayleigh number. *J. Comput. Phys.*, 371:551–563.

Wen, B., Chini, G., Dianati, N., and Doering, C. R. (2013). Computational approaches to aspect-ratio-dependent upper bounds and heat flux in porous medium convection. *Phys. Lett. A*, 377(41):2931–2938.

Wen, B., Chini, G. P., Kerswell, R. R., and Doering, C. R. (2015). Time-stepping approach for solving upper-bound problems: Application to two-dimensional Rayleigh–Bénard convection. *Phys. Rev. E*, 92(4):043012.

Wen, B., Goluskin, D., and Doering, C. R. (2022). Steady Rayleigh–Bénard convection between no-slip boundaries. *J. Fluid Mech.*, 933.

Wen, B., Goluskin, D., LeDuc, M., Chini, G., and Doering, C. R. (2020). Steady Rayleigh–Bénard convection between stress-free boundaries. *J. Fluid Mech.*, 905.

Wendt, F. (1933). Turbulente Strömungen zwischen zwei rotierenden konaxialen zylindern. *Ingenieur-Arch.*, 4(6):577–595.

White, C. M. (1929). Streamline flow through curved pipes. *Proc. R. Soc. Lond. A*, 123:645–663.

Whitehead, J. P. and Doering, C. R. (2011a). Internal heating driven convection at infinite Prandtl number. *J. Math. Phys.*, 52(9):093101.

Whitehead, J. P. and Doering, C. R. (2011b). Ultimate state of two-dimensional Rayleigh–Bénard convection between free-slip fixed-temperature boundaries. *Phys. Rev. Lett.*, 106(24):244501.

Whitehead, J. P. and Wittenberg, R. W. (2014). A rigorous bound on the vertical transport of heat in Rayleigh–Bénard convection at infinite Prandtl number with mixed thermal boundary conditions. *J. Math. Phys.*, 55(9):093104.

Williamson, C. H. K. (1996). Vortex dynamics in the cylinder wake. *Annu. Rev. Fluid Mech.*, 28(1):477–539.

Wittenberg, R. W. (2010). Bounds on Rayleigh–Bénard convection with imperfectly conducting plates. *J. Fluid Mech.*, 665:158–198.

Wunsch, C. and Ferrari, R. (2004). Vertical mixing, energy, and the general circulation of the oceans. *Annu. Rev. Fluid Mech.*, 36:281–314.

Yamamoto, K., Akita, T., Ikeuchi, H., and Kita, Y. (1995). Experimental study of the flow in a helical circular tube. *Fluid Dynam. Res.*, 16:237–249.

Yamamoto, K., Yanase, S., and Yoshida, T. (1994). Torsion effect on the flow in a helical pipe. *Fluid Dynam. Res.*, 14:259–273.

Yao, Y. and Zlatoš, A. (2017). Mixing and un-mixing by incompressible flows. *J. Eur. Math. Soc. (JEMS)*, 19(7):1911–1948.

Zhu, X., Ostilla-Mónico, R., Verzicco, R., and Lohse, D. (2016). Direct numerical simulation of Taylor–Couette flow with grooved walls: torque scaling and flow structure. *J. Fluid Mech.*, 794:746–774.

Zhu, X., Stevens, R. J., Verzicco, R., and Lohse, D. (2017). Roughness-facilitated local 1/2 scaling does not imply the onset of the ultimate regime of thermal convection. *Phys. Rev. Lett.*, 119(15):154501.